AD-A089 089 ARMY MATHEMATICS STEERING COMMITTEE F/G 9/2
PROCEEDINGS OF THE 1980 ARMY NUMERICAL ANALYSIS AND COMPUTERS C--ETC(U)
AUG 80

UNCLASSIFIED ARO-80-3 NL

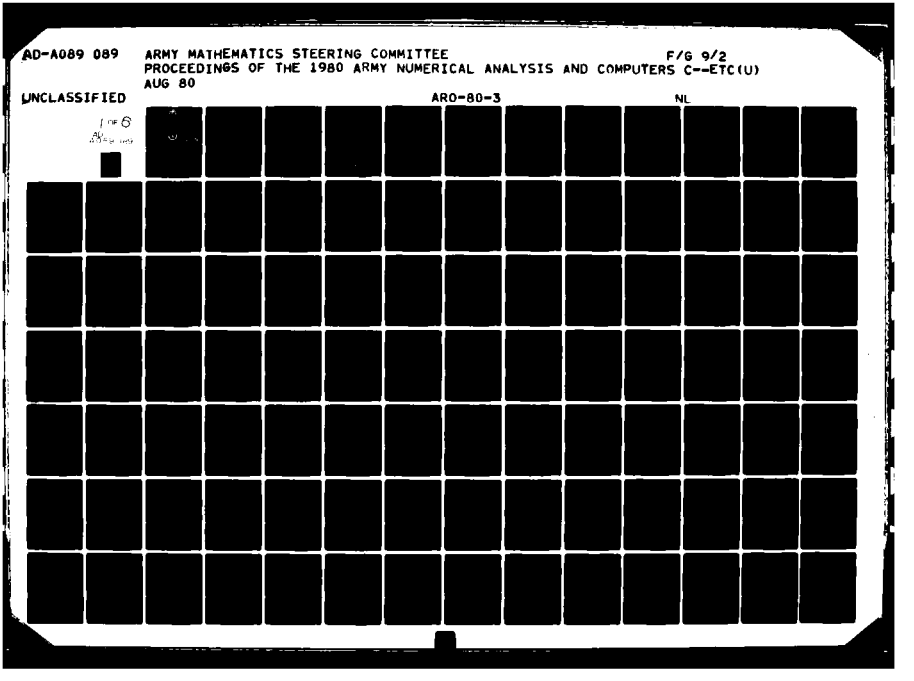

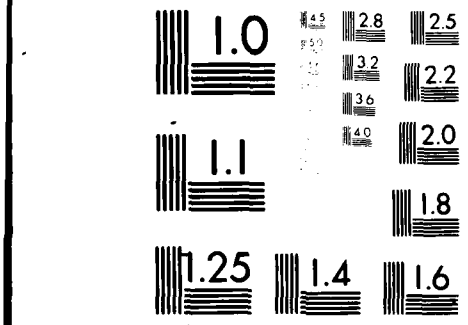

LEVEL II

12

ARO Report 80-3

PROCEEDINGS OF THE 1980 ARMY NUMERICAL ANALYSIS AND COMPUTERS CONFERENCE

Approved for public release; distribution unlimited. The findings in this report are not to be construed as an official Department of the Army position, unless so designated by other authorized documents.

SPONSORED BY
THE ARMY MATHEMATICS STEERING COMMITTEE ON BEHALF OF

THE OFFICE OF
THE CHIEF OF RESEARCH, DEVELOPMENT AND
ACQUISITION

(18) ARO

U. S. Army Research Office

(19) Report No. 80-3

(11) August 1980

(6) PROCEEDINGS OF THE 1980 ARMY NUMERICAL ANALYSIS AND COMPUTERS CONFERENCE

Sponsored by the Army Mathematics Steering Committee

(17th) Held at Moffett Field, California on 20-21 February 1980,

HOSTS

NASA Ames Research Center and the Aeromechanics Laboratory
of the Army Aviation Research and Development Command
NASA Ames Research Center, Moffett Field, California

20-21 February 1980

(12) 489

U. S. Army Research Office
P. O. Box 12211
Research Triangle Park, North Carolina

039200

FOREWORD

Going back in time to around 2225 B.C., one finds that the Babylonians made contributions to the art of computing. Their computing techniques were based on tables. They made tables of square and cube roots. One of the remarkable features of their arithmetic is that they did not insert the decimal point. So in a certain sense they employed floating point arithmetic. Since the time of the Babylonians many of the civilizations that came into being had little need for elaborate computing systems. This is certainly not the case for people living today. Computers have become a permanent part of our lives, and electronic digital computers have taken over a large portion of the work formerly done by human beings. Up to 1914, the beginning of the first world war, people seldom encountered astronomical figures in their daily work. Now, reference to such numbers as millions and billions appear in our daily newspapers. It is a fact of life today that we have to take refuge in machinery to handle the elaborate computations that commonly occur in science and engineering problems. Methods to treat some of these problems were discussed in papers presented at this symposium.

The Seventeenth Army Numerical Analysis and Computers Conference was held at the NASA Ames Research Center, Moffett Field, California on 20-21 February 1980. The co-hosts of this meeting were NASA Ames Research Center and the Aeromechanics Laboratory of the Army Aviation Research and Development Command. Drs. Irving C. Statler and James Wong served as co-chairmen of the Local Arrangements Committee. The Army Mathematics Steering Committee (AMSC), sponsor of these conferences, would like to thank these gentlemen and their assistants for all their efforts in making this an interesting and productive scientific meeting.

The theme for this year's conference was "Computation of Fluid Flows Especially Involving Shocks and Discontinuities". The computational difficulties as well as analytical treatments arising in these areas lead to interesting but troublesome problems. Some of the papers presented at this meeting shed light on many of these problems. The list of invited speakers and the title of their addresses are noted below:

Speakers and Affiliation	Title of Address
James Glimm The Rockefeller University	The Accurate Computation of Fluid Discontinuities by the Random Choice Method
T. L. Holst NASA-Ames Research Center	An Implicit Algorithm for Solving the Transonic, Conservative Full Potential Equation

Bjorn Engquist University of California- Los Angeles	Software for Hyperbolic and Parabolic Differential Equations
Jerry S. South, James D. Keller and Mohamed Hafez NASA-Ames Research Center	Computational Transonics on a Vector Computer
Paul R. Garabedian Courant Institute of Mathematical Sciences	Suppression of Shocks on Swept Wings

Members of the AMSC would like to express their appreciation for all the work expended by the speakers on preparing their papers and then presenting them at this meeting. Most of these papers are being issued in these Proceedings as an aid to the scientific community. The AMSC members would also like to thank the hosts of this conference for providing excellent classroom facilities as well as projection equipment. These enhanced the comfort as well as the appreciation of members of the audience for the scientific ideas being presented by the speakers.

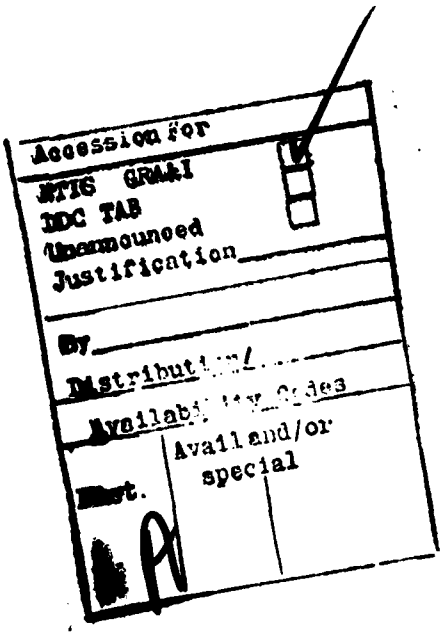

TABLE OF CONTENTS*

*This Table of Contents lists only the papers that are published in this Technical Manual. For a list of all of the papers presented at the 1979 Army Numerical Analysis and Computers Conference see the copy of the Agenda.

AGENDA FOR THE

1980 ARMY NUMERICAL ANALYSIS AND COMPUTERS CONFERENCE
20-21 February 1980
Moffett Field, California

Wednesday
20 February 1980

1245-1300 OPENING REMARKS - Dr. Irving C. Statler, Director, Aeromechanics Lab, US Army Research and Technology Laboratory (AVRADCOM) NASA-Ames Research Center, Moffett Field, California

1300-1400 KEYNOTE ADDRESS

CHAIRPERSON - Dr. Irving C. Statler, US Army Research and Technology Laboratory (AVRADCOM), Moffett Field, California

Speaker - Professor James Glimm, The Rockefeller University, New York, New York

Title - THE ACCURATE COMPUTATION OF FLUID DISCONTINUITIES *BY THE RANDOM CHOICE METHOD*

1400-1415 BREAK

1415-1615 TECHNICAL SESSION I

Chairperson - Dr. James Schmidt, Ballistic Research Laboratory, Aberdeen Proving Ground, Maryland

IMPLICIT POTENTIAL METHODS FOR THE SOLUTION OF TRANSONIC ROTOR FLOWS

Dr. F. X. Caradonna, US Army Research & Technology Labs, Moffett Field, California and Dr. J. L. Steger, Flow Simulations, Inc.

MONOTONE DIFFERENCES SCHEMES FOR A CONSERVATION LAW

Professor Mike Crandall, Mathematics Research Center, Madison, Wisconsin

DEVELOPMENT OF SHARP DISCONTINUITY TRACKING METHODS FOR EXPLOSION PROBLEMS

Dr. Gregory R. Shubin, Naval Surface Weapons Center, Silver Spring, Maryland

COMPARISON OF 3-D HYDROCODE COMPUTATIONS FOR SHOCK DIFFRACTION LOADING ON AN S-280 ELECTRICAL EQUIPMENT SHELTER

Dr. Richard E. Lottero, Ballistic Research Laboratory, Aberdeen Proving Ground, Maryland

OBLIQUE INTERACTION OF A SHOCK WAVE WITH A THREE-DIMENSIONAL TACTICAL COMMUNICATIONS CENTER

Drs. R. E. Lottero, J. D. Wortman, B. P. Bertrand and C. W. Kitchens, Jr., Ballistic Research Laboratory, Aberdeen Proving Ground, Maryland

NAVIER-STOKES SOLUTIONS FOR SPIN-UP BY A PREDICTOR-CORRECTOR MULTIPLE-ITERATION METHOD

Dr. C. W. Kitchens, Jr., Ballistic Research Laboratory, Aberdeen Proving Ground, Maryland

1415-1615 TECHNICAL SESSION II

CHAIRPERSON - Dr. Harold Law, US Army Aviation R&D Command, St. Louis, Missouri

FOURIER TRANSFORM EVALUATION

Professor J. Barkley Rosser, Mathematics Research Center, Madison, Wisconsin

APPROXIMATIONS FOR Z(G(s) F(s))

Dr. Richard E. Dickson, US Army Missile Command, Redstone Arsenal, Alabama

RADIX 65/39, A ROOT SEARCHING ALGORITHM FOR ANALYTIC EQUATIONS

Dr. Walter O. Egerland, Ballistic Research Laboratory, Aberdeen Proving Ground, Maryland

COLLOCATION APPROXIMATION TO EIGENVALUES OF ORDINARY DIFFERENTIAL EQUATIONS

Professor Carl de Boor, Mathematics Research Center, Madison, Wisconsin

COMPUTATION AND APPLICATION OF SCHWARZ-CHRISTOFFEL TRANSFORMATIONS

Professor Lloyd Trefethen, Stanford University, Stanford, California

ITERATED SCHOENBERG APPROXIMATION AND ITS APPLICATION

Mr. William S. Agee, Mathematical Services Branch, White Sands Missile Range, New Mexico

1615-1715 GENERAL SESSION I

CHAIRPERSON - Dr. Julian J. Wu, Benet Weapons Laboratory, Watervliet Arsenal, Watervliet, New York

AN IMPLICIT ALGORITHM FOR SOLVING THE TRANSONIC, CONSERVATIVE FULL POTENTIAL EQUATION

Dr. T. L. Holst, NASA-Ames Research Center, Moffett Field, California

* * * *

Thursday
21 February 1980

0830-0930 GENERAL SESSION II

CHAIRPERSON - Dr. Paul T. Boggs, US Army Research Office, Research Triangle Park, North Carolina

SOFTWARE FOR HYPERBOLIC AND PARABOLIC DIFFERENTIAL EQUATIONS

Professor Bjorn Engquist, University of California, Los Angeles, California

0930-0945 BREAK

0945-1145 TECHNICAL SESSION III

CHAIRPERSON - Dr. F. X. Caradonna, US Army Research and Technology Laboratories, Moffett Field, California

PROJECTION METHODS AND THE APPROXIMATION OF BIFURCATION BRANCHES

Professor George W. Reddien, Southern Methodist University, Dallas, Texas

A NEW METHOD FOR SOLVING HYPERBOLIC PROBLEMS

Dr. Robert MacCormack, NASA-Ames Research Center, Moffett Field, California

ON K-LINE AND KxK ITERATIVE SCHEMES: A PROBLEM ARISING IN 3-D ELLIPTIC DIFFERENCE EQUATIONS

Professor Seymour Parter, Mathematics Research Center, Madison, Wisconsin, and Dr. Michael Steuerwalt, Los Alamos Scientific Laboratory, Los Alamos, New Mexico

THE HOMOGENEOUS PROPERTIES OF THE COMPRESSIBLE NAVIER-STOKES EQUATIONS WITH APPLICATION TO FINITE DIFFERENCE METHODS

Dr. Robert T. Warming, NASA-Ames Research Center, Moffett Field, California

A TECHNIQUE FOR SYNTHESIZING THE MOTIONS OF A FLAT PLATE FOUNDATION DURING AN EARTHQUAKE

Dr. Francis E. Council, Jr., US Army Mobility Equipment R&D Command, Ft. Belvoir, Virginia

DATA-MAP, SOFTWARE FOR ANALYSIS AND DISPLAY OF AEROMECHANICS' DATA

Dr. D. J. Merkley, US Army Research & Technology Laboratory, Applied Technology Laboratory, Ft. Eustis, Virginia

0945-1145 TECHNICAL SESSION IV

CHAIRPERSON - Mr. Morton Hirschberg, Ballistic Research Laboratory, Aberdeen Proving Ground, Maryland

ANALYTICAL AND NUMERICAL CRITERIA FOR THE EVALUATION OF INTERIOR BALLISTICS CODES

Dr. James Schmidt and Mr. Thomas Mann, Ballistic Research Laboratory, Aberdeen Proving Ground, Maryland

FINITE ELEMENT COMBUSTION INSTABILITY-INTERNAL BALLISTICS ANALYSIS

Mr. Robert M. Hackett, US Army Missile Command, Redstone Arsenal, Alabama

DETERMINATION OF A BLAST FIELD BY INTEGRATION OF PRESSURE OBSERVATIONS

Dr. Aivars Celmins, Ballistic Research Laboratory, Aberdeen Proving Ground, Maryland

A QUALITATIVE ANALYSIS AND NUMERICAL STUDY OF COMBUSTION WAVES

Professor Andrew Majda, University of California, Berkeley, California

NUMERICAL PREDICTION OF RESIDUAL STRESSES IN AN OVERLOADED BREECH RING

Dr. P. C. T. Chen, Benet Weapons Laboratory, Watervliet Arsenal, Watervliet, New York

AN ADAPTIVE ALGORITHM FOR EXACT SOLUTION OF AN OVER-STRAINED TUBE

Dr. P. C. T. Chen, Benet Weapons Laboratory, Watervliet Arsenal, Watervliet, New York

1145-1300 LUNCH

1300-1400 GENERAL SESSION III

CHAIRPERSON - Dr. Billy Z. Jenkins, US Army Missile Command, Redstone Arsenal, Alabama

COMPUTATIONAL TRANSONICS ON A VECTOR COMPUTER

Messrs. Jerry S. South, James D. Keller and Mohamed Hafez, NASA-Langley Research Center, Hampton, Virginia

1400-1415 BREAK

1415-1515 TECHNICAL SESSION V

CHAIRPERSON - Mr. William S. Agee, Mathematical Services Branch, White Sands Missile Range, New Mexico

ANALYSIS OF COMPUTERIZED PRODUCTION QUEUING MODELS

Mr. James H. Donnelly, US Army Missile Command, Redstone Arsenal, Alabama

DATA BASES AND APPLICATIONS

Mr. Morton Hirschberg, Ballistic Research Laboratory, Aberdeen Proving Ground, Maryland

A TIME TO RE-THINK SMALL

Mr. C. Glenvil Whitacre, Chemical Systems Laboratory, Aberdeen Proving Ground, Maryland

1415-1515 TECHNICAL SESSION VI

CHAIRPERSON - Dr. Francis E. Council, Jr., US Army Mobility Equipment R&D Command, Ft. Belvoir, Virginia

VARIATIONAL METHODS OF CONVOLUTION INTEGRAL AND OF LARGE SPRING CONSTANTS - A NUMERICAL COMPARISON

Dr. Julian J. Wu, Benet Weapons Laboratory, Watervliet Arsenal, Watervliet, New York

COMPUTATION SCHEMES FOR SENSITIVITY COEFFICIENT OF EXTERIOR BALLISTICS WITH VELOCITY SQUARE DAMPING

Drs. C. N. Shen and Julian J. Wu, Benet Weapons Laboratory, Watervliet Arsenal, Watervliet, New York

NUMERICAL ANALYSIS ASPECTS OF THE "BLOCK-PULSE FUNCTION" METHOD FOR ANALYZING ELECTRICAL CIRCUITS

Professor Ben Noble, Mathematics Research Center, Madison, Wisconsin

1515-1615 GENERAL SESSION IV

CHAIRPERSON - Professor Ben Noble, Mathematics Research Center, Madison, Wisconsin

SUPPRESSION OF SHOCKS ON SWEPT WINGS

Professor Paul R. Garabedian, Courant Institute of Mathematical Sciences, New York University, New York, New York

1615 ADJOURN

A SHOCK TRACKING METHOD FOR HYPERBOLIC SYSTEMS

James Glimm[1,2]
Dan Marchesin[2,6]
Eli Isaacson[1]
The Rockefeller University
New York, N.Y. 10021

Oliver McBryan[3,4,5]
Courant Institute
New York University
New York, N.Y. 10012

ABSTRACT. We present a method for tracking shock discontinuities in hyperbolic systems. We apply the method to the problem of two phase flow in a porous medium, but the method is general and should be applicable to a wide range of phenomena including gas dynamics. The method is tested on an exactly soluble two-dimensional problem and is found to be very accurate. We also study a range of unstable flow problems with and without heterogeneity of the porous medium. In the case that the medium is heterogeneous, fingered shock fronts are computed and tracked. Miscible flows are studied with mobility ratios in the range 1 to 50.

INTRODUCTION. The random choice method originally developed as a theoretical tool [1], appears to be the best method for the computation of discontinuous solutions of nonlinear conservation laws in one space variable [2,3]. It allows calculations with zero diffusion. The method has been applied successfully to a number of problems including gas dynamics, chemical reactions (e.g., flame propagation), petroleum reservoir engineering, and the stability of boats against capsize.

The use of this method in two dimensions is still a research problem since numerical experiments yield mixed results. In order to extend the method from one to two dimensions, Chorin [3] used splitting in the two space directions. This extension has been applied by Chorin and Sod [4,5] to the flame chemistry and gas dynamics in an internal combustion engine. However, Colella [6] has observed that, in general, fluid discontinuities oblique to the computational grid are not resolved correctly by splitting. A similar phenomenon has been observed in applications to petroleum reservoir engineering in previous papers of this series [7,8]. A careful choice of computational grid can largely overcome this problem. Complex and highly fingered solutions are thus resolved [7,8].

The idea of a carefully chosen computational grid can be carried one step further. We present our preliminary results on a two-dimensional method which includes tracking of the discontinuity surface. Related ideas were previously proposed and tested for one space dimension [9]. Similar concepts (related to Huyghens Principle) have been developed and used by Chorin [10].

Unlike earlier shock fitting methods [11], we seek only first order accuracy. Low order methods are inherently easier to stabilize, and a careful elimination of the leading errors yields satisfactory results on coarse or moderate sized meshes. Our method seems fairly general; we believe that its scope is not limited to the petroleum reservoir applications tested so far.

The equations of two phase flow in porous media have the form

$$s_t + \text{div}\ \ vf(s) = 0, \tag{1}$$

$$v = -k(s)\ \text{grad}\ p, \tag{2}$$

$$\text{div}\ v = \text{source terms}, \tag{3}$$

where we have neglected the dispersive, or parabolic, term associated with molecular diffusion and/or capillary pressure. Here s denotes the saturation (fraction of water or solvent in the total fluid), and p is the pressure in the fluid. Also, k and f are known functions of saturation (and perhaps position) which describe the permeability and porosity of the reservoir and the viscosities of the two incompressible phases flowing in it. We solve the system (1)-(3) in a square domain with Neumann boundary conditions on p and with the source terms in (3) given by delta functions of opposite sign at diagonally opposite corners of the square. This corresponds to injection of an incompressible fluid into the square at one corner, with a corresponding outflow at the opposite corner. For simplicity we will present results here only for the case of miscible displacement. We will take the corresponding reservoir functions to be:

$$f(s) = s,$$

$$k(s) = (s + \mu^{-1/4}(1-s))^4,$$

where μ is the ratio of the viscosity of oil to the viscosity of solvent. Actually the absence of diffusion and the choice of Cauchy data imply that $s = 0$ and $s = 1$, at each point, and so the particular phenomenological function $k(s)$ chosen above, which specifies the viscosity of a mixture of two fluids in terms of the viscosities and proportions of the components, does not enter into the calculations. Similar results have been obtained for immiscible flows, with $f(s)$ a function with one point of inflection between 0 and 1.

As in [9], the discontinuous solution $s(x,y,t)$ of the hyperbolic conservation law is described at time t by

$$s(x,y,t) = \begin{cases} s_a(x,y,t) & \text{if } x,y \text{ is ahead of the front} \\ \\ s_b(x,y,t) & \text{if } x,y \text{ is behind the front.} \end{cases}$$

We imagine the functions s_a and s_b extended continuously across the front to their unphysical regions, making s double valued. Thus the front may be thought of as a cut in a Riemann surface joining the physical regions of s_a and s_b. Cauchy data are then specified at time 0 by setting $s_a = 0$ everywhere, and also $s_b = 0$ except in a small region surrounding the injection well where $s_b = 1$. The shock front is initialized at time zero by specifying a set of (ordered) points on it. The front is defined to be the piecewise linear curve which connects the points in order.

In order to update the numerical solution at each time step, we proceed as follows:

1. Advance the Front: This consists of two parts. First, we find the new position of the front using the ordinary differential equations describing the characteristics of the hyperbolic equation. Second, we modify s_a and s_b in a neighborhood of the discontinuity in order to pass any waves generated by the advancing front.

These waves typically arise fron non-convex conservation laws. (For a problem involving more state variables, we believe that waves crossing the shock can, and must, be passed between s_a and s_b at this stage by a similar method.) To modify s_a and s_b we solve one-dimensional Riemann problems along the characteristics. The modification of s_a and s_b does not involve dynamical motion of these waves -- other than the motion of the front itself.

2. Extrapolate s_a and s_b : Both s_a and s_b are extended continuously across the new position of the front to their unphysical regions.

3. Redistribute the Points Describing the Front: This is done to ensure that the portions of high curvature are resolved and that the spacing of the points is fairly uniform.

4. Update s_a and s_b: We use the splitting version of the random choice method, even though any convenient first order method could be employed.

5. Update the Elliptic Equation: See [8]. We still use the rectangular grid in a neighborhood of the front. We believe that this is the cause of the leading errors which remain. Refining the mesh near the front should eliminate these errors.

RESULTS. In order to test the validity of our tracking methods we have applied them to a problem with a known exact solution. The equations (1) - (3) are exactly solvable in the case that the velocity equation is independent of the saturation, i.e. if $\mu = 1$. As has been pointed out by Albright, Concus and Proskurowski [12], the equations may be transformed to a new coordinate system in which the flow is essentially one-dimensional. In Figure 1 we present the results of our computations for this problem on a 20x20 grid. We have superimposed the exact solution computed at the same times. Figure 1 corresponds to a miscible displacement problem with $f(s) = s$. Thus the fluid consists of either pure solvent or pure oil with no rarefaction waves, so plotting the front at a given time describes the whole solution. Similar results apply to the more general case where $f(s)$ is a function with one point of inflection. The agreement with the exact solution is in general very good except that in the area of the production well the computed solution moves somewhat too slowly. We have not attempted to use the known asymptotic form of the velocities in this region, which would presumably give a better solution. In Table I we compare the total area behind the front at several times for the exact and computed solutions on a 20x20 grid. There is agreement to within a few percent.

Table I: Comparison of Exact and Computed Solutions

Time	Exact Solvent Present	Computed Solvent Present
.0	.0	.0
.500	.129	.125
.806	.207	.202
1.035	.265	.259
1.208	.309	.302
1.505	.384	.376
2.016	.513	.504
2.349	.596	.587
2.884	.729	.721

The computation described above is principally a test of the front tracking method because, since $k(s) = 1$, the coefficients of the elliptic equation are constant. Thus no errors are introduced in the elliptic step due to lack of mesh refinement near the front.

We have also applied our front tracking method to problems where the elliptic equation is not trivial. In general, the permeability function $k(s)$ changes by a factor of μ in crossing the front. Therefore the errors introduced during the elliptic step increase with μ. For large μ, we believe that a more accurate solution of the elliptic problem near the front would improve the method. For simplicity, we again discuss only the case of miscible displacment. We present examples where the oil to solvent viscosity ratio μ is 2,5 and 50, and in the latter case we also study the case where the permeability function is given an explicit spatial dependence.

Figure 2 shows successive fronts for two different grids superimposed, when the oil-solvent viscosity ratio is $\mu = 2$. The agreement between the results for the two grids is good. Fingered solutions for a heterogeneous reservoir with $\mu = 2$ were obtained by an earlier method [8]. Figure 3 shows that tracking allows the computation of the mathematical solution in the extreme unstable regime of large viscosity ratios - here $\mu = 50$. This region was beyond the reach of the methods presented earlier in [8]. The viscosity ratio in Figure 4 is the same as that in Figure 3, but the permeability has been given an x-y dependence; specifically, it has a log-normal distribution. Figure 5 is similar, except that the length scale of the x-y dependence in the log-normal distribution has been increased. In both cases, fingering of the solution is observed. Figures 6(a) - 6(g) depict the evolution of fingers and of the associated velocity fields in the heterogeneous reservoir of Figure 5.

In Table II we present details of the amount of oil recovered at breakthrough in various cases, as well as some comparisons to experiment [13].

Table II: Oil Recovery at Breakthrough - Miscible Displacement.

	$\mu = 1$	$\mu = 2$	$\mu = 5$
Experiment	.667	.59	.46
10x10 grid	.752	.657	.548
20x20 grid	.731	.656	.503
Exact Solution	.723	-	-

References

1. Glimm, J. Solutions in the Large for Nonlinear Hyperbolic Systems of Equations. Comm. Pure Appl. Math. 18, 697 (1965).

2. Sod, G. A Survey of Numerical Methods for Compressible Fluids. J. Comp. Phys. 27, 1 (1978).

3. Chorin, A. Random Choice Solutions of Hyperbolic Systems, J. Comp. Phys. 22, 517 (1976).

4. Chorin, A. A Numerical Method for Use in Combustion Modeling.

5. Sod, G. A Numerical Method for Slightly Viscous Axisymmetric Flows with Applications to Internal Combustion Engines. J. Comp. Phys. To appear.

6. Colella, P. An Analysis of the Effect of Operator Splitting and of the Sampling Procedure on the Accuracy of Glimm's Method. University of California Thesis 1978.

7. Glimm, J., D. Marchesin and O. McBryan, Statistical Fluid Dynamics Unstable Fingers, Commun. Math. Phys., to appear.

8. Glimm, J., D. Marchesin and O. McBryan, Unstable Fingers in Two Phase Flow, Rockefeller University Preprint.

9. Glimm, J., D. Marchesin and O. McBryan, Subgrid Resolution of Fluid Discontinuities II. J. Comp. Phys., to appear.

10. Chorin, A. Flame Advection and Propagation Algorithms. University of California preprint.

11. Richtmeyer, R. and K. Morton, Difference Methods for Initial Value Problems. Interscience Publishers New York 1957.

12. Albright, N.P. Concus and W. Proskurowski, Numerical Solution of the Multidimensional Buckley-Leverett Equation by a Sampling Method. Presented at the SPE Symposium on Reservoir Simulation, Feb. 1979.

13. Haberman, B. The Efficiency of Miscible Displacment as a Function of Mobility Ratio. Trans. AIME 219, 264 (1960).

Footnotes

1. Supported in part by the NSF Grant PHY-78-08066.
2. Supported in part by the Army Research Office, ARO Grant DAAG29-78-G-0171.
3. Supported in part by the NSF Grant DMR77-04105.
4. Supported in part by the Department of Energy Grant.

5. Permanent Address: Mathematics Department, Cornell University, Ithaca, N.Y.
6. Permanent Address: Mathematics Department, Pontificia Universidade Catolica do Rio de Janeiro, Rio De Janeiro, Brazil.

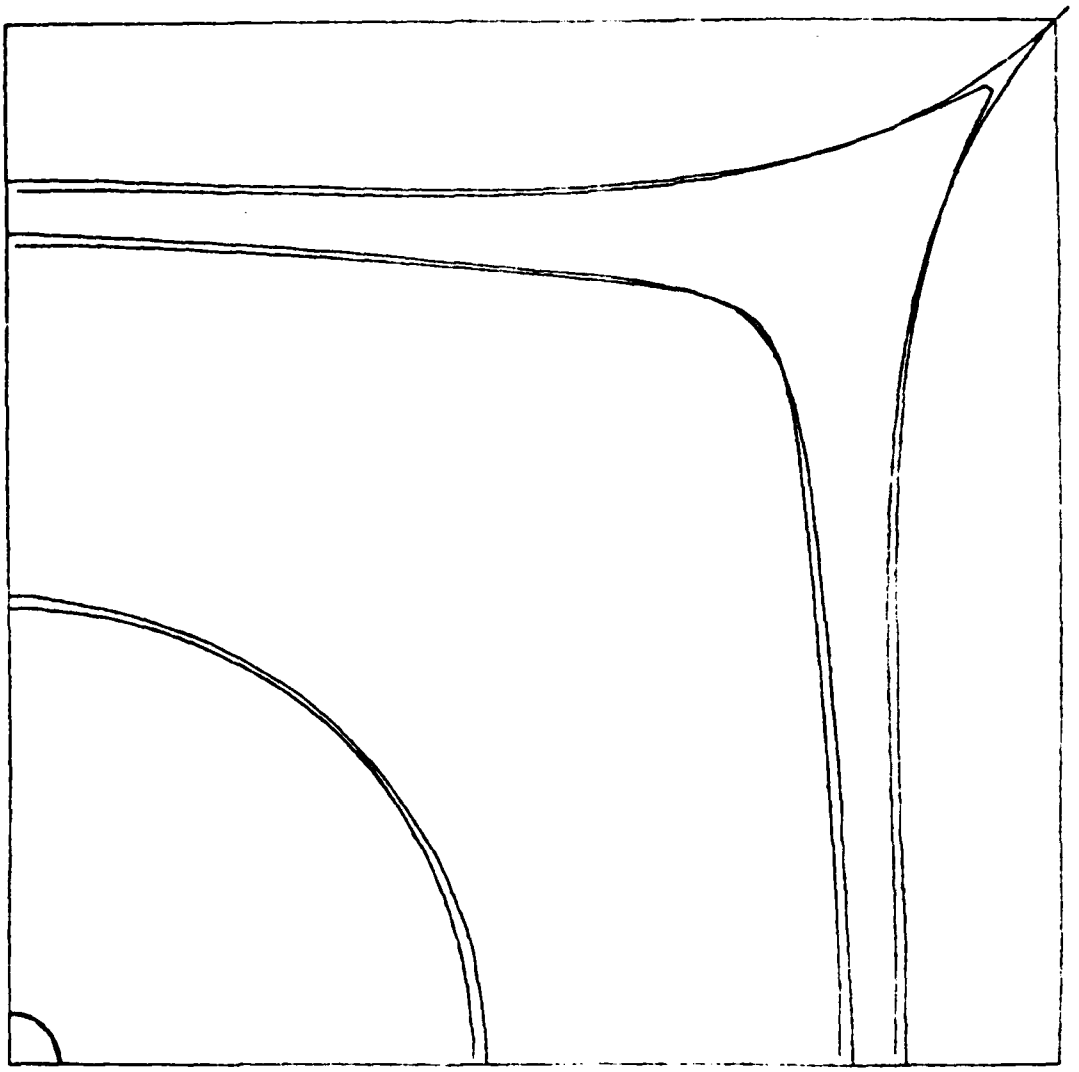

Figure 1

Miscible displacement, with equal viscosities. The exact solution and computed solution from a 20x20 grid with front tracking are plotted at equal times. The computed solution has moved faster along the boundary and slower at the tip.

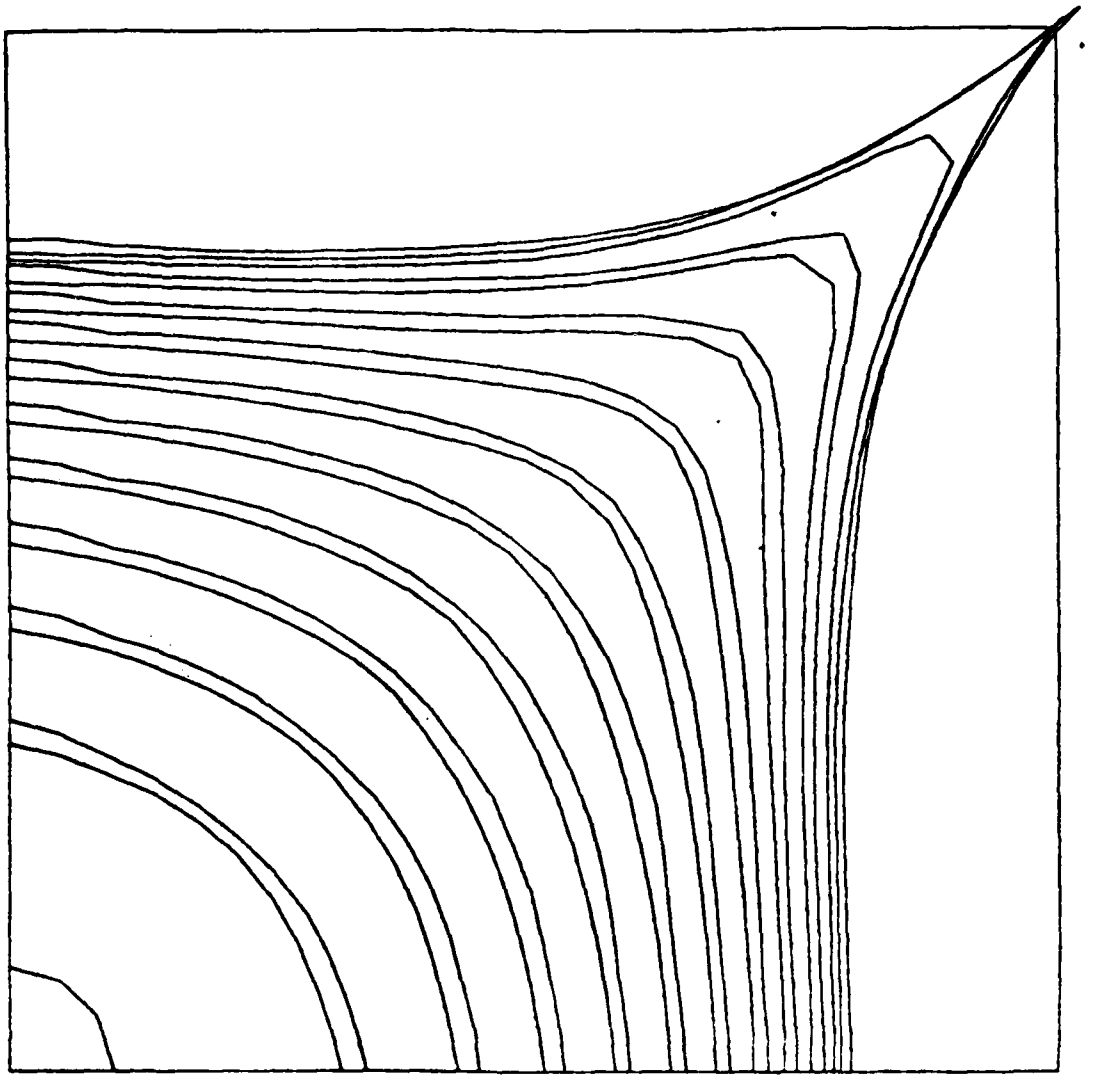

Figure 2

Miscible displacement with oil solvent viscosity ratio $\mu_o/\mu_s = 2$. The solution is computed with front tracking and plotted at successive time intervals, for a 10 x 10 and 20 x 20 grid. The coarse grid (10 x 10) solution is slightly in advance of the fine grid solution at each time step. (This solution is unstable and is not duplicated experimentally.)

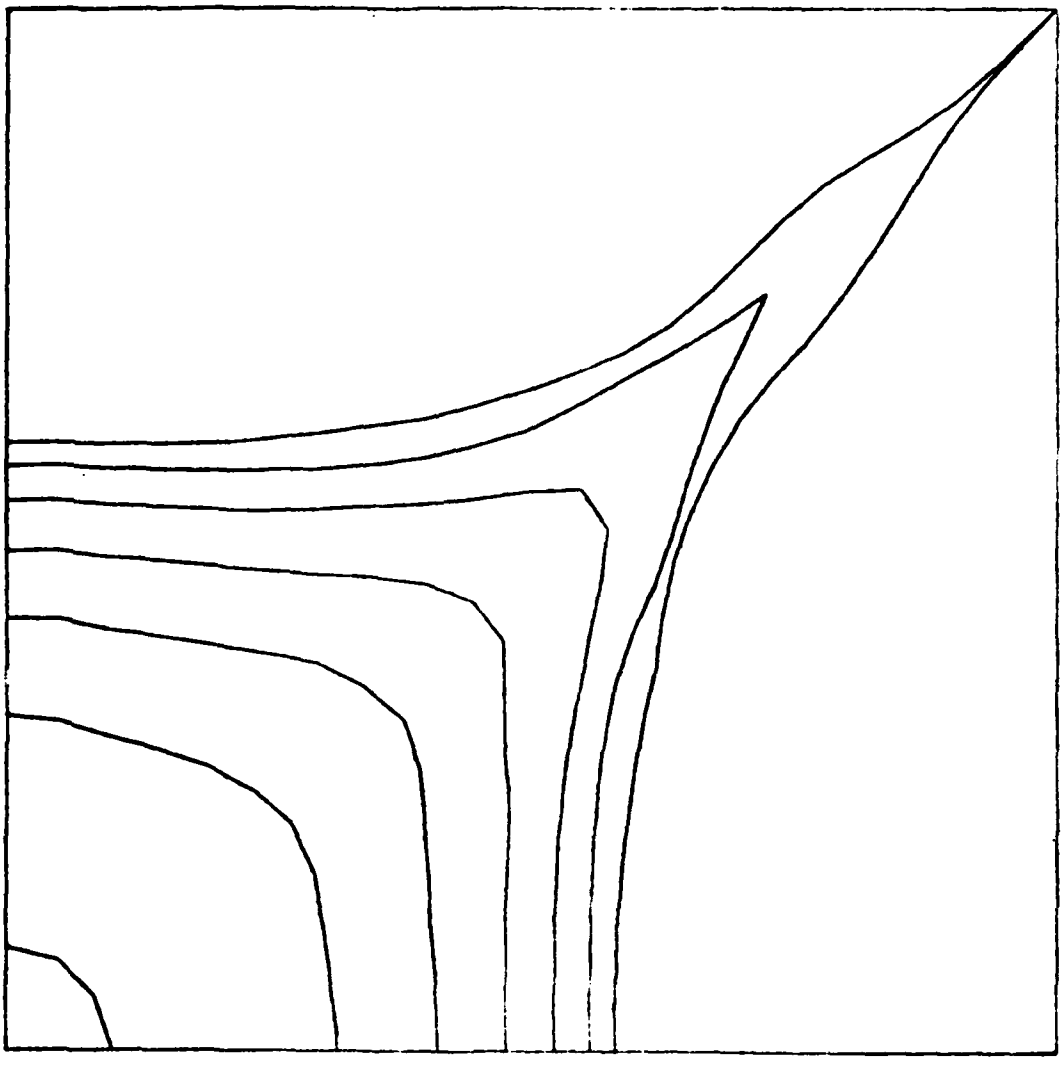

Figure 3

Miscible displacement with oil solvent viscosity ratio $\mu_o/\mu_s = 50$, computed with front tracking and a homogeneous reservoir on a 10 x 10 grid.

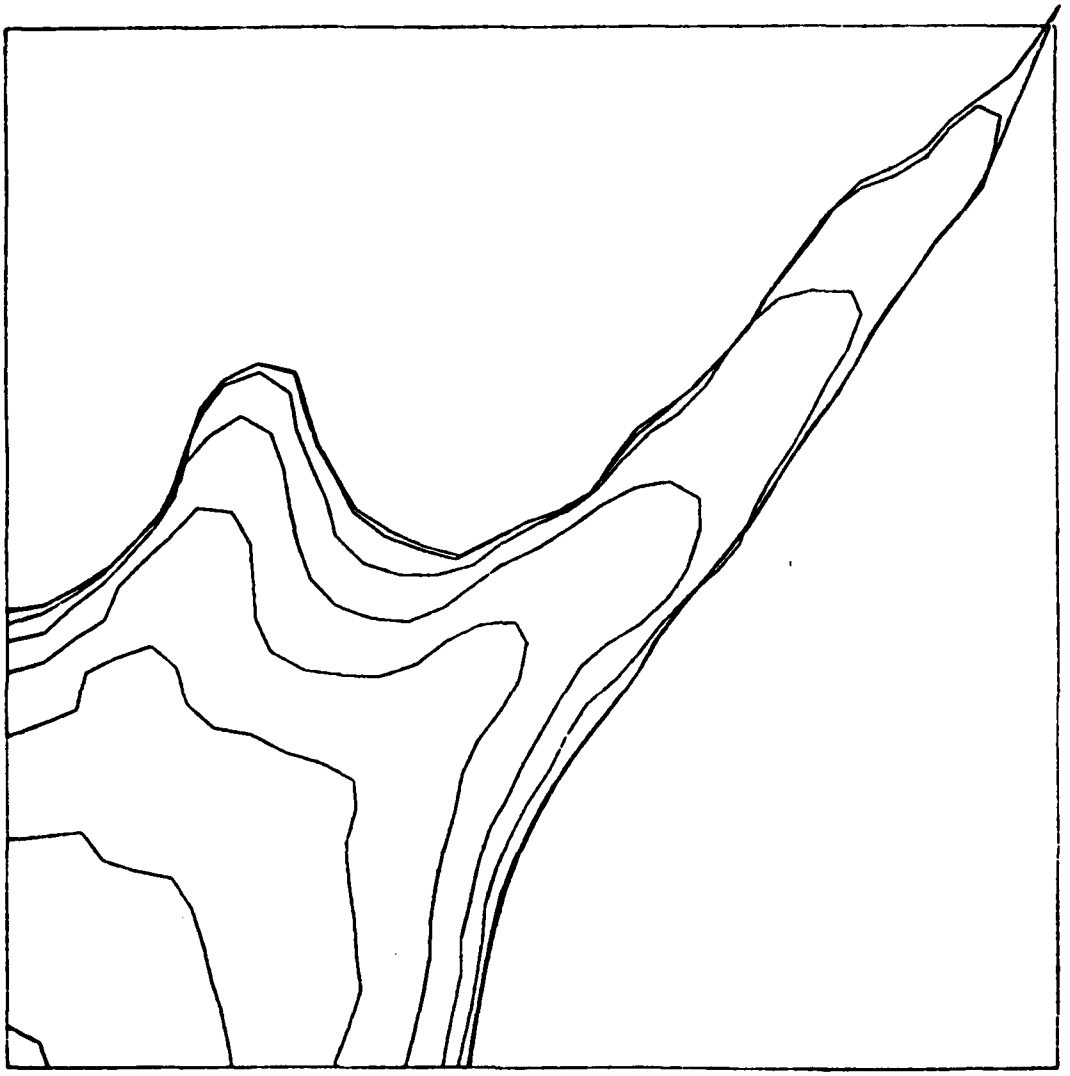

Figure 4

Miscible displacement; solvent displacing oil, with a viscosity ratio $\mu_0/\mu_s = 50$. The solution was computed on a 25x25 grid with front tracking. The reservoir was heterogeneous with log permeability normally distributed with a variance of .5 .

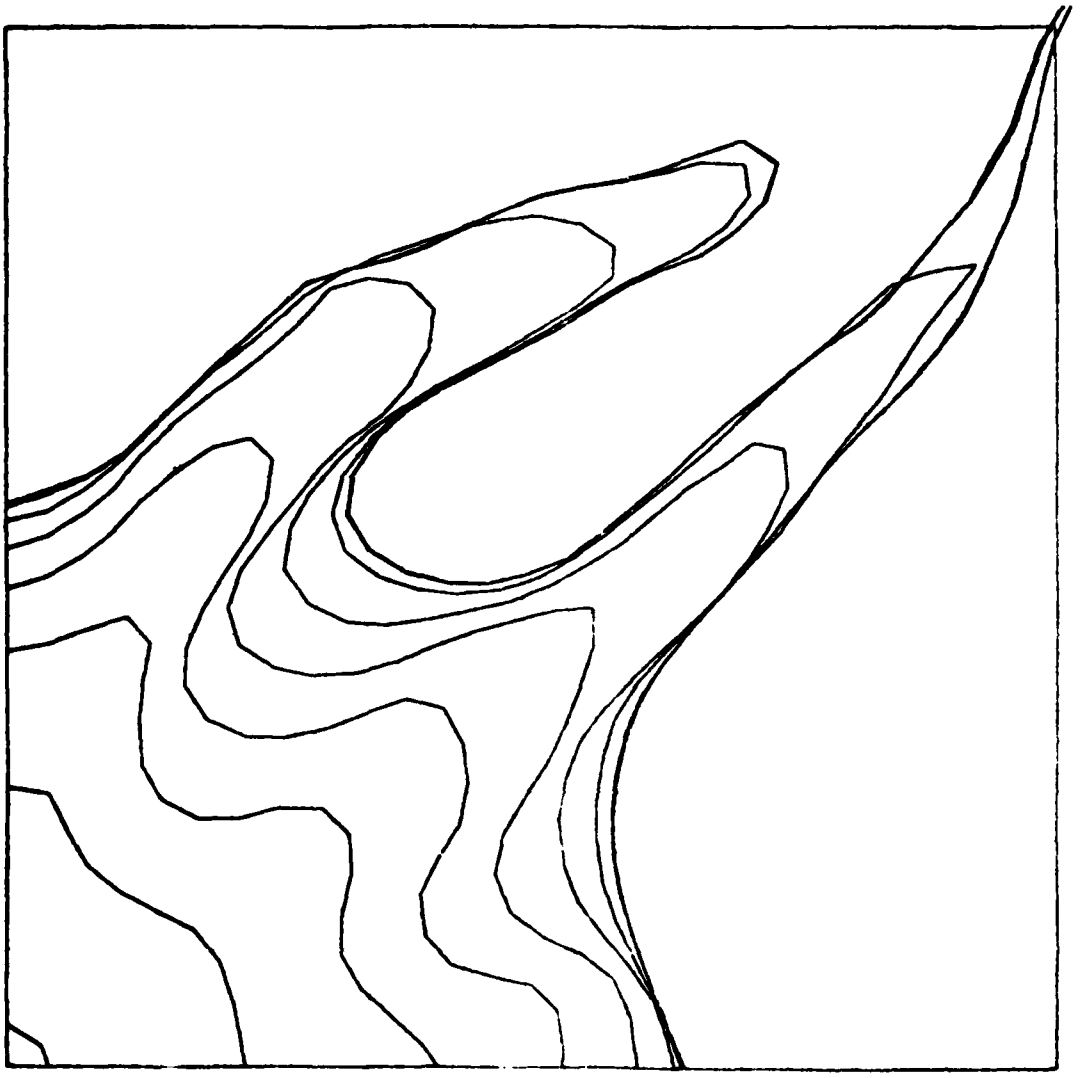

Figure 5
Miscible displacement. The length scale in the heterogeneity was increased from that of Figure 4. Individual time steps with velocity field are given in Figure 6.

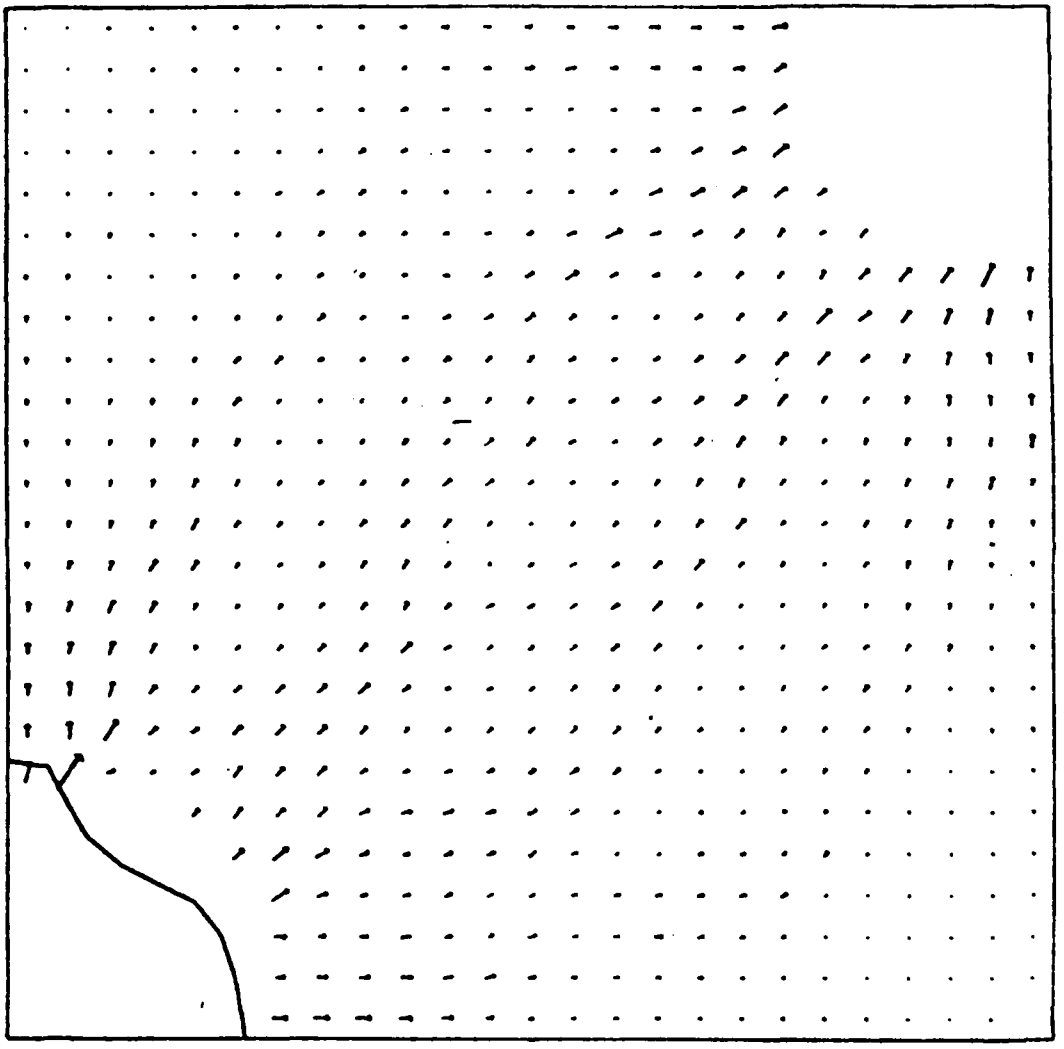

Figure 6(a)

Miscible displacement, with viscosity ratio $\mu_o/\mu_s = 50$. The front position and velocity field (lengths scaled proportional to v^2) are plotted here.

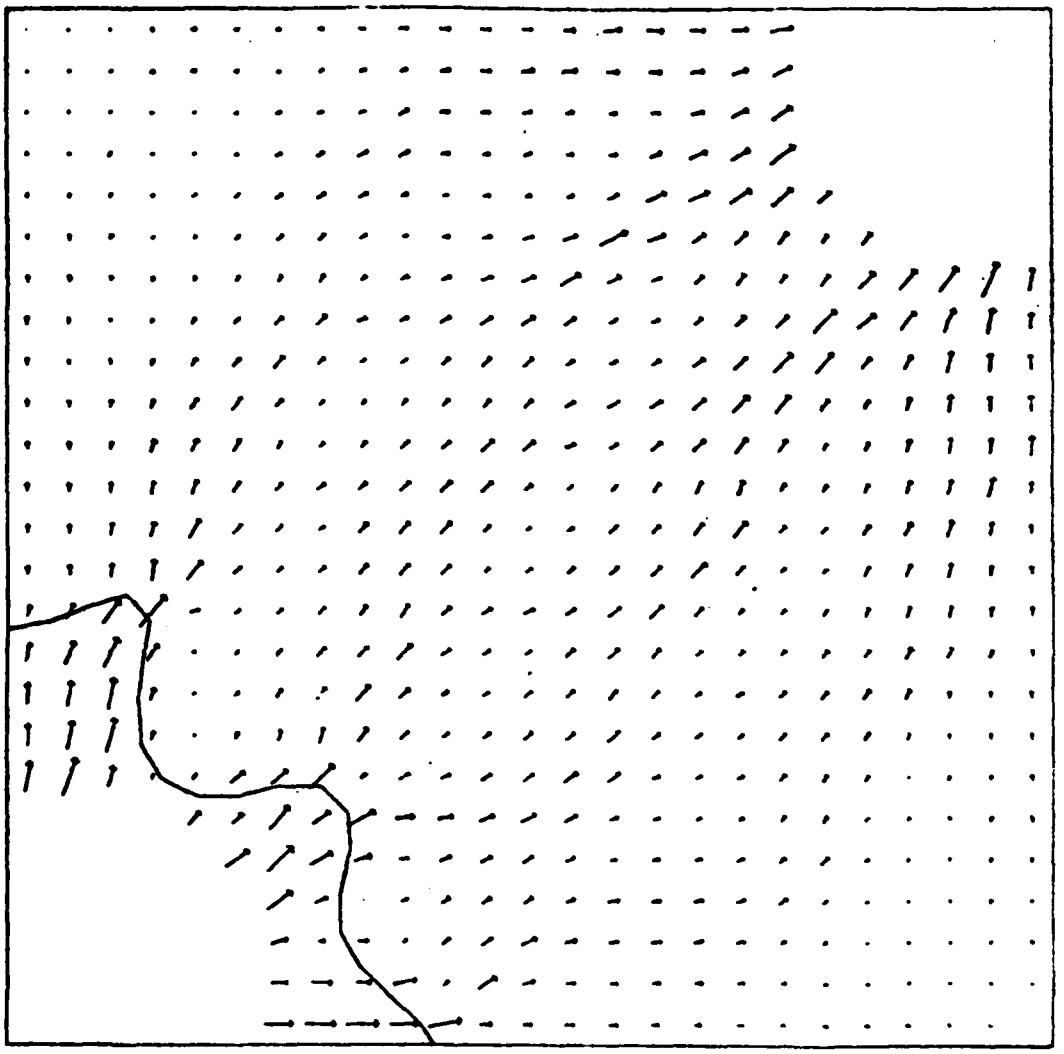

Figure 6(b)

A later time step from the same run as in Figure 6(a). In Figures 6(a)-6(f), the successive plots are separated by 15 computational time steps.

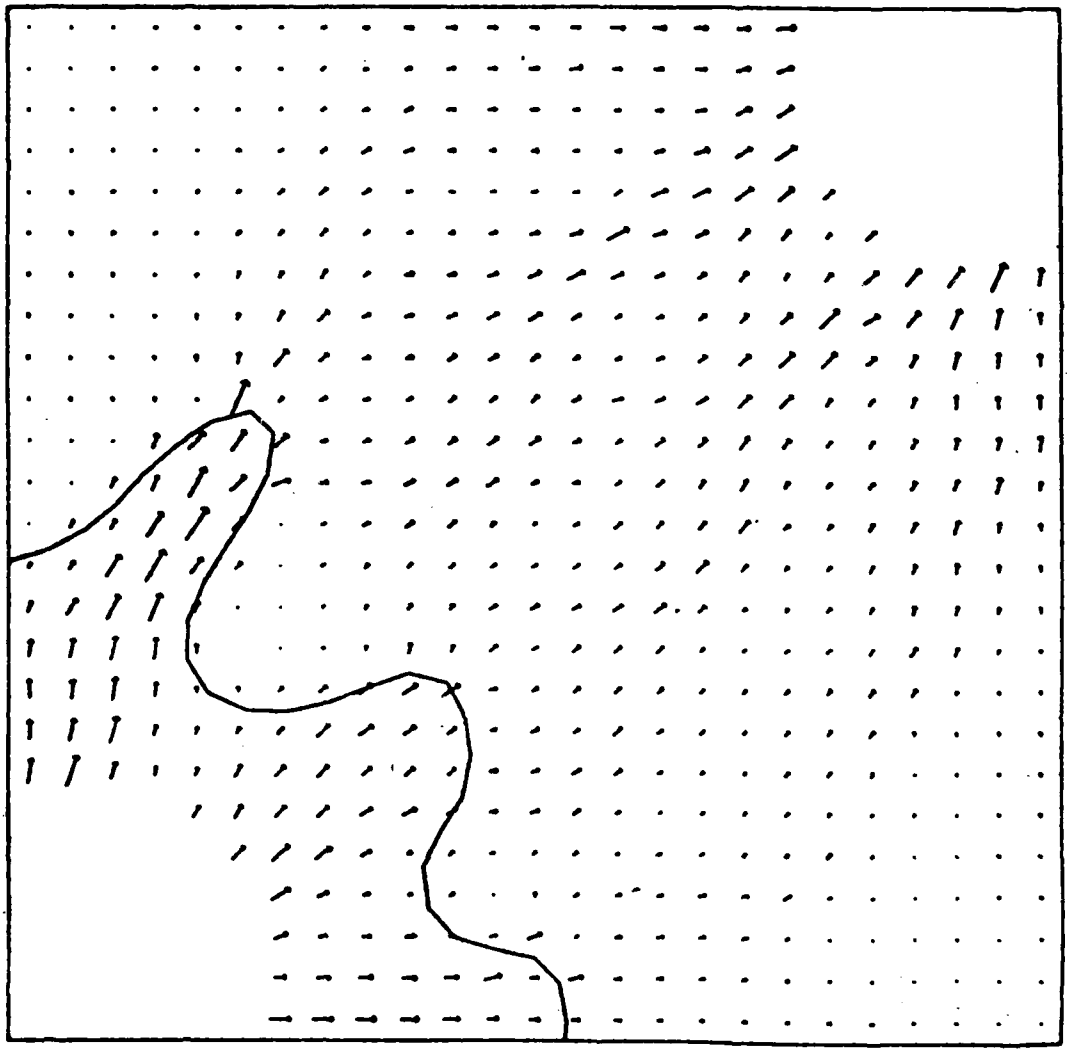

FIGURE 6(c)

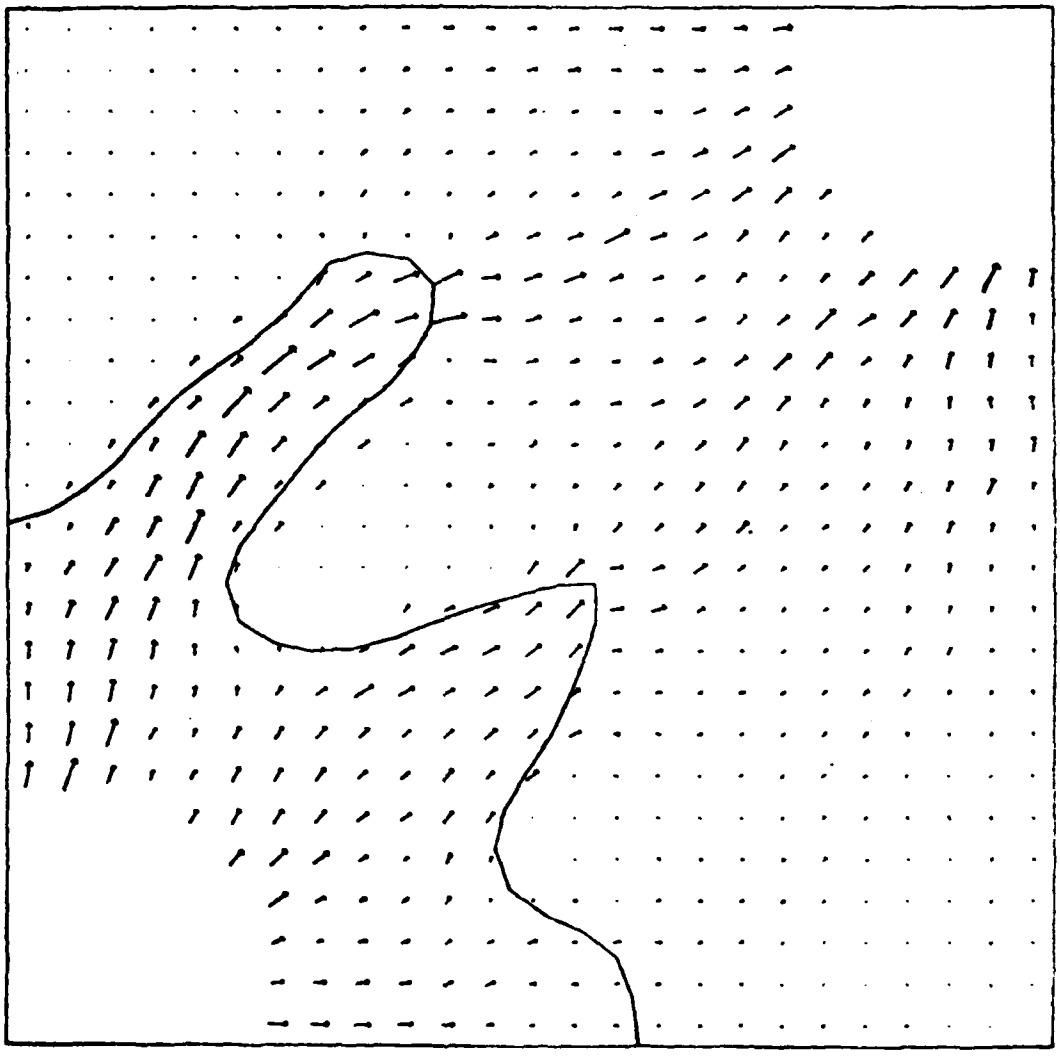

Figure 6(d)

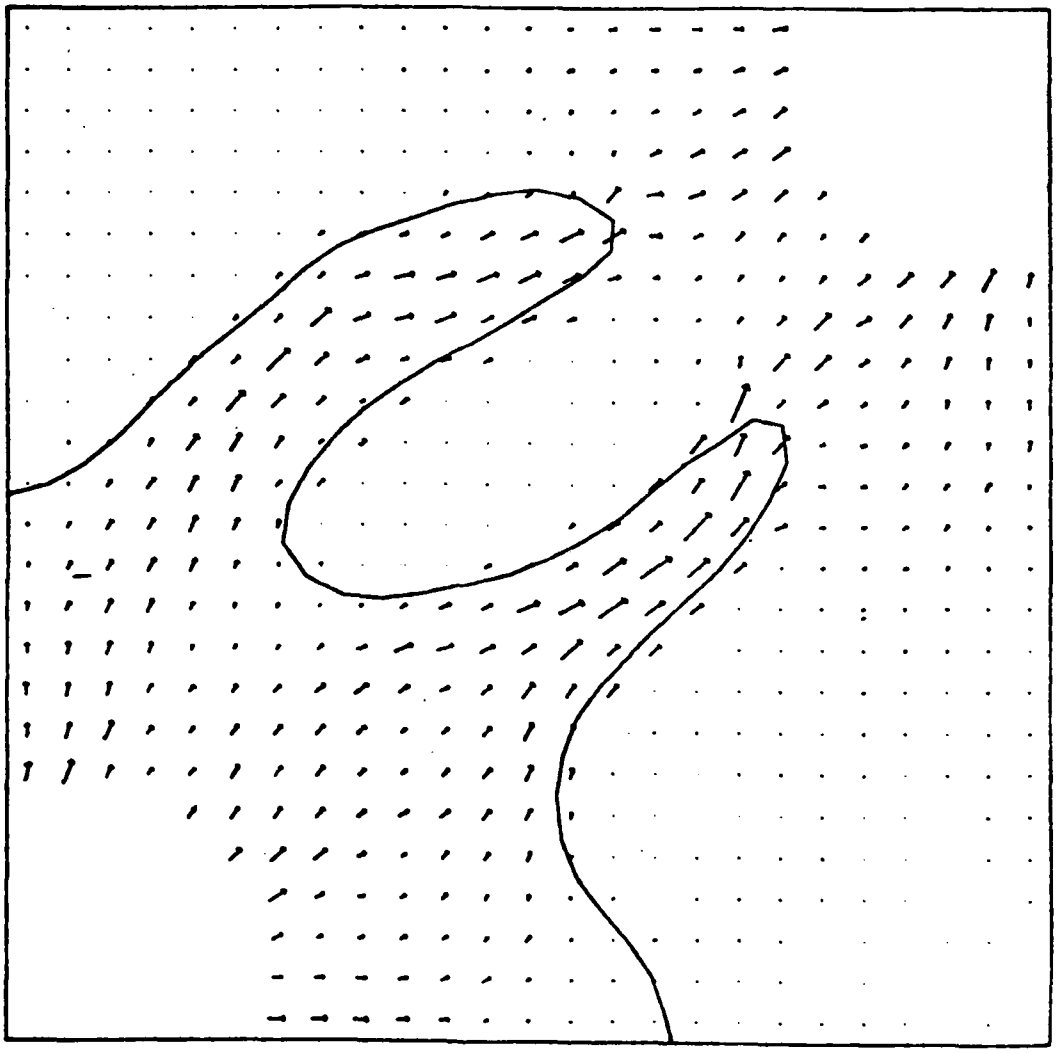

Figure 6(e)

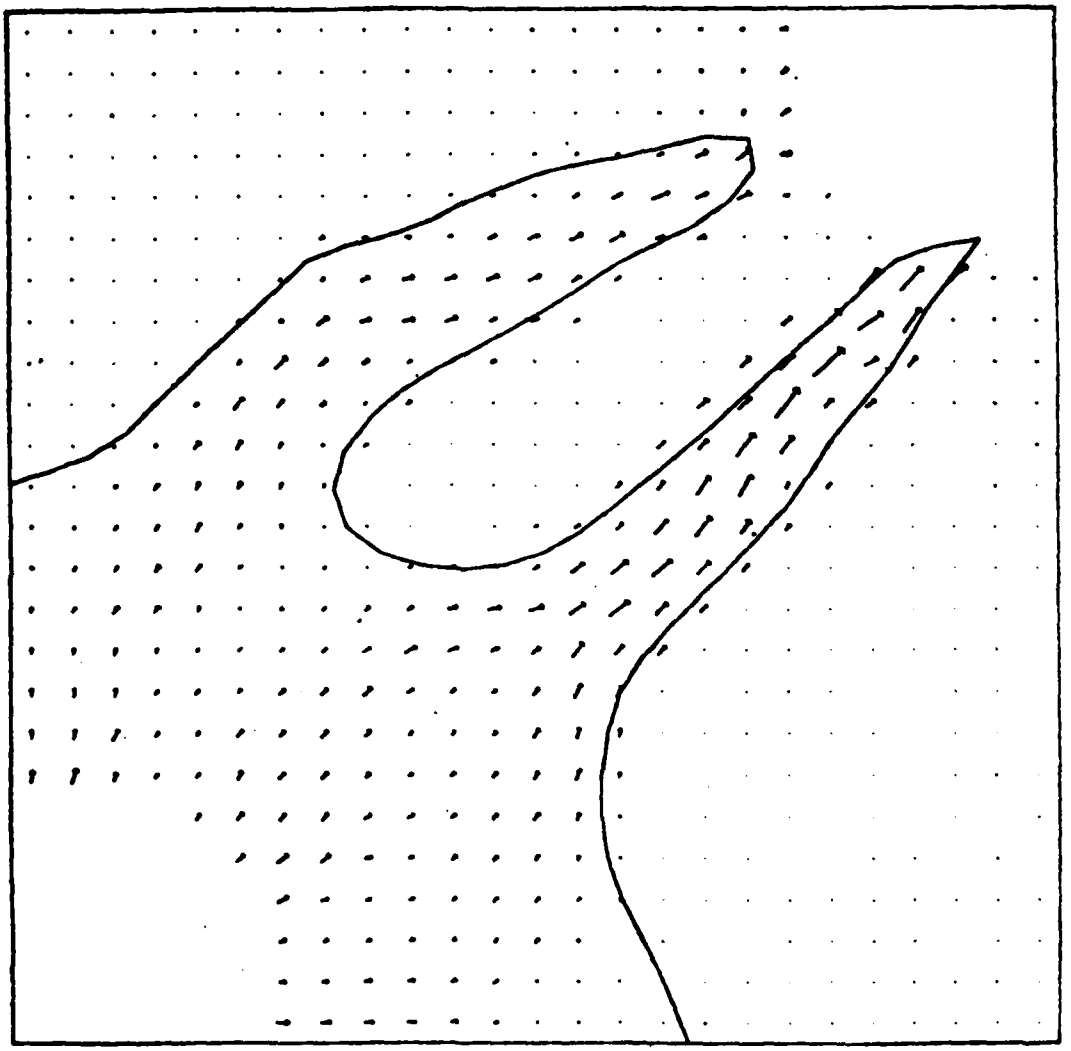

Figure 6(f)

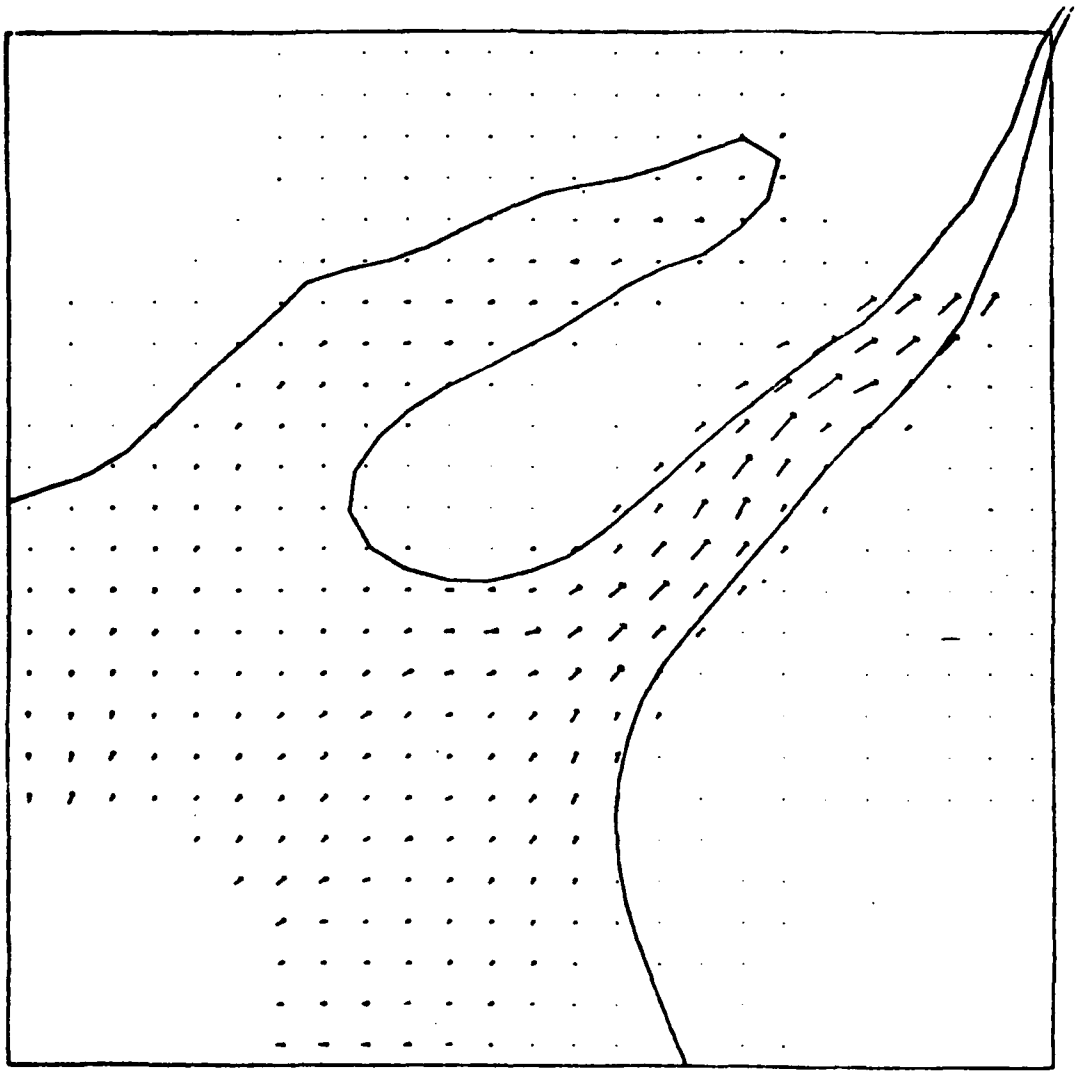

Figure 6(3)

Breakthrough contour for the oil-solvent interface.

IMPLICIT POTENTIAL METHODS FOR THE SOLUTION OF TRANSONIC ROTOR FLOWS

F. X. Caradonna
Aeromechanics Laboratory
U.S. Army Research and Technology Laboratories (AVRADCOM)
Ames Research Center, Moffett Field, California 94035

J. L. Steger
Flow Simulations Inc.
Sunnyvale, California

ABSTRACT. Two implicit potential methods capable of solving transonic rotor flow problems are developed. One method is a small disturbance technique with a general unsteady applicability. The other method is an unsteady full potential technique which maintains conservation by an appropriate expansion of the density. The two methods are compared for various test computations. Three-dimensional computations are also made and compared to actual rotor pressure data.

1. INTRODUCTION. Transonic flow is a common occurrence on modern helicopter rotors and often defines the performance limits of these machines. This flow can be quite complex, as the blade in forward flight encounters a rapidly varying Mach number, incidence, and sweep angle, and must often interact with various portions of its own wake. In addition, strong shocks can result in a high-speed stall. Even in the absence of separation effects, the shock motion and blade loadings are difficult to predict under these conditions. These problems are notoriously difficult to study experimentally and the numerical simulation of rotor flows becomes quite attractive. The potential flow approximation is the simplest model capable of simulating high-speed rotor flows. This paper describes two potential methods for simulating these flows — one, a small disturbance and the other a full potential method.

2. SMALL DISTURBANCE METHOD. The small disturbance equation is derived from the mass conservation and Bernoulli's equation,

$$\frac{\partial \rho}{\partial t} + \nabla \cdot (\rho \vec{U}) = 0 \tag{1}$$

$$\frac{\rho}{\rho_\infty} = \left[1 - \frac{\gamma - 1}{a_\infty^2}\left(\frac{\partial \phi}{\partial t} + \frac{\vec{U} \cdot \vec{U}}{2}\right)\right]^{1/\gamma - 1} \tag{2}$$

To derive a simplified equation suitable for high-speed rotor use, the above equations are recast in a blade fixed coordinate system. The resulting equation is made dimensionless, scaled, and the transonic small disturbance assumption $[(1 - M^2)/\tau^{2/3} = O(1)]$ is imposed (see ref. 1 for a detailed discussion of the derivation). The resulting equation written in conservation form is

$$A\phi_{\psi\psi} + B\phi_{x\psi} = F_x + \phi_{zz} + C\phi_{yy} + D\phi_{xy} \tag{3}$$

where

$\phi = \Phi/\Omega R c\tau^{2/3}$

$A = M^2\varepsilon^2/\tau^{2/3}$

$B = 2M^2\varepsilon f/\tau^{2/3}$

$D = Bg$

$f = y + \mu \cos\psi$

$g = x\varepsilon + \mu \sin\psi$

$C = \varepsilon^2/\tau^{2/3}$

$F = \dfrac{1 - f^2M^2}{\tau^{2/3}}\phi_x - M^2\left[\left(\dfrac{\gamma + 1}{2}\right)f\phi_x + (\gamma - 1)\varepsilon\phi_\psi\right]\phi_x$, chordwise flux term

$\mu = \Omega R/V_\infty$, rotor advance ratio

$M = \Omega R/a_\infty$, tip Mach number

$\varepsilon = c/R$, inverse of blade aspect ratio

$\psi = \Omega t$, blade azimuth

τ = blade thickness ratio

and $x = \bar{x}/c$, $z = \bar{z}\tau^{1/2}/c$, and $y = \bar{y}/R$ (barred quantities are dimensional quantities). Note that, in the above equations, the inverse aspect ratio plays the part of a reduced frequency.

Equation (3) will be solved by an implicit finite difference method. Before proceeding to discretize Eq. (3), it is first necessary to time-linearize the nonlinear flux term, F, to avoid a costly iteration process at each time step. That is, let

$$F^{n+1} = F^n + \left(\frac{\partial F}{\partial \phi_x}\right)^n \left(\phi_x^{n+1} - \phi_x^n\right) + \left(\frac{\partial F}{\partial \phi_\psi}\right)^n \left(\phi_\psi^{n+1} - \phi_\psi^n\right) . \tag{4}$$

This time-linearized flux is differenced at each midcell of the computational grid as

$$F_{i+1/2}^{n+1} = F_{i+1/2}^n + \left(\frac{\partial F}{\partial \phi_x}\right)^n \delta_i \frac{\phi_i^{n+1} - \phi_i^n}{\Delta x} + \left(\frac{\partial F}{\partial \phi_\psi}\right)\delta_n \frac{\phi_i^n - \phi_i^{n-1}}{\Delta\psi} ,$$

$$F_{i+1/2}^n = \frac{1 - f^2M^2}{\tau^{2/3}} \frac{\delta_i\phi_i^n}{\Delta x} - M^2\left[\left(\frac{\gamma + 1}{2}\right)f \frac{\delta_i\phi_i^n}{\Delta x} + \frac{\varepsilon(\gamma - 1)\delta_n\phi_i^{n-1}}{\Delta\psi}\right]\frac{\delta_i\phi_i^n}{\Delta x} \tag{5}$$

where the difference δ is defined in terms of the shift operator as

$$\delta_M = E_M^{+1} - I$$

and

$$\left(\frac{\partial F}{\partial \phi_x}\right)^n = \frac{1 - f^2M^2}{\tau^{2/3}} - \frac{M^2(\gamma + 1)f\delta_i\phi_i^n}{\Delta x} - \frac{M^2(\gamma - 1)\varepsilon\delta_n\phi_i^{n-1}}{\Delta\psi},$$

$$\left(\frac{\partial F}{\partial \phi_\psi}\right)^n = -\frac{M^2(\gamma - 1)\varepsilon\delta_i\phi_i^n}{\Delta x}.$$

To stably difference F_x in both supersonic and subsonic regions, Murman's conservative switched scheme is used (ref. 2), that is

$$F_x \to D_xF = \frac{1}{\Delta x}\left[\varepsilon_i(F_{i+1/2} - F_{i-1/2}) + (1 - \varepsilon_{i-1})(F_{i-1/2} - F_{i-3/2})\right] \qquad (6)$$

where

$$\varepsilon_i = \begin{cases} 1 & V_i > 0 \\ 0 & V_i < 0 \end{cases}$$

and

$$V = \frac{1 - M^2f^2}{\tau^{2/3}} - M^2(\gamma + 1)\phi_x - M^2(\gamma - 1)\varepsilon\phi_\psi .$$

Solutions that fully implement all the unsteady terms in Eq. (3) have been obtained in two dimensions. The numerical procedure for the two-dimensional case is the following alternating direction (ADI) scheme:

$$\left.\begin{aligned} \text{x sweep:}\quad & \frac{B}{\Delta\psi\Delta x}\delta_i(\tilde{\phi}_{i-1} - \phi_{i-1}^n)_j = D_xF + \bar{\delta}_j\delta_j\phi_{i,j}^n \\ \text{z sweep:}\quad & \frac{A}{\Delta\psi^2}\bar{\delta}_n\delta_n\phi_{i,j}^n + \frac{B}{\Delta\psi\Delta x}\delta_i(\phi_i^{n+1} - \tilde{\phi}_i)_j = \bar{\delta}_j\delta_j\phi_{i,j}^{n+1} \end{aligned}\right\} \qquad (7)$$

where $\bar{\delta}_m = E_m^{+1/2} - E_m^{-1/2}$ and F in the x-sweep is defined using $\tilde{\phi}$ in place of ϕ^{n+1}.

The boundary conditions employed (fig. 1) are undisturbed flow upstream ($\phi = 0$), an undisturbed flow or flat wall condition ($\phi = 0$ or $\phi_z = 0$) on the lateral boundaries, and zero pressure disturbance on the downstream boundary [$C_p = -2f\delta^{2/3}(\phi_x + \phi_\psi) = 0$]. The airfoil tangency condition, $\phi_z = dZ_s/dx$ ($Z_s(x)$ describes the airfoil profile), is applied on the airfoil mean surface, $z = 0$. An additional boundary is the contact discontinuity caused by the

downstream convection of vorticity from the trailing edge. Across this boundary there is a discontinuity in potential, $\Gamma = [\phi]$, described by

$$\Gamma_x + \Gamma_\psi = 0 \ , \tag{8}$$

which is obtained from pressure continuity. In addition there is a discontinuity in ϕ_{zz} across the wake. This is seen by applying Eq. (3) (in its nonconservative, two-dimensional form) across the wake to obtain

$$A\Gamma_{\psi\psi} + Bf\Gamma_{x\psi} = V\Gamma_{xx} + [\phi_{zz}] \ .$$

Substituting Eq. (8) into this expression yields

$$[\phi_{zz}] = (A - B - V)\Gamma_{xx} \tag{9}$$

A Taylor expansion gives the differencing which must account for these discontinuities:

$$\phi_{yy} \rightarrow \frac{\bar{\delta}_j \delta_j \phi_j \pm \Gamma}{\Delta y^2} \pm \frac{1}{8} [\phi_{yy}] \ . \tag{10}$$

To obtain this expression, the wake is assumed to be midway between two mesh points.

Three-dimensional nonlifting solutions to Eq. (3) in its low-frequency form (i.e., all unsteady terms except $\phi_{x\psi}$ are ignored) have also been obtained. The numerical procedure is a straightforward extension of the two-dimensional case, that is,

$$\left.\begin{aligned}
\text{x sweep:}\quad & \frac{B}{\Delta\psi\Delta x}\,\delta_i(\tilde{\phi}_{i-1} - \phi_{i-1})_{j,k} = D_x F + C\,\frac{\bar{\delta}_j\delta_j}{\Delta y^2}\,\phi^n_{i,j,k} + \frac{\bar{\delta}_k\delta_k}{\Delta z^2}\,\phi^n_{i,j,k} \\
& \qquad + \frac{D}{4\Delta x\Delta y}\,(\phi_{i+1,k+1} - \phi_{i-1,k+1} \\
& \qquad - \phi_{i+1,k-1} + \phi_{i-1,k-1})^n_j \\
\text{z sweep:}\quad & \frac{B}{\Delta\psi\Delta x}\,\delta_i(\tilde{\tilde{\phi}}_{i-1} - \tilde{\phi}_{i-1})_{j,k} = \frac{\bar{\delta}_k\delta_k}{\Delta z^2}\,(\tilde{\tilde{\phi}} - \phi^n)_{i,j,k} \\
\text{y sweep:}\quad & \frac{B}{\Delta\psi\Delta x}\,\delta_i(\phi^{n+1} - \tilde{\tilde{\phi}})_{j,k} = \frac{C}{\Delta y^2}\,\bar{\delta}_j\delta_j(\phi^{n+1} - \phi^n)_{i,j,k}
\end{aligned}\right\} \tag{11}$$

3. FULL POTENTIAL METHOD. The governing equations (1) and (2) can also be solved without making use of a small disturbance assumption. Because no terms are dropped, Eqs. (1) and (2) are frequently referred to as the unsteady full potential equations. The full potential equations surpass the small

disturbance equations in that they can account for full geometry effects and treat a more complete range of flow-field variations.

In this section a numerical procedure for the unsteady full potential equations is developed. At the current state of this development, the inertial reference frame rather than blade fixed frame is retained in Eqs. (1) and (2) and the equations are treated in only two dimensions. Although the full potential equations are solved, a thin airfoil boundary condition is presently employed for simplicity. We remark that a similar numerical algorithm was independently derived by Goorjian (ref. 3).

a) Governing Equations. Transformations can be introduced into Eqs. (1) and (2) both to simplify the treatment of boundary conditions and to cluster grid points to flow-field action regions. Since thin airfoil boundary conditions will be used, the transformation need only serve to cluster grid points. With transformation, $\xi = \xi(x)$, $\eta = \eta(z)$, Eqs. (1) and (2) take the form

$$\frac{\partial}{\partial t}\left(\frac{\rho}{J}\right) + \frac{\partial}{\partial \xi}\left(\frac{\rho \xi_x^2}{J}\frac{\partial \phi}{\partial \xi}\right) + \frac{\partial}{\partial y}\left(\frac{\rho \eta_z^2}{J}\frac{\partial \phi}{\partial \eta}\right) = 0 \tag{12a}$$

$$\rho = \left[1 - (\gamma - 1)\frac{M_\infty^2}{2}\left(2\phi_\tau + \xi_x^2 \phi_\xi^2 + \eta_z^2 \phi_\eta^2 - 1\right)\right]^{1/\gamma - 1} \tag{12b}$$

where $\rho = \bar{\rho}/\rho_\infty$, $u = \bar{u}/U_\infty$, etc., and $J = \xi_x \eta_z = 1/(x_\xi z_\eta)$ and where a uniform nonzero flow is specified at infinity, causing an appropriate change to the Bernoulli equation.

For all practical purposes, far-field boundary conditions and circulation jump conditions across the cut are identical to those previously described.

b) Conservative Form. Equation (1) is equivalent to a second-degree wave equation since $\rho = \rho(\phi)$ and thus

$$\frac{\partial \rho}{\partial t} = \frac{\partial \rho}{\partial \phi}\frac{\partial \phi}{\partial t} = -\rho^{2-\gamma}\left(\frac{\partial}{\partial t} + \phi_x \frac{\partial}{\partial x} + \phi_z \frac{\partial}{\partial z}\right)\frac{\partial \phi}{\partial t} \tag{13}$$

where $\partial\rho/\partial\phi$ is a noncommuting differential operation as determined from the Bernoulli equation. The spatial terms can be expanded in a similar way, e.g.,

$$\partial_x(\rho \phi_x) = \rho \phi_{xx} + \phi_x \rho_\phi \phi_x$$

and with rearrangement, Eq. (1) is written as

$$\phi_{tt} + 2\phi_x \phi_{xt} + 2\phi_z \phi_{zt} = (a^2 - \phi_x^2)\phi_{xx} - 2\phi_x \phi_z \phi_{xz} + (a^2 - \phi_y^2)\phi_{zz} \tag{14}$$

where $a^2 = \rho^{\gamma-1}/M_\infty^2$ (in the chosen dimensionless variables).

Equation (14) is useful in displaying the type of Eqs. (1) and (2) but in its nonconservative form it is inappropriate for "shock-capturing" (it does not give the weak solutions that model the Rankine-Hugoniot solutions). To

maintain the conservation-law form of Eq. (1) and yet still expose ϕ as the true dependent variable, the following Taylor series is introduced into the $\partial\rho/\partial t$ term

$$\rho = \rho_o + \left(\frac{\partial\rho}{\partial\phi}\right)_o (\phi - \phi_o) \tag{15}$$

where o represents a nearby known state or solution. Use of Eq. (15) allows Eq. (12a) to be rewritten as

$$\partial_t[+\hat{\beta}_o(\partial_\tau + \xi_x{}^2\phi_\xi\partial_\xi + \eta_z{}^2\phi_\eta\partial_\eta)(\phi - \phi_o)] = \partial_\xi(\hat{\rho}\xi_x{}^2\phi_\xi) + \partial_\eta(\hat{\rho}\eta_z{}^2\phi_\eta) + \partial_\tau\hat{\rho}_o \tag{16}$$

where $\beta \equiv \rho^{2-\gamma}$ and $\hat{}$ implies division by J, i.e., $\hat{\rho} = \rho/J$.

c) Numerical Algorithm. An implicit approximately factored numerical algorithm can be constructed for Eq. (16) in a similar way as for the small disturbance equation. The spatial difference operators are treated in much the same manner as they are in the steady-state relaxation algorithms (refs. 4-7). Define the operators as

$$\begin{aligned}\bar{\delta}_\xi(\hat{\rho}\xi_x{}^2\delta_\xi\phi) = {} & \left(\frac{\xi_x{}^2}{J}\right)_{i+1/2}\left[(1-\nu_{i+1})\frac{\rho_{i+1}+\rho_i}{2}\right. \\ & \left. + \nu_{i+1}\frac{(1+\theta)\rho_i + (1-\theta)\rho_{i-1}}{2}\right](\phi_{i+1} - \phi_i) \\ & - \left(\frac{\xi_x{}^2}{J}\right)_{i-1/2}\left[(1-\nu_i)\frac{\rho_i+\rho_{i-1}}{2}\right. \\ & \left. + \nu_i\frac{(1+\theta)\rho_{i-1} + (1-\theta)\rho_{i-2}}{2}\right](\phi_i - \phi_{i-1})\end{aligned} \tag{17a}$$

$$\begin{aligned}\bar{\delta}_\eta(\hat{\rho}\eta_z{}^2\bar{\delta}_\eta\phi) = {} & \left(\frac{\eta_z{}^2}{J}\right)_{j+1/2}\frac{\rho_{j+1}+\rho_j}{2}(\phi_{j+1} - \phi_j) \\ & - \left(\frac{\eta_z{}^2}{J}\right)_{j-1/2}\frac{\rho_j+\rho_{j-1}}{2}(\phi_j - \phi_{j-1})\end{aligned} \tag{17b}$$

Here $\Delta\xi = \Delta\eta = 1$ and only the varying indices are indicated. The parameter $\theta = 1$ or 2 for first- or second-order spatial accuracy in supersonic regions. The switching parameter ν is defined in a way similar to reference 5 as

$$\left.\begin{aligned}&\nu = [1 - (\rho/\rho^*)^2]c \qquad 1 \le c < 10 \\ &\nu \equiv 0 \quad \text{if} \quad \nu < 0, \text{ i.e., subsonic} \\ &\nu \equiv 1 \quad \text{if} \quad \nu > 1, \text{ i.e., supersonic}\end{aligned}\right\} \tag{18}$$

The parameter ν can be set to 1 throughout, but accuracy will be impaired unless θ is also set to 2. The operators (17a) and (17b) assume that the flow will be supersonic only in the positive x-direction. The density is found from the Bernoulli equation with ($\Delta\xi = \Delta\eta = 1$):

$$\phi_\xi\Big|_i \doteq \frac{\phi_{i+1} - \phi_{i-1}}{2} = \delta_\xi \phi_i$$

$$\phi_\eta\Big|_j \doteq \frac{\phi_{j+1} - \phi_{j-1}}{2} = \delta_\eta \phi_j$$

$$\phi_\tau\Big|^{n+1} \doteq \frac{(\phi^{n+1} - \phi^n)}{\Delta t} = \delta_\tau \phi^{n+1}$$

The metrics ξ_x and η_z are obtained from

$$\xi_x = \frac{2}{x_{i+1} - x_{i-1}}$$

$$\eta_y = \frac{2}{z_{j+1} - z_{j-1}}$$

while the term $(\xi_x^2/J)_{i+1/2}$ in Eq. (17a) is formed either as

$$\left(\frac{\xi_x^2}{J}\right)_{i+1/2} = \frac{(\xi_x^2/J)_{i+1} + (\xi_x^2/J)_i}{2} \tag{19a}$$

or

$$\left(\frac{\xi_x^2}{J}\right)_{i+1/2} = \frac{(\xi_x/J)_{i+1} + (\xi_x/J)_i}{2(x_{i+1} - x_i)} \tag{19b}$$

The terms $(\xi_x^2/J)_{i-1/2}$, $(\eta_z^2/J)_{j+1/2}$, and $(\eta_z^2/J)_{j-1/2}$ receive similar treatment. If Eq. (19a) is used, it is essential to add $-\delta_\xi(\rho_\infty \xi_x^2/J)\bar{\delta}_\xi \phi_\infty$ to the right-hand side of Eq. (16) to subtract out a numerical truncation error due to incomplete metric cancellation.

Using these operators, Eq. (16) is put in the approximately factored form (see ref. 8 for more details).

$$\left[I + \Delta t(\eta_z{}^2)\phi_\eta{}^n\delta_\eta - \Delta t \frac{J}{\beta^n} h\bar{\delta}_\eta \frac{\eta_z{}^2}{J} \rho^n\bar{\delta}_\eta\right]\times$$

$$\left[I + \Delta t(\xi_x{}^2)\phi_\xi{}^n\delta_\xi - \Delta t \frac{J}{\beta^n} h\bar{\delta}_\xi \frac{\xi_x{}^2}{J} \rho^n\bar{\delta}_\xi\right](\phi^{n+1} - \phi^n)$$

$$= \left[1 + \frac{\beta^{n-1}}{\beta^n}\right](\phi^n - \phi^{n-1}) - \frac{\beta^{n-1}}{\beta^n}(\phi^{n-1} - \phi^{n-2})$$

$$+ \Delta t \frac{\beta^{n-1}}{\beta^n}[(\xi_x{}^2)\phi_\xi^{n-1}\delta_\xi + (\eta_z{}^2)\phi_\eta^{n-1}\delta_\eta](\phi^n - \phi^{n-1})$$

$$+ \Delta t \frac{J}{\beta^n}\left[(\hat{\rho}^n - \hat{\rho}^{n-1}) + h\bar{\delta}_\xi \frac{\xi_x{}^2}{J} \rho^n\bar{\delta}_\xi\phi^n + h\bar{\delta}_\eta \frac{\eta_z{}^2}{J} \rho^n\bar{\delta}_\eta\phi^n\right] \tag{20}$$

This equation has the form

$$L_\eta L_\xi(\phi^{n+1} - \phi^n) = R \tag{21}$$

and it is implemented as an algorithm as

$$\left.\begin{aligned} L_\eta\Delta\phi^* &= R \\ L_\xi\Delta\phi^n &= \Delta\phi^* \\ \phi^{n+1} &= \phi^n + \Delta\phi^n \end{aligned}\right\} \tag{22}$$

The algorithm Eq. (22) requires only a series of scalar tridiagonal inversions and it is therefore very efficiently implemented. Computer storage equivalent to four levels of ϕ have to be supplied with ρ computed from the Bernoulli equation as needed.

4. RESULTS. A first assessment of the full potential method is to compare with previous steady solutions. This is done in Fig. 2 for the case of a circular arc profile at a small angle of attack. The particular small disturbance solution shown in this case is nonconservative and this is the cause of the discrepancy in shock location. Basically, the two numerical solutions compare well. The differences from the experimental pressures are undoubtedly due to viscous effects. For this particular computation, the switched density expression was used (Eq. (17a)). As previously mentioned, an upwind unswitched expression can be used (i.e., $\nu = 1$ in Eq. (17a)) if a higher order difference is used. This is shown in figure 3 which compares the unswitched full potential result with the same case as in figure 2. It is seen that the upwind scheme duplicates the switched density result. The overshoot in the switched

result is not inherent in switching, but probably indicates that modification of the ν expression is required.

A good unsteady solution to check out the full potential method is the slowly thickening and thinning airfoil. In this case we have a circular arc profile whose thickness τ varies as

$$M_\infty^{1/4}\tau = 0.1(10 - 15\bar{t} + 6\bar{t})\bar{t}^3 , \quad 0 \le t \le 15 , \quad \bar{t} \equiv t/15$$

$$M_\infty^{1/4}\tau = 0.1[1 - (10 - 15\bar{t} + 6\bar{t})\bar{t}^3] , \quad 15 \le t \le 30 , \quad \bar{t} = (t/15) - 1$$

The comparison in figure 4 of midchord pressure with the result of reference 9 is quite good. For this result, however, the present full potential method utilizes more unsteady terms than are absolutely required.

A case that more fully exercises the unsteady terms is the calculation of an impulsively plunged flat plate. This is a good test case because there are analytical results with which to compare. Figures 5(a)-5(c) compare both the present small disturbance and full potential results with the linear analytical results of reference 10. It is seen here that both the full potential and small disturbance cases compare well with the linear result. This is an important result as it shows that both methods are predicting both upstream and downstream propagating waves reasonably well. In contrast, the previous case (the thickening-thinning airfoil) demonstrates only the ability to handle upstream propagating waves.

The final computation is one that demonstrates the ability of potential methods to predict real transonic rotor flows — a computation of the flow on an advancing, nonlifting rotor using the three-dimensional small disturbance algorithm (Eq. (11)). The experiment in which these data were generated and some corresponding two-dimensional computations are described in reference 9. The model in question was a nearly rectangular nonlifting helicopter rotor. The unsteadiness of this flow is mainly due to the variation in the chordwise Mach number component which the blade sees. The reduced frequency of this variation is of the order of the inverse aspect ratio and is quite low. Therefore, it is appropriate to retain only the $\phi_{x\psi}$ term in Eq. (3), which amounts to assuming an infinite downstream propagation rate. Figures 6 and 7 show the numerical and experimentally obtained blade pressure distributions at azimuths of 60° and 120°, respectively. It is seen here that the small disturbance method predicts the pressure variation and shock motion quite well. It is of interest that the 120° case has much stronger shocks than the 60° case. This is indicative of the basic flow unsteadiness, as the two cases would be identical in a steady computation at the inboard stations where crossflow effects are small. In fact, this same sort of asymmetry was manifest in the thickening-thinning airfoil solution in figure 6.

5. CONCLUDING REMARKS. Potential methods seem to hold considerable promise for predicting the transonic flow on an advancing rotor blade. Two such methods — a small disturbance and a full potential method — are described here. Of the two methods, the small disturbance is the best developed, mainly because of history, smaller storage requirements, and simple geometry. Small disturbance results show excellent agreement with three-dimensional, nonlifting

rotor data. However, the limitations of this approximation, especially at lower Mach numbers and high lift, are well known. Therefore, we are developing an implicit full potential method that is fully conservative. At present the method is developed to the point of accurately predicting two-dimensional highly unsteady flows using linearized boundaries. It is clear that the method works well and will ultimately be developed into a full three-dimensional rotor flow code.

REFERENCES

1. Isom, M. P.: Unsteady Subsonic and Transonic Potential Flow Over Helicopter Rotor Blades. NASA CR-2463, Oct. 1974.

2. Murman, E. M.: Analysis of Embedded Shock Waves Calculated by Relaxation Methods. Proceedings of AIAA Computational Fluid Dynamics Conference, Palm Springs, California, July 1973, pp. 27-40.

3. Goorjian, P. M.: Computations of Unsteady Transonic Flow Governed by the Conservative Full Potential Equations Using an Alternating Direction Implicit Algorithm. NASA CR-152274, 1979.

4. Jameson, A.: Transonic Potential Flow Calculations Using Conservative Form. AIAA Second Computational Fluid Dynamics Conference Proceedings, June 1975, pp. 148-155.

5. Holst, T. L.; and Ballhaus, W. F.: Fast Conservative Schemes for the Full Potential Equation Applied to Transonic Flows. AIAA Journal, vol. 17, no. 2, Feb. 1979, pp. 145-152.

6. Holst, T. L.: A Fast Conservative Algorithm for Solving the Transonic Full-Potential Equation. AIAA Fourth Computational Fluid Dynamics Conference Proceedings, July 1979, pp. 109-121.

7. Hafez, M.; South, J.; and Murman, E.: Artificial Compressibility Methods for Numerical Solutions of the Full Potential Equation. AIAA Journal, vol. 17, Aug. 1979, pp. 838-844.

8. Steger, J. L.; and Caradonna, F. X.: A Conservative Implicit Finite-Difference Algorithm for the Unsteady Transonic Full Potential Equation. F.S.I. Rept. 79-04.

9. Ballhaus, W. F.; and Steger, J. L.: Implicit Approximate-Factorization Schemes for the Low-Frequency Transonic Equation. NASA TM X-73,082, Nov. 1975.

10. Lomax, H.; Heaslet, M.; Fuller, F.; and Sluder, L.: 2- and 3-Dimensional Unsteady Lift Problems in High Speed Flight. NACA Rept. 1077, 1952.

11. Caradonna, F. X.; and Philippe, J. J.: The Flow Over a Helicopter Blade Tip in the Transonic Regime. Vertica, vol. 2, 1978, pp. 43-60.

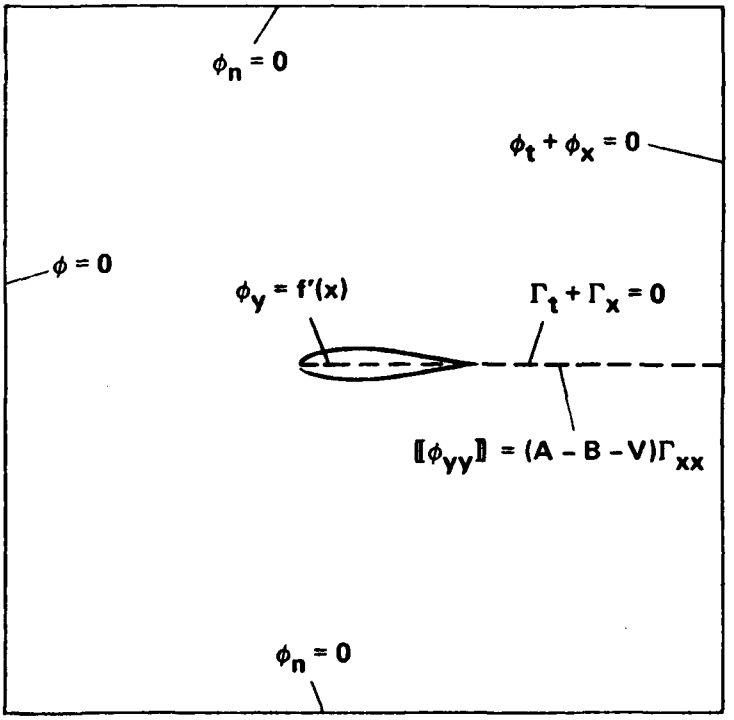

Figure 1.- Small disturbance boundary conditions.

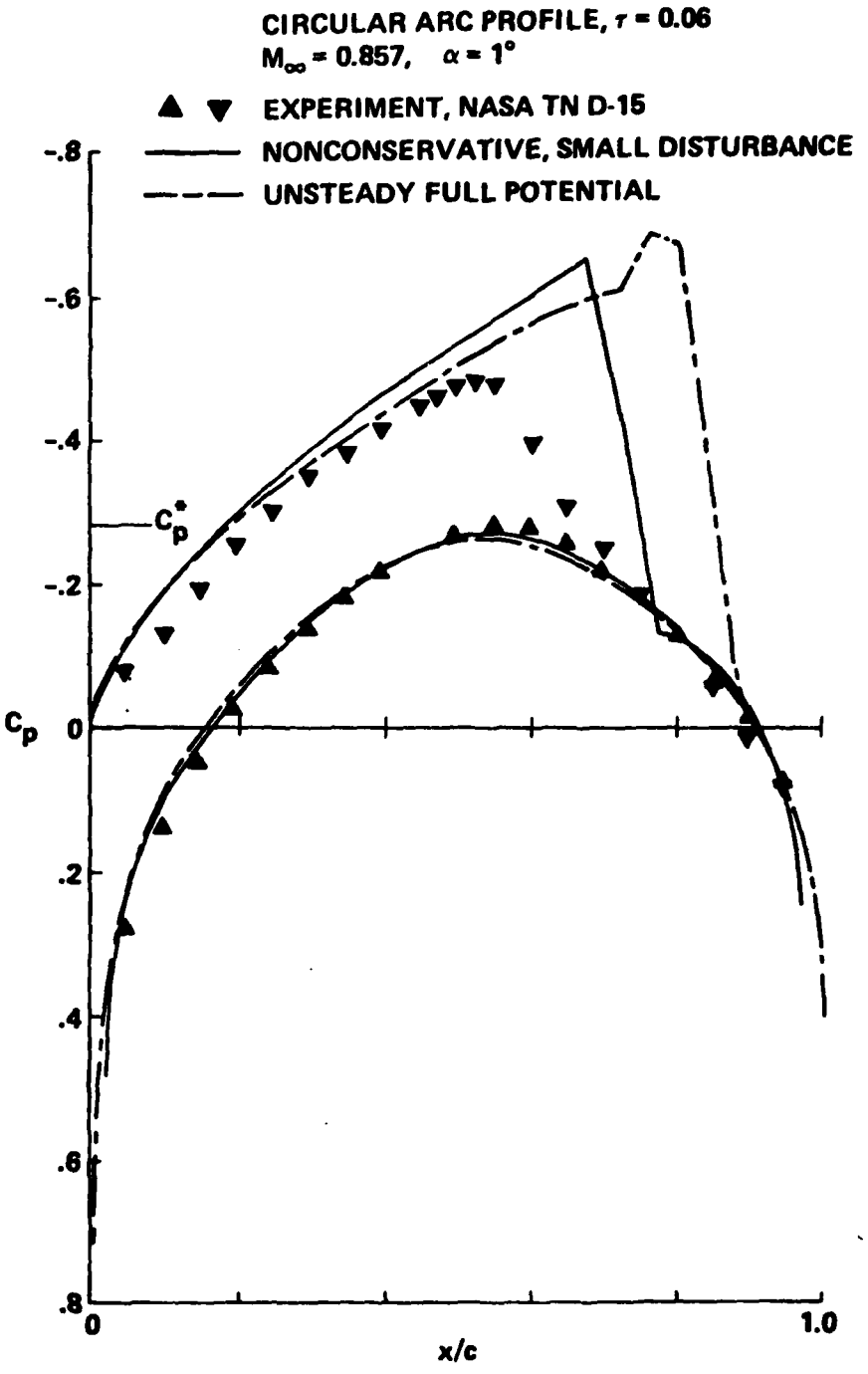

Figure 2.- Steady state flow about biconvex airfoil.

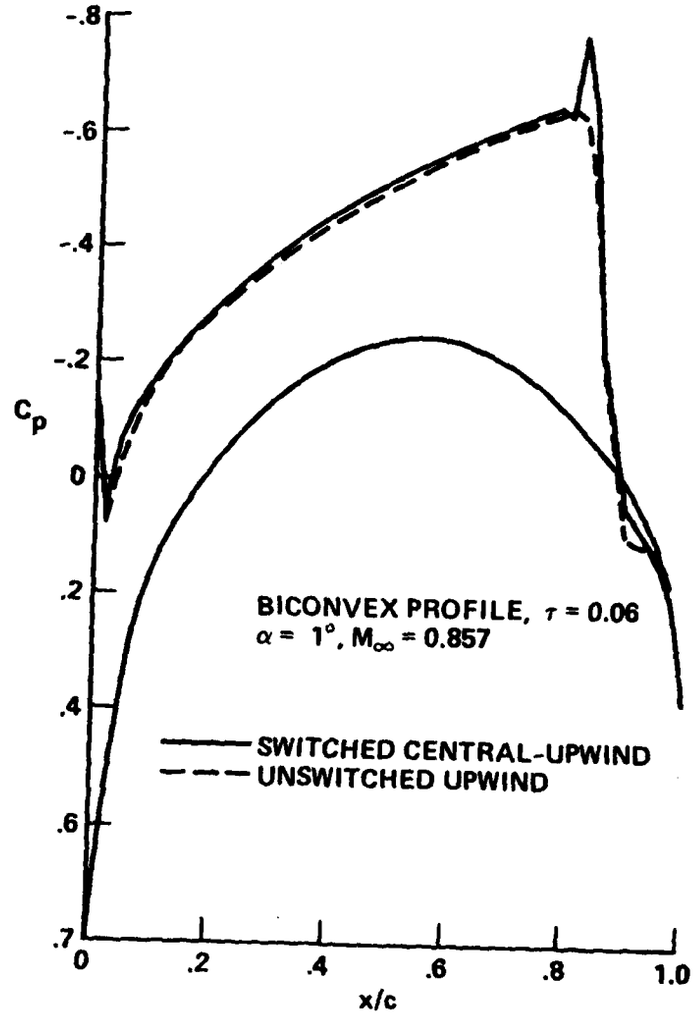

Figure 3.- Comparison of solutions obtained with $\theta = 1.8$ in Eq. 17a.

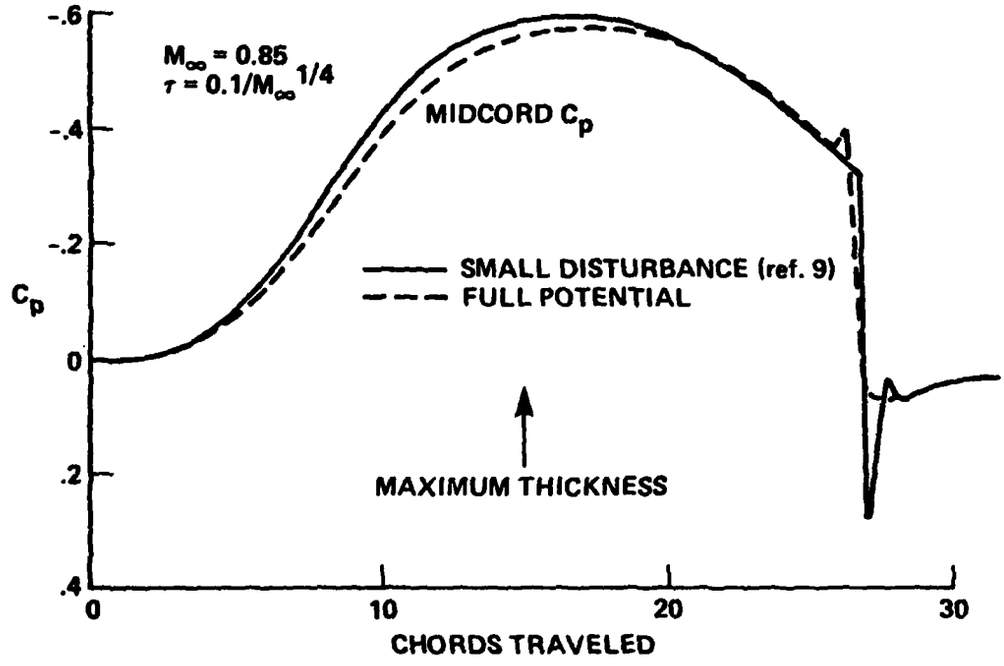

Figure 4.- Midchord pressure variation for a thickening-thinning parabolic arc airfoil.

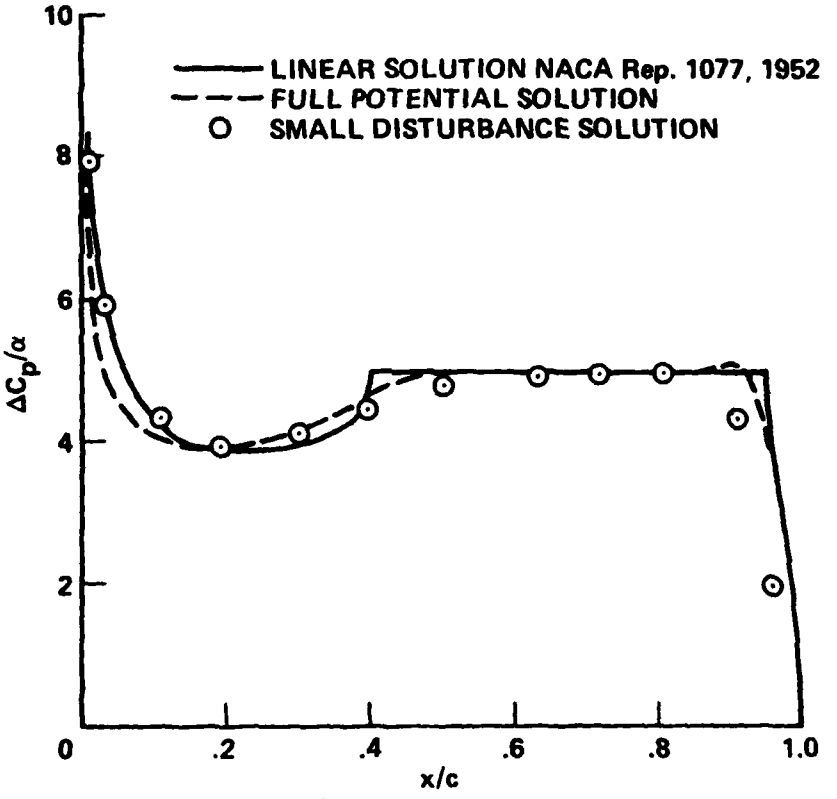

(a) M_∞ = 0.8, 0.2 chords of travel.

Figure 5.- Impulsively plunged flat plate.

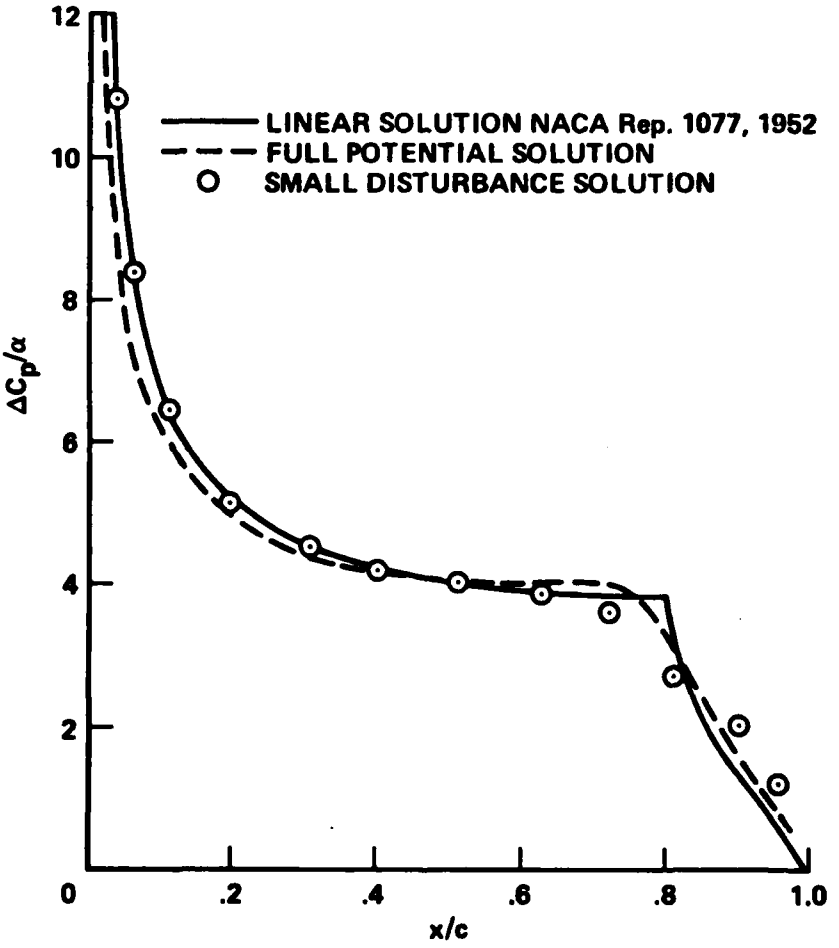

(b) M_∞ = 0.8, 0.8 chords of travel.

Figure 5.- Continued.

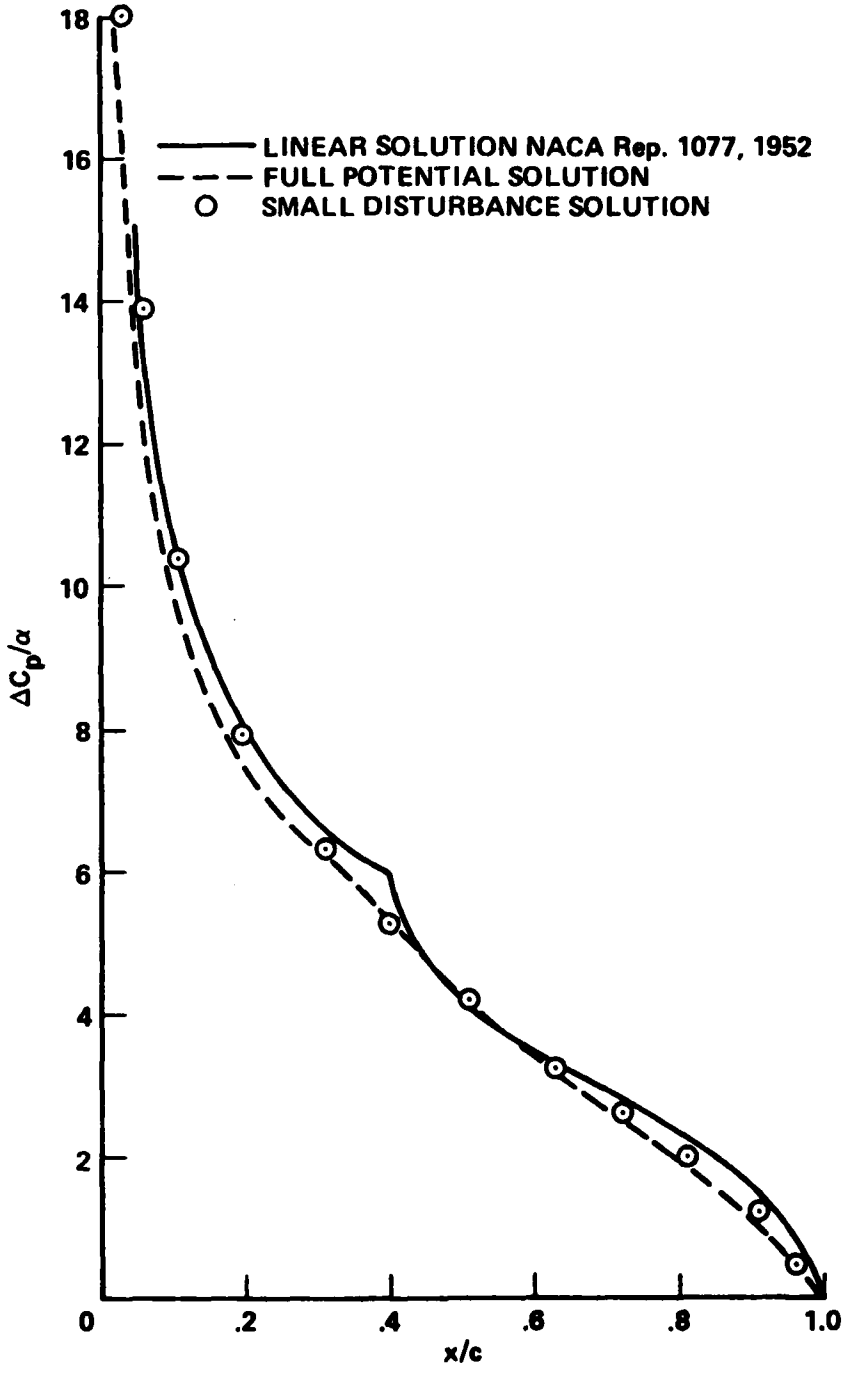

(c) M_∞ = 0.8, 2.4 chords of travel.

Figure 5.- Concluded.

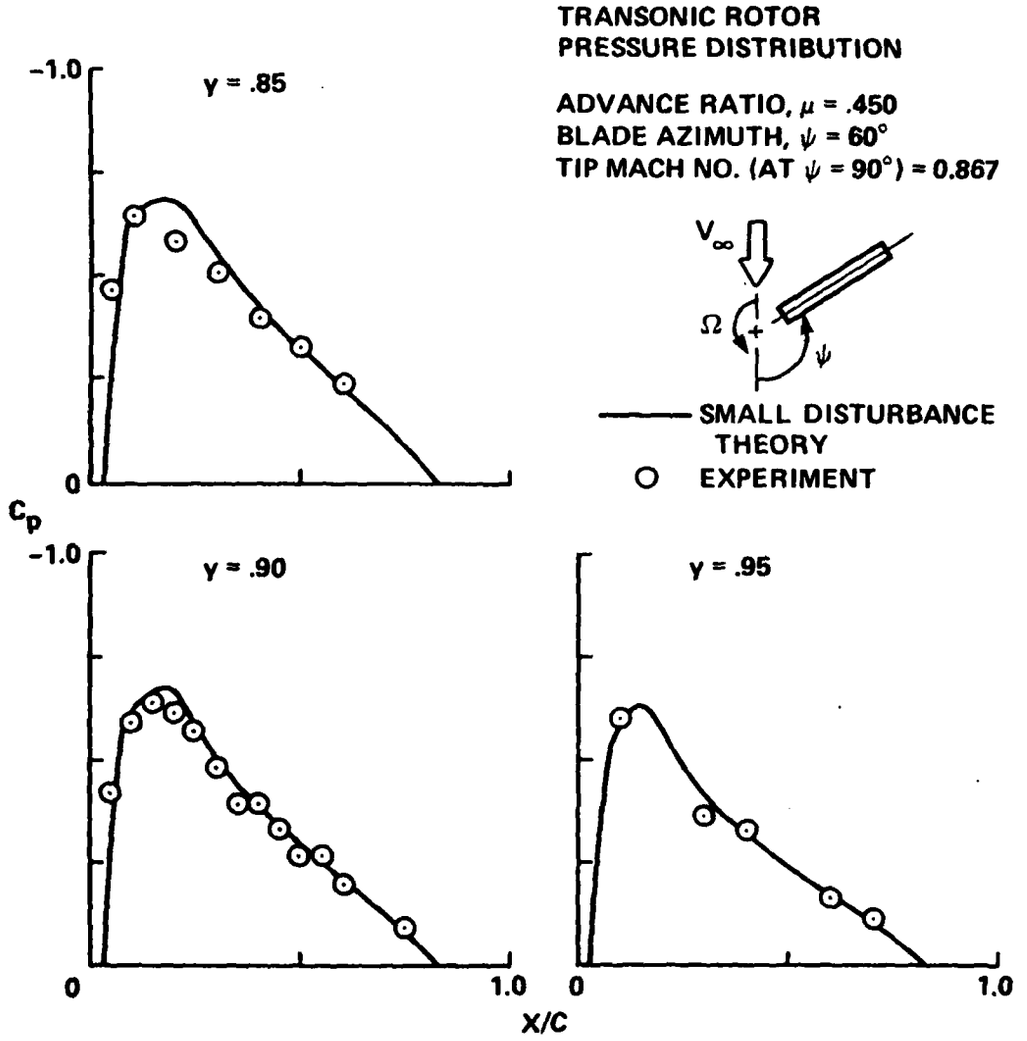

Figure 6.- Transonic rotor pressure distribution.

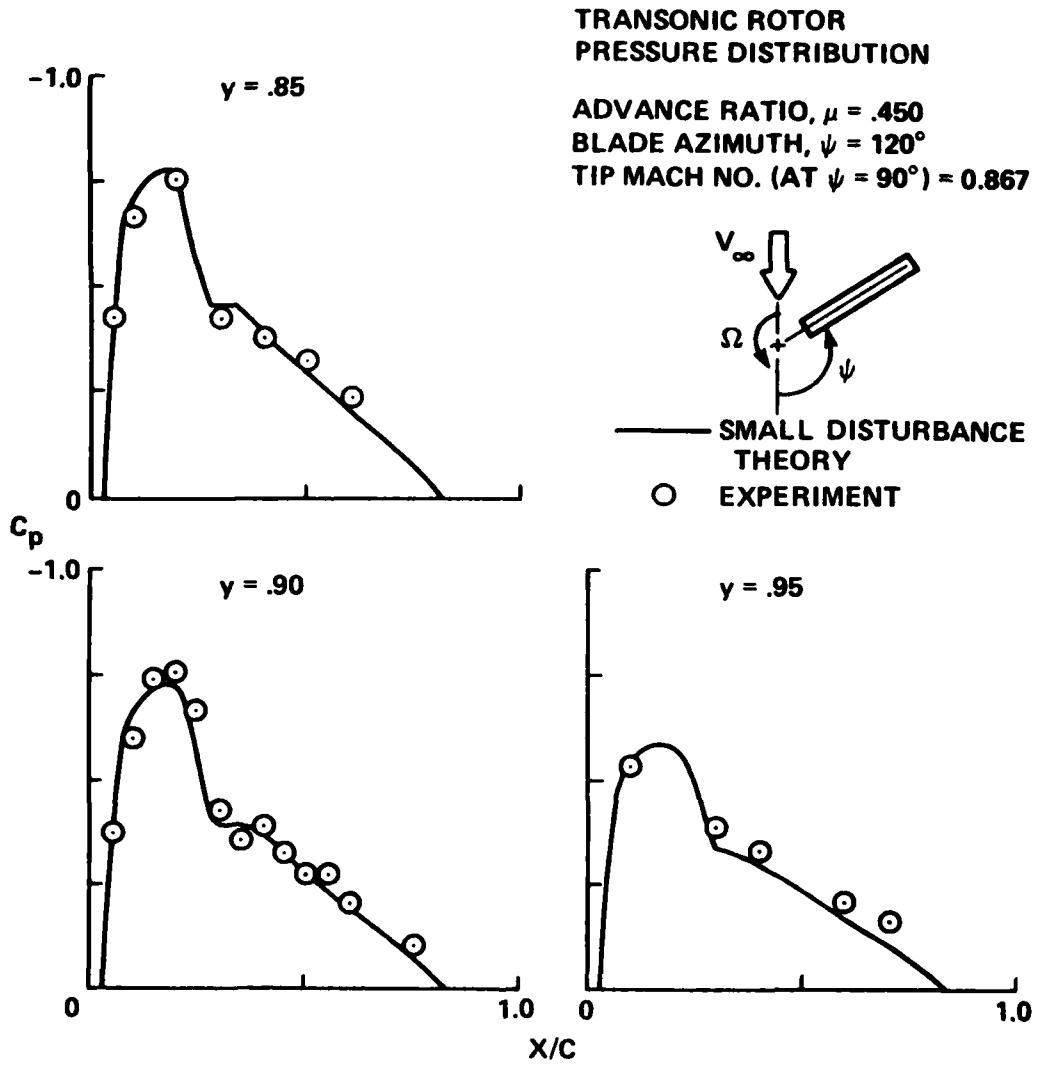

Figure 7. Transonic rotor pressure distribution.

Sharp Discontinuity Tracking Applied To Explosion Problems*

Gregory R. Shubin

Applied Mathematics Branch (R44)
Naval Surface Weapons Center
Silver Spring, Maryland 20910

February, 1980

0. Abstract

Explosion dynamics problems involve the propagation and interaction of shocks and contact discontinuities, usually in several space dimensions. Since standard finite difference methods which smear these discontinuities do not give sufficiently accurate results, a sharp discontinuity tracking method which explicitly follows the surfaces of discontinuity has been developed. This method is applied to explosion problems in one and two space dimensions.

*This material has appeared as NSWC/WOL TR 78-186

1. INTRODUCTION

Many problems of interest involve the propagation of blast waves arising from explosions, and the interaction of these waves with boundaries. In principle, a computational solution of this fluid dynamics problem should provide a cost-effective alternative to expensive physical experimentation. In reality, the computational problem is an extremely difficult one which involves the propagation and interaction of various discontinuities, both shock waves and contact discontinuities (often, interfaces between different materials), in more than one space dimension. It is of practical interest to get accurate results for the shock pressure profile (especially the peak pressure) and also to correctly predict the motion of material interfaces which significantly affect the flow field.

Most finite difference methods currently in use (both Lagrangian and Eulerian) for these explosion problems use either explicit or implicit artificial viscosity to spread or smear shocks over several computational mesh points. This falsifies the peak shock pressure and impulse. To obtain sufficient accuracy, it is necessary to use a very large number of mesh points, which becomes prohibitive for complicated multidimensional problems. While pure Lagrangian methods can follow material interfaces well and can allow areas of fine resolution to move with the fluid, they ultimately tend to break down because severe material deformation leads to distorted computational meshes. Pure Eulerian methods can handle distortion and internal slip but produce diffusion of material interfaces and do not readily allow localized resolution.

This research is aimed at developing a numerical method called "sharp discontinuity tracking" which will follow shocks and contact discontinuities accurately without introducing smearing or computational oscillations. While the method is specifically designed to handle the problem of determining the pressure history under water due to a chemical explosion in air above a water surface (herein called the "EAAW problem"), it should be applicable to other explosion dynamics problems of interest. This method allows for adequate computational resolution of physically small or shrinking regions which contain important physical phenomena, such as the air region between the expanding explosive gases and the water surface in the EAAW problem just described.

The present method is based partly on the work of Solomon et al. [References 1,2] who developed a computational method for predicting the three-dimensional steady supersonic flow field over reentry vehicles at angles of attack. Since such a steady flow problem is hyperbolic with the axial direction being a time-like coordinate, it is similar to the two-dimensional axisymmetric unsteady flow case considered here.

2. COMPUTATIONAL METHOD

A. OVERVIEW OF METHOD. The method of sharp discontinuity tracking is a finite difference method for obtaining approximate solutions of the nonlinear system of hyperbolic conservation laws (partial differential equations) which describe inviscid fluid dynamics. The proposed methodology is distinct from the usual finite difference methods since it defines explicit surfaces in the computational field which represent physical discontinuities, both shock waves and contact discontinuities. A special system of finite difference equations governs the motion of these surfaces and exactly enforces the physical boundary conditions which must hold across the discontinuities. No finite differences are taken across these surfaces. Since the discontinuities are perfectly sharp, interactions can be treated by locally exact methods. In practice it proves useful to perform a time-dependent coordinate transformation to obtain a regular mesh in which the contact surfaces are always coordinate lines and the shocks "float" through the Eulerian mesh. The regions of relatively smooth flow between the discontinuities can be accurately handled by standard second order accurate finite difference methods.

The surfaces of discontinuity represent physical shock waves and contact discontinuities. The motion of these surfaces is determined by the physical conditions which must hold across the surfaces and is also influenced by the surrounding fluids. The correct conditions linking the values of flow variables on either side of the surfaces are the Rankine-Hugoniot jump conditions for a shock, and the equality of pressure and normal particle velocity for a contact discontinuity. The surrounding fluid can influence the surface only in certain ways determined by the theory of characteristics for a system of hyperbolic partial differential equations. By selecting appropriate admissible characteristic compatibility relations and combining them with the correct physical boundary conditions, one obtains a system of differential equations which governs the motion of the surface and gives the flow variables on either side as a function of time. These differential equations are then discretized to give a system of finite difference equations for advancing the discontinuity in time.

The surfaces of discontinuity move relative to each other and will in general collide and interact. Where they meet they are locally plane and the values of flow variables on either side are explicitly known. The interaction then reduces to an algebraic problem of finding a configuration of transmitted and reflected discontinuities which satisfy all of the necessary conditions in the infinitesimal neighborhood surrounding the point of intersection. This locally exact solution is explicitly inserted into the computed flow field.

B. GOVERNING EQUATIONS FOR AXISYMMETRIC FLOW

The equations of inviscid unsteady flow are written in spherical coordinates r,θ,ϕ (Figure 1) for an axisymmetric problem ($\partial/\partial\phi \to 0$, $r \geq 0$, $0 \leq \theta \leq \pi$) as the following system of weak conservation laws:

$$\frac{\partial U}{\partial t} + \frac{\partial F}{\partial r} + \frac{\partial G}{\partial \theta} + H = 0 \tag{1}$$

where

$$U = r^2 \sin\theta \begin{pmatrix} \rho \\ \rho u \\ \rho v \\ \rho E \end{pmatrix} \qquad F = r^2 \sin\theta \begin{pmatrix} \rho u \\ \rho u^2 + p \\ \rho uv \\ u(\rho E + p) \end{pmatrix}$$

$$G = r\sin\theta \begin{pmatrix} \rho v \\ \rho uv \\ \rho v^2 + p \\ v(\rho E + p) \end{pmatrix} \qquad H = \begin{pmatrix} 0 \\ -(2p + \rho v^2) r\sin\theta \\ -r(p\cos\theta - \rho uv\sin\theta) \\ 0 \end{pmatrix} \tag{2}$$

Here ρ is the density, u is the r-component of velocity, v is the θ-component of velocity, e is the specific internal energy, and $E = e + (u^2+v^2)/2$ is the total specific energy. The pressure p is given by an equation of state for each fluid (see References 5,8 for equations of state for pentolite, air, and water) in the form

$$p = p(\rho, e) \tag{3}$$

A "main" shock wave is defined by the surface $r = s(\theta,t)$ and contact discontinuities are given as $r = c_i(\theta,t)$, $i = 1,2,\cdots I$. For the explosion in air above water, $I = 2$ and c_1 is the contact surface separating the explosive gas products from air, while c_2 is the air-water surface (plus an appropriate closure for large θ, see Figure 1). The main shock is, in general, partially in air and partially in water. These major discontinuities s and c_i are unknowns whose position and velocity is known at time = 0 and which must be advanced in time by the solution procedure. "Secondary" shocks and contact discontinuities deemed to be of less physical importance are allowed to be smeared out by the conservative finite difference scheme used for interior mesh points, as discussed below.

It is noted that the choice of the form of equations system (1) eliminates the need to specify boundary conditions on $r = 0$ and on the symmetry boundaries $\theta = 0,\pi$ since the unknown U is identically zero there. This is consistent with the fact that by symmetry, $u = v = 0$ at $r = 0$ and $v = 0$ on $\theta = 0,\pi$. However, as formulated here, the values of the primitive flow variables must be found on $\theta = 0,\pi$ in order to implement the shock and contact surface treatments. This is accomplished by solving a special set of equations which hold only on $\theta = 0$ and $\theta = \pi$; these equations are obtained by dividing (1) by $\sin\theta$ and using L'Hopital's rule to evaluate the limits $\theta \to 0,\pi$.

C. COMPUTATIONAL PROCEDURE

The computational field is viewed as being composed of regions of relatively smooth flow which are separated from each other by explicit discontinuities--either shocks or contact discontinuities. It is convenient to employ a time dependent transformation which always maps the contact discontinuities c_1, which are single-valued, piecewise smooth curves in physical space, into coordinate lines in computational space (Figure 1). It will be seen that, for the explosion in air above water (EAAW), this has the advantage of preserving computational resolution in the air region $c_1 \leq r \leq c_2$, even if $c_2 - c_1$ becomes small.

The transformation from physical to computational space is given generally as

$$\begin{aligned} X &= X(r,\theta,t) \\ Y &= Y(\theta) \\ T &= t \end{aligned} \tag{4}$$

and the governing partial differential equations (1) are expressed in the transformed computational space (X,Y,T) as

$$\frac{\partial U}{\partial T} + \frac{\partial \tilde{F}}{\partial X} + \frac{\partial \tilde{G}}{\partial Y} + \tilde{H} = 0 \tag{5}$$

where

$$\begin{aligned} \tilde{F} &= X_t U + X_r F + X_\theta G \\ \tilde{G} &= Y_\theta G \\ \tilde{H} &= H - \frac{\partial X_t}{\partial X} U - \frac{\partial X_r}{\partial X} F - \left(\frac{\partial X_\theta}{\partial X} + \frac{\partial Y_\theta}{\partial Y} \right) G \end{aligned} \tag{6}$$

Once a specific choice of transformation (4) is made, the quantities $X_t, X_r, X_\theta, Y_\theta$, and their partial derivatives are given explicitly in terms of $s(\theta,t)$, $c_1(\theta,t)$, and their partial derivatives.

For the EAAW problem, convenient choices of the transformation X are:

$$\begin{array}{ll} \text{gas region:} \\ 0 \le r \le c_1(\theta,t) & X = \dfrac{r}{c_1(\theta,t)} \\ \\ \text{air region:} \\ c_1(\theta,t) \le r \le c_2(\theta,t) & X = 1 + (k_1-1)\left[\dfrac{r-c_1(\theta,t)}{c_2(\theta,t)-c_1(\theta,t)}\right] \\ \\ \text{water region:} \\ c_2(\theta,t) \le r & X = k_1+k_2[r-c_2(\theta,t)] \end{array} \qquad (7)$$

so that $r = c_1(\theta,t)$ is mapped into $X = 1$, and $r = c_2(\theta,t)$ is mapped into $X = k_1$. Then for a given number of mesh points in the X-direction in the explosive gas region, the choices of k_1 and k_2 give the relative computational resolution in the air and water regions respectively. A convenient choice of the transformation Y is (in inverted form)

$$\theta = \pi\left(\frac{\omega^Y - 1}{\omega - 1}\right)$$

where ω is a parameter which gives graded resolution in physical space with finest resolution near $\theta = 0$ if $\omega > 1$.

A mesh function $U^k_{m,n,j}$ is defined on the uniform computational mesh

$$\text{for } j=1,2,3 \quad \begin{cases} X = m\Delta X & m = 0,1,2,\cdots,M(j) \\ Y = n\Delta Y & n = 0,1,2,\cdots,N \\ T = T_o+k\Delta T & k = 0,1,2,\cdots \end{cases}$$

where $m(1)\Delta X = 1$, $m(2)\Delta X = k_1 - 1$, $N\Delta Y = 1$, and $j=1,2,3$ for the regions of explosive gas, air, and water respectively (Figure 1). The main shock defined by $r = s(\theta,t)$ in physical space "floats" through the uniform mesh and is represented by special mesh points which are located on Y = constant lines.

It is assumed that initial data (see, e.g., Reference 8) is given $T = T_o$ for $\rho,u,v,e,p,c_i(\theta,t_o)$ and $s(\theta,t_o)$ on the spatial mesh defined above. In order to advance the solution to $T_o + \Delta T$, procedures must be given for

(i) "interior" points ($1 \le m \le M(j) - 1$, $1 \le n \le N - 1$)

(ii) points on the symmetry boundaries $\theta = 0,\pi$ ($n = 0,N$)

(iii) shock points

(iv) contact discontinuity points ($j = 1$, $m = M(1)$; $j = 2$, $m = 1$ and $m = M(2)$; $j = 3$, $m = 1$)

(v) interactions between a shock and a contact discontinuity

The solution at all points is advanced in time using finite difference predictor-corrector methods. For the interior points (i), the equations (5) are discretized and standard MacCormack [Reference 9] schemes (in this case, predictor forward differencing and corrector backward differencing in both X and Y) are used to advance the conservation vector U. The primary flow variables are easily recovered from the definition of U and the equations of state. Points on the symmetry planes (ii) are advanced in the same way, only the governing equations must be modified (as described above) before discretization. The procedures for advancing the remaining points, namely those at the shock, the contact discontinuities, and the points of discontinuity interaction, are described later.

The MacCormack finite difference scheme was chosen for its second order accuracy and its good "shock-capturing" properties (ability to reasonably smear out a shock over several mesh points), but any other predictor-corrector method could be used. For very strong captured shocks, such as the secondary shock which implodes on the origin in a spherical explosion, it is necessary to implement a computational "filter" (similar to that in Reference 10) to limit captured shock steepening. Any other shock capturing "improvement" may also be included.

Computational stability demands that ΔT be suitably restricted. A necessary (but not sufficient [Reference 11]) criterion can be derived using a geometric argument which requires that the domain of dependence of the "linearized" differential equations be contained in the domain of dependence of the finite difference equations. When this criterion is used with a multiplicative safety factor of .9, no instability is observed in actual computation.

D. ADVANCING THE MAIN SHOCK AND CONTACT DISCONTINUITIES

A crucial requirement of the present computational method is to provide an appropriate numerical treatment of the explicit surfaces which represent shocks or contact discontinuities. The known physical boundary conditions, namely the Rankine-Hugoniot jump conditions and the equality of tangential velocity across a shock, and the equality of pressure and normal velocity across a contact discontinuity, must hold exactly. However, these boundary conditions alone are not sufficient to provide equations for advancing the surface in time, but must be considered along with appropriate information obtained from the governing PDE system (1). From the theory of characteristics for hyperbolic systems of PDE's, one can derive characteristic compatability conditions (see Reference 12) which are associated with certain bicharacteristic directions. Admissible characteristic relations, that is, those associated with directions pointing away from the surface in the negative time direction, effectively determine the influence of the surrounding fluid upon the discontinuity. In the manner introduced by Kentzer (Reference 13) and used by Solomon et al. (References 1, 2), it is possible to combine the physical boundary conditions with the correct characteristic compatibility relations to obtain a system of PDE's which hold only on the surface. A finite difference approximation of these equations then provides the algorithm for advancing the surface, and the flow properties on either side, in time.

(i) CONTACT DISCONTINUITY. A contact discontinuity (c.d.) $r = c(\theta,t)$ is a material surface for the fluids on either side of the discontinuity. Hence

$$c_t - u + \frac{c_\theta}{c} v = 0 \tag{8}$$

holds at a c.d. (subscripts t,θ indicate partial derivatives). There are three admissable characteristic compatability relations which hold on each side (left and right) of the surface. Two relations correspond to a streamline and one to the Mach conoid. These compatability relations are of the form

$$\frac{\partial p}{\partial T} - A_1 \frac{\partial \rho}{\partial T} = R_1 \tag{9}$$

$$\frac{\partial}{\partial T} (D_c q_{tang}) - u \frac{\partial}{\partial T}\left(\frac{c_\theta}{c}\right) = R_2 \tag{10}$$

$$A_2 \frac{\partial p}{\partial T} + A_3 \left[\frac{\partial c_t}{\partial T} + v \frac{\partial}{\partial T}\left(\frac{c_\theta}{c}\right)\right] = R_3 \tag{11}$$

It is emphasized that (9)-(11) hold on each side of the surface, and hence represent six equations. R_1 and R_2 contain derivatives interior to the surface (Y-derivatives) and undifferentiated quantities evaluated at the surface, while R_3 contains additionally X-derivatives. A_1, A_2, and A_3 contain only undifferentiated quantities, and $D_c^2 = 1 + \left(\frac{c_\theta}{c}\right)^2$. The actual A_i and R_i are given in Appendix A. The pressure p and the normal velocity $q_{norm} = \frac{c_t}{D_c}$ are constant across the c.d., while the density ρ, energy e, and tangential velocity q_{tang} can sustain jumps.

In addition to the characteristic compatability relations we have the equation

$$\frac{\partial}{\partial T}\left(\frac{c_\theta}{c}\right) = \frac{Y_\theta}{c}\left[\frac{\partial c_t}{\partial Y} - \frac{c_t}{c}\frac{\partial c}{\partial Y}\right] \tag{12}$$

which expresses, through the chain rule, the equality of cross partials $\frac{\partial c_\theta}{\partial t} = \frac{\partial c_t}{\partial \theta}$. Also

$$\frac{\partial p}{\partial T} = \kappa_1 \frac{\partial \rho}{\partial T} + \kappa_2 \frac{\partial e}{\partial T} \tag{13}$$

holds on each side, where $\kappa_1 = \left(\frac{\partial p}{\partial \rho}\right)_e$ and $\kappa_2 = \left(\frac{\partial p}{\partial e}\right)_\rho$ are given by the appropriate equations of state. A procedure is now clear for advancing the c.d., since equations (9)-(13) provide nine equations in the nine unknowns which are (the time derivatives of) $c_t, c_\theta, p, [\rho, e, q_{tang}]_{Left}, [\rho, e, q_{tang}]_{Right}$.

(ii) SHOCK. A shock $r = s(\theta,t)$ is a surface across which the Rankine-Hugoniot jump conditions hold, namely

$$\rho Q_{norm} = \text{constant} \tag{14}$$

$$p + \rho Q_{norm}^2 = \text{constant} \tag{15}$$

$$e + p/\rho + Q_{norm/2}^2 = \text{constant} \tag{16}$$

where q_{norm} is the velocity normal to the shock in (r,θ) coordinates, $D_s = 1 + \left(\frac{s_\theta}{s}\right)^2$ and $Q_{norm} = q_{norm} - \frac{s_t}{D_s}$ is the relative velocity normal to the moving shock surface. Additionally, the tangential velocity is unchanged across a shock,

$$q_{tang} = \text{constant} \tag{17}$$

Only shocks moving into undisturbed fluid are considered here. For this case, there is only one admissible characteristic compatability relation, and it corresponds to a Mach conoid on the disturbed (high pressure) side of the shock. The compatability condition is of the form

$$\frac{\partial p}{\partial T} + A_4 \frac{\partial q_{norm}}{\partial T} = R_4 \tag{18}$$

where R_4 contains derivatives in the X-direction, derivatives interior to the shock, and undifferentiated quantities. (See Appendix A). Differentiating (14)-(16) with respect to T and solving for $\frac{\partial p}{\partial T}$ and $\frac{\partial q_{norm}}{\partial T}$, it is possible to rewrite (18) as

$$A_5 \left[\frac{\partial s_t}{\partial T} - A_6 \frac{\partial}{\partial T}\left(\frac{s_\theta}{s}\right)\right] = R_4 \tag{19}$$

where A_5 and A_6 contain only undifferentiated quantities. The equality of cross partials, expressed through the chain rule, is of the form

$$\frac{\partial}{\partial T}\left(\frac{s_\theta}{s}\right) = R_5 \tag{20}$$

so that (19) and (20) provide equations for advancing s_θ and s_t. It is then easy to get the advanced value of q_{norm} and use the Hugoniot conditions (14)-(16) to solve for all properties behind the shock.

(iii) COMMENTS. For either a shock or a c.d., we have a system of PDE's for advancing (in time) the surface and the flow variables on either side. These equations are implemented with a predictor-corrector finite difference method. Spatial differencing internal to the surface is handled in the usual predictor-forward, corrector-backward way. However, differencing in the X-direction requires special treatment since no differences can be taken across the discontinuity. Thus at the left side of discontinuities the differencing is always backward (both predictor and corrector), whereas on the right side the differencing is always forward. This procedure is only first order accurate, but it is possible (Reference 14) to add a correction term to achieve overall second order accuracy.

At the shock, finite differences are taken on a non-uniform mesh, but again it is possible to secure second order accuracy by adding a correction term. Additionally, since the shock is moving into a previously undisturbed fluid where there are no mesh points, it is necessary to insert new mesh points behind the advancing shock. This is done by quadratic interpolation of the conservation vector U using the known primary flow variables at the shock and the values of U at the mesh points along Y = constant lines behind the shock.

E. INTERACTIONS

Since the sharp discontinuity tracking method treats physically important discontinuities as explicit surfaces, it is necessary to analyze the situation which occurs when two such discontinuities interact. Considered here is the case of an air shock hitting the air-water surface obliquely. It appears that the qualitative nature of the resulting physical phenomena depends upon the incident shock strength and the angle at which the discontinuities meet [Reference 7]. For sufficiently strong shocks and sufficiently small incidence angles α, a "regular refraction" solution exists as shown in Figure 2. In a coordinate system moving along the surface with point A, the flow is pseudo-steady. Assuming locally constant states near A and locally plane discontinuities, the problem is reduced to an algebraic one of finding the twelve unknowns (ρ,u,v,e,p in regions 3 and 4, β,γ) which satisfy twelve nonlinear equations (Rankine-Hugoniot jump conditions and constancy of tangential velocity across each of R and W, state equations in regions 3 and 4, contact discontinuity conditions across the disturbed water surface).

This locally exact solution gives the necessary information to track the transmitted water shock W and the disturbed air-water interface. At present the reflected shock is allowed to be smeared out by the MacCormack finite differencing, but there is no conceptual difficulty in explicitly tracking R as well.

3. RESULTS

A. ONE DIMENSIONAL. The shock tracking method has been used successfully [1,3] in treating aerodynamic problems, but apparently has never been applied to multidimensional explosion problems. Our first efforts, however, were to develop the tracking method for spherical explosion problems in one space dimension and time. In this case, the formulation of Section 2B holds with the simplification $v = 0$, $\theta = \frac{\pi}{2}$. This type of test problem is ideally suited for the standard Lagrangian finite difference approach (as contrasted with our methods which are essentially Eulerian) since mesh distortion is no problem in one dimension. Furthermore, there are special features of the one dimensional problem which could be exploited to obtain increased computational accuracy. However, since our goal is to develop methods for multiple space dimensions, we did not employ any techniques in the one dimensional testing which wouldn't be readily extendable to more space dimensions. The following cases have been computed:

(i) Spherical Explosion of Pentolite in Water. The sequence of physical events is described in detail in [Reference 4]. Briefly, it is assumed that a pentolite sphere is centrally detonated and that the flow field is known at the instant that the detonation wave reaches the surface of the sphere ("Taylor wave" solution). At this instant a blast wave begins moving out radially into the water, followed by the contact discontinuity separating the expanding explosive gas bubble from the water. A rarefaction moves back into the explosive gases, followed by the "second shock" which implodes on the sphere's center. Computational results for peak shock pressure vs. radial distance obtained by the present method are compared (Figure 3) with those obtained by Sternberg and Hurwitz [Reference 5]. These latter results are known to agree well with experiment. It is noted that Sternberg used a sharp shock algorithm, but his method is not readily extendable to multiple dimensions. He also took advantage of the fact that, in one space dimension, the initial rarefaction which moves back into the explosive gases can be explicitly inserted into the computation. As this cannot be done in more than one dimension, this possibility was not exploited by the present method. Nevertheless, agreement between the two computational results is excellent (points of comparison other than those shown are equally close).

(ii) Spherical Explosion of Pentolite in $\gamma = 1.4$ Air. This problem is more difficult than the explosion in water case because the initial rarefaction moving back into the explosive gases is considerably stronger. Shown in Figure 4 is a comparison of the computational results for peak shock pressure vs. radius obtained with the present method (40 mesh points in explosive gas, 15 in air when main air shock at 20 charge radii), those obtained by Sternberg and Hurwitz [Reference 5], and a curve fit to experimental data derived by Goodman [Reference 6]. Agreement is generally good, despite the fact that the present method does not explicitly insert the known one dimensional rarefaction solution (as does Sternberg). The pressure profiles as a function of radius at selected times is shown in Figure 5, where the qualitative nature of the interface movement and secondary shock propagation is seen to be correct.

B. TWO DIMENSIONAL AXISYMMETRIC. In two space dimensions, the development of the method is incomplete, so that the entire EAAW problem cannot yet be handled. However, some preliminary results for a spherical explosion in air above a water surface have been obtained. These results are shown in Figures 6 and 7 for a centrally detonated explosion of a pentolite sphere located 30 charge radii above the water surface. The computation used an extremely coarse finite difference mesh composed of about 500 mesh points (approximately 25 points radially on each of 20 θ = constant lines). The 2-D axisymmetric computation was initialized with the 1-D computational results at the instant before the spherical shock hits the water surface. Figure 6 shows the main shock position at this instant and at some later times. Figure 7 shows the pressure vs. radius at these same times along the line $\theta = 0$ (straight down below the charge).

No comparison with experiment is yet possible because the computation has not been carried out sufficiently far in time. Further results cannot be obtained until an analysis is made of the various types of interactions which can occur when an oblique shock hits the water surface. This interaction must be understood in detail because the present computational method requires an explicit local handling of discontinuity interactions. This problem is more difficult than originally anticipated because the family of possible interactions appears to be very complicated, including regular refraction, Mach refraction, and refraction with bound and free precursors [Reference 7]. (So far, only regular refraction has been incorporated in the present method.) Thus this seemingly incidental aspect of the overall EAAW configuration is in fact a difficult fundamental physical problem in and of itself. Nevertheless, the preliminary computational results indicate that, once these local interactions are understood, the present computational method will prove successful for the overall explosion dynamics problem.

REFERENCES

1. Solomon, J. M., et al., "A Program for Computing Steady Inviscid Three-Dimensional Supersonic Flow on Reentry Vehicles, Vol I: Analysis and Programming," NSWC/WOL TR 77-28, 11 Feb 1977.

2. Solomon, J. M., et al., "Inviscid Flowfield Calculations for Reentry Vehicles with Control Surfaces," AIAA Journal, Vol. 15, No. 12, Dec 1977, p. 1742.

3. Moretti, G., "Floating Shock Fitting Technique for Imbedded Shocks in Unsteady Multidimensional Flows," in Proceedings of the 1974 Heat Transfer and Fluid Mechanics Institute, 1974, p. 184.

4. Sternberg, H. M. and Walker, W. A., "Calculated Flow and Energy Distribution Following Underwater Detonation of a Pentolite Sphere," Physics of Fluids, Vol. 14, No. 9, Sep 1971, p. 1869.

5. Sternberg, H. M. and Hurwitz, H., "Calculated Spherical Shock Waves Produced By Condensed Explosives in Air and Water," Proceedings of the Sixth Symposium (International) on Detonation, Coronado, Calif., Aug 1976, p. 528.

6. Goodman, H. J., "Compiled Free-Air Blast Data on Bare Spherical Pentolite," BRL Rept. 1092, Feb 1960.

7. Abd-El-Fattah, A. M., Henderson, L. F., and Lozzi, A., "Precursor Shock Waves at a Slow-Fast Gas Interface," J. Fluid Mech., Vol. 76, 1976, p. 157.

8. Walker, W. A. and Sternberg, H. M., "The Chapman-Jouguet Isentrope and the Underwater Shock Wave Performance of Pentolite," Proceedings of the 4th Symposium (International) on Detonation, ACR-126, U.S. Gov't Printing Office, 1965, p. 27.

9. MacCormack, R. W., "The Effect of Viscosity in Hypervelocity Impact Cratering," AIAA Paper No. 69-354, 1969.

10. Harten, A., "The Artificial Compression Method for Computation of Shocks and Contact Discontinuities. I. Single Conservation Laws," Comm. Pure. Appl. Math, Vol. XXX, 1977, p. 611.

11. Turkel, E., "Phase Error and Stability of Second Order Methods for Hyperbolic Problems I," Journal of Computational Physics, Vol. 15, June 1974, p. 226.

12. Courant, R. and Hilbert, D., Methods of Mathematical Physics, Vol. II, Interscience, N.Y., 1962.

13. Kentzer, C. P., "Discretization of Boundary Conditions on Moving Discontinuities," Lecture Notes in Physics, Vol. 8, Springer-Verlag, 1971, p. 108.

14. Warming, R. F. and Beam, R. M., "Upwind Second-Order Difference Schemes and Applications in Unsteady Aerodynamic Flows," Proceedings of the AIAA 2nd Computational Fluid Dynamics Conference, Hartford, Conn., 1975, p. 17.

Appendix A: A_1 and R_1 appearing in contact discontinuity and shock equations

$$A_1 = a^2 = \kappa_1 + \kappa_2 p/\rho^2 = (\text{speed of sound})^2$$

$$R_1 = -\frac{Y_\theta v}{c}\left[\frac{\partial p}{\partial Y} - a^2\frac{\partial \rho}{\partial Y}\right]$$

$$R_2 = \frac{1}{c}\left\{-Y_\theta\left(\frac{c_\theta v}{c}\frac{\partial u}{\partial Y} + v\frac{\partial v}{\partial Y} + \frac{1}{\rho}\frac{\partial p}{\partial Y}\right) + \frac{c_\theta v^2}{c} - uv\right\}$$

$$A_2 = 1.$$

In A_3 and R_3, the top sign applies for the right side of the contact discontinuity, and the bottom sign applies for the left side.

$$A_3 = \mp\frac{\rho a}{D_c}$$

$$R_3 = -a\left[\mp X_r D_s\frac{\partial p}{\partial X} + \rho a\left(X_r\frac{\partial u}{\partial X} + \frac{X_\theta}{c}\frac{\partial v}{\partial X}\right)\right]$$

$$-\frac{Y_\theta}{c}\left[\left(v \pm \frac{ac_\theta}{cD_c}\right)\frac{\partial p}{\partial Y} + \frac{\rho a}{D_c}\left(\mp v\frac{\partial u}{\partial Y} + \left(D_c a \pm \frac{c_\theta v}{c}\right)\frac{\partial v}{\partial Y}\right)\right]$$

$$-\frac{\rho a}{c}\left[a(2u + v\cot\theta) \pm \frac{v}{D_c}\left(v + \frac{c_\theta}{c}u\right)\right]$$

In R_4 and R_5, Y-differences are taken along the shock.

$$A_4 = \rho a$$

$$R_4 = -\left\{X_r(Q_{norm} + a)\left[D_s\frac{\partial p}{\partial X} + \rho a\left(\frac{\partial u}{\partial X} - \frac{s_\theta}{s}\frac{\partial v}{\partial X}\right)\right]\right.$$

$$+\frac{Y_\theta s}{D_s}\left[\left(D_s v - \frac{as_\theta}{s}\right)\frac{\partial p}{\partial Y} + \rho a\left(v\frac{\partial u}{\partial Y} + \left(D_s a - \frac{s_\theta v}{s}\right)\frac{\partial v}{\partial Y}\right)\right]$$

$$\left.+\frac{\rho a^2}{s}(2u + v\cot\theta)\right\}$$

$$A_5 = \frac{1}{D_s}\,(-\,B_3 + \rho a(1 - B_9))$$

$$A_6 = \frac{s_t s_\theta}{D_s^2 s}$$

where the terms B_3 and B_9 are defined as

$$B_3 = \alpha\left[-\,\kappa_2 Q_{norm}^2\left(\frac{s_t}{D_s}(2\rho_B - \rho) + Q_{norm}\rho_B\right)\right.$$

$$\left. - 2a^2\rho\rho_B\left(\frac{s_t}{D_s} + Q_{norm}\right)\right]$$

$$B_9 = \alpha\left[Q_{norm}\left(1 + \frac{\kappa_2}{\rho}\right)\rho_B\left(Q_{norm} + \frac{2s_t}{D_s}\right)\right.$$

$$\left. - \kappa_2 Q_{norm}\frac{s_t}{D_s} + a^2\rho_B\right]$$

$$\alpha = 1/\rho(a^2 - Q_{norm}^2)$$

and the subscript B refers to the undisturbed state ahead of the advancing shock, whereas unsubscripted variables refer to the disturbed (high pressure) side.

$$R_5 = \frac{Y_\theta}{s}\left(\frac{\partial s_t}{\partial Y} - \frac{s_t}{s}\frac{\partial s}{\partial Y}\right)$$

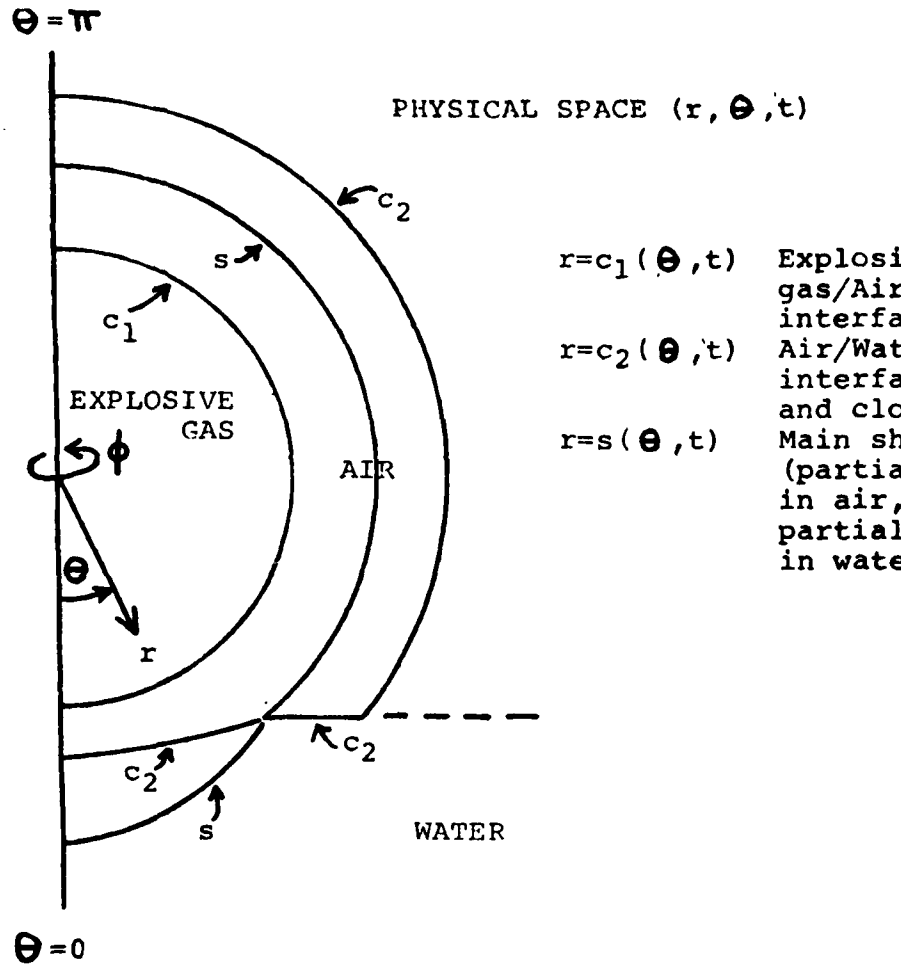

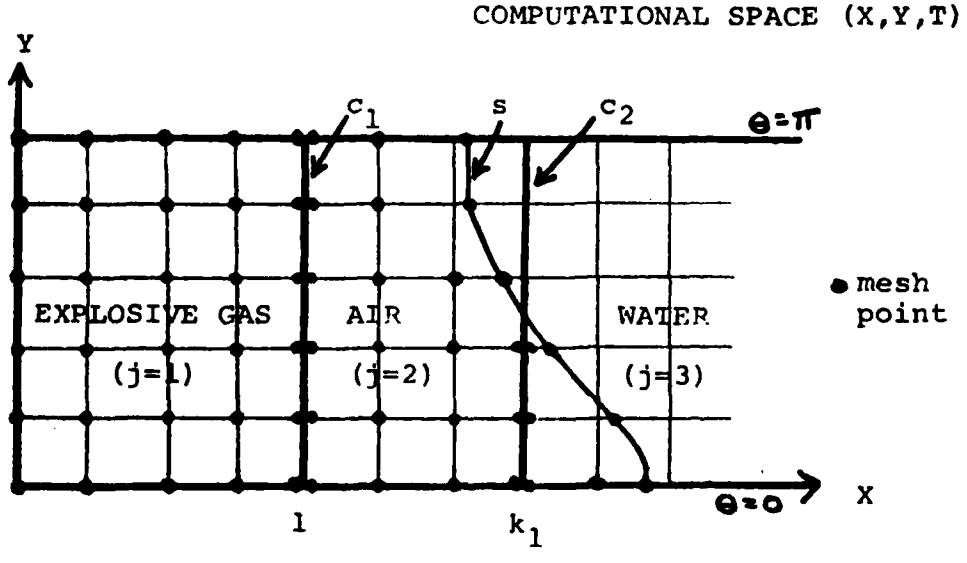

FIGURE 1 PHYSICAL AND COMPUTATIONAL SPACE FOR AXISYMMETRIC PROBLEM OF SPHERICAL EXPLOSION ABOVE AN INITIALLY FLAT WATER SURFACE

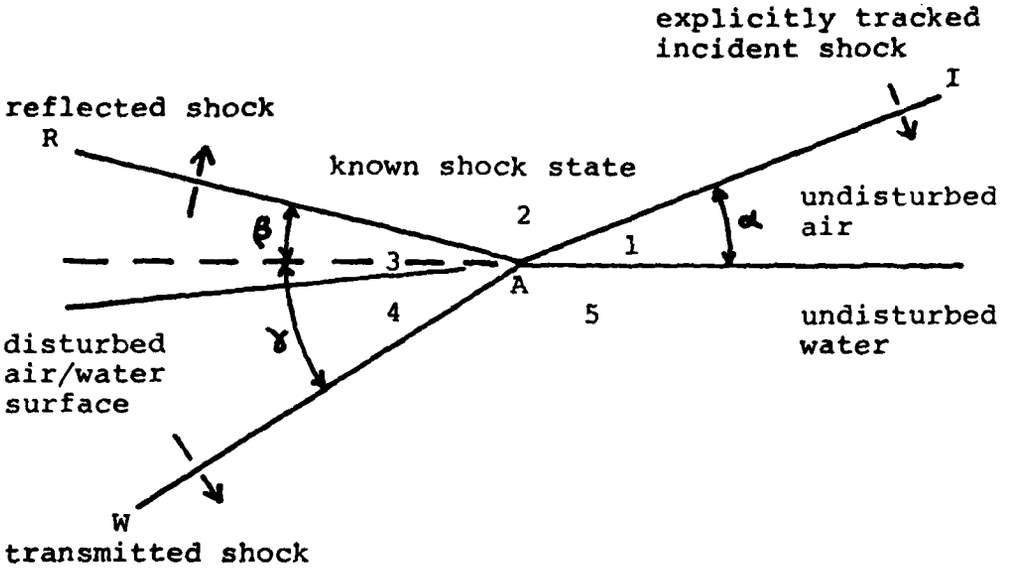

FIGURE 2 REGULAR REFRACTION OF AIR SHOCK AT AIR/WATER INTERFACE

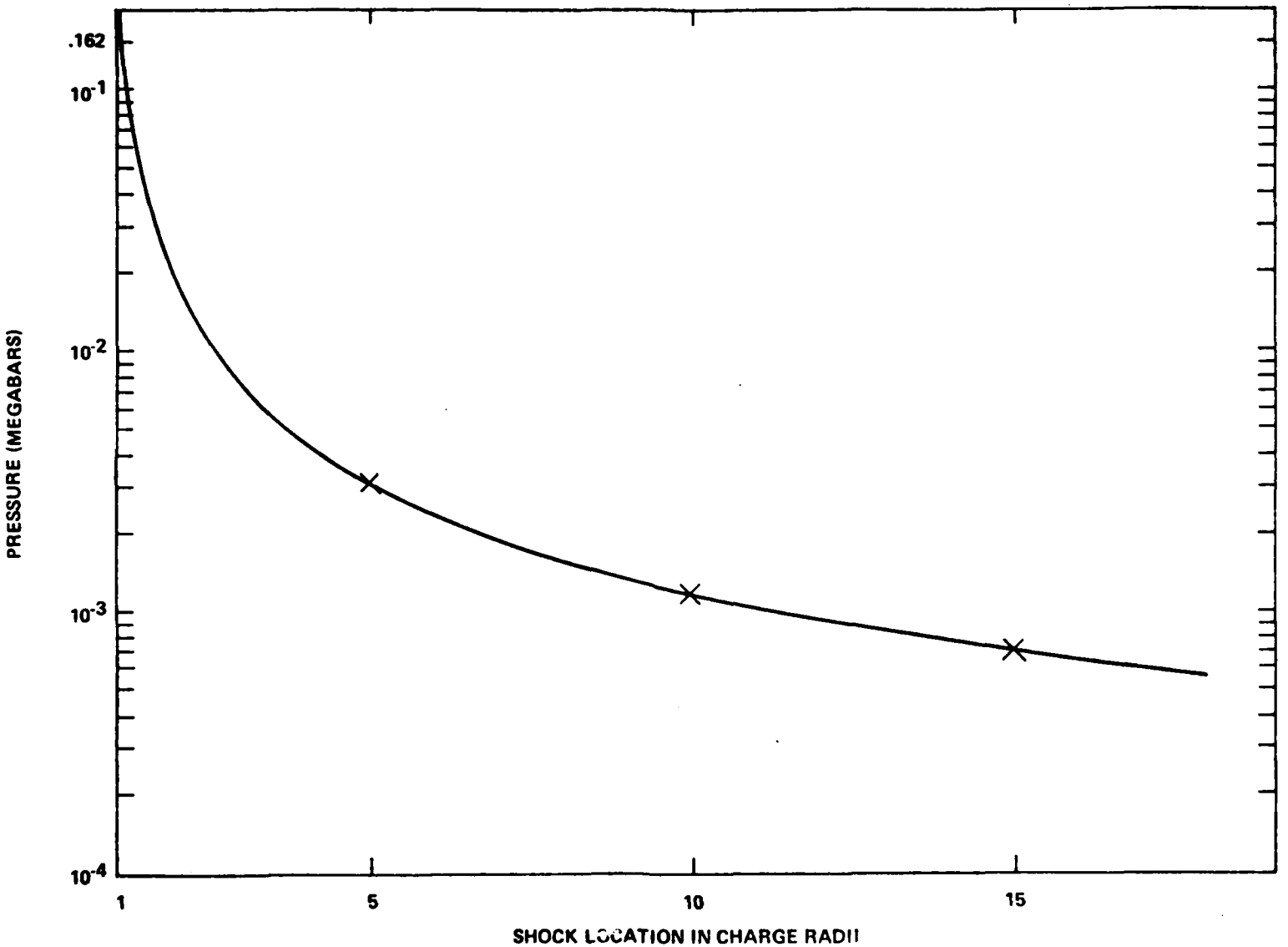

FIGURE 3: COMPUTED SHOCK PRESSURE VS. SHOCK LOCATION PENTOLITE SPHERE CENTRALLY DETONATED IN WATER (X INDICATES STERNBERG/HURWITZ RESULT – OTHER VALUES EQUALLY CLOSE)

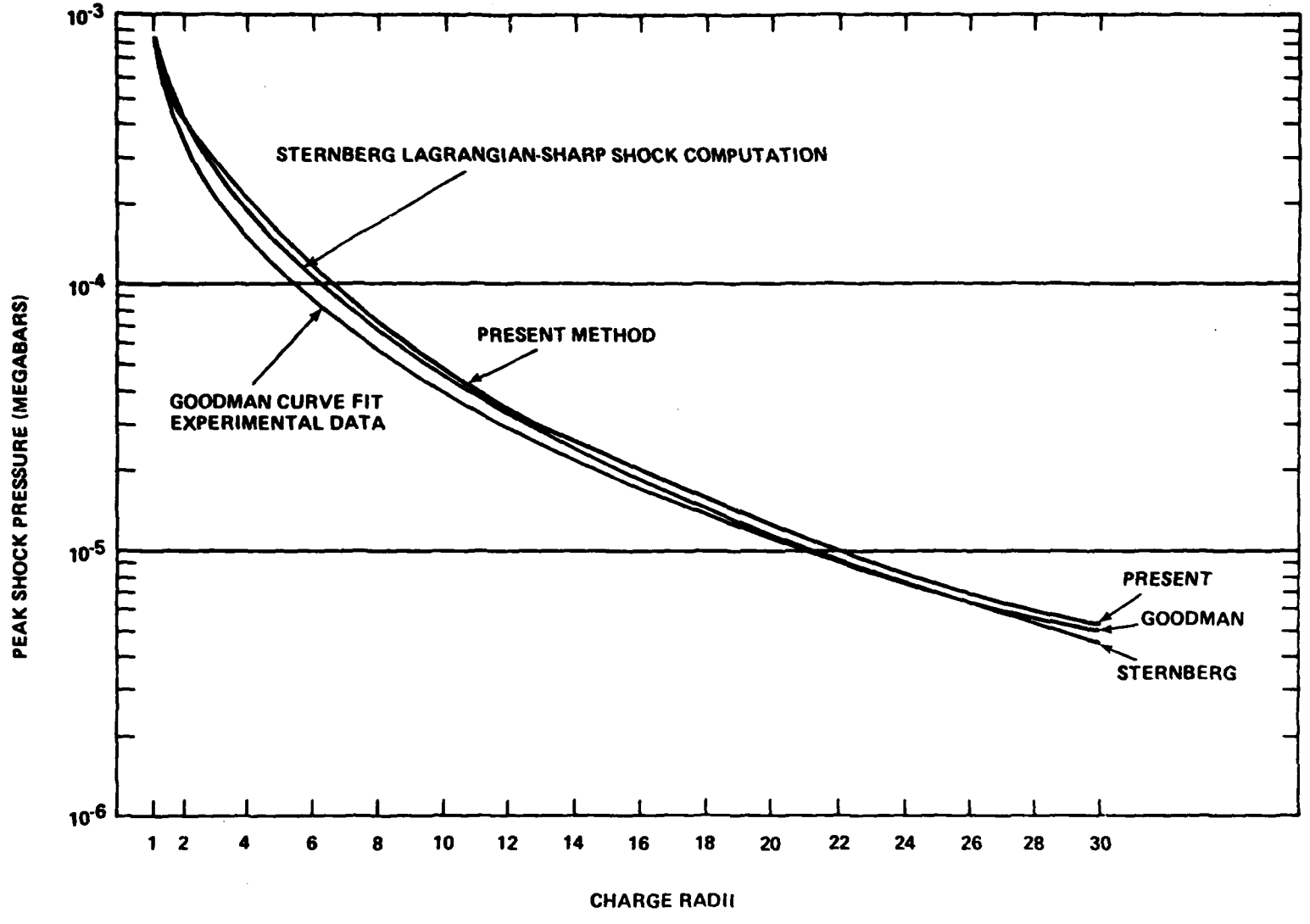

FIGURE 4: PEAK SHOCK PRESSURE VS. SHOCK LOCATION, PENTOLITE SPHERE CENTRALLY DETONATED IN γ=1.4 AIR

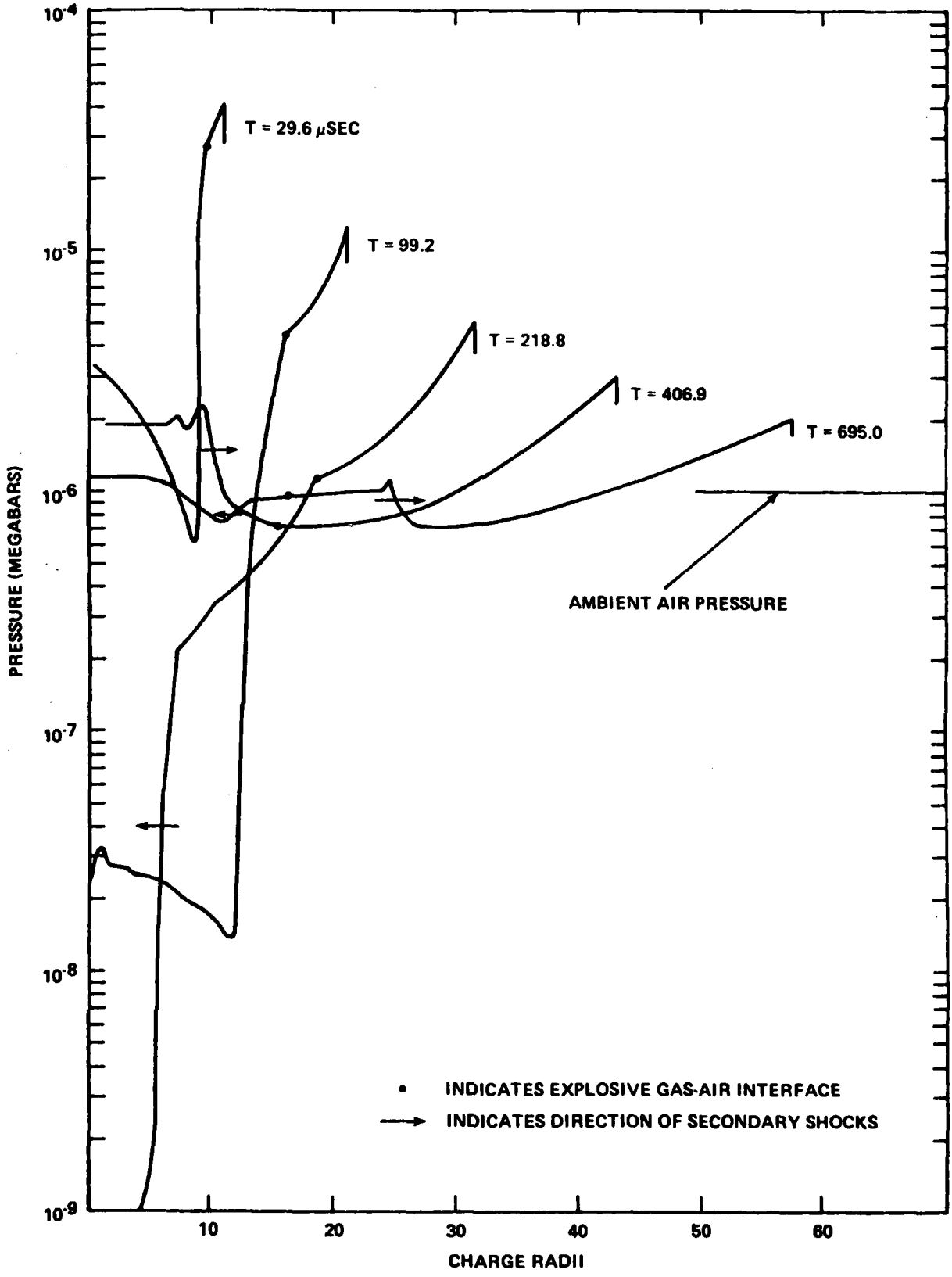

FIGURE 5: PRESSURE VS. DISTANCE AT VARIOUS TIMES, PENTOLITE SPHERE CENTRALLY DETONATED IN γ =1.4 AIR

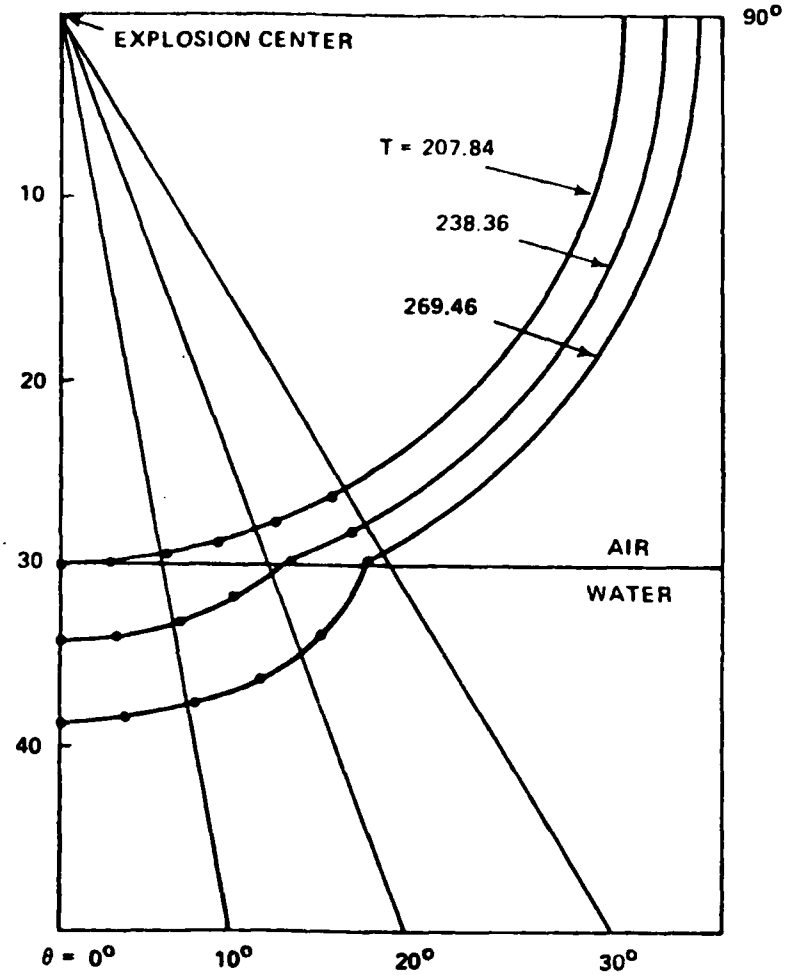

FIGURE 6: MAIN SHOCK LOCATION AT VARIOUS TIMES, PENTOLITE SPHERE CENTRALLY DETONATED IN AIR 30 CHARGE RADII ABOVE FLAT WATER SURFACE

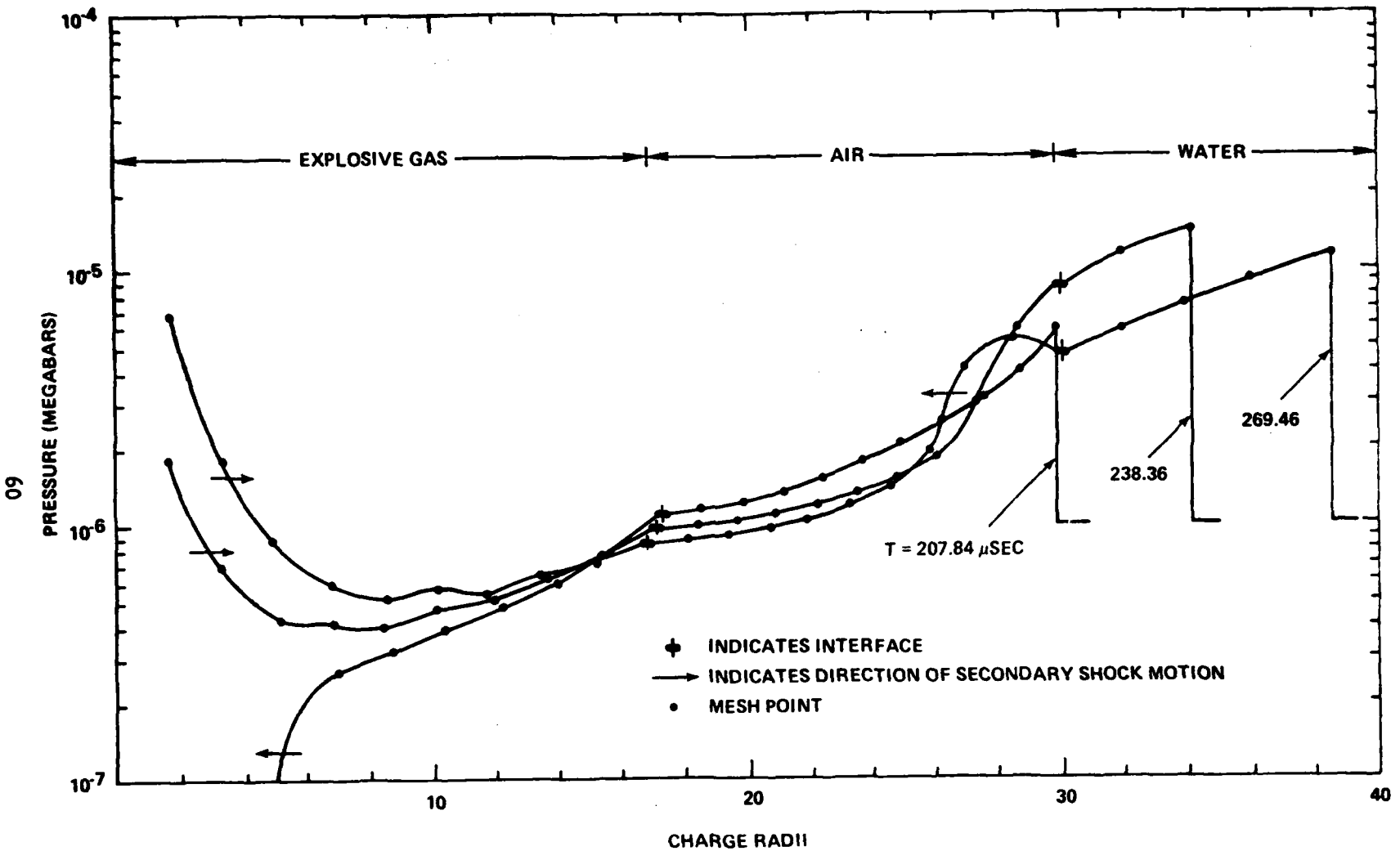

FIGURE 7: PRESSURE VS. RADIAL DISTANCE AT VARIOUS TIMES, STRAIGHT DOWN BELOW CHARGE ($\theta = 0$), PENTOLITE SPHERE CENTRALLY DETONATED IN AIR 30 CHARGE RADII ABOVE FLAT WATER SURFACE

COMPARISON OF 3-D HYDROCODE COMPUTATIONS FOR SHOCK DIFFRACTION LOADING ON AN S-280 ELECTRICAL EQUIPMENT SHELTER

Richard E. Lottero
Ballistic Research Laboratory
U.S. Army Armament Research and Development Command
Aberdeen Proving Ground, Maryland 21005

ABSTRACT

The normal shock diffraction loading on an S-280 Electrical Equipment Shelter (essentially a rectangular parallelepiped) by a 34.5 kPa (5.0 psi) shock is reported. Two different three-dimensional hydrodynamic computer codes, BAAL from the Los Alamos Scientific Laboratory and HULL from the Air Force Weapons Laboratory, are used. The results from the two hydrocodes are compared with one another, showing good agreement, and with two existing semiempirical models. Improvements to these models are suggested, as the computed results indicate that the loading for this three-dimensional shelter is significantly lower than the models predict. The effects of artifical viscosity in the hydrocodes and of the smearing of the computational shock in the finite difference grid are also discussed.

I. INTRODUCTION

Shock diffraction and drag phase loading on equipment and structures have been of significant interest to the Army ever since the introduction of nuclear weapons. Because of the inherent three-dimensional nature of such loading, the more commonly accepted method for obtaining this loading has been through field testing, dating back from atmospheric nuclear testing to the current large scale high explosive (HE) testing. Because of the high cost and necessarily complex planning involved in these tests, they are held relatively infrequently. Unpredictable anomalies such as jetting frequently occur, often with the intended targets receiving loading considerably different from that which had been expected. Space for targets and data acquisition equipment is invariably at a premium during these tests, leaving potentially valuable tests untried, and worthwhile data ungathered.

As pointed out by Taylor[1] in 1972, the accepted methods for computing shock diffraction loading on simple structures as outlined in

[1] *Taylor, W. J., "A Method for Predicting Blast Loads During the Diffraction Phase," The Shock and Vibration Bulletin, NR. 42. Part 4 of 5, Shock and Vibration Center, Naval Research Laboratory, Washington, DC., p. 135 (Jan 72).*

the U.S. Army Technical Manual TM-5-856-1[2], hereafter referred to as the Technical Manual, are no longer of sufficient accuracy for use in blast hardening and vulnerability assessment studies. Essentially, the method outlined in the Technical Manual treats a given three-dimensional structure, such as a rectangular parallelepiped, as being locally two-dimensional. Loading is then computed based on the speed at which a rarefaction wave travels across a characteristic dimension of the given target face. During the last several years, numerical methods in the form of hydrodynamic computer codes for simulating three-dimensional shock diffraction over obstacles have been advanced to the point where they can be used to complement, and in some cases replace, the use of experiments and models such as those in the Technical Manual.

A reference problem is defined, that being an S-280 Electrical Equipment Shelter being struck by a 34.5 kPa (5.0 psi) overpressure step shock. The present study includes a comparison of the HULL and BAAL hydrocodes with one another and with the Technical Manual model and Taylor's model. Improvements to the Technical Manual model are suggested, giving good agreement with the hydrocode results. The BAAL hydrocode has previously been shown to compare well with experimental shock loading on a similar rectangular parallelepiped at the same shock strength. Finally a discussion is presented on the net rotational moments on the shelter as predicted by the several methods in order to further emphasize the differences in their loading predictions.

II. REFERENCE PROBLEM

The above-mentioned shock diffraction loading problem involves an S-280 Electrical Equipment Shelter. The shelter is taken to be 3.62 m wide, 2.17 m deep, and 2.11 m high. It is sitting on the ground with one of the larger of the two different sized faces, defined here as the front face, oriented so that it is normal to the velocity vector of an oncoming one-dimensional shock wave. The shock wave is a step shock with an overpressure p^* of 34.5 kPa (5.0 psi). Ambient conditions ahead of the shock are a temperature T_1 of 288.2°K (518.7°R), a pressure p_1 of 101.3 kPa (14.7 psi), and a density ρ_1 of 1.225 kg/m^3 (.0765 lbm/ft^3). The air both ahead of and behind the shock is assumed to be a polytropic gas, with a ratio of specific heats γ of 1.4.

A simplified, locally one-dimensional, model that can be used to represent the flow field at the time that the incident shock reflects off the shelter front face is shown in Figure 1. The flow field shown

[2] *"Design of Structures to Resist the Effects of Atomic Weapons," U.S. Army Corps of Engineers, EM-1110-345-413 (1 July 1959). (Republished as TM5-856-1 in 1965).*

is that for a shock tube with a closed end. Region 1 represents the ambient air; region 2 represents the air behind the incident shock wave; region 3 represents the shock tube reservoir; region 4 represents the accelerated flow region between the expansion wave and the contact surface. Finally, region 5 is the region behind the shock wave which reflected off the rigid wall that represents the shelter front face. The theoretical peak reflected overpressure of 78.5 kPa as computed by using the one-dimensional model is an excellent reference point to use in assessing the validity of the hydrocode solutions. The initial reflection process at any given point on the front face is one-dimensional until the expansion waves coming in from the top and side edges of the front face arrive at that point.

III. SIMPLE MODELS

Prior to presenting the results of the hydrocode computations, it is worthwhile to discuss the existing models for loading on three-dimensional structures. A logical place to start is the Technical Manual. The equations presented here are for a step shock.

The Technical Manual's method for computing the loading on the front face is based on an assumed clearing time t_c, where

$$t_c = \frac{3h}{c_5} . \tag{1}$$

Here, c_5 is the sound speed on the front face of the shelter after the shock has reflected off it; for this case c_5 = 369.6 m/s. The value to be used for h is the smaller of either the height of the shelter or one-half the width; for this case h = 1.81 m. This gives a clearing time for the S-280 shelter t_c = 14.69 ms, where t_c is "... the time required to clear the front wall of reflection effects[2]." During this time, the average overpressure on the front face decreases from the peak reflected overpressure to a value

$$\bar{p}_f^* = (p_2 - p_1) + 0.85 \frac{1}{2} \rho_2 u_2^2 . \tag{2}$$

For the case under consideration here, the peak reflected overpressure on the front face is $(p_5 - p_1)$ or 78.5 kPa (11.4 psi), and $\bar{p}_f^*$ is 37.9 kPa (5.49 psi). The solid line labeled "FRONT" in Figure 2 shows the average overpressure-time history for the front face of an S-280 shelter being struck by a 34.5 kPa (5.0 psi) step shock wave as computed using this method.

Taylor[1] suggested an alternate method to estimate the loading on the front face of an obstacle, based on the number of rarefaction wave crossings. For a three-dimensional object such as the S-280 shelter there will be a succession of rarefaction waves originating from the top of the front face, reflecting in kind off the bottom boundary, plus a succession of rarefaction waves originating from the side of the front face, also reflecting in kind off the symmetry plane. In an actual occurrence of loading through shock diffraction, there would be considerable interaction between the crossing expansion waves. Because Taylor intended that the method be a simple approximation, the waves are assumed not to interact with one another. As a further simplification, the rarefaction wave speeds are assumed to be equal to the sound speed in the reflection region immediately after the incident shock reflects off the front face. In the case of the S-280 shelter, the height is 2.1 m, and the one-half width is 1.81 m. The sound speed c_5 in the reflection region is 369.6 m/s. Using Taylor's method, the required crossing time for an expansion wave running from the top to the bottom of the front face is 5.704 ms; for an expansion wave running between the side edge and the symmetry plane the crossing time is 4.897 ms. For each expansion wave crossing, the average overpressure on the front face is then computed as a percentage of the initial reflected overpressure on the front face. The values for average overpressure using the fitted curve in Figure 14 of Reference 1 are summarized in Table I, and are shown as the solid line having data points indicated with a "+" sign and labeled "FRONT" in Figure 2. The hydrocode data shown in Figure 2 will be discussed in a later section.

TABLE I. FRONT FACE AVERAGE OVERPRESSURE, TAYLOR'S METHOD

Time (ms)	Rarefaction Wave Number*	Wave Description	% Reflected Overpressure	Overpressure (kPa)
0.00	—	—	100	78.5
4.90	1	Side to Sym Plane	86.9	68.3
5.70	2	Top of Bottom	68.5	53.8
9.80	3	Sym Plane to Side	57.3	45.0
11.4	4	Bottom to Top	52.8	41.5
14.7	5	Side to Sym Plane	50.4	39.6

The time required for the incident shock wave to arrive at the plant of the back wall is

$$t_d = \frac{D}{W_i} , \qquad (3)$$

*Model stops at crossing number 5.

where D is the S-280 shelter depth, and W_i is the velocity of the incident shock. For the case under consideration here, D = 2.17 m and W_i = 386.8 m/s, so t_d = 5.616 ms. The rise time[2] required for the pressure on the back face to go from ambient at time t_d to its peak average value is

$$(t_b)_{rise} = \frac{\alpha h}{c_1}, \tag{4}$$

where α = 4.0, and h and c_1 are defined as before. Here, h = 1.81 m and c_1 = 340.3 m/s, so $(t_b)_{rise}$ = 21.28 ms. The peak average overpressure[2] on the back face is

$$(\bar{p}_b^*)_{max} = \frac{1}{2}(p_2 - p_1)\left[1 + (1 - \beta)e^{-\beta}\right], \tag{5}$$

where

$$\beta = \frac{1}{2}\frac{(p_2 - p_1)}{p_1}, \tag{6}$$

or $(\bar{p}_b^*)_{max}$ = 29.3 kPa. Because the shock wave considered here is a step shock, the model in the Technical Manual implies that the average overpressure on the back face would remain at $(\bar{p}_b^*)_{max}$ indefinitely. The overpressure time-history as computed by using this method is represented by the solid line labeled "BACK" in Figure 2. Taylor's[1] data indicate that the constant α used in Equation (4) to compute the rise time from the arrival time t_d to the time at which the average overpressure on the back face reaches the value $(\bar{p}_b^*)_{max}$ should be changed to 2.5 from 4.0. This gives a more rapid pressure rise time of 13.30 ms on the back face as compared with that computed by using the model in the Technical Manual. The overpressure-time history for the S-280 shelter back face as computed by using Taylor's method is represented by a solid line having data points indicated with a "+" sign and labeled "BACK" in Figure 2. Figure 3 shows the time-history of the average pressure difference between the front and back faces of the S-280 shelter using the methods outlined by Taylor and in the Technical Manual. The hydrocode data shown in Figure 3 will be discussed in a later section.

Taylor does not suggest an improved method for computing the average overpressure on the top and side faces of an object such as the S-280 shelter. The method outlined in the Technical Manual is

presented here for comparison with the computed hydrodynamic computer code results. From the time t = 0.0 s, when the incident shock wave reaches the plane of the front face of the target, to the time t_d at which the shock wave reaches the plane of the back face, the average overpressure on the top face varies linearly[2] from zero to

$$\bar{p}^*_{top} = \left(p_2 - p_1\right)\left[0.9 + 0.1\left(1.0 - \frac{p_2 - p_1}{p_1}\right)^2\right]. \tag{7}$$

Using the values for the reference case, $\bar{p}^*_{top}$ = 32.5 kPa at t_d = 5.616 ms. Because of vortex growth, shedding, and subsequent travel down the top face, the average overpressure is said to reach a local minimum at time

$$t_{pmin} = \frac{5D}{W_i}, \tag{8}$$

which for this case is 28.08 ms. At that time, the average overpressure on the top face is computed[2] as either

$$\bar{p}^*_{top} = \left(p_2 - p_1\right)\left[2.0 - \left(\frac{p_2 - p_1}{p_1} + 1\right)\left(\frac{h}{D}\right)^{1/3}\right], \tag{9.1}$$

or

$$\bar{p}^*_{top} = \left(p_2 - p_1\right)\left[0.5 + 0.125\left(2 - \frac{p_2 - p_1}{p_1}\right)^2\right], \tag{9.2}$$

whichever is the lesser of the two. At this time, $\bar{p}^*_{top}$ = 25.2 kPa for the S-280 shelter. After this time, there is a linear rise in the average overpressure to a value

$$\bar{p}^*_{top} = p_2 - p_1, \tag{10}$$

from the time t_{pmin} to a time

$$t = t_{pmin} + \frac{15\ D}{W_i}. \tag{11}$$

For the present case, t = 98.28 ms and $\bar{p}^*_{top}$ = 34.5 kPa, the incident shock overpressure. According to the method outlined in the Technical Manual, the geometry of the S-280 shelter is such that the times and average overpressures for the top face also apply directly to the side

face of the shelter. Figures 4 and 5 show the overpressure-time history for the top and side faces, respectively, of the S-280 shelter being struck by the 34.5 kPa overpressure step shock wave as computed by using the above method. The hydrocode data and the proposed model shown in those figures will be discussed later.

IV. HYDROCODES

Until relatively recently, methods such as those outlined in the Technical Manual were the accepted means for calculating the loading on a structure being struck by a shock wave. Taylor[1] pointed out the more serious deficiences in the simple model being used, particularly the poor modeling of three-dimensional effects, and suggested a simple but quite effective model based on wave interactions. A more generalized version of Taylor's wave interaction model has since been adapted in the TRUCK code by Hobbs, et al[3]. Two significant features of this model are the ability to model oblique loading and more complex target shapes.

However, it was apparent that a more general and accurate computational model than that offered by the simple models was needed. At the time of Taylor's[1] paper, hydrodynamic computer codes capable of solving the Euler equations (and in limited cases the Navier-Stokes equations) for two-dimensional flow were fairly well established. Significant advances were also being made in the development of hydrodynamic computer codes capable of solving three-dimensional problems, particularly at the Los Alamos Scientific Laboratory (LASL), and specifically with the implicit, arbitrary-Lagrangian-Eulerian (ALE) hydrocode BAAL[4]. The computing methods used in BAAL are described for two-dimensional flow by Hirt, Amsden, and Cook[5], and also by Amsden and Hirt[6]. The

---

[3]*Hobbs, N. P., Walsh, J. P., Zartarian, G., Lee, W. N., and Wu, Y., "TRUCK - A Digital Computer Program for Calculating the Response of Army Vehicles to Blast Waves," Contract Report ARBRL-CR-00369, U.S. Army Armament Research and Development Command, Ballistic Research Laboratory, Aberdeen Proving Ground, MD (April 1978).*

[4]*Pracht, W. E. and Brackbill, J. U., "BAAL: A Code for Calculating Three-Dimensional Fluid Flows at all Speeds with an Eulerian-Lagrangian Computing Mesh", LA-6342, Los Alamos Scientific Laboratory, Los Alamos, New Mexico (August 1976).*

[5]*Hirt, C. W., Amsden, A. A., and Cook, J. L, "An Arbitrary Lagrangian-Eulerian Computing Method for all Flow Speeds", J. Comp. Phys., 14, 227-253 (1974).*

[6]*Amsden, A. A. and Hirt, C. W., "YAQUI: An Arbitary Lagrangian-Eulerian Computer Program for Fluid Flow at all Speeds", LA-5100, Los Alamos Scientific Laboratory, Los Alamos, New Mexico (March 1973).*

extension of these methods to three-dimensional flow is described by Pracht[7]. As a result of discussions with representatives of the Ballistic Research Laboratory (BRL), LASL was contracted to perform a computation using the BAAL hydrocode, simulating the three-dimensional shock diffraction loading experiment performed by Taylor at the BRL using a solid rectangular parallelepiped as a target. The results of this computation are reported in detail by Gentry, Stein, and Hirt[8], and later in the open literature by Stein, Gentry, and Hirt[9] along with a more detailed discussion of the solution technique. Briefly, the BAAL calculation involved a solution of the inviscid Euler equations, with artificial viscosity used to stabilize flow in regions of deceleration. The BAAL code has the capability of solving the full Navier-Stokes equations. In general, the BAAL computation showed excellent agreement with the experimental pressure data for both the front and back faces. Experimental data were not taken on the top and side faces. As a result of the confidence gained in the BAAL code from this comparison, LASL was contracted to perform a second computation, this time for an S-280 Electrical Equipment Shelter being struck by a 34.5 kPa (5.0 psi) step shock wave, the reference case discussed earlier. The results of this computation are reported in detail by Lottero[10]. Using the data generated in the BAAL computation[10] for the 34.5 kPa overpressure shock wave diffracting over the S-280 shelter, and using a simple scaling model suggested by the BRL to extrapolate the 34.5 kPa data to estimate pressure-time histories for other comparable shock overpressures, Calligeros et al[11] predicted S-280 shelter responses for

---

[7]*Pracht, W. E., "Calculating Three-Dimensional Fluid Flows at all Speeds with an Eulerian-Lagrangian Computing Mesh", J. Comp. Phys. 17, 132-159 (1975).*

[8]*Gentry, R. A., Stein, L. R., and Hirt, C. W., "Three-Dimensional Computer Analysis of Shock Loads on a Simple Structure", Contract Report BRL-CR-219, U.S. Army Ballistic Research Laboratory, Aberdeen Proving Ground, MD (March 1975).*

[9]*Stein, L. R., Gentry, R. A., and Hirt, C. W., "Computational Simulation of Transient Blast Loading on Three-Dimensional Structures", Computer Methods in Applied Mechanics and Engineering 11, 57-74 (1977).*

[10]*Lottero, R. E., "Computational Predictions of Shock Diffraction Loading on an S-280 Electrical Equipment Shelter" BRL-MR-2599, U.S. Army Ballistic Research Laboratory, Aberdeen Proving Ground, MD (March 1976).*

[11]*Calligeros, J. M., Walsh, J. P., and Yaghiayan, R. P., "Structural Modeling and Response of Command, Control, and Communications Shelter Systems for Event Dice Throw", KA-TR-151, (May 1978) KAMAN AVIDYNE, Burlington, MA, Prepared under Contract No. DAAD05-74-C-0744, to be published as a BRL Contract Report.*

various shock waves for Event Dice Throw. Ethridge[12] has used the results from References 1, 9, and 10 together with experimental data to construct correlation functions for blast diffraction loading on the front and rear surfaces of a rectangular parallelepiped.

During approximately the same time period that the three-dimensional BAAL computations were being run, a three-dimensional capability was being added to the HULL[13] hydrodynamic computer code at the U.S. Air Force Weapons Laboratory (AFWL). The major differences between the HULL hydrocode and the BAAL hydrocode are that, for a hydrodynamic problem such as the one discussed here, HULL solves only the inviscid Euler equations, utilizes an explicit finite difference algorithm, and is restricted to a fully Eulerian computing mesh comprised of cells which are rectangular parallelepipeds. The AFWL wished to verify the new three- dimensional HULL against existing experimental data or proven codes. The BRL wished to gain access to another reliable three-dimensional hydrocode, as it appeared that BAAL might not be immediately available for production work. The AFWL supplied the computing facilities and the three-dimensional HULL code; the BRL supplied the test problem and the analysis of the hydrocode output.

The problem chosen for the HULL computation was the reference problem described earlier, identical to that run in the second BAAL computation[10] including the flow field grid formulation. This was chosen to gain corroboration for the BAAL computation for the S-280 shelter in time for Event Dice Throw.

V. LOADING ON SHELTER FACES

Because the HULL and BAAL codes use different conventions for naming directions and indices, the BAAL results and the flow field diagram are reproduced in part using the HULL hydrocode conventions. Figure 6 shows a three-dimensional view of the shelter in the computational flow field.

While there is just one BAAL computation for the S-280 shelter, there are two complete HULL computations, designated HULL 19.8063 (hereafter referred to as HULL A) and HULL 19.8067 (hereafter referred to as HULL B). There is also an earlier incomplete HULL computation,

---

[12] *Ethridge, N. H., "Blast Diffraction Loading on the Front and Rear Surfaces of a Rectangular Parallelepiped", BRL-MR-2784, U.S. Army Ballistic Research Laboratory, Aberdeen Proving Ground, MD (Sep 1977).*

[13] *Fry, M. A., Durret, R. E., Ganong, G. P., Matuska, D. A., Stucker, M.D., Chambers, B. S., Needham, C. E., and Westmoreland, C. D., "The HULL Hydrodynamics Computer Code", AFWL-TR-76-183, U.S. Air Force Weapons Laboratory, Kirtland Air Force Base, NM (Sep 1977).*

designated HULL 202.1 (hereafter referred to as HULL C), that contains some interesting features. All three HULL runs are for the same 34.5 kPa step shock wave. The initial formulations of the four computations are summarized in Table II. Analysis by the BRL revealed that the computation for HULL C was not valid after 19 ms simulated problem time because of the arrival of an artificial wave at the front face. The reflected wave from the front face had traveled upstream, eventually arriving at the upstream transmissive boundary through which the HULL code had been feeding the step shock. Because the algorithm for the upstream transmissive boundary was formulated to function as a simple positive image boundary, the initially constant input wave was greatly modified by the arriving compression wave and its following expansion wave. Ultimately this artificial interaction at the upstream transmission boundary caused the incoming, originally steady, wave to be almost completely turned off, with the artificial wave arriving at the front face by 19 ms simulated problem time. With the information from the analysis of HULL C and from extensive analyses of other problems by AFWL, significant improvements to 3-D HULL were made by AFWL. The problems labeled HULL A and HULL B were run at AFWL in a cooperative effort by the BRL and AFWL using the improved 3-D HULL. These two HULL runs are identical with one another in all respects except that for HULL A the shock is started at seven flow field cells upstream of the S-280 shelter front face, whereas for HULL B the shock is started at the front face of the shelter, as was the case for the BAAL run and for HULL C. Artificial viscosity was employed for both the BAAL run and HULL C; no artificial viscosity was used in HULL A or HULL B. Also, HULL C was run with a Courant-Friedrichs-Lewy (CFL) stability factor $\eta = 0.15$, while both HULL A and HULL B used $\eta = 0.50$.

Figure 7 shows a comparative plot of the average overpressure on the front face of the S-280 shelter as computed by BAAL; HULL runs A, B, and C; the Technical Manual; and Taylor's model. The two simple models both show the theoretical peak overpressure of 78.5 kPa at time zero. The first data point for the BAAL computation is at $t = 1.57$ ms, showing an average overpressure of 74.3 kPa for the front face, 5.4% below the theoretical peak value. No pressure data prior to this time were furnished to the BRL, and hence the character of the BAAL computation from $0 \leq t < 1.571$ ms is unknown. HULL C is the HULL computation that most closely resembles the BAAL computation in its general nature. These two computations use essentially the same grid; they are both started with the shock at the front face. Both computations utilize a form of artificial viscosity, applying it only in regions of deceleration, although the actual from of the BAAL viscosity function[4] is different from that used in the HULL code[14]. As may be seen in Figure 7, the HULL C computation appears to be quite stable from time

[14] *Lunn, P. W., Happ, H. J., III, and Needham, C. E., "Development of an Artificial Viscosity Function", AFWL-TR-77-53, U.S. Air Force Weapons Laboratory, Kirtland Air Force Base, NM (Sep 1977).*

TABLE II. HYDROCODE COMPUTATION SUMMARY, S-280 SHELTER, 34.5 kPa (5.0 psi) STEP SHOCK

Computation	Solution of	Grid	Artificial Viscosity	Shock Wave	Initial X Position of Shock	Computer Time & Courant-Friedrichs-Lewy Number	Simulated Real Time	Comments
BAAL[10]	Euler Equations (Implicit)	Eulerian, 8381 cells	Yes	Step, 34.475 kPa overpressure	6.2731 m, at front face	≈ 40 min (CDC 7600)	33.63 ms	Successful run
HULL A	Euler Equations (Implicit)	Eulerian, 10602 cells	No	Step, 34.475 kPa overpressure	3.3154 m, 7 cells upstream of front face	20.5 min (CDC 6600) CFL = .50	40 ms	Successful run
HULL B	Euler Equations (Explicit)	Eulerian, 10602 cells	No	Step, 34.475 kPa overpressure	6.2731 m, at front face	18.2 min (CDC 6600) CFL = .50	33.1 ms	Successful run
HULL C	Euler Equations (Explicit)	Eulerian 10602 cells	Yes	Step, 34.475 kPa overpressure	6.2731 m, at front face	time not available CFL = .15	38.4 ms	Early HULL run, Artificial waves reached front face after 19 ms simulated prob time

zero up to 19 ms, after which the solution drops off significantly due to the arrival of the artificial wave discussed earlier. The computation after 19 ms is not plotted. The HULL C computation reaches a peak average overpressure of approximately 69.0 kPa at 1.3 ms, 12.1% below the theoretical peak. From a time of 2.5 ms to 17 ms, the BAAL and HULL C computations are nearly identical. After this time, the BAAL computation tends to rise to values above the others, whereas the HULL C computation begins to converge with the other HULL computations until it is destroyed by the artificial wave. The agreement between the HULL C and BAAL runs is quite remarkable, particularly so because the HULL code is using a computational grid designed for BAAL. Normally, the HULL code uses grids in which the cell-to-cell variation in size is kept below 5 to 10% in the region where the solution is desired, or in any region through which a wave must pass on its way to the region where the solution is desired. The BAAL grid has cell-to-cell variations in size on the shelter face of 25% for each cell in the X direction, and as large as 25% for most cells in the Y and Z directions, with much larger variations in the general flow field away from the shelter. As indicated in Reference 10, the excellent agreement between the experimentally measured average overpressure and the average overpressure computed by using BAAL for the front face of a rectangular parallelepiped, using a similar grid, gives reason for confidence in the validity of the BAAL computation for the S-280 shelter front face, except for late time where it seems high and for pressure anomalies at the edges of the front face[10].

The next comparison of interest in Figure 7 is that of HULL C with HULL B. These two computations are identical with one another in all respects except that HULL B uses $\eta = 0.50$ and no artificial viscosity, and HULL C uses $\eta = 0.15$ with artificial viscosity turned on. There are significant differences between the two computations in the early diffraction phase. The HULL B computation shows an overshoot of average overpressure to a peak value at 1.0 ms of 88.5 kPa, 12.7% above the peak theoretical value of 78.5 kPa, and 28.2% above the peak average overpressure of 69.0 kPa at 1.3 ms in the HULL C computation. The HULL B computation also shows significant oscillation about the results of the HULL C computation for $t \leq 6$ ms. It is doubtful that the higher CFL number for HULL B is the primary cause of this oscillation; it is most likely due to running the code without artificial viscosity combined with having the shock started as a discontinuity at the shelter front face. It is of interest to note that at 1.6 ms (the HULL B datum closest in time to the first datum of the BAAL computation at 1.571 ms) the HULL B computation shows an average overpressure of 76.4 kPa, 2.7% below the theoretical peak reflected overpressure of 78.5 kPa.

The set-up of the HULL A computation is identical with the HULL B computation except that the HULL A computation begins with the shock located seven flow field cells upstream of the S-280 shelter front face. As may be seen in Figure 7, the movement of the shock through those seven flow field cells results in a significantly different average

overpressure-time history on the shelter front face for HULL A as compared with HULL B. Signals from the computational shock in HULL A, spatially in the form of a forward, exponentially decreasing function, arrive well ahead of the theoretical shock arrival time. These early signals are then reflected back continuously into the main portion of the oncoming computational shock wave, ultimately reducing the peak overpressure, and delaying and spreading it in time. The peak average overpressure for HULL A is 69.0 kPa, 12.1% below the theoretical peak, occurring at 4.35 ms after the theoretical arrival time of the shock wave at the front face. By 4.35 ms, the theoretical location of the shock wave is actually 1.68 m downstream of the front face, 77.5% of the distance to the plane of the back face. Gentry[8] et al show the same qualitative effect in comparing the results of a BAAL computation for a step shock started at the front face of a rectangular parallelepiped with that for an identical shock in the same grid started five flow field cells upstream of the front face. The almost exact agreement in peak average overpressure for the shelter front face between HULL C and A is most likely coincidental; the effect manifesting itself in HULL A is numerical diffusion caused by utilizing a CFL number less than 1.0 and by using a highly non-uniform grid. The X direction cell-to-cell variation between the seventh and sixth cells upstream of the shelter front face is 45.0%. The early time effects in HULL C governing the development of the peak average overpressure on the front face are due almost entirely to the effects of the modifications via artificial viscosity to the pressure difference[14,15] used to compute the accelerations in the Lagrangian phase of the HULL computation[13]. The HULL A and HULL B computations converge with one another by 20 ms, as should be expected. The HULL C computation appears to have been tending toward converging with the other HULL computations just prior to its being destroyed by the artificial wave discussed earlier.

The solutions obtained by using the method outlined in the Technical Manual and that suggested by Taylor[1] are also shown in Figure 7. All six average overpressure-time history solutions suggest that the wave interaction, or diffraction, phase on the front face lasts for about 15 ms, and is then followed by the drag phase. The Technical Manual solution for the diffraction phase is significantly different from all of the other solutions, with the one exception of being nearly identical to Taylor's solution in the early part of the diffraction phase. It agrees well with the HULL B solution throughout the drag phase, with the BAAL and HULL C solutions in the early drag phase, and with the HULL A solution shortly after the beginning of the drag phase. The solution using Taylor's model, although it is somewhat high, shows good agreement with the hydrocode solutions throughout the diffraction phase, except for regions where the hydrocode solutions show the questionable behavior discussed earlier. This good agreement,

[15] *Richtmyer, R. D. and Morton, K. W., "Difference Methods for Initial Value Problems", Second Edition, Interscience Publishers, Inc, New York, New York, 1967, pp 311-317.*

coupled with the ease with which the method may be applied, make Taylor's method most attractive for estimating front face diffraction loading. Taylor's solution for the drag phase is consistently above all of the others, except for the late-time BAAL solution. Both Taylor's method and the Technical Manual's method are exact for $t \leq 0$.

Figure 8 shows a comparative plot of the average overpressure on the back face of the S-280 shelter as computed by BAAL, HULL runs A and B, the Technical Manual, Taylor's[1] suggested improvement to the Technical Manual model, and a proposed simple model. There is excellent agreement between the three hydrocode computations. The two existing simple models[1,2] show significantly different results from the hydrocodes, particularly the model from the Technical Manual. As indicated in Reference 8, the average overpressure on the back face in the BAAL computation for the rectangular parallelepiped agrees quite well with the experimentally measured average overpressure. This led to the conclusion that the average overpressure on the back face of the S-280 shelter as computed by using BAAL may also be considered to be an accurate estimate. This conclusion is strongly reinforced by the agreement shown by HULL runs A and B. The three hydrocode computations show a significantly faster rise time required to reach the peak average overpressure, and that the peak itself is significantly higher than that predicted by the simple models. The hydrocodes also indicate a local pressure peak around 19 ms, most likely due to the interaction with one another of the weakened shocks breaking over the top and around the side faces.

It is a fairly direct matter to modify the existing model for average overpressure on the back face to better fit the hydrocode results, at least for this case. As before, Equation (3) gives $t_d = 5.62$ ms, with $\bar{p}_b^* = 0.0$ for $t \leq t_d$. It is proposed that the constant α in Equation (4) be modified so that $\alpha = 2$. The modified rise time is then $(t_b)_{rise} = 10.64$ ms. The peak average overpressure on the back face may be computed by using a modified version of Equation (5),

$$(\bar{p}_b^*)_{max} = p^*(t)_b \left(\frac{1}{2}\right)\left[1 + (1-\beta)e^{-n\beta}\right], \qquad (12)$$

with a proposed value

$$n = -\frac{1}{3},$$

with $\bar{p}_b^*$ varying linearly from a value of 0.0 at $t = t_d$ to $(\bar{p}_b^*)_{max}$ at $t = t_d + (t_b)_{rise}$. For this case, $(\bar{p}_b^*)_{max} = 32.4$ kPa at $t = 16.3$ ms.

As with the model for the top face, there is a decompression phase, lasting from

$$\left[t_d + (t_b)_{rise}\right] \leq t \leq \left[t_b + (t_b)_{rise} + \frac{(2.5)h}{c_1}\right], \qquad (13)$$

where $(\bar{p}_b^*)$ varies linearly from $(\bar{p}_b^*)_{max}$ to the value $(\bar{p}_b^*)_{drag}$. This value is found by substituting n = 0 into Equation (12), so that

$$(\bar{p}_b^*)_{drag} = p^*(t)_b \left(\frac{1}{2}\right)\left(2-\beta\right). \qquad (14)$$

This, for the step shock considered here, then represents $(\bar{p}_b^*)$ for all $t \geq \left[t_d + (t_b)_{rise} + \frac{2.5h}{c_1}\right]$. For the 34.5 kPa step shock on the S-280 shelter, $(\bar{p}_b^*)_{drag}$ = 31.5 kPa for t ≥ 29.6 ms. This modified simple model is shown in Figure 8. It fits the hydrocode data well, but its generality, like that of the simple model on which it is based, may be questionable.

It is appropriate at this time to refer back to the BAAL and HULL B plots of overpressure versus time in Figure 2 and the net loading plots shown in Figure 3. There are several reasons why only the BAAL and HULL B computations are chosen for comparison. The HULL C solution for the front face is valid only up to 19 ms, as discussed in detail earlier; the solution for the back face is no longer available, but in view of the problems associated with this computation, it would probably be of limited value. The HULL A solution shows significant deviation from the other hydrocode solutions, most likely due to the diffusion of the computational shock after its having been started seven cells upstream of the shelter front face. Both the BAAL and HULL B solutions start with the computational shock at the front face.

An important point stressed by Taylor[1] is that the method outlined in the Technical Manual significantly overestimates the net loading on a three-dimensional target, with net loading defined as the average overpressure on the front face minus that on the back face. Taylor's model predicts a significantly lower net load on the S-280 shelter than does the Technical Manual model, as pointed out earlier in Figure 3 and its accompanying discussion. As shown in Figure 2, except for the BAAL computation later in the drag phase (t > 20 ms) and the HULL B computation near t = 0, both hydrocode solutions are consistently below the front face average overpressure predicted by either Taylor's model or the Technical Manual model. Conversely, both hydrocode solutions for the back face indicate that the back face is loaded more rapidly than even Taylor suggests, peaking and remaining at average

overpressure values consistently and significantly above those predicted by either of the two models for all of the time represented here. Viewed together, the front and back face loadings from the hydrocode solutions show a greatly reduced net load on the S-280 shelter, as may be seen in Figure 3. The curves in Figure 3 suggest that the diffraction phase for the entire S-280 shelter is essentially over by 20 to 25 ms, or approximately four crossing times. During that diffraction phase, both hydrocode solutions show significantly less net loading than that predicted by Taylor[1], which is in turn significantly less than that predicted by using the model in the Technical Manual. The implication is that the whole body response of a three-dimensional target during the diffraction phase (which can be relatively long as compared with a single crossing time based on the depth of the structure) may be significantly less than the simple models predict.

By 25 ms, the net loadings from each of the two hydrocode solutions shown in Figure 3 have begun to diverge from one another, with the HULL B solution rising as time increases but remaining well below both of the simple model solutions, and the BAAL solution eventually rising above all of the others. This may be an artifact of the BAAL computation, but that is yet to be determined. From Figure 3 it may be inferred that the drag phase for the structure as a whole begins at 20 to 25 ms. For shock overpressures at which a structure such as the S-280 shelter would remain structurally functional as a result of the loading during the diffraction phase, it can be that the loading during the drag phase will determine whether or not the structure will be overturned, and hence "killed". Yet it is during the drag phase that the very limited computational and semiempirical data that are available, such as are shown in Figure 3, show significant disagreement. Additional experimental and computational data in the drag phase for three-dimensional structures are needed in order that the loading during this phase be better quantified.

Figure 4 shows a comparative plot of the average overpressure on the top face of the S-280 shelter as computed by BAAL, HULL runs A and B, the Technical Manual, and a proposed simple model. There is excellent agreement between the BAAL and HULL B computations throughout the range of simulated time. The HULL A computation agrees quite well with the other two hydrocode computations for $0 \leq t \leq 7$ ms, and for $t > 16$ ms. For $7 < t < 16$ ms, the HULL A solution shows a higher, delayed peak than do the other computations. This is most likely caused by the delayed, extended, and less severe reflection that the HULL A computation shows for the front face. The HULL A computation also shows some top face loading for $t < 0$ ms, indicating the arrival of the forward portion of the computational shock ahead of the theoretical shock arrival time.

The solid line in Figure 4 represents the average overpressure for the top face as computed by using the model suggested in the Technical Manual. The agreement with the hydrocodes for the first 6 ms, approximately equal to the time required for the theoretical shock wave to travel along the top face, is excellent. However, the model underpredicts

the peak average overpressure computed by the hydrocodes, and shows poor agreement for $t > 6$ ms. As was done for the models for the back face, the Technical Manual model for the top and side faces can be modified without much difficulty to give excellent agreement with the hydrocode results. These proposed changes follow below.

It is proposed that the following modified version of Equation (7) be used as a basis for computing the average overpressure on the top face,

$$(\bar{p}^*_{top}) = (p_2 - p_1)\left[A + (1 - A)\left(1.0 - \frac{p_2 - p_1}{p_1}\right)^2\right], \qquad (15)$$

where A is a constant whose value depends on whether the maximum, local minimum, or drag phase overpressure is to be computed. After a delay time t_d as defined in Equation (3), the maximum average overpressure on the top face, $(\bar{p}^*_{top})_{max}$, is computed by setting A = 1, so that Equation (15) reduces to

$$(\bar{p}^*_{top})_{max} = (p_2 - p_1) \ . \qquad (16)$$

From time $t = 0$ to $t = t_d$, the average overpressure increases linearly from zero to $(\bar{p}^*_{top})_{max}$. From time $t = t_d$ to a time

$$(t_{top})_{pmin} = t_d + \frac{2.0\ D}{W_i} \ , \qquad (17)$$

the average overpressure on the top faces decreases linearly from $(\bar{p}^*_{top})_{max}$ to a value $(\bar{p}^*_{top})_{pmin}$, which is computed by setting A = 0.6 in Equation (15). From time $(t_{top})_{pmin}$ to a time

$$(t_{top})_{drag} = (t_{top})_{pmin} + \frac{1.5\ D}{W_i} \qquad (18)$$

the average overpressure on the top face increases linearly from $(\bar{p}^*_{top})_{pmin}$ to a value $(\bar{p}^*_{top})_{drag}$, which is computed by setting A = 0.8 in Equation (15); after this time the average overpressure remains at $(\bar{p}^*_{top})_{drag}$. Thus, instead of dealing with several different equations as suggested in the Technical Manual[2], it is only necessary to deal with

an equation of the form of Equation (15), with A = 1.0 for the maximum, A = 0.6 for the minimum, and A = 0.8 for the drag phase average overpressures. For the S-280 shelter considered here, the simple model proposed above predicts $\bar{p}^*_{top}$ = 0.0 kPa at t = 0.0 s, $(\bar{p}^*_{top})_{max}$ = 34.5 kPa at t_d = 5.62 ms, $(\bar{p}^*_{top})_{pmin}$ = 26.7 kPa at $(t_{top})_{pmin}$ = 16.8 ms, and $(\bar{p}^*_{top})_{drag}$ = 30.6 kPa for $t \geq (t_{top})_{drag}$ = 25.3 ms. The average overpressure-time history for the top face as predicted by the modified model proposed above is shown on Figure 4.

Figure 5 shows a comparative plot of the average overpressure on the side face of the S-280 shelter as computed by BAAL, HULL runs A and B, the Technical Manual, and the proposed simple model. The proposed simple model, being a modification of the Technical Manual model, is also to be used for both the top and side faces for the S-280 shelter. Because of the geometry of the S-280 shelter, the side face is nearly equivalent in size to the one-half of the top face that is actually simulated in the hydrocode solutions, and because they have similar orientations in the flow field, the hydrocode solutions for the side face are nearly identical with those for the top face. Therefore, the same general comments regarding the relative performance of the hydrocodes and simple models for the top face loading also apply to the side face loading. As noted for the modified model proposed for the back face loading, the generality of this proposed modified model may also be limited.

VI. ROTATIONAL MOMENT

None of the simple models provide any information concerning the locations of the centers-of-overpressure on the surfaces of a target as a function of time; the wave interaction models could provide such estimates. The TRUCK code[3], which discretizes surfaces for its wave interaction computations, does provide this capability. To the extent of the credibility of the hydrocodes and the solutions gained by their use, such information is readily available[10]. Figure 9 shows the time-history of the Z location of the center-of-overpressure for the S-280 shelter front face as computed by BAAL, and by HULL runs A and B. The three hydrocode solutions show remarkable agreement with one another, although the slight differences do seem to be systematic. The center-of-overpressure stays quite close to half way up the front face for nearly all of the simulated time, except for a slight movement downward during the early part of the diffraction phase. Figure 10 shows the time-history of the Z location of the center-of-overpressure for the S-280 shelter back face as computed by the same three hydrocode runs. The back face shows considerable variation in the location of the center-of-overpressure during the diffraction phase. Prior to the arrival of the shock wave, the center-of-overpressure is arbitrarily defined as being at one-half of the height of the shelter; during that time, the average overpressure is zero by definition. The HULL A plot indicates

the arrival of the forward section of the computational shock prior to the theoretical arrival time of t = 5.62 ms at the plane of the back face.

The center-of-overpressure histories on the shelter front and back faces take on added significance when considered in conjunction with the average overpressure histories on the respective faces, just as the average loadings on the front and back faces do when looked at together in Figures 2 and 3. The simple models[1,2] predict higher loading on the front face than do the hydrocodes. For lack of a better estimate, it would probably be reasonable to use the centroid of the target face for the location of the center-of-overpressure for use with the simple model solutions for both the front and back faces. The hydrocodes indicate that such an approximation would be reasonable for the front face, but not so for the diffraction phase on the back face. During the early part of the diffraction phase, the hydrocodes predict a significantly greater average overpressure on the back face than do the simple models[1,2], acting considerably above the mid-point on the back face. During the remainder of the time simulated by the hydrocodes, the computed loading is still well above that predicted by the simple models, but with the center-of-overpressure near the area centroid. Specifically, an average of the BAAL and HULL B average overpressure on the back face over the time interval $6.6 \leq t \leq 15.8$ ms is 151% greater than that predicted by the Technical Manual, and 57% greater than that predicted by Taylor's model. For the time interval $17.2 \leq t \leq 33.4$ ms, the two hydrocode solutions average 30% greater than the Technical Manual and 8.7% greater than Taylor's model. The time-histories of the net rotational moment due to overpressure on the S-280 shelter about a line in the plane of the bottom boundary and perpendicular to the side face as computed by using BAAL, HULL B, and each of the two simple models are shown in Figure 11. As was the case for the net loading curves in Figure 3, Taylor's model[1] yields rotational moments larger than those for the Technical Manual very early in the diffraction phase and also in the drag phase, but significantly smaller values throughout the majority of the diffraction phase. The HULL B computation shows the oscillation in the solutions in the early diffraction phase discussed earlier. For $4 \leq t \leq 20$ ms the HULL B and BAAL solutions show excellent agreement with one another, predicting values well below those for the simple models. During that time interval, the hydrocodes average 47% below that predicted by the Technical Manual, and 31% below that predicted by Taylor's model. For $t > 20$ ms, the BAAL and HULL B solutions diverge significantly from one another. By 33.1 ms, the HULL B computation has reached a net rotational moment due to overpressure of 55.0 kN-m, 20.3% below the Technical Manual model's value of 69.0 kN-m, and 33.5% below the value of 82.7 kN-m obtained by using Taylor's model. By 33.6 ms, the BAAL computation has reached a net rotational moment due to overpressure 97.8 kN-m, 41.7% above the value from the Technical Manual model, 19.3% above the value from Taylor's model, and 77.8% above the value from the HULL B computation at 33.1 ms. The reason for this divergence is two-fold. The BAAL computation shows

significantly higher late-time overpressure on the S-280 shelter front face than does the HULL B computation, as shown in Figure 7, with a center-of-overpressure consistently above that for the HULL B computation, as shown in Figure 9. Conversely, the BAAL computation shows only somewhat higher late-time overpressure on the S-280 shelter back face then does the HULL B computation, as shown in Figure 8; it has a center-of-overpressure consistently below that for the HULL B computation, as shown in Figure 10. At least part of the reason for this difference in behavior between the two hydrocode solutions is the apparent anomalous behavior in the BAAL solution discussed in Reference 10.

VII. CONCLUSION

In general, the hydrocodes show good agreement with one another in predicting overpressure averaged over each of the given faces of the S-280 Electrical Equipment Shelter. They are also useful as a comparative tool in evaluating the ability of the relatively simple models discussed here to predict such loading. Additionally, the hydrocodes provide a great deal of information for which predictive models are not available and which is not readily gathered experimentally. An example of this is the use of the data from the hydrocodes to make accurate estimates of the time-history of the center-of-overpressure for use in computing rotational moments. Also, the analysis of the various hydrocode results discussed in this report has allowed some quantification of the effects of such items as the value of the CFL number, numerical diffusion caused by the finite difference grid, and artificial viscosity.

The model outlined in the Technical Manual does not appear to be suitable for predicting either the shock diffraction or the drag phase loading on a three-dimensional structure such as the S-280 Electrical Equipment Shelter. The front face loading prediction for the drag phase seems to be too high; the prediction for the drag phase appears to be reasonable. The prediction for the back face loading is too low, and is made worse by predicting too long a rise time needed for overpressure to go from zero to the predicted drag phase value. The models for predicting the loading on the top and side faces are fairly good in predicting the initial increase in overpressure with time, but underestimate the peak value to which the overpressure rises; thereafter, the models appear to be significantly in error.

Taylor's method[1] for estimating the loading on the front of a three-dimensional structure is a significant improvement over the model suggested in the Technical Manual, particularly during the diffraction phase; it appears to be somewhat high as compared with the hydrocode predictions for the drag phase. The change suggested by Taylor to be applied to the Technical Manual model for the back face loading is an improvement, but it too underpredicts the loading for all time, missing

the peak overpressure and overestimating the time required to reach the predicted peak overpressure. Taylor did not address the top and side face loading.

The empirical models suggested by Ethridge[12] provide a quick and fairly accurate means of estimating the average overpressure as a function of time on both the front and back faces of a rectangular parallelepiped. The modifications to the models in the Technical Manual for the back, top, and side faces of a rectangular parallelepiped proposed in this report also provide a quick, accurate means of estimating average overpressure, with the added feature of providing some of the detailed loading variations observed in the hydrocode computations.

The simple models do not provide a means for computing the time-history of the center-of-overpressure on the various faces of the structure. As a result, it is not possible to compute rotational moments unless assumptions are made concerning the location of the center-of-overpressure. Alternatively, center-of-overpressure models could be developed. The hydrocodes do provide this information.

The hydrocodes and the simple models all provide conflicting information during the drag phase. This late-time loading is important because it is during this time that overturning either will or will not take place. Unfortunately, relatively little experimental data have been gathered for late-time loading. This problem needs to be resolved both experimentally and computationally. Comparison of late-time loading obtained via experiment with that from inviscid codes such as HULL will also be of value in determining whether or not viscous effects should be modeled.

A more complete analysis may be found in Reference 16.

---

[16] *Lottero, R. E., "Detailed Comparison of 3-D Hydrocode Computations for Shock Diffraction Loading on an S-280 Electrical Equipment Shelter", BRL-R-( ), U.S. Army Ballistic Research Laboratory, Aberdeen Proving Ground, MD (to be published).*

REFERENCES

1. Taylor, W. J., "A Method for Predicting Blast Loads During the Diffraction Phase", The Shock and Vibration Bulletin, NR. 42. Part 4 of 5, Shock and Vibration Center, Naval Research Laboratory, Washington, DC p. 135 (Jan 72)

2. "Design of Structures to Resist the Effects of Atomic Weapons", U. S. Army Corps of Engineers, EM-1110-345-413 (1 July 1959). (Republished as TM5-856-1 in 1965).

3. Hobbs, N. P., et al, "TRUCK - A Digital Computer Program for Calculating the Response of Army Vehicles to Blast Waves", Contract Report ARBRL-CR-00369, U. S. Army Armament Research and Development Command, Ballistic Research Laboratory, Aberdeen Proving Ground, MD (April 1978).

4. Pracht, W. E. and Brackbill, J. U., "BAAL: A Code for Calculating Three-Dimensional Fluid Flows at all Speeds with an Eulerian-Lagrangian Computing Mesh", LA-6342, Los Alamos Scientific Laboratory, Los Alamos, New Mexico (August 1976).

5. Hirt, C. W., Amsden, A. A., and Cook, J. L, "An Arbitrary Lagrangian-Eulerian Computing Method for all Flow Speeds", J. Comp. Phys., 14, 227-253 (1974).

6. Amsden, A. A. and Hirt, C. W., "YAQUI: An Arbitrary Lagrangian-Eulerian Computer Program for Fluid Flow at all Speeds", LA-5100, Los Alamos Scientific Laboratory, Los Alamos, New Mexico (March 1973).

7. Pracht, W. E., "Calculating Three-Dimensional Fluid Flows at all Speeds with an Eulerian-Lagrangian Computing Mesh", J. Comp. Phys. 17, 132-159 (1975).

8. Gentry, R. A., Stein, L. R., and Hirt, C. W., "Three-Dimensional Computer Analysis of Shock Loads on a Simple Structure", Contract Report BRL-CR-219, U. S. Army Ballistic Research Laboratory, Aberdeen Proving Ground, MD (March 1975).

9. Stein, L. R., Gentry, R. A., and Hirt, C. W., "Computational Simulation of Transient Blast Loading on Three-Dimensional Structures", Computer Methods in Applied Mechanics and Engineering 11, 57-74 (1977).

10. Lottero, R. E., "Computational Predictions of Shock Diffraction Loading on an S-280 Electrical Equipment Shelter", BRL-MR-2599, U. S. Army Ballistic Research Laboratory, Aberdeen Proving Ground, MD (March 1976).

11. Calligeros, J. M., Walsh, J. P., and Yeghiayan, R. P., "Structural Modeling and Response of Command, Control, and Communications Shelter Systems for Event Dice Throw", KA-TR-151, (May 1978) KAMAN AVIDYNE, Burlington, MA, Prepared under Contract No. DAAD0574C0744, to be published as a BRL Contract Report.

12. Ethridge, N. H., "Blast Diffraction Loading on the Front and Rear Surfaces of a Rectangular Parallelepiped", BRL-MR-2784, U. S. Army Ballistic Research Laboratory, Aberdeen Proving Ground, MD (Sep 1977).

13. Fry, M. A., Durret, R. E., Ganong, G. P., Matuska, D. A., Stucker, M. D., Chambers, B. S., Needham, C. E., and Westmoreland, C. D., "The HULL Hydrodynamics Computer Code", AFWL-TR-76-183, U. S. Air Force Weapons Laboratory, Kirtland Air Force Base, NM (Sep 1977).

14. Lunn, P. W., Happ, H. J., III, and Needham, C. E., "Development of an Artificial Viscosity Function", AFWL-TR-77-53, U. S. Air Force Weapons Laboratory, Kirtland Air Force Base, NM (Sep 1977).

15. Richtmyer, R. D. and Morton, K. W., "Difference Methods for Initial Value Problems", Second Edition, Interscience Publishers, Inc., New York, New York, 1967, pp. 311-317.

16. Lottero, R. E., "Detailed Comparison of 3D Hydrocode Computations for Shock Diffraction Loading on an S-280 Electrical Equipment Shelter", BRL-R-( ), U. S. Army Ballistic Research Laboratory, Aberdeen Proving Ground, MD (to be published).

LIST OF SYMBOLS

c velocity of sound (m/s)

D the depth (m) of the target, measured in the direction of travel of the incident shock wave

h the clearing height (m), equal to the smaller of either the height of the target or one-half of its width

p static, or side-on, pressure (kPa), absolute unless otherwise indicated

T static temperature (°K)

t time (s), where $t \equiv 0.0$ when the incident shock wave arrives at the target front face, as computed according to theory

u particle velocity (m/s) with respect to an Eulerian reference frame

W wave velocity (m/s) with respect to an Eulerian reference frame

X the direction of measure of depth (m)

Y the direction of measure of width (m)

Z the direction of measure of height (m)

α a constant multiplicative factor

β $(p_2 - p_1)/2p_1$

γ the ratio of specific heats

η Courant-Friedrichs-Lewy (CFL) stability factor

ρ static density (kg/m^3), absolute unless otherwise indicated

Subscripts.

b the back face of the target

c clearing time when used with the symbol "t", the "... time required to clear the front wall of reflection effects[2]..."

drag the drag phase

f the front face of the target

AD-A089 089 ARMY MATHEMATICS STEERING COMMITTEE F/G 9/2
PROCEEDINGS OF THE 1980 ARMY NUMERICAL ANALYSIS AND COMPUTERS C--ETC(U)
AUG 80

UNCLASSIFIED ARO-80-3 NL

2 OF 6
AD
A089089

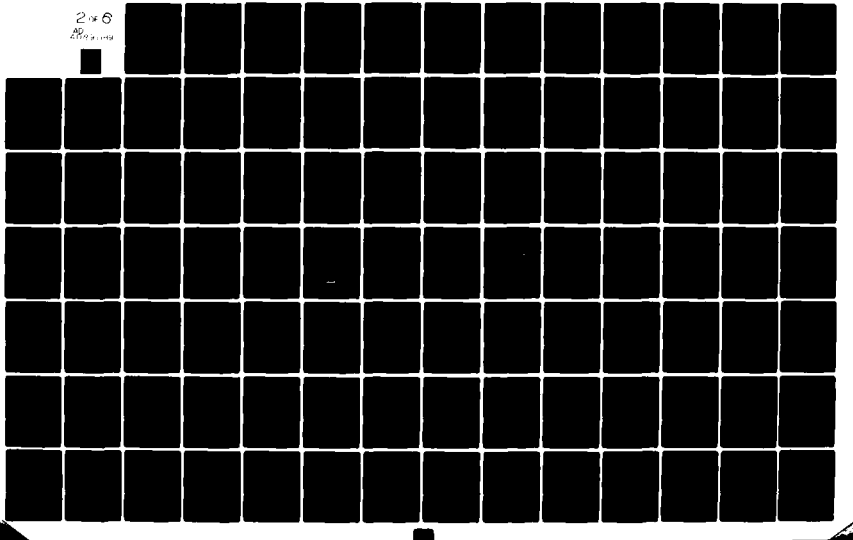

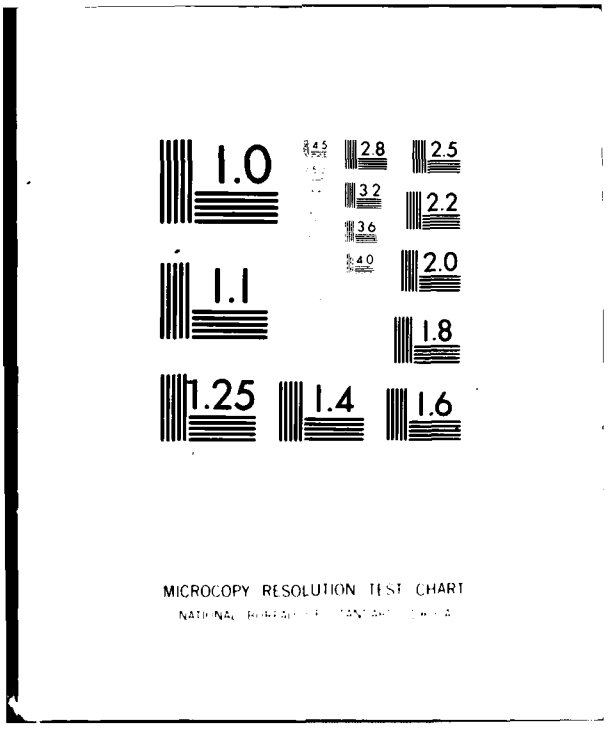
1.0
1.1
1.25
1.4
1.6
1.8
2.0
2.2
2.5
2.8
3.2
3.6
4.0
4.5
MICROCOPY RESOLUTION TEST CHART

i incident shock wave

max a peak value

pmin when used with the symbol "t", the time required for the average pressure on a target face to reach a local minimum value after having been loaded to a peak value by a shock wave

rise when used with the symbol "t", the time required for a target face to reach a peak average pressure after the initial arrival of the incident wave at that face

top the top face of the target

1 ambient, atmospheric, or reference condition, specifically that region of undisturbed gas ahead of the incoming shock wave

2 the region behind the incident shock wave

3 the region representing the shock tube reservoir

4 the region separated from the shock tube reservoir by the expansion wave, and separated from the shocked gas by the contact discontinuity

5 the region behind the reflected shock wave

Superscripts

* the value over the reference, or ambient condition (e.g., p^* represents overpressure)

- average value over a given face of the target

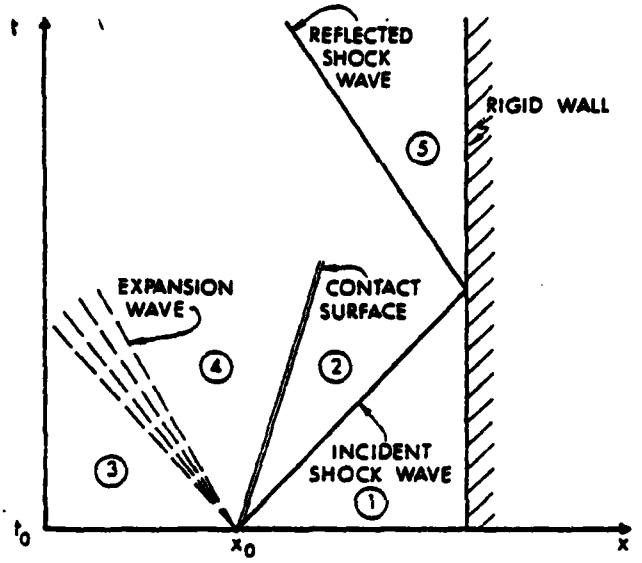

Figure 1. Simplified one-dimensional flow field.

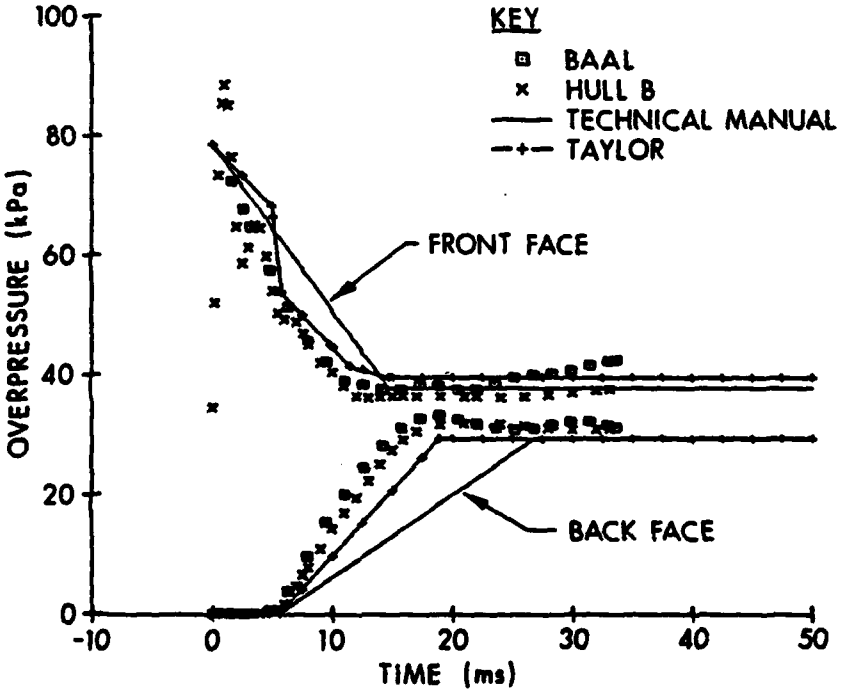

Figure 2. Front and back face average overpressure.

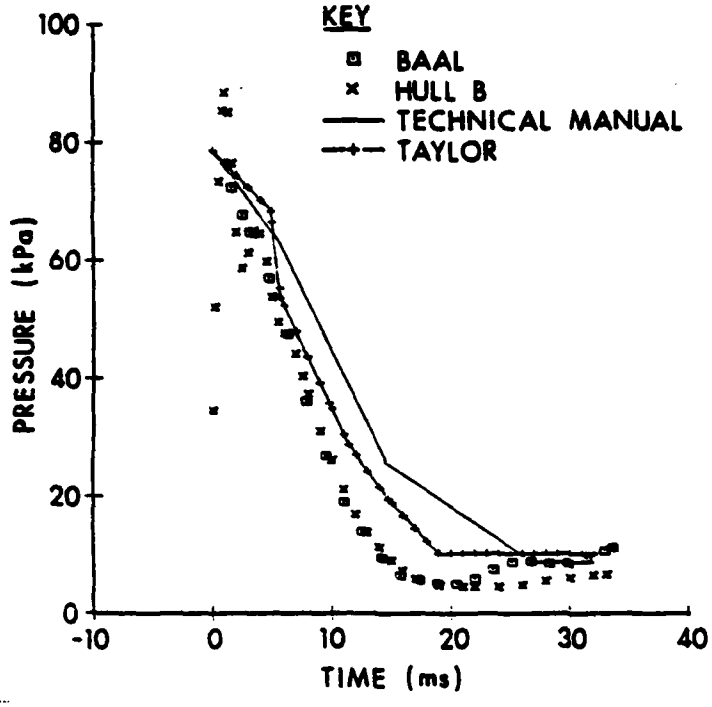

Figure 3. Average pressure difference, front face minus back face.

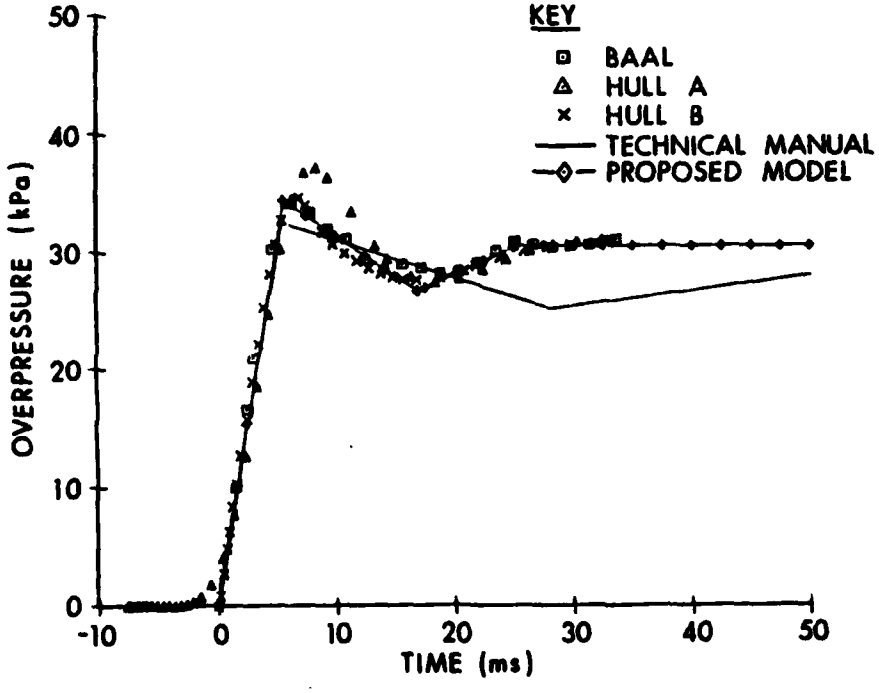

Figure 4. Top face average overpressure.

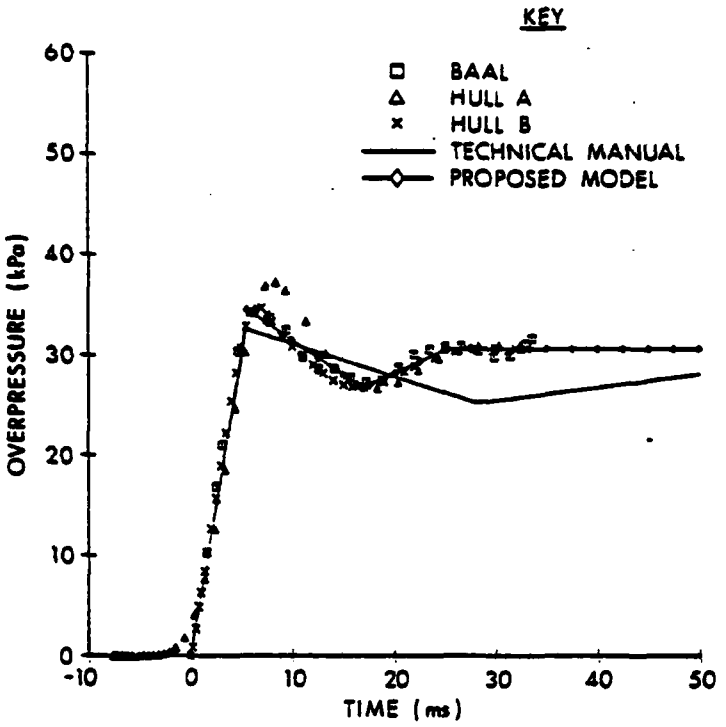

Figure 5. Side face average overpressure.

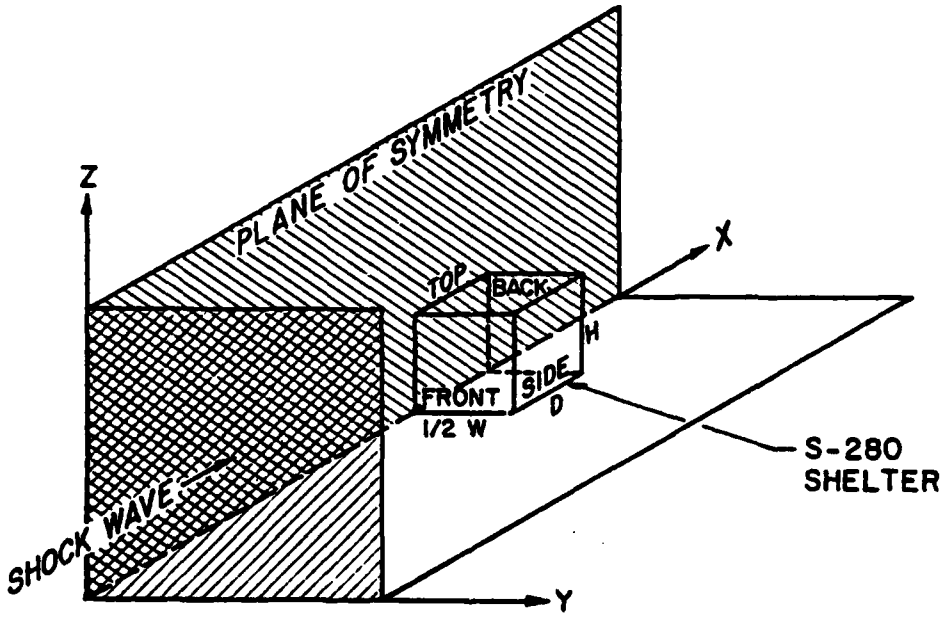

Figure 6. S-280 Electrical Equipment Shelter in the computational flow field.

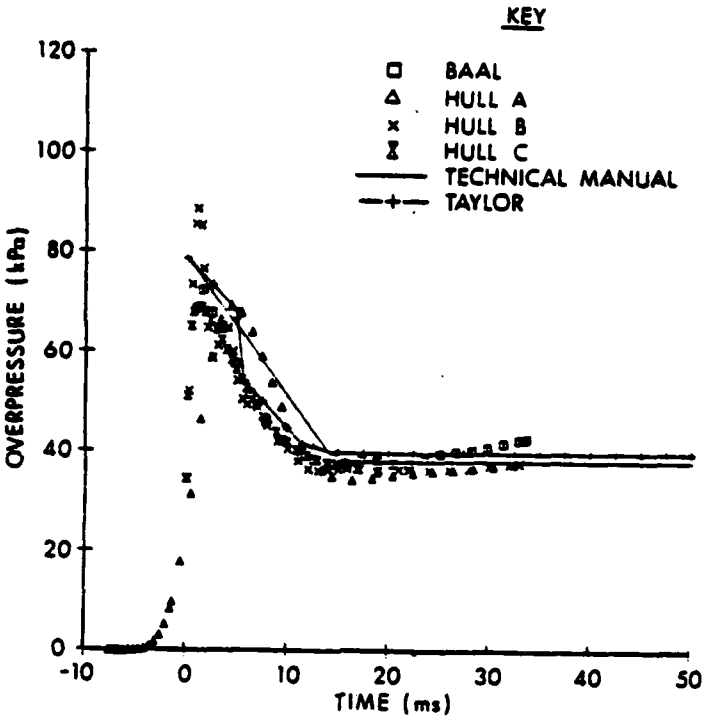

Figure 7. Front face average overpressure.

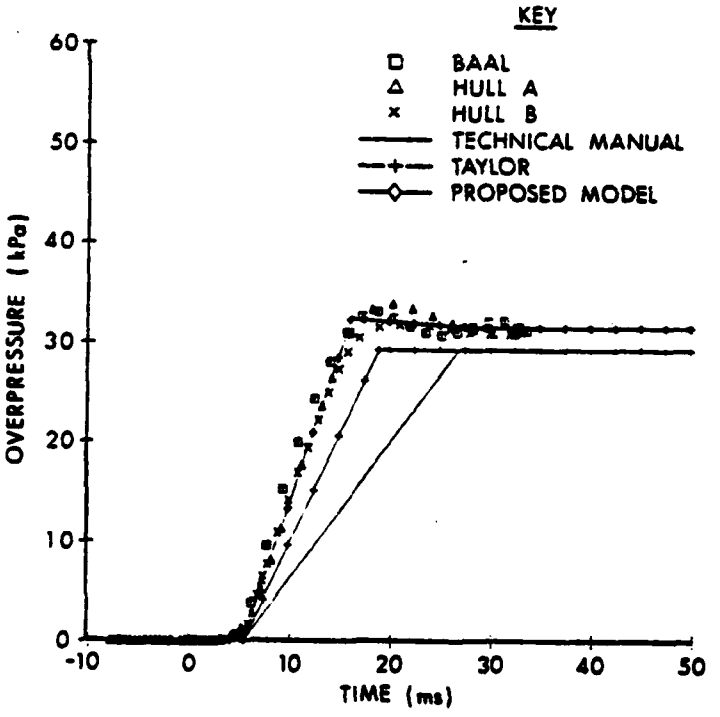

Figure 8. Back face average overpressure.

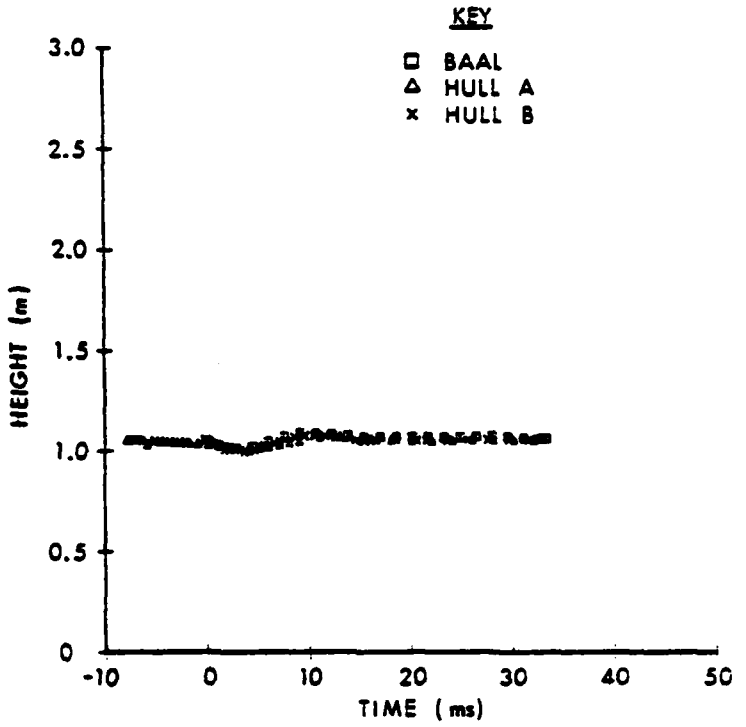

Figure 9. Height of center-of-overpressure on front face.

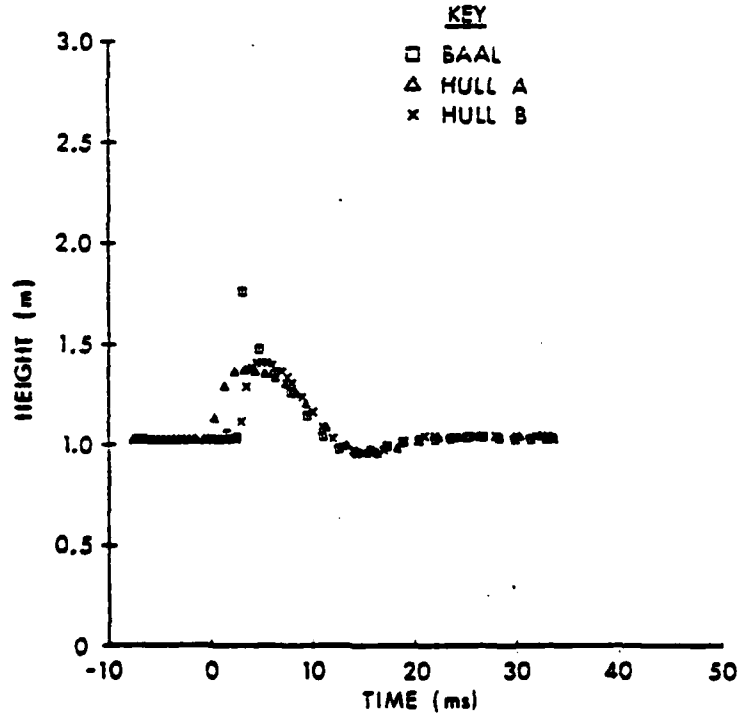

Figure 10. Height of center-of-overpressure on back face.

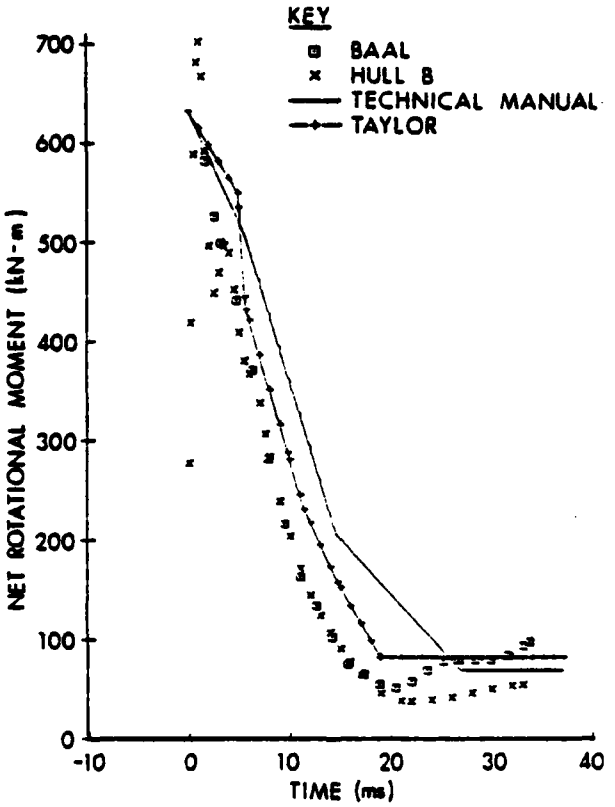

Figure 11. Net rotational moment due to overpressure.

OBLIQUE INTERACTION OF A SHOCK WAVE WITH A THREE-DIMENSIONAL TACTICAL COMMUNICATIONS SHELTER

R. E. Lottero, J. D. Wortman, B. P. Bertrand and C. W. Kitchens, Jr.
Ballistic Research Laboratory
U.S. Army Armament Research and Development Command
Aberdeen Proving Ground, Maryland 21005

ABSTRACT

Three-dimensional, unsteady finite-difference calculations with the HULL hydrocode are used to describe the shock diffraction process resulting from a shock wave striking the front of an S-280 Electrical Equipment Shelter at oblique incidence. The 52.5° obliquity of the incident 34.5 kPa (5 psi) overpressure shock on the front face produces a peak reflected overpressure that is approximately 50% larger than that for normal reflection. The numerical calculations are discussed, and evaluated by comparison with experimental pressure measurements taken in shock tube tests on a scale-model shelter. Difficulties are experienced in both the 3-D calculations and the experiment in resolving the peak reflected overpressure on the front face; comparisons for other shelter faces show good agreement. Three-dimensional and two-dimensional grid convergence studies are discussed which quantify the influence of grid size on the numerical results.

I. INTRODUCTION

It has generally been assumed that the most severe shock loading situation for a given structure occurs when the shock strikes its most vulnerable face at normal incidence. However, it is also known that when a shock wave with an overpressure $\leq$ 140 kPa (20.3 psi) strikes a target at oblique incidence, the peak reflected overpressure can be more than 50% larger than that for normal reflection[1]. This oblique interaction process is of interest from both fluid dynamic and vulnerability viewpoints. The duration and magnitude of the peak reflected overpressure are functions of the incident shock overpressure, the angle of incidence between the shock wave and the target face, and the distance along the target face measured from the leading edge. When the angle of incidence is at the critical Mach angle (to be discussed later) the reflected overpressure reaches its highest possible value. For relatively small targets, the enhanced peak reflected overpressure is difficult to measure experimentally because of its small spatial

[1] *Bertrand, B. P., "Measurements of Weak Shock Wave Reflected Pressure Histories on a 2-Dimensional Surface," ARBRL-MR-02966, U.S. Army Ballistic Research Laboratory, Aberdeen Proving Ground, Maryland (October 1979).*

extent and time duration, and the response limitations of pressure gages. The peak reflected overpressure is difficult to predict with a hydrodynamic computer code because of the general tendency of such codes, especially Eulerian codes, to smear discontinuities such as the incident and reflected shock waves.

The peak overpressure enhancement at obliquity for shock waves with an overpressure $\leq$ 140 kPa is of interest because such shock waves cover a large part of the assumed threat range from tactical nuclear weapons. The S-280 Electrical Equipment Shelter (henceforth called the S-280 shelter) houses communications equipment for many Army systems, and will be on the tactical battlefield in large numbers. The S-280 shelter is currently being hardened to decrease its blast/thermal vulnerability, and a 34.5 kPa (5.0 psi) overpressure shock wave was chosen for the present work because it represents a mid-range threat level. At normal incidence, the peak reflected overpressure for this shock wave is 78.5 kPa (11.4 psi). The critical Mach angle for a 34.5 kPa shock wave is 52.5°. At that angle, the peak reflected overpressure is estimated[1] to be as high as 122 kPa (17.7 psi), 55% greater than the value for normal incidence.

It is important from a vulnerability viewpoint to determine whether or not such a peak is of sufficient duration and spatial extent on the S-280 shelter that a 34.5 kPa overpressure shock wave represents a greater threat at 52.5° obliquity than at normal incidence. This is one of the objectives of the present study. A second objective is to use a combined experimental and computational research program to verify the three-dimensional shock loading prediction capability of the HULL[2,3] hydrocode currently at the BRL, and assess the practicability of such calculations.

II. BACKGROUND

This section provides an introduction to oblique shock diffraction. When an incident shock wave strikes a given face of a rectangular parallelepiped (such as an S-280 shelter) at some oblique angle, it also strikes another face at the complement to that angle. The initial contact between the incident shock wave and the structure occurs at the corner formed by the intersection of these two faces. This corner becomes a shock diffraction corner.

---

[2] *Fry, M. A., Durrett, R. E., Gonong, G. P., Matuska, D. A., Stucker, M. D., Chambers, B. S., Needham, C. E., and Westmoreland, C. D., "The HULL Hydrodynamics Computer Code," AFWL-TR-76-183, U.S. Air Force Weapons Laboratory, Kirtland Air Force Base, NM (September 1976).*

[3] *Fry, M. A., Needham, C. E., Stucker, M. D., Chambers, B. S., and Ganong, G. P., "AFWL HULL Calculations of Air Blast Over a Dam Slope," AFWL-TR-76-154, U. S. Air Force Weapons Laboratory, Kirtland Air Force Base, NM (October 1976).*

As the divided incident shock travels along the two faces, rarefaction waves emanating from the diffraction corner travel along the faces at the local speed of sound, following each incident shock/surface intersection point as it moves along the respective face. Depending on the angle of incidence of the shock on the face, the corner rarefaction wave will either fall continually farther behind the incident shock/surface intersection point, or it will eventually catch up. The initial reflected overpressure experienced at a given point on the surface is not relieved until the corner rarefaction wave arrives, or similar waves arrive from other parts of the flow field.

The incident shock wave of interest here is a 34.5 kPa overpressure shock. Figure 1 shows shock reflection factors (the ratio of the peak reflected overpressure to the incident overpressure) as a function of the angle of shock incidence α for this shock strength. The angle at which the corner rarefaction wave just catches up with the incident shock/surface intersection point is α_C. Regular reflection theory is valid for $0 \leq \alpha < \alpha_C$. The experimental data indicate that the peak overpressure is reached at $\alpha_M = 52.5°$, the critical Mach angle. At α_M, the intersection point between the incident and reflected shocks is on the verge of lifting off the surface, at which time a Mach stem and triple point are formed.

Information inferred[1] by measuring the Mach stem velocity for $\alpha \sim \alpha_M$ indicates that the peak reflected overpressure in this region may be even larger (122 kPa) than that indicated by the experimental data in Figure 1. The enhanced peak reflected pressure for $\alpha \sim \alpha_M$ is of interest from computational and experimental viewpoints, and may have important implications in blast vulnerability.

III. EXPERIMENTS

The experiments were conducted in the BRL ½ metre (24 inch O.D.) shock tube[4]. A 1/18.45 scale model of the S-280 shelter was constructed of aluminum, of sufficiently heavy construction that it is essentially non-responding for the shock wave strengths used here. The model dimensions are 19.58 cm (width) by 11.38 cm (height) by 11.79 cm (depth). One of the 19.58 cm by 11.38 cm faces is defined as the front face. The model was mounted in the shock tube so that the angle α between the front face and the incident shock wave front was 52.5° ± 0.5°. One of the 11.79 cm by 11.38 cm faces is defined as the windward side face, the angle between that face and the incident shock being 37.5°.

---

[4] *Coulter, G. A. and Bertrand, B. P., "BRL Shock Tube Facility for the Simulation of Air Blast Effects," BRL-MR-1685, U.S. Army Ballistic Research Laboratories, Aberdeen Proving Ground, MD (August 1965).*

Experimental shots were conducted for various overpressures and angles of incidence. The two described in Table I will be discussed here. The angle between the shock front and the shelter front face is α, p is absolute pressure, T is temperature, and E.1 and E.2 indicate the shot numbers referred to in this paper.

There were a total of eight pressure gages on the model, mounted flush to the model surface. Table II shows the gage positions where pressure measurements will be compared in detail with the hydrocode computations. The gage locations are given in a primed coordinate system, having its origin (0., 0., 0.) at the bottom corner of the leading vertical edge of the model. The front and back faces are constant X' planes, the side faces constant Y', and the top and bottom faces constant Z'. The gage positions are defined by a letter-and-number pair; the letter denotes the face and the number denotes the gage position on the face. All gages in shots E.1 and E.2 had a sensitive element diameter of 0.51 cm (.20 in), except gage F2 in shot E.2, which had a smaller diameter of 0.32 cm (.125 in) and a higher frequency response than the other gages.

IV. FINITE DIFFERENCE COMPUTATIONS

The airblast version of the HULL[2,3] hydrodynamic computer code was used for the shock diffraction computations. The HULL code currently in use at the BRL is AFWL version 8, received in September 1978, with modifications made by the BRL, and by SAI[5] under contract to the BRL. Some of the modifications were necessary to run the code on the BRL's CDC 7600; others were necessary to convert from using a SAIL[6] preprocessor for HULL to using a CDC update/SAI-POST preprocessing system. Other modifications were added to allow the input of an off-angle step shock through any combination of the left, bottom, and aft boundaries of the 3-D computational grid and the left and bottom boundaries of the 2-D Cartesian grid.

The HULL hydrocode uses an explicit time step predictor-corrector method similar to a Lax-Wendroff[7] scheme to solve the inviscid Euler equations. Detailed descriptions of the differencing method used in

---

[5] *Hasdal, J. A., Chambers, B. S., and Clemens, R. W., "Support to BRL: HULL Code Implementation on a CDC 7600," SAI-80-701-AQ, Science Applications, Inc., McLean, VA (August 1979).*

[6] *Graham, D. C., Gaby, L. P., and Rhoades, C. E., "SAIL, An Automated Approach to Software Development and Management," AFWL Interim Report 1971-6, U.S. Air Force Weapons Laboratory, Kirtland Air Force Base, NM (October 1976).*

[7] *Richtmyer, R. D. and Morton, K. W., "Difference Methods for Initial Value Problems," Interscience Publishers, Inc., John Wiley & Sons, Inc., Second Edition (1967).*

HULL are given in References 2 and 3. The computation is performed in two phases, a Lagrangian phase where flow field cells perform work on one another, and an Eulerian phase where material is fluxed across cell boundaries using a donor cell method.

Table III lists the HULL hydrocode computations described in this paper. Computation H.1, which matches experiment E.1 in shock strength and ambient conditions, will be discussed in detail in this and the next section. The remaining HULL computations, H.2 - H.7, match experiment E.2. Results from H.2 - H.7 will be discussed in the section titled "Convergence Study." The Courant-Friedrichs-Lewy number was 0.5 for all computations; artificial viscosity was not used.

The finite difference grid used for computation H.1 contains 92,512 flow field cells, with a 49 × 59 × 32 grid in the X, Y, and Z directions, respectively. The S-280 shelter model is built using 6,912 nearly cubical rigid cells, with 16 equal X direction cells (ΔX = .7366 cm), 27 equal Y direction cells (ΔY = .7253 cm), and 16 equal Z direction cells (ΔZ = .7112 cm). The rigid cells do not directly enter the computation. They are used to construct an obstacle having a perfect reflection surface. A rigid cell does require the same storage space as a hydrodynamic cell, so this space is wasted. To minimize the smearing of the computational shock as it passes through the grid prior to striking the shelter, the shock is placed well into the grid at the initial mesh generation, 2.66 cm upstream of the shelter leading edge. The shock input algorithm keeps track of the theoretical intersection of the shock wave with the boundaries, progressively moving the input shock along the boundaries as the computation proceeds.

Figure 2 shows a top view of an isobar (constant pressure) plot of the flow field for H.1 in the bottom-most plane of cells after one computational cycle. (A similar plot is not available at cycle 0.) Shock arrival time at the shelter leading edge is defined as t = 0.0. In Figure 2, the incident computational shock is indicated by the closely-spaced pressure contours. The shock is moving from the lower left corner of the figure toward the upper right corner. What appears to be a bent right end of the shock is actually the set of pressure contour identification numbers which are overwritten by the plot routine. The contour labelled "1" is not a pressure contour, but is an artificial use of the contour algorithm to show the outline of the shelter in this plane.

Figure 3 shows isobars in the same plane at t = 374.9 μs; the shock wave has passed slightly more than half-way across the shelter. Contour 5 shows the general shape of the reflected shock. Figures 2 and 3 give a qualitative indication of the flow field predicted by the 3-D HULL hydrocode. The next section provides detailed comparisons between experiment E.1 and HULL computation H.1.

V. COMPARISON OF COMPUTATIONAL AND EXPERIMENTAL RESULTS

In this section "experiment" refers to experiment E.1, and "computation" refers to computation H.1. Computation H.1 was run on the BRL's CDC 7600 for 155 computational cycles, with a total job time of 49 minutes at a cost of $776.

Figure 4 shows a comparison between the measured and the computed overpressure-time history for gage F2. The gage is located at 3/4 of the distance along the shelter front face and at 1/4 of the shelter height from the ground plane. The agreement between the two results is good, except for the initial shock interaction with the structure. Because the computational shock is spread over three or four flow field cells, it shows an earlier initial interaction and a reduced peak[8]. The agreement beyond the peak is very good, although the computed overpressure is slightly greater than that for the experiment for $0.6 \leq t \leq 1.0$ ms. The second peak in the experimental data at 1.22 ms is caused by the arrival of a secondary shock produced by the interaction of the incident shock with the model; it traveled to the shock tube wall, reflected off the wall, and returned to strike the model. A similar second peak is seen in the other comparisons in this section. It should be noted that the X's on the H.1 curve in this and the next three figures mark every fifth computed data point; they have been added primarily as a visual aid.

Figure 4 shows a measured peak reflected overpressure of 86.2 kPa occurring at .320 ms, and a corresponding computed peak of 76.2 kPa at .331 ms. The difference in time is due in part to the difficulty in establishing a zero reference time at the shelter leading edge for the experiment because of the discrete data sampling rate and the gage diameter and response time. There are similar computational problems due to the numerical diffusion of the shock wave as it travels through the finite difference grid; this causes the peak reflected overpressure to be reduced and delayed in time[8,9,10]. It was decided to establish time-zero estimates for the experiment and the computation independently and use these to compare the results.

[8] *Lottero, R. E., "Comparison of 3-D Hydrocode Computations for Shock Diffraction Loading on an S-280 Electrical Equipment Shelter," to be published in the proceedings of the 1980 Army Numerical Analysis and Computers Conference, 20-21 February, 1980, NASA-Ames Research Center, Moffett Field, CA.*

[9] *Lottero, R. E., "Detailed Comparison of 3-D Hydrocode Computations for Shock Diffraction Loading on an S-280 Electrical Equipment Shelter," to be published as a BRL report, U.S. Army Ballistic Research Laboratory, Aberdeen Proving Ground, MD.*

[10] *Gentry, R. A., Stein, L. R., and Hirt, C. W., "Three-Dimensional Computer Analysis of Shock Loads on a Simple Structure," BRL-CR-219, U.S. Army Ballistic Research Laboratory, Aberdeen Proving Ground, MD (March 1975).*

Neither the measured nor the computed peak reflected overpressure were near the expected peak of 115 kPa. The measured peak of 86.2 kPa is 25% less than the expected peak, and 16% greater than the normal reflection peak. The computed peak is 34% less than the expected peak, and 3% greater than the normal reflection peak. This is likely due to the finite gage and cell sizes which are used. In the experiment, the gage diameter is 2.6% of the span of the front face. In the computation, the cell dimension in the Y direction on the front face is 3.7% of the span, 42% larger than the gage diameter. It appears that the spatial extent of the overpressure peak is so small that it is largely integrated out even with these relatively small units of measure. Thus, it can be concluded that the overpressure peak does not make a significant contribution to the loading on the model and hence is not significant to the S-280 shelter itself. The problem of resolving the peak is still of interest from a fluid dynamics viewpoint, and will be studied further in the next section.

Figure 5 shows a comparison between the measured and computed overpressure-time histories for gage S2, located in the center of the windward side face. The angle between the shock front and this face is 37.5°. The agreement is good except for the initial shock interaction. For this angle, the expected peak reflected overpressure is essentially equal to the normal reflection overpressure of 74.2 kPa. The computational peak is 77.8 kPa, 5% greater than the normal reflection value and 7% greater than the measured peak (73.0 kPa), which is in turn 2% lower than the normal reflection peak. The peak values for this gage position will be discussed in detail in the next section.

Figure 6 shows a similar comparison for gage S1, located at the center of the leeward side face. It, too, shows a smearing of the computational shock, which has also been weakened by a rarefaction wave produced at the trailing edge of the front face. The general agreement between the curves is good. They both show a pressure plateau of 22.5 kPa for $0.6 \leq t \leq 0.9$ ms, caused by the weakened incident shock. The pressure rise which begins at .9 ms is caused by the incident shock breaking over the top face, sending another weakened shock down the leeward side face. The curves agree qualitatively, but the computed results vary from 5 to 10% less than the experimental results after .9 ms. It may be that viscous effects, which HULL cannot model, are becoming important by this time.

Figure 7 shows a similar comparison for back face gage B2. This gage is located at 3/4 of the distance along the back face, and at 1/4 of the height of the shelter from the ground plane. The agreement between the computed and the measured results is very good, except at the time of initial shock arrival (for the same reasons discussed earlier) and $t > 1.0$ ms when viscous effects may be important.

Figures 4 through 7 typify the good agreement between the computed and experimental results over the entire structure, including the top face. Good agreement is also shown when the overpressure results are integrated in time to compute overpressure impulse. Those results plus a more detailed analysis may be found in Reference 11.

VI. CONVERGENCE STUDY

Because the expected peak reflected overpressure was not obtained on the front face (gage position F2) in either the calculations or the experiment, a convergence study was performed to study the sensitivity of the peak values to both grid and gage size. It was expected that smaller grid sizes and smaller gages having higher frequency response were needed to resolve the small region of enhanced reflected overpressure on the front face. Only a limited grid refinement was possible for the 3-D computational problem because of cost and storage limitations. Most of the computational results were obtained for a representative 2-D slice of the grid for H.1, which then modeled a shelter with infinite height. Experiment E.2 was performed to study the effect of reduced gage size (.32 cm) and higher frequency response on the measured front face peak.

The grid convergence study matching shot E.2 consists of six computations: H.2 and H.3 (3-D) and H.4-H.7 (2-D). The dimensionless cell sizes in Table III are normalized by the values of ΔX, ΔY, and ΔZ on the shelter surface in H.1. The experimental gage sizes are normalized in the same way, using ΔY from H.1 for the front face gage and ΔX from H.1 for the windward side gage. Figure 8 compares the peak reflected overpressures obtained at gage position F2 on the front face. There is a systematic displacement between the 2-D and 3-D results, apparently due to differences in the finite difference algorithms; this is currently being studied. The indicated "expected" peak overpressures for E.1 and E.2 are slightly different because of differences in the incident shock strengths. These expected values are inferred from Bertrand's experimental measurements[1]. The experiments showed essentially no difference in overpressure peaks relative to the expected values. The computations show that the peak overpressure increases toward the expected value as grid size approaches zero, but the results for windward side face gage S2 indicate that part of that increase may be due to artificial sensitivity of the peak to grid size.

Figure 9 shows the results of the convergence study for gage position S2. In this case, $\alpha = 37.5°$, and the expected peak overpressures are the same as for normal reflection. The qualitative trend

[11] *Lottero, R. E., Wortman, J. D., Bertrand, B. P., and Kitchens, C. W., "Oblique Interaction of a Shock Wave with a Three-Dimensional Simple Structure, Part I, to be published as a BRL Report, U.S. Army Ballistic Research Laboratory, Aberdeen Proving Ground, MD.*

is similar to that shown in Figure 8. The computational results overshoot the expected values by as much as 20% as the grid size is decreased, indicating an undesirable sensitivity of the peak value to grid size. This difficulty is being investigated.

VII. CONCLUSIONS

This study has shown that the 3-D HULL hydrocode can produce accurate shock diffraction loading predictions for this class of problems at moderate cost. The BRL code version has been modified to treat an incident step shock moving obliquely through the 2-D and 3-D Cartesian grids. This allows the modeling of the 32.75 and 34.5 kPa (nominal 5 psi) overpressure shocks striking the front face of an S-280 Electrical Equipment Shelter at a 52.5° angle of incidence, using smooth shelter walls instead of undesirable rough "stair-stepped" surfaces formed if the shelter were rotated in the grid. The agreement between the 3-D computational and experimental results is good on all shelter faces. Errors of from -12% to -9% (H.1/E.1 and H.2/E.2, respectively) are experienced in resolving the peak reflected overpressure on the front face (F2), and +7% to +8% on the windward side face (S2); error magnitudes less than 10% are present beyond the peak. A grid convergence study has quantified the sensitivity of the peak reflected overpressure to grid size. The expected enhanced peak overpressure on the front face at 52.5° obliquity proved to be difficult to measure or compute. It is of such short duration and limited spatial extent that it is apparently unimportant as a damage mechanism for the S-280 Electrical Equipment Shelter.

REFERENCES

1. Bertrand, B. P., "Measurements of Weak Shock Wave Reflected Pressure Histories on a 2-Dimensional Surface," ARBRL-MR-02966, U.S. Army Ballistic Research Laboratory, Aberdeen Proving Ground, MD (October 1979).

2. Fry, M. A., Durrett, R. E., Ganong, G. P., Matuska, D. A., Stucker, M. D., Chambers, B. S., Needham, C. E., and Westmoreland, C. D., "The HULL Hydrodynamics Computer Code," AFWL-TR-76-183, U.S. Air Force Weapons Laboratory, Kirtland Air Force Base, NM (September 1976).

3. Fry, M. A., Needham, C. E., Stucker, M. D., Chambers, B. S., and Ganong, G. P., "AFWL HULL Calculations of Air Blast Over a Dam Slope," AFWL-TR-76-154, U. S. Air Force Weapons Laboratory, Kirtland Air Force Base, NM (October 1976).

4. Coulter, G. A. and Bertrand, B. P., "BRL Shock Tube Facility for the Simulation of Air Blast Effects," BRL-MR-1685, U.S. Army Ballistic Research Laboratories, Aberdeen Proving Ground, MD (August 1965).

5. Hasdal, J. A., Chambers, B. S., and Clemens, R. W., "Support to BRL: HULL Code Implementation on a CDC 7600," SAI-80-701-AQ, Science Applications, Inc., McLean, VA (August 1979).

6. Graham, D. C., Gaby, L. P., and Rhoades, C. E. "SAIL, An Automated Approach to Software Development and Management," AFWL Interim Report 1971-6, U.S. Air Force Weapons Laboratory, Kirtland Air Force Base, NM (October 1976).

7. Richtmyer, R. D. and Morton, K. W., "Difference Methods for Initial Value Problems," Interscience Publishers, Inc., John Wiley & Sons, Inc., Second Edition (1967).

8. Lottero, R. E., "Comparison of 3-D Hydrocode Computations for Shock Diffraction Loading on an S-280 Electrical Equipment Shelter," to be published in the proceedings of the 1980 Army Numerical Analysis and Computers Conference," 20-21 February, 1980, NASA-Ames Research Center, Moffett Field, CA.

9. Lottero, R. E., "Detailed Comparison of 3D Hydrocode Computations for Shock Diffraction Loading on an S280 Electrical Equipment Shelter," to be published as a BRL Report, U.S. Army Ballistic Research Laboratory, Aberdeen Proving Ground, MD.

REFERENCES (Cont'd)

10. Gentry, R. A., Stein, L. R., and Hirt, C. W., "Three-Dimensional Computer Analysis of Shock Loads on a Simple Structure," BRL-CR-219, U.S. Army Ballistic Research Laboratory, Aberdeen Proving Ground, MD (March 1975).

11. Lottero, R. E., Wortman, J. D., Bertrand, B. P., and Kitchens, C. W., "Oblique Interaction of a Shock Wave with a Three-Dimensional Simple Structure, Part I," to be published as a BRL Report, U.S. Army Ballistic Research Laboratory, Aberdeen Proving Ground, MD.

TABLE I. EXPERIMENTAL SHOTS

Shot Number		α	Ambient Values		Shock Overpressure
Actual	This Paper	(Degrees)	p(kPa)	T(°C)	(kPa)
24-79-126	E.1	52.5	101.42	22.25	32.75
24-79-134	E.2	52.5	101.90	24.31	34.50

TABLE II. GAGE POSITIONS

Gage Number	Face	X' (cm)	Y' (cm)	Z' (cm)
F2*	Front	0.00	14.68	2.84
B2	Back	11.79	14.68	2.84
S1	Leeward Side	5.89	19.58	5.69
S2	Windward Side	5.89	0.00	5.69

*High frequency gage, shot E.2 only.

TABLE III. HYDROCODE COMPUTATIONS

Calculation Number		Dimensions	Cell Sizes Relative to H.1
Actual	This Paper		
37.126	H.1	3-D	1.0
37.0	H.2	3-D	1.0
37.001	H.3	3-D	0.5
37.11	H.4	2-D	1.0
37.9	H.5	2-D	0.5
37.10	H.6	2-D	0.25
37.6	H.7	2-D	0.125

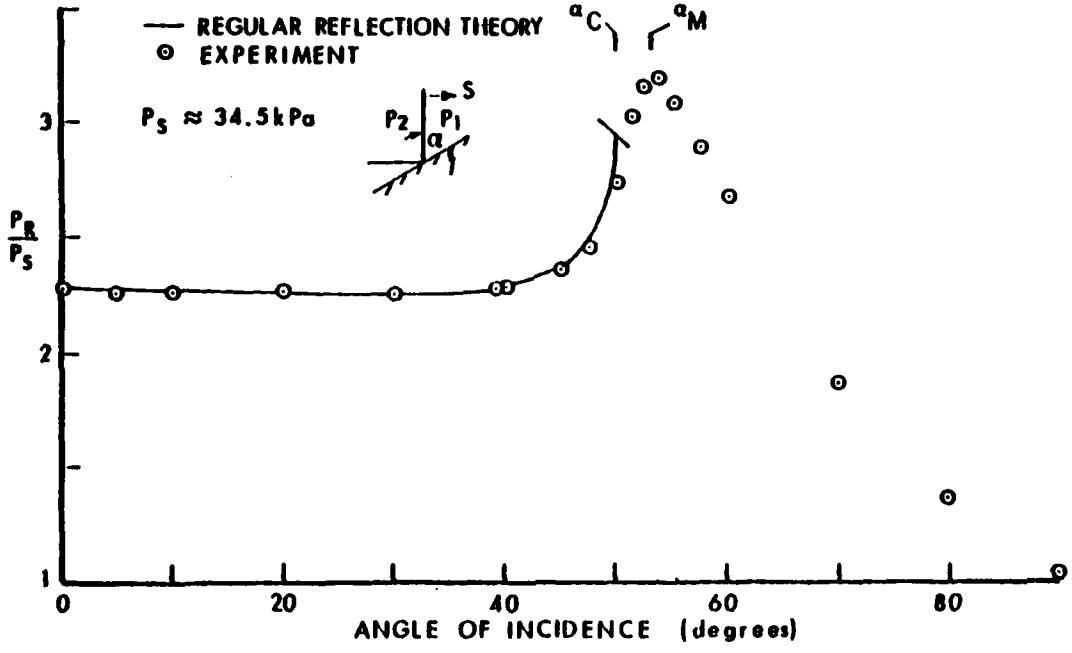

Figure 1. Experimentally determined reflection factors. (Reproduced in part from Reference 1.)

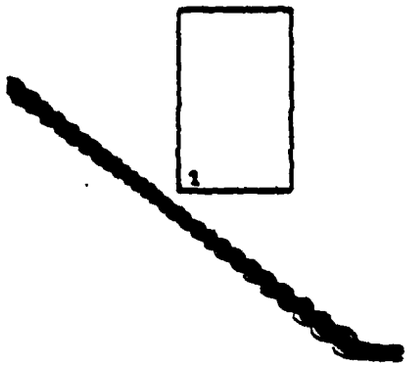

Figure 2. Isobars at t = -68.2 μs in ground plane for H.1 (qualitative view).

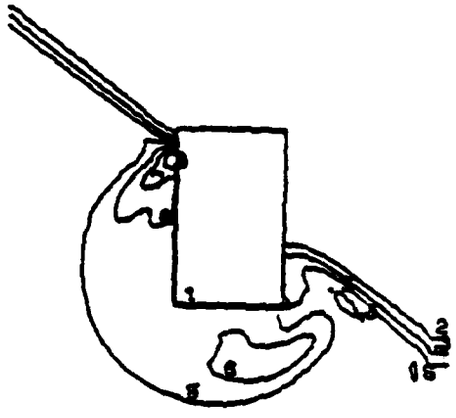

Figure 3. Isobars at t = 374.9 μs in ground plane for H.1 (qualitative view).

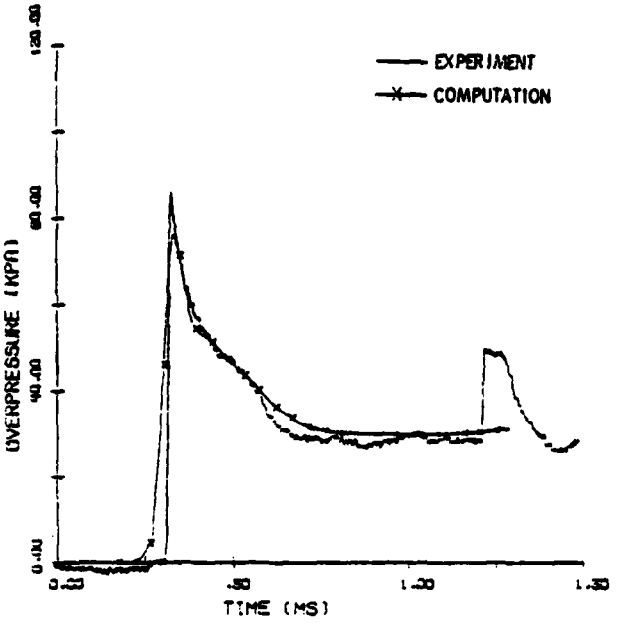

Figure 4. Comparison of measured and predicted overpressure on front face gage F2.

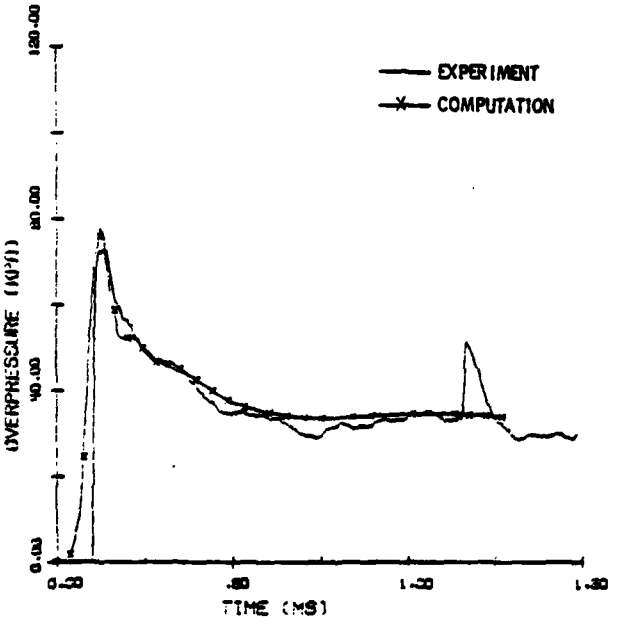

Figure 5. Comparison of measured and predicted overpressure on windward side face gage S2.

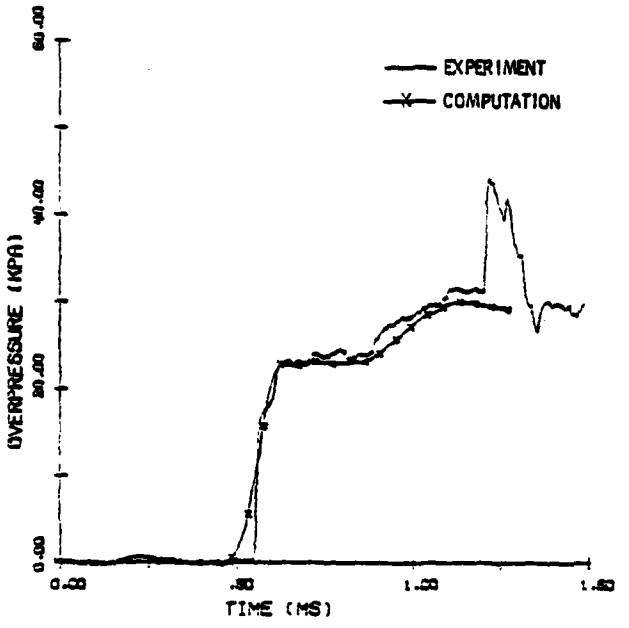

Figure 6. Comparison of measured and predicted overpressure on leeward side face gage S1.

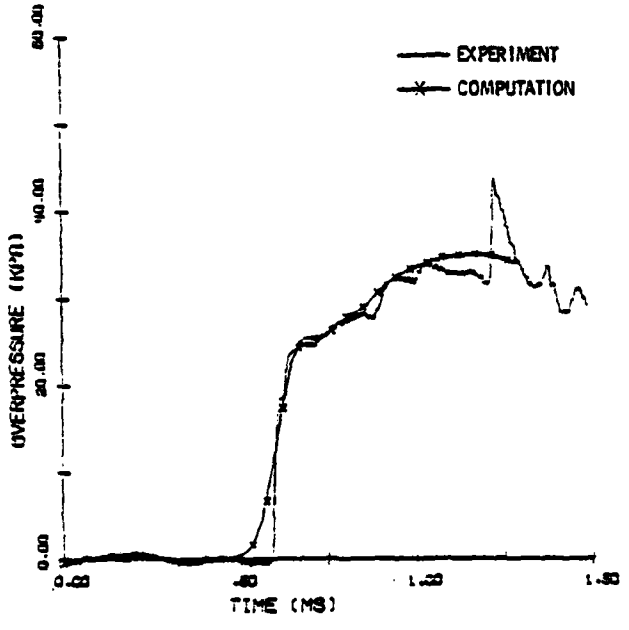

Figure 7. Comparison of measured and predicted overpressure on back face gage B2.

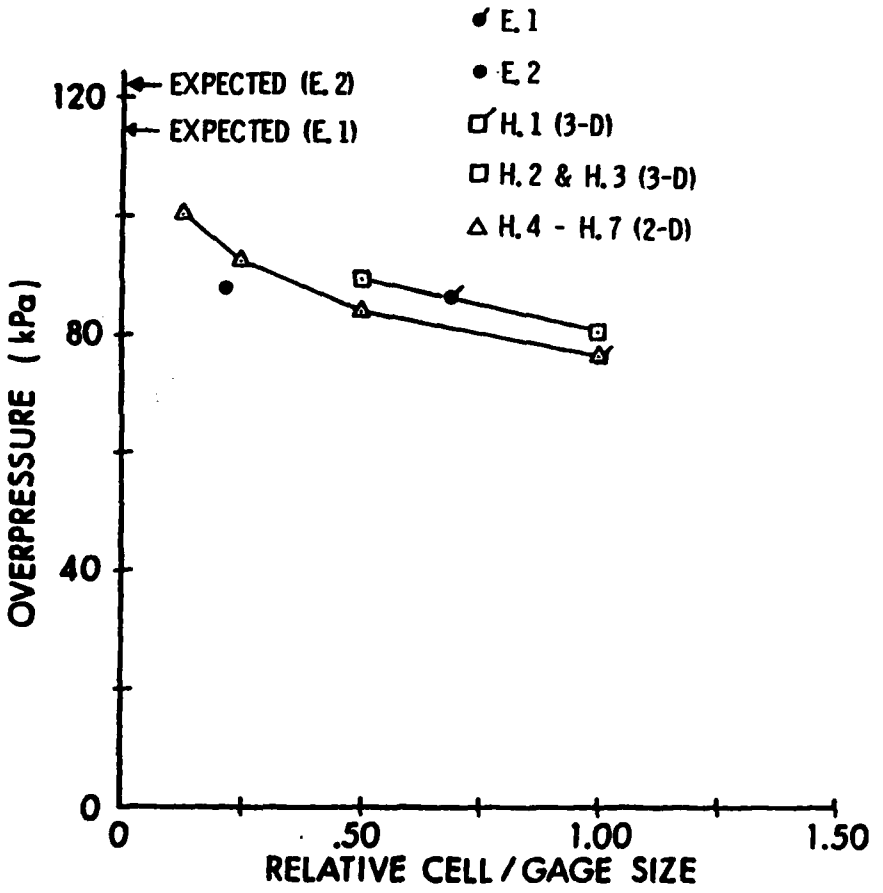

Figure 8. Peak overpressure at front face gage position F2.

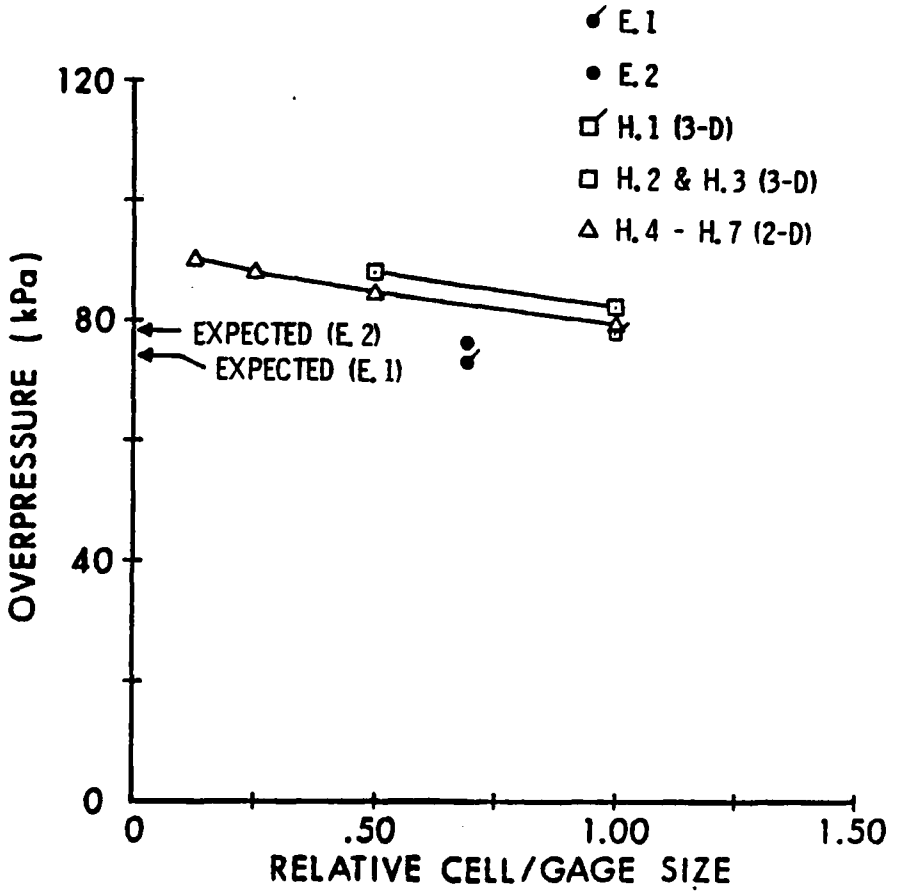

Figure 9. Peak overpressure at windward side face gage position S2.

Navier-Stokes Solutions for Spin-Up in a Filled Cylinder

Clarence W. Kitchens, Jr.

Ballistic Research Laboratory
U.S. Army Armament Research and Development Command
Aberdeen Proving Ground, Maryland

Abstract

A predictor-corrector multiple-iteration scheme is adapted and used to solve the unsteady Navier-Stokes equations. Numerical solutions for Reynolds numbers up to 50,000 are obtained for the transient spin-up flow in a cylindrical container. The grid point distribution is optimized using coordinate transformations to simultaneously resolve details of both the interior and endwall/sidewall boundary layer flows formed during spin-up. Calculations for five test problems show very good agreement with previous computations and experimental measurements. Transient phenomena occurring at early time near the sidewall, including reversed flow regions and inertial oscillations are discussed as well as certain aspects of the endwall Ekman layer flow.

Nomenclature

a	cylinder radius
$b,\bar{c},d,e$	coordinate transformation constants
c	cylinder half-height
Ek	Ekman number [$= \nu/(\Omega c^2)$]
r,R	nondimensional and dimensional radial coordinate
Re	Reynolds number [$= \Omega\, a^2/\nu$]
t,T	nondimensional and dimensional time ($t = \Omega T$)
u,v,w	r,θ,z nondimensional velocity components
z,Z	nondimensional and dimensional axial coordinate
α	cylinder aspect ratio [$= c/a$]
β	transformed radial coordinate
γ,Γ	nondimensional and dimensional circulation
ε_i	iteration convergence criteria
$\zeta,\mathbf{Z}$	nondimensional and dimensional vorticity
η	transformed axial coordinate
θ	azimuthal coordinate
ν	liquid kinematic viscosity
ψ,Ψ	nondimensional and dimensional stream function
Ω	final cylinder rotation rate
Ω_i	initial cylinder rotation rate
$\Delta\beta,\Delta\eta$	grid sizes in β and η coordinates
Δt	time step
Superscripts	
m	γ,ζ - iteration level
n	ψ - iteration level

Introduction

The objective of this work is to develop an accurate numerical procedure for solving the unsteady Navier-Stokes equations to describe transient spin-up flow occurring in a cylindrical container when it is suddenly rotated about its longitudinal axis. Knowledge of this internal flow is needed to design gun-launched projectiles which carry smoke/incendiary agents or chemical payloads. Liquid payloads enhance spin decay of projectiles[1,2] and their presence can produce flight dynamic instabilities as a result of resonance between the projectile nutational motion and inertial oscillations in the rotating liquid[3]. From a computational viewpoint this problem is instructive because it is an example of a class of internal flow problems for which computational experiments can uncover details of the flow that cannot be easily visualized or measured experimentally.

The results presented here demonstrate that a predictor-corrector multiple-iteration (PCMI) technique developed by Rubin and Lin[4] for solving steady three-dimensional boundary region problems can be successfully adapted to solve the unsteady Navier-Stokes equations. In the present approach this method is combined with the Gauss-Seidel procedure[5] and grid stretching transformations to produce an accurate procedure for describing the spin-up process. Calculations with the PCMI method have been performed for spin-up from rest and spin-up from an initial state of solid-body rotation. Numerical results have been obtained for a range of cylinder aspect ratios, α, from 0.3 to 4.4 and a range of Reynolds numbers from 215 to 50,000. Calculations performed for five test problems show very good agreement with previous

computations[6,7,8] and experimental measurements[6,9]. Numerical results have been used[10] to quantify the flow in the Ekman (or endwall) boundary layers during spin-up from rest and develop an appropriate compatibility condition for use in Wedemeyer's spin-up model[1]. Neitzel[11] successfully used the PCMI procedure developed in the present work to study the onset and temporal development of fluid dynamic instabilities during spin down in a cylinder.

Governing Equations and Boundary Conditions

The calculations employ a finite-difference analog of the unsteady axisymmetric Navier-Stokes equations formulated in cylindrical coordinates (r,θ,z). The equations are expressed in terms of ψ,ζ and γ, instead of velocity and pressure in order to simplify the numerical procedure. In dimensionless variables the governing equations are

$$\nabla^2\psi - \psi_r/r = r\zeta, \tag{1}$$

$$\zeta_t + u\zeta_r + w\zeta_z - u\zeta/r - 2\gamma\gamma_z/r^3 = (1/Re)[\nabla^2\zeta + \zeta_r/r - \zeta/r^2], \tag{2}$$

$$\gamma_t + u\gamma_r + w\gamma_z = (1/Re)\ [\nabla^2\gamma - \gamma_r/r]; \tag{3}$$

where the subscripts denote partial differentiation and

$$Re = \Omega a^2/\nu, \tag{4}$$

$$\nabla^2 = \partial^2/\partial r^2 + \partial^2/\partial z^2, \tag{5}$$

$$\gamma = rv, \tag{6}$$

$$\zeta = u_z - w_r, \tag{7}$$

with the axisymmetric stream function defined so that

$$u = \psi_z/r \text{ and } w = -\psi_r/r. \tag{8}$$

The Ekman number based on half-height is related to Re by

$$Ek = \nu/(\Omega c^2) = 1/(\alpha^2 Re). \tag{9}$$

The stream function-vorticity-circulation formulation yields an elliptic PDE, Eq. (1), and two parabolic PDEs, Eqs. (2) and (3), which are coupled. The boundary conditions impose additional coupling between ψ and ζ.

The nondimensional variables used here are defined by

$$r = R/a, \quad z = Z/a, \quad t = \Omega T,$$

$$u = U/(\Omega a), \quad v = V/(\Omega a), \quad w = W/(\Omega a), \tag{10}$$

$$\psi = \Psi/(\Omega a^3), \quad \gamma = \Gamma/(\Omega a^2), \quad \zeta = Z/\Omega.$$

The initial conditions for spin-up are

$$\psi = \zeta = 0, \ \gamma = \Omega_i r^2/\Omega \text{ for } t \leq 0. \tag{11}$$

Computational efficiency and resolution are improved by employing a symmetry boundary condition at the cylinder mid-plane, $z = \alpha$. This effectively halves the number of grid points required. The boundary conditions for $t > 0$ are

$$\psi(t, 0, z) = \gamma(t, 0, z) = \zeta(t, 0, z) = 0, \tag{12}$$

$$\psi(t, 1, z) = 0, \ \gamma(t, 1, z) = 1, \ \zeta(t, 1, z) = \psi_{rr}(t, 1, z), \tag{13}$$

$$\psi(t, r, 0) = 0, \ \gamma(t, r, 0) = r^2, \ \zeta(t, r, 0) = \psi_{zz}(t, r, 0)/r, \tag{14}$$

$$\psi(t, r, \alpha) = \zeta(t, r, \alpha) = 0, \ \gamma_z(t, r, \alpha) = 0. \tag{15}$$

The boundary conditions for vorticity along the sidewall and endwall, Eqs. (13) and (14), are derived from Eqs. (7) and (8) by imposing the no-slip conditions for velocity. Fig. 1 illustrates the coordinate system and boundaries used in the numerical calculations.

During spin-up there are viscous regions near the sidewall and endwalls which become very thin as Re becomes larger than 1000 or so, necessitating a fine grid to resolve the boundary-layer type phenomena along these walls. Analytical coordinate transformations[12]

$$\beta = \frac{\ln[(b + r)/(b - r)]}{\ln[(b + 1)/(b - 1)]} , \tag{16}$$

$$\eta = 1 + \frac{\ln[(\bar{c} + z/\alpha - 1)/(\bar{c} - z/\alpha + 1)]}{\ln[(\bar{c} + 1)/(\bar{c} - 1)]} , \tag{17}$$

with $b = (1 - d)^{-\frac{1}{2}}$ and $\bar{c} = (1 - e)^{-\frac{1}{2}}$ are used to optimize the grid point placement and transform a nonuniform grid in the physical plane into an equally-spaced grid in the computational plane. Fig. 2 shows a typical grid point distribution in the physical plane produced with Eqs. (16) and (17). The complete set of transformed equations and boundary conditions is given in Ref. 10.

Discussion of Numerical Procedure

Several methods have been used by previous investigators to solve the stream function-vorticity form of the Navier-Stokes equations. Perhaps the most popular technique is to combine the alternating-direction implicit (ADI) method[13] for the ζ and γ-equations with either an ADI or successive over-relaxation (SOR) method[14] for the ψ-equation. Briley[7,8] applied the former approach to spin-up in a cylinder. In the present approach a semi-implicit PCMI method is used to solve the ζ and γ-equations and the Gauss-Seidel method[5] is used to solve the ψ-equation.

The PCMI technique was adopted for this unsteady problem because the present author's prior experience[15] showed the method to be reliable

and easy to implement. Rubin and Lin[4] originally used the PCMI technique to investigate steady hypersonic viscous flow along a right-angle corner, imposing a symmetry condition along the diagonal. This resulted in the computation of large gradients in only one coordinate direction, which they treated implicitly. In the present application there are large gradients in two coordinate directions and some of the advantages of the PCMI technique are compromised. In adapting this technique to the present problem we chose to treat the radial direction implicitly to maintain consistency with previous work[2] based on the Wedemeyer spin-up model. This choice was advantageous in studying the early-time flow development along the sidewall and in applying the symmetry boundary conditions at $z = \alpha$. It leads, however, to an explicit time step restriction, to be discussed, that is governed by the large axial gradients in the endwall boundary layer.

In the present method all flow gradients in the z-direction are approximated by prediction and subsequent correction in this time-iterative technique. This approach eliminates cross coupling of grid points, thus reducing the size of the inversion matrices and decreasing computer time. The iteration procedure allows the boundary vorticity to converge and also allows the nonlinear terms to be approximated and then corrected, giving a more accurate simulation of the nonlinear coupling between equations.

Central difference formulae are used for all spatial derivatives at interior points, avoiding false-diffusion effects introduced by upwind difference schemes. Temporal derivatives are approximated by second-order accurate one-sided difference formulae involving three time levels.

The truncation errors for interior points are of $O(\Delta t^2, \Delta\beta^2, \Delta\eta^2)$. Ref. 10 gives the complete set of finite-difference equations used in this work, together with a discussion of the manner in which the boundary conditions were implemented. It should be noted that a first-order form for the wall vorticity boundary conditions[10] was used to obtain the results discussed in this paper. Based on test calculations for $\alpha = 1$ and $Re = 1000$, the numerical technique appears to be fully compatible with second-order accurate wall vorticity expressions.

The numerical procedure is applied by using the PCMI method to solve the difference equations for γ^{m+1} and ζ^{m+1} using the m-iterate values to form the coefficients of the nonlinear terms; where m denotes the γ and ζ-iteration level. The calculations start along the row of points adjacent to the midplane and work downward toward the endwall (see Fig. 2). The derivatives in the β-direction are treated implicitly, requiring the solution of a tridiagonal system of equations along each successive row.

At the end of each m-iterative cycle the ψ-difference equation is solved iteratively using the Gauss-Seidel method; the SOR method was used for test calculations but it did not speed up the overall procedure. The solution for ψ is obtained by starting at the interior grid point adjacent to $\beta = \eta = 0$ and sweeping first in β and then η, making use of updated values as soon as they become available. Convergence of ψ is assumed when

$$|\psi^{n+1} - \psi^{n}| \leq \varepsilon_1 \tag{18}$$

at every grid point, where n is the ψ-iteration level. Convergence is

typically achieved in 2-3 n-iterations with $\varepsilon_1 = 1 \times 10^{-7}$. The converged values for ψ are used to update the boundary values for ζ and repeat the iteration process for γ and ζ. The iteration process is assumed to converge when both

$$|\gamma^{m+1} - \gamma^m| < \varepsilon_2 \ , \tag{19}$$

$$|\zeta^{m+1} - \zeta^m| < \varepsilon_3 \tag{20}$$

at every grid point. It typically requires 2-3 m-iterations to satisfy Eqs.(19) and (20) with $\varepsilon_2 = \varepsilon_3 = 1 \times 10^{-4}$; at very early time 5-10 iterations are needed due to the severe flow unsteadiness caused by the impulsive start and the subsequent inaccuracy of the extrapolated guesses.

Stability Properties of Numerical Procedure

Rubin and Lin[4] have analyzed the interior point stability of the PCMI method for a linear model equation that approximates the unsteady two-dimensional Navier-Stokes equations. Their analysis shows that if iteration is not used the present PCMI technique has a stability restriction of the form $\Delta t < K\Delta\eta^2$, because the method is explicit in η; $\Delta\beta$ does not appear because β is treated implicitly. On the basis of their results for the case of repeated iteration, we conclude that the appropriate stability criterion for the present iterative scheme is

$$\Delta t < \text{Min}\left|\frac{\Delta\eta}{\eta_{zz}/Re + \beta_r \eta_z \psi_\beta / r}\right| \tag{21}$$

taken over all interior grid points. The term η_{zz}/Re results from the coordinate transformation in z; it vanishes if an equally-spaced grid is used in the axial direction.

Since the results of such a linear stability analysis are inconclusive, we carried out test calculations to determine the validity of Eq. (21). These studies were conducted for $\alpha = 1$ and Re = 1000, 9742 and 50,000, using three combinations of grid sizes for each Re and several different transformation parameter combinations. The results show that numerical stability is always achieved when Eq. (21) is satisfied, even when equally-spaced points are used. In limited cases numerical stability is achieved with Δt as large as 1.5 times the critical value predicted by Eq. (21). In general, the numerical studies confirm that the linear theory provides good guidance for the spin-up problem. Eq. (21) was satisfied at each time step in the illustrative examples to be discussed next.

Comparison with Previous Work

The present method has been used to treat the problems of spin-up from rest and spin-up from an initial state of solid-body rotation. We compare our results with those of Warn-Varnas et al.[6] for the latter problem. They used an ADI technique coupled with a scheme developed by Williams[16] to solve the velocity-pressure form of the Navier-Stokes equations. In their calculations they differenced the governing equations directly on a stretched grid instead of transforming to new coordinates. Their computations were verified by measurements taken with a laser doppler velocimeter (LDV) system.

Fig. 3 shows a comparison of the present calculations with results from Ref. 6 (their Fig. 13b) in terms of their quantity called "zonal velocity" (ordinate in Fig. 3), which is a scaled non-dimensional

angular velocity. The results are shown at r = 0.25 on the cylinder symmetry plane for a case with α = 0.3182, Re = 7334 and Ω_i = 0.8182Ω. The inertial oscillations excited by the sudden increase in cylinder rotation rate are clearly predicted in both computations and are in fairly good agreement with experimental measurements. Both of these numerical results appear to be within the experimental uncertainty associated with these data, according to the error analysis presented in Ref. 6. Comparisons fc · several other positions in the cylinder (not shown here) give similar agreement for both the decay of the zonal velocity and the amplitudes and phases of the inertial oscillations. The computation time and number of grid points used to obtain the numerical results in Ref. 6 are not stated. The PCMI calculations used a stretched (d = 0.3, e = 0.1) 41 × 21 (r-z) grid with 600 time steps (Δt = 0.063). Approximately 2 to 3 m-iterations, each consisting of 2-3 n-iterations, were required per time step to satisfy Eqs. (18) - (20). The complete simulation represented in Fig. 3 required 52s of CPU time on a CDC 7600 computer.

The problem of spin-up from rest has been emphasized in the present work because of its application to liquid-filled projectiles. This problem is nonlinear; the previous problem can be linearized for small $\Omega - \Omega_i$. Comparisons have been made with computations of Briley[7] and Briley and Walls[8] for spin-up from rest. They studied this problem for low Re using the ADI technique to solve the stream function-vorticity form of the Navier-Stokes equations. Fig. 4 compares values of rotational volume flow rate,

$$Q = (1/\alpha) \int_0^1 \int_0^{2\alpha} v \, dz dr, \tag{22}$$

for two cases. The quantity Q can be used to obtain a measure of the spin-up time. Briley and Walls used a uniform grid that became restrictive at moderate Re due to the small thickness of the endwall boundary layers; they obtained results for Re as large as 1167. Our calculations appear to be in good agreement with all of their results for spin-up. Neitzel's comparisons for spin-down[11], however, showed only qualitative agreement with Briley and Walls' results for Re = 1167. The observed differences are thought to be due to grid size effects.

The present computations have also been compared with LDV measurements taken by Watkins and Hussey[9]. Fig. 5 presents comparisons of azimuthal velocity along the cylinder mid-plane at four instants during spin-up for a case with α = 1.515, Re = 3076. Fig. 6 shows similar comparisons for α = 1, Re = 9741.6. The size of the symbols used to plot the experimental data in Figs. 5 and 6 approximately represents the size of the error bars that should be attached to these data. The calculations in Fig. 6 used a 21 × 21 grid with d = e = 0.10 and required 2745 time steps with Δt = 0.10. Approximately 2 m-iterations, each with 3 n-iterations, were required to satisfy Eqs (18) - (20), for a total CPU time of 69s.

The results shown in Figs. 4, 5 and 6 are representative of the "core" flow in Wedemeyer's model of spin-up from rest and they can be predicted fairly well using that model; the accuracy of the prediction increases as Re increases. However, Wedemeyer's model says very little

about the flow in the corner region, along the sidewall and in the Ekman layers. These phenomena will be discussed next.

Transient Phenomena during Spin-Up from Rest

The PCMI procedure has been used to study inertial oscillations and temporary regions of reversed secondary flow that develop and then subsequently decay during the initial stages of spin-up from rest. In a typical case[10] with $\alpha = 0.3182$ and $Re = 7334$ weak inertial oscillations develop in the flow adjacent to the sidewall immediately upon spin-up, decay in amplitude during the next few rotations and become so weak that they cannot be detected at all for $t > 40$. The phenomenon observed here is similar to that indicated in Fig. 3, except that in this case the inertial oscillations are weaker and they only occur in the rotating fluid adjacent to the sidewall. The non-rotating fluid in the interior, for instance along the mid-plane at $r = 0.25$ and $0 \leq t \leq 40$, cannot support such oscillations.

A second type of transient phenomena that has been observed in these calculations is the formation of temporary reversed flow regions along the sidewall. These regions form during the first few rotations after the impulsive start and have been observed over the parameter range $1 \leq \alpha \leq 4.3$ and $1000 < Re \leq 50{,}000$. Typical results for $\alpha = 1$, $Re = 9741.6$ are shown in Figs. 7, 8 and 9 to illustrate the reversed flow formation and decay. Each figure shows instantaneous streamlines in one-fourth of the meridional plane, the cylinder midplane being the top boundary and the sidewall being the right boundary. The results were obtained with $d = e = 0.1$ and $\Delta t = 0.05$ using a 41×41 grid. The

streamline contour interval is $\Delta\psi = 0.0004$ for each figure with the wall value set to zero. The plots indicate that a counter-clockwise meridional flow develops almost immediately after the impulsive start with no reversed flow regions present until approximately $t = 6$. Fig. 7 shows that a small reversed (clockwise) flow region has formed near the corner by $t = 6$ as indicated by the small closed contour. By $t = 13$ a second region forms, slightly higher up the sidewall from the one in Fig. 7. By $t = 20$, Fig. 8, there are four reversed flow regions present. During the next half rotation or so these reversed flow regions "collapse", or disappear, as indicated in Fig. 9 for $t = 24$. They do not redevelop for $t > 24$ and the rest of the spin-up process proceeds in a manner similar to that predicted by the Wedemeyer model.

The reversed flow regions do not develop in calculations for $\alpha = 1$, $Re < 1000$, probably because of the larger amount of viscous dissipation. At higher Re there is less viscous dissipation present and inertial effects become more pronounced. Fluid particles near the endwalls are accelerated radially outward in a spiral motion as the Ekman layer develops. These particles overshoot their "equilibrium radial position" before they turn upward from the edge of the Ekman layer near the corner. The reversed flow regions that develop along the sidewall are apparently linked to the inertial oscillations developed as swirling fluid particles travel upward along the sidewall and begin to migrate radially inward.

The calculations predict that as Re increases, both the amplitude of the inertial oscillations and the complexity of the initial flow in the corner region increases. Typical results for $\alpha = 1$ and $Re = 50,000$

show that three very small reversed flow regions develop in the corner region by t = 15. A transformed 41 × 81 grid could not sufficiently resolve the fine scales of this motion in the corner. Similar calculations for $\alpha = 1$, Re = 100,000 developed a numerical instability at t = 4.6 due to the extreme severity of the local oscillations in the corner. This result may indicate the development of a physical instability at this high Reynolds number.

Grid convergence studies have been carried out for the case depicted in Figs. 6-9 to determine the sensitivity of the results to grid size. Grids of 11 × 11, 21 × 21 and 41 × 41 were used with d = e = 0.10 and Δt = 0.20, 0.10 and 0.05, respectively. The results show that the predicted azimuthal velocity profiles are relatively insensitive to grid size. The 41 × 41 grid results are very similar to those shown in Fig. 6 for the 21 × 21 grid; typically v differs by less than 0.010 between the two cases, with a maximum difference of 0.027 occurring at early time. The comparisons do show, however, that the number of reversed flow regions formed and their times of appearance and disappearance are sensitive to grid size over this range of sizes. The 11 × 11 and 21 × 21 grids are so coarse that only the largest reversed flow region in Fig. 8 is resolved; the smaller ones in Fig. 8 and the single one in Fig. 7 are not resolved at all. All three calculations, however, predict the absence of reversed flow for $t \geq 24$. It is clear from these limited results that much finer grids near the sidewall are needed to carry out quantitative studies of the transient reversed flow regions.

Ekman Boundary Layer

The Ekman layer development at early time and its role in the subsequent spin-up process has been examined in some detail using the present procedure. Fig. 10 shows a typical computed radial velocity profile in the Ekman layer at $r = 0.76$ and $t = 8.2$ for $\alpha = 1$, $Re = 9741.6$. This profile was obtained with a 21×21 grid, and $d = 0.10$, $e = 0.02$. This grid was stretched in z to cluster almost half of the grid points into the Ekman layer. The predicted radial velocity profile is very similar to the one obtained by Rogers and Lance[17] for the steady laminar boundary layer formed on an infinite rotating disk with a non-rotating outer flow (the Von Karman problem). The small differences in Fig. 10 are due to the fact that u does not asymptotically approach zero at the edge of the Ekman layer during spin-up in a finite cylinder. The Rogers and Lance calculation, on the other hand, imposes this asymptotic behavior as a boundary condition.

Results similar to those shown in Fig. 10 have been used to quantify the Ekman layer radial mass flow rate and assess "compatibility conditions" employed in the Wedemeyer model to couple the Ekman layer and interior, or core, flows. These results show that the Ekman layer is formed within approximately the first cylinder rotation, $t = 2\pi$; thereafter, the Ekman layer radial mass flow rate at a given r monotonically decreases as t increases. This monotonic behavior of the mass flow rate is an important observation from the present work, since it indicates that non-monotonic compatibility conditions, used by several authors[9,18-20] in conjunction with Wedemeyer's model, are unrealistic approximations to the actual flow. The complete set of numerical

results from these studies has been used to develop a new monotonic compatibility condition[10].

Conclusions

A predictor-corrector multiple-iteration method has been combined with the Gauss-Seidel iteration technique to produce an effective numerical procedure for solving the unsteady Navier-Stokes equations. Test calculations for spin-up in a cylinder were shown to be in good agreement with previous calculations and experimental measurements. Computations carried out for $0.5 \leq \alpha \leq 4.4$ and $205 \leq Re \leq 50{,}000$ showed that coordinate transformations could be used to simultaneously resolve details of both the interior and boundary layer flows using a moderate number of grid points. These calculations demonstrated the presence of inertial oscillations and temporary reversed flow regions along the sidewall during spin-up from rest and quantified some aspects of the flow in the endwall Ekman layers.

Acknowledgement

The advice, encouragement and assistance of Mr. N. Gerber and Drs. G. P. Neitzel, Jr. and R. Sedney are gratefully acknowledged.

References

1. Wedemeyer, E. H., "The Unsteady Flow Within a Spinning Cylinder," J. Fluid Mech., Vol. 20, Pt. 3, 1964, pp. 383-399; also see BRL Report 1252, Aberdeen Proving Ground, MD, AD 431846, Oct. 1963.

2. Kitchens, C. W., Jr., Gerber, N. and Sedney, R., "Spin Decay of Liquid-Filled Projectiles," J. Spacecraft and Rockets, Vol. 15, No. 6, Nov-Dec 1978, pp. 348-354.

3. Stewartson, K., "On the Stability of a Spinning Top Containing Liquid," J. Fluid Mech, Vol. 5, Pt. 4, Sept. 1959, pp. 577-592.

4. Rubin, S. G. and Lin, T. C., "A Numerical Method for Three-Dimensional Viscous Flow: Application to the Hypersonic Leading Edge," J. Comp. Phys., Vol. 9, 1972, pp. 339-364.

5. Salvadori, M. G. and Baron, M. L., Numerical Methods in Engineering, Prentice-Hall, Inc., Englewood Cliffs, NJ, 1961.

6. Warn-Varnas, A., Fowlis, W. W., Piacsek, S. and Lee, S. M., "Numerical Solutions and Laser Doppler Measurements of Spin-Up," J. Fluid Mech., Vol. 85, Pt. 4, 1978, pp. 609-639.

7. Briley, W. R., "Time Dependent Rotating Flow in a Cylindrical Container," PhD Dissertation, The University of Texas at Austin, 1968, University Microfilms, Inc., 69-6121.

8. Briley, W. R. and Walls, H. A., "A Numerical Study of Time-Dependent Rotating Flow in a Cylindrical Container at Low and Moderate Reynolds Numbers," Proc. 2nd Intl. Conf. on Num. Meth. Fld. Dyn., Lecture Notes in Physics, Vol. 8, Springer-Verlag, 1970, pp. 377-384.

9. Watkins, W. B. and Hussey, R. G. "Spin-Up From Rest in a Cylinder," Phys. of Fluids, Vol. 20, No. 10, Pt. 1, 1977, pp. 1596-1604.

10. Kitchens, C. W., Jr. "Navier-Stokes Solutions for Spin-Up from Rest in a Cylindrical Container," ARBRL-TR-02193, Ballistic Research Laboratory, Aberdeen Proving Ground, MD, September 1979.

11. Neitzel, G. P., Jr., "Centrifugal Instability of Decelerating Swirl Flow within Finite and Infinite Circular Cylinders," PhD Dissertation, The Johns Hopkins University, Baltimore, MD, 1979.

12. Roberts, G. O., "Computational Meshes for Boundary-Layer Problems," Proc. 2nd Intl. Conf. on Num. Meth. Fld. Dyn., Lecture Notes in Physics, Vol. 8, Springer Verlag, 1970, pp. 171-177.

13. Peaceman, D. W. and Rachford, H. H., Jr., "The Numerical Solution of Parabolic and Elliptic Differential Equations," J. SIAM, Vol. 3, No. 1, 1955, pp. 28-41.

14. Young, D., "Iterative Methods for Solving Partial Difference Equations of Elliptic Type," Trans. Amer. Math. Soc., Vol. 76, 1954, pp. 92-111.

15. Kitchens, C. W., Jr., Gerber, N. and Sedney, R., "Study of Streamwise Vorticity Decay Downstream of a Three-Dimensional Protuberance," Bull. Am. Phys. Soc., Vol. 20, No. 11, pp. 1430.

16. Williams, G. P., "Numerical Integration of the Three-Dimensional Navier-Stokes Equations for Incompressible Flow," J. Fluid Mech., Vol. 37, 1969, pp. 727-750.

17. Rogers, M. H. and Lance, G. N., "The Rotationally Symmetric Flow of a Viscous Fluid in the Presence of an Infinite Rotating Disk," J. Fluid Mech., Vol. 7, Pt. 4, April 1960, pp. 617-631.

18. Weidman, P. D., "On the Spin-Up and Spin-Down of a Rotating Fluid, Part 2. Measurements and Stability," J. Fluid Mech., Vol. 77, Pt. 4, 1976, pp. 709-735.

19. Weidman, P. D., "On the Spin-Up and Spin-Down of a Rotating Fluid, Part 1. Extending the Wedemeyer Model," J. Fluid Mech., Vol. 77, Pt. 4, 1976, pp. 685-708.

20. Goller, H. and Ranov, H., "Unsteady Rotating Flow in a Cylinder with a Free Surface," J. Basic Eng., Trans. ASME, Vol. 90, Series D, December 1968, pp. 445-454.

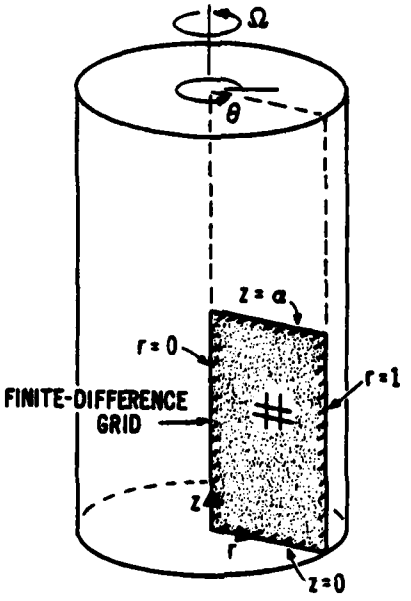

Figure 1. Geometry for spin-up calculations

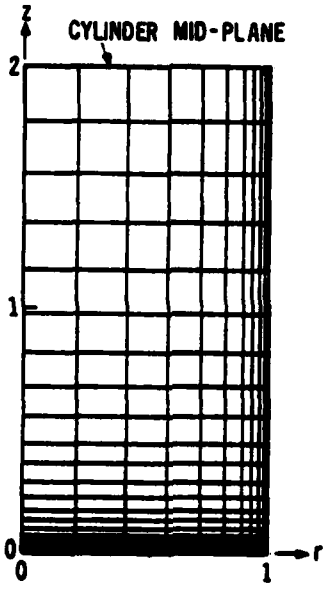

Figure 2. Typical grid point distribution in physical plane for coarse 11 × 21 grid with $\alpha = 2$ and $d = e = 0.05$

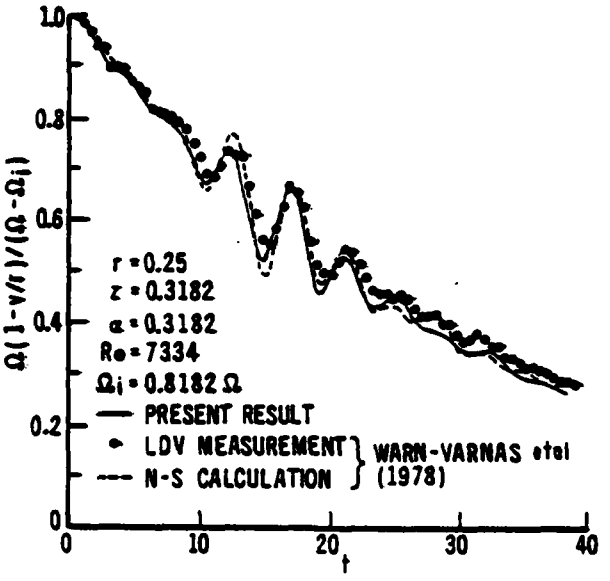

Figure 3. Inertial oscillations during spin-up from an initial state of rigid-body rotation

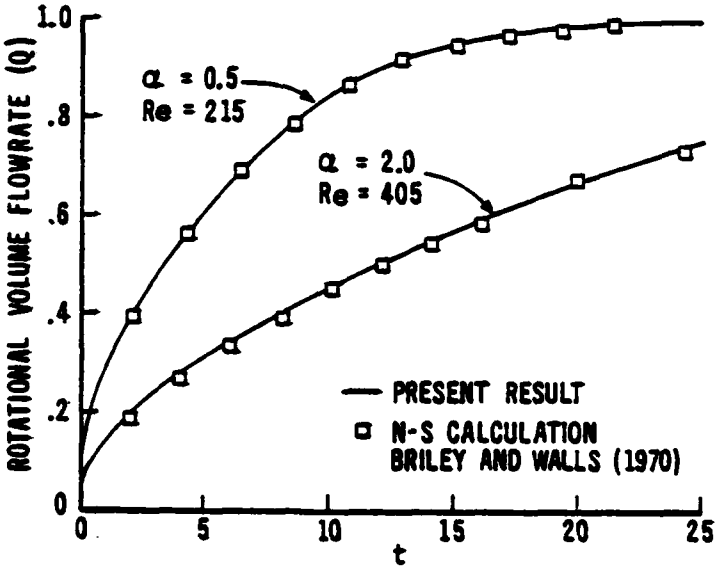

Figure 4. Rotational volume flow rate for spin-up from rest

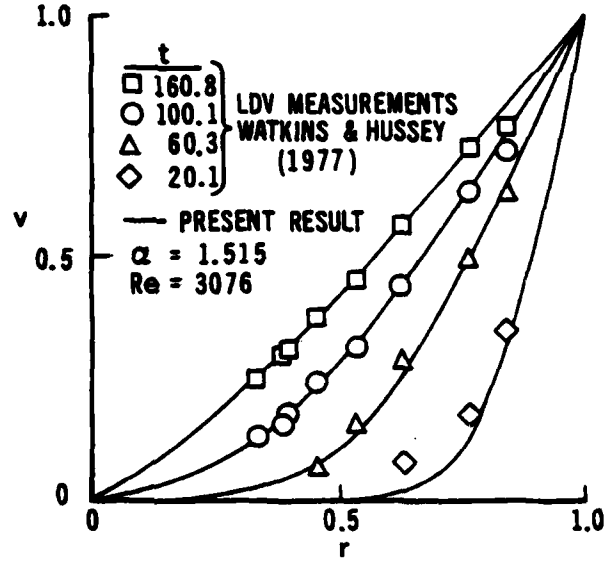

Figure 5. Azimuthal velocity profiles at cylinder mid-plane for $\alpha = 1.515$, Re = 3076

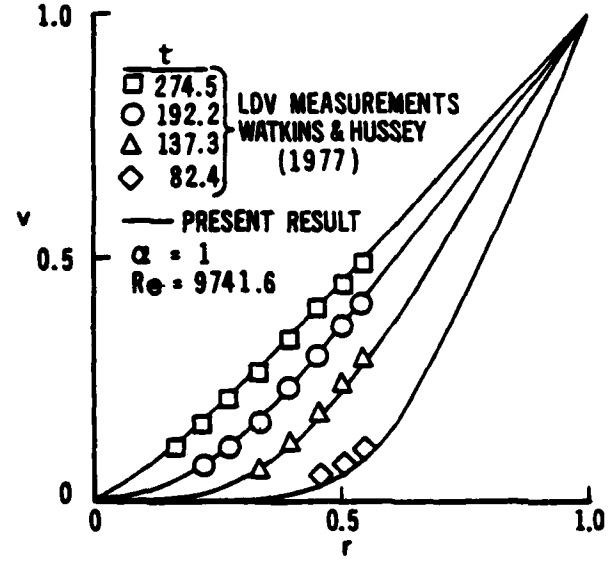

Figure 6. Azimuthal velocity profiles at cylinder mid-plane for $\alpha = 1$, Re = 9741.6

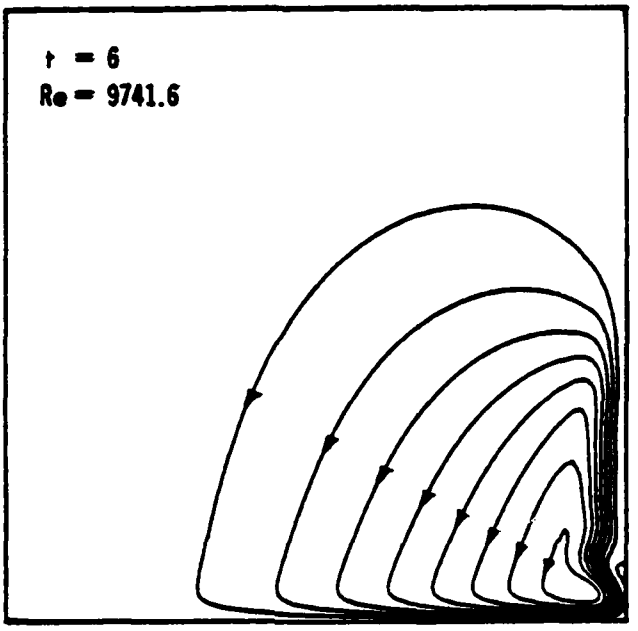

Figure 7. Instantaneous streamlines at t = 6; ψ_{min} = -0.00003, ψ_{max} = 0.00350

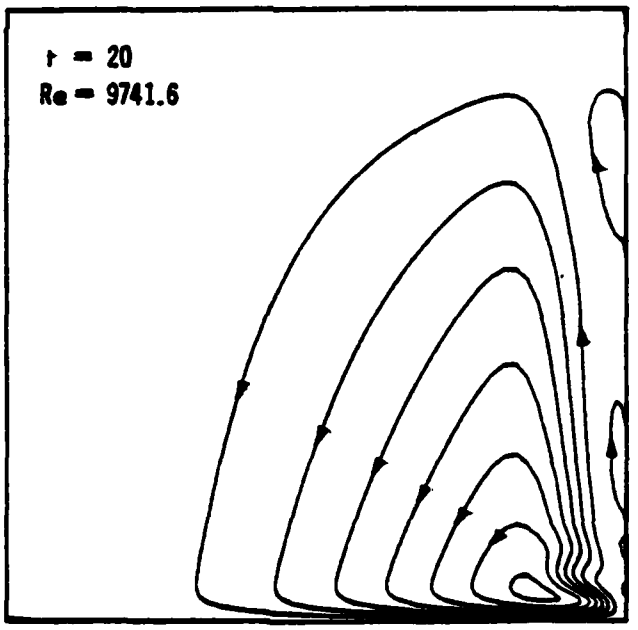

Figure 8. Instantaneous streamlines at t = 20; ψ_{min} = -0.00003, ψ_{max} = 0.00294

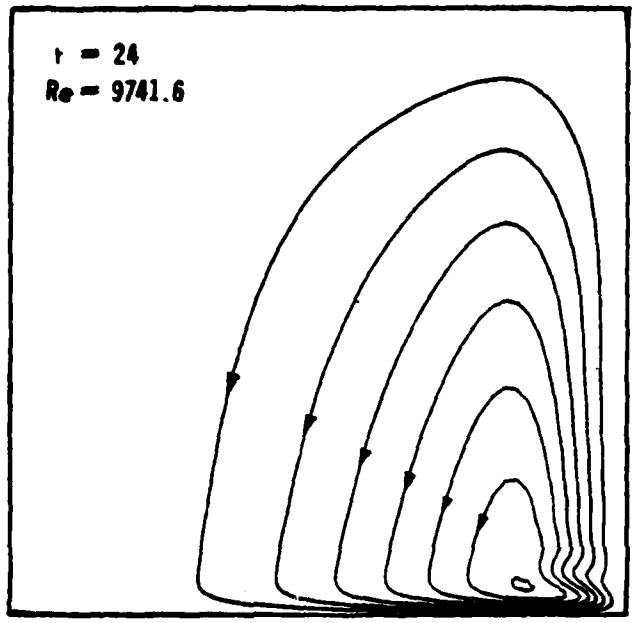

Figure 9. Instantaneous streamlines at t = 24; ψ_{min} = 0, ψ_{max} = -0.00284

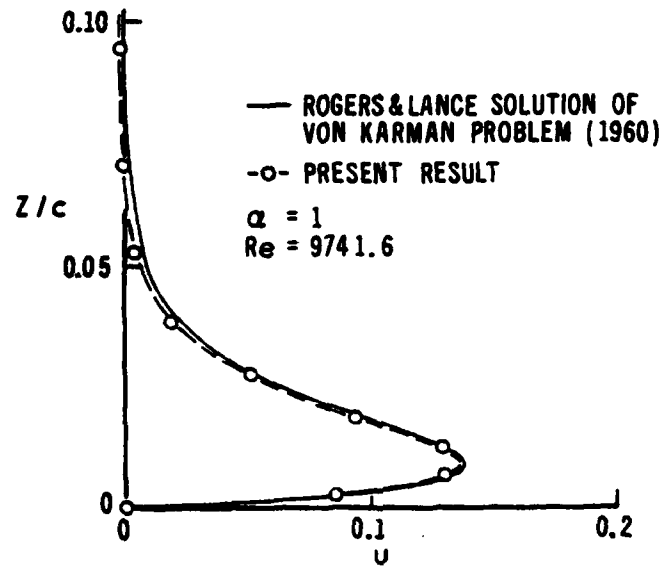

Figure 10. Radial velocity profile in Ekman layer at r = 0.76, t = 8.3 for α = 1, Re = 9741.6

FOURIER TRANSFORM EVALUATION

J. Barkley Rosser
University of Wisconsin - Madison
Mathematics Research Center
Madison, Wisconsin 53706

ABSTRACT. Methods have been given for computing Fourier transforms which are particularly efficient at chosen discrete values of the spectrum. Alternative methods based on Fourier series are presented for calculating the transform at additional values of the spectrum.

1. STATEMENT OF THE PROBLEM. The Fourier transform of $x(t)$ is defined by

$$S(f) = \int_{-\infty}^{\infty} x(t)e^{-2\pi jft}dt, \tag{1.1}$$

where $j = \sqrt{-1}$. For most cases that arise in practical problems, $|x(t)|$ falls off fairly rapidly to zero as $t \to \infty$ and as $t \to -\infty$. So, for suitable a and b, one can approximate $S(f)$ by $\bar{S}(f)$, where

$$\bar{S}(f) = \int_{-a}^{b} x(t)e^{-2\pi jft}\,dt. \tag{1.2}$$

In many cases that actually occur, $x(t)$ describes a burst of information, and one has $x(t) = 0$ for $t < -a$ or for $t > b$. In such case, one has exactly

$$S(f) = \int_{-a}^{b} x(t)e^{-2\pi jft}dt. \tag{1.3}$$

A translation of the origin gives from (1.2)

$$\bar{S}(f) = e^{2\pi jfa}\int_{0}^{a+b} x(u-a)e^{-2\pi jfu}du. \tag{1.4}$$

A change of scale gives

$$\bar{\bar{S}}(g) = \bar{S}\left(\frac{g}{a+b}\right) = (a+b)e^{2\pi jga/(a+b)}\int_{0}^{1} x((a+b)v-a)e^{-2\pi jgv}dv. \tag{1.5}$$

2. USE OF FOURIER SERIES. The analysis of Section 1 shows that, for many practical problems, and subject to a slight redefinition of $x(t)$ and $S(f)$ by a translation and a change of scale, the problem of approximating a Fourier transform can be reduced to evaluating

$$S(f) = \int_{0}^{1} x(t)e^{-2\pi jft}dt\ . \tag{2.1}$$

For functions $x(t)$ arising in practical problems, it will usually be the case that $x(t)$ is of bounded variation. We will assume this to be the case. If we consider separately the real and imaginary parts of $x(t)$, and apply the analysis at the top of page 164 of Whittaker and Watson [1], we conclude that

$$x(t) = \sum_{n=-\infty}^{\infty} a_n e^{2\pi jnt}\ . \tag{2.2}$$

Sponsored by the United States Army under Contract No. DAAG29-75-C-0024.

The series on the right converges for $0 < t < 1$ to the value

$$\tfrac{1}{2}\{x(t+0) + x(t-0)\}; \tag{2.3}$$

for $t = 0$ or $t = 1$ it converges to the value

$$\tfrac{1}{2}\{x(0+) + x(1-0)\}. \tag{2.4}$$

Also, by the analysis at the bottom of page 172 of Whittaker and Watson [1], the value of $|a_n|$ goes to zero of the order of $1/|n|$ when n goes to plus or minus infinity.

It is permissible to substitute (2.2) into (2.1) and integrate term by term. There results

$$S(f) = \frac{1}{2\pi j} \sum_{n=-\infty}^{\infty} \frac{a_n(e^{2\pi j(n-f)}-1)}{n-f}. \tag{2.5}$$

Since the $|a_n|$ go to zero of the order of $1/|n|$, the series on the right converges absolutely. If f approaches an integer m, all terms on the right of (2.5) approach zero except for the one with $n = m$, and we get

$$S(m) = a_m. \tag{2.6}$$

If we put m for f in (2.1), we get

$$S(m) = a_m = \int_0^1 x(t)e^{-2\pi jmt}dt. \tag{2.7}$$

It thus appears that we have to start by calculating $S(m)$ for quite a number of integers m. We will discuss how to do this in Sections 3 and 4. For the moment, assume that numerical estimates for enough of the a_m are available. Then estimates for $S(f)$ can be obtained by use of (2.5).

One can rewrite (2.5) as

$$S(f) = \frac{e^{2\pi j(m-f)} - 1}{2\pi j} \sum_{n=-\infty}^{\infty} \frac{a_n}{n-f}, \tag{2.8}$$

where m is some integer, usually taken near f. If f is very close to an integer m, there would be appreciable cancellation in calculating the factor in front of the summation on the right of (2.8). We can remedy this by expanding the exponential into a series. Then the factor takes the form

$$(m-f)\left\{1 + \frac{2\pi j(m-f)}{2!} + \frac{(2\pi j(m-f))^2}{3!} + \ldots\right\}. \tag{2.9}$$

One would have recourse to this only if $|m-f|$ is quite small, so that the convergence in (2.9) would be very fast.

Suppose that for some r with $0 < r < 1$ we wish to calculate $S(m+r)$ for many integers m. By (2.8), we have

$$S(r) = \frac{e^{-2\pi jr} - 1}{2\pi j} \sum_{n=-\infty}^{\infty} \frac{a_n}{n-r}, \tag{2.10}$$

$$S(1+r) - S(r) = \frac{e^{-2\pi jr} - 1}{2\pi j} \sum_{n=-\infty}^{\infty} \frac{a_n}{(n-1-r)(n-r)}, \tag{2.11}$$

$$S(m+1+r) - 2S(m+r) + S(m-1+r) = \frac{e^{-2\pi jr} - 1}{2\pi j} \sum_{n=-\infty}^{\infty} \frac{2a_n}{(n-m-1-r)(n-m-r)(n-m+1-r)}. \tag{2.12}$$

We have reasonably rapid convergence on the right of (2.10), faster convergence on the right of (2.11), and extremely rapid convergence on the right of (2.12). So we can rapidly calculate the right of (2.12) for many m's. But since the left side of (2.12) is the second central difference of the $S(m+r)$, we quickly calculate the first differences from $S(1+r) - S(r)$ by addition and subtraction. Having the first differences, we then get $S(m+r)$ from $S(r)$ by addition and subtraction.

As a practical calculating procedure, note that the coefficients of the a_n on the right side of (2.12) have the form

$$\frac{2}{(M-1-r)(M-r)(M+1-r)} \tag{2.13}$$

for various values of M. These fall off rapidly in size as $|M|$ gets large. If about two decimals of accuracy is desired, it would suffice to calculate and store values of (2.13) from about $M = -10$ to $M = 11$. Then, for each value of m, 22 multiplications and 21 additions would evaluate the sum on the right side of (2.12). As noted, this gives second differences, from which first differences and then the values of $S(m+r)$ can be calculated by additions and subtractions.

If more accuracy is desired one could use more values of M. However, it might be better to go to higher differences; this latter cannot be carried too far, since the numerators begin to increase at a distressing rate. In a later section, we will explain quite a different technique to get more accuracy.

If values of $S(m+r)$ are required for a very large number of integer values of m, it might be efficient to use the Fast Fourier Transform. An explanation how to do this will be given later.

3. ESTIMATION OF THE a_m. Obviously one has to have some sort of information about $x(t)$ if one is to make any progress. Sometimes one is lucky enough to have a formula for $x(t)$, or some algorithm by which $x(t)$ can be estimated for each given t. In a practical problem, one may have only experimentally measured values for $x(t)$, at isolated values of t. Let us assume that these values of t are equally spaced from 0 to 1. That is, one has measured (or can calculate) values of

$$x\left(\frac{k}{N}\right) \qquad \text{for } k = 0,1,2,\ldots,N.$$

Then one can approximate a_m from (2.7) by one of a number of approximate quadrature rules; see Abramowitz and Stegun [3], page 885 ff. The simplest useful approximation is by the trapezoidal rule. For (2.7) this gives

$$S(m) = a_m \cong \frac{1}{2N}\{x(0) + x(1)\} + \frac{1}{N}\sum_{k=1}^{N-1} x\left(\frac{k}{N}\right) e^{-2\pi jmk/N}. \tag{3.1}$$

Because of formulas like (2.5) and (2.8), we wish to know a_m for many values of m, both positive and negative. This could be quite a heavy calculation. If N happens to be a power of 2, or the product of a number

of small primes, one can rewrite (3.1) so that one can abridge the calculation very considerably by use of the Fast Fourier Transform. Simply redefine $x(0)$ to be

$$x(0) \text{ replaced by } \tfrac{1}{2}(x(0) + x(1)). \tag{3.2}$$

Then (3.1) can be rewritten as

$$S(m) = a_m \cong \frac{1}{N} \sum_{k=0}^{N-1} x(\tfrac{k}{N}) e^{-2\pi jmk/N} . \tag{3.3}$$

We can use the Fast Fourier Transform to get a reasonably efficient calculation of the right side of (3.3) for $-N/2 \leq m \leq (N/2) - 1$. We will shortly discuss how good an approximation this gives for a_m for $-N/2 \leq m \leq (N/2) - 1$.

The reader probably has a favorite version of the Fast Fourier Transform. If not, one can consult the original paper on the subject, namely Cooley and Tukey [5]. Some people like Brigham [6]. A particularly good explanation is given in Conte and de Boor [4]; be sure to get the third edition, as the Fast Fourier Transform does not appear in the first two editions.

If one wishes a_m for more values of m, note that the right side of (3.3) is a periodic function of m, with period N. As m reaches and passes $N/2$, the right side of (3.3) merely begins to repeat the values for m near $-N/2$. Almost certainly, the a_m do not behave this way. So for $|m| > N/2$, (3.3) must be a poorer and poorer approximation for a_m as $|m|$ increases.

We spoke earlier of estimating $S(m+r)$, where $0 < r < 1$, for a large number of values of m. If we put $m+r$ for m in (3.3), we get

$$S(m+r) \cong \frac{1}{N} \sum_{k=0}^{N-1} \{x(\tfrac{k}{N}) e^{-2\pi jrk/N}\} e^{-2\pi jmk/N} . \tag{3.4}$$

This holds also for $r = 0$, of course. Use of the Fast Fourier Transform will give values of the right side of (3.4) for $-N/2 \leq m \leq (N/2) - 1$.

By the formula for the error in the trapezoidal rule (see Abramowitz and Stegun [3], Formula 25.4.2 on page 885), the error for (3.4) is

$$- \frac{f''(\xi)}{12N^2} , \tag{3.5}$$

where

$$f(t) = x(t) e^{-2\pi j(m+r)t} \tag{3.6}$$

and ξ is a number between 0 and 1, providing $x(t)$ is twice differentiable. One term in $f''(\xi)$ would be

$$(2\pi(m+r))^2 x(\xi) e^{-2\pi j(m+r)\xi} .$$

If $|m|$ is near $N/2$, the contribution to the error from this term alone could exceed the value of a_m itself.

In other words, use of (3.1), (3.3), or (3.4) to get an approximation for $S(m+r)$ is futile unless $|m+r|$ is somewhat small compared to N.

Whether use of (3.4) involves less calculation than use of (2.10), (2.11), and (2.12) depends on how many values of m one has to deal with.

4. THE POSSIBILITY OF BETTER ESTIMATES FOR THE a_m. In the previous section, we discussed the approximation that one can get by the trapezoidal rule. If N is large and we need to know a_m only for m's of modest size, the trapezoidal rule does fairly well. Suppose we have to deal with larger m's, or the trapezoidal rule does not do well enough. There are other quadrature rules in Abramowitz and Stegun [3]. A popular one is Simpson's rule. This works only if $x(t)$ is four times differentiable. Also, N has to be even. Then Simpson's rule takes the form

$$S(m) = a_m \cong \frac{1}{6R}\{x(0) + x(1)\} + \frac{1}{3R}\sum_{k=1}^{R-1} x(\frac{k}{R})e^{-2\pi jmk/R} + \frac{2}{3R}\sum_{k=0}^{R-1} x(\frac{2k+1}{2R})e^{-2\pi jm(2k+1)/2R}, \tag{4.1}$$

where we have taken $R = N/2$. As before, if we redefine $x(0)$ to be $\frac{1}{2}\{x(0) + x(1)\}$, we get the relation

$$S(m) = a_m \cong \frac{1}{3R}\sum_{k=0}^{R-1} x(\frac{k}{R})e^{-2\pi jmk/R} + \frac{2e^{-\pi jm/R}}{3R}\sum_{k=0}^{R-1} x(\frac{2k+1}{2R})e^{-2\pi jmk/R}. \tag{4.2}$$

Each of the summations on the right can be evaluated fairly efficiently by means of the Fast Fourier Transform for $-R/2 \le m \le (R/2) - 1$, after which one can reconstitute the approximation for a_m. This gives a_m only in the range $-N/4 \le m \le (N/4) - 1$. Since each summation on the right of (4.2) is periodic with period R, one can extend (4.2) to other values of m. How far (4.2) remains a useful approximation is another question.

By Abramowitz and Stegun [3], Formula 25.4.6 on page 886, the error in (4.1) or (4.2) is

$$-\frac{f^{(4)}(\xi)}{180N^4} \tag{4.3}$$

where

$$f(t) = x(t)e^{-2\pi jmt} \tag{4.4}$$

and ξ is a number between 0 and 1. This is likely appreciably better than the error for the trapezoidal rule, especially for small $|m|$. Even for $|m|$ near $N/4$, the error could be only a few percent of the value of a_m. However, as $|m|$ increases, the error becomes too large to tolerate.

If $x(t)$ is six times differentiable and N is divisible by 4, one can use Bode's rule. This gives

$$S(m) = a_m \cong \frac{1}{90S}\left\{7\{x(0) + x(1)\}\right.$$
$$+ 14 \sum_{k=1}^{S-1} x(\frac{k}{S})\, e^{-2\pi jmk/S}$$
$$+ 12 \sum_{k=0}^{S-1} x(\frac{2k+1}{2S})\, e^{-2\pi jm(2k+1)/2S}$$
$$\left. + 32 \sum_{k=0}^{2S-1} x(\frac{2k+1}{4S})\, e^{-2\pi jm(2k+1)/4S}\right\}, \qquad (4.5)$$

where we have taken $S = N/4$. As before, if we redefine $x(0)$ to be $\frac{1}{2}\{x(0) + x(1)\}$, we get the relation

$$S(m) = a_m \cong \frac{7}{45S} \sum_{k=0}^{S-1} x(\frac{k}{S})\, e^{-2\pi jmk/S}$$
$$+ \frac{16e^{-\pi jm/2S}}{45S} \sum_{k=0}^{S-1} x(\frac{4k+1}{4S})\, e^{-2\pi jmk/S}$$
$$+ \frac{2e^{-\pi jm/S}}{15S} \sum_{k=0}^{S-1} x(\frac{2k+1}{2S})\, e^{-2\pi jmk/S}$$
$$+ \frac{16e^{-3\pi jm/2S}}{45S} \sum_{k=0}^{S-1} x(\frac{4k+3}{4S})\, e^{-2\pi jmk/S}\,. \qquad (4.6)$$

Each of the summations on the right can be evaluated fairly efficiently by means of the Fast Fourier Transform for $-S/2 \le m \le (S/2) - 1$, after which one can reconstitute the approximation for a_m. This gives a_m only in the range $-N/8 \le m \le (N/8) - 1$. Since each summation on the right of (4.6) is periodic with period S, one can extend (4.6) to other values of m. How far (4.6) remains a useful approximation is another question.

By Abramowitz and Stegun [3], Formula 25.4.14 on page 886, the error in (4.5) or (4.6) is

$$-\frac{2f^{(6)}(\xi)}{945N^6} \qquad (4.7)$$

where $f(t)$ is given by (4.4) and ξ is a number between 0 and 1. In the range $-N/8 \le m \le (N/8) - 1$, this is likely appreciably better than Simpson's rule.

In Hope [2], it is proposed to use a Gaussian type quadrature formula; see Abramowitz and Stegun [3], Formulas 25.4.29 and 25.4.30 on page 887. This requires that $x(t)$ have many derivatives. It also requires knowledge of $x(t)$ at other than regularly spaced points; if a formula is known for $x(t)$ one can manage this, but if $x(t)$ is determined at isolated points by measurement the matter is hopeless.

In Hope [2], the procedure is applied for the case that

$$x(t) = \begin{cases} \sin(200\pi t + 100\pi^2 t) & \text{for } 0 \le t \le 1 \\ 0 & \text{otherwise.} \end{cases}$$

For the method of Hope [2] to work, $x(t)$ had to be 64 times differentiable for $0 < t < 1$, and had to have computable values at very strange values of t. For the $x(t)$ given above, these conditions are satisfied.

Another difficulty with the method of Hope [2] is that the error increases very fast as m increases. Thus, in Figure 2 of Hope [2], there is a plot of the error squared as a function of m (which is called f in Figure 2). For $0 \le f \le 150$, the relative error squared is less than 10^{-8}. But as f goes from 150 to 250, the relative error squared increases from less than 10^{-8} to about 10^{-5}. It is good that the graph stopped at $m = 250$. On the whole, we can see very little to recommend in the use of Gaussian type quadrature formulas for the present purpose.

We might remark in passing that Hope [2] is very carelessly written.

(1) It is stated that the formula (2) is a trapezoidal rule approximation for (1). If one takes $\Delta f = 1$ in (2), one gets our (3.3). This is a trapezoidal rule only by virtue of the replacement (3.2), which is not used in Hope [2].

(2) There is a $\frac{1}{2}$ missing in front of the right side of (6) of Hope [2].

(3) In Figure 2 of Hope [2], a blob near the top of Figure 2 purports to show the error squared in (2) of Hope [2] (which is essentially our (3.3)) when $N = 4096$. Because the blob is near the top of the figure, this is supposed to show that a trapezoidal rule using 4096 evaluations is much poorer than the Gauss quadrature using only 1728 evaluations. The fact of the matter is that the blob in question has nothing to do with the error squared of the trapezoidal rule with $N = 4096$. For this latter, the normalized value of $|S_0(f) - S(f)|^2$, which the blob is supposed to represent, is actually about 3×10^{-9} all the way from $f = 0$ to 250. This is so small that it would have to be plotted below the bottom line of the figure, and hence is much better than the Gaussian approximation for almost half the values of f. Even the trapezoidal rule with $N = 1024$ (that is, 1024 evaluations as against the 1728 evaluations of Hope [2]) has $|S_0(f) - S(f)|^2$ running from a little below 10^{-6} at $f = 0$ up to a little over 10^{-6} at $f = 250$, which is superior to the Gauss quadrature at quite a number of values of f. Recall again that the f of Hope [2] is our m.

5. FURTHER ANALYSIS OF THE ERROR. Let N be an even integer. Define

$$x^*(t) = \sum_{n=-N/2}^{(N/2)-1} a_n e^{2\pi jnt}. \tag{5.1}$$

That is, we truncate (2.2). Then it is easily verified that for m an integer with $-N/2 \le m < N/2$ we have exactly

$$a_m = \frac{1}{N} \sum_{k=0}^{N-1} x^*(\tfrac{k}{N}) e^{-2\pi jmk/N}. \tag{5.2}$$

If N is very large, then by (2.2), $x^*(t)$ will be nearly equal to $x(t)$, so that the right side of (5.2) will be nearly equal to the right side of (3.3), so that, if we remember to make the adjustment (3.2), (3.3) will give a good approximation for a_m for $-N/2 \leq m < N/2$.

If the a_n converge rapidly to zero, then $x^*(t)$ will be a good approximation to $x(t)$ unless N is quite small. Then (3.3) will give a good approximation for a_m, and Simpson's rule or other improvements of (3.3) will not be needed.

Naturally, we cannot make the a_n for $x(t)$ converge to zero any more rapidly than they actually do. However, we can introduce new functions related to $x(t)$ for which the a_n do converge to zero more rapidly; we can then calculate $S(f)$ in terms of these new functions. This will also speed the convergence in formulas such as (2.5), (2.8), (2.10), (2.11), and (2.12).

We note that

$$\int_0^1 e^{-\alpha t} dt = \frac{1 - e^{-\alpha}}{\alpha}. \tag{5.3}$$

Differentiating both sides twice with respect to α gives

$$\int_0^1 t\, e^{-\alpha t} dt = \frac{1 - e^{-\alpha}}{\alpha^2} - \frac{e^{-\alpha}}{\alpha} \tag{5.4}$$

and

$$\int_0^1 t^2\, e^{-\alpha t} dt = \frac{2(1-e^{-\alpha})}{\alpha^3} - \frac{2e^{-\alpha}}{\alpha^2} - \frac{e^{-\alpha}}{\alpha}. \tag{5.5}$$

Now define

$$\bar{x}(t) = x(t) - t(x(1) - x(0)). \tag{5.6}$$

Then by (5.4), we have

$$S(f) = \bar{S}(f) + \{x(1) - x(0)\}\{ \frac{1 - e^{-2\pi jf}}{(2\pi jf)^2} - \frac{e^{-2\pi jf}}{2\pi jf} \}, \tag{5.7}$$

where

$$\bar{S}(f) = \int_0^1 \bar{x}(t)\, e^{-2\pi jft}\, dt. \tag{5.8}$$

Analgously to (2.2) and (2.5), we have

$$\bar{x}(t) = \sum_{n=-\infty}^{\infty} \bar{a}_n\, e^{2\pi jnt}, \tag{5.9}$$

$$\bar{S}(f) = \frac{1}{2\pi j} \sum_{n=-\infty}^{\infty} \frac{\bar{a}_n (e^{2\pi j(n-f)} - 1)}{n-f}. \tag{5.10}$$

Note first that by (5.6)

$$\bar{x}(0) = \bar{x}(1) = x(0). \tag{5.11}$$

Thus, in the approximation corresponding to (3.3) for $\bar{a}_m$ we do not need to make the adjustment (3.2). More importantly, analogously to (2.7) we have

$$\bar{S}(m) = \bar{a}_m = \int_0^1 \bar{x}(t)e^{-2\pi jmt}\,dt. \tag{5.12}$$

If we integrate by parts in this, and use (5.11), we get

$$\bar{a}_m = \frac{1}{2\pi jm} \int_0^1 \bar{x}'(t)e^{-2\pi jmt}\,dt. \tag{5.13}$$

If $\bar{x}'(t)$ is of bounded variation, which it is liable to be in any practical case, then by the analysis at the bottom of page 172 of Whittaker and Watson [1], the integral on the right of (5.13) will go to zero of the order of $1/|m|$. So $|\bar{a}_m|$ will go to zero of the order of $1/|m^2|$. This is faster convergence to zero than one could usually expect for the a_n. As noted above, this improves the situation with regard to formulas analogous to (2.5), (2.8), (2.10), (2.11), and (2.12).

Suppose that one can calculate reasonable approximations for the derivatives of $x(t)$ at $t = 0$ and $t = 1$, and that the second derivative of $x(t)$ has bounded variation. Then one can arrange for even faster convergence of the coefficients to zero. We define

$$\bar{\bar{x}}(t) = x(t) - Bt - Ct^2 \tag{5.14}$$

and choose B and C so that

$$\bar{\bar{x}}(0) = \bar{\bar{x}}(1) \tag{5.15}$$

$$\bar{\bar{x}}'(0) = \bar{\bar{x}}'(1) . \tag{5.16}$$

This we can do by taking

$$C = \tfrac{1}{2}\{x'(1) - x'(0)\} \tag{5.17}$$

$$B = x(1) - x(0) - C. \tag{5.18}$$

Then by (5.4) and (5.5), we get

$$S(f) = \bar{\bar{S}}(f) + B\{\frac{1 - e^{-2\pi jf}}{(2\pi jf)^2} - \frac{e^{-2\pi jf}}{2\pi jf}\}$$

$$+ C\{\frac{2(1-e^{-2\pi jf}}{(2\pi jf)^3} - \frac{2e^{-2\pi jf}}{(2\pi jf)^2} - \frac{e^{-2\pi jf}}{2\pi jf}\}, \tag{5.19}$$

where

$$\bar{\bar{S}}(f) = \int_0^1 \bar{\bar{x}}(t)\, e^{-2\pi jft}\,dt. \tag{5.20}$$

We reason as before. Integrating by parts in the formula analogous to (5.13), we get

$$\bar{\bar{a}}_m = \frac{-1}{4\pi^2 m^2} \int_0^1 \bar{\bar{x}}''(t)e^{-2\pi jmt}\,dt, \tag{5.21}$$

from which we conclude that $|\bar{\bar{a}}_m|$ goes to zero of the order of $1/|m^3|$.

If it happens to be possible to calculate several derivatives of $x(t)$ at $t = 0$ and $t = 1$, one can carry this process still further by an obvious generalization. Convergence of the various series will become so fast that only a few terms of the series need be taken, thus obviating the need for use of the Fast Fourier Transform.

REFERENCES

1. E. T. Whittaker and G. N. Watson, "A course of modern analysis," Cambridge University Press. 1946.

2. Lawrence L. Hope, "A fast Gaussian method for Fourier transform evaluation," Proceedings of the IEEE, vol. 63 (1975), pp. 1353-54.

3. Milton Abramowitz and Irene A. Stegun, "Handbook of Mathematical Functions," National Bureau of Standards, Applied Mathematics Series 55, 1964.

4. S. D. Conte and Carl de Boor, "Elementary numerical analysis, an algorithmic approach," third edition, McGraw-Hill Book Co., 1980.

5. J. W. Cooley and J. W. Tukey, "An algorithm for the machine calculation of complex Fourier series," Mathematics of Computation, vol. 19 (1965), pp. 297-301.

6. E. O. Brigham, "The Fast Fourier Transform," Englewood Cliffs, N.J., Prentice-Hall, 1974.

APPROXIMATIONS FOR Z[G(s) F(s)]

Richard E. Dickson
US Army Missile Command
Redstone Arsenal, Alabama 35809

I. INTRODUCTION

Z-transforms have been primarily used in the design of sample data control systems, but since its inception, it has been realized that it also had application in the digital simulation of continuous systems [1-3]. Some problems have been noted in applying z-transforms in digital simulation [4] particularly in the proper incorporation of nonzero initial conditions. These and other problems were addressed in a preliminary study [5,6]; this paper will introduce some of those as well as more recent developments.

Rather than a broad overview, only the fundamentals will be discussed in this paper. Don't be misled, the technique has been applied to the real-time digital portion of the hybrid simulation of a high spin rate air defense missile [7].

II. PRELIMINARIES

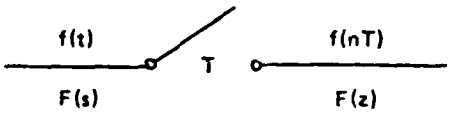

Figure 1. Time, sampled data, frequency, and sequency domains.

From the "sifting" property of the Dirac delta distribution,

$$f(nT) = \int_{-\infty}^{\infty} f(t)\ \delta(nT - t)\ dt \quad . \tag{1}$$

The Laplace transform is defined to be

$$F(s) = \int_{-\infty}^{\infty} f(t)\ u(t)\ e^{-st}\ dt \quad . \tag{2}$$

The behavior for $t < 0$ is explicitly stated in the Heaviside unit step, $u(t)$,

$$u(t) = \begin{cases} 0, & t < 0 \\ 1, & t \geq 0 \end{cases} \quad . \tag{3}$$

Of course, the derivative of $u(t)$ is $\delta(t)$.

The z-transform will be defined as a "discrete" Laplace transform,

$$F(z) = \int_{-\infty}^{\infty} \sum_{n=-\infty}^{\infty} f(t)\ \delta(nT - t)\ u(t)\ e^{-st}\ dt \quad . \tag{4}$$

and from the "sifting" property of the Dirac delta, Equation (4) becomes

$$F(z) = \sum_{n=-\infty}^{\infty} f(nT)\ u(nT)\ e^{-snT} \quad . \tag{5}$$

Letting[†]

$$z = e^{sT} \quad , \tag{6}$$

one has

$$F(z) = \sum_{n=0}^{\infty} f(nT)\ z^{-n} \tag{7}$$

which is not unexpected.

The Raggazzini-Zadeh identity may be readily deduced from the convolution properties of the Laplace transform, as follows:

$$Z[G(z)\ F(s)] = \sum_{n=-\infty}^{\infty} z^{-n}\ u(nT) \int_{-\infty}^{\infty} \sum_{k=-\infty}^{\infty} g(t)\ \delta(kT - t)\ u(t)\ f(nT - t)\ u(nT - t)\ dt \quad . \tag{8}$$

The "sifting" property of the Dirac delta yields

$$Z[G(z)\ F(s)] = \sum_{n=0}^{\infty} z^{-n} \sum_{k=0}^{n} g(kT)\ f(nT - kT) \tag{9}$$

where the summation over k = 0 to n is discrete convolution. From the Cauchy product of power series and the definition of the z-transform, Equation (7),

$$Z[G(z)\ F(s)] = G(z)\ F(z) \quad , \tag{10}$$

the Raggazzini-Zadeh identity [1].

[†] See Discussion of Reference 1; and Reference 2.

III. MEAN VALUE CONVOLUTION

It is well known that

$$Z[G(s)\ F(s)] \neq G(z)\ F(z) \tag{11}$$

and therein lies the difficulty in applying z-transforms to continuous systems. A very useful relationship would be the solution of

$$Z[G(s)\ F(s)] = \sum_{n=-\infty}^{\infty} z^{-n}\, u(nT) \int_{-\infty}^{\infty} g(t)\, u(t)\, f(nT-t)\, u(nT-t)\, dt \quad . \tag{12}$$

The mean value theorem of the integral calculus guarantees that there is some δ_k such that

$$\int_{kT}^{kT+T} g(t)\, f(nT-t)\, dt = T\, g(kT+\delta_k T)\, f(nT-kT-\delta_k T) \tag{13}$$

and Equation (12) may be rewritten

$$Z[G(s)\ f(s)] = \sum_{n=0}^{\infty} z^{-n} \sum_{k=0}^{n-1} T\, g(kT+\delta_k T)\, f(nT-kT-\delta_k T) \quad . \tag{14}$$

Since δ_k is probably different for each k, it would be difficult to proceed.

ASSUMING that

$$\delta_k = \delta \quad , \tag{15}$$

that is, δ_k is the same for all k, one has

$$Z[G(s)\ F(s)] = \sum_{n=0}^{\infty} z^{-n} \sum_{k=0}^{n-1} T\, g(kT+\delta T)\, f(nT-kT-\delta T) \quad . \tag{16}$$

This, Equation (16), is almost the form of the Cauchy product of power series except that the sum on k is to n - 1 not n. Adding and subtracting the necessary term and from the definition of the modified z-transform [8] one has

$$Z[G(s)\ F(s)] = T\, G(z,\delta)\, [F(z,-\delta) - f(-\delta T)] \quad . \tag{17}$$

The shifting theorem [8] allows further simplification,

$$Z[G(s)\ F(s)] \simeq z^{-1}\ T\ G(z,\delta)\ F\Big(z,(1-\delta)\Big) \quad . \tag{18}$$

Equations (17) and (18) will be referred to as mean value convolutions (MVC).

IV. RUNGE-KUTTA CONVOLUTIONS

It is rather easy to generalize to other convolutions using MVC [6]. Table 1 gives several convolutions based upon Runge-Kutta integrators.

TABLE 1. RUNGE-KUTTA CONVOLUTIONS

$Z[G(s)\ F(s)]$
$z^{-1}\ T\ G\left(z,\frac{1}{2}\right) F\left(z,\frac{1}{2}\right)$
$z^{-1}T\ \left[\left(1-\frac{1}{2\alpha}\right) G(z)\ F(z,1) + \left(\frac{1}{2\alpha}\right) G(z,\alpha)\ F\Big(z,(1-\alpha)\Big)\right]$
$\frac{z^{-1}T}{6}\ \left[G(z)\ F(z,1) + 4G\left(z,\frac{1}{2}\right) F\left(z,\frac{1}{2}\right) + G(z,1)\ F(z)\right]$
$\frac{z^{-1}T}{8}\ \left[G(z)\ f(z,1) + 3G\left(z,\frac{1}{3}\right) F\left(z,\frac{2}{3}\right) + 3G\left(z,\frac{2}{3}\right) F\left(z,\frac{1}{3}\right) + G(z,1)\ F(z)\right]$

In 1960, Halijak developed his trapezoidal convolution [9,3],

$$Z[G(s)\ F(s)] \simeq T\ G(z)\ F(z) - \frac{T}{2}\ [G(z)\ f(0) + g(0)\ F(z)] \tag{19}$$

which may be rewritten

$$Z[G(s)\ F(s)] \simeq \frac{T}{2}\ [G(z)(F(z) - f(0)) + (G(z) - g(0))\ F(z)] \tag{20}$$

and applying the shifting theorem, finally,

$$Z[G(s)\ F(s)] \simeq \frac{z^{-1}T}{2}\ [G(z)\ F(z,1) + G(z,1)\ F(z)] \quad , \tag{21}$$

which is the same as the second convolution in Table 1 for $\alpha = 1$. Halijak's TC has the most interesting property of having no fractional shifts.

Unfortunately, this is countered by the poor behavior in integration of a sine wave by a trapezoidal integrator when the Shannon Sampling Limit is approached [2,8]. For most applications this is not a problem since one may sample at, say, ten times the Shannon Limit of two samples per cycle, but in real-time simulation this may be a luxury one cannot afford.

Choosing $\alpha = 2/3$ yields good response for a sine wave input and appears to be the Runge-Kutta second-order integrator of choice if one is using classical numerical techniques for real-time simulation.

V. THE METHOD

Given the Raggazzini-Zadeh identity and the convolution approximations, the method for developing recurrences may now be presented.

Recalling Figure 1, one starts in the time domain with the differential equation with initial conditions, then transforms to the Laplace domain bringing in the initial conditions explicitly using

$$L\left[f^{(n)}(t)\right] = s^n F(s) - \sum_{\ell=0}^{n-1} s^{n-\ell-1}\ f^{(\ell)}(0) \quad . \tag{22}$$

Now z-transform by applying the Raggazzini-Zadeh identity or convolution approximation as appropriate.

Finally, to transform to the sample data domain, coefficients of like powers of z are equated.

A simple problem will illustrate the method. Consider the first-order constant coefficient differential equation

$$\dot{x}(t) + a\ x(t) = g(t) \quad . \tag{23}$$

Transforming to the Laplace domain, one has, using Equation (22),

$$s\ X(s) - x(0) + a\ X(s) = G(s) \tag{24}$$

and solving for X(s),

$$X(s) = \frac{G(s) + x(0)}{s + a} \quad . \tag{25}$$

Taking the z-transform, one has,

$$X(z) = Z\left[\frac{G(s)}{s + a}\right] + Z\left[\frac{x(0)}{s + a}\right] \quad . \tag{26}$$

From Equation (7) one may write

$$X(z) = x(0)\ z^{-0} + x(T)\ z^{-1} + x(2T)\ z^{-2} + \ldots \quad ; \tag{27}$$

therefore, one may apply the Raggazzini-Zadeh identity to the initial condition term,

$$Z\left[\frac{x(0)}{s + a}\right] = x(0)\ Z\left(\frac{1}{s + a}\right) \quad . \tag{28}$$

The significance of Equation (28) cannot be overstressed since the incorporation of nonzero initial conditions has been a major problem in z-transforms. Since the Raggazzini-Zadeh identity is exact, the initial conditions are incorporated exactly:

$$Z\left[\frac{x(0)}{s + a}\right] = \frac{x(0)}{1 - z^{-1}e^{-aT}} \quad . \tag{29}$$

The term with the forcing function, G(s), is another matter since the Raggazzini-Zadeh identity would not apply. Using the second convolution in Table for $\alpha = 1$, that is, trapezoidal convolution [9], one has

$$Z\left[\frac{G(s)}{s + a}\right] \simeq \frac{z^{-1}T}{2}\left[\left(\frac{1}{1 - z^{-1}e^{-aT}}\right)G(z,1) + \left(\frac{e^{-aT}}{1 - z^{-1}e^{-aT}}\right)G(z)\right] \tag{30}$$

$$\simeq \frac{z^{-1}T}{2}\ \frac{G(z,1) + e^{-aT}\,G(z)}{(1 - z^{-1}e^{-aT})} \quad . \tag{31}$$

and applying the shifting theorem

$$\simeq \frac{t}{2} \frac{(1 + z^{-1}e^{-aT})\ G(z) - g(0)}{(1 - z^{-1}e^{-aT})} \quad . \tag{32}$$

Combining Equations (32) and (29) in Equation (26),

$$X(z) \simeq \frac{\frac{T}{2}\left[(1 + z^{-1}e^{-aT})\ G(z) - g(0)\right] + x(0)}{1 - z^{-1}e^{-aT}} \tag{33}$$

Multiplying both sides by $(1 - z^{-1}e^{-aT})$, and substituting the definition of the z-transform, Equation (7),

$$(1 - z^{-1}e^{-aT}) \sum_{n=0}^{\infty} x(nT)\, z^{-n} \simeq \frac{T}{2} (1 + z^{-1}e^{-aT}) \sum_{n=0}^{\infty} g(nT)\, z^{-n} - \frac{T}{2} g(0) + x(0) \quad . \tag{34}$$

Equating coefficients of like powers of z,

$$z^{-0}: \quad x(0) = x(0) \tag{35-a}$$

$$z^{-1}: \quad x(t) - e^{-aT}\, x(0) \simeq \frac{T}{2}\left[g(T) + e^{-aT}\, g(0)\right] \tag{35-b}$$

$$z^{-n}: \quad x(nT) - e^{-aT}\, x(nT - T) \simeq \frac{T}{2}\left[g(nT) + e^{-aT}\, g(nT - T)\right] \quad . \tag{35-c}$$

It is very important to note that the general recurrence DOES NOT APPLY at n = 0. Note also that past values are decayed.

For convenience, the notation

$$x_n = x(nT) \tag{36}$$

will be used in the following equations. Table 2 gives the recurrences for the other convolutions in Table 1; References 5 and 6 contain details.

Again it is noted that past values are decayed. Of course, for a = 0, the recurrences reduce to the well-known Runge-Kutta integrations; the single integration is just a single pole at zero.

Other simple sample problems will be found in References 5 and 6. Only the results for a forced damped oscillation will be presented here for further emphasis of a point made earlier.

TABLE 2. RECURRENCES FOR A SINGLE-POLE FILTER

$x_{n+1} - e^{-aT} x_n$	
$\simeq T e^{-aT} g_n$,	$\alpha = 0$
$\simeq T e^{-aT/2} g_{n+\frac{1}{2}}$,	$\alpha = \frac{1}{2}$
$\simeq \frac{T}{4}\left[3e^{-aT/3} g_{n+\frac{2}{3}} + e^{-aT} g_n\right]$,	$\alpha = \frac{2}{3}$
$\simeq \frac{T}{2}\left[g_{n+1} + e^{-aT} g_n\right]$,	$\alpha = 1$
$\simeq \frac{T}{6}\left[g_{n+1} + 4e^{-aT/2} g_{n+\frac{1}{2}} + e^{-aT} g_n\right]$	
$\simeq \frac{T}{8}\left[g_{n+1} + 3e^{-aT/3} g_{n+\frac{2}{3}} + 3e^{-2aT/3} g_{n+\frac{1}{3}} + e^{-aT} g_n\right]$	

Given,

$$\ddot{x}(t) + 2\zeta\,\omega_0\,\dot{x}(t) + \omega_0^2 = g(t) \quad , \quad 0 < \zeta < 1 \quad , \tag{37}$$

the second step would yield

$$X(s) = \frac{G(s) + (s + 2\zeta\omega_0)\,x(0) + \dot{x}(0)}{s^2 + 2\zeta\,\omega_0\,s + \omega_0^2} \quad . \tag{38}$$

For

$$a = \zeta\,\omega_0 \tag{39}$$

and

$$\omega = (1 - \zeta^2)^{1/2}\ \omega_0 \tag{40}$$

Equation (38) may be rewritten

$$X(s) = \frac{G(s) + (s + a)\ x(0) + ax(0) + \dot{x}(0)}{(s + a)^2 + \omega^2} \tag{41}$$

the recurrence for $\alpha = 1$ is [5,6]

$$x_0 = x_0 \tag{42-a}$$

$$x_1 \simeq e^{-aT}\left[\cos \omega T + a\left(\frac{\sin \omega T}{\omega}\right)\right] x_0 + e^{-aT}\left(\frac{\sin \omega T}{\omega}\right)\ \dot{x}_0 + \frac{T}{2}\, e^{-aT}\ \left(\frac{\sin \omega T}{\omega}\right)\ g_0 \tag{42-b}$$

$$x_{n+2} \simeq (2\, e^{-aT} \cos \omega T)\ x_{n+1} - e^{-2aT}\ x_n + T\, e^{-aT}\ \left(\frac{\sin \omega T}{\omega}\right)\ g_{n+1}\ . \tag{42-c}$$

Please note that the general recurrence, Equation (42-c) DOES NOT APPLY for $n = 0$ or $n = 1$.

VI. CONCLUSIONS

Time and space do not permit a discussion of accuracy of the method [5,6,10]. Table 3 presents a summary of current work.

TABLE 3. SUMMARY OF WORK

$\frac{1}{s}$	$\frac{1}{(s + a)^n}$
Taylor Series	Fourier Series
Pole-Zero	Pole-Residue

The approach is to develop recurrence for poles other than the single pole at zero, the single integrator.

The classical Runge-Kutta integrators were developed based upon a truncated Taylor Series. For simulation of control systems, a truncated Fourier Series, truncated at the Shannon Sampling Limit, seems a more appropriate criterion since the problem is closed loop.

Normally, adjustments are made by pole-zero techniques which introduce phase shifts. Lerner's filter [11] utilized pole-residues to obtain constant time delay in the passband. Partial fraction expansions were required.

Partial fractions lead to parallel processing [2] and may reduce the start-up problem noted previously.

The adjustment of residues to improved performance is presently being studied [10] as part of an FY '80 ILIR "high risk - high payoff" effort. If the "payoff" is "high," a follow-on paper will be submitted. In the interest of "closing the loop," "feedback" is solicited.

REFERENCES

1. J. R. Raggazzini and L. A. Zadeh, "The Analysis of Sampled-Data Systems," AIEE Trans., Vol. 71, Part II, November 1952, also discussion by J. M. Salzer and reply by the authors), pp. 225-234.

2. J. M. Salzer, "Frequency Analysis of Digital Computers Operating in Real Time," Proc IRE, Vol. 42, No. 2, February 1954, pp. 457-466.

3. J. S. Rosko, Digital Simulation of Physical Systems, Reading, PA: Addison-Wesley Publishing Company, 1972.

4. R. A. Gaskill, "Fact and Fallacy in Digital Simulation," Simulation, edited by J. McLeod, New York: McGraw-Hill, 1968.

5. R. E. Dickson, Tunable Integration and Tunable Trapezoidal Convolution — A Potpourri, US Army Missile Research and Development Command, Redstone Arsenal, Alabama, 5 May 1977, Report No. TD-77-12.

6. R. E. Dickson, Trapezoidal Convolution Revisited: R-K Convolution or the Digital Simulation of Continuous Systems Via Z-Transforms, US Army Missile Research and Development Command, Redstone Arsenal, Alabama, 15 June 1978, Report No. T-78-66.

7. V. S. Grimes, Jr., Real Time Digital Model of the Rolling Air Frame, US Army Missile Research and Development Command, Redstone Arsenal, Alabama, 31 July 1978, Report No. T-78-75.

8. E. I. Jury, Theory and Application of the Z-Transform Method, New York: John Wiley and Sons, Inc., 1964.

9. C. A. Halijak, Digital Approximations of Solutions of Differential Equations Using Trapezoidal Convolution, Bendix Corporation, Bendix Systems Division, 26 August 1960, Report No. ITM-64.

10. R. E. Dickson, US Army Missile Command Laboratory Notebook 7254, 25 September 1978 to 19 December 1979, Redstone Scientific Information Center, Redstone Arsenal, Alabama.

11. R. M. Lerner, "Band-Pass Filters with Linear Phase," Proc. IEEE, Vol. 52, No. 3, May 1964, pp. 249-268.

RADIX 65/39 , A ROOT SEARCHING ALGORITHM FOR ANALYTIC EQUATIONS

WALTER O. EGERLAND

BALLISTIC RESEARCH LABORATORY,USA ARRADCOM

ABERDEEN PROVING GROUND,MD

ABSTRACT

Given a circle in the complex plane, Radix 65/39 computes all roots of an analytic equation along a chosen diameter.Each root is bracketed by two monotone sequences (Landau sequences). The algorithm is implemented in Fortran IV and presently active on the PDP 11/70. Copies of the program are available on request.

1. INTRODUCTION

Let f(z) be a bounded analytic function of $z = x + iy$ in a disk. We consider the equation $f(z)=a$ for a given (complex) constant a. To date, there is no algorithm that "exhausts" the disk in some fashion,locates all roots,determines their multiplicity,or,equally important , shows that the equation has no roots in the given disk. Towards such an ideal,we develop here an algorithm ,called Radix 65/39,that accomplishes such an exhaustion along a chosen diameter. It is based on an extension of an exclusion theorem by Landau [1]. The name Radix 65/39 is meant to reflect the connotations of the Latin word radix which include also origin and source besides root. We extended Landau's result of 65 years ago and his 1914 paper can be found in Volume 39 of BRL's Bocher collection of Mathematical Reprints.

Without loss of generality ,we shall assume in the sequel that the equation is to be solved in the unit disk U : $|z| < 1$ and that f(z) is bounded there by 1. In 2_0 we state Landau's theorem and prove its extension. For a very short proof of Landau's theorem ,the reader is referred to [3]. In 3_0 the algorithm is established . A more detailed description geared to applications is contained in [4]. The general mathematical background is covered in Carathcodory's Cambridge Tract [2].

2. EXTENSION OF LANDAU'S THEOREM

Landau's theorem can be stated as follows.

Theorem 1 (Landau's Exclusion Theorem). If f(z) is analytic in U : $|z| < 1$ and bounded by 1, then every solution ζ of the equation

$$f(z) = a \neq f(0), \quad |a| < 1$$

satisfies the inequality

$$|\zeta| \geq \left| \frac{a - a_0}{\bar{a}_0 a - 1} \right|, \quad a_0 = f(0). \tag{1}$$

The bound on ζ cannot be improved.

Thus ,the theorem establishes a disk centered at the origin that is free of zeros of the equation f(z) - a = 0. In the following theorem a Landau disk is established for an arbitrary point $z_0 \in U$ that satisfies $f(z_0) \neq a$. This generalization is the key to the algorithm.

Theorem 2. Let f(z) be analytic and bounded by 1 in U. If $z_0 \in U$, $f(z_0) \neq a$,the equation $f(z) = a, a \neq f(0)$,has no solution in the disk

$$D : \left| \frac{z - z_0}{\bar{z}_0 z - 1} \right| < \left| \frac{f(z_0) - a}{\bar{a} f(z_0) - 1} \right|. \tag{2}$$

For a proof ,let

$$t(z)=\frac{z-z_0}{\bar{z}_0 z-1}.$$

This function maps the unit disk univalently onto itself. Hence, the function

$$f(z)=f(z(t))=g(t)$$

satisfies $|g(t)|<1$, $t \in U$, and $g(0)=f(z_0)$. Since $f(z_0)\neq a$, it follows by Theorem 1 that if the equation $g(t) = a$ has the solution $t = \tau$, then

$$|\tau| \geq \left|\frac{f(z_0)-a}{\bar{a}f(z_0)-1}\right|.$$

Therefore, $z(\tau)$ is not contained in D. This completes the proof.

3. THE ALGORITHM

Letting

$$k=k(z_0)=\left|\frac{f(z_0)-a}{\bar{a}f(z_0)-1}\right|,$$

the disk D(C,R) of (2) has center

$$C=\frac{z_0(1-k^2)}{1-|z_0|^2k^2},$$

radius

$$R=k\frac{1-|z_0|^2}{1-|z_0|^2k^2},$$

and intersections with the diameter determined by z_0

$$A_0=\frac{z_0}{|z_0|}\cdot\frac{|z_0|+k}{1+|z_0|k} \tag{3}$$

and

$$B_0=\frac{z_0}{|z_0|}\cdot\frac{|z_0|-k}{1-|z_0|k}. \tag{4}$$

Definition. The algorithm is embodied in the two sequences $\{A_n\}$ and $\{B_n\}$ defined for $n=1,2,\ldots$ by

$$A_n = \frac{A_{n-1}}{|A_{n-1}|}\cdot\frac{|A_{n-1}|+k(A_{n-1})}{1+|A_{n-1}|k(A_{n-1})} \tag{5}$$

and

$$B_n = \frac{B_{n-1}}{|B_{n-1}|}\cdot\frac{|B_{n-1}|-k(B_{n-1})}{1-|B_{n-1}|k(B_{n-1})} \quad , \tag{6}$$

where A_0 , B_0 are given by (3) and (4) .

Theorem 3 . The algorithm is linearly convergent.

We carry out the proof for $\{ A_n \}$. A similar proof holds for $\{ B_n \}$. Along the ray arg z_0 , $|A_n|$ (A_n being the right endpoint of an interval that is free of zeros) is clearly monotone non-decreasing . Furthermore , $|A_n|<1$. Thus the limit $\lim_{n\to\infty}|A_n| = \alpha \leqslant 1$ exists. Since the iteration function

$$\phi(x) = argx\frac{|x|+k(x)}{1+|x|k(x)} \qquad (x = |x|\exp(iargz_0), |x|<1)$$

is continuous , it follows from (5) that $A = \alpha\ exp(iargz_0)$ satisfies the fixed point equation

$$A = \frac{A}{|A|}\cdot\frac{|A|+k(A)}{1+|A|k(A)} \quad .$$

Thus, either $A = exp(iargz_0)$ or $k(A) = 0$. If $A = exp(iargz_0)$, then, by the construction of the sequence $\{A_n\}$, $f(z) = a$ has no solution on the segment $[\ z_0\ ,\ A\ ]$. If $k(A) = 0$, then it follows from the definition of k that $f(A) = a$, i.e. that A is a root of $f(z) = a$. This proves that the algorithm is convergent. That it is linearly convergent follows from

$$\lim_{n\to\infty}\left|\frac{A-A_n}{A-A_{n-1}}\right| = 1-\frac{|f'(A)|(1-|A|^2)}{1-|a|^2} > 0.$$

That the limit is positive follows from the lemma of Schwarz-Pick. This completes the proof of the theorem.

4. MULTIPLE ROOTS

To each point on a given diameter belongs an "ascending" and "descending" sequence (Landau sequence) according to 3. Consequently ,upper and lower bounds for the modulus of a root A (that the diameter contains) can be obtained . However , since progress towards A is

essentially measured by

$$|A_n - A_{n-1}| \approx \text{Const.}\ |A - A_{n-1}|\,|f'(A)|\,,$$

"stalling " will occur in the neighborhood of a multiple root. It is a remarkable feature of the algorithm that "stalling" due to a multiple root can be avoided by the following simple device (local extraction of a root). Consider (for simplicity) the equation $f(z) = 0$ and suppose that $f(z)$ has a root of order $n = m$ at $z = \lambda$. Then $f(z)$ has the representation

$$f(z) = (z-\lambda)^m\, g(z) \quad , g(\lambda) \neq 0\,,$$

and any branch of

$$F(z) = (f(z))^{\frac{1}{m}}$$

is analytic in $|z-\lambda| < \rho$, where

$$\rho = \min(\rho_1\,,\ 1-|\lambda|)$$

and

$$\rho_1 = \min_{g(t)=0} |t-\lambda| \quad .$$

Therefore, each of the m functions

$$G(u) = F(\lambda + \rho u) \quad , \quad |u| < 1\,,$$

is analytic in U, bounded by 1, and has at $u = 0$ a zero of order 1. But this means that in the neighborhood of $z = \lambda$

$$k = |f(z)|$$

may be replaced by

$$k = |f(z)|^{\frac{1}{m}} \ .$$

Although m is not known beforehand, it can be determined interactively from the local convergence behavior of the algorithm by successively setting $n = 2,3,\ldots,m$.

REFERENCES

1. Landau,E.,Ueber eine Aufgabe aus der Funktionentheorie, The Tohoku Mathematical Journal Vol.5,Nos.3,4,June 1914.

2. Caratheodory,C.,Conformal Represenation, Cambridge Tracts No.28,Cambridge University Press,1949.

3. Egerland,W.O.,Radix 65/39 (BRL Report to appear),1980.

4. Graham,J.L. and Egerland,W.O.,Radix 65/39,An interactive Algorithm for the Solution of Analytic Equations (BRL Report to appear),1980.

COMPUTATION AND APPLICATION OF SCHWARZ-CHRISTOFFEL TRANSFORMATIONS

Lloyd N. Trefethen
Computer Science Department
Stanford University
Stanford, California 94305

ABSTRACT. We discuss the problem of numerically computing Schwarz-Christoffel transformations, which map the unit disk in the complex plane conformally onto the interior of a polygon. A program is described which solves this problem reliably to high accuracy for bounded or unbounded image polygons. Some applications to fluids and electrical problems are given.

1. INTRODUCTION. Conformal mapping is a relatively underdeveloped area of numerical analysis, but nevertheless a number of techniques are known. The best understood problem in this area is the problem of mapping the unit disk D conformally onto a simply connected region Ω with a smooth boundary Γ, or vice versa. Available techniques for this task include Theodorsen's method [7,8], Symm's method [8,10], a method based on solving the Cauchy-Riemann equations [1], and a method based on matching the behavior of a power series on Γ [3]. The majority of methods (and the first two in this list) are based on integral equations. All of them begin by discretizing the boundary Γ in some way. For a thorough discussion of numerical conformal mapping as of 1964, see the book by Gaier [4].

Our concern here is the special case in which Γ is a polygon. This problem differs from the first one in two important ways. First, the boundary can be fully described by a finite set of parameters. Second, the derivative of the solution map from D to Ω will necessarily have a singularity at each vertex. The presence of these singularities suggests that methods designed for smooth boundaries are likely to perform poorly when Γ is a polygon, unless special care is taken. This is indeed the case. On the other hand the finiteness of the geometry suggests that the problem of mapping onto polygons is inherently simple and need not be subject to discretization error. Both facts point to the desirability of using a specialized technique for the conformal mapping of polygons.

Such a technique is the numerical implementation of the Schwarz-Christoffel transformation, and our aim here is to sketch the methods with which we have dealt with this problem. The result has been a computer program that accurately maps the unit disk onto the interior of an arbitrary bounded or unbounded polygon. Several innovations make the program substantially faster and more reliable than previous programs for implementing the Schwarz-Christoffel transformation. A fuller presentation may be found in [11] and [12].

For mixed problems that involve general regions whose boundaries contain sharp corners, very little has been done. One promising approach, which has been implemented by Davis [2], is based on a generalization of the Schwarz-Christoffel formula to general regions.

2. THE SCHWARZ-CHRISTOFFEL TRANSFORMATION; FORMULATION OF THE PARAMETER PROBLEM AS A NONLINEAR SYSTEM OF EQUATIONS. Let Ω be a region in the complex w-plane bounded by a polygon P with N vertices $w_1, \ldots, w_N$. Some of the w_k may lie at $w = \infty$, but for simplicity we shall suppose here that all are finite. Let the external angle of P at w_k be $\pi\beta_k$. Then for any set of points $z_1, \ldots, z_N$ in counterclockwise order on the circle $|z| = 1$, and for any complex

constants C and w_c, the Schwarz-Christoffel formula

$$w(z) = w_c + C \int_0^z \prod_{k=1}^{N} (1 - z'/z_k)^{-\beta_k} \, dz' \qquad (1)$$

defines an analytic function of z in the unit disk with $w(0) = w_c$. The Schwarz-Christoffel theorem asserts: given $w_c \in \Omega$, there is some choice of C and $\{z_k\}$ (let us call these points prevertices) such that (1) defines a conformal map (one-to-one, nonvanishing derivative) of the unit disk D onto Ω.

The central question is, how can we find a correct set of values C and $\{z_k\}$? This is known as the parameter problem. In general the solution can only be found numerically. The method we have used — and this is an old idea — is to formulate the problem as a system of nonlinear equations in the unknowns $\{z_k\}$, $1 \le k \le N-1$. (There is one free parameter in the conformal map, which we absorb by setting $z_N = 1$.) Now the correct prevertices $\{z_k\}$ will satisfy $N-1$ equations specifying the lengths of the sides of P,

$$|w_{k+1} - w_k| = \left| C \int_{z_k}^{z_{k+1}} \prod_{j=1}^{N} (1 - z'/z_j)^{-\beta_j} \, dz' \right|, \quad 1 \le k \le N-1 . \qquad (2)$$

These equations constitute the nonlinear system we attempt to solve numerically for the unknowns $z_1, \ldots, z_{N-1}$. (C is not treated as a primary unknown, but is replaced in (2) by the function of $\{z_k\}$ determined by

$$w_N - w_c = C \int_0^{z_N} \prod_{k=1}^{N} (1 - z'/z_k)^{-\beta_k} \, dz' . \quad) \qquad (3)$$

It can be shown that any set of prevertices $\{z_k\}$ that satisfies (2) defines a solution of the Schwarz-Christoffel mapping problem, and that there is exactly one such solution set.

The unknowns $\{z_k\}$ are not arbitrary complex numbers: they all lie on $|z| = 1$, and they lie in counterclockwise order. We must impose these two constraints in the process of seeking the solution of the parameter problem. First, it is natural to work not with z_k but with its (real) argument,

$$\theta_k = \arg z_k , \quad 0 \le \theta_k < 2\pi . \qquad (4)$$

This eliminates the first constraint. Not so obvious but also important, it turns out that a second change of variables can eliminate the constraints $\theta_k < \theta_{k+1}$. We define

$$y_k = \log \frac{\theta_k - \theta_{k-1}}{\theta_{k+1} - \theta_k} , \quad 1 \le k \le N-1 \qquad (5)$$

(with $\theta_0 \equiv \theta_N$), and now it is easy to see that there is a one-to-one correspondence between arbitrary sets of real numbers $y_1, \ldots, y_{N-1}$ and sets of real numbers $\theta_1, \ldots, \theta_{N-1}$ constrained by $\theta_k < \theta_{k+1}$.

This means of eliminating constraints is a trick, but its effect is to make (2) much easier to solve numerically. In fact, it turns out that (5) also leads to a formulation of the Schwarz-Christoffel problem that is better conditioned and better scaled than the original one.

(2) has now become a system in N-1 real unknowns $\{y_k\}$, and it can be solved by any robust nonlinear equations solver. We have used the routine NS01A, by M.J. Powell [9]. This is an early "hybrid" code, combining a steepest descent method with an approximation of Newton's method. The results have been very encouraging: in experiments involving several hundred polygons, the program has converged from the trivial initial guess $y_k \equiv 0$ ($\{z_k\}$ equally spaced around $|z| = 1$) in all but four or five cases involving highly irregular geometries.

3. NUMERICAL INTEGRATION BY COMPOUND GAUSS-JACOBI QUADRATURE. So far we have described only half of the computational problem; the rest is the task of evaluating the Schwarz-Christoffel integral efficiently. During the iterative solution of the parameter problem, (2) and (3) must be evaluated many times for various sets of trial prevertices $\{z_k\}$. After the parameter problem is solved, each evaluation of the Schwarz-Christoffel map at a point $z \in D$ will require a further integration as in (1).

The technique we have used takes advantage of the fact that although the prevertices $\{z_k\}$ vary during the solution of the parameter problem, the angles $\{\beta_k\}$ do not. Suppose we choose to evaluate (2) along the straight line segment from z_k to z_{k+1}. At each endpoint the integrand has a singularity of the form $(1 - z/z_j)^{-\beta_j}$, but otherwise it is smooth. Therefore by a linear change of variable it is easy to convert (2) to an integral over [-1,1] of the form

$$I \equiv \int_{-1}^{1} (1+x)^{\alpha} (1-x)^{\gamma} f(x)\, dx \qquad (6)$$

where $\alpha = -\beta_k$, $\gamma = -\beta_{k+1}$, and $f(x)$ is analytic throughout [-1,1]. Every integral we need to evaluate in Schwarz-Christoffel computations can be brought to the form (6), and in each case α and γ will be drawn from the fixed set $\{0\} \cup \{-\beta_k\}$.

This is a natural situation in which to apply Gauss-Jacobi quadrature [5]. A Gauss-Jacobi quadrature formula is a rule of the form

$$I \cong \sum_{k=1}^{NPTS} w_k f(x_k) \qquad (7)$$

for some positive integer NPTS, in which the numbers w_k are positive weights and the points x_k are nodes in (-1,1). The formula is constructed to take the singularities in (6) implicitly into account, and to be optimal in the sense that it yields the exact value for I whenever f is a polynomial of degree $\leq 2\,NPTS - 1$.

Gauss-Jacobi quadrature nodes and weights can be computed rapdily to high accuracy. We have used the program GAUSSQ by Golub & Welsch [6] for this purpose. Since the angles $\{\beta_k\}$ remain fixed, nodes and weights need only be computed once at the start of all computations.

One complication must be introduced if Gauss-Jacobi quadrature is to evaluate the Schwarz-Christoffel integral efficiently in any but the simplest problems. It happens that in practice, even when P is a reasonably regular polygon, the correct prevertices $\{z_k\}$ are often spaced exceedingly irregularly around the unit circle. It is easily possible, for example, to have $\theta_2 - \theta_1 \sim 1$, $\theta_3 - \theta_2 \sim 10^{-4}$. In such a case the integral (2) from z_1 to z_2 has a singularity at z_3 very close to the interval of integration, which transforms in (6) to a singularity very close to 1 . As a result pure Gauss-Jacobi quadrature would require on the order of 10^4 nodes to achieve high accuracy, costing a thousand times as many evaluations of $f(x)$ as one would like to allow.

Our solution is to use a form of compound Gauss-Jacobi quadrature. Before evaluating any integral such as (2), the program determines how close the nearest singularity z_j $(j \neq k, k+1)$ is to one of the endpoints and subdivides the interval of integration at that endpoint if it is too close. An appropriate Gauss-Jacobi rule is then applied on each subinterval, and the division is managed in such a way that no subinterval is longer than twice the distance to the nearest singularity. Because of the simplicity of the geometry of the disk, this is easy to do.

By this means we maintain a minimum density of quadrature nodes relative to the smoothness of the integrand at each point in each integral. The result is an integration procedure that, in practice, requires about $2d$ integrand evaluations in each integration to achieve d decimal digits of accuracy.

4. COMPUTATION OF THE INVERSE MAP. Now that $w(z_0)$ can be computed for given $z_0 \in D$, the problem of computing $z(w_0)$ for given $w_0 \in \Omega$ is relatively easy. The value sought is the unique solution in D of the nonlinear equation

$$w(z) - w_0 = 0 . \tag{8}$$

If a reasonably good initial guess is known, (8) can be solved rapidly by Newton's method. At each iteration a derivative $w'(z)$ will be required, and this is just C times the integrand in (1).

To get a sufficiently good initial guess for the Newton iteration, we reformulate (8) as an initial value problem involving an ordinary differential equation in one complex variable. From (1), $z(w)$ must satisfy

$$\begin{aligned} z(w_c) &= 0 , \\ \frac{dz}{dw} &= \frac{1}{C} \prod_{k=1}^{N} (1 - z/z_k)^{+\beta_k} , \end{aligned} \tag{9}$$

and since $w(z)$ has a nonvanishing derivative this differential equation is well behaved throughout Ω . In principle, therefore, $z(w_0)$ can be computed by choosing

a path from w_c to w_0 and integrating (9) numerically along that path. Our program does this to low accuracy by means of the routine ODE by Shampine and Gordon, and then switches to Newton's method as a more efficient means of achieving high accuracy.

This hybrid scheme evaluates the inverse map $z(w)$ in about four times the time it takes to evaluate the forward map $w(z)$.

5. THE SCPACK PACKAGE. The methods described here have been implemented in a package of Fortran programs in double precision called SCPACK [12]. Including the routines associated with the library programs GAUSSQ, NSO1A, and ODE, SCPACK consists of about 33 subroutines and 3000 lines of code. To obtain a copy, send me a tape with desired DCB parameters or contact me for further information.

6. EXAMPLES. Figure 1 shows three conformal maps, two of them onto bounded polygons and the third onto a polygon with three vertices at infinity. In each case the images of the radius vectors from $z = 0$ to the prevertices $z = z_k$ in the unit disk have been drawn, together with the images of a set of concentric circles in the disk. All intersections evidently form right angles, as they must. Observe that contour lines bend tightly around reentrant corners, revealing the large gradients there, but avoid the backwater regions near outward-directed corners and vertices at infinity.

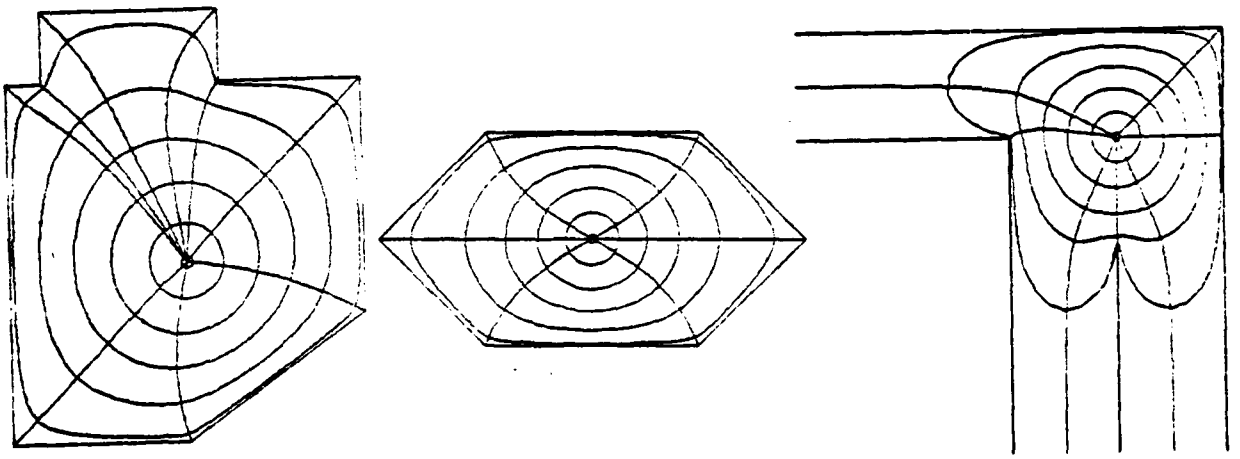

Figure 1. Three conformal maps of the unit disk. Contours within each plot are images of concentric circle in the disk at radii .03, .2, .4, .6, .8, .97 , and of radii from the center of the disk to the prevertices z_k .

A familiar application of conformal mapping is to problems of ideal incompressible flow in two dimensions. Such flow is governed by Laplace's equation $\nabla^2\phi = 0$, where ϕ is a scalar velocity potential. The plots of Figure 2 show streamlines for ideal flow through a pair of infinite channels. In each case one Schwarz-Christoffel map has mapped the given region to the unit disk, and a second (trivial) one has mapped the disk to an infinite channel with parallel straight sides, where Laplace's equation has a simple solution. The streamlines shown are images of straight parallel lines in this channel.

Figure 2. Streamlines for ideal incompressible flow in two infinite channels.

The other best-known applications of conformal mapping are to electric potential problems in the plane. In Figure 3 we have considered the problem of steady DC current flow through a polygonally shaped resistor. One end is held at one fixed voltage V_0, another at a second voltage V_1, and the sides in between are insulated. Such problems come up in the design of integrated circuits.

Like the previous one, this problem is governed by Laplace's equation. The difference is that here the boundary conditions are more complicated. First we reduce the polygon to the unit disk by a Schwarz-Christoffel transformation. Then we apply the Schwarz-Christoffel formula a second time, but without solving a second parameter problem: we let $z_1, \ldots, z_4$ be the four points on $|z| = 1$ at which the boundary conditions must change, set $\pi\beta_1 = \ldots = \pi\beta_4 = \pi/2$, pick arbitrary values for C and w_c, and consider the image of the disk under (1). It is a rectangle with the special property that the four distinct boundary components of the original resistor map to its four sides. So once again Laplace's equation has a trivial solution: a regular grid in this rectangle gives streamlines and lines of constant voltage, which have been mapped back to the problem domain in Figure 3.

As a bonus, the resistance of the polygonal resistor may easily be seen to be a simple number. It is the length of the conformally equivalent rectangle divided by its width — in this example, 3.3762593 .

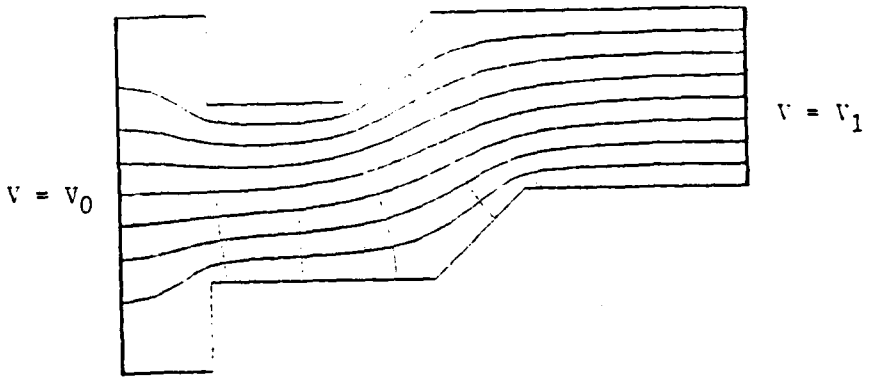

Figure 3. Streamlines and equipotential lines in a polygonal resistor.

examples we have considered in this section required on the order computer time on the IBM 370/168.

ACKNOWLEDGMENTS. This project was proposed and guided by Prof. Peter Henrici of the ETH in Zurich, Switzerland. It was supported in part by ONR contract N00014-75-C-1132 and in part by a National Science Foundation Graduate Fellowship.

REFERENCES.

[1] Chakravarthy, S. and Anderson, D., Numerical Conformal Mapping, Math. Comp. 33 (1979), pp. 953-969.

[2] Davis, R. T., Numerical methods for coordinate generation based on Schwarz-Christoffel Transformations, 4th AIAA Comp. Fluid Dynamics Conf. Proceedings, 1979.

[3] Fornberg, B., A Numerical Method for Conformal Mappings, to appear in SIAM J. Sci. Stat. Comp.

[4] Gaier, D., Konstruktive Methoden der Konformen Abbildung. Springer Tracts in Natural Philosophy, vol. 3. Springer, Berlin, 1964.

[5] Gautschi, W., A Survey of Gauss-Christoffel Quadrature Formulae, to appear in Christoffel memorial volume of papers, Birkhäuser.

[6] Golub, G. and Welsch, J., Calculation of Gaussian Quadrature Rules, Math. Comp. 23 (1969), pp. 221-230.

[7] Gutknecht, M., Solving Theodorsen's Integral Equation for Conformal Maps with the Fast Fourier Transform, parts I-III, to appear.

[8] Henrici, P., Fast Fourier Methods in Computational Complex Analysis, SIAM Review 21 (1979), pp. 481-527.

[9] Powell, M. J., A Fortran Subroutine for Solving Systems of Non-linear Algebraic Equations, Tech. Report AERE-R. 5947, Harwell, England (1968).

[10] Symm, G. T., An Integral Equation Method in Conformal Mapping, Numer. Math. 9 (1966), pp. 250-258.

[11] Trefethen, L. N., Numerical Computation of the Schwarz-Christoffel Transformation, SIAM J. Sci. Stat. Comp. 1, 1980.

[12] Trefethen, L. N., SCPACK Version 1.1 Users Guide, unpublished.

ITERATED SCHÖENBERG APPROXIMATION AND ITS APPLICATION

William S. Agee, Robert H. Turner, Barbara A. Dunn
Mathematical Services Branch
Data Sciences Division
US Army White Sands Missile Range
White Sands Missile Range, New Mexico 88002

ABSTRACT. A simple method of local approximation and its application to the approximation of simple functions and to the approximation and smoothing of noisy data sequences is described. The local approximation method which we call iterated Schöenberg approximation (ITSH) was developed at White Sands Missile Range for approximation or smoothing of noisy data when little is known beforehand about the character of the data or noise. At last years Army Numerical Analysis and Computers Conference, Carl deBoor described and proved the convergence properties of this iterated Schöenberg method. In order to obtain a feeling for the approximation ability of ITSH, its approximation error is compared with the error obtained from least squares spline approximation for some known functions. When approximating or smoothing a noisy data sequence for which little or nothing is known about either the data or noise, it is necessary to make the location of the knots data dependent. This can be accomplished by examining the estimation error and adding knots in the vicinity of any trend occurence. This sequence of spline fitting and error analysis is continued until the estimation error is free of trends. A local fitting approximation, whose estimation requires only a minimal amount of computation, is very attractive for this application. The performance of iterated Schöenberg approximation method for this type of application is illustrated with WSMR tracking data.

1. INTRODUCTION. At the 1979 Army Numerical Analysis and Computers Conference Carl deBoor [1] proved several properties of a simple curve fitting method which we have developed at White Sands Missile Range. This curve fitting method, which we call iterated Schöenberg approximation (ITSH) for reasons which will become obvious, is a spline based fitting method. It is a local approximation method, i.e., the approximation at any particular value, say t, of the independent variable is mainly dependent on observed data points (t_i, y_i) for which t_i is close to t and is only very weakly dependent on (t_i, y_i) which are far from t. The iterated Schoenberg method is also computationally very fast.

In trajectory data reduction at WSMR it is often desirable to preprocess noisy measurement data sequences. We may want to simultaneously preprocess many, possibly long data sequences, each having one or two thousand data points, in order to accomplish one or more of the following objectives: (1) Estimation of measurement noise variances to be used in later least squares processing, (2) detection and rejection of outliers in measurement data, (3) synchronizing measurement times, (4) resolving measurement ambiguities.

Most often, very little is known about either the dynamic character of the measurements or the character of the measurement noise. For this reason

we make the final choice of the knots in the spline fit data dependent. This is accomplished by starting with a sparse, tentative set of knots, computing a spline approximation, and examining the fitting error and adding knots in the vicinity of any trends in the error. This sequence of spline fitting and error analysis is continued until the estimation error is free of trends. A local spline fitting method such as the ITSH method which requires only a minimal amount of computation to compute a new spline fit after adding knots is very attractive for this application.

2. SCHÖENBERG AND ITERATED SCHÖENBERG APPROXIMATION. Let $\{T_i, i = 1, N\}$ be a set of knot locations and let $y(t_j)$ be a set of data points to be fitted by a spline approximation. Suppose we fit a spline curve of order k, the most common value of k being four, using the Schoenberg, variation diminishing approximation,

$$\hat{y}(t_j) = \sum_{B_i(t_j) \neq 0} y(t_i^*) B_i(t_j), \tag{1}$$

where the values t_i^* are the knot averages

$$t_i^* = \frac{1}{K-1} \sum_{\ell=1}^{K-1} t_i + \ell \tag{2}$$

The $B_i(t_j)$ are the B-splines of order K and the sum in (1) is taken over the B-splines which are non-zero at t_j. The Schoenberg approximation in (1) is a very fast method of curve fitting since the coefficients of the B-splines in (1) are merely function values and require essentially no computation. Although the Schoenberg approximation produces a fit which assumes the shape of the data sequence, the magnitude of the fitting errors are often quite large. If these errors are visually examined, one notices that the errors, although quite large, are also smooth and that they, in turn, could be well approximated by a Schoenberg approximation. This observation forms the basis of the iterated Schoenberg approximation method. The following sequence of steps describes our iterated Schoenberg method for curve fitting.

3. ITERATED SCHÖENBERG METHOD.

a. Compute Schoenberg fit to data

$$\hat{y}(t_j) = \sum_{B_i(t_j) \neq 0} y(t_i^*) B_i(t_j) \tag{3}$$

b. Compute residuals

$$r(t_j) = y(t_j) - \hat{y}(t_j) \tag{4}$$

c. Compute Schoenberg fit to residuals

$$\hat{r}(t_j) = \sum_{B_i(t_j) \neq 0} r(t_i^*)B_i(t_j) \tag{5}$$

d. Update approximation

$$\hat{y}(t_j) \longleftarrow \hat{y}(t_j) + \hat{r}(t_j) \tag{6}$$

e. Repeat steps b, c, and d until $|\hat{r}(t_j)|$ are acceptably small.

4. CONVERGENCE OF THE ITERATED SCHÖENBERG METHOD (DE BOOR). Let the Schoenberg approximation be represented as an operator V

$$\hat{y} = Vy = \Sigma y(t_i^*)B_i \tag{7}$$

Then we can represent an arbitrary term $\hat{y}^{(n)}$ in the iterated Schoenberg fitting sequence as,

$$\hat{y}^{(n)} = \hat{y}^{(n-1)} + V(y-\hat{y}^{(n-1)}) \tag{8}$$

If this process converges, we must have

$$Vy = V\hat{y}^{(\infty)} \tag{9}$$

This condition is equivalent to

$$\Sigma y(t_i^*)B_i = \Sigma \hat{y}^{(\infty)}(t_i^*)B_i \tag{10}$$

The above outline demonstrates that, if the process converges, it converges to the spline interpolant to the set of points $\{y(t_i^*), i = N\}$. de Boor showed that indeed the process does converge since $||I - B||_\infty < 1$, where B is the matrix, $B = [B_i(t_j^*)]$. Furthermore, de Boor demonstrated that the slowly varying components of $y(t_i)$ are well approximated more quickly than the rapidly varying components of $y(t_i)$. Thus, some smoothing is obtained by stopping the iteration early.

5. APPLICATION TO A DOUBLE HUMP FUNCTION. The double hump function,

$$y(t) = \frac{1}{.01+(t-.3)^2} + \frac{1}{.015+(t-1.2)^2} \quad 0 \leq t \leq z$$

provides a good first illustration of the application of the iterated Schoenberg curve fitting procedure. Two hundred equally spaced samples, $y(t_i)$, $t_i = .01 \cdot i$, $i = 0, 199$, were generated. Knot positions for this

examples were preselected at T_i = 0, .19, .23, .30, .43, .50, .59, .87, 1.04, 1.10, 1.20, 1.31, 1.41, 1.61, 1.99. No noise was added to the data points. Figs. 1 and 2 plot y(t) and $5r^{(n)}(t)$, where $r^{(n)}(t)$ is the residual after the $n^{\underline{th}}$ cycle of Schoenberg iteration, for n = 1, 4. We see that after four iterations, the fit has converged well enough so that error is everywhere less than 0.5. Fig. 3 plots y(t) and $5r^{(n)}(t)$ for n = 9, 10. Although the error after the 10th iteration is smaller than the error after the fourth iteration, the approximation at the fourth iteration is probably adequate for most purposes. This early convergence is even more satisfactory for the more commonly encountered data sequences which vary less wildly than the double hump function used in this illustration. As a comparison to the error in the ITSH approximation Fig. 4 plots 5r(t), where r(t) is the error in the least squares spline approximation to $y(t_i)$, i = 0, 199, using the specified knots. There are almost no discernible differences in the error $5r^{(10)}(t)$ from the ITSH approximation and the error 5r(t) from the least square approximation. Again it must be emphasized that for any practical applications the error in the early iterations of ITSH, say n = 3 or 4, will be nearly as small as the error in a least square approximation.

FIGURE 1

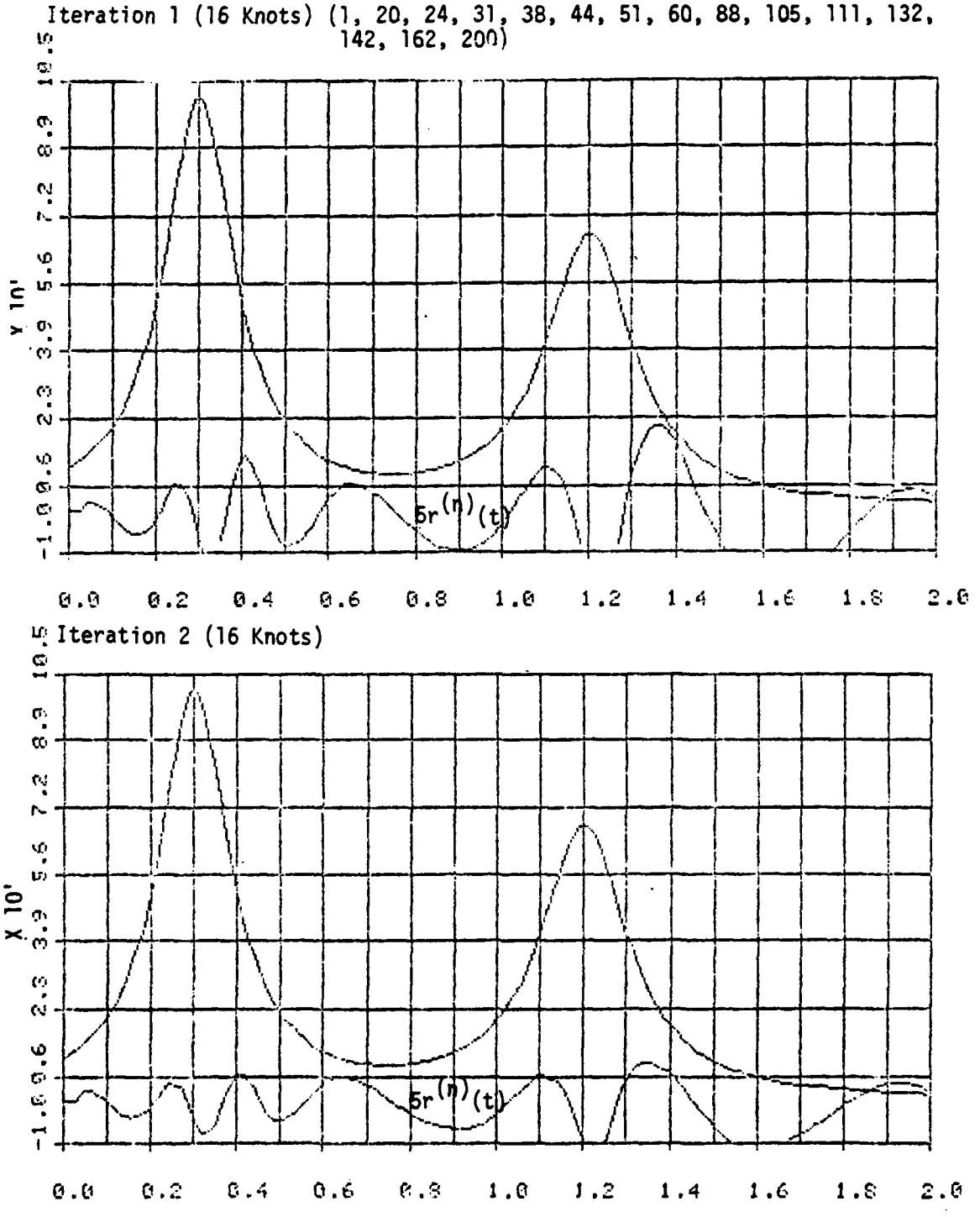
Iteration 1 (16 Knots) (1, 20, 24, 31, 38, 44, 51, 60, 88, 105, 111, 132, 142, 162, 200)
Y 10'
-1.0 0.6 2.3 3.9 5.6 7.2 8.9 10.5
$\delta r^{(n)}(t)$
0.0 0.2 0.4 0.6 0.8 1.0 1.2 1.4 1.6 1.8 2.0
Iteration 2 (16 Knots)
X 10'
-1.6 0.6 2.3 3.9 5.6 7.2 8.9 10.5
$\delta r^{(n)}(t)$
0.0 0.2 0.4 0.6 0.8 1.0 1.2 1.4 1.6 1.8 2.0

FIGURE 2

Iteration 3 (16 Knots) (1, 20, 24, 31, 38, 44, 51, 60, 88, 105, 111, 121, 132, 142, 162, 200)

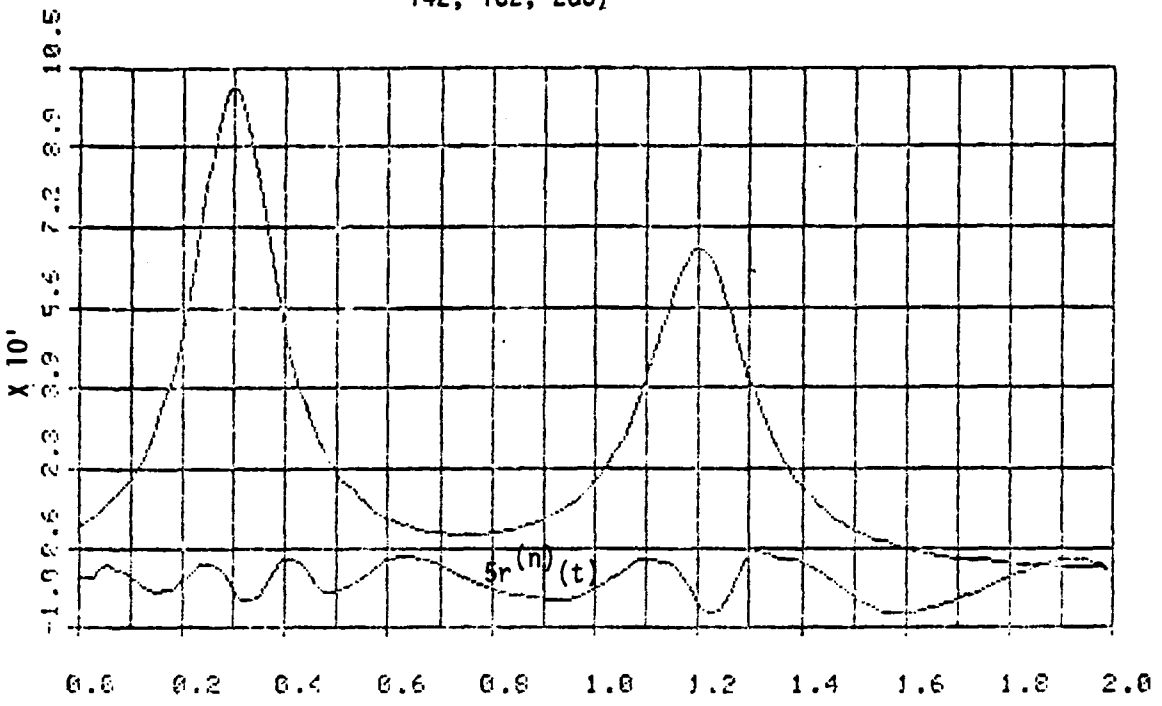

Iteration 4 (16 Knots)

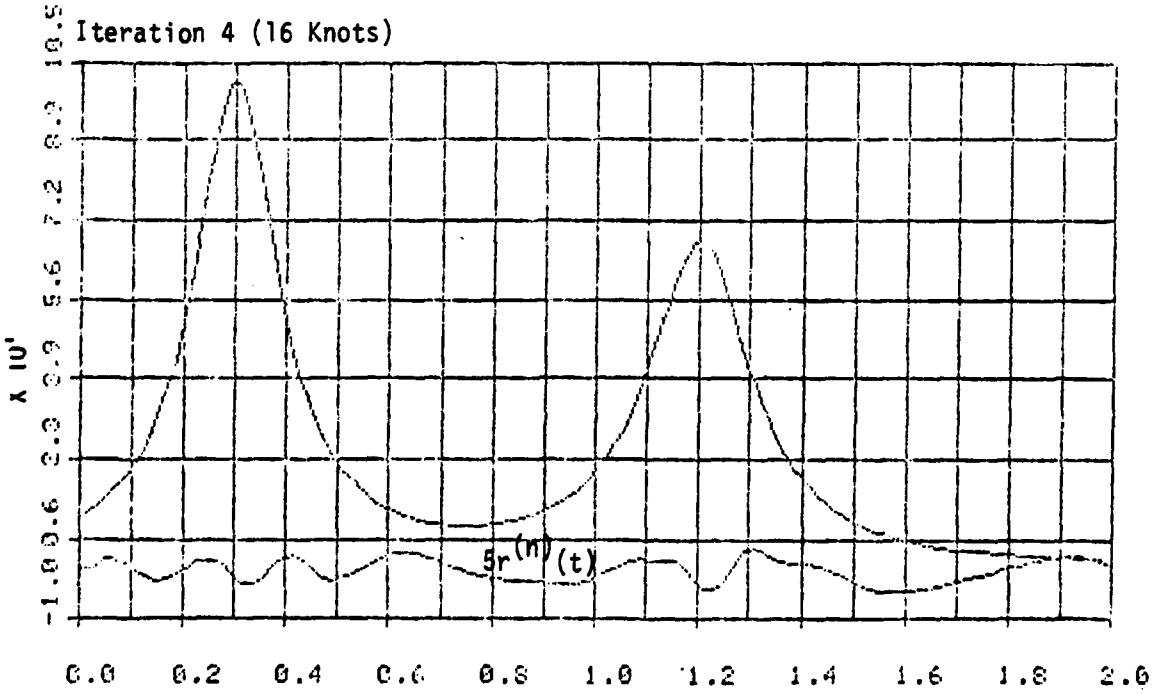

FIGURE 3

Iteration 9 (16 Knots) (1, 20, 24, 31, 38, 44, 51, 60, 88, 105, 111, 121, 132, 142, 162, 200)

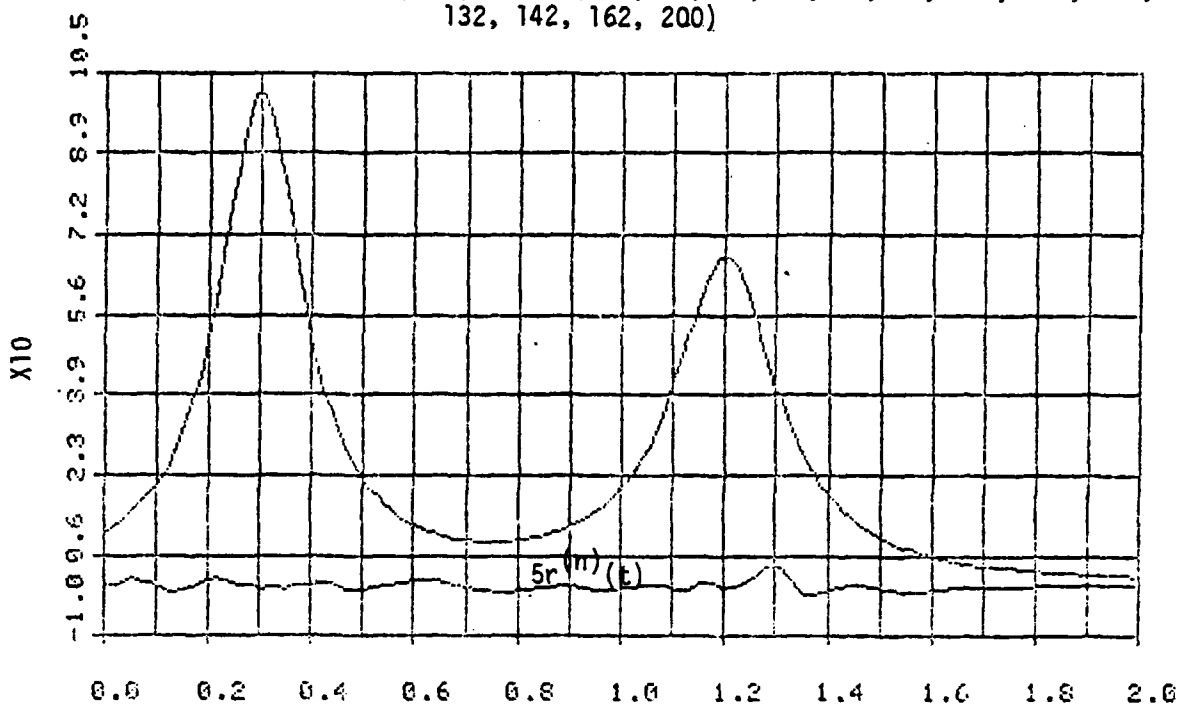

Iteration 10 (16 Knots)

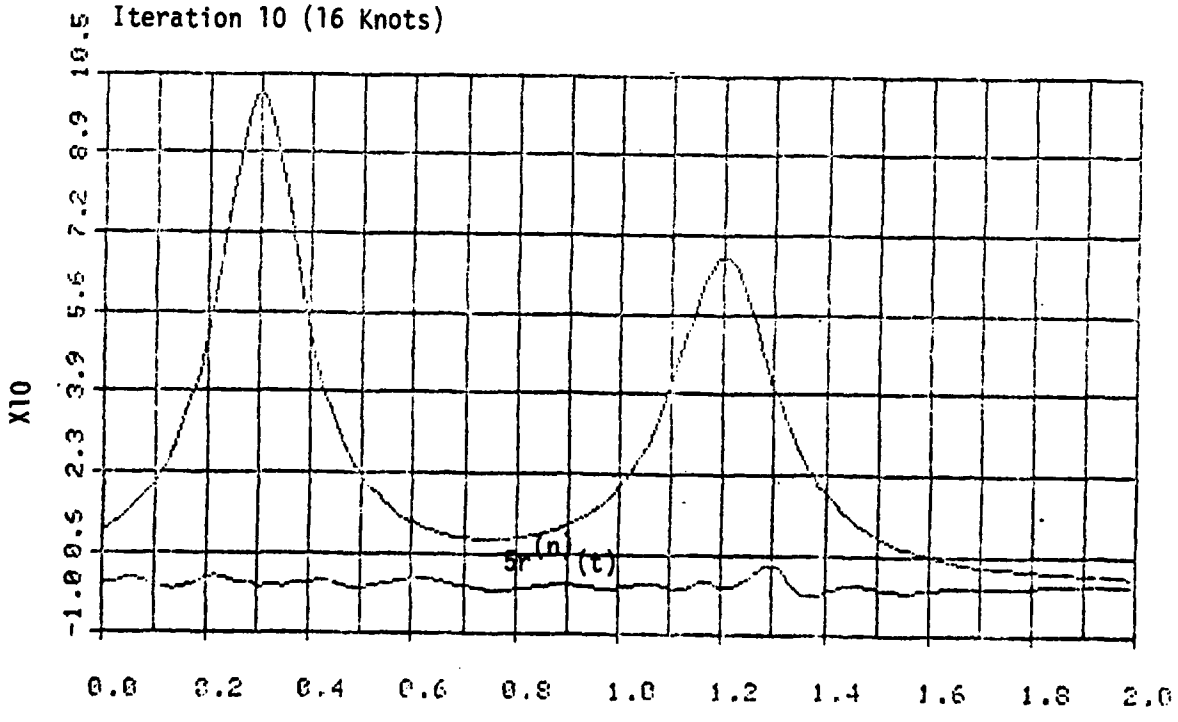

FIGURE 4

16 Knots 1, 20, 24, 31, 38, 44, 51, 60, 88, 105, 111, 132, 142, 162, 200

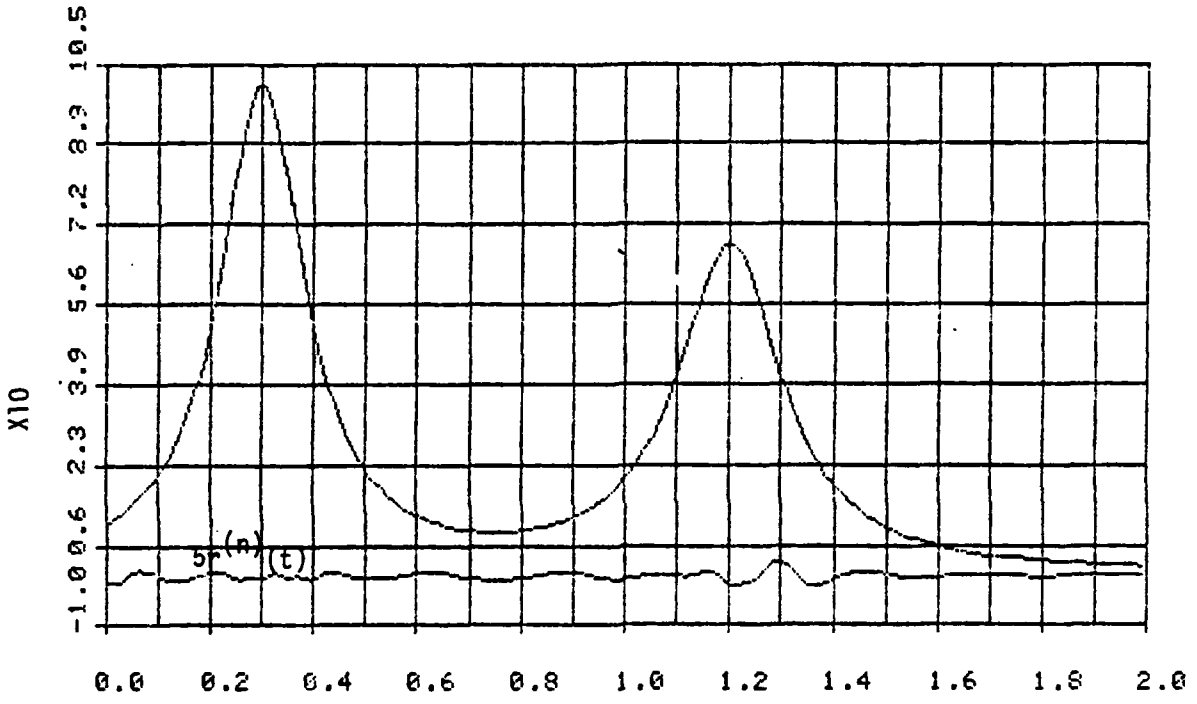

6. KNOT ADDITION TECHNIQUES. When no a priori assumptions are made either about the character of the additive noise which might have corrupted the measurements or about the dynamic character of the measurements themselves, it will not be possible to make a good a priori choice of the knot positions. Thus, the choice of the knots will have to be data dependent. At least two distinct ways of making the knots data dependent have been proposed in the literature. One method is to make a pass through the entire data set to examine the dynamic character of the data and place the knots at the points where the largest excursions from a baseline occurs. Such a technique is proposed by Soames [2]. Another distinctly different method is to initially select a rather arbitrary and small set of knots. Using this knot set, a spline curve is fit to the data and the residuals from the fit are examined for trends. If a trend is identified in any knot interval, a new knot is added in this interval (subject to the condition that there be some specified minimum number of data points in each of the new knot intervals). This process of spline fitting, examining the residuals for trends and adding knots is continued until there are no identifiable trends in the residuals or there are too few points in a knot interval. This type of procedure was proposed by Powell [3]. Only the latter type of procedure is considered here. We have tried several different techniques for identifying trends in the residuals to the spline fit.

Let $r(t_i)$, $i = 1, M$ be the residuals in the spline fit for any knot interval. The test for trends proposed by Powell is to compute a serial correlation coefficient for the residuals.

$$S = \frac{\sum_{i=1}^{M} (r(t_i)-\bar{r})(r(t_{i+1})-\bar{r})}{\sum_{i=1}^{M} (r(t_i)-\bar{r})^2} \tag{11}$$

where

$$\bar{r} = \frac{1}{M} \sum_{i=1}^{M} r(t_i) \tag{12}$$

If $s_1 \leq S \leq s_2$, no new knot is added in this knot interval. If either $S < s_1$ or $S > s_2$, a new knot is placed at the center of the knot interval, subject to having a specified minimum number of points in each of the resulting knot intervals. The specific values of s_1 and s_2 to be used depend on the sample size M. For a table of s_1 and s_2 versus M, see Ezekiel and Fox [4]. The values of s_1 and s_2 are in the neighborhood of $s_1 = -.4$ and $s_2 = .33$.

A second possible test for identifying trends in the residual is to use the Von Neuman ratio, V, which is the ratio of the mean square successive difference to the variance.

$$V = \frac{\sum_{i=1}^{M} (r(t_{i+1})-r(t_i))^2}{\sum_{i=1}^{M} (r(t_i)-\bar{r})^2} \tag{13}$$

If $v_1 \leq V \leq v_2$, no new knot is added in the interval. If either $V < v_1$ or $V > v_2$ a new knot is placed at the center of the interval. Values for v_1 and v_2 are dependent upon M. Tables of v_1 and v_2 are given in Ezekiel and Fox. Common values for v_1 and v_2 are in the neighborhood of $v_1 = 1.37$ and $v_2 = 2.85$.

A third method for identifying trends in a knot interval is to use a local estimate of the signal to noise ratio of the residuals. Let d_{i+3}, $i = 1, M-3$ be the third differences of the residuals.

$$d_{i+3} = r(t_{i+3}) - 3r(t_{i+2}) + 3r(t_{i+1}) - r(t_i) \tag{14}$$

We examine the ratio,

$$S_x^2/S_n^2 = \frac{\frac{1}{M-1}\sum_{i=1}^{M} (r(t_i)-\bar{r})^2}{\frac{1}{20(M-4)}\sum_{i=1}^{M-3} (d_{i+3}-\bar{d})^2}, \tag{15}$$

where

$$\bar{d} = \frac{1}{M-3}\sum_{i=1}^{M-3} d_{i+3} \tag{16}$$

If $S_x^2/S_n^2 < R_0$, it is concluded that there is no trend in the interval. Otherwise, a knot is added at the center of the knot interval subject to the restriction that there be a minimum number of points in each of the resulting knot intervals.

7. APPLICATION OF KNOT ADDITION. In order to illustrate the application of Iterated Schoenberg approximation in conjunction with a knot addition scheme, we again use the double hump function used in the previous examples. For this application, we add random Gaussian noise having mean zero and unit variance to the sampled values of the double hump function. Since ITSH uses sample values or interpolated sample values as coefficients in the approximation, the noisy sample values are locally smoothed in this application prior to use in the approximation. For the following example the smoothed values are obtained by taking the median of an odd number samples centered at each sample data point. We also use the signal to noise ratio criterion as a means of detecting in the residuals for this example.

The initial approximation to the noisy double hump function is computed using the five knot positions, T_i = 0, .31, .59, 1.21, 1.99. Figures 5 and 6 plot the double hump function, $y(t)$, and $5r^{(n)}(t)$, where $r^n(t)$ is the residual after the nth cycle of ITSH, for n = 1, 4. Figure 7 plots $y(t)$ and $5r^{(n)}(t)$ for n = 9, 10. In each of these plots, the residuals have obvious trends which indicates that the five knots used are totally inadequate for approximating $y(t)$. The signal to noise ratio trend detector determines that a trend exists in each of the four knot intervals so that an additional knot is positioned at the center of each of the original knot intervals, making a total of nine knots.

FIGURE 5

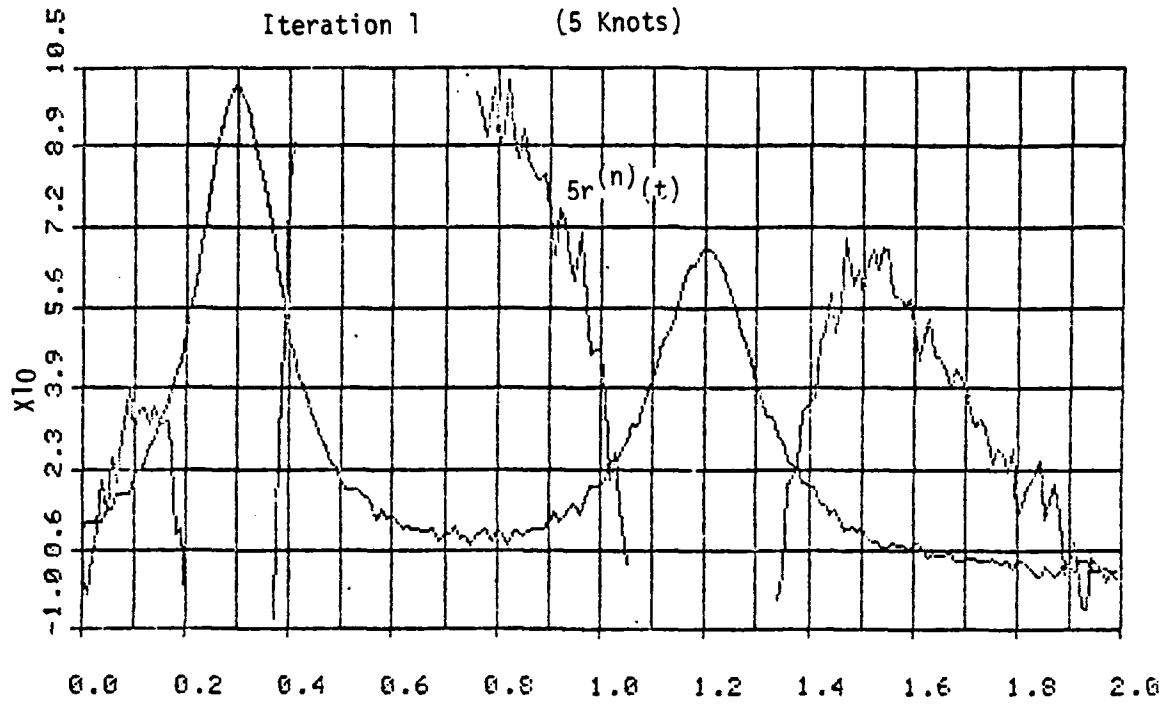
Iteration 1
(5 Knots)
X10
10.5
8.9
7.2
5.6
3.9
2.3
0.6
-1.0
$5r^{(n)}(t)$
0.0
0.2
0.4
0.6
0.8
1.0
1.2
1.4
1.6
1.8
2.0

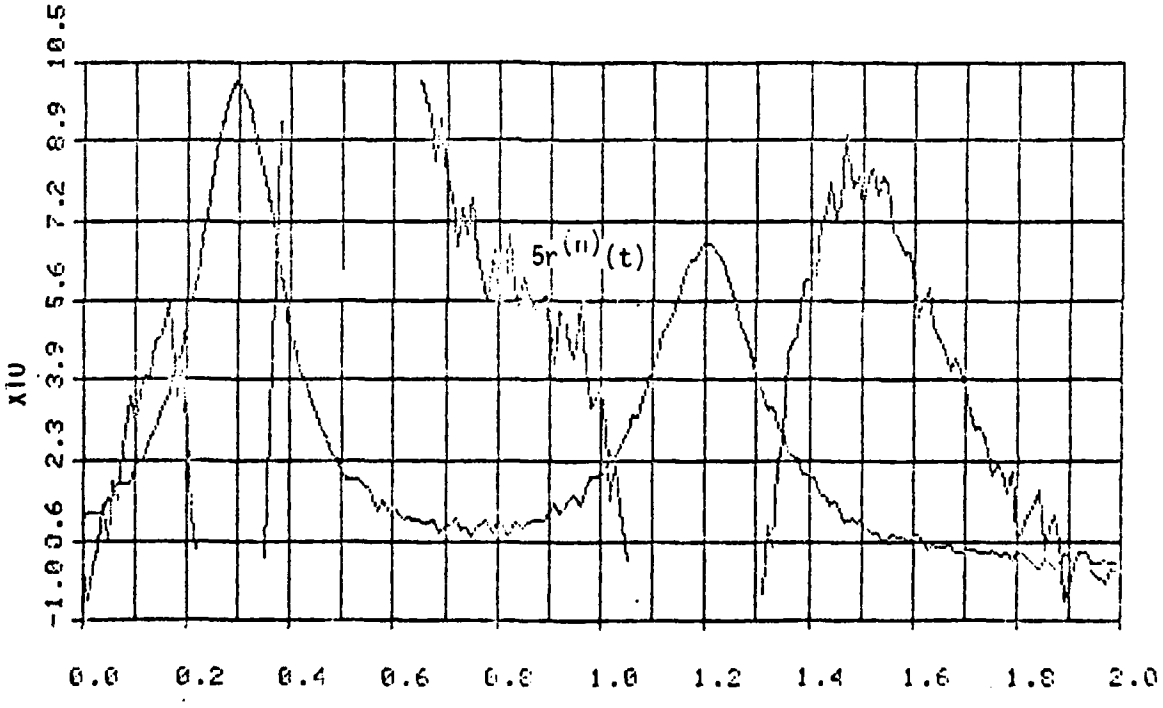
X10
10.5
8.9
7.2
5.6
3.9
2.3
0.6
-1.0
$5r^{(n)}(t)$
0.0
0.2
0.4
0.6
0.8
1.0
1.2
1.4
1.6
1.8
2.0

AD-A089 089 ARMY MATHEMATICS STEERING COMMITTEE F/G 9/2
PROCEEDINGS OF THE 1980 ARMY NUMERICAL ANALYSIS AND COMPUTERS C--ETC(U)
AUG 80

UNCLASSIFIED ARO-80-3 NL

3 of 6
AD A089089

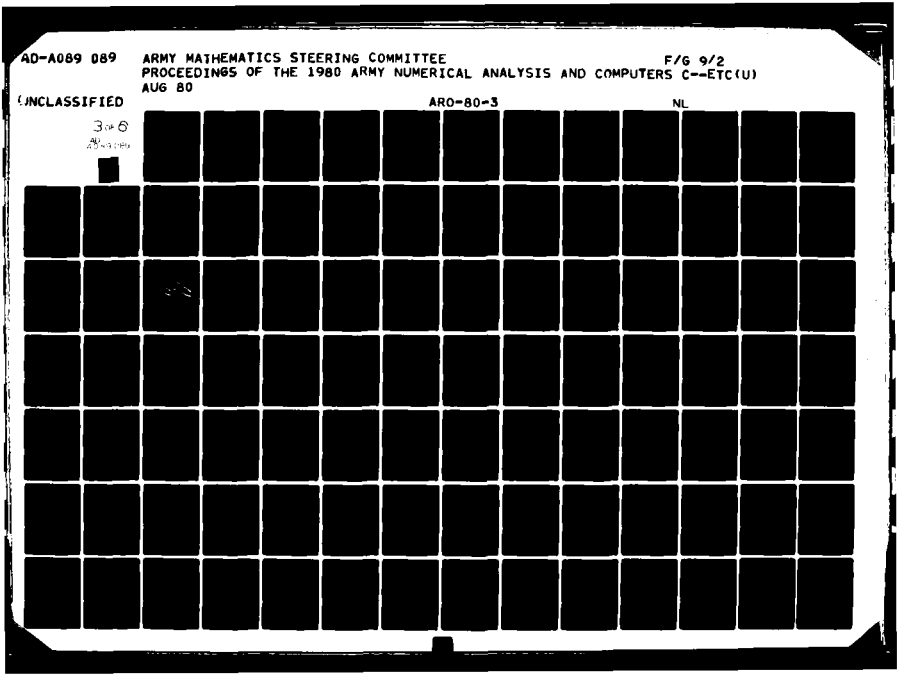

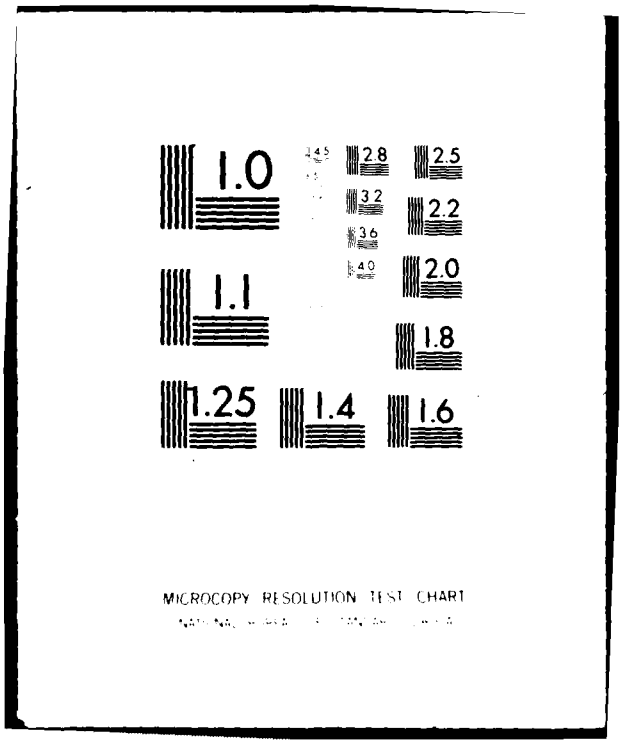
1.0
2.8
2.5
3.2
2.2
3.6
4.0
2.0
1.1
1.8
1.25
1.4
1.6
MICROCOPY RESOLUTION TEST CHART

FIGURE 6

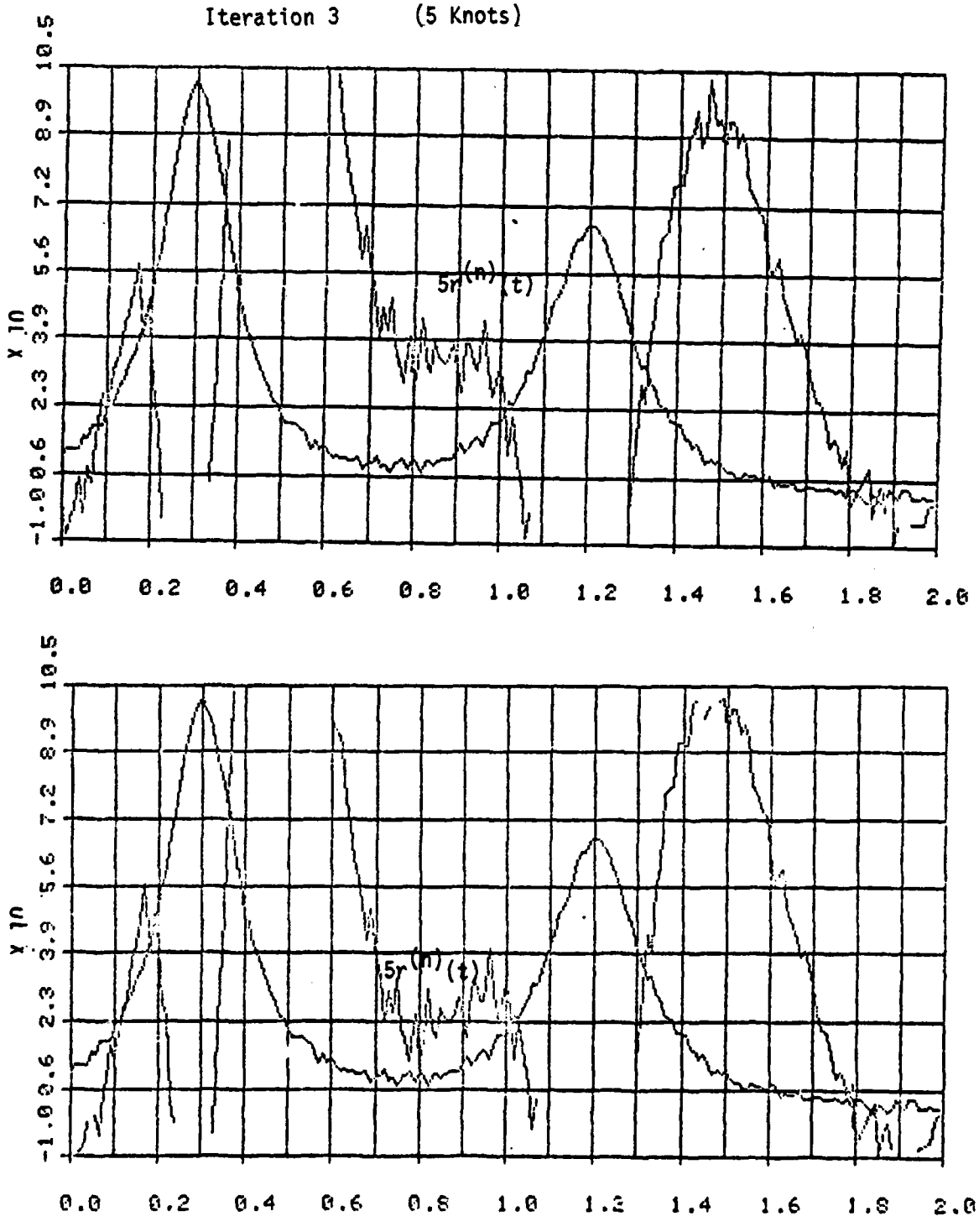
Iteration 3 (5 Knots)
X 10
10.5
8.9
7.2
5.6
3.9
2.3
0.6
-1.0
$5r^{(n)}(t)$
0.0
0.2
0.4
0.6
0.8
1.0
1.2
1.4
1.6
1.8
2.0

FIGURE 7

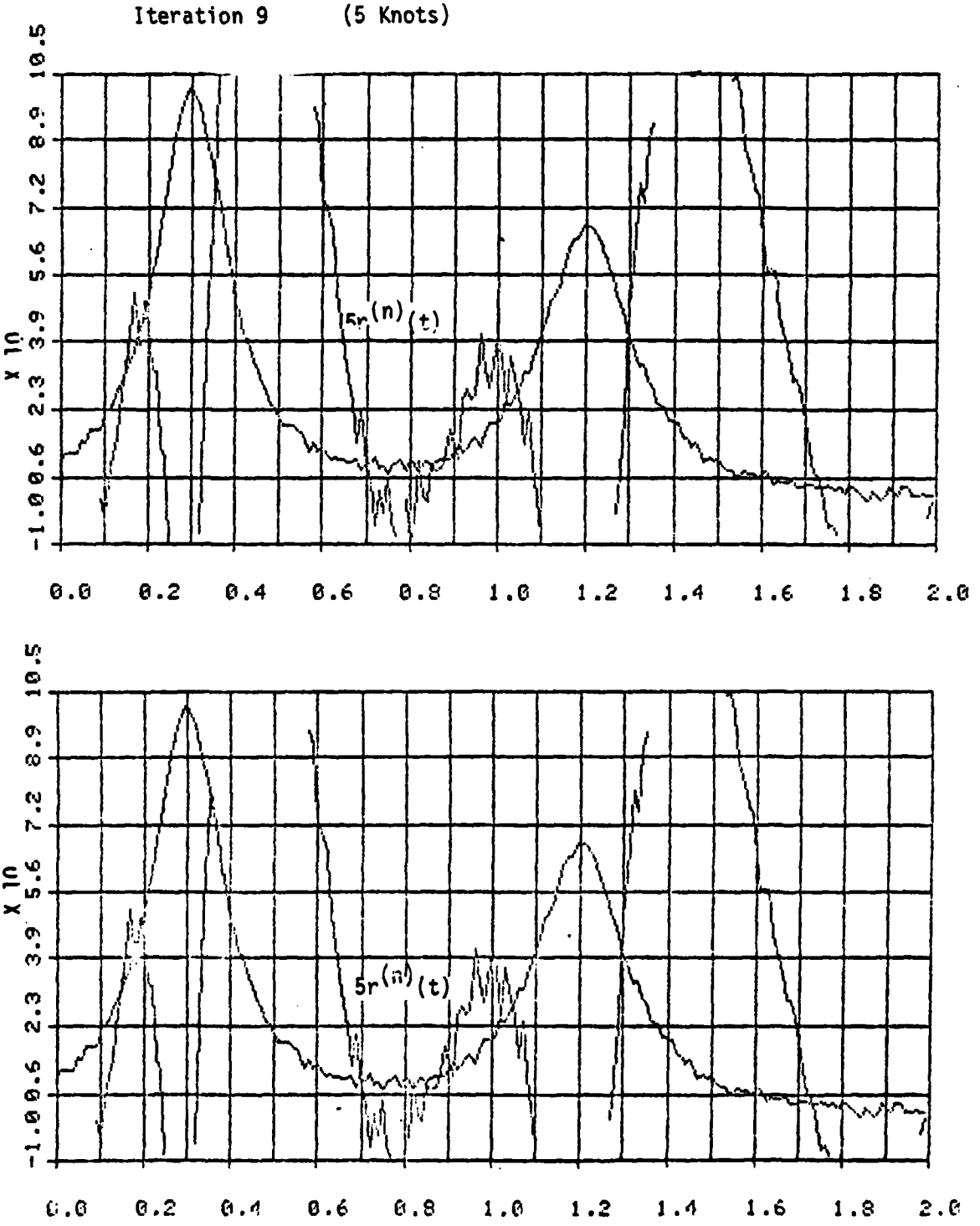
Iteration 9 (5 Knots)
X 10
10.5
8.9
7.2
5.6
3.9
2.3
0.6
-1.0
$5r^{(n)}(t)$
0.0
0.2
0.4
0.6
0.8
1.0
1.2
1.4
1.6
1.8
2.0

Figures 8 and 9 plot y(t) and $5r^{(n)}(t)$, n = 1, 4 from the ITSH approximation using nine knots, T_i = 0, .16, .31, .46, .59, .91, 1.21, 1.61, 1.99. Figure 10 shows y(t) and $5r^{n}(t)$ for n = 10. These plots again indicate that the nine knots used are inadequate and the signal to noise ratio criterion dictates that additional knots should be placed in five of the knot intervals. The ITSH approximation is reapplied using the fourteen knots, T_i = 0, .16, .24, .31, .39, .46, .59, .91, 1.07, 1.21, 1.42, 1.61, 1.81, 1.99. Figures 11 and 12 plot the function and residual for the first four iterations of ITSH using fourteen knots. From these residual plots one can see that the fit to the noisy double hump function has improved considerably and the residuals appear to be more random than before. In fact, the trend detection scheme add only two knots, a T = 1.15 and T = 1.32 making a total of sixteen knots. Figures 13, 14 and 15 plot $5r^{(n)}(t)$ for n = 1, 4 and n = 9, 10. The residuals appear to be rather random. This observation is confirmed by the failure of the signal to noise ratio criterion to detect a trend in all but one of the knot intervals. A trend was detected in the interval [.24, .31] but addition of a knot in this interval was prohibited by the requirement that there be at least seven data points in any knot interval.

FIGURE 8

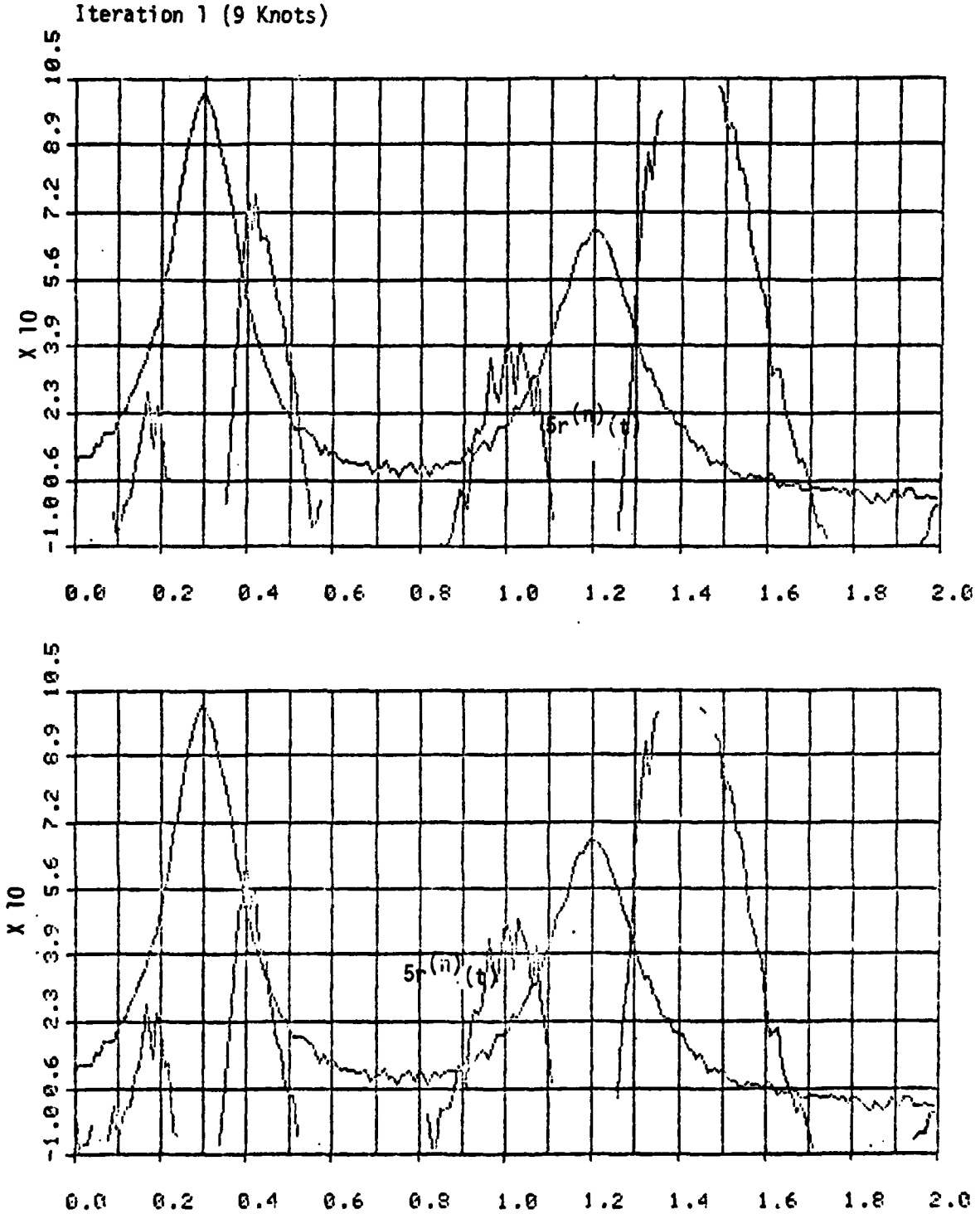
Iteration 1 (9 Knots)
X 10
10.5
8.9
7.2
5.6
3.9
2.3
0.6
-1.0
$\delta r^{(n)}(t)$
0.0
0.2
0.4
0.6
0.8
1.0
1.2
1.4
1.6
1.8
2.0

FIGURE 9

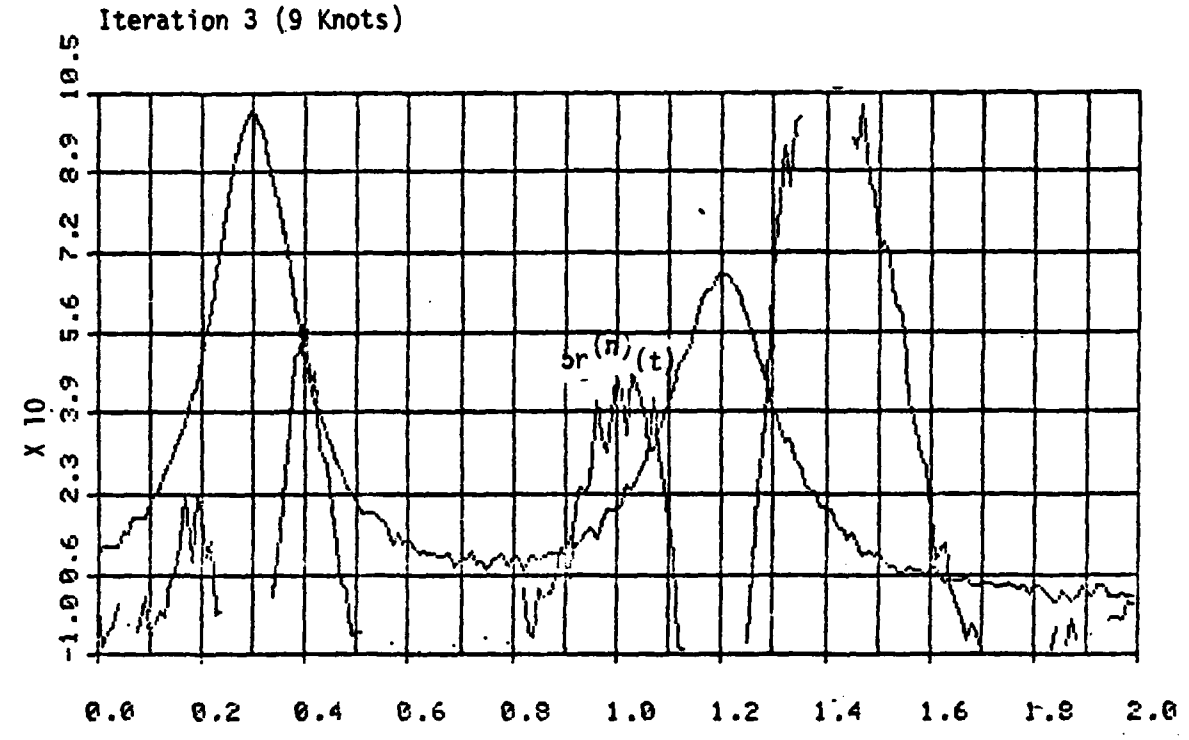
Iteration 3 (9 Knots)
X 10
10.5
8.9
7.2
5.6
3.9
2.3
0.6
-1.0
$\delta r^{(n)}(t)$
0.0
0.2
0.4
0.6
0.8
1.0
1.2
1.4
1.6
1.8
2.0

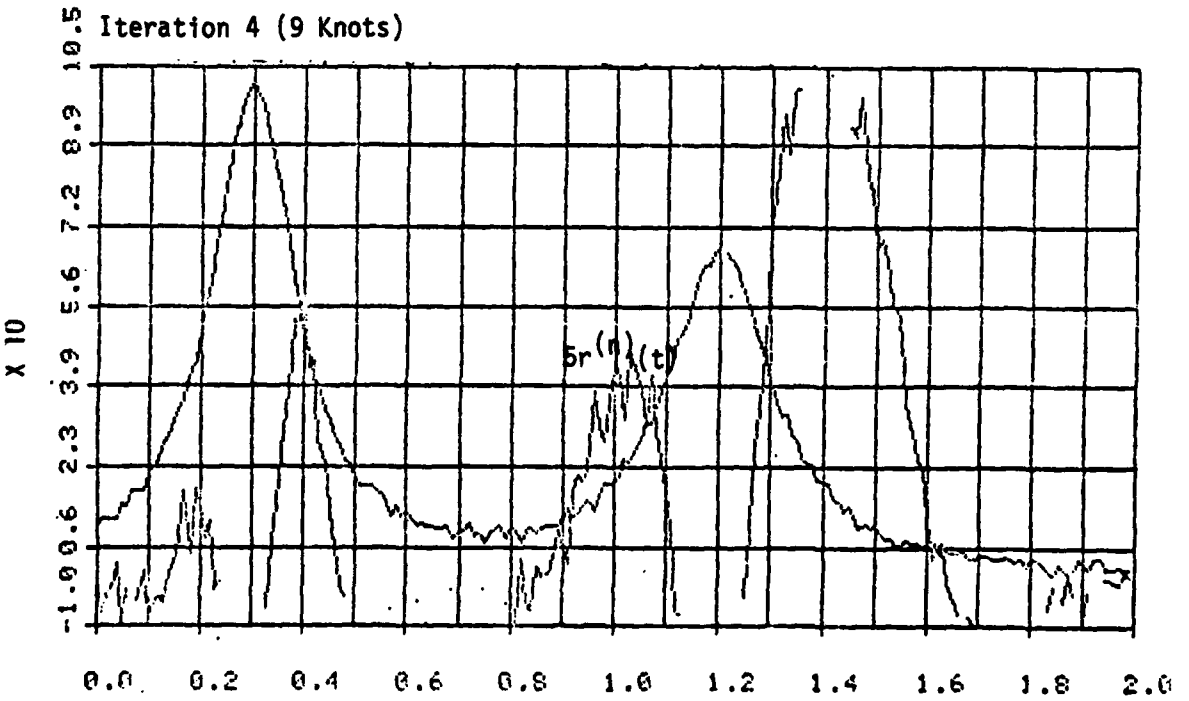
Iteration 4 (9 Knots)
X 10
10.5
8.9
7.2
5.6
3.9
2.3
0.6
-1.0
$\delta r^{(n)}(t)$
0.0
0.2
0.4
0.6
0.8
1.0
1.2
1.4
1.6
1.8
2.0

FIGURE 10

Iteration 10 (9 Knots)

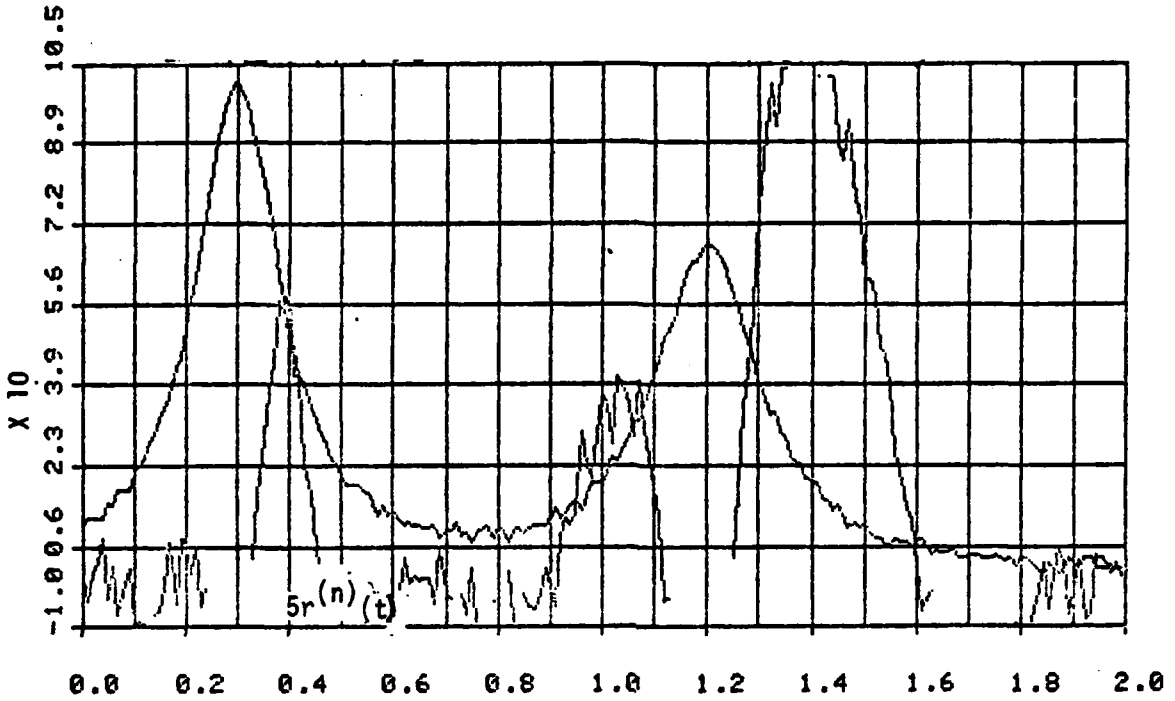

FIGURE 11

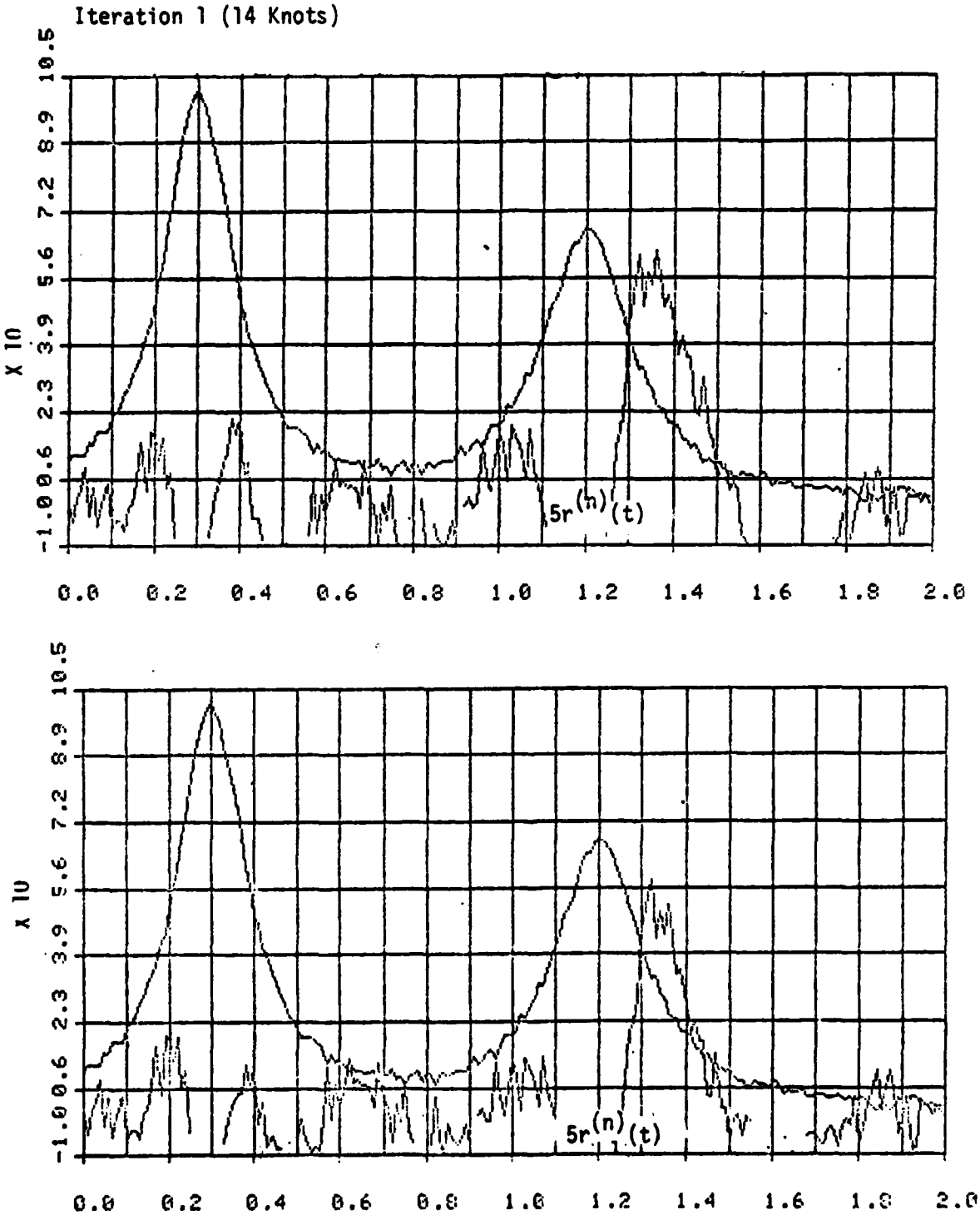
Iteration 1 (14 Knots)
X 10
10.5
8.9
7.2
5.6
3.9
2.3
0.6
-1.0
$5r^{(n)}(t)$
0.0
0.2
0.4
0.6
0.8
1.0
1.2
1.4
1.6
1.8
2.0
X 10
10.5
8.9
7.2
5.6
3.9
2.3
0.6
-1.0
$5r^{(n)}(t)$
0.0
0.2
0.4
0.6
0.8
1.0
1.2
1.4
1.6
1.8
2.0

FIGURE 12

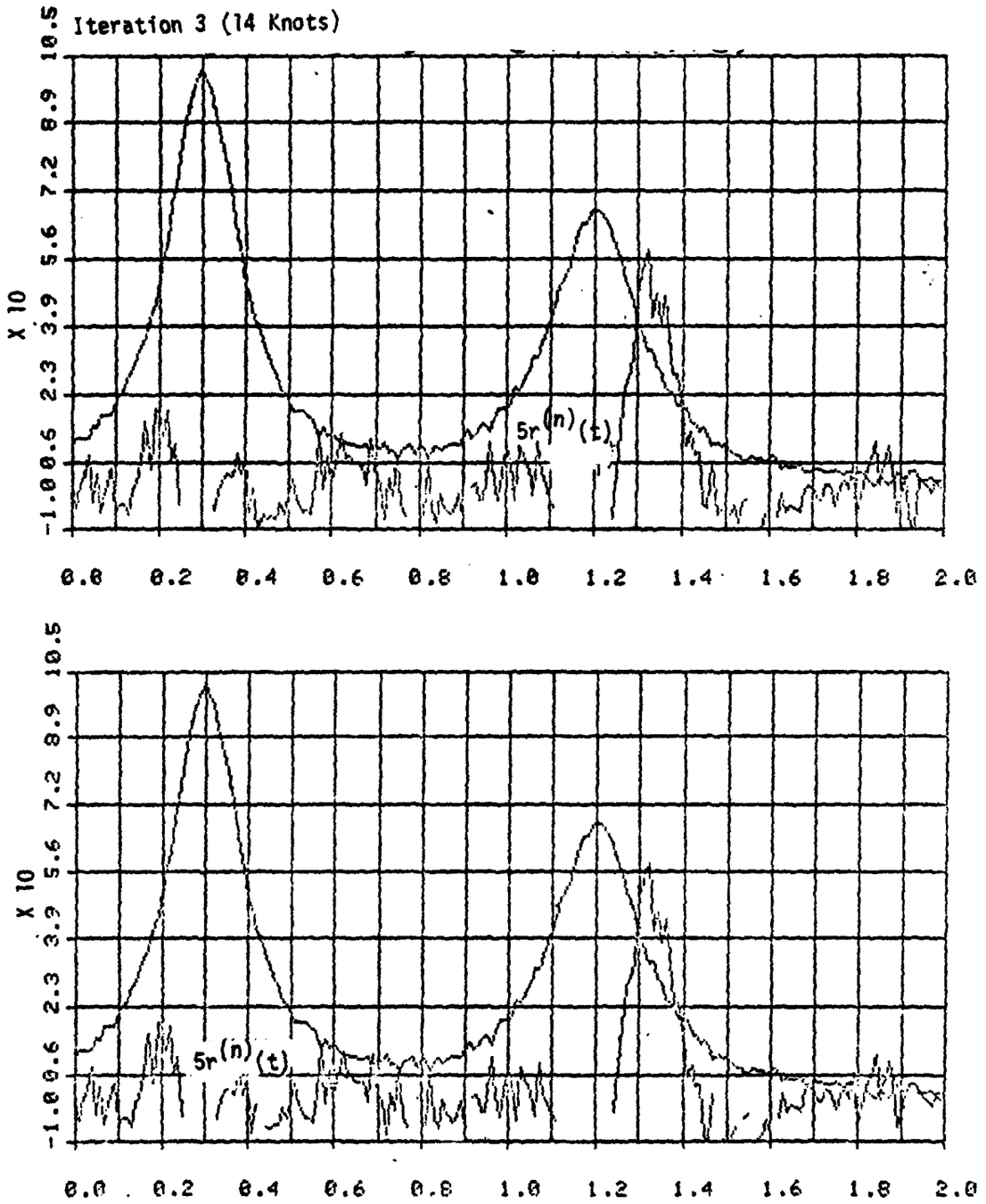
Iteration 3 (14 Knots)
X 10
10.5
8.9
7.2
5.6
3.9
2.3
0.6
-1.0
$5r^{(n)}(t)$
0.0
0.2
0.4
0.6
0.8
1.0
1.2
1.4
1.6
1.8
2.0

FIGURE 13

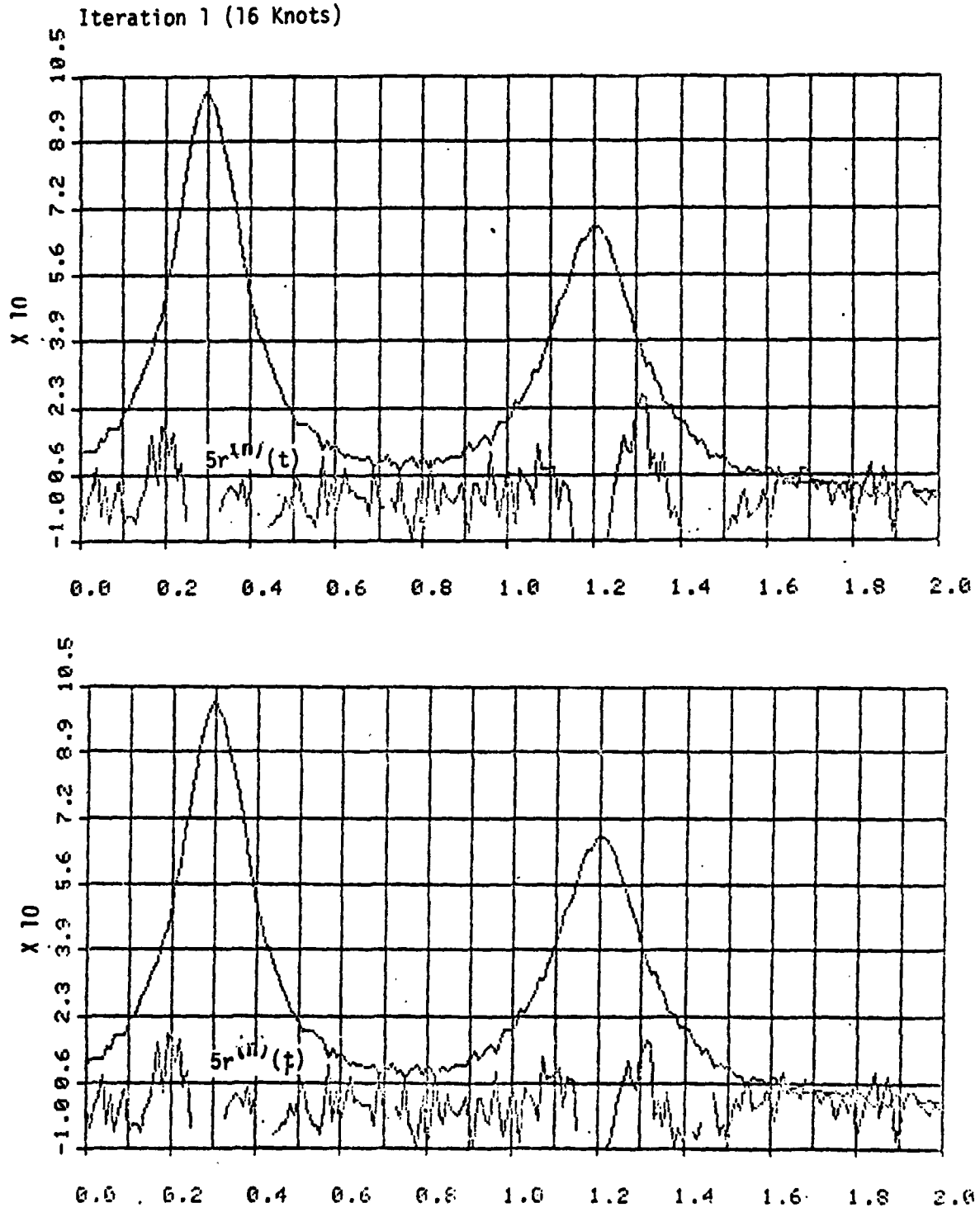
Iteration 1 (16 Knots)
X 10
10.5
8.9
7.2
5.6
3.9
2.3
0.6
-1.0
$5r^{(n)}(t)$
0.0
0.2
0.4
0.6
0.8
1.0
1.2
1.4
1.6
1.8
2.0
X 10
10.5
8.9
7.2
5.6
3.9
2.3
0.6
-1.0
$5r^{(n)}(t)$
0.0
0.2
0.4
0.6
0.8
1.0
1.2
1.4
1.6
1.8
2.0

FIGURE 14

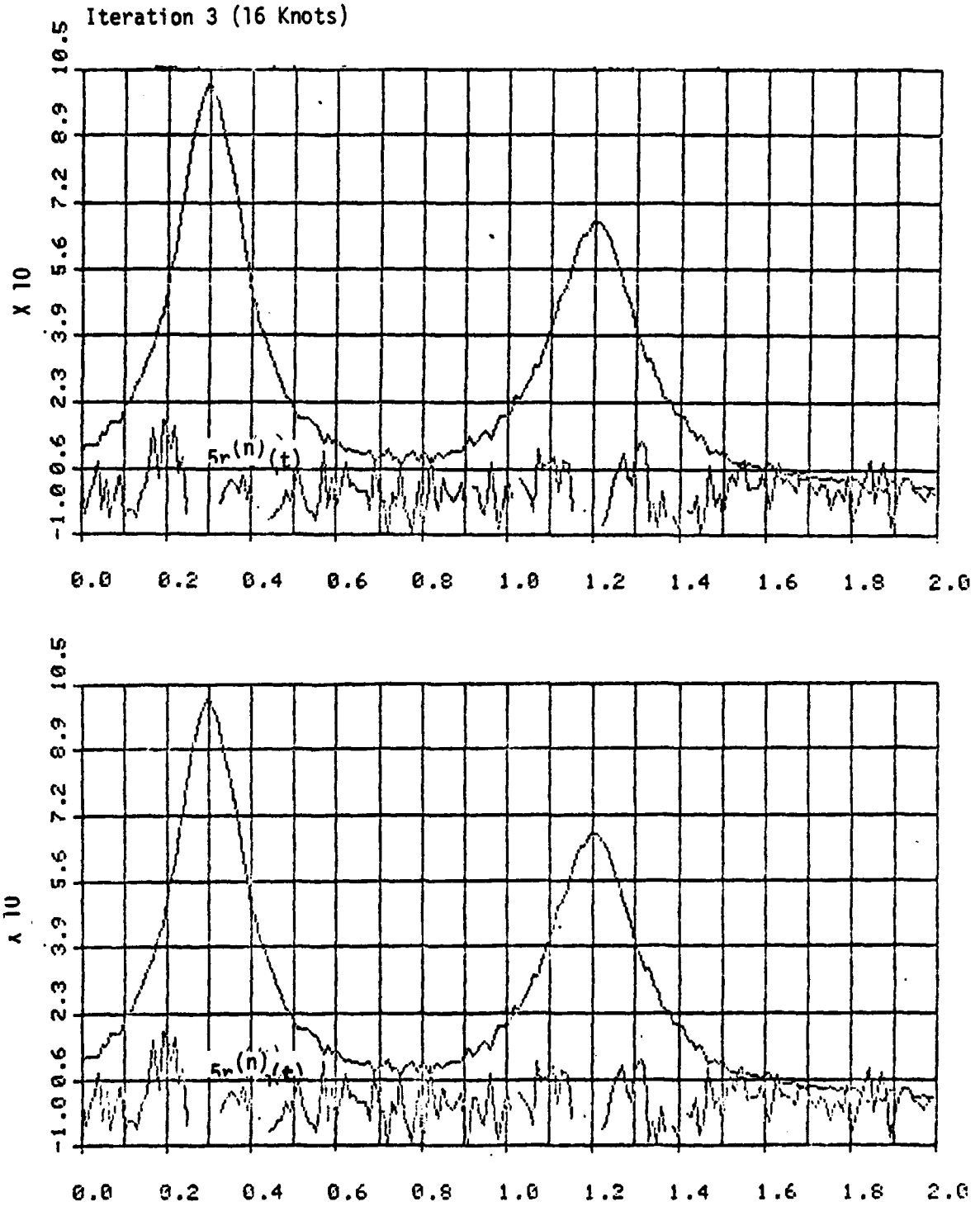
Iteration 3 (16 Knots)
X 10
10.5
8.9
7.2
5.6
3.9
2.3
0.6
-1.0
$s_r(n)(t)$
0.0
0.2
0.4
0.6
0.8
1.0
1.2
1.4
1.6
1.8
2.0

FIGURE 15

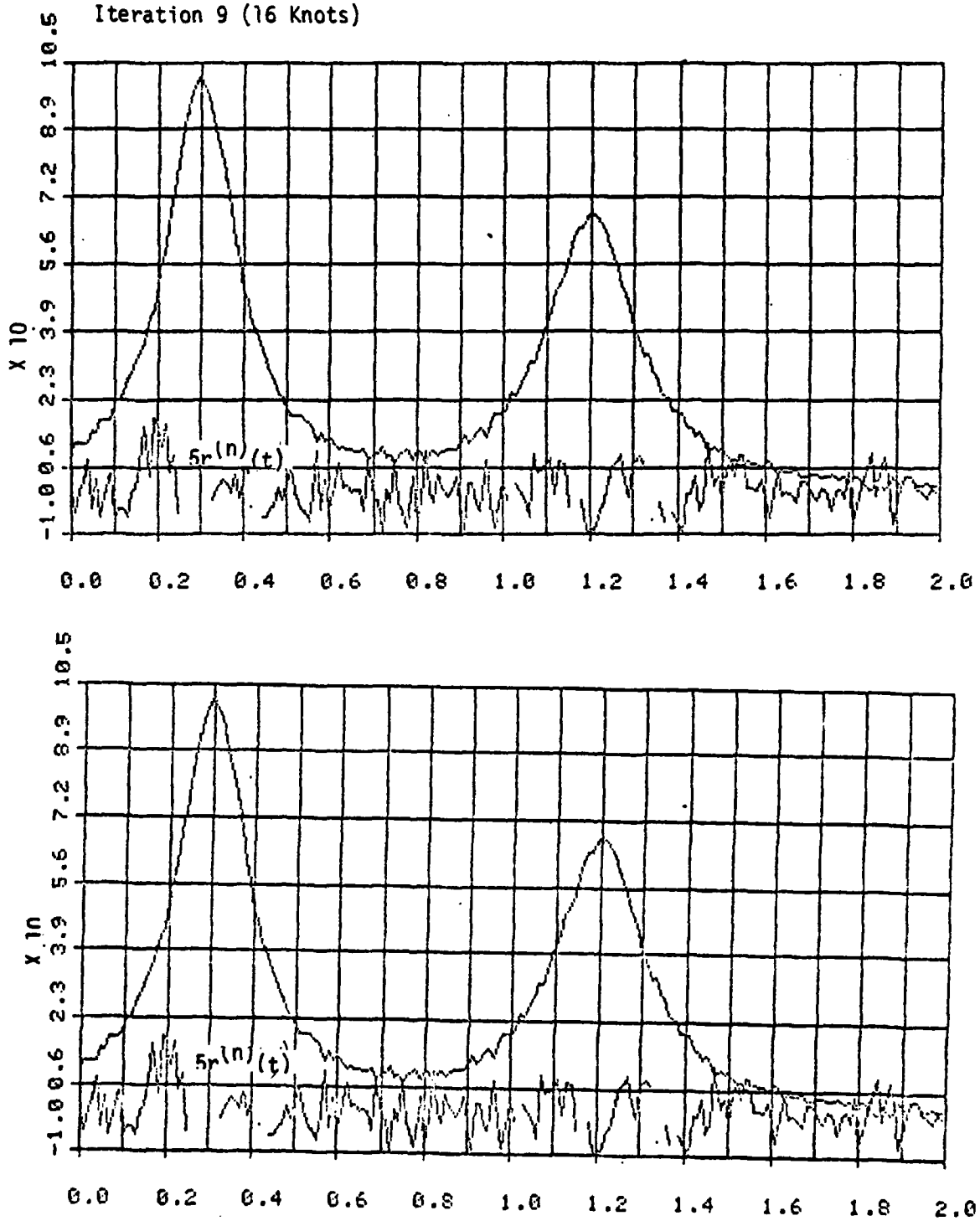
Iteration 9 (16 Knots)
X 10
10.5
8.9
7.2
5.6
3.9
2.3
0.6
-1.0
$5r^{(n)}(t)$
0.0
0.2
0.4
0.6
0.8
1.0
1.2
1.4
1.6
1.8
2.0
X 1n
$5r^{(n)}(t)$

REFERENCES

1. de Boor, C, (1979), "How Does Agee's Smoothing Method Work?", Proceedings of the 1979 Army Numerical Analysis and Computers Conference.

2. Soames, R, (1976), "VP-Splines, An Extension of Twice Differentiable Interpolation", Proceedings of the 1976 Army Numerical Analysis and Computers Conference.

3. Powell, M., (1970), "Curve Fitting by Splines in One Variable, Numerical Approximation to Functions and Data", J. G. Hayes, Ed., Athlone Press.

4. Ezekiel, M., and Fox, K., (1959), "Methods of Correlation and Regression Analysis", John Wiley, New York.

AN IMPLICIT ALGORITHM FOR SOLVING THE TRANSONIC, CONSERVATIVE FULL-POTENTIAL EQUATION

Terry L. Holst
Applied Computational Aerodynamics Branch
Ames Research Center, NASA, Moffett Field, California 94035

ABSTRACT. A fast, fully implicit approximate factorization algorithm (AF2), designed to solve the conservative transonic full-potential equation in either two or three dimensions, is described. The algorithm uses an upwind bias of the density coefficient for stability in supersonic regions. This provides an effective upwind difference of the streamwise terms for any orientation of the velocity vector (i.e., "rotated differencing"), and thereby greatly enhances the reliability of the algorithm. Computed results for both airfoils and simplified wings demonstrate substantial improvement in convergence speed for the new algorithm relative to standard successive-line overrelaxation algorithms. In addition, results from a simplified vector computer efficiency analysis indicate that this AF2 algorithm is suitable for use on vector computers.

1. INTRODUCTION. An implicit approximate factorization algorithm (AF2) for solving the low-frequency (unsteady) transonic small-disturbance equation in two and three dimensions was introduced in reference 1. This algorithm has been subsequently applied as a relaxation algorithm for solving the steady transonic small-disturbance potential equation in two-space dimensions (ref. 2) and the conservative full-potential equation in both two-space dimensions (refs. 3-5) and three space dimensions (ref. 6). For all steady formulations, significant improvement in convergence speed for AF2 has been obtained relative to the conventional transonic relaxation procedure, successive-line overrelaxation (SLOR).

Several general guidelines for the construction of implicit approximate factorization (AF) schemes can be formulated by considering the two-level iteration procedure

$$NC^n + \omega L\phi^n = 0 \tag{1}$$

where C^n is the correction $(\phi^{n+1} - \phi^n)$; $L\phi^n$ is the residual, which is a measure of how well the finite-difference equation is satisfied by the nth level velocity-potential solution (ϕ^n); and ω is a relaxation parameter. The iteration scheme given by equation (1) can be considered as an iteration in pseudo time where the n superscript indicates the time-step level of the solution, that is, $(\ )^{n+1} - (\ )^n \sim \Delta t(\ )_t$. The operator N determines the type of iterative procedure, and therefore determines the rate at which the solution procedure converges. Classical successive overrelaxation schemes (SOR) or SLOR schemes effectively use only a portion of the L operator in forming the N operator. As a consequence, the iteration scheme is relatively simple, but the convergence rate may be very slow. In the present AF approach,

the philosophy is to choose a representation for N that closely approximates L. This, in theory, will produce a scheme with good convergence characteristics. The procedure for obtaining N consists of two steps: (1) linearize L and (2) factor the linearized result. There are usually two factors for two-dimensional algorithms and three factors for three-dimensional algorithms. The resulting scheme retains the simplicity of having to perform only narrow-banded scalar matrix inversions (for the present case, bidiagonal and tridiagonal). The effects of both the error terms resulting from the factorization and the linearization are removed from the solution simultaneously by means of the iteration scheme. Because each grid point is influenced by every other grid point during each iteration, much faster convergence can be obtained.

Stability in the present full-potential formulation for supersonic regions of flow has been achieved by adding an artificial viscosity term similar to that introduced in reference 7. However, in the present formulation, addition of the artificial viscosity term is achieved by using an upwind bias of the density coefficient. This strategy greatly simplifies the solution procedure and effectively allows the simple two- and three-banded matrix form of the AF scheme to be retained over the entire flow field, even in regions of supersonic flow. Other studies (refs. 8-11) have used similar steady-state differencing procedures in a wide variety of problems to further substantiate this differencing procedure as being both reliable and flexible.

Although fully implicit algorithms such as AF2 offer potentially large benefits in terms of fast convergence, the final computational efficiency levels may be radically affected by the newer vector computer architectures. These new vector computers generally feature either parallel (Illiac IV) or pipeline (CDC STAR) hardwares and very efficiently manage vectorizable algorithms, but in some cases very inefficiently manage algorithms that do not vectorize. Therefore, a simple analysis based on vector length categorization of floating point operation counts is used to estimate the efficiencies of several full-potential algorithms on a model pipeline vector computer. The full-potential algorithms studied are all three dimensional and include explicit, semi-implicit (SLOR) and fully implicit (AF2) algorithms. The results indicate that a high degree of vectorization is possible for the present AF2 algorithm.

2. GOVERNING EQUATIONS. The three-dimensional full-potential equation written in strong conservation-law form is given by

$$(\rho\phi_x)_x + (\rho\phi_y)_y + (\rho\phi_z)_z = 0 \tag{2a}$$

$$\rho = \left[1 - \frac{\gamma - 1}{\gamma + 1}\left(\phi_x^2 + \phi_y^2 + \phi_z^2\right)\right]^{1/\gamma-1} \tag{2b}$$

The density (ρ) and velocity components (ϕ_x, ϕ_y, and ϕ_z) are nondimensionalized by the stagnation density (ρ_s) and the critical sound speed (a_*), respectively; x, y, and z are Cartesian coordinates in the streamwise, spanwise, and vertical directions, respectively; and γ is the ratio of specific heats.

The two-dimensional conservation-law form of the full-potential equation is simply obtained by dropping all y-derivative terms from equation (2).

Equation (2) expresses mass conservation for flows that are steady, isentropic, and irrotational. The corresponding shock-jump conditions are valid approximations to the Rankine-Hugoniot relations for many transonic flow applications. A comparison of isentropic and Rankine-Hugoniot shock polars is given in reference 12.

Equation (2) is transformed from the Cartesian coordinate physical domain to the surface-oriented coordinate computational domain by using a general independent variable transformation (see fig. 1). This transformation, indicated by

$$\left.\begin{aligned} \xi &= \xi(x,y,z) \\ \eta &= \eta(x,y,z) \\ \zeta &= \zeta(x,y,z) \end{aligned}\right\} \tag{3}$$

maintains the strong conservation-law form of equation (2) as discussed in references 13-16. The full-potential equation written in the ξ-η-ζ coordinate system is given by

$$\left(\frac{\rho U}{J}\right)_\xi + \left(\frac{\rho V}{J}\right)_\eta + \left(\frac{\rho W}{J}\right)_\zeta = 0 \tag{4a}$$

$$\rho = \left[1 - \frac{\gamma - 1}{\gamma + 1}\left(U\phi_\xi + V\phi_\eta + W\phi_\zeta\right)\right]^{1/\gamma - 1} \tag{4b}$$

where

$$\left.\begin{aligned} U &= A_1\phi_\xi + A_4\phi_\eta + A_5\phi_\zeta \\ V &= A_4\phi_\xi + A_2\phi_\eta + A_6\phi_\zeta \\ W &= A_5\phi_\xi + A_6\phi_\eta + A_3\phi_\zeta \end{aligned}\right\} \tag{5a}$$

$$\left.\begin{aligned} A_1 &= \xi_x^2 + \xi_y^2 + \xi_z^2 \\ A_2 &= \eta_x^2 + \eta_y^2 + \eta_z^2 \\ A_3 &= \zeta_x^2 + \zeta_y^2 + \zeta_z^2 \\ A_4 &= \xi_x\eta_x + \xi_y\eta_y + \xi_z\eta_z \\ A_5 &= \xi_x\zeta_x + \xi_y\zeta_y + \xi_z\zeta_z \\ A_6 &= \eta_x\zeta_x + \eta_y\zeta_y + \eta_z\zeta_z \end{aligned}\right\} \tag{5b}$$

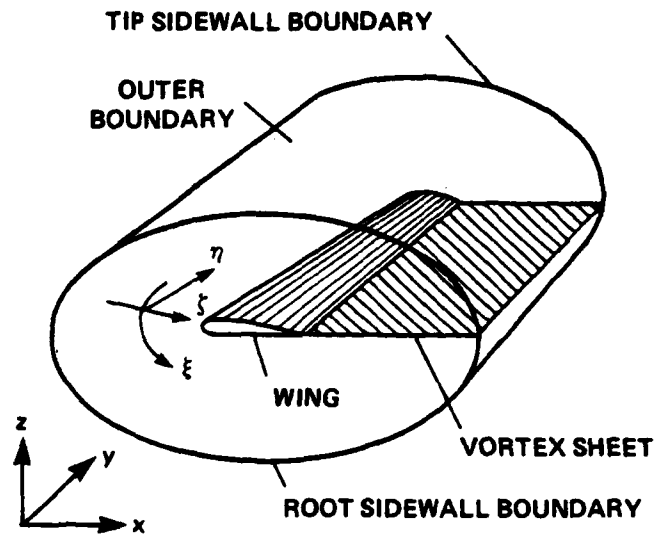

(a) Physical domain.

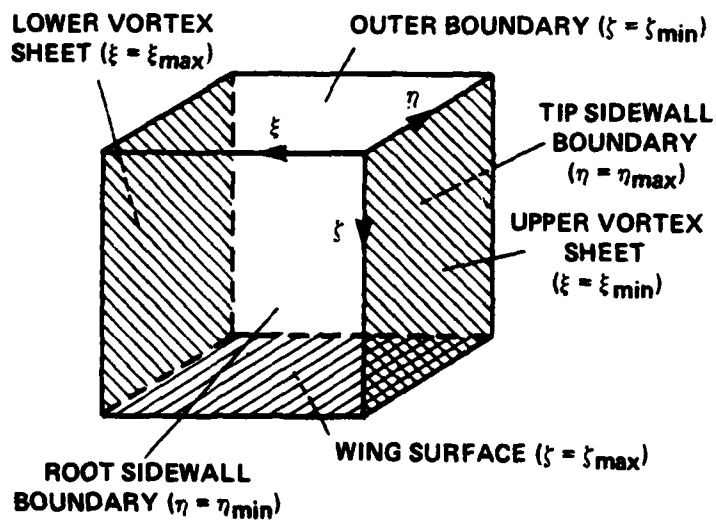

(b) Computational domain.

Figure 1.- Schematic of general $(x,y,z) \leftrightarrow (\xi,\eta,\zeta)$ transformation.

and

$$J = \xi_x\eta_y\zeta_z + \xi_y\eta_z\zeta_x + \xi_z\eta_x\zeta_y - \xi_z\eta_y\zeta_x - \xi_y\eta_x\zeta_z - \xi_x\eta_z\zeta_y \tag{5c}$$

The quantities U, V, and W are contravariant velocity components along the ξ, η, and ζ directions, respectively; A_1 - A_6 depend on the metric relations

$$\left.\begin{aligned}
\xi_x &= J(y_\eta z_\zeta - y_\zeta z_\eta) \\
\xi_y &= J(x_\zeta z_\eta - x_\eta z_\zeta) \\
\xi_z &= J(x_\eta y_\zeta - x_\zeta y_\eta) \\
\eta_x &= J(y_\zeta z_\xi - y_\xi z_\zeta) \\
\eta_y &= J(x_\xi z_\zeta - x_\zeta z_\xi) \\
\eta_z &= J(x_\zeta y_\xi - x_\xi y_\zeta) \\
\zeta_x &= J(y_\xi z_\eta - y_\eta z_\xi) \\
\zeta_y &= J(x_\eta z_\xi - x_\xi z_\eta) \\
\zeta_z &= J(x_\xi y_\eta - x_\eta y_\xi)
\end{aligned}\right\} \tag{6}$$

and J is the Jacobian of the transformation. The two-dimensional form of the full-potential equation, written in the computational domain (ξ-ζ coordinates), is obtained by dropping all y and η terms in equations (4)-(6); that is, all y and η derivatives as well as all derivatives of y and η are set to zero. An exception to this is that y_η and η_y must be set equal to one.

The transformed full-potential equation (eq. (4)) is only slightly more complicated than the original Cartesian form (eq. (2)), provided the quantities A_1-A_6 and J are considered as known constants. Several significant advantages are offered by this very general form. The main advantage is that boundaries associated with the physical domain are transformed to boundaries of the computational domain. This aspect is illustrated in figure 1 where the physical and computational domains for a typical transformation are shown. The computational coordinates, ξ, η, and ζ, are in the wraparound, spanwise, and radial-like directions, respectively. The inner wing boundary transforms to $\zeta = \zeta_{max}$, and the outer physical boundary transforms to $\zeta = \zeta_{min}$. Note that no restrictions have been placed on the shape of the outer boundary. Arbitrarily shaped outer boundaries, including wind-tunnel walls, may be used. The symmetry-plane boundary transforms to $\eta = \eta_{min}$, and the wing-tip boundary transforms to $\eta = \eta_{max}$. The last two sides of the computational domain are formed from the upper and lower cuts along the vortex sheet. Additional discussion regarding the general transformation used in the present study is given in reference 6.

3. GRID GENERATION. The grid-generation scheme used in this study is a simple extension of the two-dimensional scheme presented in reference 4; it is described in reference 6. Basically, this scheme uses numerically generated solutions of Laplace's equation (or Poisson's equation) to establish regular and smooth finite-difference meshes around arbitrary bodies. In the present case, the finite-difference mesh for each spanwise plane (η = constant plane) is generated using the two-dimensional algorithm. This requires solution of the following two Laplace equations in each spanwise plane:

$$\xi_{xx} + \xi_{zz} = 0 , \qquad \zeta_{xx} + \zeta_{zz} = 0 \tag{7}$$

These equations are transformed to (and solved in) the computational domain. The quantities ξ and ζ are the independent variables, and x and z are the dependent variables. A fast approximate factorization relaxation algorithm is used to solve the resulting transformed equations (ref. 4). This establishes values for x and z in each spanwise plane. Coordinate values in the spanwise direction (y values) are established by a simple stretching formula. Given the values of x, y, and z at each grid point, the values of the metric quantities (eq. (5)) are easily computed using finite-difference formulas. Details of this procedure are given in reference 6.

4. FULL-POTENTIAL EQUATION ALGORITHM

Spatial Differencing. A finite-difference approximation to equation (3), suitable for both subsonic and supersonic flow regions is given by

$$\overleftarrow{\delta}_\xi\left(\frac{\tilde{\rho}U}{J}\right)_{i+1/2,j,k} + \overleftarrow{\delta}_\eta\left(\frac{\bar{\rho}V}{J}\right)_{i,j+1/2,k} + \overleftarrow{\delta}_\zeta\left(\frac{\hat{\rho}W}{J}\right)_{i,j,k+1/2} = 0 \tag{8}$$

The operators $\overleftarrow{\delta}_\xi( )$, $\overleftarrow{\delta}_\eta( )$, and $\overleftarrow{\delta}_\zeta( )$ are first-order accurate backward difference operators in the ξ, η, and ζ directions, respectively, and are defined by

$$\begin{aligned}
\overleftarrow{\delta}_\xi( )_{i,j,k} &= ( )_{i,j,k} - ( )_{i-1,j,k} \\
\overleftarrow{\delta}_\eta( )_{i,j,k} &= ( )_{i,j,k} - ( )_{i,j-1,k} \\
\overleftarrow{\delta}_\zeta( )_{i,j,k} &= ( )_{i,j,k} - ( )_{i,j,k-1}
\end{aligned} \tag{9}$$

The standard $\Delta\xi$, $\Delta\eta$, and $\Delta\zeta$ quantities are all equal to 1; therefore, they have been omitted. The density coefficients, $\tilde{\rho}$, $\bar{\rho}$, and $\hat{\rho}$ are upwind evaluations of the density and are defined by

$$\bar{\rho}_{i+1/2,j,k} = [(1 - \nu)\rho]_{i+1/2,j,k} + \nu_{i+1/2,j,k}\rho_{i+r+1/2,j,k} \tag{10a}$$

$$\bar{\rho}_{i,j+1/2,k} = [(1 - \nu)\rho]_{i,j+1/2,k} + \nu_{i,j+1/2,k}\rho_{i,j+s+1/2,k} \tag{10b}$$

$$\hat{\rho}_{i,j,k+1/2} = [(1 - \nu)\rho]_{i,j,k+1/2} + \nu_{i,j,k+1/2}\rho_{i,j,k+t+1/2} \tag{10c}$$

The density is computed in a straightforward manner by using equation (4b). The quantity ν is a switching function controlling the level of upwinding in the spatial difference scheme. Further discussion about the calculation of density and the definition of ν will be presented subsequently. The r, s, and t indices control the upwind direction and are defined by

$$\begin{aligned} r &= \mp 1 \quad \text{when} \quad U_{i+1/2,j,k} \gtrless 0 \\ s &= \mp 1 \quad \text{when} \quad V_{i,j+1/2,k} \gtrless 0 \\ t &= \mp 1 \quad \text{when} \quad W_{i,j,k+1/2} \gtrless 0 \end{aligned} \tag{11}$$

The differencing scheme, given by equations (8)-(11), maintains an upwind influence for supersonic regions anywhere in the general ξ-η-ζ finite-difference mesh for any orientation of the velocity vector. Thus, the effect of rotated differencing is closely approximated (ref. 5). This aspect greatly enhances the stability and reliability of the present algorithm for many difficult strong shock-wave cases.

Two variations for computing the density have been studied using the two-dimensional version of the algorithm. (The two-dimensional algorithm is obtained by eliminating all η terms and dropping j subscripts in eqs. (8)-(11).) The first variation involves the calculation of the density at mesh points (i,k) (refs. 4,5). Simple averages are then used to obtain the density at the required half points i+1/2,k and i,k+1/2. The second variation involves the calculation of density at the mesh cell centers (i+1/2, k+1/2) (refs. 6, 11, 17). Simple averages are used again to obtain the density at the required half points. In each case, values of ϕ_ξ, ϕ_ζ, U, and W required in the density calculation are computed with standard second-order-accurate finite-difference formulas. Calculation of the density at the cell centers produces sharper shock waves and better resolution of the re-expansion singularity at the foot of the shock wave. This is because the computational module for the latter version extends over fewer grid points and thereby causes less smearing of the solution. The first variation for computing the density, by virtue of its increased dissipation, is more easily stabilized for strong shock-wave calculations. Density values in the three-dimensional scheme are computed and stored at i+1/2,j,k. Values of the density required at i,j+1/2,k and i,j,k+1/2 are determined by simple four-element averages. Values of the density required in the ξ-derivative term of equation (8) (i.e., $\rho_{i+1/2,j,k}$) are computed with the smallest possible computational module in the ξ direction. Therefore, shock waves should be optimally captured in regions where the ξ coordinate is nearly streamwise.

Use of the present upwinded density coefficients in an otherwise centrally differenced scheme, is equivalent to adding an artificial-viscosity-type term to a standard centrally differenced scheme. The equivalent artificial viscosity term is given by

$$-\Delta\xi\left(\nu\rho_\xi \frac{|U|}{J}\right)_\xi - \Delta\eta\left(\nu\rho_\eta \frac{|V|}{J}\right)_\eta - \Delta\zeta\left(\nu\rho_\zeta \frac{|W|}{J}\right)_\zeta \tag{12}$$

To obtain the scheme of equation (8), the ρ_ξ, ρ_η, and ρ_ζ derivatives of equation (12) must be differenced with a backward difference when U, V, and W are positive and with a forward difference when they are negative.

The artificial viscosity coefficient ν strongly affects the stability of the present scheme and is defined as follows:

$$\nu_{i+1/2,j,k} = \begin{cases} \max[(M^2_{i,j,k} - 1)C, 0] & \text{for } U_{i+1/2,j,k} > 0 \\ \max[(M^2_{i+1,j,k} - 1)C, 0] & \text{for } U_{i+1/2,j,k} < 0 \end{cases} \tag{13}$$

The parameter C is a user-specified constant and is given a value between 1.0 and 2.0. Use of larger values of C increases the amount of upwinding and, therefore, the effective amount of artificial viscosity added to the difference scheme. For subsonic regions ν is zero, making the spatial difference scheme entirely second-order-accurate and centrally differenced. In supersonic regions, as the Mach number increases, the density coefficients and, therefore, the spatial-differencing scheme, are increasingly retarded in the upwind direction. An additional constraint placed on ν is $\nu \le 1$. This improves stability and, in some cases, improves the convergence rate. Expressions for ν at $i,j+1/2,k$ and $i,j,k+1/2$ are required in equations (10b) and (10c) and are defined similarly to $\nu_{i+1/2,j,k}$.

AF2 Iteration Scheme. The AF2 fully implicit approximate factorization scheme applied to the three-dimensional full-potential equation (refs. 1,6), can be expressed by choosing the N operator of equation (1) as follows:

$$\alpha NC^n_{i,j,k} = -\left[\left(\alpha - \frac{1}{A_k}\vec{\delta}_\eta A_j \overleftarrow{\delta}_\eta\right)\left(A_k - \frac{1}{\alpha}\vec{\delta}_\xi A_i \overleftarrow{\delta}_\xi\right) - \alpha E^{+1}_\zeta A_k\right](\alpha + \overleftarrow{\delta}_\zeta)C^n_{i,j,k} \tag{14}$$

where

$$A_i = \left(\frac{\tilde{\rho}A_1}{J}\right)^n_{i-1/2,j,k}, \quad A_j = \left(\frac{\bar{\rho}A_2}{J}\right)^n_{i,j-1/2,k}, \quad A_k = \left(\frac{\hat{\rho}A_3}{J}\right)^n_{i,j,k-1/2} \tag{15}$$

The $\tilde{\rho}$, $\bar{\rho}$, and $\hat{\rho}$ coefficients are defined by equations (10a) to (10c) and the operator E^{+1}_ζ is a shift operator given by

$$E_\zeta^{+1}(\ )_{i,j,k} = (\ )_{i,j,k+1} \tag{16}$$

The quantity α (eq. 14) is an acceleration parameter which may be considered as the inverse of a pseudotime step, Δt^{-1}. The best approach for choosing α is to use a sequence of values ranging from small to large time steps. The small time steps are particularly effective for reducing high-frequency errors, and the large time steps are effective for reducing the low-frequency errors. A suitable sequence with analytically estimated endpoints (α_L, α_H) is given in reference 3. Note that one form of the two-dimensional AF2 iteration scheme is obtained from equation (14) by simply setting the η difference equal to zero (ref. 4).

Multiplying out the three factors of equation (14) yields an approximation to the L operator defined by equation (8) plus a number of error terms. This approximate L operator does not have the mixed-derivative terms contained in the exact L operator and has been effectively linearized; that is, all the coefficients used in equation (14), A_i, A_j, and A_k, are evaluated at the nth iteration level. In spite of these approximations, unconditional linear stability exists for this scheme; it is discussed in references 1, 4, and 18. Because this scheme is implicit, each point in the finite-difference mesh influences every other point during each iteration. As a result, evolution of the solution proceeds at a much faster rate, relative to explicit or semi-implicit algorithms.

The AF2 scheme is implemented in three steps as follows:

Step 1:
$$\left(\alpha - \frac{1}{A_k}\vec{\delta}_\eta A_j \overleftarrow{\delta}_\eta\right) g_{i,j}^n = \alpha\omega L\phi_{i,j,k}^n + \alpha A_{k+1} f_{i,j,k+1}^n \tag{17}$$

Step 2:
$$\left(A_k - \frac{1}{\alpha}\vec{\delta}_\xi A_i \overleftarrow{\delta}_\xi\right) f_{i,j,k}^n = g_{i,j}^n \tag{18}$$

Step 3:
$$(\alpha + \overleftarrow{\delta}_\zeta) C_{i,j,k}^n = f_{i,j,k}^n \tag{19}$$

Here, ω is a relaxation factor equal to 1.8 for all cases presented; $g_{i,j}^n$ is an intermediate result stored at each grid point in a given k plane; that is, g is a two-dimensional storage array, and $f_{i,j,k}^n$ is an intermediate result stored at each point in the finite-difference mesh. In step 1, the g array is obtained by solving a tridiagonal matrix equation for each ξ = constant line in the kth plane. In step 2, the f array is obtained from g by solving a tridiagonal matrix equation for each η = constant line, again for just the kth plane. Next, step 1 is used to obtain the g array for the k - 1 plane, and then step 2 is used to obtain the f array for the k - 1 plane, etc. This process continues until all values of f in the three-dimensional mesh are established. Then, by using step 3, the correction array is obtained from the f array by solving a simple bidiagonal matrix equation for each ζ = constant line in the entire finite-difference mesh. With this sweeping procedure all coefficients, A_i, A_j, and A_k are required only once per iteration and, therefore, do not have to be stored in

three-dimensional arrays. The nature of this AF2 factorization places a sweep-direction restriction on the step 1-2 combination and on step 3. The step 1-2 combination must be swept in the direction of the decreasing k subscript, that is, from the wing boundary toward the outer boundary (see fig. 1). The step 3 sweep must proceed in the opposite direction, that is, from the outer boundary toward the wing. There are no sweep-direction limitations placed on any of the three sweeps due to flow direction.

Initiation of step 1 at the wing boundary ($k = NK$) requires knowledge of f at $NK + 1$ which is generally unobtainable. A simple solution is to set f at $NK + 1$ equal to zero. Because the present iteration scheme is written in the correction form, f must approach zero as the solution converges. This boundary condition is therefore consistent with the steady-state solution and seems to provide acceptable performance. A similar boundary condition is required for g at $\eta = \eta_{min}(j = 1)$ and $\eta = \eta_{max}(j = NJ)$; it is implemented by imposing $(g_\eta)_{i,1} = (g_\eta)_{i,NJ} = 0$.

Temporal Damping. For the AF2 factorization, the N operator must be written so that either the ξ-, η-, or ζ-difference approximation to the full-potential equation is split between two factors. This construction generates either a $\phi_{\xi t}$-, $\phi_{\eta t}$-, or $\phi_{\zeta t}$-type term and, if it is properly upwind-differenced (ref. 19), provides time-dependent dissipation to the convergence process. When a particular coordinate direction is split (e.g., the ξ direction), the resulting $\phi_{\xi t}$ difference direction is fixed by the construction of the AF2 algorithm; that is, the term is either backward or forward differenced over the entire mesh. Due to the wraparound ξ coordinate, a backward-differenced $\phi_{\xi t}$ is upwind differenced below the wing and downwind differenced above the wing; a forward-differenced $\phi_{\xi t}$ is downwind differenced below and upwind differenced above. Therefore, a problem with $\phi_{\xi t}$ arises either above or below the wing. Following the two-dimensional algorithm development (ref. 4) the ζ-difference approximation is split between two factors. This allows control over the other more important coordinate directions (ξ and η) because the $\phi_{\xi t}$ and $\phi_{\eta t}$ terms are added to the iteration scheme explicitly and are not part of the factorization construction. The $\phi_{\eta t}$ and $\phi_{\xi t}$ terms are included by adding

$$\mp\beta_\eta \left| V_{i,j,k} \right| \vec{\vec{\delta}}_\eta \quad \text{and} \quad \mp\alpha\beta_\xi \vec{\vec{\delta}}_\xi \tag{20}$$

inside the brackets of the first and second sweep equations (17) and (18), respectively. The parameter β_ξ is fixed to 0.0 in subsonic regions and specified as needed in supersonic regions. The parameter β_η is a user-specified constant, fixed over the entire mesh. For all cases presented in this study, $\beta_\eta = 0$. The double-arrow notation on the ξ- and η-difference operators indicates that the difference is always upwind. For the η direction, a backward difference is used when the η contravariant velocity component ($V_{i,j,k}$) is positive; a forward difference is used when V is negative. The sign is chosen in each case so that the addition of $\phi_{\eta t}$ and $\phi_{\xi t}$ increases the magnitude of the first- and second-sweep diagonal coefficients, respectively. Additional discussion about temporal damping can be found in references 4 and 6.

Boundary Conditions. The wing surface boundary condition is that of flow tangency (i.e., no flow through the wing surface), and requires the ζ contravariant velocity component at the wing surface to be zero ($W = 0$). This boundary condition is implemented by

$$\left(\frac{\rho W}{J}\right)_{i,j,NK+1/2} = -\left(\frac{\rho W}{J}\right)_{i,j,NK-1/2} \tag{21}$$

where $k = NK$ is the wing surface. In expressions where ϕ_ζ is required at the wing surface, the $W = 0$ boundary condition is used again to obtain

$$\phi_\zeta\Big|_{wing} = -\frac{A_5}{A_3}\,\phi_\xi - \frac{A_5}{A_3}\,\phi_\eta \tag{22}$$

Thus, a value of ϕ_ζ at the wing surface can be obtained without using a one-sided difference on ϕ.

In the present study, a special wing geometry has been chosen to evaluate the new three-dimensional AF2 algorithm, namely, flow past an arbitrary wing mounted between parallel walls. The purpose of this model problem is to simulate the flow past a wing in a wind tunnel. The parallel sidewalls are treated with the same tangency boundary condition used for the wing surface ($V = 0$). Details about the implementation of this boundary condition are given in reference 6.

5. COMPUTED RESULTS. The implicit algorithm discussed in the previous section has been coded into a transonic airfoil analysis computer code (TAIR) and a transonic wing analysis computer code (TWING). Details of the TAIR and TWING codes are given in references 4 and 6, respectively. Three versions of the AF2 algorithm have been investigated using the TAIR code; they are designated by (1) standard AF2, (2) AF2 ($\tilde{\rho}_{LHS} \to 1$), and (3) AF2 ($\tilde{\rho}_{LHS} \to 1$, $\phi_{xt} \to 0$). The first version (standard AF2) refers to the two-dimensional AF2 scheme presented in reference 4. The second version (AF2, $\tilde{\rho}_{LHS} \to 1$) is the same as scheme 1, with the additional constraint that all density coefficients are removed from the left-hand side of the iteration scheme; that is, all the density coefficients are removed from the N operator, equation (14). To provide appropriate scaling, the residual (right-hand side of the iteration scheme) is divided by the density, $\rho^n_{i,j,k}$. This kind of simplification was tried in reference 8 for an ADI-type algorithm and produced stable results. The third version is the same as scheme 2, with the additional constraint that all ϕ_{xt} is removed from the iteration scheme. Stability for this case is more difficult to maintain and often requires larger values of the constant C (see eq. (13)), which increases the degree of upwinding in the residual operator.

Convergence histories for these three algorithm variations applied to a typical transonic calculation (NACA 0012 airfoil, $M_\infty = 0.75$, $\alpha = 1°$) are shown in figure 2. All three variations converge, but the standard AF2 scheme is two to three times faster than the other two schemes. It is interesting to

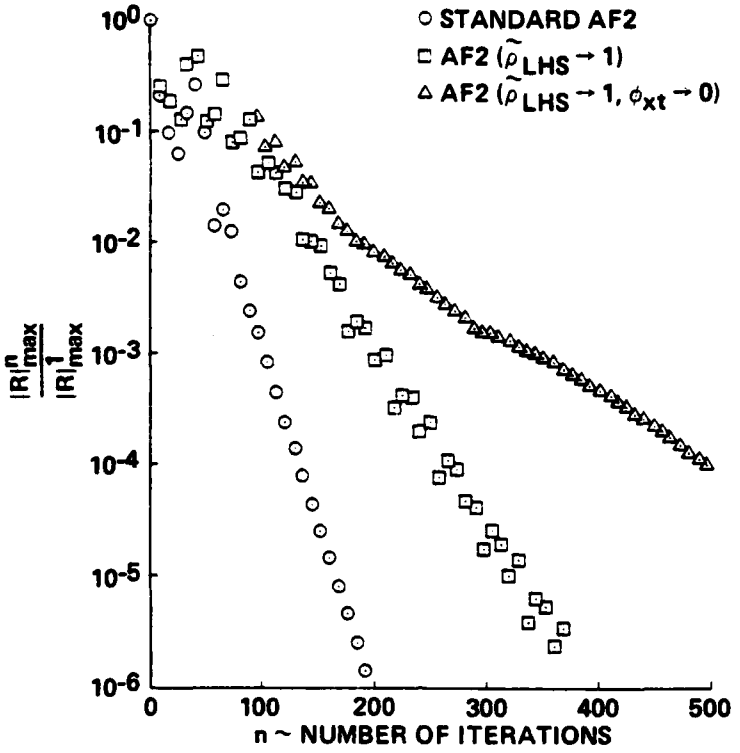

Figure 2.- Convergence history comparison for three versions of the AF2 algorithm: NACA 0012 airfoil, $M_\infty = 0.75$, $\alpha = 1°$.

note that the coefficients of the matrices being inverted in the third case are stationary, that is, invariant with iteration. In addition, these matrices are also symmetrical, which is generally an undesirable characteristic of transonic relaxation schemes leading to instability. Another interesting point is that removal of the density upwinding, but not the density itself, from the left-hand side of the iteration scheme (i.e., replacing $\tilde{\rho}_{LHS} \rightarrow \rho_{LHS}$), produces a convergence rate almost identical to the standard AF2 convergence rate. Therefore, inclusion of at least the density in the N operator, but not necessarily the upwinded or retarded density, as well as inclusion of $\phi_{\xi t}$, is very important for rapid convergence but not always necessary for achieving stability.

Several examples from the TAIR computer code, using the standard AF2 iteration scheme, are now presented. The first test case involves the Korn airfoil (airfoil 75-06-12, ref. 20) at a free-stream Mach number of 0.74 and an angle of attack of 0°. This calculation was obtained by using TAIR in the default mode. This simply means that all parameters affecting the convergence rate including the relaxation factor (ω), the acceleration parameters (α_k), and the temporal damping coefficient (β_ξ) are either held fixed or are adjusted automatically by internal computer code logic. This feature greatly simplifies operation of TAIR and improves reliability, especially for inexperienced users. However, the convergence speed of TAIR in the default mode is

about 10% to 50% below optimum, depending on the particular case. For more details about the default mode feature see reference 6.

The pressure coefficient distribution for this slightly off-design Korn airfoil calculation is compared in figure 3 with a result obtained from the GRUMFOIL computer code (ref. 21); the calculations are in excellent agreement. The GRUMFOIL computer code is similar to TAIR in that both codes solve the conservative full-potential equation, but different in that TAIR uses the AF2 iteration scheme and GRUMFOIL uses a hybrid direct-solver/SLOR iteration scheme (ref. 7). This hybrid iteration scheme is composed of one direct-solver iteration (which is very effective for reducing low-frequency errors but is unstable for supersonic regions) followed by several (10 is the default) SLOR iterations. The purpose of the SLOR iterations is to smooth

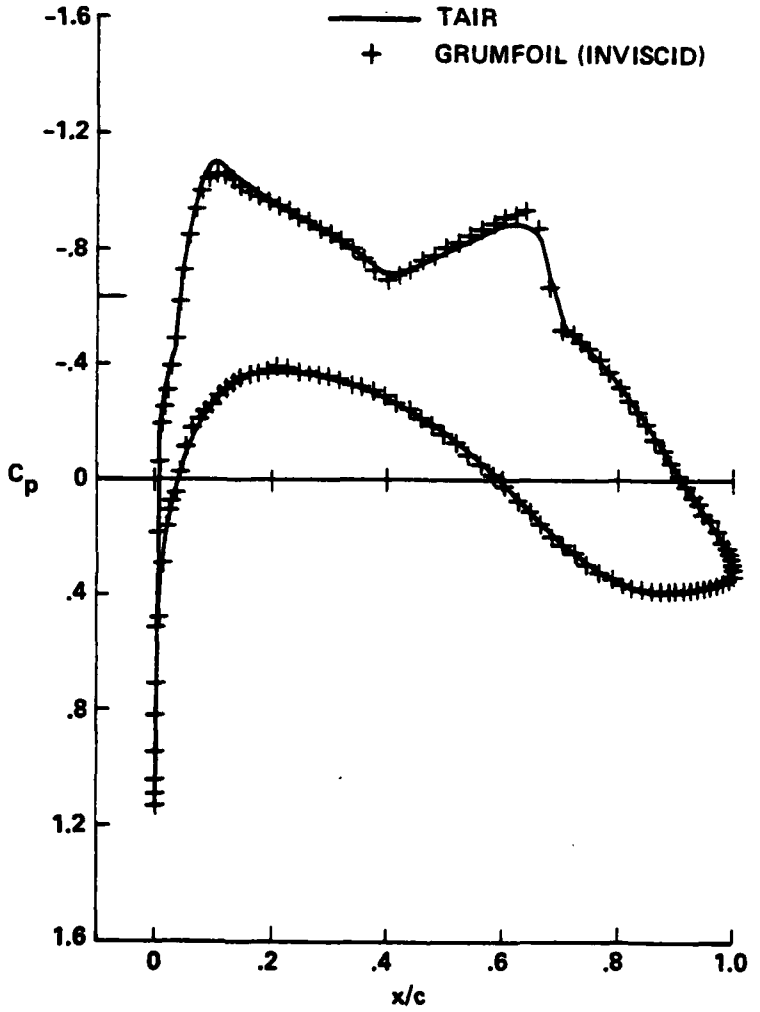

Figure 3.- Pressure coefficient comparison: Korn airfoil, $M_\infty = 0.74$, $\alpha = 0°$.

high-frequency errors generated by the direct-solver step in regions of supersonic flow. The boundary-layer option available in GRUMFOIL has not been used in any of the results presented herein. All GRUMFOIL results are computed on a 148 × 32 mesh; the TAIR results are computed on a 149 × 32 mesh.

The rms error (E_{rms}) convergence-history curves for the Korn airfoil calculation are presented in figure 4. The E_{rms} at iteration n is defined by

$$E^n_{rms} = \left[\frac{\sum_{i=1}^{NI} \left(C^n_{P_i} - C_{P_i} \right)^2}{\sum_{i=1}^{NI} C^2_{P_i}} \right]^{1/2} \tag{23}$$

where $C^n_{P_i}$ is the surface pressure coefficient at the ith grid point and the nth iteration; C_{P_i} is the surface pressure coefficient at the ith grid

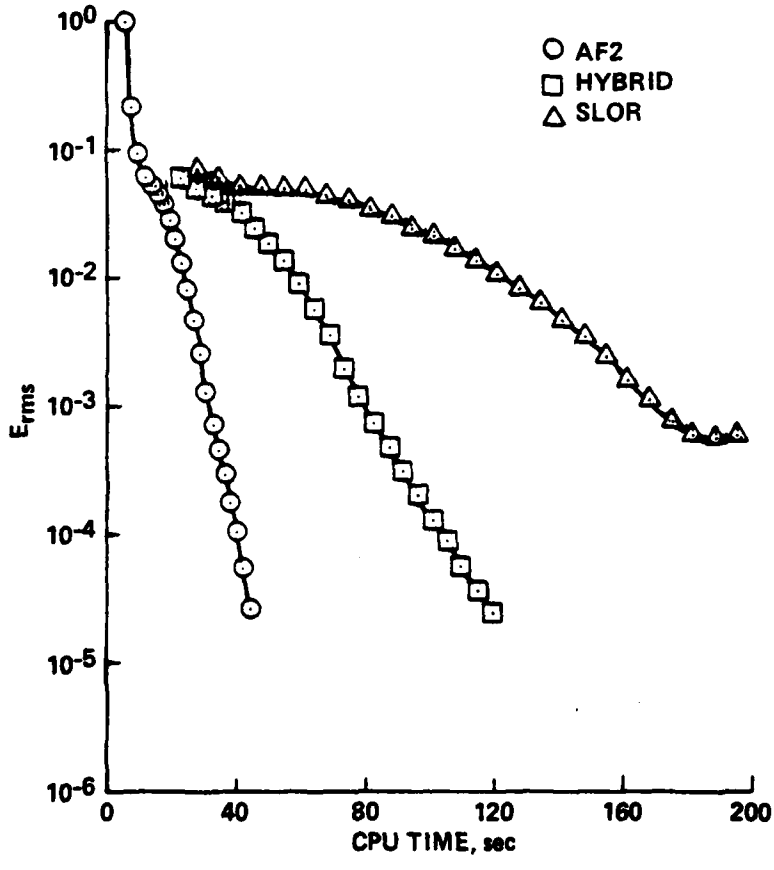

Figure 4.- Two-dimensional convergence histories: Korn airfoil, $M_\infty = 0.74$, $\alpha = 0°$.

point taken from the converged solution; and NI is the total number of surface grid points. Using E_{rms} to compare convergence performance is a much more quantitively correct procedure than using the standard maximum residual quantity. (See refs. 3 and 22 for a more complete explanation of this point.)

The three curves shown in figure 4 correspond to the following iteration schemes: (1) AF2, (2) hybrid, and (3) SLOR. The SLOR scheme is simply the hybrid iteration scheme without benefit of the direct-solver step (see ref. 7). Convergence for the SLOR scheme has been approximately optimized by a trial-and-error adjustment of the relaxation parameter. Each convergence-history curve is constructed by plotting E_{rms} vs CPU time (Ames CDC 7600 computer). The hybrid case has been computed with default values for all relaxation parameters. Set-up times, that is, the CPU time required for grid generation, initialization, and coarse- and medium-mesh calculations, are included in each convergence-history curve. The AF2 curve includes 6 sec for grid generation and initialization. The hybrid and SLOR curves use coarse-medium-fine mesh sequences. Converged results from the coarse mesh are interpolated onto the medium mesh and then from the medium mesh onto the fine mesh, thus providing a good initial guess for the fine-mesh calculation. The set-up times for these cases are 23 sec for the hybrid case and 28 sec for the SLOR case. For this calculation the AF2 scheme is about 2.5 times faster than the hybrid scheme and about 5 times faster than SLOR.

Solutions with M_∞ Near Unity. As the free-stream Mach number approaches unity, interesting airfoil shock-wave patterns develop. These solutions were the subject of discussion in references 5, 6, 8, and 23. An example calculation about an NACA 0012 airfoil at $M_\infty = 0.95$ and $\alpha = 0°$ is shown in figure 5. The Mach number contours clearly illustrate the existence of a so-called "fishtail" shock-wave pattern downstream of the airfoil trailing edge. The angle of attack produces lift ($C_L = 0.43$) and, therefore, desymmetrizes the fishtail shock-wave structure. The oblique shock emanating from the trailing-edge upper surface has been strengthened while the oblique shock emanating from the trailing-edge lower surface has been weakened and is almost nonexistent. The normal shock above the airfoil is much stronger than the normal shock below the airfoil. This difficult calculation demonstrates the convergence reliability of the present transonic solution procedure.

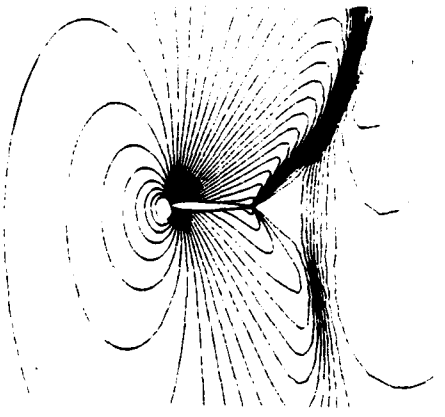

Figure 5.- Mach number contours: NACA 0012 airfoil, $M_\infty = 0.95$, $\alpha = 4°$.

Convergence history curves for this case — including E_{rms}, maximum residual ($|R|_{max}$), number of supersonic points (NSP), and lift coefficient (C_L) convergence histories — are presented in figure 6. Convergence is achieved in approximately 20 sec of CPU time (Ames CDC 7600 computer), or

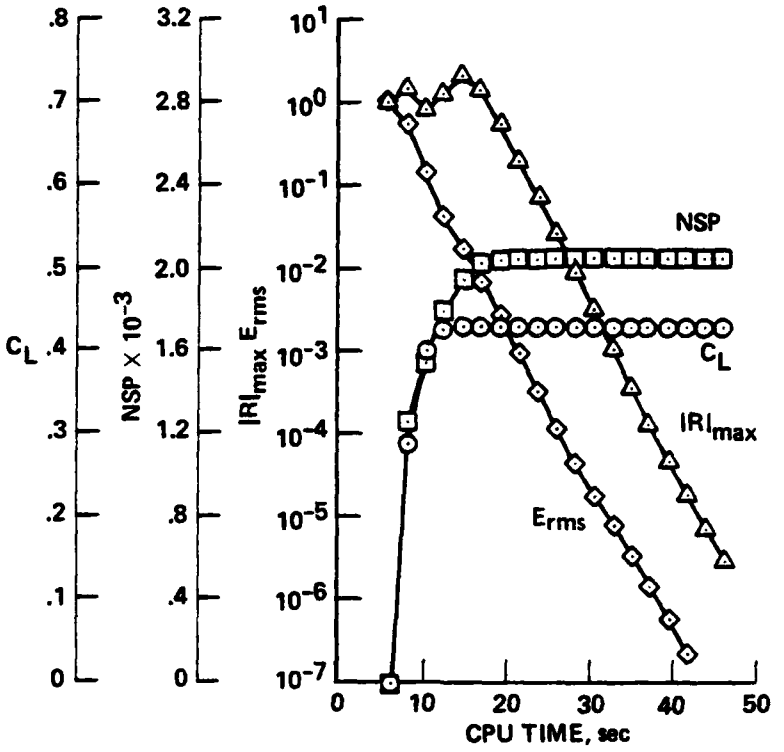

Figure 6.- Two-dimensional convergence histories: NACA 0012 airfoil, $M_\infty = 0.95$, $\alpha = 4°$.

116 iterations, and is indicated by constant values of both NSP and C_L. The steady-state value of NSP is just over 2,000, which represents about 45% of all mesh points. At this point, $|R|_{max}$ has dropped only slightly and E_{rms} has dropped by over 2.5 orders of magnitude. This apparent discrepancy is partially due to the fact that the airfoil surface solution, which is effectively monitored by E_{rms}, converges before the downstream fishtail shock-wave pattern. Another cause is that during the initial phase of convergence, in which the residual is nearly constant, the position of the shock sonic line is rapidly being adjusted. This excites high-frequency errors and, therefore, keeps the residual artificially high, even though E^n_{rms} is rapidly decreasing. Establishment of convergence for such a small reduction in the maximum residual is a characteristic behavior of many strong shock calculations in which the present algorithm is used. Use of a three-order-of-magnitude reduction in $|R|_{max}$ as a convergence criterion for the present case world require E_{rms} to be reduced by 5 orders of magnitude, which represents more iterations (by a factor of 2) than necessary.

Three-Dimensional Solutions. Results from the transonic wing analysis code (TWING) are presented in this section. All calculations were made with the density coefficients upwinded in only the ξ and η directions. For the

present case, this was sufficient; however, for cases with stronger shocks at the trailing edge, density upwinding along the ζ direction would probably be required. All results have been computed with $\alpha_L = 0.4$, $\alpha_H = 4.0$, and β_ξ ranging from 0.1 to 0.5. The larger values of β_ξ were required for the larger aspect ratio cases.

Figures 7-9 show the results of a nonlifting wing calculation with the following characteristics: NACA 0015 wing, $M_\infty = 0.86$, $\lambda = 30°$, and AR = 1.9. Figures 7 and 8 show the wing planform Mach number contours at 20 and 80

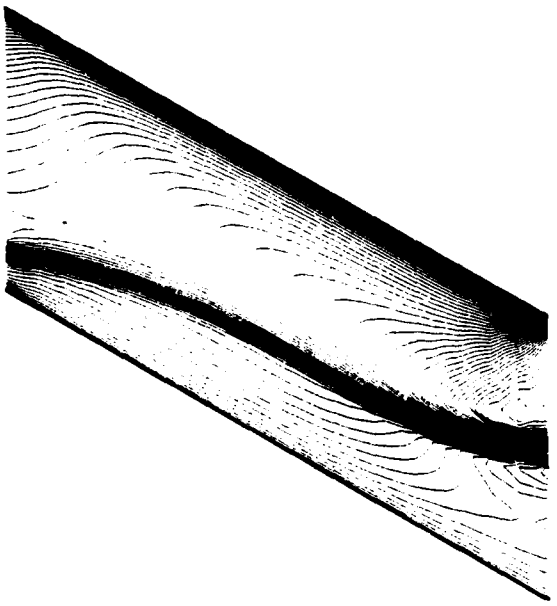

Figure 7.- Wing planform Mach contours (20 iterations): NACA 0015 wing, $M_\infty = 0.86$, $\alpha = 0°$, $\lambda = 30°$, AR = 1.9.

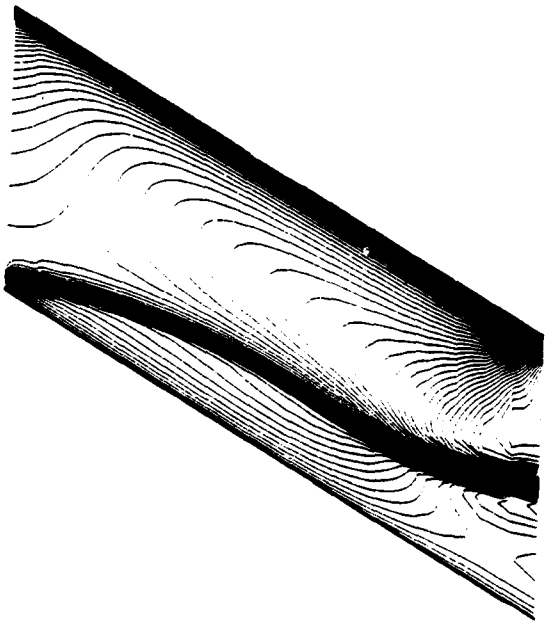

Figure 8.- Wing planform Mach contours (fully converged): NACA 0015 wing, $M_\infty = 0.86$, $\alpha = 0°$, $\lambda = 30°$, AR = 1.9.

iterations, respectively. In just 20 iterations, a reasonable approximation to the final solution is already established. As expected, the shock wave approaches both sidewalls perpendicularly. Near center span the shock wave is swept, approximately parallel to the wing leading and trailing edges. The spanwise shock-strength gradient is quite large. This is indicated by both the Mach contours given in figure 8 and the surface C_p distributions given in figure 9. The maximum local Mach numbers are 1.26 in the root, 1.33 in the center span, and 1.78 in the tip planes. A large part of this spanwise shock-strenth gradient is caused by the tip sidewall-wing interaction, which is essentially the opposite of a three-dimensional relief effect. The existence of the tip sidewall constrains the streamlines to remain in the tip plane. The wing sweep induces a spanwise component of velocity which in effect squeezes the streamlines toward the tip plane. This increases the Mach number and therefore the shock strength in the tip-plane region.

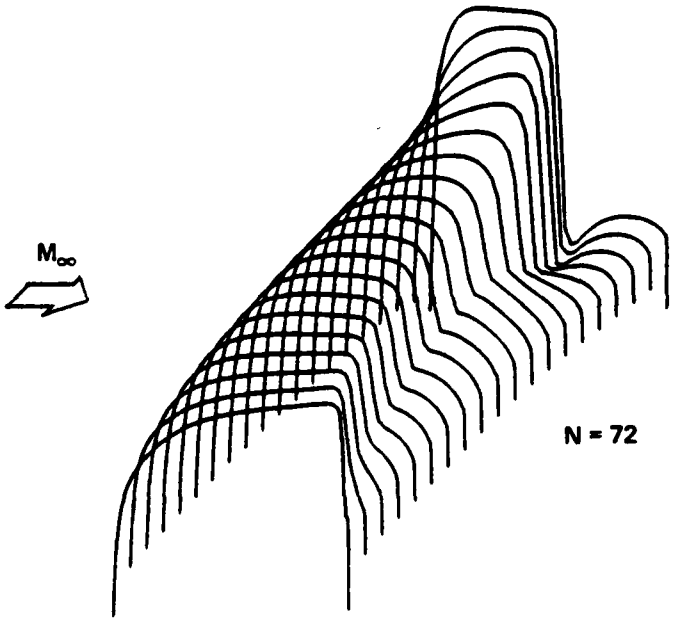

Figure 9.- Three-dimensional pressure coefficient distribution: NACA 0015 wing, $M_\infty = 0.86$, $\alpha = 0°$, $\lambda = 30°$, AR = 1.9.

The TWING calculation presented here was computed with 23,200 ($58 \times 20 \times 20$) grid points. Because of the wraparound mesh, all 58 points in the ξ direction lie on the wing surface. Each iteration of the three-dimensional algorithm requires about 2.1 sec of CPU time on the Ames CDC 7600 computer. For the case just presented, this equates to a total run time of less than 3 min to achieve plottable accuracy. Cases with weaker shock waves are faster. For subcritical cases the run time is faster still, requiring only about a minute of CPU time. These times include CPU time for metric recalculation every iteration. Another version of TWING, using disk storage to store all metric quantities, actually requires less CPU time per iteration (1.8 sec); however, it is slightly more expensive, because of the additional I/O access charges. This, of course, is a characteristic of the Ames CDC 7600 charging algorithm.

6. ALGORITHM EFFICIENCY ON VECTOR COMPUTERS. The use of computational fluid dynamics as a relatively fast and inexpensive aircraft design tool is finding increased acceptance in the aircraft industry (refs. 24, 25). Use of these tools and the development of new, more efficient numerical algorithms, however, requires faster and more cost-effective computers. In this regard vector computers, such as the Burroughs Illiac IV, the CDC STAR-100, and the CRAY-1, show considerable promise. These vector machines offer greatly enhanced computing speeds arising from the ability to operate on many

calculations simultaneously, parallel machines, and/or in an assembly line fashion, pipeline machines (more discussion regarding vector computer architectures can be found in ref. 26). Because of the nature of the speed enhancement, these machines tend to favor certain classes of algorithms. It remains to be seen how existing algorithms, as well as new ones, will lend themselves to these new computer architectures. The purpose of the present study is to compare various full-potential algorithms on a model pipeline vector computer and, therefore, determine if any fundamental limitations regarding efficient vector computing exist.

Algorithm Model. The simplified model used to simulate the various full-potential algorithms is now discussed. The basic elements of this model are as follows: (1) perform a floating point operation count for the algorithm, preferably from an existing computer code; and (2) subdivide the operation count according to vectorizability (plane, line, scalar), that is, all operations which can be vectorized into planes are placed into the plane category, all line vectorizable operations are placed into the line category, etc. Further discussion on the subject of algorithm vectorizability along with examples is presented in reference 26. Included in the present analysis are boundary condition operations (when possible) as well as "penalty operations" involved with data transposes. Overhead operation counts involved with do loop logic, addressing calculations, etc. are not included. In view of the simple nature of the present algorithm model, only idealistic estimates for algorithm performance are expected. The primary utility of the present model is in providing an optimistic upper bound for the performance of an algorithm on a vector computer. In addition, since all algorithms are modeled with the same assumptions, the present analysis provides a simplified basis for the comparison of different algorithms.

Computer Model. Once statistical data for each algorithm are obtained, computational efficiencies using a pipeline vector computer model are determined. All results assume in-core operation only. Rules used to establish the computer model are as follows: All floating point operations (including addition, subtraction, multiplication, and division) are modeled by the following performance curve:

$$e = \frac{S_o R}{1 + R(S_o - 1)} \tag{24}$$

where

$$S_o = \left.\frac{de}{dR}\right|_{R=0} = \frac{Ap + L_{max}}{Ap} \tag{25}$$

In equations (24) and (25), e is the efficiency, defined as the ratio of actual MFLOPS rate (million floating point operations per second) to the maximum MFLOPS rate, R is the ratio of vector length (dictated by the algorithm) to the maximum vector length allowed by the hardware, A is the vector

pipe startup time in clocks, and p is the number of pipes. The maximum MFLOPS rate is defined by

$$\text{MFLOPS}_{max} = \frac{L_{max}}{A + L_{max}/p} \frac{10^{-6}}{c} \tag{26}$$

where c is the clock time in nanoseconds. The model computer performance curve, given by equations (24)-(26), is typical for existing pipeline vector computers; it is displayed in figure 10. Values for each of the machine-dependent parameters defined in equations (24)-(26), are also displayed in figure 10.

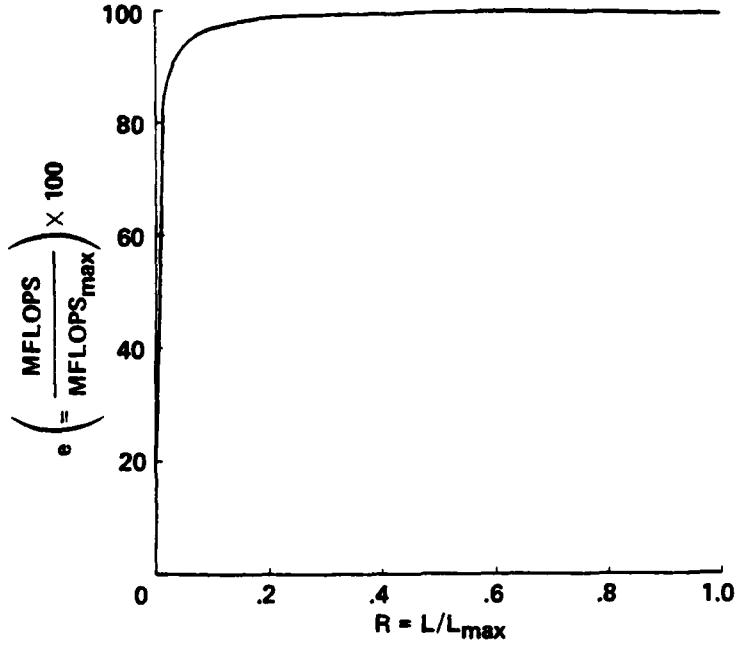

Figure 10.- Computer model performance curve; $S_o = 300$, $L_{max} = 65{,}536$, Ap = 219.

The next aspect of the computer model concerns the establishment of a transpose penalty. The transpose operation is required by some algorithms (usually implicit algorithms) to reorder data in memory, thus allowing contiguous memory access during execution of vector operations. For the present computer model, data transposition efficiency e_t is determined by $e_t = c_{TP}e$, where e is the standard efficiency obtained from equation (24). In all cases, a value of 0.25 was used for the transpose penalty coefficient c_{TP}. This value produces reasonable agreement with typical pipeline vector computers.

The scalar computational efficiency e_s is determined by assuming one scalar result every five clocks. This yields a scalar efficiency for the present model computer of 0.05. This value corresponds to an idealistic upper

bound on scalar performance and, therefore, is consistent with the present analysis.

Once individual efficiencies have been computed for each vector length — that is, efficiencies for plane operations, e_p; line operations, e_ℓ; scalar operations, e_s; and transpose operations, e_t — the overall efficiency is computed as follows:

$$e = \frac{1}{(R_p/e_p) + (R_\ell/e_\ell) + (R_s/e_s) + (R_t/e_t)} \tag{27}$$

where

$$\left.\begin{aligned} R_p &= N_p/N_{TOT} \\ R_\ell &= N_\ell/N_{TOT} \\ R_s &= N_s/N_{TOT} \\ R_t &= N_t/N_{TOT} \end{aligned}\right\} \tag{28}$$

and

$$N_{TOT} = N_p + N_\ell + N_s$$

In equations (27) and (28), N_p and N_ℓ are the number of planar and line vectorizable operations, respectively, N_s is the number of scalar operations, and N_t is the number of transposes.

Vector Computer Efficiency Results. Results of the present vector computer efficiency study are shown in figures 11 and 12. The efficiency e is plotted vs the degree of planar vectorization (% planar) for a mesh consisting of 10^5 points ($n \times n \times n$ where $n = 46$) in figure 11 and 5×10^5 points ($n \times n \times n$ where $n = 79$) in figure 12. The solid curves indicate % scalar = constant lines and are displayed for 0, 2, 4, 8, 16, 32, and 64% scalar content. This type of plot or "efficiency map" displays all the possible algorithm combinations composed of plane, line, and scalar operations. As such, it represents a good format for comparing different algorithms or algorithm coding philosophies.

Theoretical efficiencies for four full-potential algorithms are compared in figures 11 and 12. These three-dimensional algorithms are (1) AF2 (with and without transpose penalty), (2) SLOR, (3) ZEBRA II (see ref. 11), and (4) ADI (with and without transpose penalty). For the grid with 10^5 points (fig. 11), ZEBRA II is the most efficient algorithm (86%); ADI is 67%, AF2 49%, and SLOR 32%. The SLOR algorithm is least efficient because it inherently contains a relatively large number of scalar operations (5% for the model algorithm version considered here and potentially larger percentages for other versions). The transpose penalty associated with the ADI algorithm is much larger than that associated with AF2 because ADI has twice as many transposes. The efficiency map shown in figure 12 is very similar to the

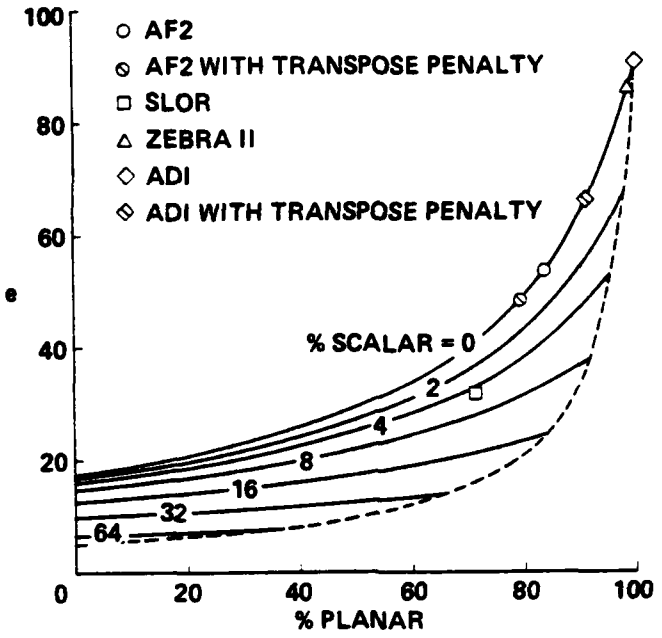

Figure 11.- Algorithm efficiency on a model pipeline vector computer: 10^5 grid points.

efficiency map of figure 11. The biggest overall difference is that all algorithms gain in efficiency as the grid dimensions are increased. This, of course, is a direct result of increased vector lengths.

The rate of execution, that is, the efficiency, of a particular algorithm is only one of three important considerations needed to determine total execution time for a solution. The other two considerations are number of operations per iteration and number of iterations required for a solution. The implicit schemes (e.g., AF2) lose ground relative to explicit schemes in the first two categories, but overwhelmingly gain ground in the last category. Ultimate algorithm supremacy can only be determined by collectively considering all three categories. Such a comparison is displayed in table 1. The number of iterations per solution has been estimated from two-dimensional results. The AF2 algorithm is fastest on the model computer, being about 7 times faster than SLOR. The ADI and ZEBRA II algorithms are next in speed, being about 5 and 3 times faster than SLOR, respectively.

One last comment concerning efficient computation on vector computers is in order. The type of vector computer modeled in the present study attains most of its efficiency only when large vectors are utilized, for example, planar vectors. Other vector computers do exist that attain very efficient operation (~100%) with much shorter vectors, for example, line vectors. Also, different computer hardwares provide for different alternatives for data transposition — some machines have no transpose penalties at all. Because of these features, implicit algorithms may provide even larger savings in overall

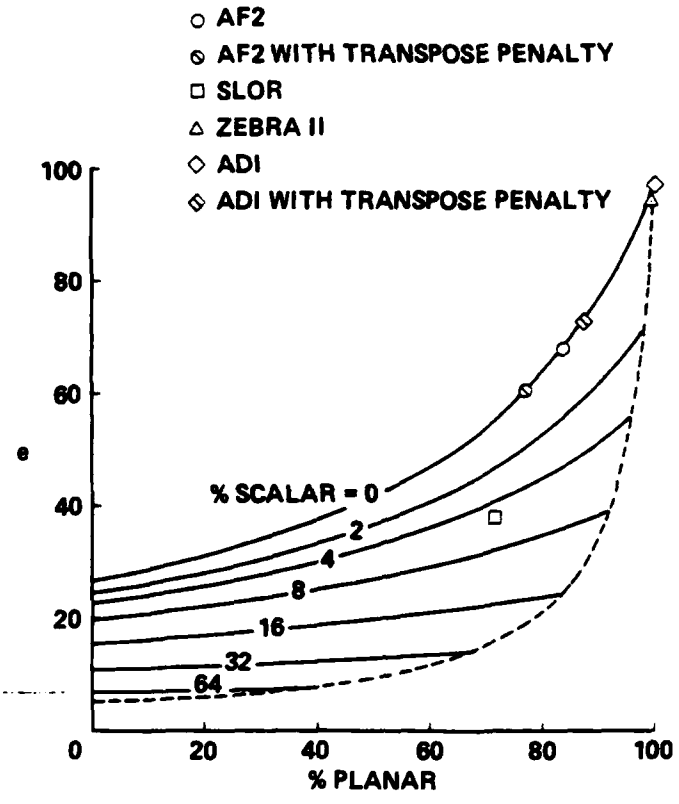

Figure 12.- Algorithm efficiency on a model pipeline vector computer: 5×10^5 grid points.

TABLE 1.- TOTAL EXECUTION TIME COMPARISON FOR SEVERAL FULL-POTENTIAL ALGORITHMS ON A MODEL PIPELINE VECTOR COMPUTER

Algorithm	e (10^5 mesh)	Operations per grid point	Iterations/ solution	$\frac{\text{Time}}{(\text{Time})_{\text{SLOR}}}$
SLOR	32%	160	~600	1.00
AF2	49%	200	~100	0.14
ADI	67%	210	~200	0.21
ZEBRA II	86%	130	~600	0.30

computer times. The exact amount of savings can only be determined when all these features are considered.

6. CONCLUSIONS. A fast, implicit algorithm for solving the conservative full-potential equation in both two and three dimensions is presented. Stability in supersonic regions is maintained by using an upwind evaluation of the density coefficient along all coordinate directions. This provides an effective upwind difference of the streamwise terms for any orientation of the velocity vector (i.e., rotated differencing), and thereby greatly enhances the reliability of the present algorithm. The present scheme has been used to compute a number of difficult two-dimensional test cases, including cases with "fishtail" shock-wave patterns. The rapid convergence of these difficult cases demonstrates the reliability and efficiency of the present transonic flow solution procedure.

The present fully implicit AF2 algorithm has been compared with both the standard transonic-solution procedure, successive-line overrelaxation (SLOR), and a hybrid (direct-solver/SLOR) scheme. The surface C_p distributions produced by these schemes are in good agreement. Based on CPU time, the rms error in the surface pressures is reduced approximately 5 to 7 times faster by the AF2 algorithm than by SLOR, and approximately 2 to 3 times faster by the AF2 algorithm than by the hybrid scheme.

A three-dimensional solution for a swept wing mounted between parallel walls is also presented. For this calculation a strong shock wave extends across the entire wingspan, indicating a high degree of reliability for the three-dimensional AF2 algorithm. Convergence histories indicate that the convergence rate improvement experienced in two dimensions carries over to the three-dimensional version of the fully-implicit algorithm.

A simple analysis based on vector length categorization of floating point operation counts has been developed and used to estimate the computational efficiency of several full-potential algorithms on a model pipeline vector computer. Despite penalties imposed by vectorization of implicit schemes, results indicate that a high degree of efficiency can be obtained from implicit algorithms, including the present AF2 algorithm.

ACKNOWLEDGMENTS

The author expresses gratitude to P. Buning and A. Wray, Ames Research Center, for many helpful discussions during the course of the vector computer efficiency study.

REFERENCES

1. Ballhaus, W. F.; and Steger, J. L.: Implicit Approximate Factorization for the Low-Frequency Transonic Equation. NASA TM X-73,082, 1975.

2. Ballhaus, W. F.; Jameson, A.; and Albert, J.: Implicit Approximate Factorization Schemes for the Efficient Solution of Steady Transonic Flow Problems. AIAA J., vol. 16, no. 6, 1978, pp. 573-579.

3. Holst, T. L.; and Ballhaus, W. F.: Fast Conservative Schemes for the Full Potential Equation Applied to Transonic Flows. NASA TM-78469, 1978. (Also AIAA J., vol. 17, no. 2, Feb. 1979, pp. 145-152.)

4. Holst, T. L.: An Implicit Algorithm for the Conservative, Transonic Full Potential Equation Using an Arbitrary Mesh. AIAA Paper 78-1113, July 1978. (Also AIAA J., vol. 17, no. 10, Oct. 1979, pp. 1038-1045.)

5. Holst, T. L.; and Albert, J.: An Implicit Algorithm for the Conservative, Transonic Full Potential Equation with Effective Rotated Differencing. NASA TM-78570, 1979.

6. Holst, T. L.: A Fast, Conservative Algorithm for Solving the Transonic Full-Potential Equation. AIAA Fourth Computational Fluid Dynamics Conference Proceedings, July 1979, pp. 109-121.

7. Jameson, A.: Transonic Potential Flow Calculations Using Conservative Form. AIAA Second Computational Fluid Dynamics Conference Proceedings, June 1975, pp. 148-155.

8. Hafez, M. M.; Murman, E. M.; and South, J. C.: Artificial Compressibility Methods for Numerical Solution of Transonic Full Potential Equation. AIAA Paper 78-1148, July 1978. (Also AIAA J., vol. 17, no. 8, Aug. 1979, pp. 838-844.)

9. Eberle, A.: A Finite Volume Method for Calculating Transonic Potential Flow Around Wings from the Pressure Minimum Integral. Technical Translation, NASA TM-75,324, 1978.

10. Eberle, A.: Transonic Potential Flow Computations by Finite Elements: Airfoil and Wing Analysis, Airfoil Optimization. Lecture at the DGLR/GARTEUR 6 Symposium, Transonic Configurations, Bad Harzburg, Germany, June 1978.

11. South, J. C.; Keller, J. D.; and Hafez, M. M.: Vector Processor Algorithms for Transonic Flow Calculations. AIAA Fourth Computational Fluid Dynamics Conference Proceedings, July 1979, pp. 247-255.

12. Steger, J. L.; and Baldwin, B. S.: Shock Waves and Drag in the Numerical Calculation of Isentropic Transonic Flow. NASA TN D-6997, 1972.

13. Lapidus, A.: A Detached Shock Calculation by Second-Order Finite Differences. J. Comput. Phys., vol. 2, 1967, pp. 154-177.

14. Viviand, H.: Conservative Forms of Gas Dynamic Equations. La Recherche Aerospatiale, no. 1, Jan.-Feb. 1974, pp. 65-68.

15. Vinokur, M.: Conservative Equations of Gas Dynamics in Curvilinear Coordinate Systems. J. Comput. Phys., vol. 14, Feb. 1974, pp. 105-125.

16. Steger, J. L.: Implicit Finite Difference Simulation of Flow About Arbitrary Geometries with Application to Airfoils. AIAA Paper 77-665, June 1977. (See also AIAA J., vol. 16, no. 7, July 1978, pp. 696-686.)

17. Jameson, A.: Transonic Flow Calculations. VKI Lecture Series 87, Mar. 15-19, 1976.

18. Holst, T. L.: An Implicit Algorithm for the Transonic Full-Potential Equation in Conservative Form. Presented at the Fourth International Symposium on Computing Methods in Applied Sciences and Engineering, Versailles, France, Dec. 1979. (Proceedings to appear in Lecture Notes in Physics.)

19. Jameson, A.: Iterative Solution of Transonic Flows over Airfoils and Wings, Including Flows at Mach 1. Commun. Pure & Appl. Math., vol. 27, 1974, pp. 283-309.

20. Bauer, F.; Garabedian, P.; Korn, D.; and Jameson, A.: Supercritical Wing Sections. Lecture Notes in Economics and Mathematical Systems, 108, Springer Verlag, 1975.

21. Melnik, R. E.: Wake Curvature and Trailing Edge Interaction Effects in Viscous Flow over Airfoils. Advanced Technology Airfoil Research, NASA CP-2045, Mar. 1978, pp. 255-270.

22. Ballhaus, W. F.: A Fast Implicit Solution Procedure for Transonic Flows. Lecture Notes in Physics, Computing Methods in Applied Sciences and Engineering, Springer-Verlag, 1977, pp. 90-102.

23. Newman, P. A.; and South, J. C.: Conservative Versus Nonconservative Differencing: Transonic Streamline Shape Effects. NASA TM X-72,827, 1976.

24. Chapman, D. R.: Computational Aerodynamics Development and Outlook. AIAA J., vol. 17, no. 12, Dec. 1979, pp. 1293-1313.

25. Gessow, A.; and Morris, D. J.: A Survey of Computational Aerodynamics in the United States. NASA SP-394, 1977.

26. Bailey, F. R.: A View Toward Future Fluid Dynamics Computing. AIAA Paper 78-1112, July 1978.

COMPUTATION OF BIFURCATION BRANCHES USING PROJECTION METHODS

E. J. Doedel
Computer Science Department
Concordia University
Montreal, Quebec

G. W. Reddien
Mathematics Department
Southern Methodist University
Dallas, Texas 75275

ABSTRACT. Both theoretical and computational results are given for the application of projection methods to compute bifurcation branches for solutions to systems of ordinary differential equations. A normalization is given in the Hopf case that enables one to compute around turning points.

1. INTRODUCTION. Several authors have recently studied the computation of solution branches bifurcating at singular points for operator equations. Included here are Keller [5], Atkinson [1], Weiss [13], Rheinboldt [8], Westreich and Varol [14], Seydel [9,10], Weber [12], Hassard and Wan [4] and Langford [6] among many others. These papers consider problems in which one of the key assumptions in the analysis of numerical methods is not satisfied, namely that the desired solution be isolated. This assumption has been fundamental to the analysis of projection methods for boundary value problems. We will extend the known results on the approximation of bifurcation branches in several ways here. We will explicitly consider the use of projection methods, e.g. collocation with splines. Results published to date deal mainly with finite difference methods or more constructive iterative methods based on asymptotic expansions. Our results are more general than those obtained for difference methods in that we allow more general parameter dependence. In the Hopf case, we introduce a new normalization condition and reparameterization to facilitate computation around turning points for the branches.

Section 2 of this paper contains a sketch of our theoretical results justifying the use of projection methods. Section 3 contains computational details in the Hopf case.

2. CONVERGENCE RESULTS. We are interested in two problems. The first has the form

$$\text{(a)} \quad D^m u + \sum_{j=0}^{m-1} a_j(x) D^j u = f(\mu, u) \quad , \quad 0 < x < 1$$

$$\text{(b)} \quad Bu = 0 \qquad \text{(2.1)}$$

where μ is a real parameter, $u(x)$, $a_j(x)$ and $f(\mu,u)$ are real-valued functions and (2.1)(b) represents m real, linear, homogeneous boundary conditions which contain derivatives of u up to order m-1 at x=0 and

x=1. We consider the approximation of solution branches to (2.1) as the parameter μ varies by using projection methods. As an example, let Y_n be the polynomial splines of degree m+k and in C^{m+p} over a partition Δ_n of [0,1]. Let $\{\xi_i\}$ denote a set of collocation points in [0,1]. Then we approximate the solution to (2.1) by solving

$$(2.2) \qquad D^m u_n(\xi_i) + \sum_{j=0}^{m-1} a_j(\xi_i) D^j u_n(\xi_i) = f(\mu, u_n(\xi_i))$$

where $u_n \in Y_n$ and $Bu_n = 0$. For collocation at Gauss points one has $p = -1$. For details on the set up of collocation and other projection methods, see Reddien [7]. Following [7], (2.1) can be expressed in operator form as $v + T(\mu,v) = 0$ (let $v = D^m u$) under suitable assumptions on B, and (2.2) can be written analogously in the form $v_n + P_n T(\mu, v_n) = 0$. Based on these formulations, our approximation results are developed. For simplicity, the known solution branch will be taken to be the zero branch, i.e. $T(\mu,0) = 0$. Let $F(\mu,v)$ be a C^2 mapping from $R \times X \to X$ where X is a Banach space. We later will define F using I+T. We assume (H1) that $F(\mu,0) = 0$ for $|\mu-\mu^*|<1$, (H2) $\text{Null}(F_v(\mu^*,0))$ and $X/\text{Range}(F_v(\mu^*,0))$ are one-dimensional, and (H3) $f_{\mu v}(\mu^*,0)\phi_0$ is not in $\text{Range}(F_v(\mu^*,0))$, where ϕ_0 spans $\text{Null}(F_v(\mu^*,0))$. Let Z be any complement of $\text{Null}(F_v(\mu^*,0))$ in X. We will need the following basic result [2].

Theorem 2.3. (Crandall and Rabinowitz) Let (H1)-(H3) hold. Then there is a neighborhood U of $(\mu^*,0)$ in RxX, an interval I=(-a,a) and continuous functions $\phi: I \to R$ and $\psi: I \to Z$ so that $\phi(0)=\mu^*$, $\psi(0)=0$ and

$$F^{-1}(0) \cap U = \{(\phi(\alpha), \alpha\phi_0 + \alpha z) : |\alpha| < a\} \cup \{(\mu,0) : (\mu,0) \in U\}$$

Moreover, ϕ and ψ are C^2 mappings.

We define $F(\mu,v) = v+T(\mu,v)$ and assume T is such that F satisfies (H1), (H2) and (H3). We assume in addition that (H4) there exists a neighborhood U of $(\mu^*,0)$ in R x X so that $P_n T_v(\mu,v) \to T_v(\mu,v)$ and $P_n T_{\mu v}(\mu,v) \to T_{\mu v}(\mu,v)$ uniformly for (μ,v) in U as $n \to \infty$. Hypothesis (H4) follows easily for the problem (2.1) with the usual collocation projectors [7] in (2.2).

Our convergence proof is an application of the Kantorovich theorem on the convergence of Newton's method. The following version can be applied.

Theorem 2.4. Let P be a mapping defined on a Banach space X_1 into a

Banach space X_2 and let $B(x_0,\rho)$ denote the open ball of radius ρ about x_0. Let P be a C^2 mapping and let:

(1) $||P''(x)|| \leq k$ on $B(x_0,\rho)$

(2) $P'(x_0)$ is onto with $||P'(x_0)^{-1}|| \leq \beta$

(3) $||P'(x_0)^{-1}P(x_0)|| \leq \eta$

(4) $\rho_0 \equiv \dfrac{1 - (1-2h\eta)^{\frac{1}{2}}}{h}$ with $h \equiv \beta\eta k$

satisfy $\rho_0 < \rho$ and $h \leq \frac{1}{2}$. Then $P(x)=0$ has a solution x^* in $\bar{B}(x_0,\rho)$ which is computable by Newton's method starting from x_0. Define $a = (1+(1-2h)^{\frac{1}{2}})\eta/h$. If $a \leq \rho$, then x^* is the unique solution to $P(x)=0$ in $\bar{B}(x_0,\rho_0)$.

Rewrite the problem $F(\mu,v)=0$ in the form $F(\mu,a\phi_0+az)=0$, z in Z, where ϕ_0 and z are defined as earlier. Define

$$f(a,\mu,z) = \begin{cases} a^{-1}F(\mu,a\phi_0+az) & a \neq 0 \\ F_v(\mu,0)(\phi_0+z) & a=0 \end{cases} \tag{2.5}$$

We write (2.1) then in the equivalent form $f(a,\mu,z)=0$. Computationally, a, ϕ_0 and z do not have to be identified, although to do so is often helpful [6]. We further define $F_n(\mu,a\phi_0+az) = P_n\phi_0 + az + P_nT(\mu,aP_n\phi_0+az)$ and define $f_n(a,\mu,z)$ as in (2.5). Then (2.2) can be written in the form $f_n(a,\mu,z)=0$ for fixed a.

To establish our convergence result we apply the Kantorovich theorem to f_n. We take $P: R \times Z \to X$ to be defined by $P(\mu,z) = f_n(a,\mu,z)$. Let $X_1 = R \times Z$ and $X_2 = X$. The proof is a relatively straight forward computation using the fact that from the proof of the Crandall-Rabinowitz theorem, it follows that the map $(\mu,z) \to f(a,\mu,z)$ is continuously Fréchet differentiable and the Fréchet derivative has a bounded inverse at $(0,\mu^*,0)$. We will omit the details.

Theorem 2.6. Let conditions (H1)-(H4) be satisfied. Then there exists an integer N and a real number $a_0 > 0$ so that for all $n \geq N$ and $0 \leq a \leq a_0$, there is a unique solution to the equation $v_n + P_nT(\mu_n,v_n)=0$ of the form $v_n = aP_n\phi_0 + az_n$, z_n in P_nX. Moreover, the following error estimate holds:

$$||(\mu_n,v_n) - (\phi(a\eta), a\phi_0 + a\psi(a))||_\infty =$$
$$O(||\phi_0+\psi(a) - P_n(\phi_0+\psi(a))||_\infty).$$

We have shown that for a fixed value of α_0, accurate approximations are well defined in the vicinity of the bifurcation point. Convergence rates follow from Theorem 2.6 using results in [7].

Hopf bifurcation can be analyzed in an analogous manner. We consider the system

$$\frac{du}{dt} + F(\mu,u)=0 \tag{2.7}$$

where $u\varepsilon R^m$ and $F:RxR^M \to R^m$. Let Ω be a neighborhood of 0 in RxR^m and (A1) let F be in $C^2(\Omega,R^m)$ and (A2) $F(\mu,0)=0$ for $(\mu,0)$ in Ω. We let (0,0) be the Hopf bifurcation point. Define the unknown period to be $2\pi\rho$ and let $\tau=\rho^{-1}t$. Then (2.7) becomes

$$du/d\tau + \rho F(\mu,u)=0 \tag{2.8}$$

and we seek 2π-periodic solutions. We replace τ by t in what follows.

The Banach spaces of 2π-periodic functions in $C^1(R,R^m)$ and $C(R,R^m)$ will be denoted by $C^1_{2\pi}$ and $C_{2\pi}$ respectively with the usual [3] L^∞-norms.

Define $L_0 = F_u(0,0)$. In order to guarantee the existence of periodic solutions near (0,0) we assume (A3) that (a) i is an algebraically simple eigenvalue of L_0 (b) $ni\notin\sigma(L_0)$ for n = 0,2,3, and (A4) by defining continuously differentiable functions $\beta(\mu)$ and $x(\mu)$ near $\mu = 0$ so that

$$F_u(\mu,0)\, x(\mu) = \beta(\mu)\, x(\mu),$$

$\beta(0) = i$ and $x(0)$ spans $\text{Null}(L_0 - iI)$, that $\text{Re}\beta'(0) = 0$.

These assumptions guarantee the existence of continuously differentiable functions (ρ,μ,u): $(-\eta,\eta) \to R \times R \times C^1_{2\pi}$, $\eta>0$, so that

(a) $\rho(\alpha)$, $\mu(\alpha)$, $u(\alpha)$ is a nontrivial solution of (2.8) for α in $(-\eta,\eta)$ and $\alpha \neq 0$ and (b) $\mu(0) = 0$, $u(0) = 0$ and $\rho(0) = 1$. This solution branch is unique up to a translation in t.

For numerical methods, we again consider projection methods as given for example in (2.2). That is, let X_n be a finite dimensional subspace of $C^1_{2\pi}$ and let $Y_n = DX_n \subset C^1_{2\pi}$. We let P_n be a continuous linear projection mapping $C_{2\pi}$ onto Y_n and assume (A5) that $P_n \to I$ as $n \to \infty$. Additionally, we assume that for sets of functions S in $C^1_{2\pi}$ that are uniformly bounded in the norm of $C^1_{2\pi}$, that $P_n \to I$ uniformly over S. Thus we develop approximations u_n to the solution u of (2.8) by solving

$$u_n' + \rho_n P_n F(\mu_n,u_n) = 0,\ u_n \varepsilon X_n. \tag{2.9}$$

Existence, uniqueness and error estimates for solution branches follow again by using a Newton's method argument. The details will appear elsewhere. The basic idea is based on results in [3]. Let ϕ_0 in $C^1_{2\pi}\backslash\{0\}$ satisfy $\phi_0' + L_0\phi_0 = 0$. Let V be a complement of Null $(\frac{d}{dt} + L_0)$ in $C^1_{2\pi}$. Define $H(\rho,\mu,u) = u' + \rho F(\mu,u)$. Then the role of $f(\alpha,\mu,u)$ in the simple bifurcation is played by

$$G(\alpha,\rho,\mu,v) = \begin{cases} \alpha^{-1} H(\rho,\mu,\alpha(\phi_0 + v)) & \alpha\neq 0 \\ H_u(\rho,\mu,0)(\phi_0 + v) & \alpha = 0 \end{cases}$$

where G is a mapping defined on RxRxRxV.

Theorem 2.10. Let conditions (A1)-(A5) be satisfied. Then there exists an integer N and a real number $\alpha_0 > 0$ so that for all $n \geq N$ and $0 < \alpha < \alpha_0$, there is a unique solution (ρ_n,μ_n,u_n) to (2.9) where $u_n = \alpha(P_n\phi_0 + v_n)$, v_n in V. Moreover,

$$||(\rho_n,\mu_n,u_n) - (\rho(\alpha),\mu(\alpha),\alpha\phi_0 + \alpha v(\alpha))||_\infty =$$
$$0(||P_n u_0' - u_0'||_\infty + ||P_n\phi_0 - \phi||_{C^1}).$$

Uniqueness results are somewhat weaker in this case since solutions to (2.8) can be translated. Normalizations are given in the next section.

3. COMPUTATIONAL CONSIDERATIONS. We treat the switching of branches and computations for simple bifurcation using normalizations developed and described by H.B. Keller in the important [5]. Thus we omit details of this case and give only our treatment of Hopf bifurcation as it is apparently new. We present a general continuation method that allows for computation past turning points without added difficulty in the Hopf case. The branch switching techniques of Keller are applicable here. Computational methods for periodic branches have been given by Hassard and Wan [4] and also Langford [6].

The computation of branches of periodic solutions away from a Hopf point is frequently based on their assumed stability. If a branch is unstable and if the system (2.8) consists of two equations, then one can simply replace t by -t. In all other cases direct initial value techniques will be difficult to implement especially if turning points are present along the branch of periodic solutions. Our procedure enables the computation to proceed past turning points as well as along unstable branches. The period of ρ in (2.8) is treated as an unknown; periodicity is imposed as a side condition; and two additional equations regulate the stepsize along the branch and anchor the periodic solution.

Suppose (ρ_0,μ_0,v) is a 2π-periodic solution to (2.8). To find a neighboring solution (ρ,μ,u) a distance s from the given solution, add the condition

$$\theta_1(\rho-\rho)^2 + \theta_2^2(\mu-\mu_0)^2 + \theta_3^2 \|u - v\|_2^2 = s^2 \tag{3.1}$$

where the θ_i are fixed weights and $\|\cdot\|_2$ is the L^2-norm. Eq (3.1) was discretized using Simpson's rule in our computations. Accuracy here is not important. For each $s \neq 0$ the solution u to (2.8)-(3.1) is isolated and unique up to translation in time. For numerical computations u can be anchored by requiring $(u(0) - v(0)) \perp v'(0)$, i.e. that

$$(u(0) - v(0)) \perp f(\mu_0, v(0)) = 0. \tag{3.2}$$

At a Hopf point (μ_0, v_0), $f(\mu_0, v_0) = 0$. It is known that the periodic branch has the asymptotic expansion $u(t,s) = v_0 + s\phi_0(t) + 0(s^2)$ where the function ϕ_0 was defined in Section 2. Thus to switch onto the periodic branch we replace (3.2) by $(u(0) - v(0))^T \phi_0(0) = 0$. The full system can be shown to be well-posed.

The dynamic behavior of a single first order chemical reaction in a continuously stirred tank reactor can be modelled by the ordinary differential equations

$$\begin{aligned} u_1' &= -u_1 + B \cdot Da(1-u_2)e^{u_1} - \beta u_1 \\ u_2' &= -u_2 + Da(1-u_2)e^{u_1} \end{aligned} \tag{3.4}$$

where B, β and Da are dimensionless parameters. An extensive numerical treatment of this problem is reported in [11]. We discretized (3.4) using collocation at Gauss points and continuous quadratic splines. See [7] for definitions. The associated mesh was redistributed regularly along a solution branch to approximately equidistribute arclength. Along periodic branches for (3.4), the solution changes rapidly in a very small interval. Moreover, the location of this interval does not remain fixed. Thus equidistributing the mesh resulted in significant improvement of the numerical results. Using an adaptive mesh, 71 mesh points, and with β=3, B=14, the corresponding bifurcation diagram of [11] was recovered. See Figure 4.1. The solid curve represents the branch of periodic solutions, while the steady state branch appears dashed. A typical result is given in Figure 4.2 where an insufficient number of ten uniformly distributed mesh points is used. Note the abundance of extraneous solutions. The ability of the method to compute past turning points is illustrated here.

REFERENCES

1. K. E. Atkinson, The numerical solution of a bifurcation problem, SIAM J. Numer. Anal. 14(1977), 584-599.
2. M. G. Crandall and P. H. Rabinowitz, Bifurcation from simple eigenvalues, J. Functional Analysis 8(1971), 321-346.

3. M. G, Crandall and P. H. Rabinowitz, The Hopf bifurcation theorem, TSR #1604, Mathematics Research Center, Madison, Wisconsin, 1976.
4. B. Hassard and Y.-H. Wan, Bifurcation formula derived from the center manifold theory, to appear in J. Math. Anal. Appl.
5. H. B. Keller, Bifurcation and nonlinear eigenvalue problems, in Applications of Bifurcation Theory, P. H. Rabinowitz, ed., Academic Press(1977), 359-384.
6. W. F. Langford, Numerical computation of bifurcation problems for ordinary differential equations, Numer. Math. 28(1977), 171-190.
7. G. W. Reddien, Projection methods for two-point boundary value problems, SIAM Review, April(1980).
8. Werner C. Rheinboldt, Numerical methods for a class of finite dimensional bifurcation problems, SIAM J. Numer. Anal. 15(1978), 1-11.
9. R. Seydel, Numerical computation of branch points in ordinary differential equations, Numer. Math. 32(1979), 51-68.
10. Rudiger Seydel, Programme zur numerische Behandlung von Verzweigungsproblemen bei nichtlinearen Gleichungen and Differentialgleichungen, TUM-M8006, Technische Universitat Munchen, February, 1980.
11. A. Uppal, W. H. Ray and A. B. Poore, On the dynamic behavior of continuous stirred tank reactors, Chen. Eng. Sci. 29(1974), 967-985.
12. Helmut Weber, Numerische Behandlung von Verzweigungsproblemen, Numer. Math. 32 (1979), 17-29.
13. Richard Weiss, Bifurcation in difference approximations to two-point boundary value problems, Math. Comp. 29(1975), 746-760.
14. David Westreich and Yaakov L. Varol, Numerical bifurcation at simple eigenvalues, SIAM J. Numer. Anal. 16(1979), 538-546.

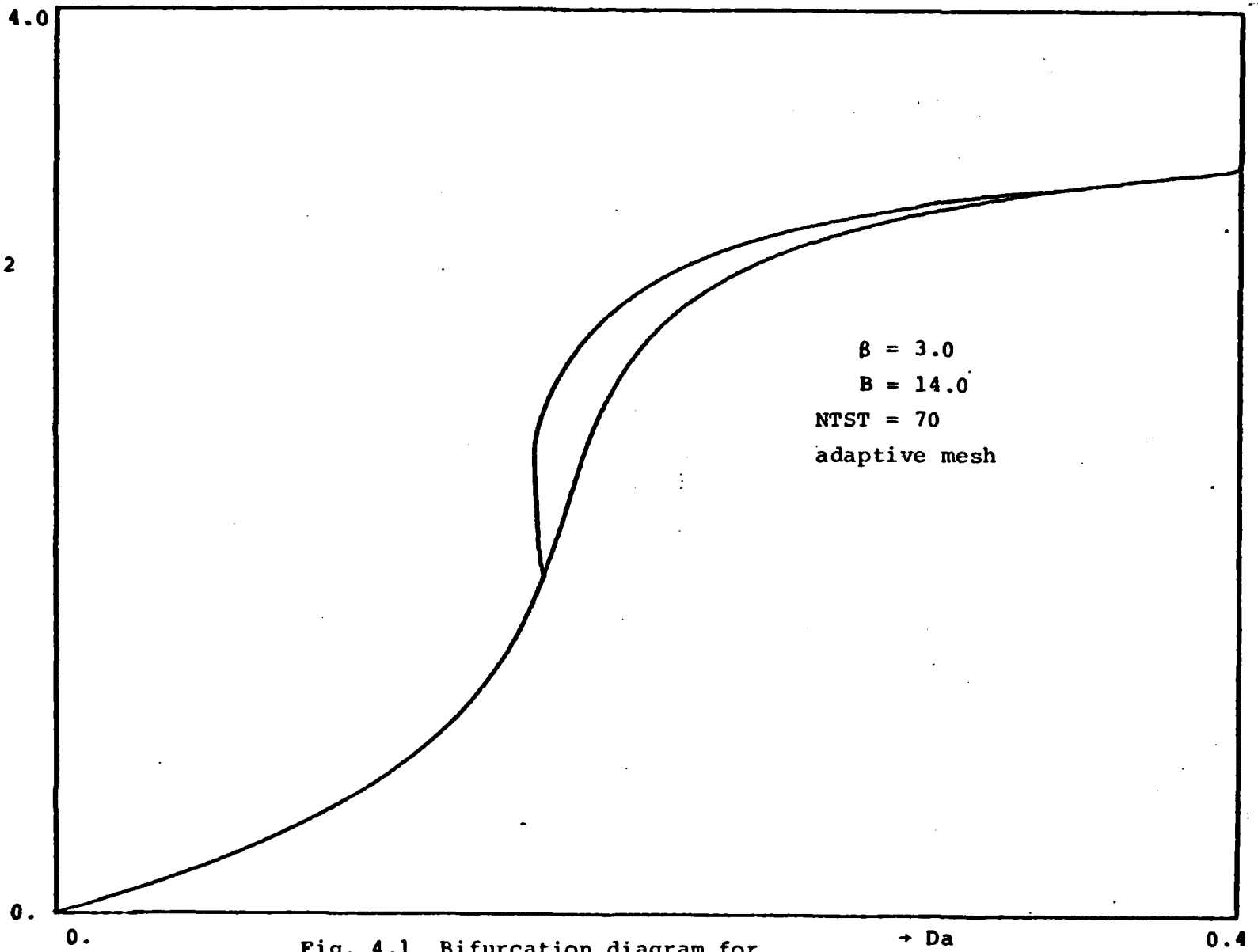

Fig. 4.1 Bifurcation diagram for equation 3.4

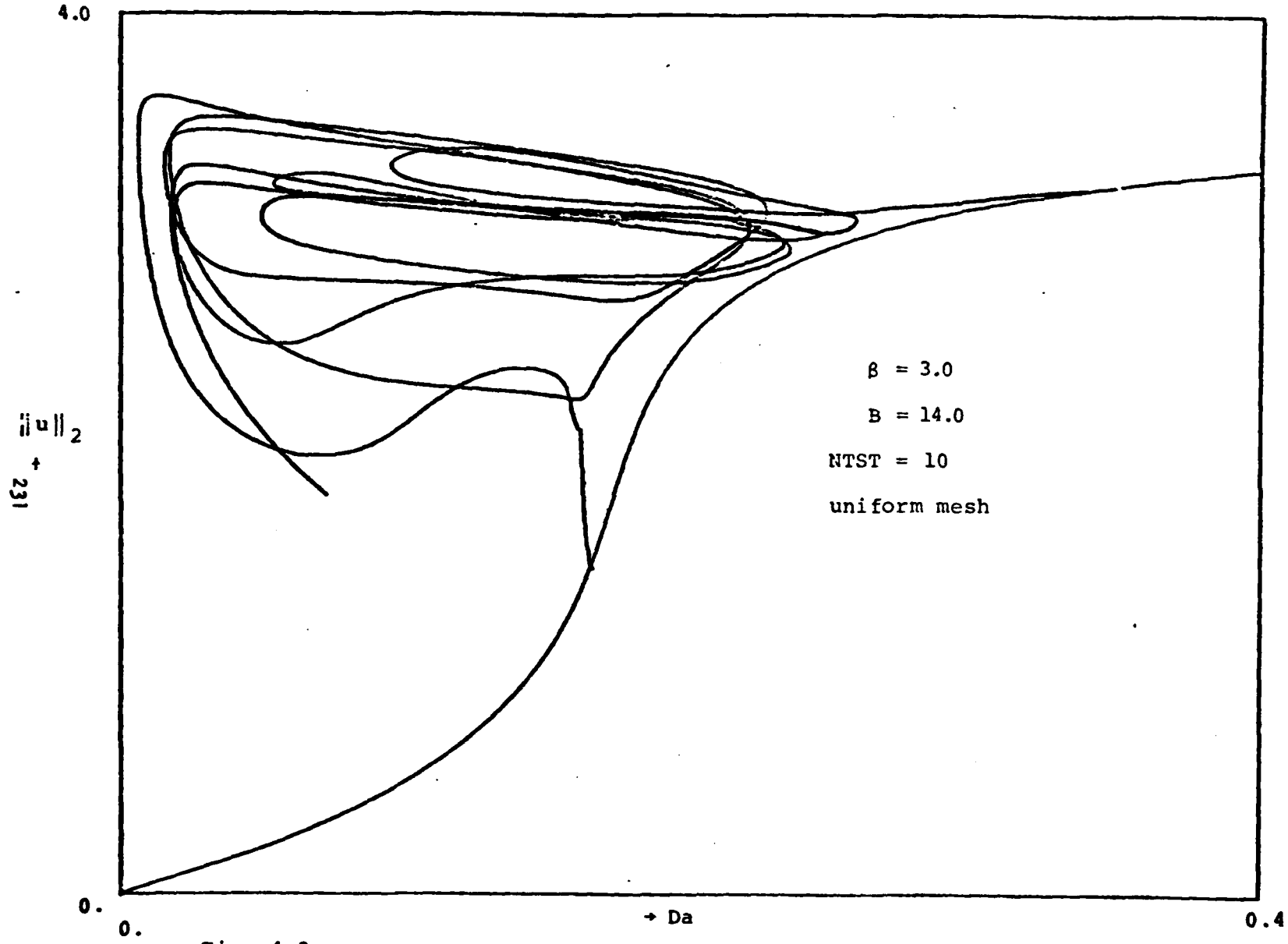

Fig. 4.2 Effect of an inaccurate discretization on the bifurcation diagram of equation 3.4

ON K-LINE AND K × K BLOCK ITERATIVE SCHEMES FOR A PROBLEM ARISING IN 3-D ELLIPTIC DIFFERENCE EQUATIONS*

Seymour V. Parter[1]

and

Michael Steuerwalt[2]

Dedicated to Garrett Birkhoff
on the occasion of his seventieth birthday

[1]Computer Sciences Department, University of Wisconsin-Madison, Madison, WI 53706

[2]University of California, Los Alamos Scientific Laboratory, Los Alamos, NM 87545

*This work was supported by the U.S. Department of Energy under Contract No. W-7405-ENG-36, and by the Office of Naval Research under Contract No. N00014-76-C-0341.

ON K-LINE AND K × K BLOCK ITERATIVE SCHEMES FOR A PROBLEM ARISING IN 3-D ELLIPTIC DIFFERENCE EQUATIONS

by

Seymour V. Parter

and

Michael Steuerwalt

ABSTRACT

Novel computer architectures and a desire to solve three-dimensional problems have together aroused new interest in iterative methods for computing solutions to elliptic difference equations. Block iterative methods are particularly attractive for vector machines, such as the CRAY-1. Schemes that take the basic block to be a plane reduce a three-dimensional elliptic system to two-dimensional systems, to which block methods are again applicable. We analyze the convergence rate of k-line and k × k block iterative methods for solving these two-dimensional problems.

---

1. INTRODUCTION

Some years ago there was great interest in iterative methods for solving elliptic difference equations: see [1, 12, 13, 21, 22, 23, 24]. Recently there has been more emphasis on finite element equations ([2, 4, 5, 20, 25]) and direct methods of solution ([7, 8, 11, 17, 18]). Nevertheless, in practice, particularly in the case of three-dimensional problems (see [9, 11, 19]), finite difference equations are frequently used and they are commonly solved by an iterative method, usually some variant of the SOR method. Furthermore, the advent of new computer architectures, "vector machines" and "parallel processors," has stimulated a search for iterative schemes that are particularly efficient for these machines.

We examine two block schemes that arise in this way. Consider the three-dimensional model problem

$$
\begin{aligned}
& -\Delta_h(3)\, U = f \quad , \quad (x_i, y_j, z_n) \in \Omega \\
& U = g \quad , \quad (x_i, y_j, z_n) \in \partial\Omega
\end{aligned}
\tag{1.1}
$$

where

$$
(x_i, y_j, z_n) = (ih, jh, nh) \quad , \quad 0 \leq i,j,n \leq P + 1 \tag{1.2}
$$

are the grid points in the unit cube Ω with

$$
h = \frac{1}{P + 1} \quad , \tag{1.3}
$$

and $\Delta_h(3)$ is the usual 7 point discrete approximation to the Laplace operator, given by

$$
(\Delta_h(3))_{ijn} = \begin{cases} \dfrac{U_{i+1,j,n} - 2\,U_{ijn} + U_{i-1,j,n}}{h^2} + \\ \dfrac{U_{i,j+1,n} - 2\,U_{ijn} + U_{i,j-1,n}}{h^2} + \\ \dfrac{U_{i,j,n+1} - 2\,U_{ijn} + U_{i,j,n-1}}{h^2} \end{cases} . \tag{1.4}
$$

Suppose that one has decided to use a "plane" iterative method, probably block SOR where each block is the set of unknowns

$$
\tilde{U}_n = \left\{ U_{i,j,n} \; ; \; 1 \leq i,j \leq P \right\} \tag{1.5}
$$

associated with a plane n = constant. Now we must solve the equations in each plane. With $V = \tilde{U}_n$, these equations can be written as

$$(1.6) \qquad 6V_{ij} - V_{i+1,j} - V_{i-1,j} - V_{i,j+1} - V_{i,j-1} = F_{ij}, \quad 1 \le i,j \le P .$$

We consider two block iterative schemes for the solution of (1.6). These are

(i) <u>k-line iterative scheme</u>: In this scheme each block consists of the unknowns V_{ij} associated with the points on k consecutive horizontal lines. These blocks are indexed by a single index, say s. We have

$$(1.7) \qquad \tilde{V}_s = \left\{ V_{i,k(s-1)+\mu} \; ; \; 1 \le \mu \le k \right\} .$$

(ii) <u>k × k block iterative scheme</u>: In this scheme each block consists of the unknowns V_{ij} associated with the points in a k × k square. It is easiest to describe this block with a double index (r,s). The (r,s) block is

$$(1.8) \qquad \tilde{V}_{rs} = \left\{ V_{k(r-1)+i,k(s-1)+j} \; ; \; 1 \le i,j \le k \right\} .$$

Because each of these block structures satisfies block property A (see [1, 22, 24]) the spectral radii of the Gauss-Seidel method and the SOR method (as well as the optimal overrelaxation parameter ω_b) are determined by the spectral radius of the block Jacobi scheme.

From the analysis of the corresponding block iterative methods applied to the two-dimensional Poisson problem (see [3, 14, 15]), one might expect that these spectral radii behave like 1/k. Unfortunately, this is not the case. In fact, if $\rho(SkL)$ and $\rho(SkB)$ are the spectral radii of the block Jacobi iterative methods based on the blocks (1.7) and (1.8) respectively, applied to (1.6), we find that both $\rho(SkL)$ and $\rho(SkB)$ have nonzero limits as $k \to \infty$!

In Section 3 we give the results for the case k = 1. These results are obtained immediately by tensor product methods.

In Section 4 we begin our analysis of $\rho(SkL)$ and $\rho(SkB)$. We use a variant of "separation of variables" to reduce the problem to a one-dimensional eigenvalue problem involving tridiagonal matrices.

In Section 5 we obtain the basic estimates of the spectral radii; loosely speaking, if $P/k \geq 2$, then

$$\rho(SkL) \to 2 - \sqrt{3} + 0(h^2) = .267949 + 0(h^2) \tag{1.9}$$

$$\rho(SkB) \to 1/2\ (3 - \sqrt{5}) + 0(h^2) = .381966 + 0(h^2)\ .$$

Two sets of approximate values for $\rho(SkL)$ and $\rho(SkB)$ are given in the following tables. For $k \geq 3$ the results are correct up to a term that is $0(h^2)$.

k	$\rho_1(SkL)$	$\rho_2(SkL)$
1	$1/2 - 3\pi^2h^2/8$	$1/2 - 3\pi^2h^2/8$
2	$1/3 + 0(h)$	$1/3 + 0(h)$
3	.268541 ± .185(-1)	.286398 ± .684(-3)
4	.267987 ± .483(-2)	.272772 ± .443(-4)
6	.267949 ± .344(-3)	.268293 ± .221(-6)
8	.276949 ± .247(-4)	.267974 ± .114(-8)
12	.267949 ± .127(-6)	.267949 ± .302(-13)
14	.267949 ± .913(-8)	.267949
18	.267949 ± .471(-10)	
24	.267949 ± .178(-13)	
27	.267949	

Figure 1.

k	ρ_1(SkB)	ρ_2(SkB)
1	$2/3 - \pi^2h^2/3$	$2/3 - \pi^2h^2/3$
2	$1/2 + 0(h)$	$1/2 + 0(h)$
3	.384848 ± .515(-1)	.432468 ± .390(-2)
4	.382296 ± .187(-1)	.400477 ± .477(-2)
6	.381972 ± .266(-2)	.384625 ± .934(-5)
8	.381966 ± .387(-3)	.382353 ± .196(-6)*
12	.381966 ± .824(-5)	.381974 ± .888(-10)
14	.381966 ± .120(-5)	.381967 ± .189(-11)
16	.381966 ± .175(-6)	.381966 ± .409(-13)
18	.381966 ± .256(-7)	.381966
24	.381966 ± .795(-10)	
30	.381966 ± .247(-12)	
36	.381966	

Figure 2.

In these tables the shorthand .185(-1) stands for $.185 \times 10^{-1}$. Note that the tolerances for ρ_2 are smaller than the tolerances for ρ_1, even though the estimates ρ_1 appear to converge more rapidly.

As we indicated above, the Jacobi spectral radius determines the spectral radii of the Gauss-Seidel and SOR methods. For the Gauss-Seidel scheme, neglecting $0(h^2)$ terms,

$$\rho(S_\infty L\text{-}GS) = \rho(S_\infty L)^2 = .071797 \tag{1.10}$$

$$\rho(S_\infty B\text{-}GS) = \rho(S_\infty B)^2 = .145898 \quad .$$

The optimal ω for the SOR method is given by

$$\omega_b = 2 / \left(1 + \sqrt{1-\rho^2}\right)$$

where ρ is the spectral radius of the Jacobi method (see [22]), and with this choice of ω

$$\rho(SOR) = \omega_b - 1 \quad .$$

Hence

$$\rho(S\infty L\text{-}SOR) = .018624 \tag{1.11}$$
$$\rho(S\infty B\text{-}SOR) = .039406 \quad .$$

Figures 1 and 2 show that in a plane iterative method for (1.1) the inner iterations to solve (1.6) need not use a very large k. Indeed, at k = 8 the spectral radii have essentially reached their asymptotic values.

We describe some computational results in Section 6. Finally, in Section 7 we briefly discuss block iterative methods for two- and three-dimensional problems in the context of vector machines such as the CRAY-1.

But one important comment should be made now. Our analysis seems to be very special and perhaps limited to model problems. On the other hand, standard elliptic problems of great generality can be analyzed by the methods of [3, 13, 15]. Unfortunately, those methods do not, and apparently cannot, apply to the strongly diagonally dominant problem (1.6). Elliptic problems discussed in the earlier works are regular problems, while (1.6) corresponds to a two-dimensional discrete singular perturbation problem

$$-h^2 \Delta_h(2)\, U + 2\, U = F \quad . \tag{1.12}$$

For this reason, and to distinguish from the notation used in [15], we designate the spectral radii as $\rho(SkL)$ and $\rho(SkB)$.

We are indebted to Dan Boley, Bill Buzbee, and Molly Mahaffy for much support and encouragement during the evolution of this work. Bill Buzbee aroused our interest in the problem and provided the basic support, as well as many fruitful discussions. Dan

Boley wrote the original code that was used for experimentation and optimization of the results of [3]. Molly Mahaffy revised Boley's code and carried out the computations described in Section 6. These computations were performed on the Cray-1 at the Los Alamos Scientific Laboratory.

2. Iterative Methods

In this section we describe the basic iterative schemes of interest. Consider a system of linear equations

$$AX = Y \tag{2.1}$$

where A is an R × R matrix. Block iterative schemes for the solution of (2.1) are completely described by describing a partition of the R-vectors into blocks. Specifically, suppose we imagine all R-vectors X partitioned into block vectors of the form

$$X = (X_1, X_2, \ldots, X_{R'})^t \tag{2.2}$$

where each X_j is itself an R_j-vector and (of course)

$$\sum_{j=1}^{R'} R_j = R \ . \tag{2.3}$$

Corresponding to this partition of vectors the matrix A is naturally partitioned into blocks

$$A = A_{ij} \ .$$

where each A_{ij} is itself an $R_i \times R_j$ matrix. The block Jacobi

iterative scheme associated with this block structure is now given by

$$A_{jj}\, X_j^{(\nu+1)} = -\sum_{j \neq s} A_{js}\, X_s^{(\nu)} + Y_j \quad . \tag{2.4}$$

The corresponding Gauss-Seidel iterative scheme is

$$A_{jj}\, X_j^{(\nu+1)} = -\sum_{j>s} A_{js}\, X_s^{(\nu+1)} - \sum_{j<s} A_{js}\, X_s^{(\nu)} + Y_j \quad , \tag{2.5}$$

while the successive overrelaxation (SOR) iterative scheme with overrelaxation parameter ω is

$$A_{jj}\, X_j^{(\nu+1)} = -\omega \sum_{j>s} A_{js}\, X_s^{(\nu+1)} - \omega \sum_{j<s} A_{js}\, X_s^{(\nu)} + A_{jj}(1-\omega)\, X_s^{(\nu)} + \omega\, Y_j \quad . \tag{2.6}$$

In every case we have a splitting

$$A = M - N \quad , \tag{2.7}$$

and the iterative scheme takes the form

$$M\, X^{(\nu+1)} = N\, X^{(\nu)} + Y \quad . \tag{2.8}$$

In particular, for the block Jacobi scheme

$$M = \text{diagonal}\ (A_{ii}). \tag{2.9}$$

For any such splitting, let

$$\rho = \max \left\{ |\lambda| \ ; \ \det(\lambda M - N) = 0 \right\} . \tag{2.10}$$

It is well known ([6, 10, 22]) that if A is nonsingular then the iterates $X^{(\nu)}$ converge to the unique solution X of (2.1) independently of $X^{(0)}$ if and only if

$$\rho < 1 \quad . \tag{2.11}$$

Returning to our problem (1.6), we see that our vector X is an R-vector, with $R = P^2$, corresponding to the two-dimensional grid vector $\tilde{U}_n = V$. Furthermore, (1.7) and (1.8) define two distinct partitions of V.

It is not difficult to see that both partitions lead to Jacobi iterative schemes that satisfy block property A. Hence the Gauss-Seidel spectral radius and the SOR spectral radius, as well as the optimal choice of ω, are determined by the spectral radius ρ of the Jacobi iterative scheme.

The problem studied in this report is: for each of the block Jacobi schemes, k-line and k × k block, determine the asymptotic behavior of ρ as $P \to \infty$ (i.e., as $h \to 0$).

We therefore study the generalized eigenvalue problem

$$\lambda M V = N V \tag{2.12}$$

where M is given by (2.9) for the two partitions (1.7), (1.8). In addition to block property A these splittings also have the following properties:

$$\begin{aligned} &M = M^* = M^t, \quad N = N^* = N^t \ , \\ &M \text{ is positive definite,} \\ &N \text{ is nonnegative (each of its entries is nonnegative),} \\ &M \text{ is an M-matrix (its inverse is nonnegative).} \end{aligned} \tag{2.13}$$

3. Estimating ρ, k = 1

The case k = 1 is easily handled by the method of tensor products: see [12, 23]. Here we merely record the results.

Let $\rho(S1L)$ denote the spectral radius of the Jacobi iterative scheme based on a block partition into single lines. Then

$$\rho(S1L) = \frac{2 \cos \pi h}{6 - 2 \cos \pi h} \cong \frac{1}{2} \left(1 - \frac{3}{4} \pi^2 h^2\right) . \tag{3.1}$$

Let $\rho(S1^2B)$ denote the spectral radius of the 1×1 block Jacobi iterative scheme. This is "point" relaxation and we have

$$\rho(S1^2B) = \frac{4 \cos \pi h}{6} \cong \frac{2}{3} \left(1 - \frac{1}{2} \pi^2 h^2\right) . \tag{3.2}$$

4. Estimating ρ, $k \geq 2$. Preliminaries

In this section we develop some general properties of our particular Jacobi iterative schemes. We use these properties to reduce the problems to one-dimensional eigenvalue problems essentially via "separation of variables."

Because our splittings satisfy block property A we know that <u>if</u> λ <u>is an eigenvalue of (2.12), so is</u> $-\lambda$ (see [22, 23, 24]). M is positive definite and N is symmetric, so all the eigenvalues of (2.12) are real (see [6]), and thus ρ is characterized by

$$\rho = \max_{X \neq 0} \frac{(NX, X)}{(MX, X)} \tag{4.1}$$

where $(\ ,\ )$ denotes the usual vector inner product

$$(X, Y) = X^t \overline{Y} = \sum x_i \overline{y}_i . \tag{4.2}$$

Let $k \geq 2$ be a fixed integer less than P. Assume that P is chosen so that k divides P -- that is, for some integer Q,

$$P = kQ . \tag{4.3}$$

A unified approach to our two problems is provided by the following convenient representation of N in each case. Consider the one-dimensional operator $\tilde{N}$ acting on vectors

$$(4.4) \qquad \phi = (\phi_1, \phi_2, \ldots, \phi_p)^t$$

as follows: for $1 \le s \le Q-1$, $0 \le j \le k-1$,

$$(4.5) \qquad (\tilde{N}\,\phi)_{ks+j} = \begin{cases} 0 & , \quad 2 \le j \le k-1 \\ \phi_{ks+1}, & j = 0 \\ \phi_{ks} & , \quad j = 1 \end{cases} .$$

Let N_x and N_y be the two-dimensional operators which act on grid vectors $V = (V_{ij})$ in the following manner: N_x acts on V only in the x direction, i.e., the first subscript, and in that direction N_x acts as $\tilde{N}$. Similarly N_y acts on V only in the y direction. For example, for $1 \le s \le Q-1$, $0 \le i \le k-1$

$$(4.6) \qquad (N_x\,V)_{ks+i,j} = \begin{cases} 0 & , \quad 2 \le i \le k-1 \\ V_{ks+1,j}, & i = 0 \\ V_{ks,j} & , \quad i = 1 \end{cases} .$$

A careful examination of the two partitions of the matrix A yields the first lemma.

Lemma 4.1: For the k-line Jacobi iterative scheme

$$(4.7a) \qquad N = N_y \quad .$$

For the $k \times k$ block Jacobi iterative scheme

$$(4.7b) \qquad N = N_x + N_y \quad .$$

Lemma 4.2: Let $\rho(SkL)$ and $\rho(SkB)$ be the spectral radii of the k-line and $k \times k$ block Jacobi iterative schemes respectively. Then

$$\frac{1}{k+1} + 0(h) \leq \rho(SkL) \leq \frac{1}{3} \quad , \tag{4.8a}$$

$$\frac{2}{k+2} + 0(h) \leq \rho(SkB) \leq \frac{1}{2} \quad . \tag{4.8b}$$

Proof: We first obtain the lower bounds of (4.8). Let $U = (U_{ij})$ be the grid vector

$$U_{ij} = \sin \pi ih \cdot \sin \pi jh \quad . \tag{4.9}$$

Then

$$\frac{(NU,U)}{(MU,U)} = \frac{(NU,U)}{(AU,U) + (NU,U)} \quad .$$

However, U is an eigenvector for A and

$$AU = (6 - 4 \cos \pi h)U \cong (2 + 0(h^2))U \quad ,$$

whence

$$\frac{(NU,U)}{(MU,U)} = \frac{(NU,U)}{(2 + 0(h^2))\ (U,U) + (NU,U)} \quad . \tag{4.10}$$

A direct calculation using the "smoothness" of U and the form of $\tilde{N}$ (see [3, 14, 15]) shows that

$$\begin{aligned} (N_x U,U) &= (2/k + 0(h))\ (U,U) \\ (N_y U,U) &= (2/k + 0(h))\ (U,U) \quad . \end{aligned} \tag{4.11}$$

We put (4.7) and (4.11) into (4.10) and use (4.1) to obtain the lower bounds of (4.8).

Let V be an eigenvector associated with the eigenvalue ρ. Then

$$\rho M V = N V \quad .$$

Subtracting ρNV from both sides gives

$$A V = \mu N V \tag{4.12a}$$

where

$$\mu = \frac{1 - \rho}{\rho} \quad . \tag{4.12b}$$

Hence

$$(AV,V) = \mu(NV,V) \quad . \tag{4.13}$$

It is an easy matter to see, using the explicit eigenvalue of A or the Gerschgorin theorem, that

$$(AV,V) \geq 2(V,V) \quad . \tag{4.14a}$$

Moreover, the definition of N shows that

$$(N_y V,V) \leq (V,V) \tag{4.14b}$$

$$\left(\left[N_x + N_y\right] V,V\right) \leq 2 (V,V) \quad . \tag{4.14c}$$

Thus (4.13) and (4.14a), together with (4.14b) or (4.14c), show that $2 \leq \mu$ or $2 \leq 2\mu$, respectively. The upper bounds of (4.8) now follow at once.

Let

$$\sigma = \frac{1}{\mu} \quad . \tag{4.15}$$

We rewrite (4.12a) as

$$\sigma A V = N V \quad . \tag{4.16}$$

Any positive eigenvalue σ of (4.16) corresponds to a positive eigenvalue λ of (2.12) and conversely via the relationships

$$\sigma = \frac{\lambda}{1 - \lambda} \tag{4.17a}$$

$$\lambda = \frac{\sigma}{1 + \sigma} \quad . \tag{4.17b}$$

Because σ is a monotone increasing function of λ (and conversely) we seek the largest positive eigenvalue σ of (4.16). But A^{-1} is a positive matrix and $N \neq 0$ is a nonnegative matrix, so by the Perron-Frobenius theory [22] the largest positive eigenvalue of (4.16) is its spectral radius, and the associated eigenvector V may be taken nonnegative.

Let us study the eigenvalue problem (4.16). Because A is positive definite and N is symmetric there is a complete set of eigenvectors $V^{(\nu)}$, $\nu = 1, 2, \ldots, P^2$.

We attempt to apply "separation of variables" to this eigenvalue problem.

Case 1: The k-line scheme.

For each n, $1 \leq n \leq P$, let

$$V_{ij}^{(n)} = \sin \pi i n h \, \phi_j^{(n)} \quad , \quad 1 \leq i,j \leq P \quad . \tag{4.18}$$

Substitution into (4.16) with $N = N_y$ yields

$$\sigma A_n \phi^{(n)} = \tilde{N} \phi^{(n)} \quad , \tag{4.19a}$$

where A_n is the tridiagonal matrix

$$A_n = [-1, 6 - 2 \cos \pi nh, -1] \quad . \tag{4.19b}$$

Each A_n is positive definite, so each eigenvalue problem (4.19a) has P linearly independent eigenvectors, say $\phi^{(n)}(r)$, r = 1, 2, ..., P. Now the vectors given by

$$V_{ij}^{(n)} = \sin \pi inh \, \phi_j^{(n)}(r) \tag{4.20}$$

are P^2 linearly independent eigenvectors of (4.16). Hence all the eigenvalues of (4.16) are given by the eigenvalues of the P eigenvalue problems (4.19a), n = 1, 2, ..., P.

We therefore seek the largest positive eigenvalue σ of the P eigenvalue problems (4.19a). However, each A_n is not only positive definite but also an M-matrix, i.e., A_n^{-1} is a positive matrix. Because $\tilde{N}$ is a nonnegative matrix, the largest positive eigenvalue of (4.19a) is also the spectral radius of that problem. Moreover, the associated eigenvector $\phi^{(n)}$ may be taken nonnegative. Assume that has been done. Then both V, the eigenvector of (4.16) associated with σ, and $\phi^{(n)}$, the eigenvector of (4.19a) associated with σ, must be nonnegative. Therefore the representation (4.20) shows that we must have n = 1. We summarize these facts in the following lemma.

Lemma 4.3: Consider the k-line iterative scheme with $2 \leq k < P$ and (4.3) holding. Then

$$\rho(SkL) = \frac{\sigma}{1 + \sigma}$$

where σ is the largest positive eigenvalue, and the spectral radius, of the eigenvalue problem

(4.21) $$\sigma A_1 \phi = \tilde{N} \phi$$

and A_1 is given by (4.19b) with $n = 1$.

Case 2: The $k \times k$ block scheme.

This case is a bit more complicated, so we proceed with a more formal development of the argument.

Lemma 4.4: Let $N = N_x + N_y$. Consider the eigenvalue problem (4.16) Let $\bar{\sigma}$ be the largest positive eigenvalue. Then $\bar{\sigma}$ is a simple eigenvalue: there is only one linearly independent eigenvector associated with $\bar{\sigma}$. Moreover, the associated eigenvector may be taken to be strictly positive.

Proof: Consider the matrix $A^{-1}N$. Because A^{-1} is a positive matrix and N is a nonnegative matrix not identically zero, every column of $A^{-1}N$ is either the zero vector or a strictly positive vector. Let T be the permutation matrix which collects the positive columns into the first r columns, so that

(4.22) $$B = T^t A^{-1} N T = \begin{bmatrix} B_{11} & 0 \\ B_{21} & 0 \end{bmatrix} .$$

Here B_{11} is an $r \times r$ positive matrix and B_{21} is a $(P^2 - r) \times r$ positive matrix. Let

$$U = \begin{bmatrix} X \\ Y \end{bmatrix}$$

be an eigenvector of B with associated eigenvalue λ. Then

(4.23a) $$B_{11} X = \lambda X ,$$

(4.23b) $$B_{21} X = \lambda Y .$$

Thus λ and X are an eigenvalue and associated eigenvector of B_{11}. In particular, if $\lambda = \bar{\sigma}$ then, because B_{11} is strictly positive, there is only one linearly independent eigenvector X and X can be taken strictly positive. Since (4.23b) determines Y uniquely in terms of X, the lemma is proven.

We are now ready to reduce the eigenvalue problem (4.16) to a one-dimensional problem.

Lemma 4.5: Let $N = N_x + N_y$ and consider the eigenvalue problem (4.16). Let $\bar{\sigma}$ be the largest positive eigenvalue. Then $\bar{\sigma}$ is also determined as the largest positive eigenvalue of the eigenvalue problem

$$\sigma B \phi = \tilde{N} \phi \tag{4.24}$$

where

$$\phi = (\phi_1, \phi_2, \ldots, \phi_p)^t \tag{4.25a}$$

and B is the tridiagonal matrix

$$B = [-1, 3, -1] \quad . \tag{4.25b}$$

Proof: The matrix B is both an M-matrix and positive definite. Therefore the eigenvalue problem (4.24) has P linearly independent eigenvectors. Moreover, if σ_0 is the largest positive eigenvalue the associated eigenvector ϕ^0 may be taken strictly positive.

Let σ be an eigenvalue of (4.24) and let ϕ be an associated eigenvector. Let the grid vector V be given by

$$V_{ij} = \phi_i \phi_j \quad . \tag{4.26}$$

Then

$$\sigma(AV)_{ij} = \sigma \phi_i (B\phi)_j + \sigma \phi_j (B\phi)_i \quad .$$

We apply (4.24) to see that

$$\sigma(AV)_{ij} = \phi_i(\tilde{N}\phi)_j + \phi_j(\tilde{N}\phi)_i$$
$$= (N_y V)_{ij} + (N_x V)_{ij} = (NV)_{ij} \quad .$$

In other words, the grid vector V is an eigenvector of (4.16) with associated eigenvalue σ. In particular, if $\sigma = \sigma_0$ and $\phi = \phi^0$ then the grid vector V is not only an eigenvector of (4.16), it is a strictly positive eigenvector! Hence, by virtue of lemma 4.4, the V so obtained is an eigenvector of (4.16) associated with $\bar{\sigma}$, the largest positive eigenvalue of (4.16). This proves the lemma.

5. Estimating ρ, $k \geq 3$

In this section we study the one-dimensional eigenvalue problems (4.21), (4.24). We shall first reduce the problem still further by eliminating from (4.21) and (4.24) variables corresponding to those equations in which

$$(\tilde{N}\phi)_j = 0$$

In order to do this we require a specific representation of the solution of tridiagonal systems of equations.

Let $k \geq 3$ be fixed.

Lemma 5.1: Consider the system of linear equations

(5.1a) $$-\phi_{j-1} + \beta\phi_j - \phi_{j+1} = 0 \quad , \qquad j = 1, 2, \ldots, k-2$$

where ϕ_0 and ϕ_{k-1} are given and

(5.1b) $$\beta > 2 \quad .$$

Let E_j, $j = 0, 1, \ldots, k-2$ be generated by the recursive scheme

$$E_0 = 0$$

(5.2)
$$E_j = \frac{1}{\beta - E_{j-1}} \quad , \qquad j = 1, 2, \ldots, k-2,$$

and set

$$a_k = E_1 E_2 \cdots E_{k-2} \quad ,$$

(5.3)
$$b_k = E_{k-2} \quad .$$

Then

(5.4a) $$\phi_1 = b_k \phi_0 + a_k \phi_{k-1} \quad ,$$

(5.4b) $$\phi_{k-2} = a_k \phi_0 + b_k \phi_{k-1} \quad .$$

Furthermore

(5.5) $$0 < E_j \leq E_{j+1} \leq 1 \quad ,$$

and as k tends to ∞

(5.6a) $$b_k = E_{k-2} \to \frac{1}{2}\left(\beta - \sqrt{\beta^2 - 4}\right),$$

(5.6b) $$a_k \to 0 \quad .$$

Proof: The formulae (5.4a), (5.4b) are obtained from the well known algorithm for solving diagonally dominant tridiagonal systems; see [16, 10]. The monotonicity of the E_j and the bound given in (5.5) are also well known and easily established by induction. Finally, if $k \to \infty$ then E_{k-2} must converge to E_∞, a solution of

$$E^2 - \beta E + 1 = 0 \quad .$$

Because one root is bigger than 1 and the other is smaller, the bound (5.5) implies that E_∞ must be the smaller root. This proves (5.6a), and (5.6b) follows immediately.

Returning to the eigenvalue problems (4.21) and (4.24), let $1 \le s \le Q-2$ and consider the equations satisfied by ϕ_{ks+2}, ϕ_{ks+3}, ..., ϕ_{ks+k-1}. For the corresponding equations we have $(\tilde{N}\phi)_j = 0$. Hence

$$(5.7) \qquad -\phi_{ks+j-1} + \beta\phi_{ks+j} - \phi_{ks+j+1} = 0 \quad , \quad j = 2, 3, \ldots, k-1$$

where ϕ_{ks+1} and $\phi_{k(s+1)}$ can be taken as known. In these equations

$$(5.8a) \qquad \beta = 6 - 2\cos \pi h$$

for the eigenvalue problem (4.21) and

$$(5.8b) \qquad \beta = 3$$

for the eigenvalue problem (4.24). In either case we use lemma 5.1 together with the equations numbered ks for $s = 2, 3, \ldots, Q-1$ and the equations numbered $ks + 1$ for $s = 1, 2, \ldots, Q-2$ to eliminate ϕ_{ks+j}, $j = 2, 3, \ldots, k-1$ and $s = 1, 2, \ldots, Q-2$. For example, the ks equation is

$$\sigma\left[-\phi_{ks-1} + \beta\phi_{ks} - \phi_{ks+1}\right] = \phi_{ks+1} \ .$$

If $2 \le s \le Q-1$, then with the appropriate choice of a_k and b_k we have

$$\phi_{ks-1} = b_k\,\phi_{ks} + a_k\,\phi_{k(s-1)+1} \ .$$

We thus obtain for $2 \le s \le Q-1$

$$(5.9) \qquad \sigma\left[-a_k\,\phi_{k(s-1)+1} + (\beta - b_k)\,\phi_{ks} - \phi_{ks+1}\right] = \phi_{ks+1} \ .$$

Similarly, the (ks + 1) equation is

$$\sigma \left[- \phi_{ks} + \beta \phi_{ks+1} - \phi_{ks+2} \right] = \phi_{ks} \quad .$$

If $1 \leq s \leq Q-2$, then with the appropriate choice of a_k and b_k we have

$$\phi_{ks+2} = a_k \phi_{k(s+1)} + b_k \phi_{ks+1} \quad .$$

Thus we have, for $1 \leq s \leq Q-2$,

$$\sigma \left[- \phi_{ks} + (\beta - b_k)\phi_{ks+1} - a_k \phi_{k(s+1)} \right] = \phi_{ks} \quad . \tag{5.10}$$

Now we must eliminate $\phi_1, \phi_2, \ldots, \phi_{k-1}$ and $\phi_{k(Q-1)+2}, \phi_{k(Q-1)+3}, \ldots, \phi_{kQ}$. In these cases we have a system of k - 1 unknowns. However, the procedure is exactly the same. We collect our results in

Lemma 5.2. Let $\sigma \neq 0$ and ϕ be an eigenvalue and eigenvector respectively of (4.21) or (4.24). Let a_k, b_k, and b_{k+1} be given by (5.3) with the appropriate choice of β, either (5.8a) or (5.8b). Let

$$\xi_{2s-1} = \phi_{ks} \quad , \quad s = 1, 2, \ldots, Q-1 \quad , \tag{5.11a}$$

$$\xi_{2s} = \phi_{ks+1} \quad , \quad s = 1, 2, \ldots, Q-1 \quad . \tag{5.11b}$$

Let

$$\mu = 1/\sigma \quad , \quad \gamma = 1 + \mu \quad . \tag{5.11c}$$

Then γ and $\xi_1, \ldots, \xi_{2(Q-1)}$ satisfy the homogeneous system

(5.12a) $$(\beta - b_{k+1})\xi_1 - \gamma\,\xi_2 = 0$$

(5.12b) $$-\gamma\,\xi_1 + (\beta - b_k)\xi_2 - a_k\,\xi_3 = 0$$

(5.12c) $$-a_k\,\xi_{2s} + (\beta - b_k)\xi_{2s+1} - \gamma\xi_{2s+2} = 0,$$
$$s = 1, 2, \ldots, Q-3$$

(5.12d) $$-\gamma\,\xi_{2s+1} + (\beta - b_k)\xi_{2s+2} - a_k\xi_{2s+3} = 0,$$
$$s = 1, 2, \ldots, Q-3$$

(5.12e) $$-a_k\,\xi_{2(Q-2)} + (\beta - b_k)\xi_{2(Q-2)+1} - \gamma\,\xi_{2(Q-1)} = 0$$

(5.12f) $$-\gamma\,\xi_{2(Q-2)+1} + (\beta - b_{k+1})\xi_{2(Q-1)} = 0 \quad .$$

Moreover, let μ_0 be the smallest positive number for which the system (5.12) possesses a nontrivial solution; then $\gamma_0 > 1$ and

(5.13) $$\rho = \frac{1}{1 + \mu_0} = \frac{1}{\gamma_0} \quad .$$

Proof: It is only necessary to verify the characterization of μ_0 or γ_0 given by (5.13). However, this is an immediate consequence of our earlier characterization of σ as the largest eigenvalue of (4.21) or (4.24).

Corollary: Consider equations (5.12) with b_{k+1} replaced by b_k. Let $\hat{\gamma}$ be the smallest positive value ≥ 1 of γ so that these modified equations have a nontrivial solution. Also, consider the system (5.12) with b_k replaced by b_{k+1}. Let $\bar{\gamma}$ be the smallest positive value of γ so that these modified equations have a nontrivial solution. Then

(5.14) $$\bar{\gamma} \leq \gamma_0 \leq \hat{\gamma} \quad .$$

Proof: Because

$$b_k \leq b_{k+1}$$

we see that

$$\beta - b_{k+1} \leq \beta - b_k \quad .$$

When γ is a small positive number the tridiagonal matrix of (5.12) is positive definite. If we increase some diagonal elements (for instance, replace $\beta - b_{k+1}$ by $\beta - b_k$) we increase all the eigenvalues. Thus increasing some diagonal elements means we must raise γ to make the system singular. Therefore

$$\gamma_0 \leq \hat{\gamma} \quad .$$

Similarly, replacing b_k by b_{k+1} makes the diagonal smaller and γ need not be so large. This proves (5.14).

Having established this corollary, we proceed to estimate the quantities $\bar{\gamma}$ and $\hat{\gamma}$. First we rearrange the matrices of interest.

Lemma 5.3: Let $\tilde{A}$ be the symmetric tridiagonal matrix

$$\tilde{A} = \begin{bmatrix} \bar{\beta} & -\gamma & & & & & \\ -\gamma & \bar{\beta} & -a_k & & & & \\ & -a_k & \bar{\beta} & -\gamma & & & \\ & & -\gamma & \bar{\beta} & -a_k & & \\ & & & & & -\gamma & \\ & & & & -\gamma & \bar{\beta} & \end{bmatrix}$$

of order 2(Q - 1). Let T be the permutation matrix corresponding to the permutation

$$(5.15) \qquad (2j - 1) \to j \ , \quad 2j \to (Q - 1) + j \ ,$$

so that, letting e_j denote the jth unit vector,

$$(5.16) \qquad T = \left[e_1, e_3, \ldots, e_{2Q-3}, e_2, e_4, \ldots, e_{2(Q-1)} \right] \ .$$

Then

$$(5.17a) \qquad T^t \tilde{A} T = \tilde{B}$$

where

$$(5.17b) \qquad \tilde{B} = \begin{bmatrix} \bar{\beta} I & E \\ E^t & \bar{\beta} I \end{bmatrix}$$

and E is the tridiagonal matrix $[-a_k, -\gamma, 0]$ of order Q - 1.

Proof: Direct computation.

We remark that in the application of this lemma we will set $\bar{\beta} = \beta - b_k$ or $\bar{\beta} = \beta - b_{k+1}$.

Now let

$$(5.18) \qquad V = \begin{bmatrix} X \\ Y \end{bmatrix}$$

be a nontrivial null vector of $\tilde{B}$, so that

$$(5.19) \qquad \tilde{B} V = 0 \ .$$

Then (5.19) is equivalent to the pair of equations

(5.20a) $$E^t E Y = \bar{\beta}^2 Y \ ,$$

(5.20b) $$E E^t X = \bar{\beta}^2 X \ .$$

A computation shows that

(5.21) $$E^tE = \begin{bmatrix} a_k^2 + \gamma^2 & a_k \gamma & & & \\ a_k \gamma & a_k^2 + \gamma^2 & a_k \gamma & & \\ & & & & \\ & & & a_k^2 + \gamma^2 & a_k \gamma \\ & & & a_k\gamma & \gamma^2 \end{bmatrix} ;$$

that is, E^tE is the constant tridiagonal matrix $[a_k\gamma, a_k^2 + \gamma^2, a_k\gamma]$ except that the (Q-1,Q-1) term is γ^2 rather than $a_k^2 + \gamma^2$. The matrix EE^t is identical to E^tE except that the (1,1) and (Q-1,Q-1) terms are interchanged.

Lemma 5.4: Let $\bar{\gamma}$ and $\hat{\gamma}$ be defined as in the corollary to lemma 5.2. Then

(5.22) $$\beta - b_{k+1} - a_k \le \bar{\gamma} \le \gamma_0 \le \hat{\gamma} \le \beta - b_k - a_k(1 - 0(h^2)) \le \beta - b_k + a_k$$

and from (5.13) we have

(5.23) $$\frac{1}{\beta - b_k + a_k} \le \frac{1}{\beta - b_k - a_k + a_k\, 0(h^2)} \le \rho$$
$$\le \frac{1}{\beta - b_{k+1} - a_k} \quad .$$

Proof: Consider the case of $\bar{\gamma}$. Then $\bar{\beta} = \beta - b_{k+1}$. From (5.20a) we see that if $\gamma = \bar{\gamma}$ then $\bar{\beta}^2$ is an eigenvalue of E^tE. Thus by the Gerschgorin Theorem [6]

$$\bar{\beta}^2 \le a_k^2 + \bar{\gamma}^2 + 2a_k\bar{\gamma} = (a_k + \bar{\gamma})^2 \quad .$$

This establishes the left hand inequality of (5.22).

Consider the case of $\hat{\gamma}$. Then $\bar{\beta} = \beta - b_k$. For $\gamma < \hat{\gamma}$ the matrix $\tilde{B}$ is positive definite. Therefore at $\gamma = \hat{\gamma}$ the smallest eigenvalue of $\tilde{B}$ is zero. Thus $-\bar{\beta}$ is the smallest eigenvalue of

$$\tilde{B}_0 = \begin{bmatrix} 0 & E \\ E^t & 0 \end{bmatrix} .$$

If η is an eigenvalue of $\tilde{B}_0$, so is $-\eta$. Moreover, η is an eigenvalue of $\tilde{B}_0$ if and only if η^2 is an eigenvalue of E^tE. We conclude when $\gamma = \hat{\gamma}$ that $\bar{\beta}^2$ is the largest eigenvalue of E^tE. Let $\eta_1 > \eta_2 > \cdots > \eta_{Q-1}$ be the eigenvalues of E^tE. From the inclusion theorem [6, p. 149] and the known eigenvalues of the tridiagonal matrix [1, 0, 1] of order Q - 2, we deduce that

$$\eta_j \ge a_k^2 + \gamma^2 + 2\, a_k\gamma \cos\frac{j\pi}{Q-1} \ge \eta_{j+1} \quad , \; 1 \le j \le Q-2 \quad .$$

Thus

$$\bar{\beta}^2 \ge a_k^2 + \hat{\gamma}^2 + 2a_k\,\hat{\gamma}\,\left[1 - \frac{1}{2}\left(\frac{\pi}{Q-1}\right)^2\right]$$
$$\ge a_k^2 + \hat{\gamma}^2 - 2a_k\hat{\gamma} = (\hat{\gamma} - a_k)^2 \quad .$$

It is easy to see that $\hat{\gamma} \leq \bar{\beta}$, whence

$$\bar{\beta}^2 \left[1 + \frac{a_k}{\bar{\beta}} \left(\frac{\pi}{Q - 1}\right)^2\right] \geq (a_k + \hat{\gamma})^2 \quad .$$

This proves the right hand inequalities of (5.22).

Remark: It is important to observe that the coefficient of the $0(h^2)$ term includes a_k. Since $a_k \to 0$ rapidly, this term is truly negligible.

Corollary: Let $k \to \infty$. Then

$$\rho \to \frac{1}{2} \left[\beta - \sqrt{\beta^2 - 4}\right] \quad . \tag{5.24}$$

Proof: It follows from (5.6) that

$$\rho \to \frac{1}{\beta - E_\infty} \quad \text{as } k \to \infty \ .$$

However, equation (5.2) shows that

$$\frac{1}{\beta - E_\infty} = E_\infty = \frac{1}{2} \left[\beta - \sqrt{\beta^2 - 4}\right] \quad .$$

Theorem 5.1: Consider the k-line Jacobi iterative scheme where k divides P and $k < P$. Let $\rho(SkL)$ denote the spectral radius of this scheme. Then the results shown in Figure 1 are correct up to a term which is $0(h^2)$.

Proof: The result for $k = 1$ follows from (3.1). The result for $k = 2$ follows from (4.8a). The results for $k \geq 3$ were obtained from a computation based on (5.23) with $\beta = 4$. The column ρ_1 was computed with the coarse lower bound of (5.23), and ρ_2 with the fine lower bound.

Theorem 5.2: Consider the $k \times k$ block Jacobi iterative scheme where k divides P and $k < P$. Let $\rho(SkB)$ denote the spectral radius of this scheme. Then the results shown in Figure 2 are correct.

Proof: The result for $k = 1$ follows from (3.2). The result for $k = 2$ follows from (4.8b). The results for $k \geq 3$ were obtained from a computation based on (5.23) with $\beta = 3$.

6. Computational Results

Using codes originally prepared by D. L. Boley (see [3]), Molly Mahaffy computed approximate spectral radii for the Gauss-Seidel iterative scheme using k lines and $k \times k$ blocks. These spectral radii were computed by the power method. The Gauss-Seidel method was chosen because the general theory shows that the Jacobi iterative scheme has both ρ and $-\rho$ as eigenvalues while the Gauss-Seidel scheme has a simple eigenvalue on the spectral radius. Furthermore, we also have

$$\rho(\text{Gauss-Seidel}) = \left[\rho(\text{Jacobi})\right]^2 .$$

The results are contained in the following tables. In all cases $P = 128$. As with Figures 1 and 2, the columns ρ_1^2 and ρ_2^2 were computed using the coarser and finer bounds of (5.23), respectively.

k-line Iterative Scheme

k	ρ_1^2 (Theory)	ρ_2^2 (Theory)	ρ^2(Computed)
4	.071840 ± .259(-2)	.074404 ± .242(-4)	.07662
8	.071797 ± .132(-4)	.071810 ± .608(-9)	.07167
16	.071797 ± .351(-9)	.071797	.07164
32	.071797	.071797	.07164
64	.071797	.071797	.07164

Figure 3.

k × k Block Iterative Scheme

k	ρ_1^2 (Theory)	ρ_2^2 (Theory)	ρ^2 (Computed)
4	.146498 ± .143(-1)	.160382 ± .382(-3)	.16620
8	.145898 ± .296(-3)	.146194 ± .150(-6)	.14631
16	.145898 ± .134(-6)	.145898 ± .311(-13)	.14590
32	.145898 ± .271(-13)	.145898	.14590
64	.145898	.145898	.14590

Figure 4.

We emphasize that Theorems 5.1 and 5.2 do not require that $k/P \to 0$, but only that $k < P$. The computations show this clearly. For instance, in Figures 3 and 4 we see that with $P = 128$ and $k = 64$, the largest acceptable value, ρ^2 has essentially attained its asymptotic value. These results seem to contradict the intuitive feeling that, were M to include a much larger part of A, the spectral radius of $M^{-1}N$ would be much smaller.

7. Block iterative methods and vector machines

The asymptotic convergence rate of the iterative method (2.8) is $-\ln \rho$, where ρ is the spectral radius of $M^{-1}N$ (see [22, page 67]). Equation (5.23) shows that the spectral radii and asymptotic convergence rates of block methods for (1.6) are only very weakly dependent on P. In contrast, these characteristics depend strongly on P when the block methods are applied to regular problems. For example, the spectral radius of the k-line Jacobi method for the model problem in two dimensions is

$$\rho(kL) = 1 - k\pi^2h^2 + O(h^3) \tag{7.1}$$

(see [15]), and so, neglecting higher order terms,

$$\rho(kL\text{-}GS) = 1 - 2k\pi^2h^2 \tag{7.2}$$

$$\rho(kL\text{-}SOR) = 1 - \sqrt{8k}\,\pi h, \text{ with optimal } \omega\ . \tag{7.3}$$

Comparison of Figure 1 with (7.1)-(7.3) shows that the asymptotic convergence rate of the k-line SOR method is a factor of $O(P/\sqrt{k})$ greater for (1.6) than for a regular problem on the same mesh, and for the k-line Gauss-Seidel and Jacobi methods is $O(P^2/k)$ greater. These conclusions also hold for k × k block methods. The singular perturbation helps -- so much so that k-line SOR with moderate k beats fast direct methods for (1.6).

A k-plane iterative method is the three-dimensional analogue of a k-line scheme in two dimensions. As shown in [15], the k-plane, k × k line, and k × k × k block Jacobi methods for (1.1) have respective spectral radii

$$\rho(kP) = 1 - 3k\pi^2h^2/2 + O(h^3)$$
$$\rho(k^2L) = 1 - 3k\pi^2h^2/4 + O(h^3)$$
$$\rho(k^3B) = 1 - k\pi^2h^2/2 + O(h^3) .$$

Choice of a block method is influenced by storage requirements, data transmission rates, and the underlying organizational structure of the data. The last point is particularly telling for three-dimensional problems, where the data structure may forbid any convenient access except by planes. Often these considerations force us to use 1-plane methods for (1.1). The spectral radius of the plane SOR scheme that gives rise to (1.6) is

$$\rho(1P\text{-SOR}) = 1 - \sqrt{12}\,\pi h + O(h^2), \text{ with optimal } \omega .$$

An iterative sweep can be made quickly if the systems (2.4), (2.5), or (2.6) can be solved quickly. These systems are typically banded with half-bandwidth k. On the Cray-1 they can be solved with vector tridiagonal or vector band routines, written especially for that machine, that run at speeds of 40 to 90 million floating point operations (add, subtract, multiply, or divide of floating point numbers) per second. To get advantageously long vectors, the k lines or k × k blocks may be grouped in red-black order. Similar considerations apply to other vector machines.

REFERENCES

[1] R. J. Arms, L. D. Gates, and B. Zondek. A method of block iteration. J. SIAM 4 (1956), 220-229.

[2] K. Aziz and I. Babuska, editors. The mathematical foundations of the finite element method with applications to partial differential equations. Academic Press, New York (1973).

[3] D. L. Boley, B. L. Buzbee, and S. V. Parter. On block relaxation techniques. University of Wisconsin M.R.C. report No. 1860 (June 1978). Also, Proceedings of the 1978 Army Numerical Analysis and Computer Conference, ARO Report 78-3, 277-295.

[4] C. de Boor, editor. Mathematical Aspects of Finite Elements in Partial Differential Equations. Academic Press, New York (1974).

[5] J. H. Bramble and A. H. Schatz. Rayleigh-Ritz-Galerkin methods for Dirichlet's problem using subspaces without boundary conditions. Comm. Pure Appl. Math. 23 (1970), 653-675.

[6] J. L. Franklin. Matrix Theory. Prentice-Hall, Englewood Cliffs, N.J. (1968).

[7] Alan George. Nested dissection of a regular finite element mesh. SINUM 10 (1973), 345-363.

[8] Alan George. Numerical experiments using dissection to solve n by n grid problems. SINUM 14 (1977), 161-179.

[9] L. E. Grosch. Poisson Solvers on a Large Array Computer. Proceedings of the 1978 LASL Workshop on Vector and Parallel Processors, Los Alamos Scientific Laboratory, Los Alamos, NM (1978), 93-132.

[10] E. Isaacson and H. B. Keller. Analysis of Numerical Methods. John Wiley and Sons, New York (1966).

[11] M. J. Kasic, Jr. A direct Poisson solver on Star. Proceedings of the 1978 LASL Workshop on Vector and Parallel Processors, Los Alamos Scientific Laboratory, Los Alamos, NM (1978), 137-164.

[12] H. Keller. On some iterative methods for solving elliptic difference equations. Quart. Appl. Math. 16 (1958), 209-226.

[13] S. V. Parter. On estimating the 'rates of convergence' of iterative methods for elliptic difference equations. Trans. Amer. Math. Soc. 114 (1965), 320-354.

[14] S. V. Parter. Multi-line iterative methods for elliptic difference equations and fundamental frequencies. Numerische Math. 3 (1961), 305-319.

[15] S. V. Parter and M. Steuerwalt. Another look at iterative methods for elliptic difference equations. Report (to appear).

[16] R. D. Richtmyer and K. W. Morton. Difference Methods for Initial Value Problems (2nd ed.). Interscience, New York (1967).

[17] D. J. Rose. A graph-theoretic study of the numerical solution of sparse positive definite systems of linear equations. Graph Theory and Computing, R. C. Read, editor, Academic Press, New York (1972).

[18] D. J. Rose and R. A. Willoughby, editors. Sparse Matrices and their Applications. Plenum Press, New York (1972).

[19] A. H. Sameh, S. C. Chen, and D. J. Kuck. Parallel Poisson and biharmonic solvers. Computing 17 (1976), 219-230.

[20] G. Strang and G. J. Fix. An Analysis of the Finite Element Method. Prentice-Hall, Englewood Cliffs, NJ (1973).

[21] R. S. Varga. Factorization and normalized iterative methods. Boundary Problems in Differential Equations, R. E. Langer, editor, University of Wisconsin Press (1960), 121-142.

[22] R. S. Varga. Matrix Iterative Analysis. Prentice-Hall, Englewood Cliffs, NJ (1962).

[23] David M. Young. Iterative Solution of Large Linear Systems. Academic Press, New York (1971).

[24] David M. Young. Iterative methods for solving partial difference equations of elliptic type. Trans. Amer. Math. Soc. 76 (1954), 92-111.

[25] O. C. Zienkiewicz. The finite element method: from intuition to generality. Appl. Mech. Rec. 23 (1970), 249-256.

THE HOMOGENEOUS PROPERTIES OF THE COMPRESSIBLE NAVIER-STOKES EQUATIONS WITH APPLICATION TO FINITE DIFFERENCE METHODS

R. F. Warming, Richard M. Beam, and J. L. Steger*
Computational Fluid Dynamics Branch
Ames Research Center, NASA, Moffett Field, California 94035

ABSTRACT. The conservation-law form of the compressible Navier Stokes equations has the remarkable property that the nonlinear flux vectors are homogeneous functions of degree one. This property leads to many interesting identities of both theoretical and practical importance. For example, one particular identity allows alternating direction implicit methods and explicit and implicit fractional step algorithms to be easily derived for the nonlinear equations of gasdynamics by using Pade approximants to exponential matrix operators. For the hyperbolic terms, the homogeneous property permits the splitting of flux vectors into subvectors by similarity transformations so that each subvector has associated with it a specified eigenvalue spectrum. As a consequence of flux vector splitting, new explicit and implicit dissipative finite-difference schemes are developed for first-order hyperbolic systems of equations. Appropriate one-sided spatial differences for each split flux vector are used throughout the computational field even if the flow is locally subsonic. The resulting dissipative schemes are very robust when applied to flow fields with discontinuities. The results of some numerical computations are included. (A preliminary written version of the material on flux vector splitting appeared in NASA TM 78605, July 1979.)

*Present address: Flow Simulations, Inc., 298 Sunnyvale Ave., Sunnyvale, California 94086

A TECHNIQUE FOR SYNTHESIZING THE MOTIONS OF A FLAT PLATE FOUNDATION DURING AN EARTHQUAKE

Francis E. Council, Jr.

U. S. Army Mobility Equipment Research and Development Command

Fort Belvoir, VA 22060

Abstract

A time history is synthesized by means of a computer of accelerations in a flat plate foundation by first solving the partial differential equations for describing the displacements in the foundation by means of a Green's tensor and Parseval's relation. These equations are coupled to similar type equations for describing the displacements in the surrounding medium by means of variational techniques. The resulting equations are then coupled to those for describing the motions of a building. A comparison of the results obtained by the model discussed in this paper and another model was accomplished by taking frequency spectrums of both time histories of the accelerations and then comparing both frequency spectrums with an observed frequency spectrum of a building.

I. INTRODUCTION. One of the standard approaches for describing the displacements in a medium is to use Navier's equations of linear elasticity. These partial differential equations are difficult to separate into orthogonal modes such that independant solutions for the various displacements are obtained. A different approach is used in this paper, the coupling of the equations is maintained as the equations for the displacements are solved. Similar type equations for the displacements in the surrounding medium and the foundation are coupled together by means of variational techniques and are then modified with a foundation-structure interaction. The results of the model discussed in this paper and another model are compared by comparing the frequency spectrums of accelerations of both models with an observed frequency spectrum during an earthquake of the building which both models had been applied to.

Although finite element methods could have been used for describing the motion of the foundation, the methods used were those of continuum mechanics. Since the dynamics of the structure of a building that is attached to the foundation are better described by finite element methods, the problem arises as to how the two approaches can be joined together. This joining of approaches can be accomplished relatively easily by the properties of Dirac delta functions.

II. DISPLACEMENT FUNCTIONS FOR THE FOUNDATION. The Navier's equations for describing displacements in the foundation are given as

$$(\lambda+2\mu)U_{1,11} + 2\mu U_{1,12} + 2\mu U_{1,13} - \rho\cdot\frac{\partial^2 U_1}{\partial t^2} = F_1 \qquad (1)$$

$$2\mu U_{1,12} + (\lambda+2\mu)U_{2,22} + 2\mu U_{3,23} - \rho\cdot\frac{\partial^2 U_2}{\partial t^2} = F_2 \qquad (2)$$

$$2\mu U_{1,31} + 2\mu U_{2,32} + (\lambda+2\mu)U_{3,33} - \rho\cdot\frac{\partial^2 U_3}{\partial t^2} = F_3 \qquad (3)$$

where U_1, U_2 and U_3 are the displacements and ρ is the density of the medium. If operator notation is used where

$$[L]\,\vec{U} = \vec{F} \qquad (4)$$

and

$$[L][G] = [\delta] \qquad (5)$$

with $[L]$, $[G]$, and $[\delta]$ being tensors of rank two and $\vec{U}$ and $\vec{F}$ being tensors of rank one, then

$$[G] = -[L]^{-1}[\delta] \tag{6}$$

and

$$\vec{U} = \int [G] \vec{F} \, dx_1 dx_2 dx_3 dt \, . \tag{7}$$

The techniques by which $[G]$ and $\vec{U}$ are obtained have been developed by Council [1]. Consequently, the elements of the Green's tensor are identified as

$$[G] = \begin{bmatrix} G_{11} & G_{12} & G_{13} \\ G_{21} & G_{22} & G_{23} \\ G_{31} & G_{32} & G_{33} \end{bmatrix} \tag{8}$$

where

$$G_{11}(X_1 X_2 X_3, T;\ x_1 x_2 x_3 t) = \frac{1}{DP}\{(\lambda+2\mu)^2 \exp(i(X_3+X_2-(\frac{\lambda+2\mu}{\rho})^{\frac{1}{2}}T)) - (2\mu)^2 \exp(i(X_1+X_2+X_3-(\frac{\lambda+2\mu}{\rho})^{\frac{1}{2}}T))\}\{\delta(\vec{X}-\vec{x})\delta(T-t)\}, \tag{9}$$

$$G_{12}(X_1 X_2, X_3 T;\ x_1, x_2, x_3, t) = \frac{1}{DP}\{(2\mu)^2 \exp(i(X_1+X_2+X_3 - (\frac{\lambda+2\mu}{\rho})^{\frac{1}{2}}T)) - (\lambda+2\mu)(2\mu)\exp(i(X_3 - \frac{\lambda+2\mu}{\rho})^{\frac{1}{2}}T))\}\{\delta(\vec{X}-\vec{x})\delta(T-t)\}, \tag{10}$$

$$G_{13}(X_1, X_2, X_3, T;\ x_1, x_2, x_3, t) = \frac{1}{DP}\{(2\mu)^2 \exp(i(X_1+X_2+X_3-(\frac{\lambda+2\mu}{\rho})^{\frac{1}{2}}T)) - 2\mu(\lambda+2\mu)\exp(i(X_2 - (\frac{\lambda+2\mu}{\rho})^{\frac{1}{2}}T)\}\{\delta(\vec{X}-\vec{x})\delta(T-t)\}, \tag{11}$$

$$G_{21}(X_1,X_2,X_3,T;x_1,x_2,x_3,t) = \frac{1}{DP}\{(2\mu)^2\exp(i(X_1+X_2+X_3 - (\frac{\lambda+2\mu}{\rho})^{1/2}T)) \tag{12}$$

$$- 2\mu(\lambda+2\mu)\exp(i(X_3-(\frac{\lambda+2\mu}{\rho})^{1/2}T)\}\{\delta(\vec{X}-\vec{x})\delta(T-t)\} ,$$

$$G_{22}(X_1,X_2,X_3,T;x_1,x_2,x_3,t) = \frac{1}{DP}\{(\lambda+2\mu)^2\exp(i(X_1+X_2-(\frac{\lambda+2\mu}{\rho})^{1/2}T)) \tag{13}$$

$$-(2\mu)^2\exp(i(X_1+X_2+X_3- (\frac{\lambda+2\mu}{\rho})^{1/2}T\}\{\delta(\vec{X}-\vec{x})\delta(T-t)\} ,$$

$$G_{23}(X_1,X_2,X_3,T;x_1,x_2,x_3,t) = \frac{1}{DP}\{(2\mu)^2\exp(i(X_1+X_2+X_3- (\frac{\lambda+2\mu}{\rho})^{1/2}T)) \tag{14}$$

$$-(2\mu)(\lambda+2\mu)\exp(i\ (X_1- (\frac{\lambda+2\mu}{\rho})^{1/2}T)\}\{\delta(\vec{X}-\vec{x})\delta(T-t)\} ,$$

$$G_{31}(X_1,X_2,X_3,T;x_1,x_2,x_3,t) = \frac{1}{DP}\{(2\mu)^2\exp(i(X_1+X_2+X_3-(\frac{\lambda+2\mu}{\rho})^{1/2}T)) \tag{15}$$

$$-2\mu(\lambda+2\mu)\exp(i(X_2-(\frac{\lambda+2\mu}{\rho})^{1/2}T)\}\{\delta(\vec{X}-\vec{x})\delta(T-t)\} ,$$

$$G_{32}(X_1,X_2,X_3,T;x_1,x_2,x_3,t) = \frac{1}{DP}\{(2\mu)^2\exp(i(X_1+X_2+X_3-(\frac{\lambda+2\mu}{\rho})^{1/2}T)) \tag{16}$$

$$-2\mu(\lambda+2\mu)\exp(i(X_1-(\frac{\lambda+2\mu}{\rho})^{1/2}T)\}\{\delta(\vec{X}-\vec{x})\delta T-t)\} ,$$

$$G_{33}(X_1,X_2,X_3,T;x_1,x_2,x_3,t) = \frac{1}{DP}\{(\lambda+2\mu)^2\exp(i(X_1+X_2-(\frac{\lambda+2\mu}{\rho})^{1/2}T) \tag{17}$$

$$-(2\mu)^2\exp(i(X_1+X_2+X_3-(\frac{\lambda+2\mu}{\rho})^{1/2}T)\}\{\delta(\vec{X}-\vec{x})\delta(T-t)\} ,$$

with

$$DP = \{(\lambda+2\mu)^3\exp(i(X_1+X_2+X_3-(\frac{\lambda+2\mu}{\rho})^{1/2}T)) + (2\mu)^3 \tag{18}$$

$$-[(\lambda+2\mu)(2\mu)^2(\exp(i(X_1-(\frac{\lambda+2\mu}{\rho})^{1/2}T)) + \exp(i(X_3-(\frac{\lambda+2\mu}{\rho})^{1/2}T)$$

$$+ \exp(i(X_3- (\frac{\lambda+2\mu}{\rho})^{1/2}T)))]\} .$$

III. MATCHING OF DISPLACEMENT FUNCTIONS BY VARIATIONAL TECHNIQUES.

With the Green's tensor and the displacement function for the foundation having been found, then this displacement function must be matched to the displacement function for the surrounding medium in terms of the boundary conditions. The surrounding medium and the foundation are considered as being continuous with each other, i.e., a component of the displacement function of the surrounding medium is continuous with the same component of the displacement function of the foundation. Since the two displacement functions were developed such that individual components are orthogonal, only one component at a time need be considered.

Let the subscript $_S$ of a displacement function refer to the surrounding medium and the subscript $_F$ of a displacement function refer to the foundation. The individual components of the displacement functions would be U_{S1}, U_{S2}, U_{S3}, and U_{F1}, U_{F2}, U_{F3}, respectively. As an example, consider the displacements which are perpendicular to the fault line and parallel to the surface. Displacement functions for the foundation in terms of the displacement functions in the surrounding medium which hold true in regions close to the boundary can be constructed such that

$$U_{F1}(X_1,X_2,X_3,T) = \left(\frac{U_{F1}(X_1,X_2,X_3,T)}{U_{S1}(X_1,X_2,X_3,T)} \right) \Big|_{X_1=X_1} U_{S1}(X_1,X_2,X_3,T) \tag{19}$$

and

$$U_{F1}(X_1,X_2,X_3,T) = \left(\frac{U_{F1}(X_1,X_2,X_3,T)}{U_{S1}(X_1,X_2,X_3,T)} \right) \Big|_{X_1=X_1+a_1} U_{S1}(X_1,X_2,X_3,T) \tag{20}$$

where the symbols $|_{X_1=X_1}$ and $|_{X_1=X_1+a_1}$ indicate that evaluation is performed with X_1 as a constant. In the preceding equations, a_1 is the distance between the two faces. In order to maintain continuity of the displacement functions in the foundation, then these two equations may be used to form a constraint equation,

$$g_1 = \left\{ \frac{U_{F1}(X_1,X_2,X_3,T)}{U_{S1}(X_1,X_2,X_3,T)} \Big|_{X_1=X_1+a_1} - \frac{U_{F1}(X_1,X_2,X_3,T)}{U_{S1}(X_1,X_2,X_3,T)} \Big|_{X_1=X_1} \right\} U_{S1}(X_1,X_2,X_3,T) \tag{21}$$

A similar constraint equation for the other two vertical faces is obtained as

$$g_2(X_1,X_2,X_3,T) = \left\{ \frac{U_{F2}(X_1,X_2,X_3,T)}{U_{S2}(X_1,X_2,X_3,T)} \Big|_{X_2=X_2+a_2/2} \right. \tag{22}$$

$$\left. - \left(\frac{U_{F2}(X_1,X_2,X_3,T)}{U_{S2}(X_1,X_2,X_3,T)} \right) \Big|_{X_2=X_2-a_2/2} \right\} U_{S2}(X_1,X_2,X_3,T)$$

The constraint equation for the horizontal surfaces of the foundation is different since the upper surface is not in contact with the surrounding medium, but a displacement function does exist in the foundation, even at the surface. Consequently,

$$g_3(X_1,X_2,X_3,T) = \left\{\left(\frac{U_{F3}(X_1,X_2,X_3,T)}{U_{S3}(X_1,X_2,X_3,T}\right)\Big|_{X_3=X_3-a_3} - \frac{U_{F3}(X_1,X_2,X_3,T)}{U_{S3}(X_1,X_2,X_3,T)}\Big|_{X_3=0}\right\} U_{S3}(X_1,X_2,X_3,T) + U_{F3}(X_1,X_2,X_3,T) \tag{23}$$

The three constraint equations are then used to form a new equation such that

$$I(X_1,X_2,X_3,T) = U_{F1}(X_1,X_2,X_3,T) + \sum_{i=1}^{i=3} \lambda_i g_i \tag{24}$$

with the Euler-Lagrange equation being used such that the Lagrange multipliers, $\lambda_1,\lambda_2,\lambda_3$ are evaluated. The three equations that are obtained from the last equation with the Euler-Lagrange equation being used are

$$\begin{aligned} U_{F1,1} + \lambda_1 g_{1,1} + \lambda_2 g_{2,1} + \lambda_3 g_{3,1} &= 0 \\ U_{F1,2} + \lambda_1 g_{1,2} + \lambda_2 g_{2,2} + \lambda_3 g_{3,2} &= 0 \\ U_{F1,3} + \lambda_1 g_{1,3} + \lambda_2 g_{2,3} + \lambda_3 g_{3,3} &= 0 \end{aligned} \tag{25}$$

With three equations and three unknowns, namely the Lagrangian multipliers λ_1 , λ_2 , and λ_3 ,then the Lagrangian multipliers are obtained by means of simultaneous equations as

$$\begin{aligned} \lambda_1 &= A_1/D \\ \lambda_2 &= A_2/D \\ \lambda_3 &= A_3/D \end{aligned} \tag{26}$$

where

$$A_1 = U_{F1,1}g_{2,2}g_{3,3} + U_{F1,3}g_{2,1}g_{3,2} + U_{F1,2}g_{3,1}g_{2,3} - U_{F1,3}g_{2,2}g_{3,1} - U_{F1,1}g_{2,3}g_{3,2} - U_{F1,2}g_{3,3}g_{2,1} \quad (27)$$

$$A_2 = U_{F1,2}g_{1,1}g_{2,3} + U_{F1,1}g_{3,2}g_{1,3} + U_{F1,3}g_{3,1}g_{1,2} - U_{F1,2}g_{1,3}g_{3,1} - U_{F1,3}g_{3,2}g_{1,1} - U_{F1,1}g_{3,3}g_{1,2} \quad (28)$$

$$A_3 = U_{F1,3}g_{1,1}g_{2,2} + U_{F1,2}g_{2,1}g_{1,3} + U_{F1,1}g_{1,2}g_{2,3} - U_{F1,1}g_{1,3}g_{2,2} - U_{F1,2}g_{1,1}g_{2,3} - U_{F1,3}g_{1,2}g_{1,3} \quad (29)$$

and

$$D = g_{1,1}g_{2,2}g_{3,3} + g_{1,3}g_{2,1}g_{3,2} + g_{1,2}g_{3,1}g_{2,3} - g_{1,3}g_{2,2}g_{3,1} - g_{1,1}g_{2,3}g_{3,2} - g_{1,2}g_{3,3}g_{2,1} \quad (30)$$

The actual programming of this problem requires an awareness that the displacement functions U_S and U_F were derived as wave equations such that complex quantities are considered. The equations have been derived in such a fashion that the other components of the displacement functions are derived in a similar fashion, the difference being that the subscript 1 of U_{F1} and U_{S1} is changed to 2 and 3 for the other two equations.

IV. FOUNDATION-STRUCTURE INTERACTION. Consider a rectangular foundation with the dimension a_1 along the X_1 axis, a_2 along the X_2 axis, and a_3 along the X_3 axis with the vertical face closest to the epicenter being at a distance X_1. This same face is considered as being parallel to the fault line, and displacement vectors in terms of coordinates at the corners of the upper surface can be expressed as

$U_1(X_1, a_2/2, 0, T)$, $U_2(X_1, a_2/2, 0, T)$, $U_3(X_1, a_2/2, 0, T)$

$U_1(X_1, -a_2/2, 0, t)$, $U_2(X_1, -a_2/2, 0, T)$, $U_3(X_1, -a_2/2, 0, T)$

$U_1(X_1 + a_1, a_2/2, 0, t)$, $U_2(X_1 + a_1, a_2/2, 0, t)$, $U_3(X_1 + a_1, a_2/2, 0, T)$

$U_1(X_1 + a_1, -a_2/2, 0, T)$, $U_2(X_1 + a_1, -a_2/2, 0, T)$, $U_3(X_1 + a_1, -a_2/2, 0, T$

The components of the displacement at the center of the foundation are expressed as

$$U_1(X_1 + a_1/2, 0, 0, T),\ U_2(X_1 + a_1/2, 0, 0, T),\ U_3(X_1 + a_1/2, 0, 0, T)$$

while the displacement vectors at the midponts of the sides are expressed respectively as

$$U_1(X_1, 0, 0, T),\ U_2(X_1, 0, 0, T),\ U_3(X_1, 0, 0, T)$$

$$U_1(X_1 + a_1, 0, 0, T),\ U_2(X_1 + a_1, 0, 0, T),\ U_3(X_1 + a_1, 0, 0, T)$$

$$U_1(X_1 + a_1/2, a_2/2, 0, T),\ U_2(X_1 + a_1/2, a_2/2, 0, T),$$
$$U_3(X_1 + a_1/2, a_2/2, 0, T)$$

$$U_1(X_1 + a_1/2, -a_2/2, 0, T),\ U_2(X_1 + a_1/2, -a_2/2, 0, T),$$
$$U_3(X_1 + a_1/2, -a_2/2, 0, T)$$

With the upper surface of the foundation being considered, the previous sets of vectors can be generalized as

$$U_1\left(X_1 + \frac{a_1 i}{2} - \frac{a_1}{2}, -a_2 + \frac{a_2 j}{2}, 0, T\right)$$

$$U_2\left(X_1 + \frac{a_1 i}{2} - \frac{a_1}{2}, -a_2 + \frac{a_2 j}{2}, 0, T\right)$$

$$U_3\left(X_1 + \frac{a_1 i}{2} - \frac{a_1}{2}, -a_2 + \frac{a_2 j}{2}, 0, T\right)$$

where $1 \leq i \leq 3$, $1 \leq j \leq 3$.

The previous statements show how the time dependent displacements for any location of the foundation can be found, this information is used with relationships for the foundation-structure interaction. The foundation-structure interaction expression is the one used by Wood [2]. The $(\ddot{U}_g)$ of equation 10.6 of the report by Wood is identified with $\ddot{U}_1$ if the second derivative with respect to time of the U_1 of equation (6.6) of [1] is taken. $(\ddot{U}_g + \ddot{u}_b)$ is identified with $\ddot{U}^*_{F1}$ where U_{F1} of equation (24) of this paper is a displacement function of the foundation and where U^*_{F1} is the U_{F1} modified by considering foundation-structure interaction. The equations developed by Wood imply that the accelerations of the foundation are considered as being measured at the center of mass of the foundation.

The equations that were derived in this dissertation deal with a three dimensional situation rather than a two dimensional situation as discussed in the report by Wood. This was done in order to have a greater applicability to the foundation which has three dimensions and because the basic equations from which the displacements in the foundation and the surrounding medium dealt with a three dimensional situation with the respective partial differential equations being coupled. If the second derivative with respect to time of one of the equations dealing with horizontal displacements of the foundation is taken, it must then be modified such that the effect of foundation-structure interaction can be included. One way of considering interaction is to use the report by Wood.

If equation (10.6) of the report by Wood is modified in terms of the equations of this paper, it is written as

$$\sum_{j=1}^{N} m_j(\ddot{U}^*_{F1} + \ddot{u}_j) + m_b\ddot{U}'_{F1} = F_b(t) \tag{31}$$

where $\ddot{U}'_{F1}$ is the foundation acceleration with foundation-structure interaction included. The expression

$$\sum_{j=1}^{N} m_j(\ddot{U}_{F1} + \ddot{u}_j)$$

may be replaced by $S_b(t)$ of the report by Wood such that

$$S_b(t) + m_b\ddot{U}'_{F1} = F_b(t) \tag{32}$$

If the foundation-structure interaction is not included, then the previous equation is written as

$$m_b\ddot{U}_{F1} = F_b(t) \tag{33}$$

Since $F_b(t)$ is the same for the two equations, then after taking the Fourier transform of the two equations and setting them equal to each other where $S_b(\omega) = H_{11}(\omega)$ then

$$\ddot{U}'_{F1}(\omega) = \ddot{U}'_{F1}(\omega) - H_{11}(\omega)/m_b \,. \tag{34}$$

V. COMPARISON OF RESULTS. There are some difficulties in attempting to compare results as obtained by the techniques developed in this paer and the results which are currently in the literature. As stated by Crouse and Jennings [3] , except for the limiting static case, the dynamic impedance functions have not been evaluated for the case of a perfectly bonded rigid plate on an elastic half space. Although Wood has considered embedment of the foundation, his approach is essentially an empirical one with his use of a spring and dashpot model. A limitation of his approach is that he considers a foundation which is square in shape. Kabori et al [4] discuss a rectangular foundation resting on an elastic half space but disadvantages of his approach are that the foundation is not embeded and also that closed form solutions are not obtained. This paper addresses the conditions of an embeded foundation in which the upper surface is rectangular.

The actual comparisons were made by comparing the results obtained by the techniques of this paper with the results obtained from actual observations and comparing the results obtained by the Wood model with the same results from actual observations. The two comparisons were then examined to see which gave a better agreement with observed results. One way of comparing results is to compare the frequency spectrums of a time history of the accelerations of the foundation as obtained by the model developed in this paper occuring in response to a synthesized earthquake and a frequency spectrum of a time history of the accelerations of the foundation obtained by the response of the Wood model to the same synthesized earthquake with a frequency spectrum of the accelerations of the same foundation which was obtained from observations made during an actual earthquake.

The observed results that were used as a basis of comparison are shown in Figure 1 which was taken from the report by Wood. This figure is a smoothed distribution of the amplitudes of the frequencies associated with the Fourier transform of the accelerations observed in the basement of a building. Each of the signifigant peaks is approximated by a Gaussian distribution; by observing the amplitude of the peak, the frequency at which the peak is a maximum and the width of the peak at half amplitude, then constants may be evaluated in order that each of the peaks can be described with a distribution function. The function describing the frequency spectrum of the accelerations of the basement of the building affected by a seismic disturbance, noise excluded, is then a sum of distribution functions as shown in equation (35).

$$\begin{aligned}\psi(\omega) = {} & 2.4\ \exp\left(-(\omega-1.1)^2 \ell n\left(2/(.08)^2\right)\right) \\ & + 3.8\ \exp\left(-(\omega-2.3)^2 \ell n\left(2/(0.2)^2\right)\right) \\ & + 4.1\ \exp\left(-(\omega-2.8)^2 \ell n\left(2/(0.3)^2\right)\right) \\ & + 2.2\ \exp\left(-\omega-4.0\right)^2 \ell n\left(2/(0.3)^2\right)\end{aligned} \tag{35}$$

FOURIER AMPLITUDE SPECTRUM

JPL BUILDING BSMT. E-W DIRECTION.

FROM ACCELERATION RECORD. 0.-40. SEC.

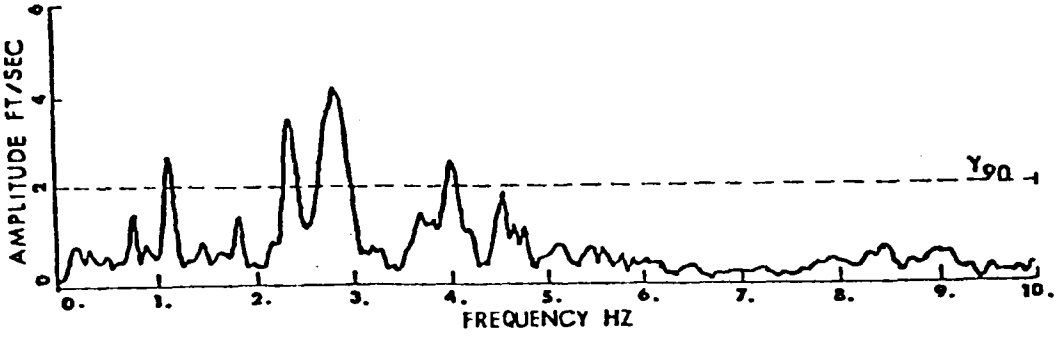

Figure 1

The actual comparisons were made in the following manner. As input to equation (10.12) of the report by Wood, the Fourier transform of the time history of one of the horizontal accelerations of the surrounding medium as obtained from the equations of this paper was used. The amplitudes obtained by the use of the Wood model were compared with the amplitudes obtained by means of equation (35) for the same frequencies; the two frequency distributions were normalized and a standard deviation of the differences between the two distributions was obtained. The Fourier transform was performed by means of a Fast Fourier Transform [5] as was the standard deviation [6] . The results as obtained by a time history of the accelerations of the foundation by means of the equations developed in this paper were compared with actual results in a similar manner. The acceleration time history of the foundation along the same coordinate axis as was used for the Wood model was changed to a frequency spectrum by means of the Fast Fourier Transform which was then modified to include foundation-structure interaction with the same foundation-structure interaction expression that Wood used. The two standard deviations that had been obtained were then compared with each other.

The standard deviations of the differences associated with the Wood model was 2.5492, the standard deviation of the differences associated with the model developed in this paper was 1.6010. Since the standard deviation of the differences obtained by the use of the model developed in this paper as compared with the standard deviation of the differences obtained by the use of the Wood model was smaller, then the model developed in this paper can be considered as an improvement as to agreement with physical reality.

REFERENCES

1. Council, F. E., "A New Technique for the Solution of Navier's Equations," Transactions of the Twenty-Fifth Conference of Army Mathematicians, ARO Report 80-1, pp 185-214.

2. Wood, John H., "Analysis of the Earthquake Response of a Nine-Story Steel Frame Building During the San Fernando Earthquake," Report No. EERL 72-04, California Institute of Technology Earthquake Engineering Research Laboratory, Pasadena, California, October, 1972.

3. Crouse, Charles B. and Jennings, Paul C., "Soil-Structure Interaction During the San Fernando Earthquake," Bulletin of the Seismological Society of America, Vol. 65, No. 1, Feb. 1975, P 15.

4. Kobori, T., Menoi, R. and Suzuki, T., "The Dynamical Ground Compliance of a Rectangular Foundation of a Viso-elastic Stratum," Bull. Disas. Prev. Res. Inst., Kyoto University, Vol. 20, Part 4, No. 183, March, 1971, pp 279-329.

5. IBM, "System/360 Scientific Subroutine Package (360A-CM-034) Version II, Programmer's Manual," International Business Machine Corp., Data Processing Division, 112 East Post Road, White Plains, N. Y., 10601, 1967, p 154.

6. Ibid p 16.

DATA-MAP, Software for Analysis, Management and Display of Aeromechanics' Data

Donald J. Merkley
Applied Technology Laboratory
US Army Research and Technology Laboratories (AVRADCOM)
Fort Eustis, VA

ABSTRACT. DATA-MAP (Data from Aeromechanics' Test and Analytics - Management and Analysis Package) is a computer software system which provides direct access to large data bases, performs analysis and derivations, and provides the user with various options for output display, interactively or through batch processing. DATA-MAP was designed to utilize the Operational Loads Survey data but is general enough to accommodate other large, time based, data sets resulting from test or analysis. The need for and evolution of the software system is discussed. The processing and output capabilities of DATA-MAP are described and examples are presented, with a discussion of DATA-MAP applications from a user's viewpoint.

1. INTRODUCTION. The need for the system is derived from the Operational Loads Survey (OLS), a flight test conducted using an US Army AH-1G to gain experimental insight of rotor aerodynamic environments and structural dynamics of helicopters (Reference 1). A comprehensive data base was acquired of rotor aerodynamic forces, aeroelastic loads, blade motions, acoustics and the attendant responses of the control system and airframe that result from flying operational maneuvers. Continuous and simultaneous data was recorded from 387 transducers for 224 different flight conditions. Over 72,000 separate functions of time were digitized and recorded on 175 magnetic tapes. A computer program was developed to retrieve the raw data; however, it was inconvenient, time consuming and discouraged potential users. It was difficult to manage such a large data base without the proper software tools. The Applied Technology Laboratory (ATL), US Army Research and Technology Laboratories (AVRADCOM) developed the functional descriptions for such a software system to utilize the OLS data base and yet be general enough to use with other data sets, both analytical and test.

The functional descriptions required the system to provide access, data reduction, and a variety of formats of presentation of digitized data. In addition, operation in batch, interactive and interactive graphics modes were required. The functional descriptions also included a need for a high degree of user interaction and computer generated

step-by-step explanations of user inputs, user options, and menus of data available for processing. Most analytical methods commonly used for helicopter test data analysis, selectable by the user in any appropriate combination, were specified. Modular design requirements were stressed to permit other methods to be added as the need arises. Design requirements included execution on an IBM 360 Model 65 with Time Sharing Option (TSO), Tektronix 4014 graphic terminal, Houston Instruments DP-1 incremental plotter, and IBM 2741 typewriter terminal. The mandatory computing language was FORTRAN IV.

Bell Helicopter Textron, Scientific and Technical Computing, was selected as principle performer to develop this software, which is now known as DATA-MAP. DATA-MAP meets all of the above mentioned design requirements with an easy to learn user oriented format (Reference 2).

2. DATA-MAP CAPABILITIES. DATA-MAP consists of two major programs, the File Creation Program and the Processing Program, as well as several utility programs. The basic execution sequence is illustrated in Figure 1. The File Creation Program reads data from some storage medium (digital tape or disc), selectively transfers data to a direct access disc called the Master File and creates a directory of the data thus stored. The Master File is then the data input source for the Processing Program. The Processing Program retrieves data from the Master File, accepts user commands interactively or in batch mode, processes the data, and outputs data in graphic or printed formats. The Processing Program provides the user with various analyses that may be performed on the basic data contained on the Master File and, in addition, certain parameters may be derived from the basic data. The computational capabilities available to the user in the Processing Program are detailed in Figure 2. These analyses and derivations can be performed in multiple dimensions (e.g., time, chord, and radius). Sequences of analyses and/or derivations can be performed on a set of data in any appropriate combination.

Basic data and processed outputs can be presented in various formats as shown in Figure 3. Simple X-Y plots or multiple-curve X-Y plots are available. The user also has the options of specifying log-log or semi-log axes, scaling on X and Y and whether the plot has grids and/or tic marks. When X-Y plots are produced on the Tektronix 4014 terminal, the user may specify that the crosshair cursor be activated immediately after the plot is completed. The crosshairs may be used to evaluate points on the screen in user coordinates. Three-dimensional outputs in the form of contour plots and surface perspective drawings in rectangular and cylindrical coordinate systems are available. Auto scaling is available on all plots or the user may specify the scale values. All output options are available on a Tektronix 4014 terminal in the interactive graphics mode of operation or on an incremental plotter in the batch mode. Printed listings are available in either mode, or on an interactive typewriter terminal.

AD-A089 089 ARMY MATHEMATICS STEERING COMMITTEE F/G 9/2
PROCEEDINGS OF THE 1980 ARMY NUMERICAL ANALYSIS AND COMPUTERS C--ETC(U)
AUG 80

UNCLASSIFIED ARO-80-3 NL

4 OF 6
AD A089089

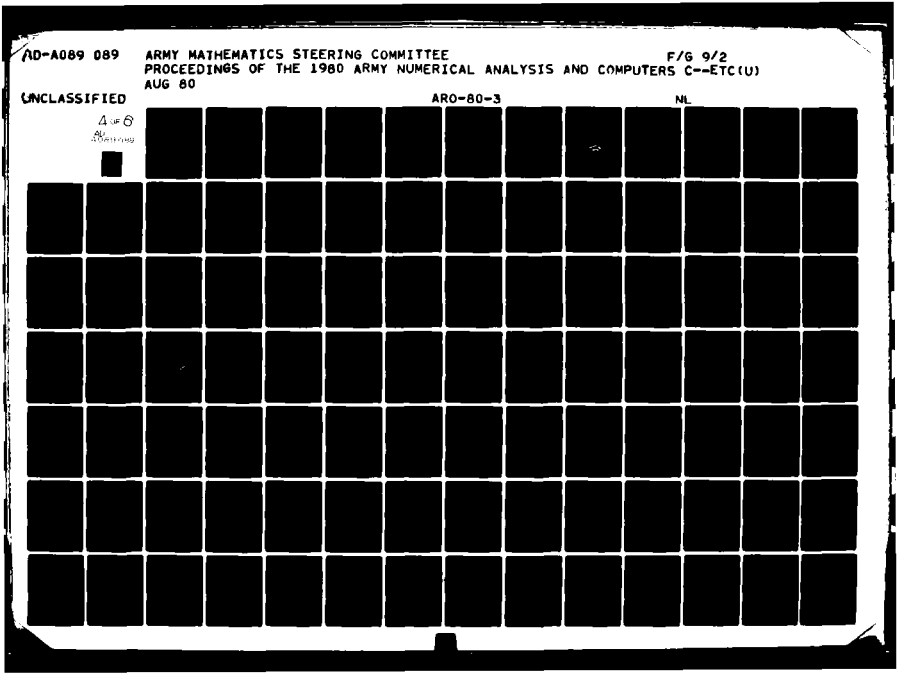

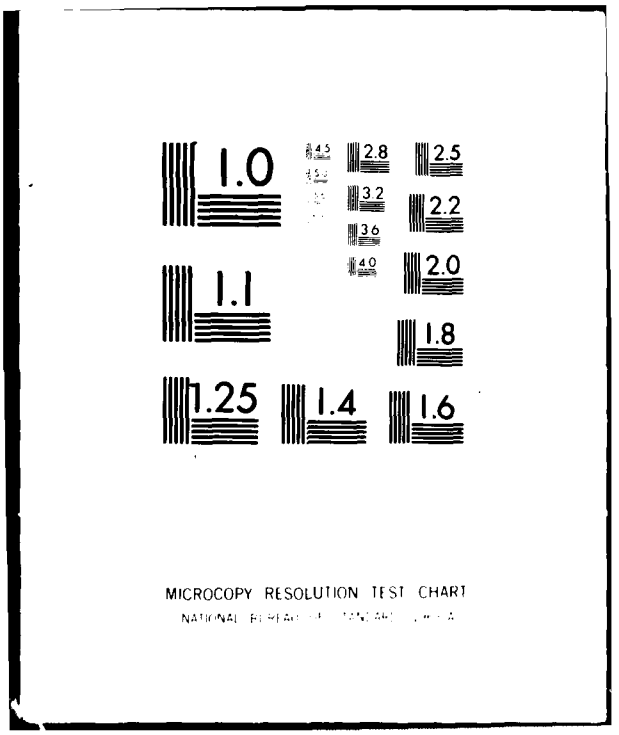
1.0
2.8
2.5
3.2
2.2
3.6
4.0
2.0
1.1
1.8
1.25
1.4
1.6
MICROCOPY RESOLUTION TEST CHART

Four utility programs are provided in the system. Two of them are for file initialization in the Master and Command Sequence Files. The Command Sequence File is a permanent disc file on which sequences of command steps can be stored. Another utility program is provided for users to develop complete input sequences for the File Creation Program in an interactive mode. Questions are asked to prompt input for every possible specification. The output of the program is a data set which can then be specified as the user input for the File Creation program. This program assures the user that his input to the File Creation Program is correct in syntax and that all possible specifications have been considered, and is particularly useful to new users of DATA-MAP. A File Maintenance Program is provided such that a designated data base monitor at each user installation can maintain the Master File. Various functions are provided in the File Maintenance Program such as listing the contents of the Master File, location of each partition, the date each was created, its user's name and the last date the partition was accessed. The contents of each partion may also be listed. Partitions may be deleted, saved on tape or restored through use of this program.

3. USER CONVENIENCE. DATA-MAP was designed with consideration of the user. All user instructions are free field format with logical meaning and structure, and are identical for the interactive and batch modes. Many types of errors are detected in the input process and there are defaults for some entries.

Help Mode

When an invalid entry is detected the program prints a message indicating the erroneous entry and converts to the Help mode. In the Help mode, the user will be instructed as to the meaning of each remaining entry and, where possible, which allowed options are available for each entry, including the current default value for the entry, if one exists. If the user is confused at any time during the instruction input, all he need do is enter a question mark, ?, which will cause the program to prompt the user for the proper input.

Scratch Files

Rather than printing or plotting the results of any process, the user may choose to have the processing program store the output on a scratch file. Once data has been stored on a scratch file, that data can be used as input to an analysis or derivation or simply used for display. One of the primary advantages provided by scratch files is the ability to perform sequences of processes on the same data.

Info File

The Info File is provided as a device to simplify user specification of large numbers of data channels representing like parameters, geometric

positions of the parameters, and labeling information for output processes. When specifying large amounts of input data with the Info File, the user simply references the appropriate group by name.

CANCEL COMMAND

By entering CANCEL, all input entered for the step to that point is canceled and the program returns to the beginning of a new step. CANCEL at the beginning of a step is ignored.

COMMAND SEQUENCING

The Command Sequencing function allows the user to create, modify, execute, or delete sequences of command steps. These sequences are stored on a permanent disc file so that sequences created in one run of the Processing Program can be executed in other runs of this program. In these separate runs, the operating mode (i.e., Batch, Interactive, Interactive Graphics) may be different. There are three motivations for using the Command Sequence capability:

- The user may want to enter instructions interactively using the error checking process, but without execution of steps, and then execute the identical instructions in batch mode.

- The user may want to enter instructions interactively inspect the results immediately and then obtain line printer and incremental plotter versions of printout and plots from batch without retyping the instructions.

- The user may have long sequences of instructions to enter which are generally the same for all given executions but which involve a small number of changes.

4. IMPROVEMENTS. Improvements to DATA-MAP are currently being made to enhance its graphics, analysis and operational capabilities in order to expand its versatility and usefulness as an engineering tool. The improvements have been identified through exercising DATA-MAP and planning for future use of the system. Figure 4 indicates the types of improvements that are being made. These improvements are anticipated to be fully functional by July 1980.

The Data Transfer File provides a uniform format for test or simulation data in order to ease the problem of interfacing varied data bases with DATA-MAP. Figure 5 illustrates the manner in which the Data Transfer File will interface various data with the File Creation Program. The File Creation Program and the Processing Program are being modified to handle the Data Transfer File. The Rotorcraft Flight Simulation Program (C-81) is an existing general purpose flight simulation program which can analyze performance, stability and control, rotor loads, and aeroelastic stability for

single, compound, tandem, or side-by-side helicopter rotor configurations in hover, transition, cruise or high speed flight. The C-81 program is being modified to write the simulation data to the Data Transfer File for access by DATA-MAP. This will not only provide the ability to analyze and display the simulated data, but also directly compare the simulated data with test results. DATA-MAP will also be improved to include certain processing capabilities. Some of these improvements are specifically conceived to facilitate direct comparison or correlation of data from different data bases.

5. APPLICATIONS. DATA-MAP has fostered numerous applications as shown in figure 6. The potential for future applications of the system is good.

Two in-house projects are in progress at the Applied Technology Laboratory utilizing the OLS data. Report-quality graphics are being generated by DATA-MAP which will be used to document these projects. Several other in-house projects are planned for future work.

Other activities include international cooperation with the United Kingdom under the auspices of The Technical Coordinating Panel (TTCP). Helicopter flight test data, recorded by the Royal Aircraft Establishment, has successfully been partitioned on the Master File, and processed by DATA-MAP. This data along with selected OLS data, will form the basis of a joint Aerodynamic Loads Work Session at ATL in March 1980 with participants from the US Army, NASA and the Royal Aircraft Establishment.

DATA-MAP has been installed at the NASA-Ames Research Center on a VAX 11/780 computer to reduce and analyze rotor data obtained in the 40x80 Wind Tunnel. DATA-MAP is also being investigated to support the Transonic Dynamics Tunnel facility at the NASA-Langley Research Center.

Contractors use of DATA-MAP to date, has been limited. Several contractual investigations have successfully applied the system, thereby reducing the workload of the analyst while producing high quality graphics (references 3 and 4). The contractors' use of DATA-MAP will increase as they become aware of its versatility and usefulness as an engineering tool, and are encouraged to use the system. Contractors may be required in the future, to deliver experimental and analytical data to the Army in a format that provides for easy interfacing with DATA-MAP, where practicable.

DATA-MAP can play a major role in the validation and verification of new analytical methods through statistical correlation with available test data. DATA-MAP may also be incorporated into large software systems, such as the Second Generation Comprehensive Helicopter Analysis System (references 5, 6, and 7) as a post processor to perform basic output options.

6. CONCLUSIONS. DATA-MAP is a data analysis and management system that has been shown to be versatile and user oriented. It provides an engineering user, not necessarily computer oriented, a powerful tool to interactively analyze and interpret a vast amount of data which may otherwise be unmanageable. Most of the derivations and some of the analysis procedures are helicopter oriented; however, other processing capabilities, data management features and the graphics functions can readily be used for non-helicopter applications. The management and engineers at the Applied Technology Laboratory are enthusiastic about DATA-MAP's capabilities and are pursuing the establishment of a standard Data Item which will require future data bases to be put in a format that will readily interface with DATA-MAP whenever practicable.

References

1. Shockey, G. A., Cox, C. R. and Williamson, J. W., "AH-1G Helicopter Aerodynamic and Structural Loads Survey", Bell Helicopter Textron, USAAMRDL-TR-76-39, Eustis Directorate, US Army Air Mobility R&D Laboratory, Fort Eustis, Virginia, February 1977.

2. Philbrick, R. B. and Eubanks, A. L., "Operational Loads Survey-Data Management System, Volume I - User's Manual, Volume II - Systems Manaul", Bell Helicopter Textron, USARTL-TR-78-52A and B, Applied Technology Laboratory, US Army Research and Technology Laboratories (AVRADCOM), Fort Eustis, Virginia, January 1979.

3. Tangler, J. L., "Analysis of Low-Speed Helicopter Flight Test Data", Bell Helicopter Textron, USARTL-TR-79-19, Applied Technology Laboratory, US Army Research and Technology Laboratories (AVRADCOM), Fort Eustis, Virginia, August 1979.

4. Van Gaasbeck, J., "Validation of the Rotorcraft Flight Simulation Program C-81 Using Operational Loads Survey Flight Test Data", Bell Helicopter Textron, USAAVRADCOM-TR-80-D-4, Applied Technology Laboratory, US Army Research and Technology Laboratories (AVRADCOM), Fort Eustis, Virginia, (to be published).

5. "The Predesign Phase of the Second Generation Comprehensive Helicopter Analysis System," Computer Sciences Corporation, USARTL-TR-78-41, US Army Research and Technology Laboratories (AVRADCOM), Fort Eustis, Virginia, October 1978.

6. Hamrick, T., Copeland, D., Tarzanin, F., Staley, J., Hunt, L., and Burns, G., "Predesign of the Second Generation Comprehensive Helicopter Analysis System," Sciences Applications, Inc. USARTL-TR-78-42, Applied Technology Laboratory, US Army Research and Technology Laboratories (AVRADCOM), Fort Eustis, Virginia, December 1978.

7. "Predesign of the Second Generation Comprehensive Helicopter Analysis System," Control Data Corporation, USARTL-TR-78-43, Applied Technology Laboratory, US Army Research and Technology Laboratories (AVRADCOM), Fort Eustis, Virginia, October 1978.

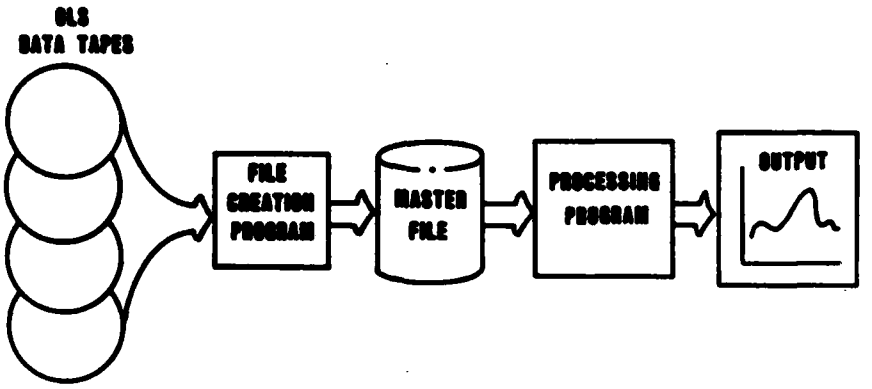

FIGURE 1. DATA-MAP EXECUTION SEQUENCE

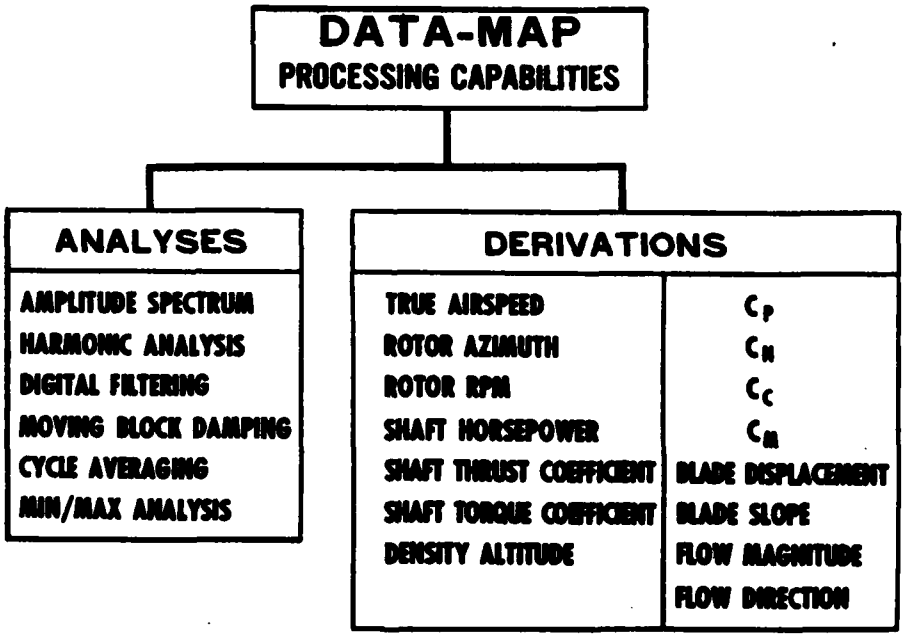

FIGURE 2. DATA-MAP PROCESSING CAPABILITIES

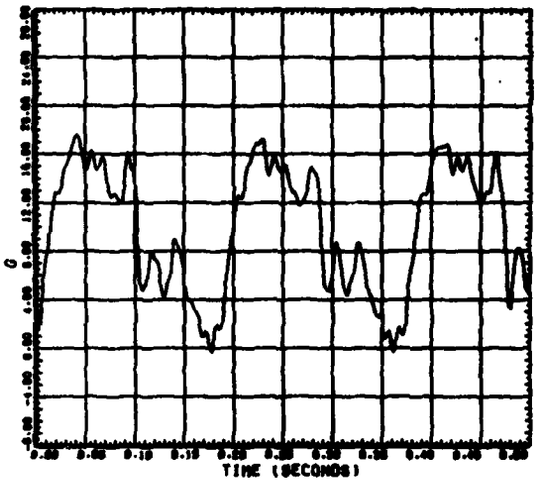

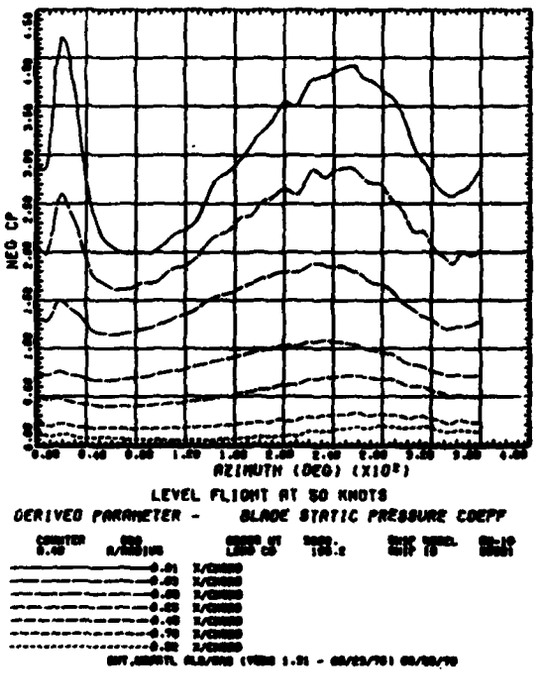

FIGURE 3. DATA-MAP OUTPUT OPTIONS

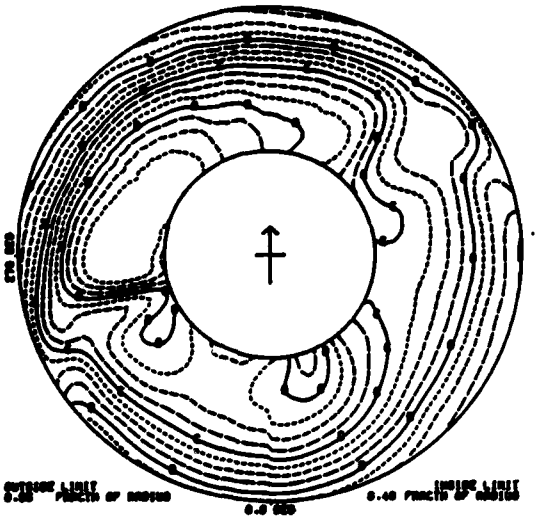

LEVEL FLIGHT AT 50 KNOTS

DERIVED PARAMETER - NORMAL FORCE COEFFICIENT

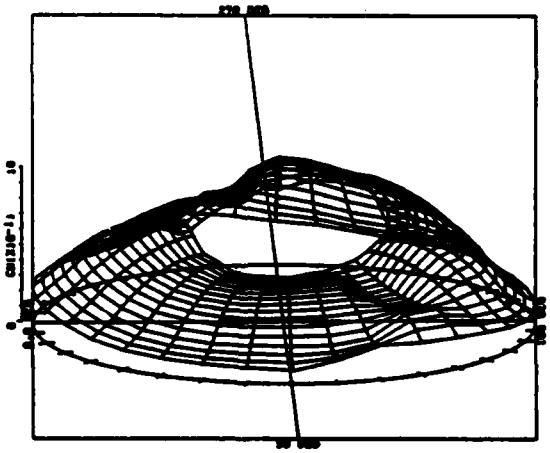

LEVEL FLIGHT AT 50 KNOTS

DERIVED PARAMETER - NORMAL FORCE COEFFICIENT

FIGURE 3. CONTINUED

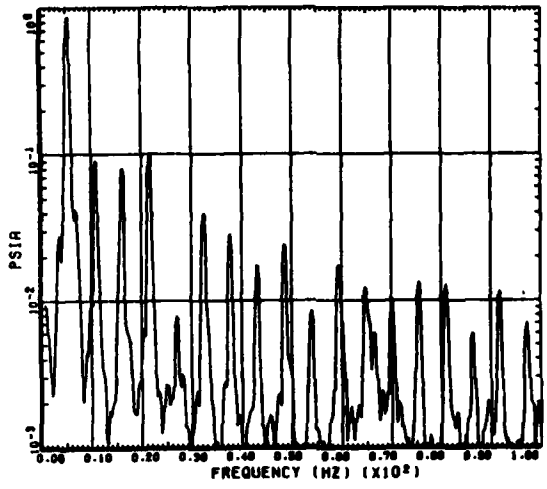

FIGURE 3. CONCLUDED

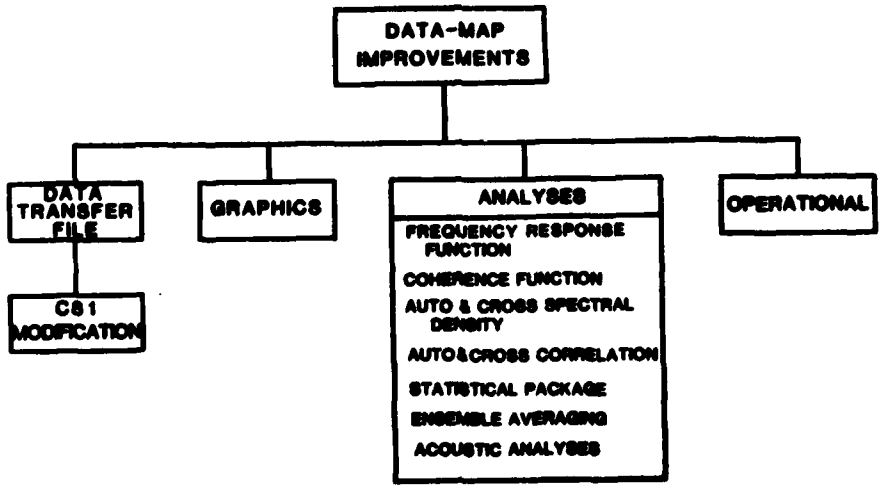

FIGURE 4. DATA-MAP IMPROVEMENTS

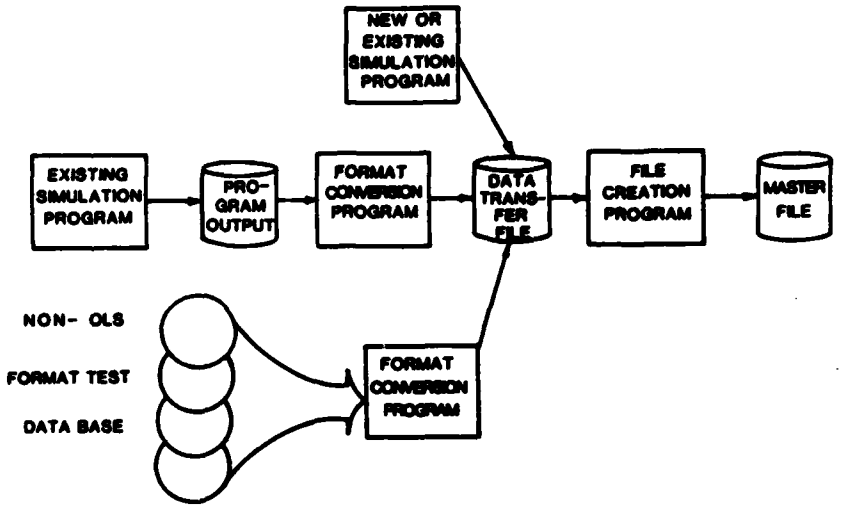

FIGURE 5. INTERFACING DATA-MAP WITH NON-OLS FORMATTED DATA

- 2 ATL HOUSE TASKS
  - A REPRESENTATIVE SUMMARY OF THE OLS DATA
  - APPLICATION OF THE OLS DATA
    - COMPRESSIBILITY
    - VORTEX INTERACTION
    - STAGNATION POINT AND ANGLE OF ATTACK
    - MODEL PARTICIPATION FACTORS
    - SIMULTANEOUS DATA
- TTCP HAG-4 WORKSHOPS
- IMPROVEMENTS TO ROTORCRAFT FLIGHT SIMULATION PROGRAM, C-81
- BEARINGLESS MAIN ROTOR DATA BASE
- ANALYSIS OF LOW-SPEED HELICOPTER FLIGHT-TEST DATA
- B/V C-80 POSTPROCESSOR
- NASA ACOUSTICS
- NASA-AMES INSTALLATION
- NASA TIP EFFECTS (40×80) WT TEST SUPPORT
- NASA-LANGLEY TRANSONIC DYNAMICS TUNNEL SUPPORT

FIGURE 6. DATA-MAP APPLICATIONS

ANALYTICAL AND NUMERICAL CRITERIA FOR THE EVALUATION OF INTERIOR BALLISTICS CODES

James A. Schmitt
Thomas L. Mann
Interior Ballistics Division
US Army ARRADCOM Ballistic Research Laboratory
Aberdeen Proving Ground, MD 21005

ABSTRACT. The initial validation program for a new, state-of-the-art, transient, two-phase, two-dimensional, interior ballistics algorithm ALPHA is presented. The verification of the ballistic cycle simulation for a simplified gun, the Lagrange gun, is made by comparing the computed results with the analytical solution for the core flow and by applying consistency tests on the numerical results. The ALPHA simulation of the two-dimensional, one-phase flow in the Lagrange gun is shown to be more accurate than previous calculations.

I. INTRODUCTION. At the ARRADCOM Ballistic Research Laboratory (BRL), a new, state-of-the-art, two-phase, two-dimensional, interior ballistics algorithm ALPHA is being developed under contract to Scientific Research Associates, Inc.[1] ALPHA will simulate the high pressure, turbulent, viscous, gas flow, and burning propellant motion behind an accelerating projectile as well as the heat transfer to the gun tube wall. The consistently split linearized, block-implicit scheme developed by Briley and McDonald[2] is employed to solve the two-phase, averaged equations. The validation of the basic models and the numerical technique in an interior ballistics environment is an important and necessary task. As the algorithm is being developed, we at the BRL are taking finished segments and testing them for accuracy. By this process, we hope to have a substantial in-house capability with a tested algorithm when the complete code is delivered. This paper describes the initial validation program and its findings.

The intial phase of the validation program consists of the 150mm and 20mm Lagrange gun simulations. The Lagrange gun consists of a projectile in a perfectly smooth cylindrical tube closed at one end. The flat based projectile is initially held fixed and an inert hot gas at high pressure is introduced in the enclosed cavity. The ballistic cycle of the Lagrange gun resembles that of a real gun, if the assumption is made that the propellant burns completely before the projectile moves. The Lagrange gun is used as a benchmark problem to validate the resolution of ALPHA's multiple-length-scale capability, the accuracy of its unsteady viscous gas flow simulation, and the accuracy of the core flow coupling to the projectile motion.

Without viscosity the gas flow in the Lagrange gun is one-dimensional and is governed by the rarefaction wave propagation. The rarefaction wave is generated by the motion of the projectile and traverses the distance between the projectile and breech several times before the projectile does exit the tube. Under the further assumptions of isentropic expansion of each element of gas, and of constant covolume, Love and Pidduck[3] developed an analytic solution for the flow field and projectile motion. Although the formulas for the gas properties become extremely complicated after the rarefaction wave reaches the projectile for the first time, the gas flow during the complete ballistic cycle for a 150mm Lagrange gun is calculated in Reference 3. If the gas within the gun is viscid, the flow is two-dimensional because of the tube wall boundary layer and the radial flow throughout the flow field. The radial flow is caused by the interaction of the larger core axial velocity which governs the projectile motion and the slower axial velocity in the tube wall boundary layer. Because of this disparity in the axial velocity in the radial direction, the gas particles in the boundary layer do not keep up with the projectile. Hence, a mass deficit is generated near the corner of the projectile and tube wall. To rectify this deficiency, a radial component of the velocity develops which is toward the wall near the projectile and toward the center-line away from the projectile. Although no analytic solution exists for the two-dimensional case, a computer simulation of the flow field was calculated by Heiser and Hensel[4] for a 20mm gun. Heiser and Hensel calated the values of the flow field variables at the projectile base, the velocity and thermal boundary layers along the tube wall, and the radial velocity distribution in the flow.

Section II lists the governing equations, states the boundary conditions and summarizes the numerical procedure used in ALPHA. In Section III, the results of the one-dimensional Lagrange gun are given. Using Love and Pidduck's projectile base pressure formula which is valid until the rarefaction wave reaches the projectile, a mesh and time-step resolution study, and an analysis of ALPHA's time-step selection procedures are made. The accuracy of the pressure and projectile velocity calculations from the start of the projectile motion to muzzle-time are determined by comparing them to Love and Pidduck's analytic calculations for the 150mm gun. Section IV contains the two-dimensional ALPHA results for the 20mm gun. These results are compared to Heiser and Hensel's. The ALPHA velocity boundary layer thicknesses as a function of time and position are compared to those which assume a similiarity solution. Section V contains the conclusions.

II. GOVERNING EQUATIONS AND NUMERICAL METHOD. The gas flow within the Lagrange gun is assumed to be single phase, compressible, laminar, viscous, heat conducting, and axisymmetric. The flow is also assumed to obey Stoke's relation of viscosity and Fourier's law of heat conduction. For this case, the governing partial differential equations in Ref. 1 can be written as:

$$\frac{\partial \rho}{\partial t} + \frac{1}{r}\frac{\partial}{\partial r}(r\rho u) + \frac{\partial}{\partial z}(\rho w) = 0 \quad , \tag{1}$$

$$\frac{\partial}{\partial t}(\rho u) + \frac{1}{r}\frac{\partial}{\partial r}(r\rho u^2) + \frac{\partial}{\partial z}(\rho uw) = -\frac{\partial P}{\partial r} + \frac{\partial}{\partial r}\left[\frac{2}{3}\mu\left(2\frac{\partial u}{\partial r} - \frac{u}{r} - \frac{\partial w}{\partial z}\right)\right] + \frac{2\mu}{r}\left(\frac{\partial u}{\partial r} - \frac{u}{r}\right) + \frac{\partial}{\partial z}\left[\mu\left(\frac{\partial u}{\partial z} + \frac{\partial w}{\partial r}\right)\right] , \tag{2}$$

$$\frac{\partial}{\partial t}(\rho w) + \frac{1}{r}\frac{\partial}{\partial r}(r\rho uw) + \frac{\partial}{\partial z}(\rho w^2) = -\frac{\partial P}{\partial z} + \frac{1}{r}\frac{\partial}{\partial r}\left[\mu r\left(\frac{\partial w}{\partial r} + \frac{\partial u}{\partial z}\right)\right] + \frac{\partial}{\partial z}\left[\frac{2}{3}\mu\left(2\frac{\partial w}{\partial z} - \frac{\partial u}{\partial r} - \frac{u}{r}\right)\right] , \tag{3}$$

$$\frac{\partial}{\partial t}(\rho h) - \frac{\partial P}{\partial t} + \frac{1}{r}\frac{\partial}{\partial r}(r\rho uh) + \frac{\partial}{\partial z}(\rho wh) = u\frac{\partial P}{\partial r} + w\frac{\partial P}{\partial z} - \Phi - \frac{1}{r}\frac{\partial}{\partial r}(rq_r) - \frac{\partial}{\partial z}(q_z) \quad , \tag{4}$$

where t, r, z, ρ, u, w, P, μ, h, Φ, q_r, and q_r are the time, radial coordinate, axial coordinate, density, radial velocity, axial velocity, pressure, viscosity, specific enthalpy, dissipation function, radial component of the heat flux vector and the axial component of the heat flux vector, respectively. The specific enthalpy is defined by $h = c_v T + P/\rho$, where T is the gas temperature. The heat flux vector is given as $(-k\,\partial T/\partial r, -k\,\partial T/\partial z)$. The pressure is given by the Noble-Abel equation of state $P(1-\eta\rho) = \rho RT/M$, where R is the universal gas constant, and M is the molar mass with the value of 23.8 g/mole. The specific heats (c_v and c_p), the ratio of specific heats (γ) and the covolume (η) are given constants. The viscosity coefficient μ is defined by Sutherland's law $\mu = c_1 T^{3/2}/(c_2 + T)$ where $c_1 = 1.458 \times 10^{-6}$ kg/(s·m·$K^{1/2}$) and $c_2 = 110.33$K. The thermal conductivity k is given by $k = c_p \mu/Pr$, where the Prandtl number Pr is $4\gamma/(9\gamma - 5)$. The dissipation function Φ is defined by

$$\Phi = \frac{2}{3}\left[\frac{1}{r}\frac{\partial}{\partial r}(ru) + \frac{\partial w}{\partial z}\right]^2 - 2\mu\left[\left(\frac{\partial u}{\partial r}\right)^2 + \left(\frac{u}{r}\right)^2 + \left(\frac{\partial w}{\partial z}\right)^2\right] - \mu\left[\frac{\partial u}{\partial z} + \frac{\partial w}{\partial r}\right]^2 \quad . \tag{5}$$

The motion of the projectile is assumed frictionless and is governed by the equation

$$m_p \frac{dw_p}{dt} = \iint_{\substack{\text{Projectile} \\ \text{Area}}} P(r,z_p,t)dA, \qquad (6)$$

where, m_p, z_p, and w_p are the mass, position, and axial velocity of the projectile. The gas properties and gun parameters that are not listed above vary with the simulation and are given in Table 1.

TABLE 1. GEOMETRY AND GAS PROPERTIES FOR THE 150MM AND 20MM LAGRANGE GUN SIMULATIONS

150mm	Uniform Cross Section	20mm
1.698m	Combustion Chamber Length	.175m
6.0m	Bore Length	1.115m
50kg	Projectile Mass	.120kg
$1.0 \times 10^{-3} m^3/kg$	Noble-Abel Gas	$1.08 \times 10^{-3} m^3/kg$
1.222	Gamma	1.271
621.09 MPa	Initial Pressure	300 MPa
2666.8K	Initial Temperature	3000K

The boundary conditions at the breech and projectile are the same for all the simulations; i.e., no-slip, adiabatic walls. The boundary conditions along the center-line are the symmetric conditions; $u = 0$, $\partial w/\partial r = 0$, $\partial T/\partial r = 0$, $\partial \rho/\partial r = 0$. Along the tube wall, the conditions vary according to the simulation and are given in the appropriate section. The density at a no-slip wall is determined by the normal momentum equation at the wall. The initial conditions for each simulation are given in Table 1.

The Eqs. 1-5 are solved numerically by the Briley and McDonald split linearized block implicit scheme.[2] All the ALPHA calculations are performed using a fully implicit time-step (backward difference) and centered spatial differences. In the ALPHA algorithm certain terms in the governing equations can be lagged by one time-step in order to simplify the implementation of the algorithm and to enhance its efficiency. The viscosity coefficient μ, the dissipation function Φ, all mixed second order partial derivatives, and the thermal conductivity k are lagged in these simulations. The computational mesh in the axial direction is an accordian type mesh, i.e., the first and last axial grid points are attached to the breech and projectile, respectively, and the mesh expands as the projectile accelerates down the gun tube. The details of the computational mesh for each simulation are given in the appropriate section.

Because the boundaries of the Lagrange gun are assumed adiabatic, the total energy within the computational domain should remain constant throughout a simulation. A conservation test for mass and total energy is incorporated into ALPHA. The deviation of these quantities from their initial values is monitored throughout the calculations.

Since mesh lines lie on the computational boundaries in the ALPHA algorithm, the axial velocity at the mesh point at the corner formed by the gun tube wall and projectile base is double-valued. If this mesh point is viewed as part of the tube wall, its axial velocity should be zero. If this mesh point is viewed as part of the projectile, its axial velocity should be the velocity of the projectile. For all the calculations reported in this paper, the former is used. No significant difference in the flow field occurs when the latter is chosen.

III. ONE-DIMENSIONAL LAGRANGE GUN. The geometry and gas properties for the 20mm and 150mm gun simulations are listed in Table 1. For the one-dimensional calculation, the computational domain (the enclosed cavity behind the projectile) has four cells in the radial direction, and a uniform mesh in the axial direction. Along the tube wall symmetry boundary conditions are stipulated. The gas in the simulations is viscous but the symmetry condition at the wall prevents a boundary layer from forming. A measure of the viscous effects in this flow is the deviation of the pressure P and density ρ from the isentropic relation

$$\frac{P}{\rho}\,\frac{1}{1-\eta\rho} = \frac{P_o}{\rho_o}\,\frac{1}{1-\eta\rho_o} \quad , \tag{7}$$

where the subscript zero denotes the initial values. In every one-dimensional calculation, the deviation of the left hand side of Eq. (7) is less than 1.4 percent from the right hand side. Hence, the viscous effects of the gas are believed to be negligible and the ALPHA simulations represent Love and Pidduck's case.

Because the Briley and McDonald scheme is implicit, the time-step selection is not coupled to the spatial mesh. Consequently, both the mesh and time-step must be chosen by the user. A mesh and time-step refinement study reveals the controlling truncation error mechanism. The study is performed with a uniform spatial mesh and constant time-step for the 20mm Lagrange gun. The calculations simulate the rarefaction wave propagation to the breech, its reflection and its return to the projectile. Because the pressure is a significant flow variable in a ballistic cycle, we compare the computed pressure value to Love and Pidduck's analytic value at the time the rarefaction wave reaches the projectile (t = .24201 ms). The largest difference between the pressure values occurs at this time and is listed in Table 2. The tabulated results show that for the 10 μs and 5 μs time-step runs, the time truncation error dominates the spatial truncation error and that only for sufficiently small time-steps does a mesh refinement significantly increase the accuracy. Because muzzle-times are of the order of milliseconds, a constant time-step of the order of microseconds would cause a lengthy calculation. To increase the accuracy of the results in Table 2 as well as the algorithm's efficiency, higher order temporal finite differencing should be employed.

TABLE 2. MESH AND TIME-STEP REFINEMENT FOR THE ONE-DIMENSIONAL 20MM LAGRANGE GUN

CONSTANT TIME-STEP (μs)	% DEVIATION*	
	11 MESH (Δz_o = 17.50mm)	22 MESH (Δz_o = 8.33mm)
10	2.82	2.80
5	2.09	2.04
2.5	1.59	1.49
1.25	1.39	1.13

*In base pressure values between Love and Pidduck and ALPHA at t = .24201 ms.

Initially, ALPHA had two time-step selection procedures for transient calculations - a constant time-step and a variable time-step based on the maximum relative percent change in the velocity components and density. For the runs recorded in Table 3, the variable time-step was increased by 25 percent if the maximum change was less than 4 percent, was decreased by 20 percent if the maximum change was greater than 6 percent, and was not altered if the maximum change was between 4 percent and 6 percent. The results in Table 3 indicate that the variable time-step does not produce sufficiently accurate results for this class of problems. For example, consider the 22 axial mesh and the initial time-step Δt_o = 1.25 μs. The computational work column indicates that the variable time-step selection procedure increases the Δt, because the computational work for the variable time-step is less than the constant time-step. In fact, the maximum Δt for this case is 10 μs. The final percent deviation between the 1.25 μs and 10 μs variable time-step runs are quite close. Consequently, a significantly smaller initial time-step for the variable selection does not insure a comparably more accurate solution. Furthermore, one has expended 84 percent more computational work for only a 8.4 percent increase in accuracy. The same behavior can also be seen for the 11 axial mesh runs. Because neither time-step selection procedure produces a highly accurate result with good efficiency, a new time-step selection procedure should be developed.

TABLE 3. COMPARISON OF VARIABLE AND CONSTANT TIME-STEP SELECTION PROCEDURES FOR THE ONE-DIMENSIONAL 20MM LAGRANGE GUN

MESH (UNIFORM)	INITIAL TIME-STEP Δt_o (μs)	PERCENT DEVIATION* (Δt_{max}=10 μs) VARIABLE	CONSTANT	RELATIVE COMPUTATIONAL WORK** VARIABLE	CONSTANT
22 (Δz_o = 8.33mm)	10	2.14	2.80	3.8	1.7
22	5	2.04	2.04	4.7	3.3
22	1.25	1.96	1.13	7.0	13.2
11 (Δz_o = 17.50mm)	10	2.25	2.82	2.1	1
11	1.25	2.08	1.39	3.8	7.8

*In base pressure values between Love and Pidduck and ALPHA at t = .24201 ms

**Number of finite difference nodes evaluated to reach t = .24201 ms

Questions on the optimal choice of mesh and time-step selection procedure are not addressed. However, it is clear from Table 3 that for a comparable amount of computational effort, the accuracy can vary substantially depending on the mesh and time-step. For example, the calculation with a 11 mesh and a constant time-step of 1.25 μs takes only 11 percent more computational work than calculation with the 22 mesh and variable time-step (Δt_o = 1.25 μs), and yet the accuracy is 29 percent better.

For the one-dimensional 150mm gun simulation a 89 uniform axial mesh is used. Because the existing time-step selection procedures are not adequate for this class of problems and because the axial rarefaction wave propagation within the tube governs the entire flow field, a time-step selection procedure based on the wave speed and the axial computational mesh is utilized, i.e.,

$$\Delta t = \sigma \cdot \frac{\Delta z_{max}}{(a+w)_p} \quad , \tag{8}$$

where $(a+w)_p$ is the sound speed plus the gas axial velocity at the projectile base and σ is a input constant. This axial Courant-Friedrichs-Lewy type condition is not used for any numerical stability reasons but as a compromise time-step selection procedure. In the initial phase of the simulation, the axial mesh size and the quantity $(a+w)_p$ do not change significantly, thus, Eq. (8) approximates a constant time-step. In the final phase the mesh size increases dramatically (by a factor of 4 or 5) and a time-step selection based on Eq. (8) allows a larger time-step as the spatial truncation error also increases. This time-step selection attempts to perserve some of the accuracy of a constant time-step while allowing a faster calculation. Furthermore, the objection of the variable time-step selection procedure is eliminated because a smaller value of the constant σ consistently makes the time-step smaller for a given mesh and improves the accuracy of the calculation. For the 150mm gun, the constant σ is set to one.

Figure 1 shows the Love and Pidduck's calculated pressure decrease due to the rarefaction wave propagation. The displacement of the projectile and subsequent gas expansion causes the rarefaction wave. At t=0, the pressure is at its initial value. At t = .4772 ms, the position of the rarefaction wave (given by the slope discontinuity) is midway between the projectile and breech. At t = .9544 ms, the rarefaction wave reaches the breech where it is reflected. This wave arrives back at the displaced projectile at t = 2.117 ms. The rarefaction wave is again reflected and

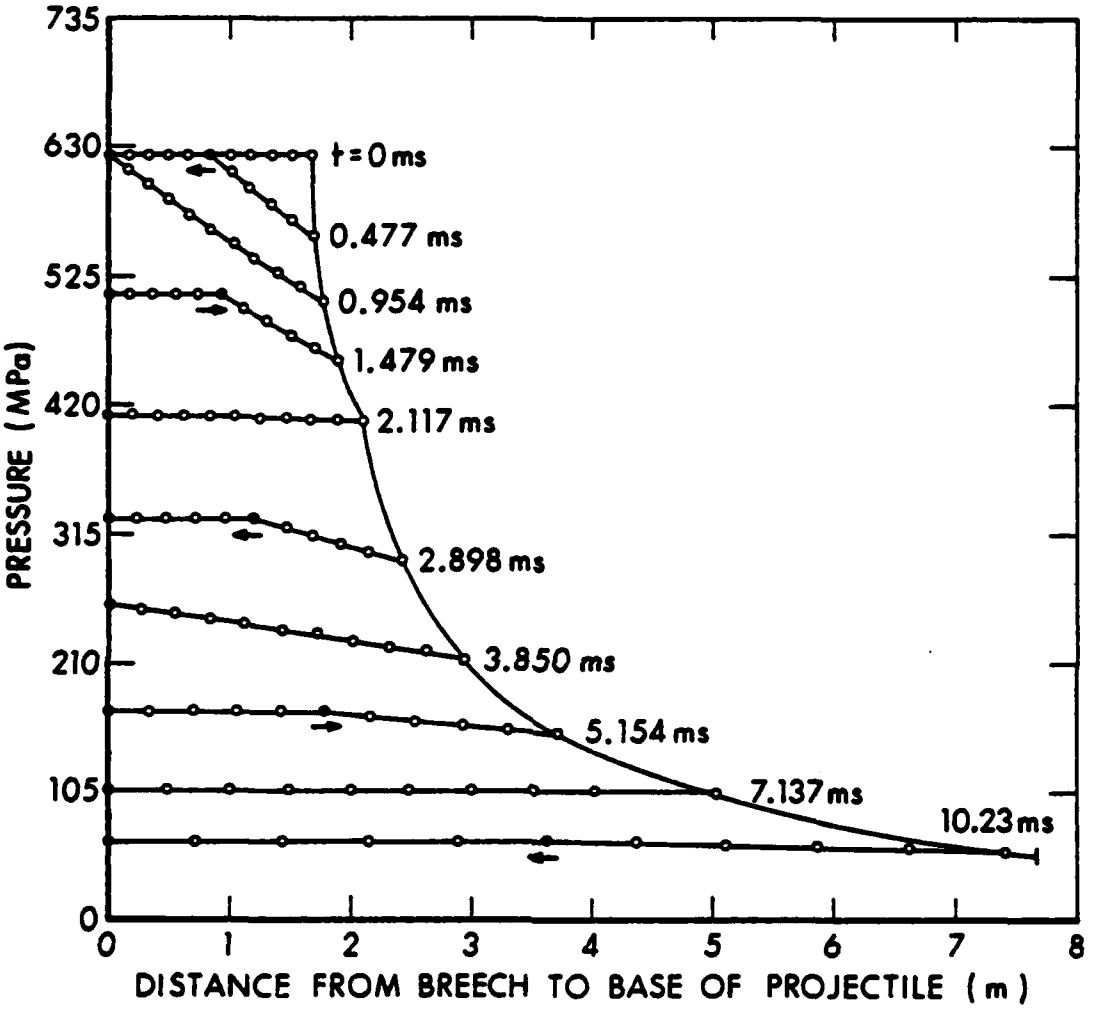

Figure 1. Love and Pidduck's Pressure Profiles for the 150mm Lagrange Gun (Adapted from Ref. 3).

the entire process is repeated. At muzzle time, t = 10.58 ms, the rarefaction wave is approximately halfway to the breech for the third time. The magnitude in the slope discontinuity of the pressure curve decreases with time due to the equilibration of the pressures during the gas expansion. The projectile's position curve shows a distinct slope discontinuity when the rarefaction wave reaches the projectile for the first time. At the second arrival t = 7.137 ms, the magnitude of the slope discontinuity is extremely small and cannot be discerned in Figure 1. The ALPHA results are plotted in Figure 2. Although the times at which the pressure profiles are plotted do not coincide with those of Love and Pidduck, the same features seen in Figure 1 are present in Figure 2.

Figure 3 shows a detailed comparison of Love and Pidduck's pressure profile with ALPHA's pressure profile at t = 2.898 ms. At the breech and projectile (away from the rarefaction wave) the difference between the pressure values are less than 0.2 percent. At the rarefaction wave, the difference is less than 1.1 percent. The slope discontinuity in the analytic solution is smeared out in the numerical calculation. The ALPHA pressure history at the projectile is compared with the analytic values in Figure 4. Throughout most of the calculation, the values differ by less than 0.4 percent. The deviation increases significantly to over 2 percent when the rarefaction wave reaches the projectile. This is consistent with results in Figure 3, i.e., the accuracy of the pressure value at the rarefaction front is less than at a distance from it. The decrease in the accuracy of the ALPHA pressure values for t > 6 ms is due to the increase truncation error generated by the expanding axial mesh. Figure 5 shows the comparison of the projectile velocity histories. The ALPHA values are within 0.6 percent of Love and Pidduck's values through muzzle-time.

IV. TWO-DIMENSIONAL LAGRANGE GUN. The no-slip boundary condition along the tube wall is imposed for this calculation. Because the gas is viscous, a two-dimensional flow develops. The tube wall is assumed to be adiabatic as is the breech and projectile. The computational grid at t = 0 is given in Table 4. Grid concentrations along the tube wall and projectile are used in order to resolve the boundary layer and radial flow near the projectile, respectively. The time-step procedure for this run is the minimum time-step which is generated by the variable time-step procedure and by Eq. (8). The rationale for this time-step is based on the facts that the variable time-step procedure has been used to accurately compute compressible boundary layers and that the time-step given by Eq. (8) produces at most a 2.3 percent error in the pressure values for the rarefaction wave propagation in the 150mm gun. By using the minimum, both phenomena which occur in this two-dimensional problem should be accurately computed. For this simulation, the constant σ is set to one.

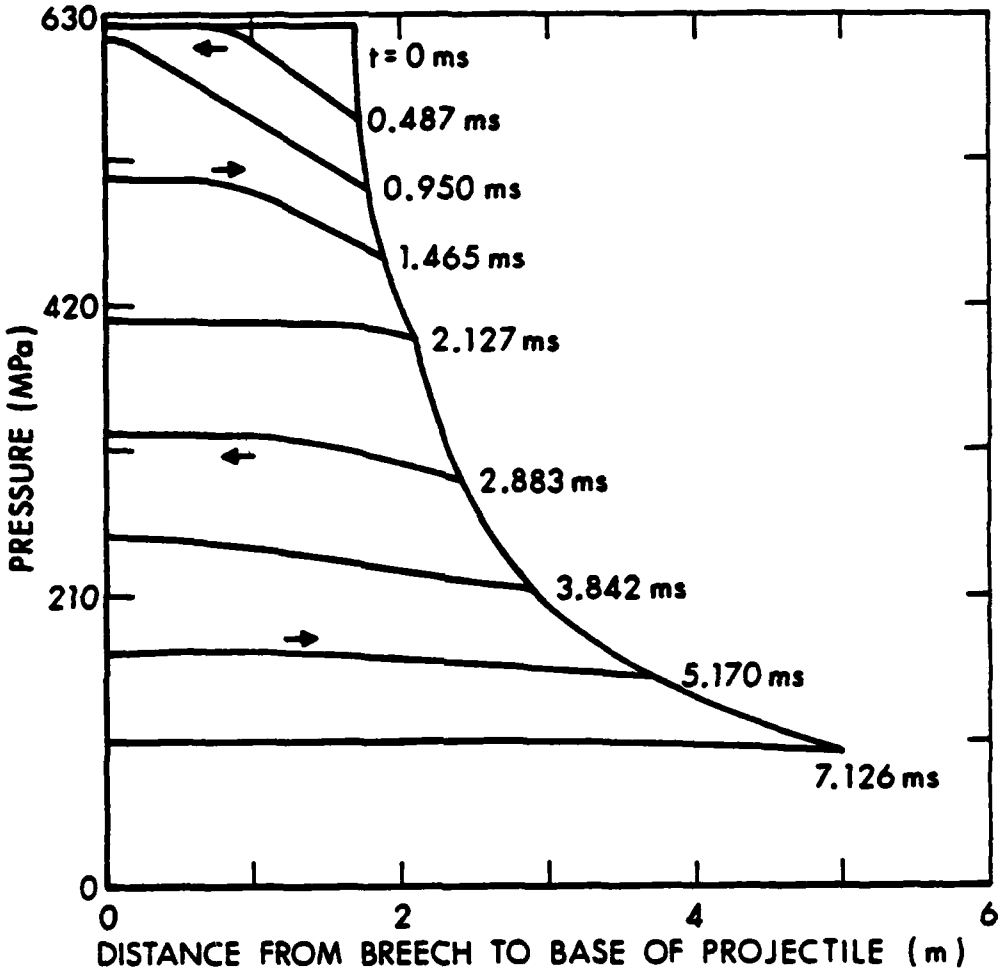

Figure 2. Pressure Profiles for the 150mm Lagrange Gun Computed by ALPHA.

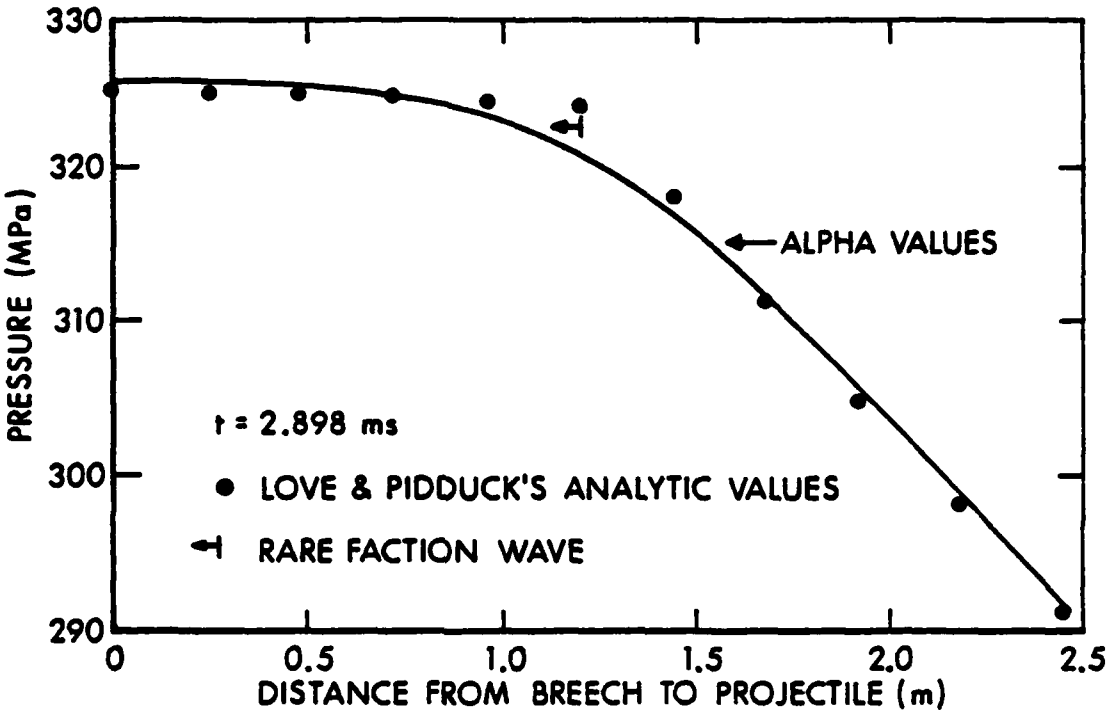

Figure 3. Comparison of Pressure Profiles After Rarefaction Wave Has Been Reflected From the Projectile for the 150mm Lagrange Gun.

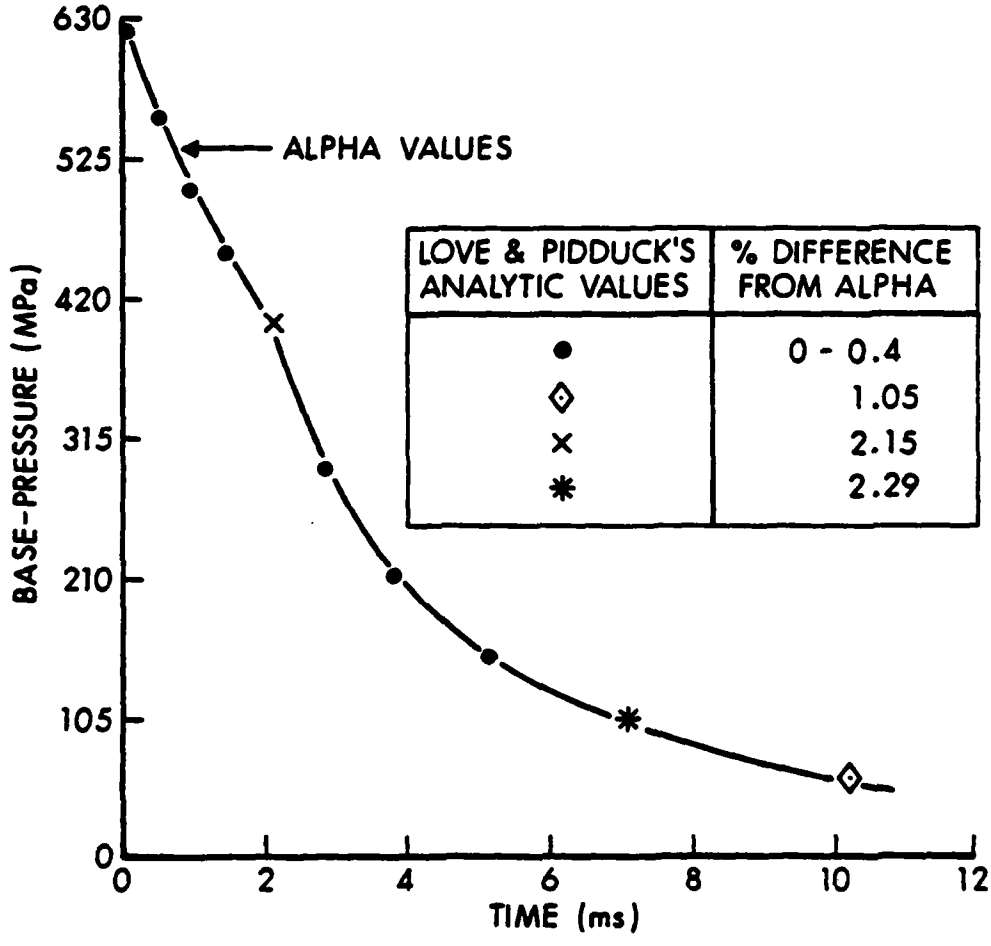

Figure 4. Comparison of the Projectile Base Pressure Histories for the 150mm Lagrange Gun.

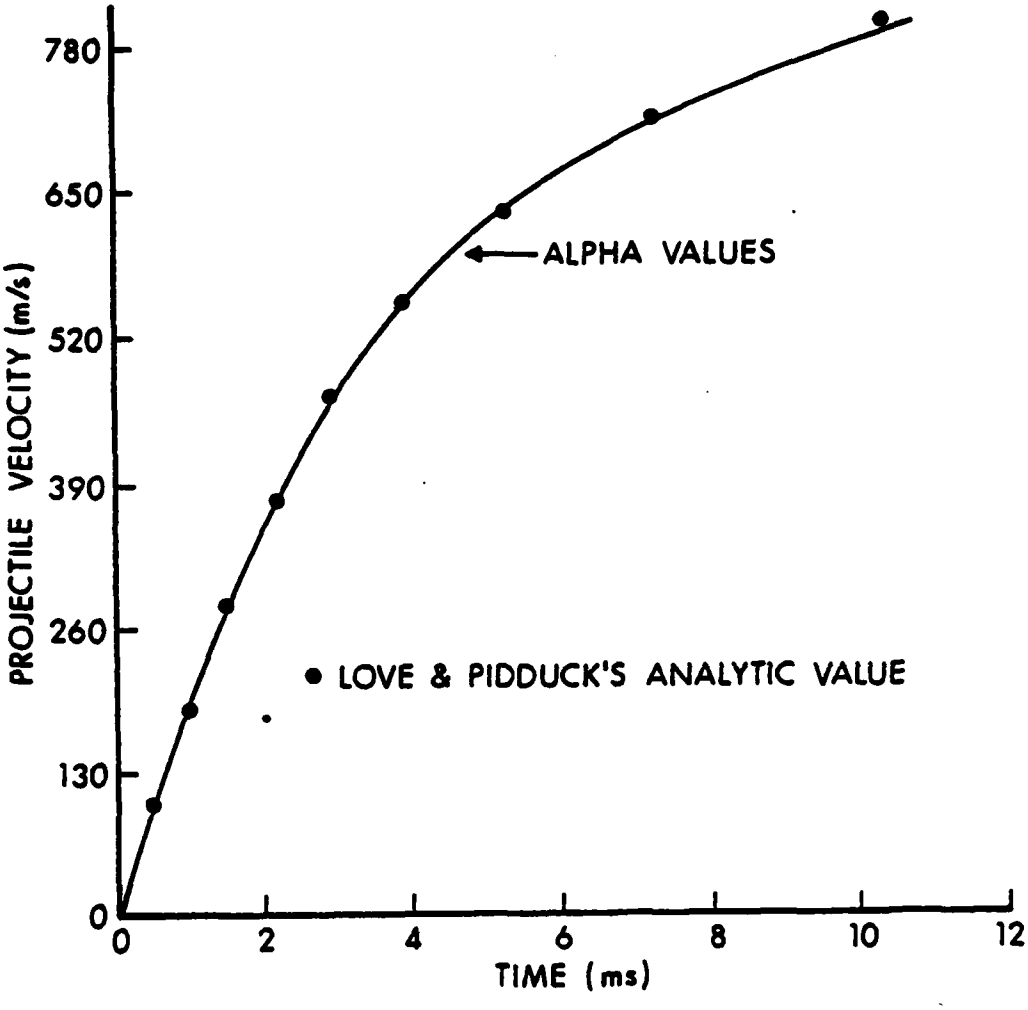

Figure 5. Comparison of the Projectile Velocity Histories for the 150mm Lagrange Gun.

TABLE 4. COMPUTATIONAL MESH FOR THE TWO-DIMENSIONAL 20MM LAGRANGE GUN SIMULATION

NUMBER	RADIAL INCREMENTS (MM)	AXIAL INCREMENTS (MM)
1	.00778 (Tube Wall)	.00276 (Projectile)
	.01155	.00362
	.01713	.00468
	.02541	.00607
5	.03764	.00786
	.05568	.01017
	.08218	.01318
	.12087	.01706
	.17692	.02210
10	.25710	.02861
	.36977	.03704
	.52395	.04796
	.72696	.06207
	.97971	.08035
15	1.26983	.10395
	1.56520 (Midway)	.13448
	1.81402	.17388
	1.95821 (Center Line)	.22474
		.29029
20		.37465
		.48303
		.62193
		.79940
		1.02524
25		1.31119
		1.67080
		2.11928
		2.67246
		3.34532
30		4.14922
		5.08793
		6.15246
		7.31528
		8.52543
35		9.70698
		10.76340
		11.58988
		12.09234
		12.20841
40		11.92313 (Midway)
		11.27290
		10.33597
		9.21362
		8.00911
45		6.81124
		5.68545
		4.67230
		3.79072 (Breech)

The gun geometry, gas parameters, initial conditions (see Table 1), and boundary conditions used in the simulation are identical to those used by Heiser and Hensel.[4] Despite this duplicate setup, the computed muzzle-velocities differ greatly: Heiser and Hensel computed over a 700 m/s muzzle-velocity (see Figure 6) while ALPHA's value is less than 600 m/s (see Figure 7). To determine the more accurate calculation, the Love and Pidduck rarefaction wave arrival time at the projectile was compared to the calculated times. Although the development of the boundary layer along the tube wall may alter somewhat the rarefaction wave propagation, the rarefaction wave arrival times for the one-dimensional and two-dimensional simulations should be comparable. Taking the slope discontinuity in the projectile pressure history curves as the arrival time of the rarefaction wave at the projectile, we find that the arrival time computed by Heiser and Hensel is 96 percent larger than Love and Pidduck's value of .24201 ms and that computed by ALPHA is 4 percent smaller. Consequently, we feel that the ALPHA result is the more accurate. Because a higher pressure is maintained at the projectile base for a longer time in Heiser and Hensel's simulation, the muzzle-velocity is larger and the muzzle-time is shorter. The dashed curves in Figure 6 are Heiser and Hensel's results for a breechless gun (the rarefaction wave never returns to the projectile).

The axial velocity near the center-line for a given time can be approximated well by a linear profile with the axial velocity equal to zero at the breech, and equal to the projectile velocity at the projectile base. Furthermore, the gun tube wall is at rest. This configuration resembles that for the steady Falkner-Skan similarity solution for the boundary layer with a linear core velocity. The boundary layer thicknesses away from the projectile base are almost constant as are the boundary layer thicknesses in the corresponding Falkner-Skan solution (see Figure 8). In the similarity solution the boundary layer thickness is given by

$$\delta = K \left[\frac{\bar{\mu} \bar{z}}{\bar{\rho} \bar{w}} \right]^{1/2} , \tag{9}$$

where K is a proportionality constant and $\bar{\mu}$, $\bar{\rho}$, $\bar{z}$, $\bar{w}$, are the gas viscosity coefficient, gas density, axial position, and axial gas velocity in the core flow, respectively. The value of the constant K at specific times is computed at a calibration point (the second axial mesh point from the breech) from Eq. (9) by using the core values and the 99 percent velocity boundary layer thickness value which is calculated from the ALPHA velocity field. Once the constant K is determined, a "theoretical" value of the boundary layer thickness via Eq. (9) can be computed for the given time and for any position from the ALPHA center-line values of $\bar{\mu}$, $\bar{\rho}$, and $\bar{w}$. The comparisons

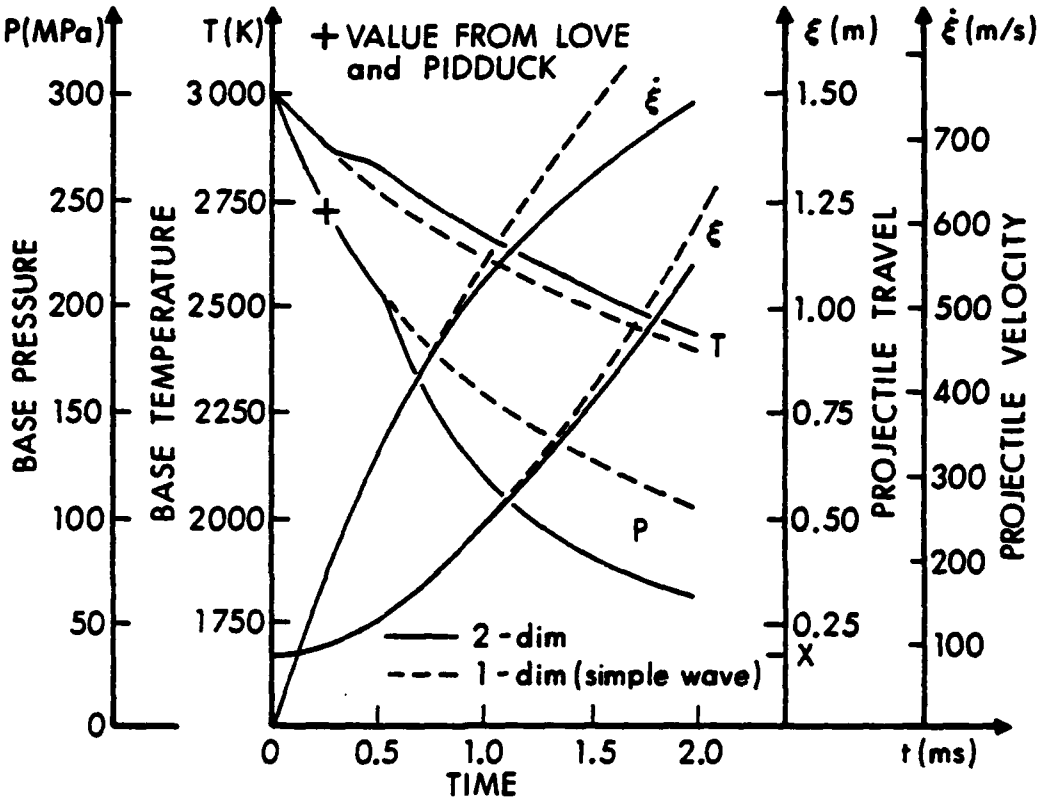

Figure 6. Heiser and Hensel's Projectile Histories
(Adapted from Ref. 4)

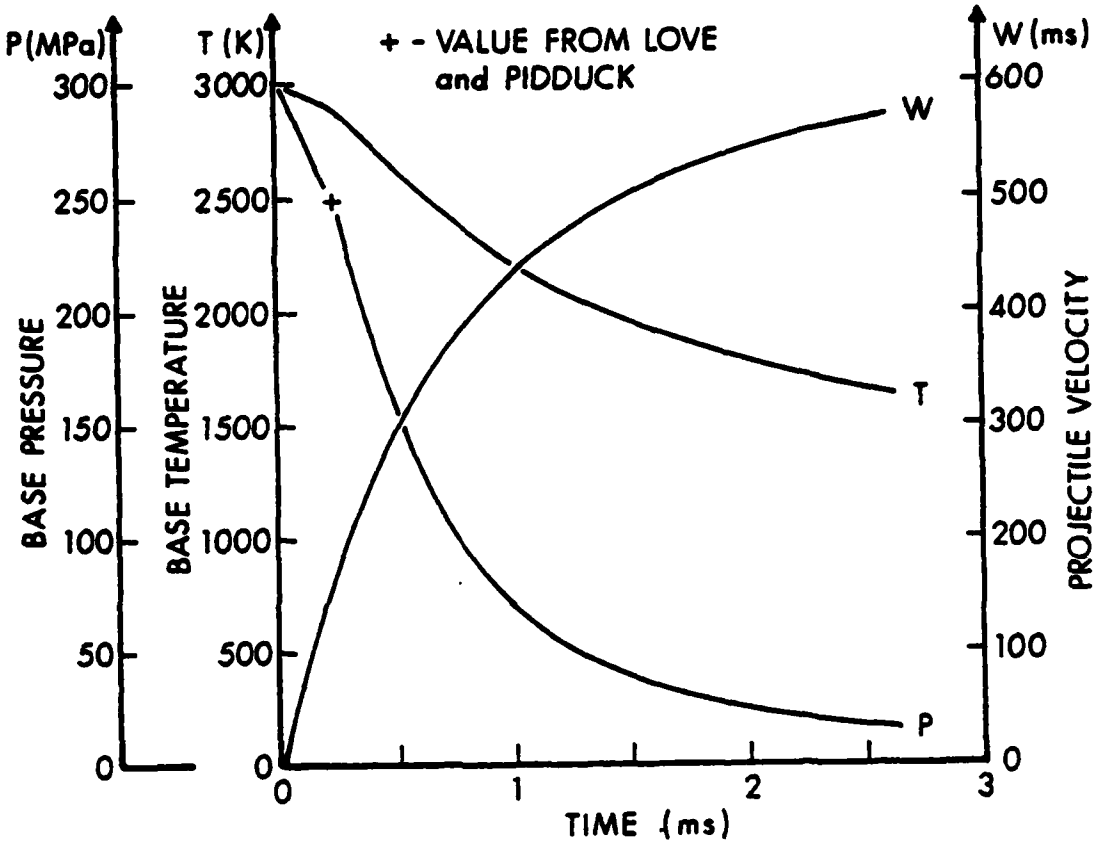

Figure 7. Projectile Histories Computed By ALPHA.

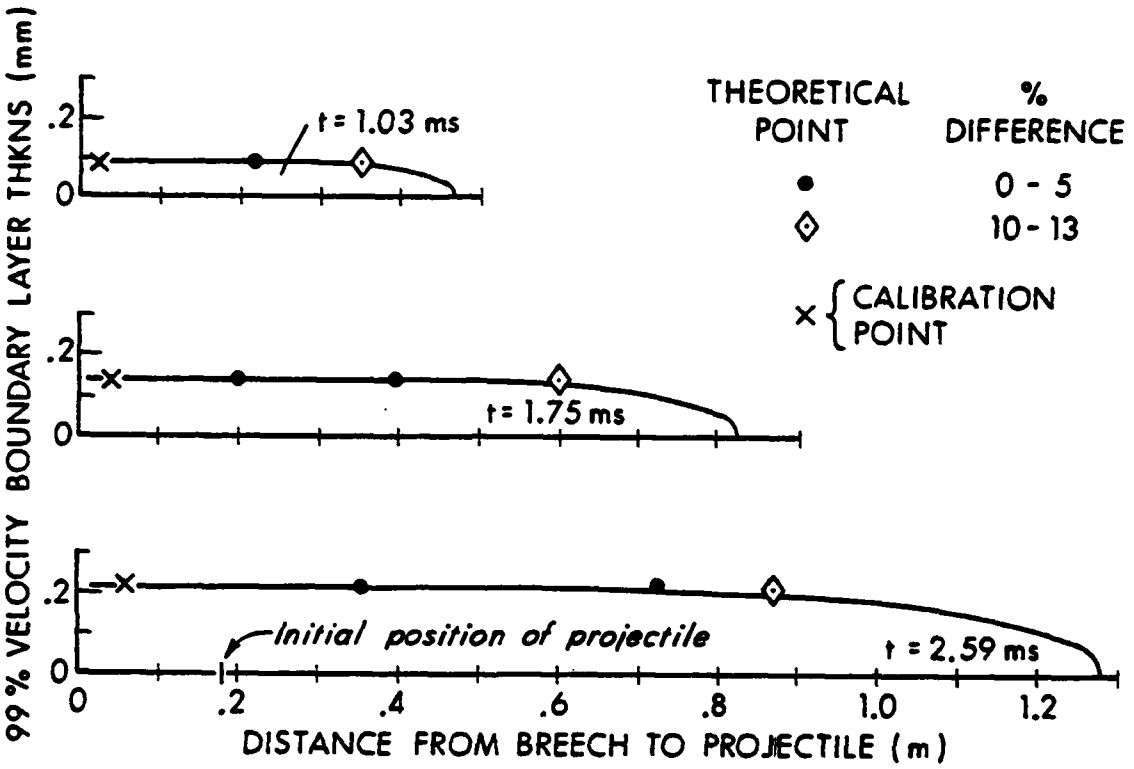

Figure 8. Comparison of the Velocity Boundary Layer Thickness (Given by ALPHA and by Eq. (9)).

between these "theoretical" values and the actual 99 percent velocity boundary layer values are given in Figure 8. Away from the projectile base, these values differ by no more than 5 percent, and the ALPHA values seem to be self-consistent. The boundary layer thickness is the largest at muzzle-time when it reaches .22mm. Heiser and Hensel's velocity boundary layers thickness are less than .1mm. This discrepancy is reasonable because Heiser and Hensel predicted a larger core velocity which increases the core Reynolds number and decreases the boundary layer thickness.

A typical velocity field computed by ALPHA is shown in Figure 9. Because the radial velocity is of the O(1 m/s) and the axial velocity is of the O(100 m/s), different plotting scales are used. Figure 9 shows only the velocity vectors for a selected number of mesh points. If the velocity vectors at each mesh point would be shown, the high concentration of grid points would obscure the flow picture near the wall and projectile. The ALPHA velocity field does not change qualitatively but only quantitatively in time. The axial flow in the core accelerates from zero at the breech to the projectile velocity. The tube wall boundary layer can clearly be seen. Figure 9 does not show the small non-zero radial velocity in the interior of the computational domain and away from the projectile, because their magnitudes are so small. Close to the projectile, the radial flow reverses direction and significantly increases in magnitude. The radial flow is developed in order to rectify the mass deficit at the corner of the projectile and wall which is caused by the boundary layer along the wall. Figure 10 shows Heiser and Hensel's velocity field at two times. Despite the fact that these velocity fields are near muzzle-time and are only 0.1 ms apart, they differ significantly in the radial component. The ALPHA velocity field is more consistent with the flow field mechanisms.

V. CONCLUSION. The initial validation program for ALPHA via the Lagrange gun reveals several important facts. (1) Higher order temporal finite differencing schemes should be used to increase ALPHA's accuracy and efficiency. (2) A better time-step selection procedure should be developed for the class of problems involving unsteady wave propagation. (3) Despite a relatively coarse core mesh and large time-step, ALPHA can compute the one-dimensional rarefaction wave propagation to within 2.3 percent and projectile motion to within 0.6 percent. (4) ALPHA's simulation of the two-dimensional Lagrange gun is more accurate than previous calculations. (5) The gun tube wall boundary layer thickness computed by ALPHA is consistent. (6) ALPHA calculations conserve mass and energy to within 0.3 percent for a complete simulation.

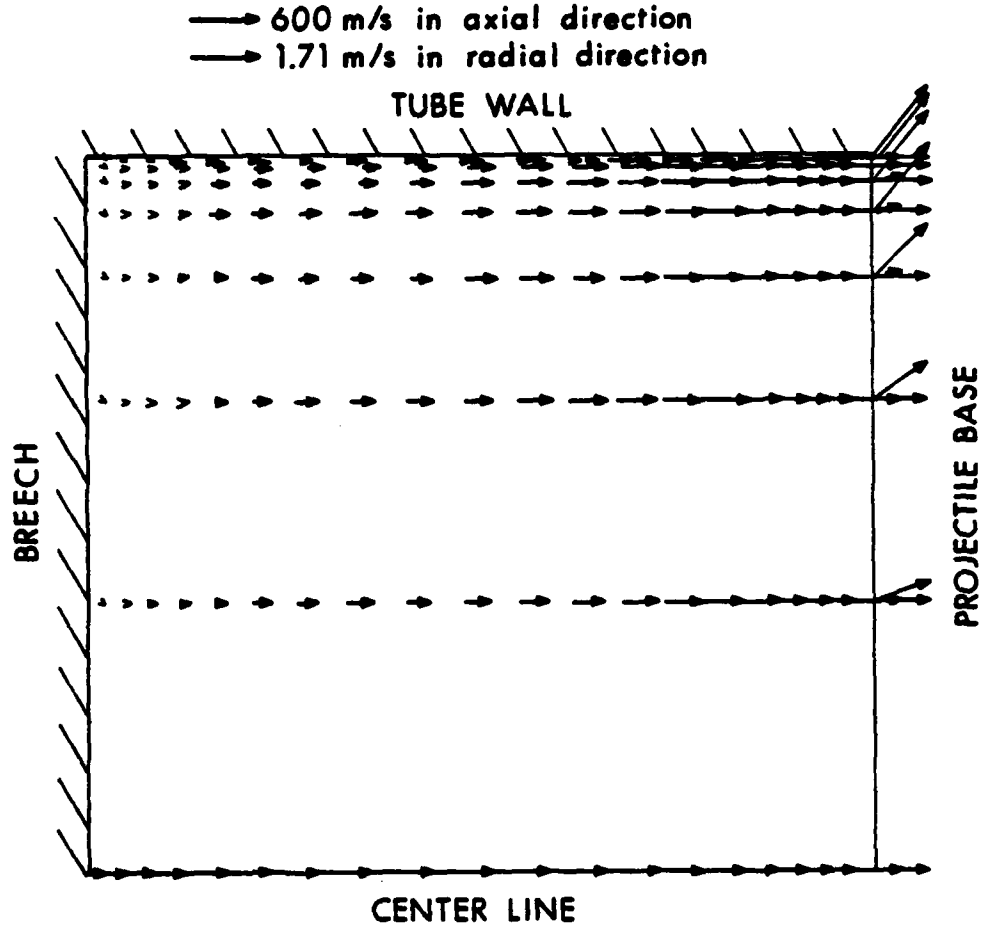

Figure 9. Edited ALPHA Velocity Profile at t = 2.589 ms.

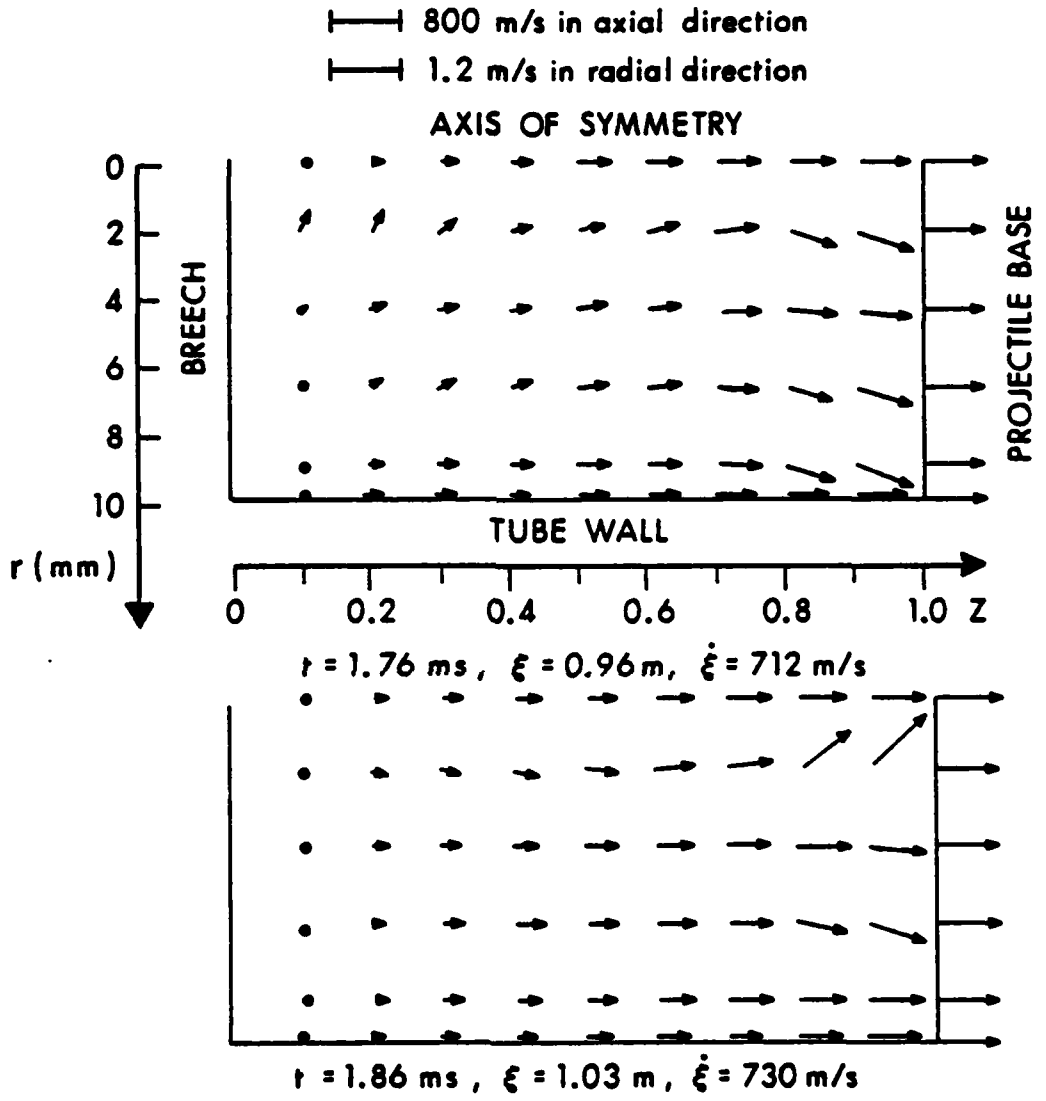

Figure 10. Heiser and Hensel's Computed Velocity Profiles (Adapted from Ref. 4).

The importance of the analytical solution of Love and Pidduck in this study cannot be over emphasized. This analytic solution is used, at least partially, in forming four out of the six conclusions above. Furthermore, in the initial validation program of a new code, an analytic solution is superior to experiments, because the uncertainties in the experimental set-up and the errors in the measurements, are absent.

The future work with ALPHA consists of testing higher order temporal finite difference schemes and time-step selection procedures for the Lagrange gun environment. A detailed study of the radial flow and its effects on the temperature field especially near the projectile as well as the affects of the multi-valued corner point (at the intersection of the gun tube wall and projectile base) on the flow field will be studied.

ACKNOWLEDGMENT

The authors have benefited from many discussions with Dr. Howard J. Gibeling at Scientific Research Associates, Inc., regarding the ALPHA algorithm.

REFERENCES

1. H.J. Gibeling, R.C. Buggeln, H. McDonald, "Development of a Two-Dimensional Implicit Interior Ballistics Code", Contract Report ARBRL-CR-00411, USA ARRADCOM BRL, APG, MD, January 1980.

2. W.R. Briley and H. McDonald, "Solution of the Multidimensional Compressible Navier-Stokes Equations by a Generalized Implicit Method", J. Comp. Phys., 24, pp. 372-397, 1977.

3. E.H. Love and F.B. Pidduck, "Lagrange's Ballistic Problem", Phil. Trans. Roy. Soc., 222, pp. 167-226, 1921-22.

4. R. Heiser and D. Hensel, "Calculation of the Axisymmetric Unsteady Compressible Boundary Layer Flow Behind a Moving Projectile", Proceedings of the Fourth International Symposium on Ballistics, 1978.

FINITE ELEMENT COMBUSTION INSTABILITY - INTERNAL BALLISTICS ANALYSIS

Robert M. Hackett
U.S. Army Missile Laboratory
Propulsion Directorate
Redstone Arsenal, Alabama 35809

ABSTRACT. Using sophisticated numerical analysis techniques, it is now possible to predict the instability of a solid propellant rocket motor subjected to small, combustion amplified disturbances. This capability is of considerable importance because of the probability of combustion instability in certain motors and the attendant jeopardy to successful motor and system operation. It is also important that the solid rocket motor designer be able to utilize this analysis capability, in conjunction with the internal ballistics analysis, which has been the key design component. Clearly, the integrated utilization of both techniques can provide a more efficient motor design procedure.

This paper describes the development of a finite element combustion instability analysis package for solid propellant rocket motors, which can be automatically coupled with an internal ballistics code to predict system response at any time from ignition to burnout. The program provides for the automatic coupling of the output from the ballistics code to a mesh generator so that the cavity-grain geometry is redefined in such a manner that a new finite element mesh for cavity and solid propellant is created at any selected time during the period of performance. Thus, the mesh corresponding to any burn distance can be automatically generated. The stability computations are based on the state-of-the-art in linear analysis of combustion instability: the irrotational motions of an inviscid, compressible fluid are coupled to the motion of a nearly incompressible, linearly viscoelastic solid, and the effect of the flow field and combustion on the acoustic oscillations is determined.

The analysis package is operational in status and has been employed to predict the combustion response of various types of solid propellant rocket systems. Agreement with a limited number of closed-form solutions and experimental observations has been obtained.

1. INTRODUCTION. The phenomenon of oscillatory combustion instability in solid rocket motors results from the responsiveness of the combustion process to oscillations in the flow environment. Because of the high probability of combustion instability in low signature motors and the attendant jeopardy to successful motor and system performance, the capability of instability prediction is of unquestioned importance. The state-of-the art in the field of linear analysis of combustion instability is based on a perturbation of the acoustic field in the burning propellant and an evaluation of the growth/decay coefficient associated with the acoustic pressure waves; a positive coefficient indicates an amplification of the waves and, therefore, instability,

and a negative value implies attenuation of the waves and stability.

In early 1975 the development of a Standardized Stability Prediction Method for Solid Rocket Motors (ref. 1) was begun by Aerojet Solid Propulsion Company under contract with the Air Force. It was decided that this method would employ the NASTRAN finite element fluid analysis option which was developed for rocket acoustic cavity analysis (refs. 2,3,4,5). The NASTRAN finite element analysis is axisymmetric and approximates the effect of radial slots (fig. 1) on the cavity acoustics. As long as the slot width is relatively narrow, the approximation provides an accurate model of the cavity acoustic response, but as the slot width increases, the accuracy diminishes. The NASTRAN option as used in the standardized method does not provide for the coupling of the vibratory response of the solid propellant grain to that of the acoustic cavity and hence does not provide a means of evaluating the damping of the acoustic oscillations by the propellant grain response. An additional limiting feature of the standardized method is that it employs a post processor, separate from the other analyses, for evaluating the growth/decay coefficient.

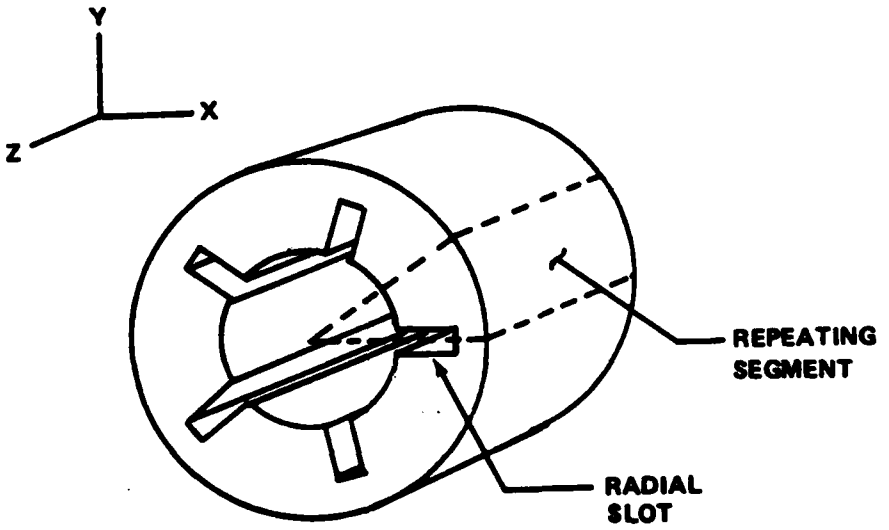

Figure 1. Three-dimensional cavity-solid propellant model.

The three-dimensional analysis package presented herein was developed primarily to provide 1) more generality, and therefore more accuracy in modeling complex cavity geometries, 2) a means of predicting the damping of acoustic oscillations by the solid propellant grain, 3) an integrated program designed solely for the purpose of combustion instability prediction with ease of use, and 4) a means of coupling the combustion instability analysis to an internal ballistics analysis. The developed package possesses all of these positive features as well as certain inherent, somewhat unappealing features associated with

"bigness" which will be pointed out later in the paper.

The main aspects of the developed three-dimensional code are listed below and will be elaborated upon subsequently in the paper:

1) utilizes a three-dimensional finite element mesh generator especially adapted to provide input to the program

2) utilizes the principle of dihedral symmetry which enables a consideration of only the smallest repeating geometrical segment

3) couples the response of the gas cavity with that of the solid propellant grain to enable the calculation of the frequency of the coupled system and the damping provided by the propellant grain

4) provides for modeling the propellant grain as a nearly incompressible material (which differs from the common minimum potential energy formulation)

5) utilizes the principle of condensation, wherein, in this case, the fluid pressure degrees-of-freedom are designated "master" and the solid propellant displacement and mean pressure parameter degrees-of-freedom are designated "slave." This enables a major reduction in the size of the problem: the number of equations is reduced from the total number of degrees-of-freedom of the coupled system to the number of fluid pressure degrees-of-freedom

6) provides the option of considering the response of the gas cavity alone (which models the cavity boundaries as being "acoustically hard"). This option might be utilized in certain cases where a savings in computer costs or storage is a dominant consideration. In this case the condensation approach previously described obviously would not be taken

7) calculates the three-dimensional potential flow field

8) evaluates the stability integrals for the calculation of the net driving/damping coefficient for each mode.

2. FINITE ELEMENT MESH GENERATION. It is only necessary to develop a finite element mesh for one repeating segment (fig. 1) of the total cavity-grain rocket geometry. This is true because of the employment of the principle of dihedral symmetry in the program. Although the three-dimensional element used in the program for both the cavity region and the propellant grain is a tetrahedron (ref. 6), the mesh is that of bricks, each brick, or quasi-hexahedron, being comprised of five basic tetrahedra. The breakdown of the quasi-hexahedra into tetrahedra is performed internally. The mesh generator is an

efficient routine which automatically creates the complete finite element mesh, for both cavity and solid propellant regions, from a minimal amount of input. Each repeating segment is sectioned in the longitudinal or z-direction, with each section comprised of a number of quadrilateral parts which are identified by a counterclockwise listing of their part boundary curves. Part boundary curves may be ellipses as well as straight lines and their points of intersection are designated by I,J indices as shown in figure 2.

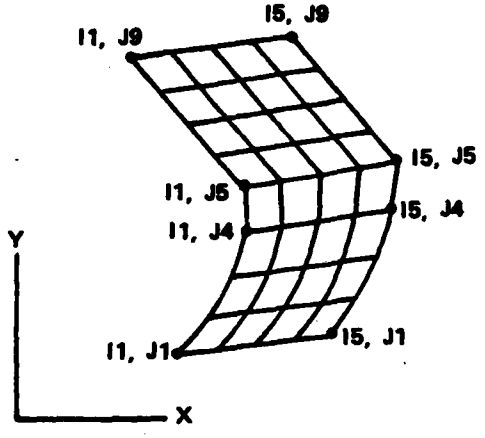

PART 1 (CAVITY)

I1, J1 TO I5, J1 (CURVE 1)
I5, J1 TO I5, J4 (CURVE 2)
I5, J4 TO I1, J4 (CURVE 3)
I1, J4 TO I1, J1 (CURVE 4)

PART 2 (CAVITY–SOLID PROPELLANT INTERFACE)

I1, J4 TO I5, J4 (CURVE 3)
I5, J4 TO I5, J5 (CURVE 2)
I5, J5 TO I1, J5 (CURVE 5)
I1, J5 TO I1, J4 (CURVE 4)

PART 3 (SOLID PROPELLANT)

I1, J5 TO I5, J5 (CURVE 5)
I5, J5 TO I5, J9 (CURVE 6)
I5, J9 TO I1, J9 (CURVE 7)
I1, J9 TO I1, J5 (CURVE 8)

Figure 2. Finite element mesh definition for cavity-solid propellant.

By coupling the output of a standard internal ballistics analysis computer code with the mesh generator one can obtain a combustion instability analysis at any stage of performance, i.e., at any instant from ignition of the propellant to burnout, as illustrated in figure 3. This has been done through the definition of additional part boundary curves, which conform to the geometry of the different zones of burning for the differing cavity-grain configurations. With the transfer of a small number of geometric parameters from the output of the internal ballistics code to the mesh generator, a complete combustion instability analysis can be initiated and automatically performed. The designation of these parameters and a detailed description of the development of the coupling program are found in references 7 and 8. Presently the coupling of an internal ballistics analysis with the combustion instability analysis is limited to the consideration of axisymmetric and star cross-section geometries, but increased part boundary curve definition is a matter of expansion of the program, not of additional development.

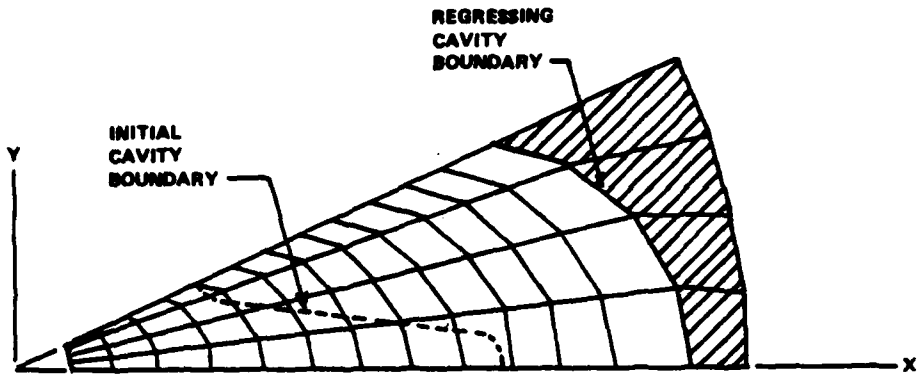

Figure 3. Finite element model of repeating segment with cavity-solid propellant interface defined by ballistics analysis output.

3. DIHEDRAL SYMMETRY. If a geometrically defined body is made up of identical segments symmetrically arranged with respect to an axis, the degrees-of-freedom for a finite element analysis can be transformed into uncoupled symmetrical components, thereby greatly reducing the number of equations which must be solved simultaneously (ref. 9). A further reduction can be effected if each segment has a plane of reflective symmetry. Dihedral symmetry is the term applied to this latter condition. It can be seen from figure 1 that a typical solid rocket geometry meets this requirement and, therefore, the principle of dihedral symmetry can be employed in a three-dimensional (cylindrical coordinate) analysis. The application of the principle to this problem is explained in detail in reference 10 and will not be reproduced here, but the resulting analysis will be discussed.

Employing the principle of dihedral symmetry, the program computes three distinct types of acoustic harmonics: the zero harmonic, the K harmonics, and the N/2 harmonic. The zero harmonic exists for all cases. The number of possible K harmonics is given by

$$K = 1, \ldots, L \tag{1}$$

where the harmonic index L is given by

$$L = \frac{N - 1}{2} \text{ (if N is an odd number)} \tag{2a}$$

$$= \frac{N - 2}{2} \text{ (if N is an even number)} \tag{2b}$$

where N is the number of radial slots or lobes. The N/2 harmonic exists only when N is even. Referring to the geometry of figure 1, then, one could calculate the zero, first, and second harmonics, the latter two being K harmonics. The longitudinal modes associated with

each harmonic are calculated as requested by the user. The result of this calculation (eigensolution) is the natural circular frequency associated with each acoustic mode and the corresponding acoustic pressure distribution (normalized acoustic pressure at each finite element nodal point) for the smallest repeating segment. The pressure distribution for each of the other segments is then simply calculated automatically through the dihedral transformation matrix. The acoustic velocity components (constant for the region occupied by each cavity tetrahedral element) are computed from the acoustic pressure nodal point values for those cavity elements which are adjacent to the propellant grain.

The theoretical formulation of the complete three-dimensional finite element analysis, in which the natural circular frequency, the acoustic pressure distribution, and the element acoustic velocities are calculated, is given in reference 11 and will not be repeated here. Reference 12 also presents the theoretical finite element formulation which was used in the development of this program.

4. COUPLED RESPONSE. The presence of the solid propellant grain can significantly shift the acoustic system frequency from that of the gas phase alone, a portion of the acoustic energy being dissipated by the deformable solid material. This effect can be one of the more significant sinks for acoustic energy in both large and small rocket motors, the amount of damping depending on the grain geometry and mechanical properties and on the acoustic mode shape and natural frequency.

In order to evaluate the coupled cavity-solid propellant grain response it is necessary to model, by the finite element method, both cavity and grain. This, of course, greatly increases the size of the problem to be solved, from the standpoint of number of initial degrees-of-freedom. The coupled finite element formulation of reference 12, which is coded in the three-dimensional program, is expressed in matrix form by:

$$\left(\begin{bmatrix} F & 0 \\ -U^T & K \end{bmatrix} - \lambda^2 \begin{bmatrix} C & U \\ 0 & \begin{matrix} M & 0 \\ 0 & 0 \end{matrix} \end{bmatrix} \right) \begin{Bmatrix} p \\ \Delta \\ H \end{Bmatrix} = 0 \qquad (3)$$

where $[F]$ is the fluid inertia matrix, $[C]$ is the fluid compressibility matrix, $[K]$ is the solid stiffness matrix, $[M]$ is the solid consistent mass matrix, $[U]$ is the matrix which couples acoustic pressure degrees-of-freedom to solid displacement degrees-of-freedom, $\{p\}$ is the acoustic pressure vector, $\{\Delta\}$ is the solid displacement vector, $\{H\}$ is the mean pressure parameter vector (to be elaborated upon later), and λ^2 is the eigenvalue of the coupled system.

The structural damping can be attributed to the out-of-phase re-

sponse of the solid propellant grain, which is measured in terms of the complex shearing modulus of the grain, which, in turn, results in a complex eigenvalue for the coupled system. The imaginary part of the complex eigenvalue obtained from the eigensolution is the natural circular frequency of the coupled system while the real part is the structural damping rate.

Since the complex shearing modulus is frequency dependent, a series of iterations may be necessary before the accurate value of complex modulus for input into the program is determined.

5. PROPELLANT GRAIN MODELING. Since the propellant grain is only accurately modeled as a nearly incompressible material, the well-known standard Navier displacement formulation, in conjunction with the Ritz procedure, would lead to inaccuracies in the finite element modeling of the grain. In order to avoid this situation the solid finite element formulation utilized in this program is that of a linear displacement-linear mean pressure tetrahedron (ref. 13). It is similar to the Herrmann variational formulation (ref. 14), which employs a linear displacement function and a constant mean pressure function. The finite element modeling of the propellant grain used in this program is outlined in detail in reference 12 and will not be repeated here.

6. EIGENVALUE ECONOMIZER - CONDENSATION. The extraction of eigenvalues and eigenvectors is a much more expensive operation than is the solution of simultaneous linear equations. It requires roughly twice as much time to extract a single eigenvalue as to do a single "static" analysis. In order to reduce or "condense" the number of degrees-of-freedom in the eigensolution, the following technique is utilized in the three-dimensional program. Further details of the method are found in reference 15.

The original formulation of the coupled system is given by equation 3, where the number of degrees-of-freedom is equal to the number of cavity nodal point pressures, plus the number of solid propellant nodal point displacement components, plus the number of solid propellant nodal point mean pressure parameter values (one at each propellant grain nodal point), for the analyzed repeating segment. The condensed formulation is given by:

$$\left(\left[F_r\right] - \lambda^2 \left[C_r\right]\right)\left\{p\right\} = 0 \tag{4}$$

where

$$\left[F_r\right] = \left[\begin{array}{c|c} I & \\ \hline K^{-1}U^T & \end{array}\right]^T \left[\begin{array}{c|c} F & 0 \\ \hline -U^T & K \end{array}\right] \left[\begin{array}{c|c} I & \\ \hline K^{-1}U^T & \end{array}\right] \tag{5a}$$

and

$$\left[C_r\right] = \left[\begin{array}{c} I \\ \hline K^{-1}U^T \end{array}\right]^T \left[\begin{array}{c|c} C & U \\ \hline O & \begin{array}{c|c} M & O \\ \hline O & Q \end{array} \end{array}\right] \left[\begin{array}{c} I \\ \hline K^{-1}U^T \end{array}\right] \tag{5b}$$

where I is the identity matrix. The relationship between initial and reduced degrees-of-freedom is

$$\left\{\begin{array}{c} p \\ \hline \Delta \\ \hline H \end{array}\right\} = \left[\begin{array}{c} I \\ \hline K^{-1}U^T \end{array}\right] \{p\} \tag{6}$$

7. UNCOUPLED RESPONSE. Although one of the most important features of the three-dimensional program is the coupled cavity-propellant response, the option of a cavity analysis alone is available to the user. In this case the cavity-solid propellant interface is modeled as an "acoustically hard" boundary. The cavity only option would greatly reduce the solution time and cost and would, in some cases, perhaps suffice. The user need make only two simple adjustments to the input data, and these adjustments are described in the user's guide to the three-dimensional code (ref. 16).

8. POTENTIAL FLOW CALCULATION. A separate operation is carried out in the sub-routine which performs a potential flow analysis for the purpose of determining the mean flow field in the rocket cavity. As in the case of the eigensolution, only the smallest repeating geometrical segment need be considered, and, for this calculation, only the cavity portion of the segment with the proper boundary conditions. The same general formulation of the finite element model equations of motion is utilized except that, in this case, the fluid is considered to be incompressible. The mass flow into the cavity from the burning propellant surface is modeled as a cavity-solid propellant interface nodal point quantity. It is calculated by summing the interface surface areas associated with each nodal point lying on the cavity-solid propellant interface. The solution of the resulting set of linear equations for the mean flow velocity components (constant for each cavity tetrahedron) is explained in reference 11 and will not be discussed here.

9. EVALUATION OF STABILITY INTEGRALS. The final operation consists primarily of the evaluation of the stability integrals associated with the various driving/damping coupling mechanisms which occur in the cavity chamber in the presence of combustion and flow. The stability integrals presently incorporated into the program are those derived in reference 17 for the three-dimensional case, along with the flow-

turning formulation also found in reference 17. The use of linear pressure (and therefore constant velocity) tetrahedral elements to represent the cavity region enables an explicit evaluation of the stability integrals, given the acoustic nodal point pressures and element velocities and the mean flow element velocities from the finite element solutions. At present the code does not contain a routine for evaluating nozzle damping or particulate damping. These additional calculations will be added.

The evaluation of stability integrals is for the purpose of calculating the driving/damping coefficient, α, a fact well-known to the combustion community. A positive α indicates a stable mode. The net value of α computed by the three-dimensional code is a summation of the computed values of α_{PC} (pressure coupling), α_{VC} (velocity coupling), α_{FT} (flow-turning), and α_{SD} (structural damping). The value of α_{SD} is obtained from the complex eigensolution described in an earlier section; the other three α-values are obtained from the evaluation of the stability integrals. It is known that the pressure coupling mechanism always drives the acoustic oscillations, that the velocity coupling mechanism may either drive or damp the oscillations, and that the flow-turning mechanism always damps the oscillations. Response factors (refs. 18 and 19) are input into the program as multiples of the stability integrals for the calculation of the α's obtained from the different coupling mechanisms. These propellant grain-dependent response functions are obtained from other analyses and utilized as direct input into the three-dimensional program.

10. COMPARISON WITH ANALYTICAL SOLUTIONS AND EXPERIMENTAL OBSERVATIONS. In order to affirm the accuracy and usefulness of any numerical analysis package it is necessary to make comparisons of results obtained numerically with available analytical closed-form solutions and experimentally obtained results. In the case of a complex analysis procedure such as that of combustion instability, available bases of comparison are limited in both regards. The following results are presented to support the contention of accuracy and utility of the developed package.

Analytical Comparisons. A right circular cylindrical cavity 254mm long and 254mm in diameter was modeled using an 18° repeating segment consisting of 32 quasi-hexahedral elements, 4 in the radial direction and 8 in the longitudinal direction. Acoustic frequencies corresponding to the first and second longitudinal modes (1L and 2L), the first tangential mode (1T), the first tangential-first longitudinal mode (1T-1L), and the first radial mode (1R) were solved for and are compared with the corresponding analytically obtained frequencies of the cavity. The values are shown in table 1.

Table 1. Numerically and Analytically Calculated Acoustic Frequencies For Cylindrical Cavity.

Mode	Frequency (Hz)	
	Analytical Solution	Finite Element Solution
1L	2000	1988
2L	4000	4042
1T	2400	2378
1T-1L	3124	3151
1R	4994	5033

As described earlier, a separate potential flow calculation is made in the combustion instability analysis package for the purpose of evaluating the stability integrals. A comparison of the finite element potential flow solution with the analytical solution for the cylindrical cavity is shown in figure 4.

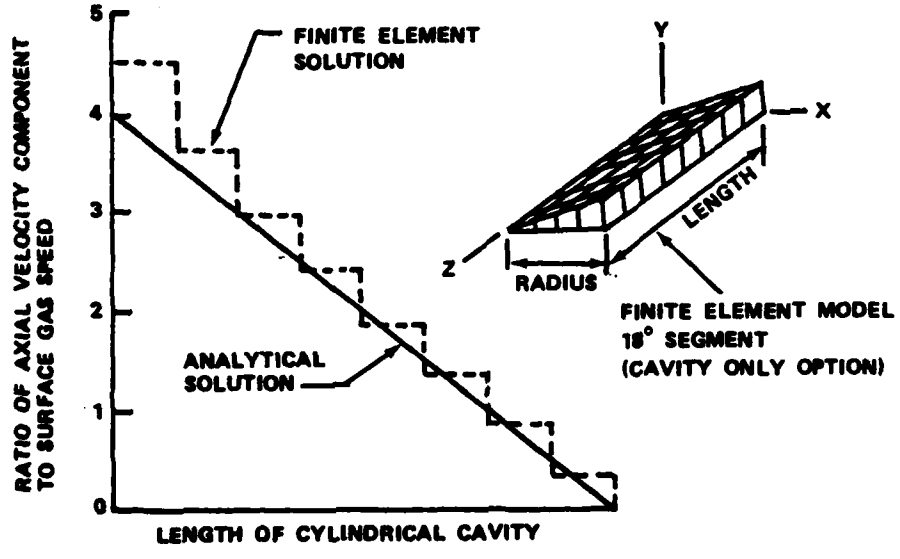

Figure 4. Comparison of finite element and analytical potential flow field solutions for a circular cylinder.

The accuracy of the finite element frequency calculations is seen in table 1. These results are highly favorable, especially when considering the relatively small number of elements used to model the cavity. The somewhat less satisfying agreement in the case of the finite element potential flow solution can be attributed to the relatively small number of elements, especially near the exhaust end of the cavity where the axial velocity component has its largest value.

Additional comparisons with closed-form solutions of the same type have yielded results similar to those cited here.

Experimental Comparisons. The experimental data used for comparison purposes were obtained from Hercules, Inc., Allegany Ballistics Laboratory (ABL) in Cumberland, Maryland and result from testing of an early experimental model of the Smokeless CHAPARRAL Motor Assembly, conducted in early 1977. The finocyl geometry of the pulsed motor and the finite element model consisted of a small diameter-to-length ratio cylindrical cavity having four radial slots over approximately one-third of the cavity length. Experimental longitudinal mode frequency and stability data can be compared to corresponding finite element analysis results in table 2. The test data and numerical results found in table 2 correspond to a burn distance of 8.03mm. The finite element analyses were performed on the CDC 6600 computer at Redstone Arsenal. The lack of close agreement observed when comparing corresponding net α-values can to some extent be attributed to the use of somewhat inaccurate values of response factors, which are presently considered in the program as properties of the propellant, but which are also flow-dependent. However, the qualitatively good agreement between corresponding values can be observed.

Table 2. Smokeless CHAPARRAL Data and Finite Element Analysis Results.

Test Data		Finite Element Analysis	
Frequency (Hz)	$\alpha(sec^{-1})$	Frequency (Hz)	$\alpha(sec^{-1})$
323	-94		
290	-41	307	-198
644	-266		
640	-290	593	-220
909	-192		
927	-145	909	-148

The results from additional finite element analyses of the early experimental model of the Smokeless CHAPARRAL Motor Assembly are shown in table 3. The most notable aspect of this set of finite element analysis results is the prediction of instability in some of the tangential modes (positive values of α). This compares quite favorably with ABL tests of the same assembly, which exhibited clear instabilities in tangential modes. Also, ABL test results showed 5-6 separate tangential modes evident in the frequency range of 9000-20,000 Hz.

Table 3. Higher Acoustic Mode Finite Element Analysis Results For Smokeless CHAPARRAL Motor.

Harmonic	Mode	Frequency (Hz)	α (sec^{-1})
K (=1)	1	7992	-147
	2	13,476	+ 33
	3	15,303	- 55
	4	15,915	+ 46
	5	17,907	- 92
N/2 (=2)	1	8981	-232
	2	15,948	+162
	3	20,516	-119
	4	23,693	- 62
	5	25,644	- 85

The comparisons between numerical and experimental results, which can be made from tables 2 and 3, would appear to support the contention that the developed finite element package can be of valuable use in predicting the instability of solid rocket systems.

11. CONCLUSIONS. The developed computer package performs a linear analysis of the irrotational motions of an inviscid, compressible fluid coupled to the motions of a nearly incompressible, linearly viscoelastic solid, performs a linear potential flow analysis of the irrotational motions of an inviscid, incompressible fluid, and then determines the effect of the flow field and of combustion on the calculated acoustic oscillations. There are obvious limitations attached to any code which is as basic as the restrictions listed above dictate, but it is felt that the developed code presented herein is probably as sophisticated as the present state-of-the-art warrants. It is viewed as having much potential as both a design and a research tool. As the state-of-the-art in combustion technology advances, it is felt that the code can be relatively easily revised and updated to include the new technology; at least it was designed with that provision in mind.

One of the most attractive features of the code is the ease of use. Other extremely important attributes are the fact that it is three-dimensional, that it performs a coupled cavity-solid propellant analysis (or, alternatively, a cavity-only analysis), and that all analyses are automatically linked. Features of the code which do not enhance its reputation also exist, and they too should be pointed out. It is a large program requiring a large amount of storage and it may require long run times, as is the case with any three-dimensional finite element program. Presently, the entire program is in-core computation, but this will, in all probability, be modified. The eigenvalue routine used in the analysis may not be the most efficient one available. This

possibility is currently being investigated, and if a more efficient routine can be found, it will be used in place of the one presently employed. In certain instances a two-dimensional (axisymmetric) uncoupled analysis provides sufficient accuracy, and for such cases use of the three-dimensional code might not have merit.

It is felt that the demonstrated attributes of the three-dimensional code far outweigh any foreseen disadvantages, and that it can provide the means of performing important, and heretofore impossible, analyses.

REFERENCES

1. Standardized Stability Prediction Method for Solid Rocket Motors, Vol. II (Multidimensional Computer Program Users Manual, by D.P. Dudley and R.D. Waugh) and Vol. III (Axial Mode Computer Program Users Manual, by R.L. Lovine and R.C. Waugh), Aerojet Propulsion Company, Sacramento, California, February 1976.
2. Herting, D.N., "Application Manual for NASTRAN Acoustic Cavity Analysis," The MacNeal-Schwendler Corporation, Report MS 116-2. May 1971.
3. Herting, D.N., J.A. Joseph, L.R. Kuusinen and R.H. MacNeal, "Acoustic Analysis of Solid Rocket Motor Cavities by a Finite Element Method," The MacNeal-Schwendler Corporation, Report MS 116-3.
4. NASTRAN Cyclic Symmetry Capability User's Guide, The MacNeal-Schwendler Corporation, EC-180, July 1972.
5. Analysis of a Solid Rocket Motor Cavity, The MacNeal-Schwendler Corporation, Report MS 200, November 22, 1972.
6. Zienkiewicz, O.C., The Finite Element Method in Engineering Science, McGraw-Hill, London, 1971.
7. Hackett, R.M., "A Coupled Interior Ballistics-Finite Element Combustion Instability Analysis Procedure," Technical Report T-78-72, US Army Missile Research and Development Command, Redstone Arsenal, Alabama, July 1978.
8. Hackett, R.M., "A Coupled Interior Ballistics Finite Element Combustion Instability Analysis Procedure - Part II," Technical Report T-79-68, US Army Missile Command, Redstone Arsenal, Alabama, June 1979.
9. MacNeal, R.H., R.H. Harder and J.B. Mason, "NASTRAN Cyclic Symmetry Capability," TM X-2893 NASTRAN: Users' Experiences, NASA, September 1973, pp. 395-421.
10. Hackett, R.M., "Three-Dimensional Acoustic Analysis of Solid Rocket Motor Cavities," Technical Report RK-76-7, US Army Missile Command, Redstone Arsenal, Alabama, November 1975.
11. Hackett, R.M., "Three-Dimensional Finite Element Acoustic Analysis of Solid Rocket Motor Cavities," Journal of Spacecraft and Rockets, v 13, n 10, October 1976, pp 585-588.

12. Hackett, R.M., and R.S. Juruf, "Three-Dimensional Finite Element Analysis of Acoustic Instability of Solid Propellant Rocket Motors," Proceedings of the 13th Annual Meeting of the Society of Engineering Science, Inc., Hampton, Virginia, November 1976, pp. 1641-1651.
13. Hughes, T.J.R. and H. Allik, "Finite Elements for Compressible and Incompressible Continua," Proceedings of the Symposium on Application of Finite Element Methods in Civil Engineering, Vanderbilt University, Nashville, Tennessee, November 1969, pp. 27-62.
14. Herrmann, L.R., "Elasticity Equations for Incompressible and Nearly Incompressible Materials by a Variational Theorem," Journal of the American Institute of Aeronautics and Astronautics, v 3, n 10, October 1965, pp. 1896-1900.
15. Cook, R.D., Concepts and Applications of Finite Element Analysis, John Wiley & Sons, Inc., 1974.
16. Hackett, R.M., "User's Manual for FLAP3," Technical Report TK-77-4, US Army Missile Research and Development Command, Redstone Arsenal, Alabama, July 1977.
17. Final Report - T-Burner Testing of Metallized Solid Propellants, Report No. AFRPL-TR-74-28 (F.E.C. Culick - Editor) Air Force Rocket Propulsion Laboratory, Edwards, California, October 1974.
18. Hart, R.W. and F.T. McClure, "Combustion Instability: Acoustic Interaction with a Burning Propellant Surface," Journal of Chemical Physics, v 30, June 1959, pp. 1501-1514.
19. Price, E.W., "Experimental Solid Rocket Combustion Instability," Tenth Symposium (International) On Combustion, The Combustion Institute, 1965, pp. 1067-1082.

NUMERICAL PREDICTION OF RESIDUAL STRESSES IN AN OVERLOADED BREECH RING

P. C. T. Chen
U.S. Army Armament Research and Development Command
Benet Weapons Laboratory, LCWSL
Watervliet, NY 12189

ABSTRACT. This paper describes a numerical technique for predicting the residual stresses in an overloaded breech ring. The numerical approach used is the finite element method based on the incremental stress-strain matrix and a computer program has been developed. The material behavior is characterized by the von Mises' yield criterion, Prandtl-Reuss flow equations and isotropic hardening rule. A piecewise linear representation for the stress-strain curve is used. The numerical results of the stresses in all elements are obtained for four contact conditions. The location and magnitude of the maximum fillet stress are determined as a function of loading. Residual stresses resulting from elastic unloading are calculated. A satisfactory agreement between numerical and experimental results has been reached.

1. INTRODUCTION. In guns with a sliding breech mechanims, breech ring failures have been observed originating from the lower fillet in the vicinity of the contact region. The observations indicate that high tensile stress produced by stress concentration at the fillet was responsible for the failure. In order to reduce the chance of failure and extend the fatigue life, an exploratory study on the autofrettage of a breech mechanism was initiated. The technique is based on the production of beneficial residual stresses through coldworking to counteract the high operating stresses induced by firing.

A photoplastic model made of aluminum block and polycarbonate ring was designed (ref. 1). The maximum fillet stresses for an elastic load as well as an elastoplastic load were determined experimentally. Residual stress resulting from removing maximum test load was calculated. A numerical investigation of the photoplastic model was made by using NASTRAN (ref. 2). The numerical results are in good agreement with the experimental data in the elastic range of loading but not in the plastic range. Furthermore, NASTRAN program stops before the maximum test load is reached and residual stress after complete unloading cannot be calculated.

This paper describes a numerical technique for predicting the residual stresses in an overloaded breech ring. The numerical approach used is the finite element method based on the incremental stress-strain matrix and a

computer program has been developed. The material behavior is characterized by the von Mises' yield criterion, Prandtl-Reuss flow equations and isotropic hardening rule. A piecewise linear representation for the stress-strain curve is used. The numerical results of the stresses in all elements are obtained for four contact conditions. The location and magnitude of the maximum fillet stress are determined as a function of loading. Residual stresses resulting from elastic unloading are calculated. A satsifactory agreement between numerical and experimental results has been reached.

2. METHOD AND PROGRAM. The finite element method used here is of the incremental type since solutions to problems involving material nonlinearity are best obtained by solving a sequence of linear problems associated with an incremental application of the loading. The formulation of the governing matrix equation is developed by using the incremental stress-strain matrix in conjunction with the stationary principle for elastic-plastic solids. Following the procedure outlined in reference 3, we have developed a finite element computer program for solving two dimensional elastic-plastic problems of rotational symmetry. The element type is either triangular (ref. 4) or quadrilateral (ref. 5) and both were implemented in analyzing gun tube problems. For the present problem, the plane stress case was implemented. The field displacement is based on the linear displacement function in a triangular element. Small strain condition is used to derive the kinematical matrix [B]. The material behavior is characterized by the Mises yield criterion, Prandtl-Reuss flow equations and isotropic hardening rule. A piecewise linear representation for the effective stress-strain curve is used. As derived in reference 3, the incremental form of the constitutive matrix [D] for an elastic-plastic element ($\sigma \geq \sigma_o$) can be written as

$$\{\Delta\sigma\} = [D]\ \{\Delta\varepsilon\}$$

$$\{\Delta\sigma\}^T = \lfloor \Delta\sigma_x,\ \Delta\sigma_y,\ \Delta T_{xy} \rfloor$$

$$\{\Delta\varepsilon\}^T = \lfloor \Delta\varepsilon_x,\ \Delta\varepsilon_y,\ \Delta\gamma_{xy} \rfloor$$

and

$$[D] = \frac{E}{A_3}\begin{bmatrix} \sigma_y'^2+2A_1 & & \text{SYM.} \\ -\sigma_x'\sigma_y'+2\nu A_1 & \sigma_x'^2+2A_1 & \\ -\dfrac{\sigma_x'+\nu\sigma_y'}{1+\nu}T_{xy} & -\dfrac{\sigma_y'+\nu\sigma_x'}{1+\nu}T_{xy} & \dfrac{A_2}{2(1+\nu)}+\dfrac{2H'(1-\nu)\sigma}{9E} \end{bmatrix} \quad (1)$$

where E, ν are Young's modulus, Poisson's ratio, respectively.

$$A_1 = \frac{2H'}{9E}\bar{\sigma}^2 + \frac{T_{xy}^2}{1+\nu}, \quad A_2 = \sigma_x'^2 + 2\nu\sigma_x'\sigma_y' + \sigma_y'^2,$$

$$A_3 = 2(1-\nu^2)A_1 + A_2, \quad \sigma_x' = (2\sigma_x - \sigma_y)/3,$$

$$\sigma_y' = (2\sigma_y - \sigma_x)/3, \quad H' = \Delta\bar{\sigma}/\Delta\bar{\varepsilon}^P,$$

$$\bar{\sigma} = [\sigma_x^2 + \sigma_y^2 - \sigma_x\sigma_y + 3T_{xy}^2]^{1/2},$$

$$\Delta\bar{\varepsilon}^P = 2/3\,[(\Delta\varepsilon^P{}_x)^2 + (\Delta\varepsilon^P{}_y)^2 + (\Delta\varepsilon^P{}_z)^2 + \tfrac{1}{2}(\Delta\gamma^P{}_{xy})^2]^{1/2} \qquad (2)$$

and σ_o is the yield stress in simple tension or compression. For an elastic element in which $\sigma < \sigma_o$, the constitutive matrix is

$$[D] = \frac{E}{1-\nu^2}\begin{bmatrix} 1 & \nu & 0 \\ \nu & 1 & 0 \\ 0 & 0 & (1-\nu)/2 \end{bmatrix}. \qquad (3)$$

The stiffness matrix [k] for a triangular element is represented by

$$[k] = [B]^T[D][B]t\Delta \qquad (4)$$

where t denotes the thickness and Δ is the area of the triangular. Four triangular elements are used to construct a quadrilateral element as shown in reference 5. The element stiffness matrix is determined by static condensation and the kinematical matrix is formed by averaging over four triangulars. The stresses and strains are calculated at the centroid of each element.

The computer program developed for the plane-stress elastic-plastic problems was a modification of the previous program for the axisymmetric case (ref. 4 and 5). The overlay feature was utilized for reducing the core storage requirement. Disk was used as an auxiliary storage device for the current element information and for solving the large system of equation by partition. A tape may be used to store the final results for output plotting and also for restarting this program from a point of completion of a given loading sequence. The computer used is IBM 360 Model 44.

3. MODEL AND LOADING. A two-dimensional photoplastic model of aluminum block and polycarbonate ring was designed (ref. 1). The breech ring was made of 0.12 inch thick LEXAN plate and the top of the ring was fixed. This material has a Poisson's ratio of 0.38 in the elastic state and a limiting value of 0.5 in the plastic state. The stress-strain (σ-ε) curve for LEXAN beyond the proportional limit can be described by the modified Ramberg-Osgood equation in the following form

$$E\varepsilon/\sigma_B = \sigma/\sigma_B + (3/7)(\sigma/\sigma_B)^n \quad \text{for} \quad \sigma_A \leq \sigma \leq \sigma_C \tag{5}$$

and the values of five parameters are E = 325 Ksi, n = 11.5, σ_A = 6.2 Ksi, σ_B = 8.7 Ksi, σ_C = 9.576 Ksi, where E is Young's modulus, n is a parameter, σ_A is the proportional limit, σ_B is the secant yield strength having a slope equal to 0.7 E and σ_C is the flow stress at which the slope of the stress-strain curve is zero. A piecewise linear representation for the effective stress-strain curve is used in this numerical study and the values for 11 data points other than the origin are

$$(\varepsilon_i,\ \sigma_i \text{ in Ksi}) = (.018621,\ 6.),\ (.020401,\ 6.5),$$

$$(.022480,\ 7.0),\ (.025158,\ 7.5),\ (.028988,\ 8.0),$$

$$(.034934,\ 8.5),\ (.044635,\ 9.0),\ (.051679,\ 9.25),$$

$$(.060781,\ 9.50),\ (.064043,\ 9.596),\ (.1,\ 9.576)\ . \tag{6}$$

The dimensionless slope ω_i is defined by

$$\omega_i = E^{-1}(\sigma_{i+1}-\sigma_i)/(\varepsilon_{i+1}-\varepsilon_i) \tag{7}$$

and we can calculate $(H'/E)_i = \omega_i/(1-\omega_i)$ for i = 1,...,10.

A finite-element representation for one half of the breech ring is shown in Figure 1. The other half is not needed because of symmetry. There are 224 grid points and 189 quadrilateral elements in this model. The grids 1 to 8 are constrained in x-direction only while grids 217 to 224 are held fixed. The top portion of the breech ring is omitted because this is believed to have little effect on the maximum stress information near the lower fillet. In fact this belief has been confirmed by obtaining the elastic solution for another finite element model with additional 70 quadrilateral elements in the top portion. The difference between these two models for the maximum tensile stress is only 1.3%. The aluminum block is regarded as rigid and the load is transmitted to the ring through contact. Initially the block is in full contact with the ring. As load increases, a gap develops in the central portion. The width of central gap under the full test load (2F = 1144 pounds) was observed

experimentally to be about 5 inches. Our elastic-plastic finite-element program in its present form cannot be used to determine the width of contact and the force distribution as functions of loading. Guided by the experimental information on the width of central gap, we have chosen four contact conditions in this numerical investigation. The points of contact are at nodes (33, 41, 49, 57) for case 1, at nodes (41, 49, 57) for case 2, at nodes (49, 57, 65) for case 3 and at nodes (57, 65) for case 4. The width of contact and the force distribution in each case are assumed to remain unchanged during loading and only the total force (2F) is allowed to increase. The force distribution may be uniform or non-uniform and both types have been used in this study. Initially we apply a small force to obtain elastic solution and the total force (2F*) required to cause incipient plastic deformation is calculated by using Mises yield criterion. Then we apply the additional force in increments until the maximum test load is reached. The load increments we chose are non-uniform because our experience indicates that smaller increments should be used as plastic deformation becomes bigger. Our choice for the present investigation is an arithmetic decreasing sequence generated automatically in the program. If 10 incremental steps are used, then

$$\lfloor \Delta F_j \rfloor = \frac{1}{145} \lfloor 19,18,\ldots,11,10 \rfloor (5.72-F^*) \quad \text{for } j = 1,\ldots,10 \qquad (8)$$

It is important to choose a proper set of increments in order to obtain good results at reasonable cost. To reach the maximum test load of 2F = 1144 pounds, we used 11 increments for the four contact conditions and 22 increments for the second and third cases. The difference between 11 and 22 incremental loadings for the maximum tensile stress is found to be within 1%. The restart feature of the program has been used for the second contact condition to increase the total force from 1144 pounds to 1300 pounds in 7 additional steps. The increments are again non-uniform.

4. RESULTS AND DISCUSSIONS. The numerical results of the stresses in all elements were obtained for the overloaded breech ring under different contact conditions. Some of them are presented below in Figures 2-7. The major principal stresses in elements along the contact region and fillet are shown in Figures 2-5, for the four contact conditions under uniform load distributions. In each of these figures, we presented two sets of data corresponding to the load levels at the initial yielding (F*) and at the maximum test load (F = 572 pounds). The incipient plastic deformation first occurs in element 99 for the first two cases and in element 50 for the last two cases. The values of load level for the four cases are F* = 312.8, 321.9, 221.7, 169.2 pounds. The initial yielding is tensile in element 99 and compressive in element 50. It is interesting to find out that the location of the maximum tensile stress is in element 99 for all contact conditions under either uniform or non-uniform load distributions and this location remains unchanged as the total force

increases. Since this location is of sufficient distance away from the contact regions, it seems to suggest that Saint Vennant's principle can be applied to this problem in the elastic as well as plastic range of loading. The values of the maximum tensile stress based on the four contact conditions with uniform load distribution are 2029, 1972, 1939, 1936 psi at F = 100 pounds and 9532, 9361, 9174, 9119 psi at F = 572 pounds. It should be noted that the stresses in the finite element program were calculated at the centroid of each element but only one principal stress at the boundary was measured. The values of the maximum tensile stress at the fillet based on experimental approach are 2222 psi at F = 100 pounds and 9300 psi at F = 572 pounds. For the purpose of comparison, the boundary stress is determined by extrapolation using the calculated results for those elements along the radial direction through element 99. This is illustrated in Figure 6 for the second case of contact condition. Similar figures for the other three cases are not shown. Three curves are plotted in Figure 6 and they represent the major principal stresses for three load levels at the initial yielding, maximum test load and complete unloading after reaching the maximum load. The residual stresses after complete unloading are determined by assuming that the unloading process is purely elastic. Our numerical results reveal no reverse yielding. In extrapolating the boundary stress, we shall remember that the maximum tensile stress shall not exceed the flow stress of 9576 psi. As seen in Figure 6, a comparison between the numerical and the experimental results for the maximum tensile stress indicates that a satisfactory agreement has been reached. In Figure 7, two principal stresses as well as the residual stresses in element 99 are shown as functions of loading. Only the second case of contact conditions is presented here for illustration. The residual stress is determined by assuming a purely elastic unloading resulting from various stages of loading. The minor principal stress (σ_2) is found to be a nearly linear function of loading and its residual value is very small. The value of the principal stress angle for all contact conditions and for all load levels is found to lie within -26° to -27° with respect to the x-axis. As can be seen in Figure 7, the major principal stress (σ_1) and its residual value increase in magnitude as the total contact force increases but they are of opposite sign. Therefore, the production of compressive residual stress in an overloaded breech ring is beneficial because it can counteract the high operating tensile stress induced by firing. As a result of prestressing during the process of manufacturing, the elastic carrying capacity and fatigue life can be increased and thus the chances of breech failures can be reduced. Furthermore, the finite element program developed here is a useful tool in redesigning breech rings or blocks.

REFERENCES

1. Y. F. Cheng, "Photoplastic Study of Residual Stress in an Overloaded Breech Ring," Technical Report ARLCB-TR-78018, November, 1978.

2. P. C. T. Chen and G. P. O'Hara, "NASTRAN Analysis of a Photoplastic Model for Sliding Breech Mechanism," Proceedings 1979 Army Numerical Analysis and Computer Conference, pp. 237-254.

3. Y. Yamada, N. Yoshimura, and T. Sakurai, "Plastic Stress-Strain Matrix and Its Application for the Solution of Elastic-Plastic Problems by the Finite Element Method," International Journal of Mechanical Science, Vol. 10, pp. 343-354, 1968.

4. P. C. T. Chen, "Elastic-Plastic Solution of a Two-Dimensional Tube Problem by the Finite Element Method," Transactions of Nineteenth Conference of Army Mathematicians, ARO Report 73-3, pp. 763-784, 1973.

5. P. C. T. Chen, "Numerical Solution of Gun Tube Problems in the Elastic-Plastic Range," Proceedings 1977 Army Numerical Analysis and Computer Conference, pp. 423-439.

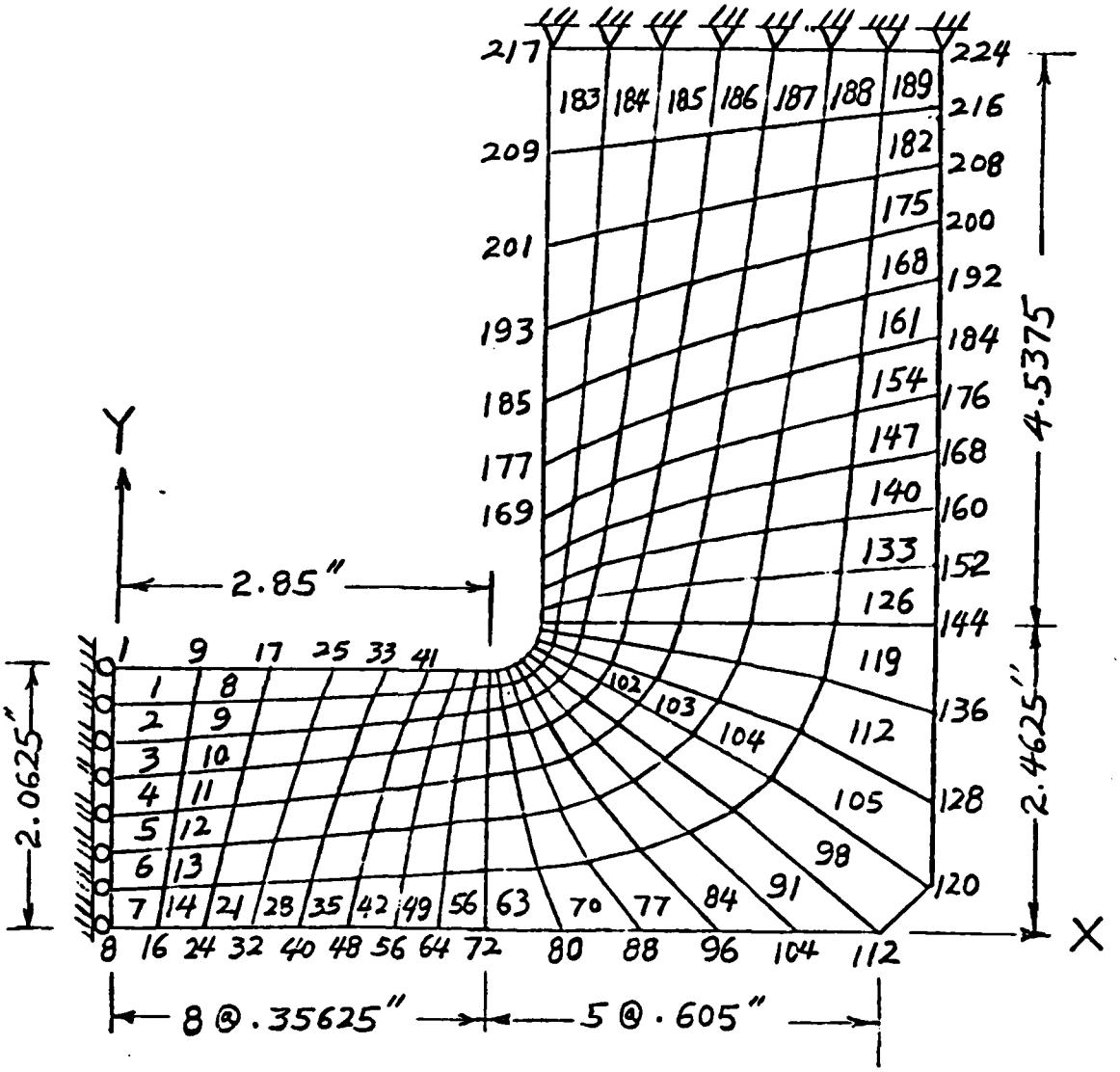

Figure 1. A Finite Element Model for Breech Ring

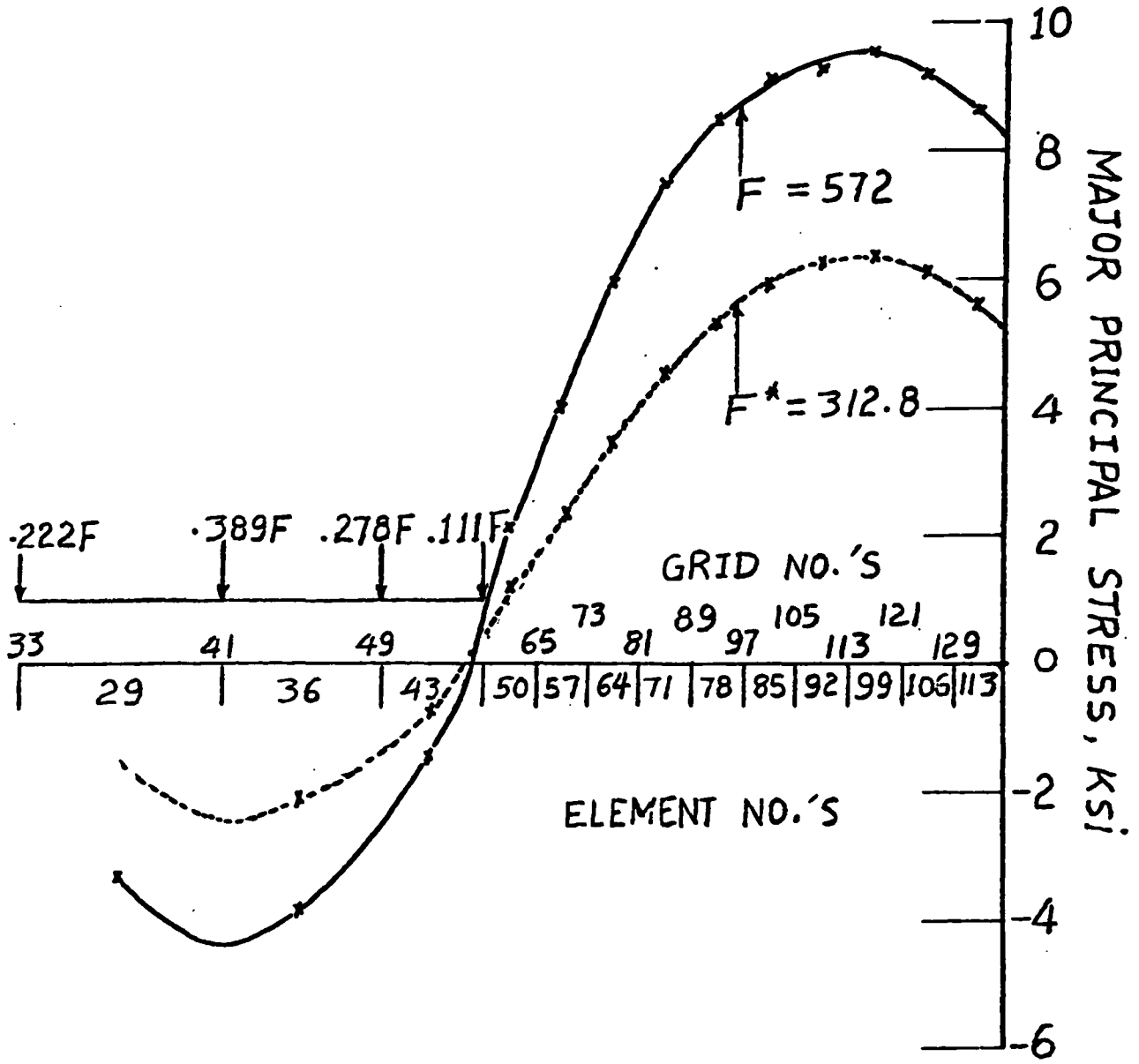

Figure 2. Major Principal Stress Aong the Boundary Elements for Case 1

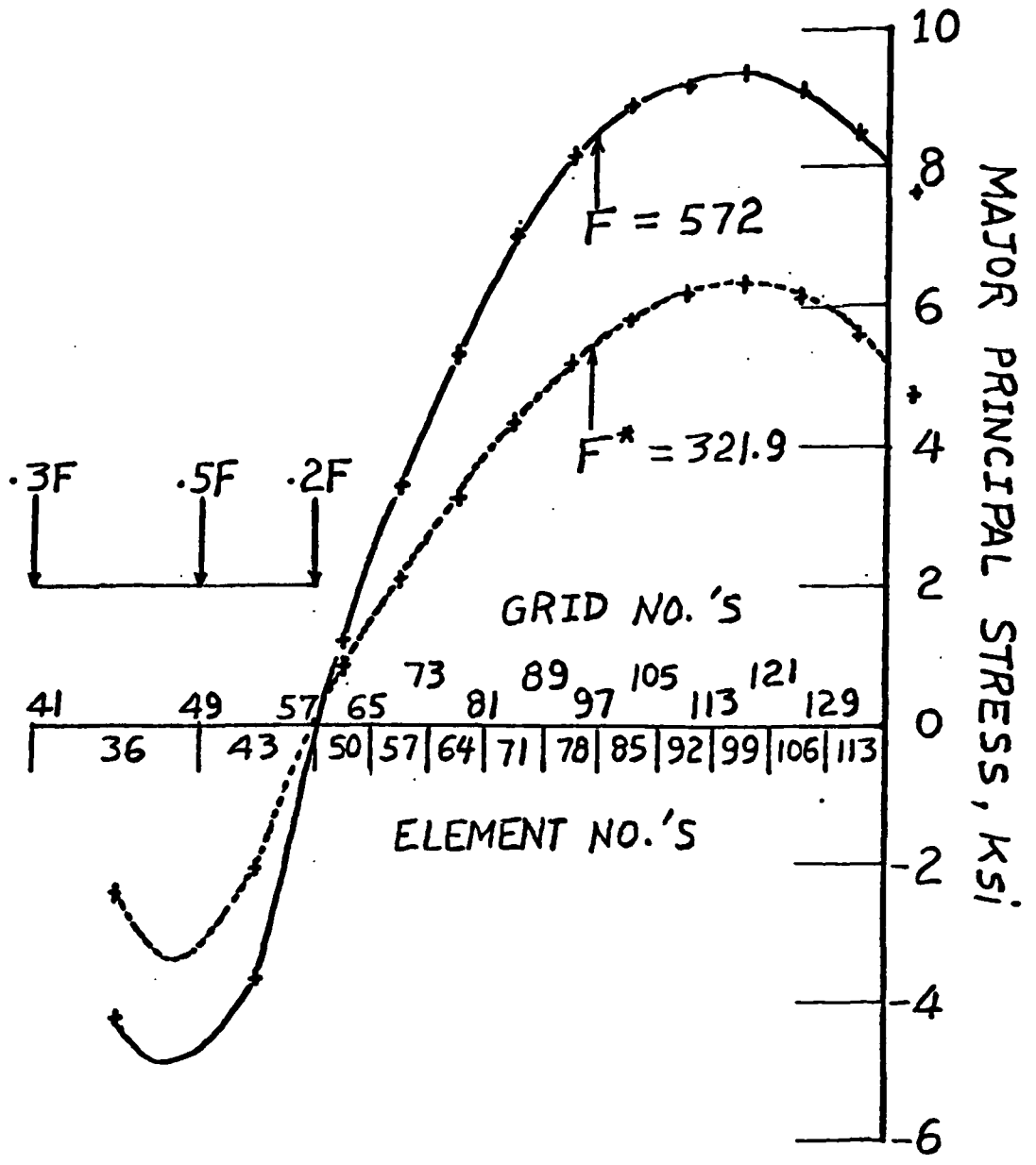

Figure 3. Major Principal Stress Along the Boundary Elements for Case 2

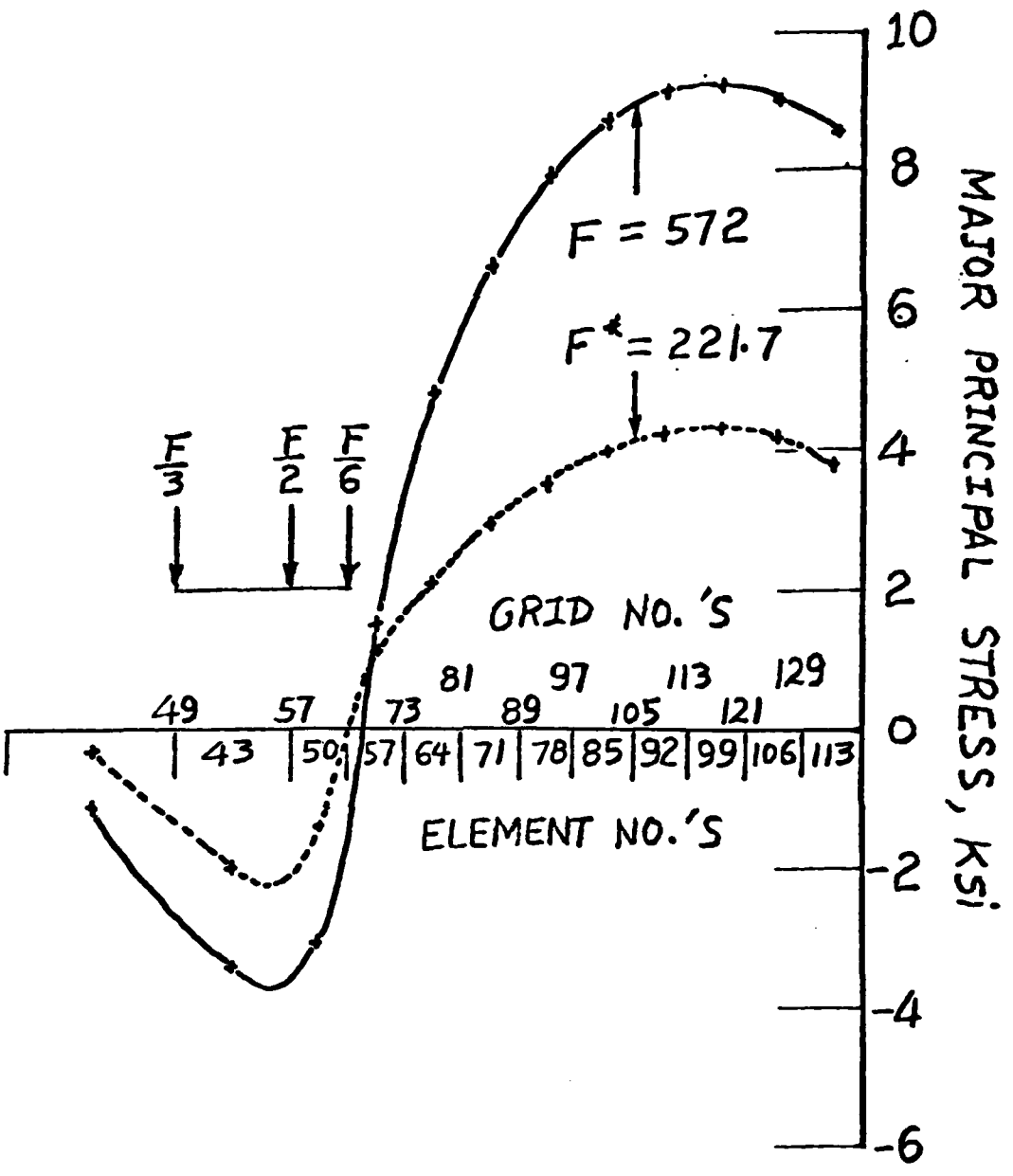

Figure 4. Major Principal Stress Along the Boundary Elements for Case 3

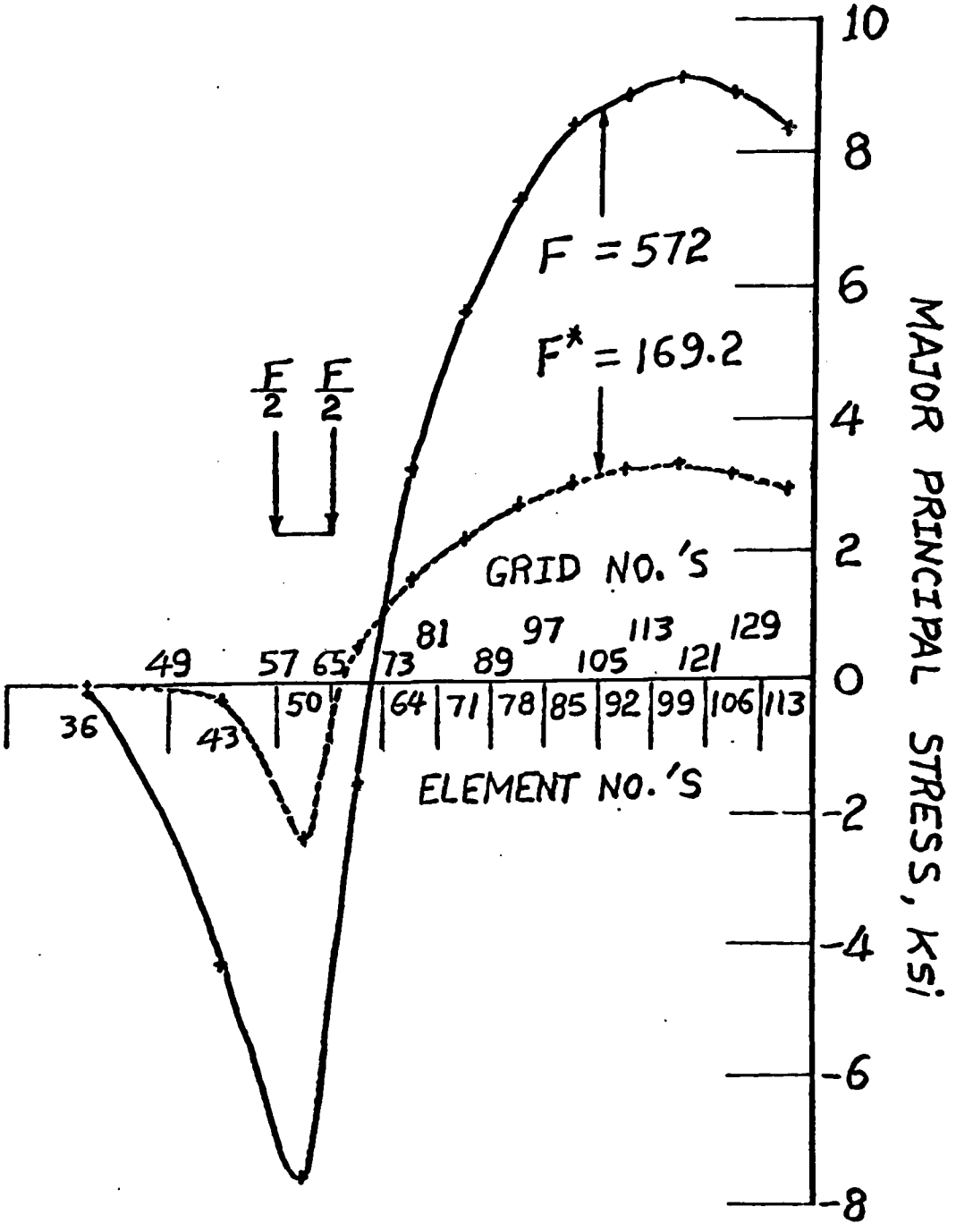

Figure 5. Major Principal Stress Along the Boundary Elements for Case 4

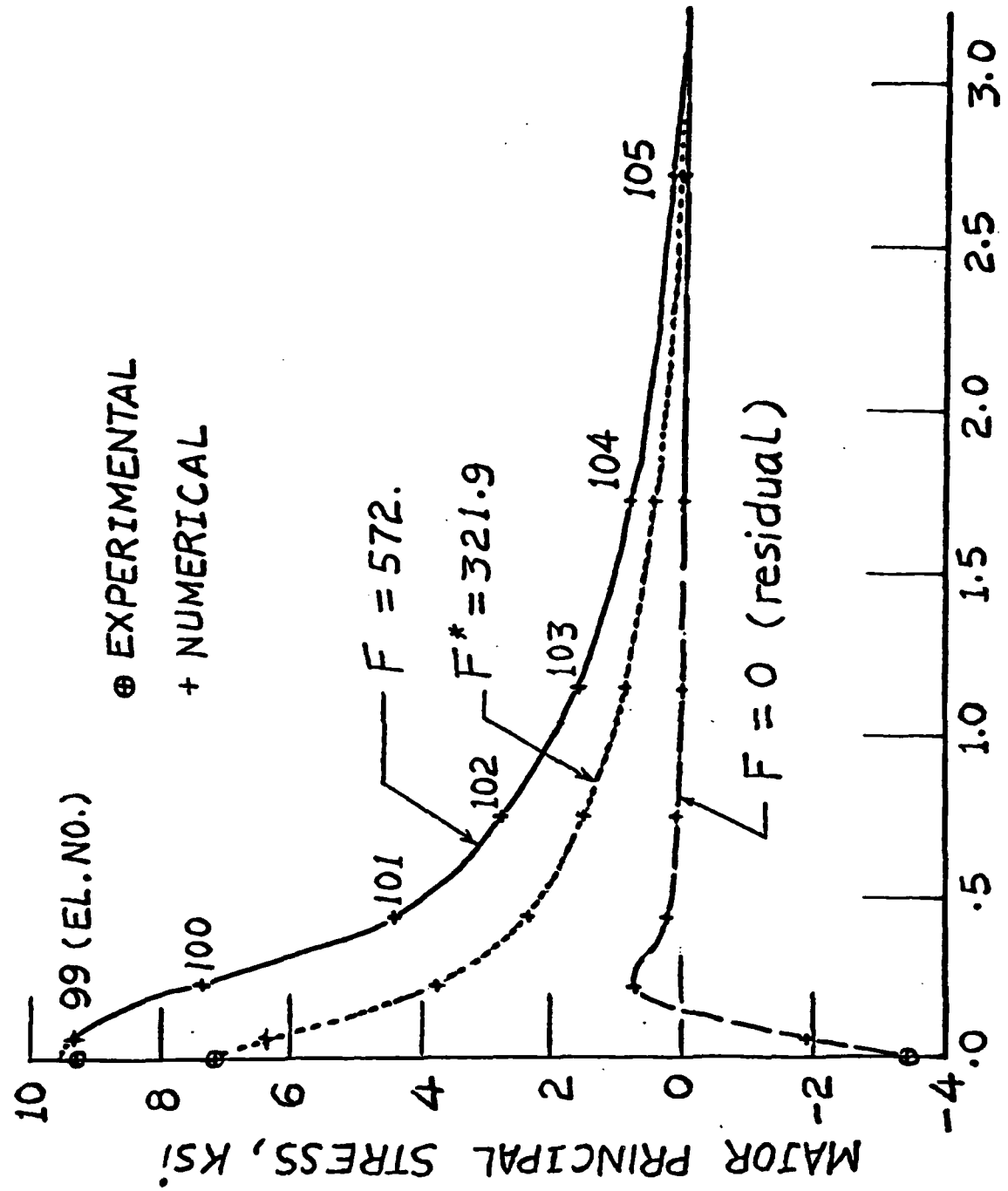

Figure 6. Determination of the Maximum Tensile Stress for Case 2

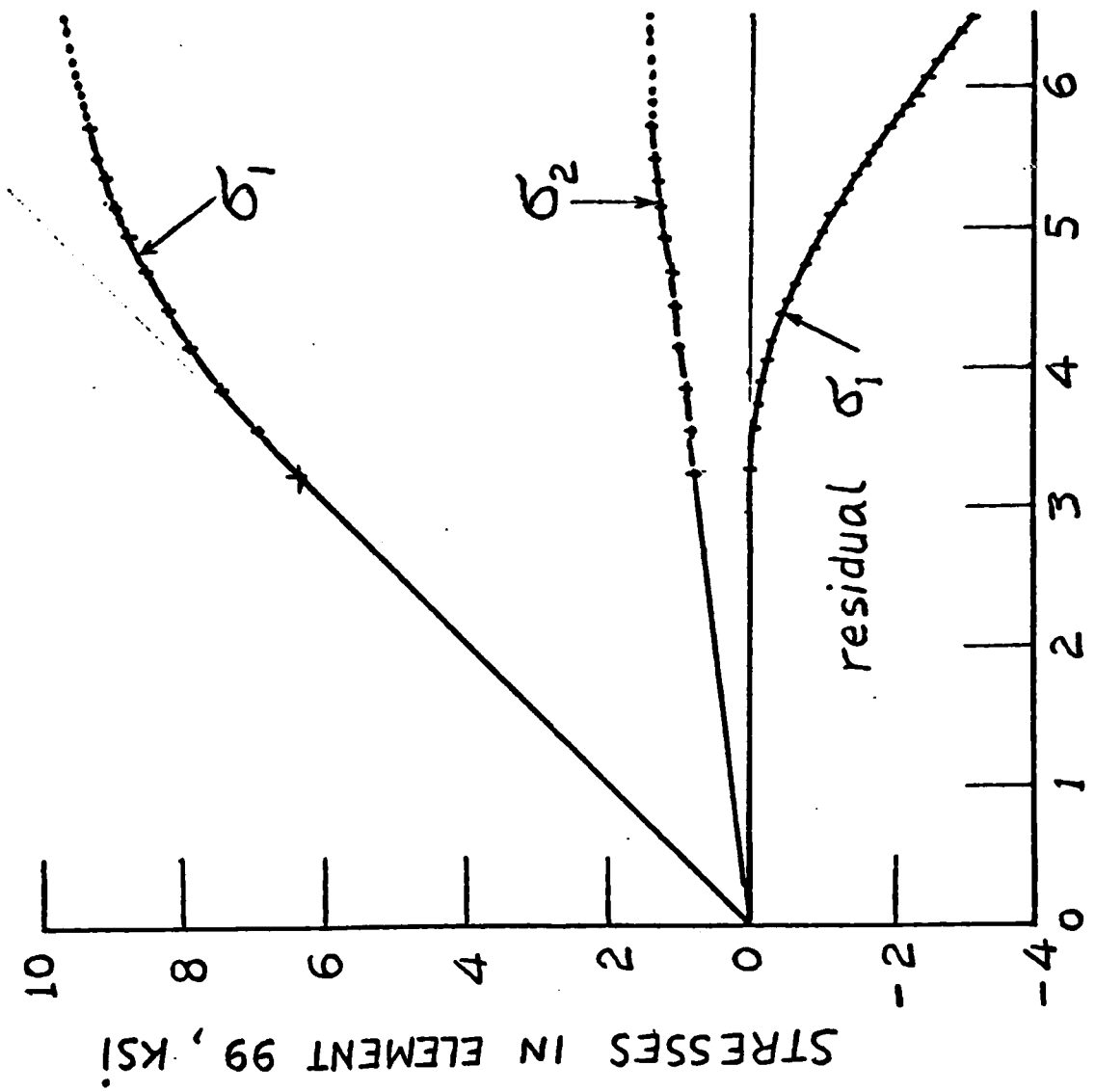

Figure 7. Stresses in Element 99 as functions of Contact Force for Case 2

AN ADAPTIVE ALGORITHM FOR EXACT SOLUTION OF AN OVER-STRAINED TUBE

P. C. T. Chen
U.S. Army Armament Research and Development Command
Benet Weapons Laboratory, LCWSL
Watervliet, NY 12189

ABSTRACT. An adaptive algorithm to generate exact solution has been developed for the plane-strain problem of a thick-walled tube overstrained by internal or external pressure. The material obeys the von Mises' yield criterion, the Prandtl-Reuss flow theory and the isotropic hardening rule. The ideally-plastic material is treated as a special case. The formulation is based on the finite-difference method in conjunction with a scaled incremental-loading approach. One additional grid point will become yielded in each load step. The grid sizes and load increments are determined in the program. For a given percentage of overstrain and a desired solution accuracy, the stresses and strains can be obtained in an efficient way.

1. INTRODUCTION. In a previous paper (ref. 1), a new finite-difference approach was developed for solving the axisymmetric plane-strain problems subjected to internal or external pressure beyond the elastic limit. The material was assumed to obey the von Mises' yield criterion, the Prandtl-Reuss flow theory and the isotropic hardening rule. The ideally-plastic material was treated as a special case. The new formulation is simpler than other finite-difference methods for ideally-plastic materials (ref. 2) and strain-hardening materials (ref. 3). The load increments used in all steps were fixed and equal. Accurate numerical results can be obtained by reducing the grid sizes and load increments.

In the present paper, an adaptive algorithm to generate more accurate solution will be developed for the plane-strain problem of an overstrained tube. The load increments in all steps are varied and determined automatically in the program. One additional grid point will become yielded in each load step. To reach 100% overstrain, the number of steps are equal to the number of grids. For a given percentage of overstrain and a desired solution accuracy, the stresses and strains can be obtained in a much more efficient manner.

2. BASIC EQUATIONS. Assuming small strain and no body forces in the axisymmetric state of plane strain, the radial and tangential stresses, σ_r and σ_θ, must satisfy the equilibrium equation,

$$r(\partial\sigma_r/\partial r) = \sigma_\theta - \sigma_r \; ; \qquad (1)$$

and the corresponding strains, ε_r and ε_θ, are given in terms of the radial displacement, u, by

$$\varepsilon_r = \partial u/\partial r \quad , \quad \varepsilon_\theta = u/r \ . \tag{2}$$

It follows that the strains must satisfy the equation of compatibility

$$r(\partial\varepsilon_\theta/\partial r) = \varepsilon_r - \varepsilon_\theta \ . \tag{3}$$

The material is assumed to be elastic-plastic, obeying Mises' yield criterion, Prandtl-Reuss flow theory and isotropic hardening law. The complete stress-strain relations can be rewritten in an incremental form (ref. 4)

$$d\sigma_i = d_{ij}d\varepsilon_j \quad \text{for} \quad i,j = r,\theta,z \tag{4}$$

and

$$d_{ij}/2G = \nu/(1-2\nu) + \delta_{ij} - \sigma_i'\sigma_j'/S \ , \tag{5}$$

where E is Young's modulus, ν is Poisson's ratio, δ_{ij} is the Kronecker delta,

$$S = \frac{2}{3}\,(1 + \frac{1}{3}\,H'/G)\sigma^2 \quad , \quad 2G = E/(1+\nu) \quad , \tag{6}$$

$$\sigma_m = (\sigma_r+\sigma_\theta+\sigma_z)/3 \quad , \quad \sigma_i' = \sigma_i - \sigma_m \quad , \tag{7}$$

$$\sigma = (1/\sqrt{2})[(\sigma_r-\sigma_\theta)^2 + (\sigma_\theta-\sigma_z)^2 + (\sigma_z-\sigma_r)^2]^{1/2} \geq \sigma_o \quad , \tag{8}$$

and σ_o is the yield stress in simple tension or compression. For a strain hardening material, H' is the slope of the effective stress/plastic strain curve

$$\sigma = H(\int d\varepsilon^p) \ .$$

For an ideally-plastic material, $H' = 0$. When $\sigma < \sigma_o$ or $d\sigma < 0$, the state of stress is elastic and the third term in equation (4) disappears. Consider a thick-walled cylinder of inner radius a and external radius b. The tube is subjected to inner pressure p and/or external pressure q. The elastic solution for this problem is well-known

$$\left.\begin{matrix}\sigma_r \\ \sigma_\theta\end{matrix}\right\} = \pm\,\frac{(q-p)}{b^2/a^2-1}\,(\frac{b}{r})^2 + \frac{p-q(b/a)^2}{b^2/a^2-1} \quad , \tag{9}$$

$$\sigma_z = \nu(\sigma_r+\sigma_\theta) \quad ,$$

and the pressure p* or q* required to cause initial yielding can be determined by using the Mises' yield criterion.

3. FINITE-DIFFERENCE FORMULATION. For pressure beyond the elastic limit, an incremental approach of the finite-difference formulation is used. At the beginning of each incremental loading, Δp or Δq, the distribution of displacements, strains and stresses are assumed to be known and we want to determine Δu, $\Delta\varepsilon_r$, $\Delta\varepsilon_\theta$, $\Delta\sigma_r$, $\Delta\sigma_\theta$, $\Delta\sigma_z$ at all grid points. The cross section of the tube is divided into n rings with

$$r_1=a, r_2, \ldots, r_k=\rho, \ldots, r_{n+1}=b, \tag{10}$$

where ρ is the radius of the elastic-plastic interface.

Since the incremental stresses are related to the incremental strains by the incremental form (Eq. (4)) and $\Delta u = r\Delta\varepsilon_\theta$, there exists only two unknowns at each station that have to be determined for each increment of loading. The unknown variables in the present formulation are $(\Delta\varepsilon_\theta)_i$, $(\Delta\varepsilon_r)_i$, for $i = 1,2,\ldots n,n+1$.

The equation of equilibrium (Eq. (1)) and the equation of compatibility (Eq. (3)) are valid for both the elastic and the plastic regions of a thick-walled tube. The finite-difference forms of these two equations at $i = 1,\ldots,n$ are given by

$$\begin{aligned}(r_{i+1}-2r_i)(\Delta\sigma_r)_i - (r_{i+1}-r_i)(\Delta\sigma_\theta)_i + r_i(\Delta\sigma_r)_{i+1} \\ = (r_{i+1}-r_i)(\sigma_\theta-\sigma_r)_i - r_i[(\sigma_r)_{i+1} - (\sigma_r)_i]\end{aligned} \tag{11}$$

for the equation of equilibrium, and

$$\begin{aligned}(r_{i+1}-2r_i)(\Delta\varepsilon_\theta)_i - (r_{i+1}-r)(\Delta\varepsilon_r)_i + r_i(\Delta\varepsilon_\theta)_{i+1} \\ = (r_{i+1}-r_i)(\varepsilon_r-\varepsilon_\theta)_i - r_i[(\varepsilon_\theta)_{i+1} - (\varepsilon_\theta)_i]\end{aligned} \tag{12}$$

for the equation of compatibility.

With the aid of the incremental stress-strain relations (Eq. (4)), Eq. (11) can be rewritten as

$$\begin{aligned}&[(r_{i+1}-2r_i)(d_{12})_i + (-r_{i+1}+r_i)(d_{22})_i](\Delta\varepsilon_\theta)_i \\ &+ [(r_{i+1}-2r_i)(d_{11})_i + (-r_{i+1}+r_i)(d_{21})_i](\Delta\varepsilon_r)_i \\ &+ r_i(d_{12})_{i+1}(\Delta\varepsilon_\theta)_{i+1} + r_i(d_{11})_{i+1}(\Delta\varepsilon_r)_{i+1} \\ &= (r_{i+1}-r_i)(\sigma_\theta-\sigma_r)_i - r_i[(\sigma_r)_{i+1} - (\sigma_r)_i] \quad .\end{aligned} \tag{13}$$

The boundary conditions for the problem are

$$\Delta\sigma_r(a,t) = -\Delta p \quad , \quad \Delta\sigma_r(b,t) = -\Delta q \quad . \tag{14}$$

Using the incremental relations (Eq. (4)), we rewrite Eq. (11) as

$$(d_{12})_1(\Delta\varepsilon_\theta)_1 + (d_{11})_1(\Delta\varepsilon_r)_1 = -\Delta p \quad . \tag{15}$$

and

$$(d_{12})_{n+1}(\Delta\varepsilon_\theta)_{n+1} + (d_{11})_{n+1}(\Delta\varepsilon_r)_{n+1} = -\Delta q \quad . \tag{16}$$

Now we can form a system of 2(n+1) equations for solving 2(n+1) unknowns, $(\Delta\varepsilon_\theta)_i$, $(\Delta\varepsilon_r)_i$, for $i = 1,2,\ldots,n,n+1$. Equations (15) and (16) are taken as the first and last equations, respectively, and the other 2n equations are set up at $i = 1,2,\ldots,n$ using Eqs. (12) and (13). The final system is an unsymmetric band matrix with the nonzero terms clustered about the main diagonal, two below and one above.

4. INCREMENTAL LOADING - FIXED VS. SCALED. When the total applied pressure p or q is given, it is natural to divide the loading path into m equal fixed increments with

$$\Delta p = (p-p^*)/m \quad , \quad \Delta q = (q-q^*)/m \quad . \tag{17}$$

These fixed increments need not be equal for all steps and any sequence of m increments can be supplied by the user. The fixed increments were applied until the total pressure or a given percentage of overstrain is reached. The percentage of overstrain is defined as $(\rho-a)/(b-a) \times 100\%$. The accuracy of the numerical results will depend upon the values of m and n used. Large values of m and n will yield better results at greater cost. For each value of n = 20, 50, 100,..., we may set m = n, 2n, 4n, 8n,..., to discuss the convergence. The numerical results suggest that a sequence of decreasing load-increments is a better choice than that of equal increments.

In the following, a method to generate a sequence of load-increments is described. The method is based on a scaled incremental loading approach (ref. 4). In each step, a dummy load-increment such as Δp is applied and the incremental results $\Delta\sigma_i$ for $i = r,\theta,z$ at all grids are determined. For all grid points at which $\sigma = ||\sigma_i|| < \sigma_o$, we compute the scaler α's by the formula

$$\alpha = \frac{1}{2}\{\Gamma + [\Gamma^2 + 4||\Delta\sigma_i||^2(\sigma_o{}^2 - ||\sigma_i||^2)]^{1/2}/||\Delta\sigma_i||^2 \quad , \tag{18}$$

where

$$\Gamma = ||\sigma_i||^2 + ||\Delta\sigma_i||^2 - ||\sigma_i + \Delta\sigma_i||^2 \quad , \tag{19}$$

and $||\sigma_i||$, $||\Delta\sigma_i||$, $||\sigma_i + \Delta\sigma_i||^2$ are computed by

$$||\sigma_i||^2 = \frac{1}{2}\left[(\sigma_r-\sigma_\theta)^2 + (\sigma_\theta-\sigma_z)^2 + (\sigma_z-\sigma_r)^2\right] \quad . \tag{20}$$

Let λ be the minimum of the α's. Then λ is the load-increment factor just sufficient to yield one additional point. A sequence of $\lambda^{(j)}$ can be determined for all steps $j = 1,2,\ldots,m$ and the updated results are

$$p^{(j)} = p^{(j-1)} + \lambda^{(j)}\Delta p^{(j)}$$

$$\sigma_i^{(j)} = \sigma_i^{(j-1)} + \lambda^{(j)}\Delta\sigma_i^{(j)} \quad , \text{ etc.} \tag{21}$$

5. NUMERICAL RESULTS AND DISCUSSIONS. The numerical results for a thick tube with $b/a = 2$, $\nu = .3$ subjected to internal pressure only were obtained. The elastic-perfectly-plastic case ($H' = 0$) as well as strain-hardening case ($H' = E/9$) were considered. Both fixed and scaled incremental loading approaches were used. The pressure p^* required to cause initial yielding is $.4323\ \sigma_o$.

In order to compare the rate of convergence based on two incremental loading procedures, we consider an elastic-perfectly-plastic case. The numerical results were shown in Tables 1 and 2. Based on the equal load-increments, the effect of m and n on the internal pressure and bore displacement can be seen in Table 1. Larger values of m and n will yield better results except the bore displacement for 100% overstrain. If the scaled incremental loading approach is used, the load-increments for all steps are calculated and m = n x 100% overstrain. The numerical results for the pressure, displacement, axial stress at the inside and the maximum hoop stress were shown in Table 2. A comparison of Tables 1 and 2 indicates that the scaled incremental loading approach is much more accurate and efficient than the equal incremental loading approach. For example, to reach 50% overstrain with n = 20, 10 scaled load-increments can give better results than 2044 equal load-increments.

Finally, we consider a strain-hardening tube subjected to internal pressure only. The numerical results were based on the scaled incremental loading and the following parameters: $b/a = 2$, $\nu = .3$, $H' = E/9$, $n = 100$. The stresses and strains as functions of overstrain percentage were obtained. In Figures 1 and 2, we show the residual stresses resulting from 50% and 100% overstrain. The effect of favorable residual stresses of an autofrettaged tube is well known. A simple and efficient approach to compute accurate residual stresses is important.

TABLE 1. CONVERGENCE STUDY BASED ON FIXED LOAD-INCREMENTS IN A PLANE-STRAIN TUBE ($b/a = 2$, $\nu = .3$, $H' = 0$), $\Delta p = (p-p^*)/m$.

	50% O.S.			100% O.S.		
n	m	P/σ_o	$\frac{E}{\sigma_o}\frac{U_a}{a}$	m	P/σ_o	$\frac{E}{\sigma_o}\frac{U_a}{a}$
20	14	.7597	2.1779	18	.8532	4.1528
	30	.7480	2.1382	38	.8322	4.0422
	62	.7422	2.1169	78	.8222	4.2663
	126	.7393	2.0991	159	.8198	5.2851
	252	.7374	2.0924	317	.8161	4.6004
	508	.7369	2.0897	637	.8143	4.1516
	1020	.7367	2.0904	1277	.8134	4.1538
	2044	.7366	2.0898	2556	.8128	4.0463
50	39	.7347	2.0497	50	.8200	3.9683
	77	.7308	2.0387	98	.8123	3.8637
	156	.7269	2.0142	199	.8081	3.8473
	391	.7261	2.0168	497	.8058	4.1184
	793	.7257	2.0152	1006	.8046	3.9444
100	77	.7249	1.9963	99	.8085	3.7437
	154	.7231	1.9913	198	.8062	4.2167
	236	.7235	1.9982	301	.8037	3.7931
	391	.7227	1.9952	498	.8022	3.7641
200	152	.7211	1.9781	196	.8047	4.3750
	311	.7211	1.9831	398	.8018	3.9207
	720	.7203	1.9802	920	.8003	3.8174

TABLE 2. CONVERGENCE STUDY BASED ON SCALED LOAD-INCREMENTS IN A PLANE-STRAIN TUBE ($b/a = 2$, $\nu = .3$, $H' = 0$).

O.S.	n	P/σ_o	$\frac{E}{\sigma_o}\frac{U_a}{a}$	Max. σ_θ/σ_o	σ_z/σ_o at r=a
	20	.7276	2.0710	.8879	-.1106
	50	.7225	2.0078	.8919	-.1071
50%	100	.7205	1.9877	.8932	-.1056
	200	.7193	1.9776	.8939	-.1047
	400	.7189	1.9731	.8942	-.1045
	20	.8079	3.9786	1.1251	-.2199
	50	.8027	3.7835	1.1251	-.2127
100%	100	.8004	3.7224	1.1251	-.2098
	200	.7990	3.6920	1.1251	-.2081
	400	.7982	3.6770	1.1251	-.2072

REFERENCES

1. Chen, P. C. T., "A Finite-Difference Approach to Axisymmetric Plane-Strain Problems Beyond the Elastic Limit," Transactions Twenty-Fifth Conference of Army Mathematicians, pp. 455-466, January 1980.

2. Hodge, P. G. and White, G. N., "A Quantitative Comparison of Flow and Deformation Theories of Plasticity," J. Appl. Mech., Vol. 17, 1950, pp. 180-184.

3. Chu, S. C., "A More Rational Approach to the Problem of an Elasto-Plastic Thick-Walled Cylinder," J. of the Franklin Institute, Vol. 294, 1972, pp. 57-65.

4. Yamada, Y., Yoshimura, N., and Sakurni, T., "Plastic Stress-Strain Matrix and Its Application for the Solution of Elastic-Plastic Problems by the Finite Element Method," Int. J. Mech. Sci., Vol. 10, 1968, pp. 343-354.

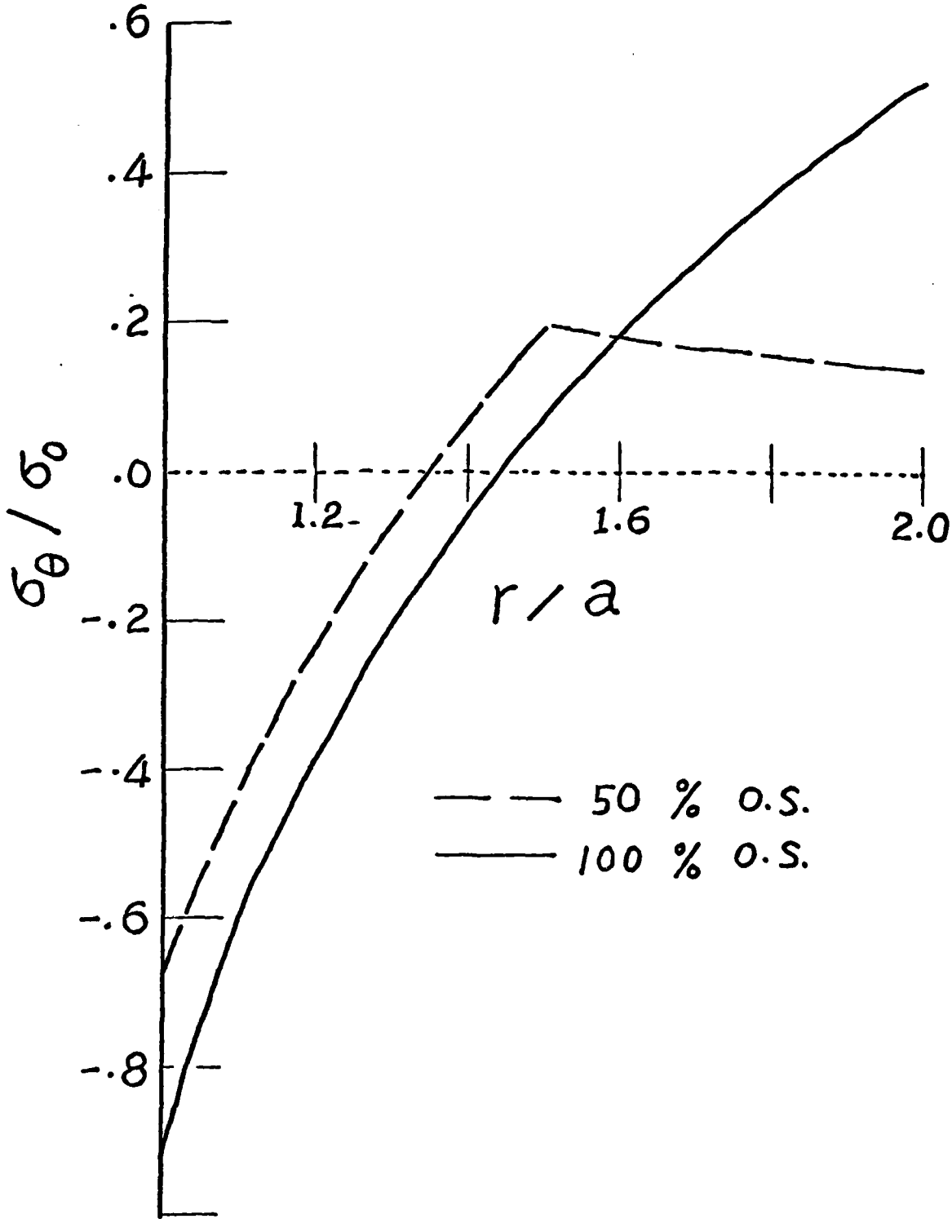

Figure 1. The residual tangential stress distribution in an overstrained tube (b/a = 2.0, ν = 0.3, ω = 0.1, n = 100).

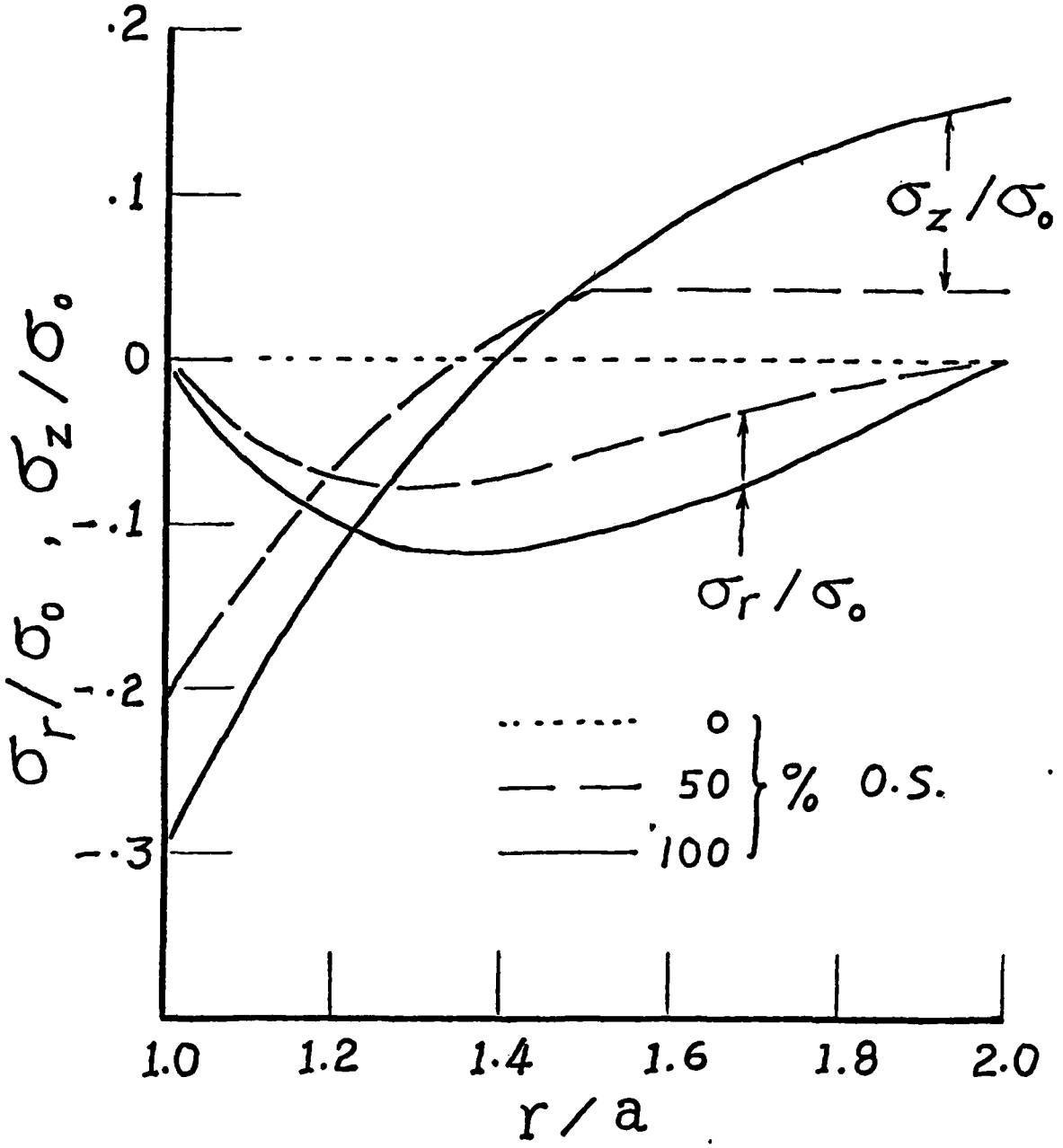

Figure 2. The residual radial and axial stress distribution in an overstrained tube (b/a = 2.0, ν = 0.3, ω = 0.1, n = 100).

COMPUTATIONAL TRANSONICS ON A VECTOR COMPUTER

Jerry C. South, Jr., and James D. Keller
NASA Langley Research Center
Hampton, Virginia 23665

and

Mohamed M. Hafez
Flow Research Company
Kent, Washington 98031

ABSTRACT. This paper discusses algorithms for solving the transonic full-potential equation in conservative form on a vector computer, such as the CDC CYBER-200 series or the CRAY-1. Recent research with the "artificial density" method for transonics has led to development of some new iteration schemes which take advantage of vector-computer architecture without suffering significant loss of convergence rate. Several schemes were tested and results are shown comparing the computational rates of one of the promising schemes on several different computers.

1. INTRODUCTION. In the last decade, significant progress has been made in the analysis of three-dimensional aerodynamic configurations at transonic speeds. The key element in this progress has been the development of reliable relaxation methods for solution of the nonlinear potential equation in various forms. In many cases, useful results have been obtained with these methods on standard, "serial-type" computers such as the CDC 6000-series and the IBM 360-series machines. However, production-type runs of 3-D transonic codes use excessive amounts of computer resources. An example is the Caughey-Jameson (ref. 1) transonic wing code FLO 22 used extensively throughout the Government and aircraft industry: A medium parabolic-coordinates grid of 192 × 16 × 32 (chord × normal × span) takes about 1,700 seconds on a CYBER-175 computer, with an accounting cost of about $500. It is estimated that the inclusion of a sophisticated 3-D boundary-layer interaction scheme might triple the cost.

Furthermore, the finest grid which can be operated in the CYBER-175 with the FLO 22 code is 192 × 24 × 32, which has been found to provide inadequate resolution of certain features of the flow such as swept, oblique, weak shock waves where the flow before and after the shock is supersonic. A more desirable grid for resolving such features seems to be about 300 × 32 × 32, well beyond the capacity of most existing high-speed serial computers. There is thus an increasing interest in operating these codes on more powerful computers in terms of both memory and speed, such as the CRAY-1, CDC STAR-100, CYBER-203, or ILLIAC-IV.

The current relaxation methods used in the 3-D transonic codes are not suitable for the vector-architecture computers just mentioned. For example, one of the most reliable and widely-used methods is line successive overrelaxation (LSOR); its convergence

rate depends partly on using the latest available values from the previous line while solving for the current line; hence, the lines cannot be solved simultaneously. Use of old values of the preceding line would reduce the method to line Jacobi and (assuming stability) allow simultaneous solution of all lines; however, the convergence rate would be intolerably slow, negating the advantages of the fast computational rate of the vector or parallel computer. It is clearly desirable to search for methods that can take advantage of the long-vector operational capabilities of such machines as STAR without suffering significant loss in convergence rate compared to established serial-computation methods.

Some progress has been made in this direction already. Smith et al. (ref. 2) carried out a preliminary study of "vectorizing" the LSOR algorithm in FLO 22. The serial version of the code has the option to use either vertical or horizontal line relaxation; the vector version used the horizontal line algorithm to achieve the longer vector length (192 to 300). Speed gains of the STAR-100 over the CYBER-175 ranged from 2 to 3, indicating that far greater vector lengths and less serial, or scalar, operations were required for the STAR-100 to approach its potential efficiency. Keller and Jameson (ref. 3) studied a three-iteration level, explicit, point relaxation scheme for the 2-D small-disturbance equation, with vector lengths equal to the number of points in a plane. Their results indicated that such a code, with vector operations of length I × J of order 10^3 or more approached the full potential of the STAR-100 capability; however, the explicit scheme took about three times as many cycles on a given mesh as LSOR, so some of the benefits were lost. Their net gain over a good serial LSOR version on CYBER-175 was 1.8, although the vector-code computational rate was 250,000 points/second. Redhed et al. (ref. 4) discussed an alternating-line SOR method for a 3-D transonic wing code, wherein the odd and even vertical lines in a cross-flow (Y-Z) plane were solved separately; the computation of the equations (residual and tridiagonal coefficients) was a vector length equal to half the cross-plane dimension J × K/2 = 28 × 20/2 = 280, while the even- and odd-line tridiagonal solutions were carried out with J/2 = 14 length vectors. This procedure represented a compromise in that it retained the essentials of the relatively successful LSOR algorithm, while achieving an increase in vector length for a significant part of the calculation. The net result for this algorithm on STAR-100 was a speed gain of 3.4 over the CYBER-175 LSOR code. Obviously, a larger speed ratio would have been obtained using a finer mesh; the 64 × 28 × 20 mesh employed in reference 4 should be considered as a coarse 3-D mesh. Reference 4 rightly concluded that more study is needed to eliminate the short-vector operations. Hotovy and Dickson (ref. 5) presented a "3-color checkerboard" algorithm for use on STAR-100 for a 2-D transonic small-disturbance equation. The third "color" in the checkerboard pattern of solution was required in their algorithm because of the update of the (i-2,j) point in the upwind difference for ϕ_{xx} at supersonic points. Their algorithm

required that point to be at the same iteration level as the (i,j) point; and, hence, they could not both belong to the same vector or "color." The vector lengths in the algorithm were 1/3 of the mesh points in the I × J plane. The algorithm suffered from the same defect as did the explicit scheme of reference 3, in that it required about 3 times as many cycles as a good LSOR version; the net speed ratio was about 2 when the 3-color checkerboard on STAR was matched against LSOR on CYBER-175.

In this paper, we present a new algorithm which solves the 2-D and 3-D full-potential equation in conservation form. The scheme is based on the artificial density formulation of the potential equation studied in references 6 to 8. With this formulation, transonic full-potential calculations are rather easily vectorized. In the following section, the artificial density method is discussed briefly. Improved procedures are given which avoid erratic behavior at shocks. Subsequent sections discuss some properties of vector-processor machines, iteration algorithms, and numerical results.

2. THE ARTIFICIAL DENSITY METHOD. The artificial density method has been proposed in references 6 to 8 as a simple method for introducing dissipation into the difference analog of the conservative full-potential equation. The idea is to solve the equation

$$(\bar{\rho}\phi_x)_x + (\bar{\rho}\phi_y)_y + (\bar{\rho}\phi_z)_z = 0$$

where

$$\bar{\rho} = \rho - \mu\Delta s \rho_s$$

$$\rho = \left(M_\infty^2 a^2\right)^{\frac{1}{\gamma - 1}}$$

$$a^2 = \frac{1}{M_\infty^2} + \frac{\gamma - 1}{2}(1 - q^2)$$

$$q^2 = \phi_x^2 + \phi_y^2 + \phi_z^2$$

$$\mu = \max\,(0,\ 1 - a^2/q^2)$$

The term $\Delta s \rho_s$ in the $\bar{\rho}$-equation is the product of the step length along a streamline and the streamwise density gradient. The use of $\bar{\rho}$ in the potential equation instead of the isentropic density ρ produces a dissipative difference scheme when correct differencing is used. In references 7 and 8, the isentropic density was calculated at the node points using the velocity components centered there. The difference operator requires the density values at midpoints of line segments connecting node points; hence, these midsegment values were obtained by averages of the adjacent node-point values. In reference 7, this convenience was carried through to the calculation of the artificial density $\bar{\rho}$,

$$\bar{\rho}_{ij} = \rho_{ij} - \mu_{ij} (\rho_s \Delta s)_{ij}$$

where upwind formulas were used for the approximation to $\rho_s \Delta s$. The midsegment values of $\bar{\rho}$ were calculated as averages. A similar procedure was used in reference 8. In both references 7 and 8, it was noted that overshoots (nonphysical expansions) occurred just ahead of a shock wave and that it was usually necessary to multiply the switch function μ by a constant or variable factor to increase the amount of dissipation. This procedure tends to cause more smearing of the shocks, and a reliable prescription for selecting the factor from one case to the next is not known. South and Jameson (ref. 9) relate this erratic behavior to two sources: (1) The mislocation of the switch function, μ, and (2) calculation of the midsegment densities by averaging nodal-point values. In reference 9, the difficulty is cured if the switch function μ_i, defined at the node point i rather than at the midsegment $i+\frac{1}{2}$, is used in the expression for $\bar{\rho}_{i+\frac{1}{2}}$ and if the midsegment values of the density are calculated using the midsegment values of the velocities as in references 6, 10, or 11. Two-dimensional results illustrating these points are given in figures 1 to 3. Figures 1 and 2 compare the nodal point and midcell evaluation of artificial density for a nonlifting NACA 0012 airfoil and $M_\infty = 0.85$ and 0.92, respectively. These results, and all others in this paper, use the planar, small-disturbance boundary condition at the airfoil mean chord line. The $M_\infty = 0.92$ case exhibits a "fishtail" shock pattern, with an oblique shock at the trailing edge followed by a normal shock in the wake. The nodal-point density evaluation gives nonphysical overshoots (which could be diminished at the expense of more smearing), while the midcell density yields sharp shocks with no discernible overshoots. Figure 3 shows the midcell method alone for $M_\infty = 1.2$, with a bow shock ahead and an oblique shock at the tail. Again the results show a sharp shock without overshoots.

It has been found that the question of iterative schemes for solving the artificial-density difference equations is an

issue almost separate from the artificial density formulation. Indeed, fairly simple iteration schemes could be applied to the difference equations irrespective of how the artificial viscosity is introduced. Based on these simplified iteration schemes, new methods for transonics are especially effective on a vector or parallel computer as discussed in a later section. First, calculations on vector computers are discussed in the following section.

3. VECTOR PROCESSOR PROPERTIES. The advent of the new vector processor type of large-scale computers (CDC STAR-100, CDC CYBER-203, CRAY-1, ILLIAC IV, and Texas Instrument ASC) will have a significant impact on iterative algorithms used for transonic flow calculations. There are currently two types of vector processors. The first type gets its speed by having a number of parallel processors which can perform the same operation on different sets of operands simultaneously. An example of this type is the ILLIAC IV. The second type is the pipeline processor which does operations on streams of operands in assembly-line fashion. CDC STAR-100, CYBER-203, and CRAY-1 are examples of this second type. Vector computers are most efficient when the algorithms used call for the same operations to be done on a number of different pairs of operands (or vectors) independently. The parallel processors operate at their fastest rate when the vector length is equal to the number of processors. The CDC pipeline-type processors continue to operate more efficiently as the vector length increases. Another feature of such machines is that as the ratio of vector speed to scalar speed increases, it becomes even more important to avoid scalar operations. For example, if vector operations can be done 20 times faster than scalar operations and a code does 90 percent of its operations in vector mode and 10 percent in scalar mode, then the 10 percent of the operations which are scalar will take 69 percent of the time. The main improvement of the CYBER-203 over the STAR-100 is that the CYBER-203 has a much faster scalar speed than the STAR-100.

As discussed in the Introduction, the methods in wide use for transonics today are not very suitable for vector computers; they involve short-vector operations and over 10-percent scalar work. The following section discusses transonic algorithms which use moderate-to-long vectors and which appear to minimize the scalar work.

4. ITERATION ALGORITHMS. So far the search for efficient iterative schemes for vector processors has developed into a study of compromises. We have examined several explicit, implicit, and semi-implicit schemes including second-order Richardson iteration, checkerboard SOR, checkerboard leapfrog, alternating line SOR, and approximate factorization. Details of these schemes can be found in reference 12. The scheme which has proven to be most efficient on the CDC vector processors is a point scheme which mimics a full-plane SOR. We call this scheme ZEBRA II. It is a cross-plane checkerboard, where the horizontal lines $j + k$ odd are black and the lines $j + k$ even

are white. Each plane i = constant is thus a checkerboard pattern. The algorithm is, in its simplest form for an unstretched grid,

$$B\Delta\phi_{ijk} = \frac{\Delta X^2 R_{ijk}}{\bar{\rho}_{avg}} + \beta\Delta\phi_{i-1,jk}$$

where

$$\Delta X^2 R_{ijk} = \bar{\rho}_{i+\frac{1}{2},jk}\left(\phi^n_{i+1,jk} - \phi^n_{ijk}\right)$$

$$- \bar{\rho}_{i-\frac{1}{2},jk}\left(\phi^n_{ijk} - \phi^{n+1}_{i-1,jk}\right)$$

$$+ \left[\bar{\rho}_{i,j+\frac{1}{2},k}\left(\phi^\nu_{i,j+1,k} - \phi^n_{ijk}\right)\right.$$

$$\left. - \bar{\rho}_{i,j-\frac{1}{2},k}\left(\phi^n_{ijk} - \phi^\nu_{i,j-1,k}\right)\right]\left(\frac{\Delta x}{\Delta y}\right)^2$$

$$+ \left[\bar{\rho}_{ij,k+\frac{1}{2}}\left(\phi^\nu_{ij,k+1} - \phi^n_{ijk}\right)\right.$$

$$\left. - \bar{\rho}_{ij,k-\frac{1}{2}}\left(\phi^n_{ijk} - \phi^\nu_{ij,k-1}\right)\right]\left(\frac{\Delta x}{\Delta z}\right)^2$$

$\nu = n$ for j + k odd

$\nu = n+1$ for j + k even

$$B = \frac{2}{\omega_x} + \beta + \frac{2}{\omega_y}\left(\frac{\Delta x}{\Delta y}\right)^2 + \frac{2}{\omega_z}\left(\frac{\Delta x}{\Delta z}\right)^2$$

The term β is the coefficient of the added ϕ_{xt}; the algorithm possesses "natural" ϕ_{xt} in that the ϕ-values at the i+1 plane are old, while the values at i-1 are new. We use a simple scheme for automatically increasing or decreasing β as needed. Generally, an estimate for the spectral radius based on both the maximum residual and the average residual is calculated. Let

$$SRM = |R|^{n}_{max} \Big/ |R|^{n-1}_{max}$$

$$SRA = |R|^{n}_{avg} \Big/ |R|^{n-1}_{avg}$$

Then β is changed according to:

$$\left.\begin{array}{l} \text{if (SRM + SRA)} > \text{SRMAX} \\ \text{and } \beta^{n} < \text{BMAX} \end{array}\right\} \longrightarrow \beta^{n+1} = 1.2\beta^{n}$$

$$\text{if (SRM + SRA)} < 2.0 \longrightarrow \beta^{n+1} = 0.98\beta^{n}$$

Typically, the parameters which have been quite successful for stretched Cartesian meshes are:

$$1.9 \leq \omega_x < 2.0, \quad \omega_y = \omega_z = 2.0$$

$$\text{SRMAX} = 2.1$$
$$\text{BMAX} = 2.0$$
$$\beta^{o} = 0.25$$

The usual behavior of the convergence process is a transient adjustment of the supersonic region and shock movement, followed by a fairly smooth decrease of the error with an attendant reduction in β. The three cases of figures 1 to 3 were solved easily by the 2-D version of ZEBRA II; the latter two should be considered as rather severe tests of an iterative scheme. So far, the ZEBRA II algorithm has been the most reliable method tested of those considered herein.

ZEBRA II has two features which are advantageous for vector processors. First, the algorithm uses vector instructions most of which are of length $0(J \times K)$ or longer; typical vector lengths range from 400 to 1,000. Second, the storage occurs in a natural

order, so that a virtual memory system will have no excessive paging. The ϕ-array is the only 3-D array stored as consecutive cross-planes; all other arrays are 2-D. For example, STAR-100 is a virtual memory machine, and the code and all 2-D arrays were stored on one large page. The other large pages available in core were left for the ϕ-array. On the STAR-100 computer at Langley Research Center, which has about 1/2-million-word (64-bit) storage, it would be possible to run cases with as many as 10,000 points in a cross-plane and still have a small number of page faults per iteration (depending on how many points are in the x-direction). When all of the values of the potential function will not fit in core, it is possible to have the number of page faults per iteration equal to 2 plus the number of large pages (65,000 words) which will not fit in core.

5. NUMERICAL RESULTS. A pilot code was written to test different algorithms for 3-D transonic flow around a wing at an angle of attack. The calculations reported here are for $\alpha = 2^{o}$, $M_{\infty} = 0.85$, NACA 0012 airfoil section, leading-edge sweep angle = trailing-edge sweep angle = 15^{o}, on a grid $I \times J \times K = 70 \times 16 \times 30$. All runs were 400 cycles. Figure 4 shows the convergence history of the ZEBRA II scheme and line successive overrelaxation (LSOR). The two converge at nearly the same rate.

The pilot code was first operated on several different machines without any vectorization. The times are shown in the table. Note that the STAR-100 is slow (about the speed of a CDC 6600) in scalar mode, but that the CYBER-203 (an improved version of the STAR-100) is much faster (almost as fast as a 7600); and, when the optimizing compiler is used on the CYBER-203, it is much faster still (almost as fast as the CRAY-1).

The code was then modified to take advantage of the vector processing capabilities of these computers. The modifications for the CRAY-1 were minor. The only changes necessary were to rearrange loops by introducing temporary vectors so that the compiler could generate vector instructions. For the CRAY-1 results in this paper, only a portion of the code was vectorized. The calculations of the density and the maximum residual were not vectorized. It is estimated that a completely vectorized code on the CRAY-1 would run in about 80 seconds. The modifications on the STAR-100 and CYBER-203 were not as easy to make. The code was rewritten using explicit vector instructions.

The two types of vector processor computers used in this study have different architectures. The CRAY-1 reaches its full speed with short vector lengths while the speed of the STAR-100 and CYBER-203 increases as the vector length increases. The results shown in this paper were computed on a grid with (30×16) 480 points in each cross-plane. On this size problem, the STAR-100 computational rate is 144,000 points/second. When the number of points in the cross-plane is increased to (60×32) 1,920, the computational rate increases to 208,000 points/second.

Thus, the STAR-100 and CYBER-203 have an additional advantage as the problem size increases. Finally, it should be emphasized that the 32-bit arithmetic capability of STAR-100 can be utilized to push the larger problem computational rate to 460,000 points/second and double the available core size.

6. CONCLUDING REMARKS. The artificial density method for computational transonics has opened the door to the development of new algorithms which are more efficient on vector computers such as STAR-100, CYBER-203, and CRAY-1 than current "serial" methods such as LSOR. The architecture of the new computers suggests compromises which must be made in order to best utilize the capabilities of these machines. A good vector algorithm for the CDC vector processors is one in which the data is processed in a natural contiguous pattern; the vectors are of moderately long length (400 to 1,000, say); and the convergence rate is not much slower than good standard methods. One method which fits these requirements is ZEBRA II, which is essentially a cross-plane, point-relaxation, checkerboard method.

The numerical results illustrate some of the compromises that must be made. The ZEBRA II scheme works efficiently on both CRAY-1 and STAR-100, with run times of about 1 minute for a 3-D lifting wing with planar boundary conditions, Cartesian coordinates, and the full-potential equation. STAR-100 32-bit arithmetic capability would yield run times of 26 seconds. This run time represents a speed gain of 10 over CDC 7600 and 17 over the CYBER-175. Doubling the number of mesh points in each cross-plane direction increases the relative speed gain of STAR-100 by 30 percent.

It remains to be studied as to how well the ZEBRA II scheme, or some variant of it, can be made to work in other coordinate systems, such as the parabolic coordinates used in the Jameson-Caughey FLO 22 wing code. Further, it would be valuable to obtain some hard data on vectorization of some of the new implicit approximate factorization methods.

ACKNOWLEDGMENT. The third author wishes to express his appreciation to Donald Lovell of Flow Research Company and Frank Chism of United Computing Systems, Inc., for their help during the development of the CDC 7600 and CRAY-1 computer codes.

REFERENCES.

1. Jameson, Antony; and Caughey, David A.: Numerical Calculation of the Transonic Flow Past a Swept Wing. ERDA Res. and Dev. Rep. COO-3077-140, New York University, June 1977.

2. Smith, Robert E.; Pitts, Joan I.; and Lambiotte, Jules J.: A Vectorization of the Jameson-Caughey NYU Transonic Swept-Wing Computer Program FLO-22-VI for the STAR-100 Computer. NASA TM-78665, March 1978.

3. Keller, James D.; and Jameson, Antony: Preliminary Study of the Use of the STAR-100 Computer for Transonic Flow Calculations. AIAA Paper 78-12, Jan. 1978.

4. Redhed, David D.; Chen, Allen W.; and Hotovy, Steven G.: New Approach to the 3-D Transonic Flow Analysis Using the STAR-100 Computer. AIAA J., vol. 17, no. 1, Jan. 1979, pp. 98-99.

5. Hotovy, Steven G.; and Dickson, L. J.: Evaluation of a Vectorizable 2-D Transonic Finite Difference Algorithm. AIAA Paper 79-0276, Jan. 1979.

6. Holst, Terry L.; and Ballhaus, William F.: Conservative Implicit Schemes for the Full Potential Equation Applied to Transonic Flows. NASA TM-78469, March 1978.

7. Hafez, Mohamed M. Hafez; South, Jerry C., Jr.; and Murman, Earll M.: Artificial Compressibility Methods for Numerical Solution of Transonic Full Potential Equation. AIAA Paper 78-1148, July 1978.

8. Holst, Terry L.: An Implicit Algorithm for the Conservative Transonic Full Potential Equation Using an Arbitrary Mesh. AIAA Paper 78-1113, July 1978.

9. South, Jerry C., Jr.; and Jameson, Antony: Recent Advanced in Computational Transonics. Conference on Computers in Aerodynamics, Polytechnic Institute of New York, Farmingdale, N.Y., June 4-5, 1979. To appear in special issue of Computers and Fluids.

10. Jameson, Antony: Transonic Potential Flow Calculations Using Conservation Form. Proc. AIAA 2nd Comp. Fld. Dyns. Conf., Hartford, Conn., June 1975, pp. 148-161.

11. Jameson, Antony: Numerical Computation of Transonic Flows With Shock Waves. Symposium Transonicum II, Proc. International Union of Theoretical and Applied Mechanics, Göttingen, Sept. 8-13, 1975, eds., K. Oswatitsch and D. Rues, Springer-Verlag, 1976.

12. South, Jerry C., Jr.; Keller, James D.; and Hafez, Mohamed M.: Vector Processor Algorithms for Transonic Flow Calculations. AIAA Paper 79-1457, July 1979.

TIMING COMPARISON FOR ZEBRA II ALGORITHM
FOR TRANSONIC FLOW

MACHINE AND CODE VERSION	CPU TIME (SEC)
STAR-100 scalar code	2,272
CYBER-175 scalar code	724
CYBER-203 scalar code	487
CDC 7600 scalar code	443
CYBER-203 scalar code, optimizing compiler	243
CRAY-1 scalar code	222
CRAY-1 partially vectorized code*	144
STAR-100 vectorized code**	80
CYBER-203 vectorized code	74

*It is estimated that a fully vectorized code would run in about 80 seconds on the CRAY-1.

**STAR-100 and CYBER-203 have 32-bit arithmetic capability also via the SL/1 language. It is estimated that the CPU time for such a case would be about 36 seconds on the STAR-100.

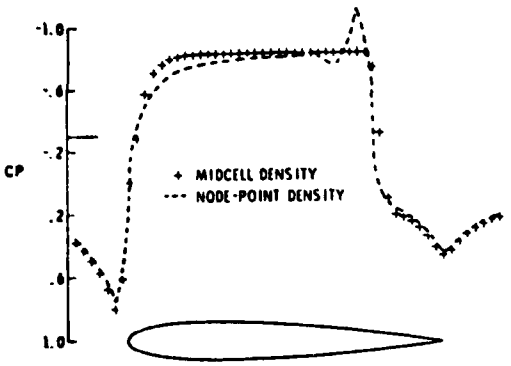

Figure 1. - Pressure distribution for NACA airfoil. M_{∞}=.85, α = 0, 121 × 25 mesh.

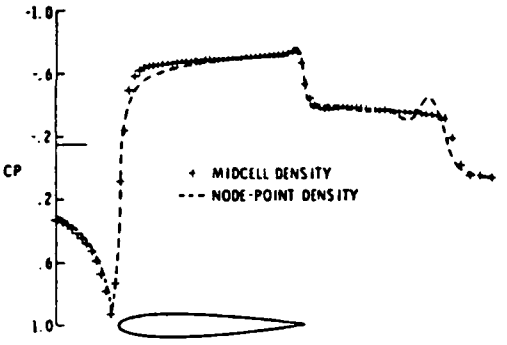

Figure 2. - Pressure distribution for NACA airfoil. M_{∞}=.92, α = 0, 121 × 49 mesh.

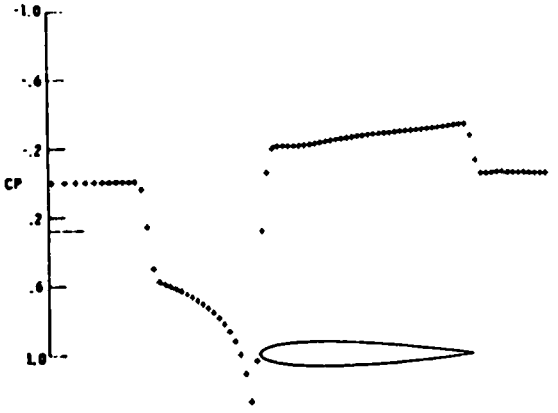

Figure 3. - Pressure distribution for NACA 0012 airfoil. Midcell density, M_{∞} = 1.2, α = 0, 121 × 61 mesh.

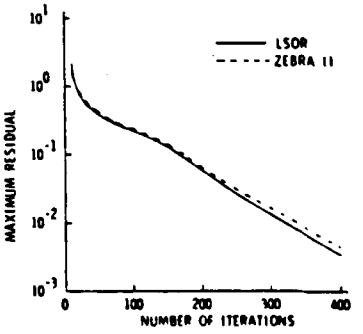

Figure 4. - Convergence history for 3-D transonic code.

ANALYSIS OF COMPUTERIZED PRODUCTION QUEUEING MODELS

James H. Donnelly
U.S. Army Missile Command
Engineering Directorate
Redstone Arsenal, Alabama 35809

Robert E. Shannon
The University of Alabama in Huntsville
Department of Industrial
and Systems Engineering
Huntsville, Alabama 35807

ABSTRACT. This paper addresses a proposed systematic methodology for use in analyzing biased and autocorrelated simulation data. The objective for using the methodology is to determine the best manner in which to operate a simulation model to permit computation of a minimum mean-squared-error estimate for the stationary mean of a simulated process. A mean-squared-error estimate provides an optimum trade-off between estimator bias squared and variance. Areas of special attention in this paper include computer aided analysis of nonstationary processes, time series analysis and analysis of queueing model data.

1. INTRODUCTION. On occasion during the planning and execution of computerized simulation experiments, an experimentor has to face the situation in which a simulation model will generate a transient, autocorrelated nonterminating series of random observations. Then, observing that the simulation experiment does not have some natural stopping point, the experimentor must set a limit e to the maximum number of simulation observations created. However, if the simulation experiment should not exit its transient warm up phase within the constraining limit, the observations from a transient distribution may have to be used for [illegible] purposes. Unfortunately, if estimates for stationary process [illegible] based upon transient data, the estimates will generally

be unreliable. Assuming that both transient and autocorrelated model behavior is unavoidable, the following question surfaces: which methodology and what criterion or criteria should be used for estimating so that the resulting estimates will be meaningful?

Given the preceding question and some general interest in the estimation of an initially transient process' stationary mean, the specific area under consideration in this paper is the development of a systematic methodology to determine the best manner in which to conduct a simulation experiment to obtain an estimate for the steady state process mean. The purpose of the methodology is to provide an experimentor with a quantitative procedure with which to select from one of four alternatives available for the conduct of a simulation experiment. The four choices are: conduct one long simulation run and retain all observations; conduct one long run and discard warm up observations; replicate and retain all observations or; replicate and discard warm up observations [1].

Three essential parameters which result from the use of the methodology are: N, an integer which specifies the number of independent simulation runs to be conducted in a simulation experiment; W, an integer which specifies the number of warm up observations to discard in each simulation run of an experiment; and L, an integer which specifies the number of observations saved in each simulation run of an experiment and used for estimation purposes. The integers N, W and L are subject to the constraint $N(W+L) \leq M$, where M is a budget constraint which denotes the total number of response observations that may be created in each simulation experiment. Use of N, W and L for the conduct of a simulation experiment should lead to operating conditions that permit the computation of an approximately minimum mean-squared-error estimate for the stationary mean.

The systematic methodology approach is presented in Section 2, and to show how the methodology works, a simple autoregressive process example is explored in Section 3. The example demonstrates the feasibility of the methodology per se and suggests its applicability to more complex

time series processes. Section 4 delves into the application of the methodology to a simple queueing process.

2. METHODOLOGY APPROACH. The approach pursued in the development of a methodology for analysis of transient autocorrelated data is based upon the theoretical works of Wold [2] and their subsequent practical extension by Box and Jenkins [3]. Furthermore, the methodology has also been influenced by Fishman's use of the mean-squared-error criterion as a figure of merit for use in nonstationary simulation experiments [4], and Turnquist and Sussman's use of a budget constraint to limit simulation experiments [5].

Wold's efforts during the nineteen-thirties have led to general recognition of the following three time series models:

$$X_t = \phi_1 X_{t-1} + \phi_2 X_{t-2} + \ldots + \phi_p X_{t-p} + a_t \tag{2.1}$$

$$X_t = a_t - \theta_1 a_{t-1} - \theta_2 a_{t-2} - \ldots - \theta_q a_{t-q} \tag{2.2}$$

$$X_t = \phi_1 X_{t-1} + \phi_2 X_{t-2} + \ldots + \phi_p X_{t-p} + a_t - \theta_1 a_{t-1} - \theta_2 a_{t-2} - \ldots - \theta_q a_{t-q} \tag{2.3}$$

Where equation (2.1) defines an autoregressive AR(p) process, equation (2.2) defines a moving average MA(q) process, and equation (2.3) defines an autoregressive moving average ARMA(p,q) process. The variable X_t represents a current value, whereas the X_{t-1}, X_{t-2},... variables represent lagged values of the variable X_t. The variables a_t, a_{t-1}, a_{t-2}, ... represent random disturbances or shocks and are generally assumed NID(0, σ_a^2). The coefficients ϕ_1, ϕ_2,..., ϕ_p and θ_1, θ_2,..., θ_q represent model parameters. Theoretically, p and q can be finite or infinite depending upon the particular process represented.

Although theoretically satisfying, Wold's models were not overly practical because of the lack of an efficient methodology for selecting and fitting an appropriate model to a given time series. This troublesome problem was overcome by Box and Jenkins with their development of

a methodology for rapid identification and fitting of an appropriate AR, MA or ARMA model to time series data. Their methodology entails estimation of the autocorrelation and partial autocorrelation functions to provide visibility into the underlying mechanism of an unknown process. Essentially, the Box and Jenkins approach employs inspection of estimated autocorrelation and partial autocorrelation functions to detect stationarity, trend, seasonality and randomness in time series data as well as to tentatively identify an appropriate model. The estimated autocorrelation coefficients are further used for the estimation of model parameters.

Working with the assumption that it is possible to characterize many transient, discrete event, stochastic processes by the use of surrogate models such as one of Wold's family of models, the following protocol has been investigated in an attempt to develop a computer aided methodology which will lead to a minimized mean-squared-error estimator:

1. Specify a simulation experiment budget constraint M and initial condition x_o.
2. Operate the simulation model to create h time series observations $\{x_t ; t=1,2,\ldots, h\}$ such that $219 \leq h \leq M$.
3. Separate the series at x_d such that $h - 50 = d$.
4. Attempt to identify an ARMA(p,q) model for the series $\{x_t ; t=d+1, d+2, \ldots, h\}$ by employing Box and Jenkins' techniques [3] for model identification and tentative estimation of model parameters.
5. Apply the Hooke-Jeeves pattern search technique [6] to optimize the estimates for parameters such that the estimates will satisfy the entire series $\{x_t ; t=0,1,2,\ldots, h\}$.
6. Perform a Chi-square test to test if the estimated shock terms $\{\hat{a}_t ; t=1,2,\ldots, h\}$ generated by the Hooke-Jeeves pattern search are normally distributed about a zero mean.
7. Based upon steps 1 through 6, use the selected ARMA(p,q) model to generate a surrogate time series $\{y_t ; t=1,2,\ldots, h\}$.
8. Perform a two tailed paired t test to test the hypothesis that the stationary means for the two series $\{x_t\}$ and $\{y_t\}$ came from

the same population.

9. Based upon the results of the Chi-square and two tailed paired t tests, if the selected surrogate model is an adequate fit, the following parameters and expectations are derived based upon the selected model, the initial condition x_o and the constraint $N(W+L) \leq M$:

   a. The ARMA(p,q) process stationary mean as h approaches infinity as a limit

   $$\hat{\hat{\mu}} = \lim_{h \to \infty} E[Y_h | x_o] \tag{2.4}$$

   b. The expected value for $\bar{Y}_{N,W,L}$

   $$E[\hat{\mu}] = E[\bar{Y}_{N,W,L} | x_o]$$

   $$E[\hat{\mu}] = E[1/N \sum_{i=1}^{N} (1/L \sum_{t=W+1}^{W+L} Y_t^{(i)})] \tag{2.5}$$

   where (i) is an index which indicates a particular replication, e. g., i = 1,2,..., N.

   c. The variance for $\bar{Y}_{N,W,L}$

   $$VAR[\hat{\mu}] = VAR[\bar{Y}_{N,W,L} | x_o]$$

   $$VAR[\hat{\mu}] = VAR[1/N \sum_{i=1}^{N} (1/L \sum_{t=W+1}^{W+L} Y_t^{(i)})] \tag{2.6}$$

10. Given the results of derivations (2.4), (2.5) and (2.6), the mean-squared-error objective function is minimized through exhaustive enumeration with respect to N, W and L.
    That is:

    $$\text{Min MSE } (\bar{Y}_{N,W,L} | x_o) = VAR[\hat{\mu}] + [E[\hat{\mu}] - \hat{\hat{\mu}}]^2 \tag{2.7}$$

    subject to:
    $N(W+L) \leq M$
    N, W and L integers and ≥ 0.

11. Perform a sensitivity analysis to determine if N, W and L are sensitive to the estimates for the parameters used in the ARMA

(p,q) model. Extreme sensitivity of N, W and L to model parameters will shed some doubt as to the value of W and L and perhaps N.

12. When N, W and L have been determined, the simulation experiment can be continued in consonance with N, W and L and the stationary mean estimated using only (N)(L) of the data. For example, the average $\bar{X}$ is computed in the following manner:

$$\bar{X} = [1/N \sum_{i=1}^{N} 1/L \sum_{t=W+1}^{W+L} X_t^{(i)}] \qquad (2.8)$$

The resulting estimate for the stationary mean will be approximately optimal when measured in terms of the mean-squared-error criterion.

The preceding steps will be expanded upon in Section 3. Figure 2-1 portrays the flow of the methodology and highlights key decision points.

3. AN APPLICATION. To demonstrate the utility of the methodology, a simple AR(1) autoregressive model of the form

$$X_t = \phi(X_{t-1} - \mu) + \mu + a_t \qquad (3.1)$$

where

$$0 < \phi < 1$$

$$E[a_t] = 0$$

$$E[a_s a_t] = \begin{cases} \sigma_a^2 & , \quad s = t \\ 0 & , \quad s \neq t \end{cases}$$

was used to generate a stochastic process $\{X_t ; t=1,2,\ldots, \infty\}$ where observations are recorded at discrete equidistant points in time $t=1,2,\ldots$. Model parameters were specified as: $\phi = 0.9$, $\mu = 10.0$, $\sigma_a^2 = 1.0$ and $a_t = NID(0, \sigma_a^2)$. Budget constraint M was set equal to 1000 and to induce transient behavior, x_o was set equal to 30.

The model was run to collect h = 250 observations and the last fifty observations were used to estimate the autocorrelation and partial autocorrelation functions. Figure 3-1 displays graphical plots for both functions; these plots are normally used for process identification. Examination of Figure 3-1 readily indicates that an autoregressive model of the first order, e. g., an AR(1) model, is a likely candidate for a

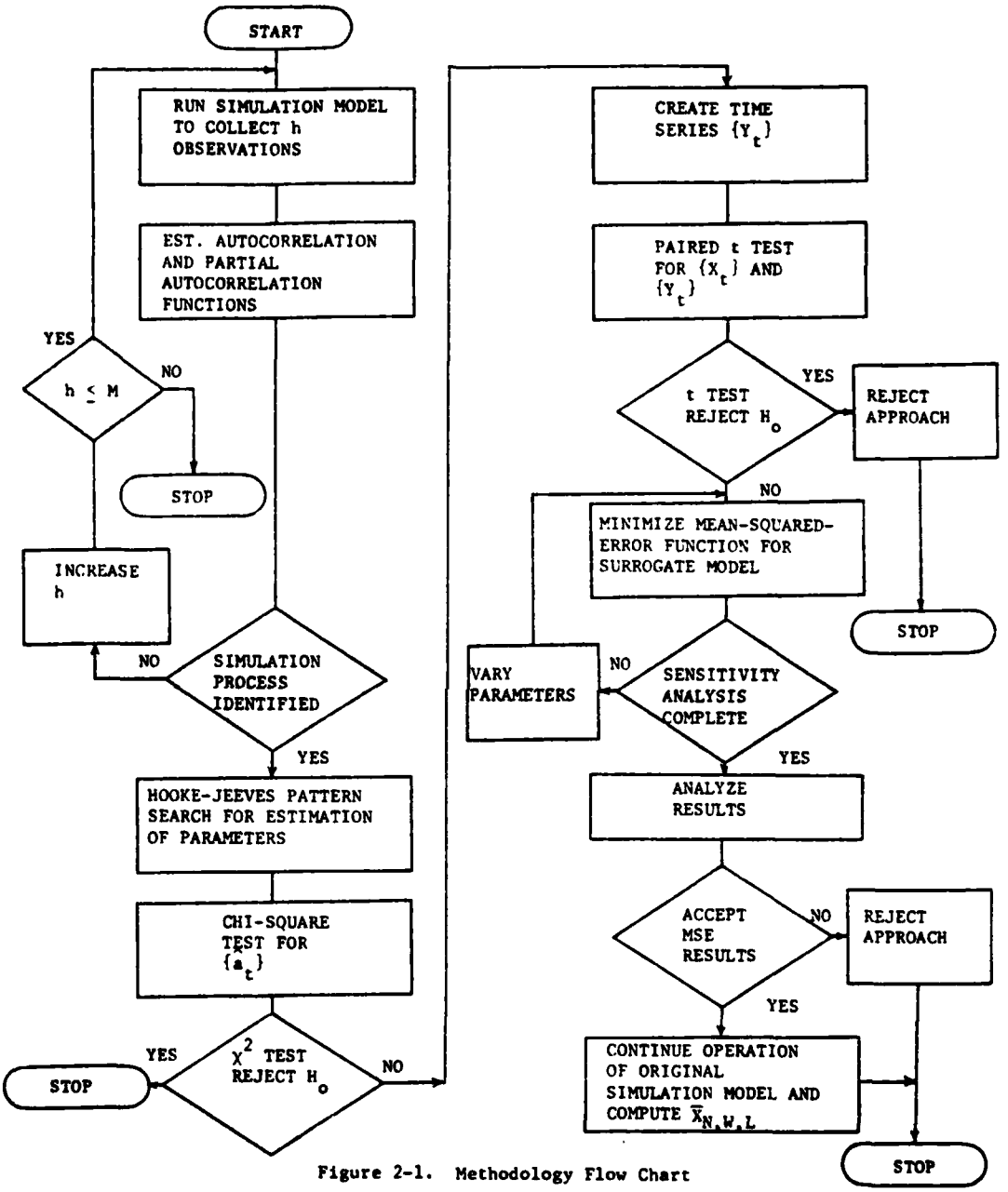

Figure 2-1. Methodology Flow Chart

model to characterize the process. Of course this is a correct choice, however, in a practical situation the underlying model structure which generated the two hundred and fifty observations would not be known a priori.

Given the assumption that an AR(1) model is adequate, the average for the last fifty observations and the autocorrelation coefficient r_1, which is used as an initial estimate for ϕ, were used to initialize a Hooke-Jeeves pattern search algorithm.

The Hooke-Jeeves pattern search method is used in a fasion similar to the Box and Jenkins non-linear least squares method in that a vector of estimated parameters

$$(\hat{\phi}\ \ \hat{\theta}\ \ \hat{\hat{\mu}}) = (\hat{\phi}_1, \hat{\phi}_2, \ldots, \hat{\phi}_p, \hat{\theta}_1, \hat{\theta}_2, \ldots, \hat{\theta}_q, \hat{\hat{\mu}}) \tag{3.2}$$

is used to compute a sum of squared shock terms $S(\hat{\phi}, \hat{\theta}, \hat{\hat{\mu}})$ where

$$S(\hat{\phi}, \hat{\theta}, \hat{\hat{\mu}}) = \sum_{t=1}^{h} \hat{a}_t^2 \tag{3.3}$$

The a_t are the estimated shock terms given a specific ARMA model, estimated parameters and the original time series observations. For an AR(1) model, each $\hat{a}_t$ is estimated in the following manner:

$$\hat{a}_t = x_t - \hat{\phi}(x_{t-1} - \hat{\hat{\mu}}) - \hat{\hat{\mu}},\ t=1,2,\ldots,\ h \tag{3.4}$$

where x_o and x_t are the original time series data.

The Hooke-Jeeves pattern search routine attempts to minimize $S(\hat{\phi}, \hat{\theta}, \hat{\hat{\mu}})$ by individually varying each of the parameters in the vector $(\hat{\phi}, \hat{\theta}, \hat{\hat{\mu}})$ by small increments to search for smaller and smaller values for the squared sum of shock terms $S(\hat{\phi}, \hat{\theta}, \hat{\hat{\mu}})$.

Upon completion of the Hooke-Jeeves pattern search, the estimated shock terms $\{\hat{a}_t\ ;\ t=1,2,\ldots,\ h\}$ were standardized and subjected to a Chi-square test to test the hypothesis that the $\hat{a}_t$ are NID(0, $\hat{\sigma}_a^2$). The Chi-square test was conducted at the $\alpha = 0.05$ significance level and with eight degrees-of-freedom. The Chi-square test is designed to have ten cells for data, hence the need for $h \geq 219$ observations. One degree-of-freedom is lost due to an inherent characteristic of the test and the other due to the need to estimate σ_a^2. The mean for the probability distribution of $\hat{a}_t$ is assumed equal to zero.

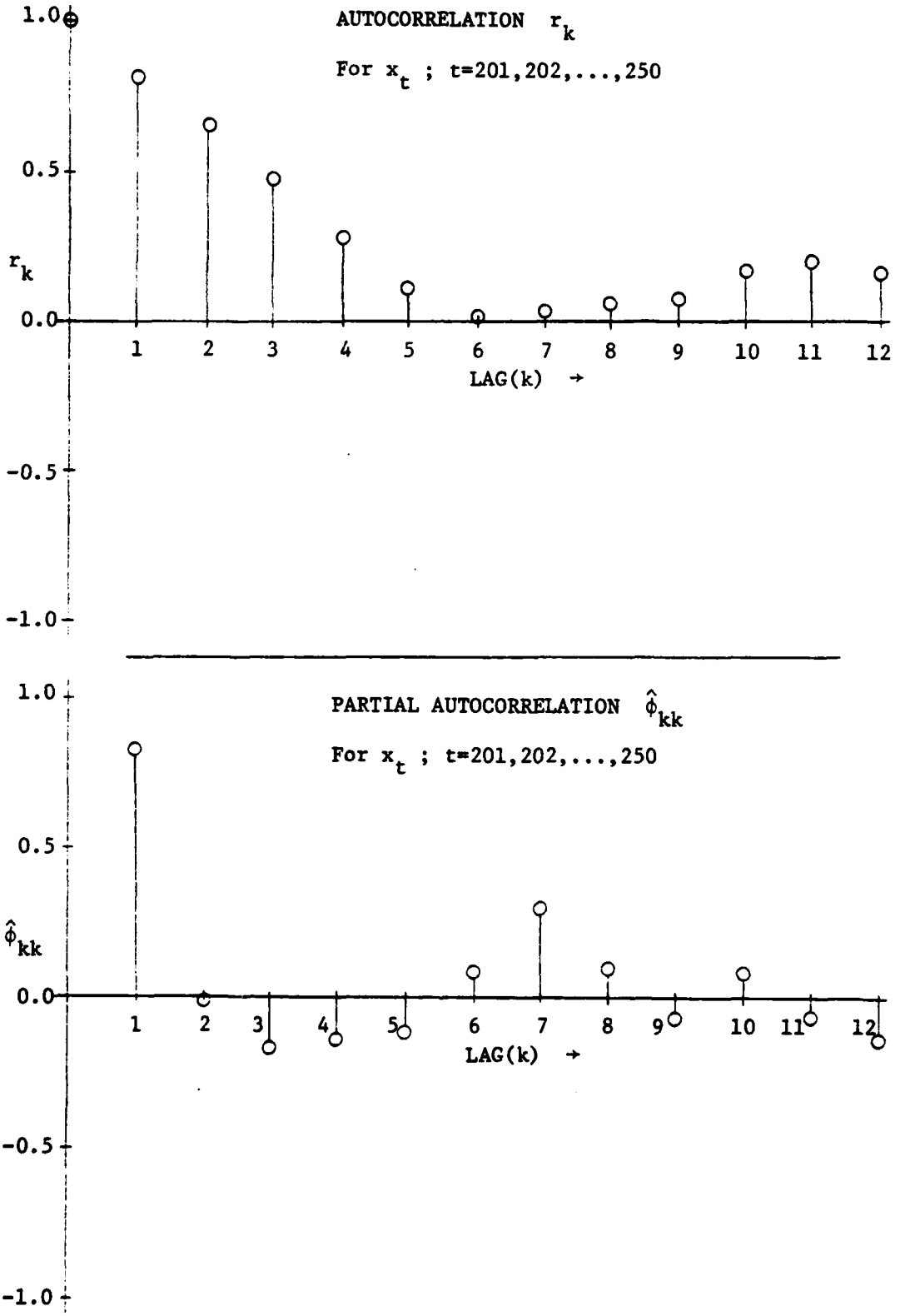

Figure 3-1. Autocorrelation and Partial Autocorrelation Functions

Table 3-1 presents a summary for the information used to initialize the Hooke-Jeeves pattern search and the results that were forthcoming. The $\hat{\hat{\mu}}$ term shown in Table 3-1 is an estimate for the process stationary mean.

Table 3-1

Hooke-Jeeves Pattern Search

H-J Input		H-J Estimated Parameters			χ^2 Statistic
$\bar{x}$	r_1	$\hat{\hat{\mu}}$	$\hat{\sigma}_a^2$	$\hat{\phi}$	
13.087	0.816	10.043	0.955	0.897	5.718

Since the Chi-square statistic $\chi^2 = 5.718$ was found to be less than the table value of $\chi^2_{0.05,8} = 15.5$ [7], the Hooke-Jeeves estimated parameters are tentatively accepted prior to additional testing with a two tailed paired t test. To conduct the two tailed paired t test, an independent surrogate time series $\{y_t ; t=1,2,\ldots, h\}$ was generated with the initial condition $y_o = x_o$. The parameters used in the surrogate model are those that were generated by the Hooke-Jeeves pattern search. Given the original series $\{x_t, t=1,2,\ldots, h\}$ and the surrogate series $\{y_t ; t=1,2,\ldots, h\}$, a pair-by-pair two tailed paired t test was conducted to test the hypothesis that the means for the two series came from the same parent population. The two tailed paired t test was conducted at a significance level of $\alpha = 0.05$ with an associated two hundred and forty-nine degrees-of-freedom. For the two series tested, the statistic $t = -0.730$, therefore, the absolute value of t was less than a table value of $t_{0.05/2,249} = \pm 1.960$ [7], and the surrogate model mean was not rejected as being equal to the $\{x_t\}$ series mean. Based on the Chi-square test and the two tailed paired t test, the surrogate series $\{y_t\}$ and model were considered an adequate characterization for the series $\{x_t\}$.

Having obtained an adequate surrogate model, for example

$$Y_t = 0.897(Y_{t-1} - 10.043) + 10.043 + a_t \qquad (3.5)$$

$$y_o = 30$$

a_t = NID(0, 0.955)

the mean-squared-error for $\bar{X}$, or rather its surrogate $\bar{Y}$, was derived and minimized in terms of N, W and L through exhaustive enumeration. The mean-squared-error for $\bar{Y}$ is obtained by derivation of equation (2.7) for an AR(1) model, which after a modest amount of effort leads to the objective function and constraints:

$$\text{Min } \hat{MSE}\left[\bar{Y}_{N,W,L} \mid x_o\right] = \frac{(x_o - \hat{\hat{\mu}})^2 \hat{\phi}^2 (\hat{\phi}^W - \hat{\phi}^{W+L})^2}{L^2 (1 - \hat{\phi})^2} +$$

$$\frac{\hat{\sigma}_a^2}{LN(1 - \hat{\phi})^2} \left[1 - \frac{\hat{\phi}(1 - \hat{\phi}^L)}{L(1 - \hat{\phi}^2)} \left[2 + \hat{\phi}^{2W+1} (1 - \hat{\phi}^L) \right] \right] \quad (3.6)$$

subject to:

$N(W+L) \leq M$

N, W and L integers and ≥ 0.

Minimization of (3.6) resulted in the following optimal values: N = 1, W = 19 and L =981 given a budget constraint M = 1000. In contrast, the exact values for N, W and L for the model given in equation (3.1) are: N = 1, W = 20 and L = 980.

Sensitivity analysis, e. g., varying each of the estimates $\hat{\phi}$, $\hat{\hat{\mu}}$ and $\hat{\sigma}_a^2$ plus and minus one per cent and noting the change in mean-squared-error value, indicated that the mean-squared-error for the particular test case studied was sensitive to the estimate for ϕ, but rather insensitive to the estimates for μ and σ_a^2. Table 3-2 presents a summary for the effects of parameter variation on the estimated mean-squared-error and N, W and L.

Table 3-2

MSE Sensitivity

Parameter Estimates		$\hat{MSE}$	N	W	L	% Δ MSE Change
$\hat{\hat{\mu}}$	1.071×10^{1}	9.110×10^{-2}	1	19	981	0.006
	1.082×10^{1}	9.110×10^{-2}	1	19	981	% Ref.
	1.093×10^{1}	9.109×10^{-2}	1	19	981	-0.006
$\hat{\sigma}_a^2$	9.453×10^{-1}	9.019×10^{-2}	1	19	981	-0.995
	9.548×10^{-1}	9.110×10^{-2}	1	19	981	% Ref.
	9.644×10^{-1}	9.200×10^{-2}	1	19	981	0.995
$\hat{\phi}$	8.879×10^{-1}	7.703×10^{-2}	1	18	982	-15.442
	8.969×10^{-1}	9.110×10^{-2}	1	19	981	% Ref.
	9.058×10^{-1}	1.094×10^{-1}	1	21	979	20.085

Figure 3-2 depicts the trade-off between estimator bias squared and variance as a function of discarded warm up observations. It is interesting to note that when a similar experiment was conducted with $x_o = \mu$, the resulting value for W was W = 0. Hence, and as expected, warm up observations should not be discarded when the AR(1) simulation experiment is initialized with x_o set equal to the steady state process mean.

4. QUEUEING APPLICATION. Given initial success with an AR(1) model, an attempt was made to determine optimum operating conditions in terms of N, W and L for a M/M/1 queueing process. A queueing model was run with a traffic intensity $\rho = 0.8$, an initial condition $x_o = 0$ and a budget constraint M = 1000. The model response variable, X_t, was the waiting time of each customer in the system.

Application of the methodology to the first 250 observations indicated that an AR(1) model was an adequate surrogate for the queueing model. Based upon minimization of the mean-squared-error for the surrogate AR(1) model, N, W and L were determined to be N = 1, W = 0 and L = 1000. This result is in consonance with the findings of Wilson and Pritsker [8] who determined that if a M/M/1 model is started with its initial condition set equal to the process stationary mode (e. g., $x_o = 0$) then, no warm up observations should be discarded to achieve

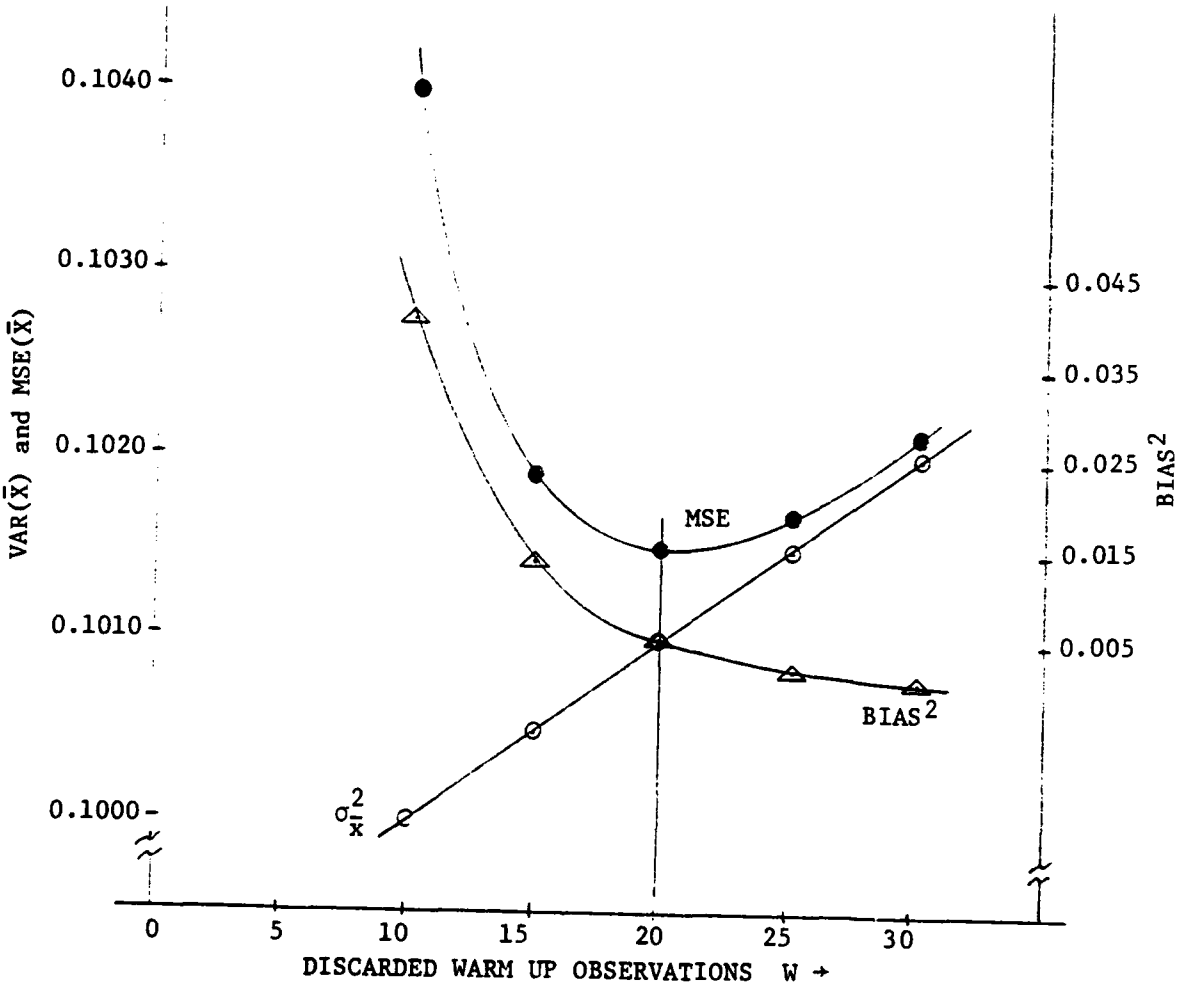

Figure 3-2. Trade-Off Between Bias^2 and Variance

a minimum mean-squared-error estimator for the process mean.

5. CONCLUSIONS. The preceding discussion has presented a systematic methodology for estimation of N, W and L to achieve an approximately minimized mean-squared-error estimator. The mean-squared-error criterion provides a performance measure with which to conduct an optimal trade-off between estimator bias squared and variance given a budget constraint M. If a discrete event autocorrelated time series experiment is executed using the values estimated for N, W and L and the constraint M, a minimized mean-squared-error sample average can be computed. Numerous elementary test cases have been executed using BASIC software with a microcomputer and favorable results have been achieved.

A corollary benefit of the methodology is that it provides a mechanism for an experimentor to evaluate the possible penalty associated with data stream truncation and independent simulation replications. It is anticipated that the methodology could be used to estimate superior simulation model initial conditions and that the surrogate model approach could be used for analysis of complex simulation processes.

6. REFERENCES.

1. Shannon, Robert E., Systems Simulation: The Art and Science, Prentice-Hall, Inc., Englewood Cliffs, New Jersey, 1975.

2. Wold, Herman, A Study in the Analysis of Stationary Time Series, Almquist and Wiksell, Stockholm, 1954.

3. Box, George E. P. and Gwilym M. Jenkins, Time Series Analysis: Forecasting and Control, Holden-Day, Inc., San Francisco, California, 1976.

4. Fishman, George S., "Bias Conisderations in Simulation Experiments," Operations Research, Vol. 20, No. 4, July-August 1972, pp. 785-790.

5. Turnquist, Mark A. and Joseph M. Sussman, "Toward Guidelines for Designing Experiments in Queueing Simulation," Simulation, Vol. 28, No. 5, May 1977, pp. 137-144.

6. Gottfried, Byron S. and Joel Weisman, Introduction to Optimization Theory, Prentice-Hall, Inc., Englewood Cliffs, New Jersey, 1973.

7. Duncan, Acheson J., Quality Control and Industrial Statistics, Third Edition, Richard D. Irwin, Inc., Homewood, Illinois, 1965.

8. Wilson, James R. and A. Alan B. Pritsker, "Evaluation of Startup Policies in Simulation Experiments," Simulation, Vol. 31, No. 3, September 1978, pp. 79-89.

AD-A089 089 ARMY MATHEMATICS STEERING COMMITTEE F/G 9/2
PROCEEDINGS OF THE 1980 ARMY NUMERICAL ANALYSIS AND COMPUTERS C--ETC(U)
AUG 80

UNCLASSIFIED ARO-80-3 NL

5 of 6
AD A089089

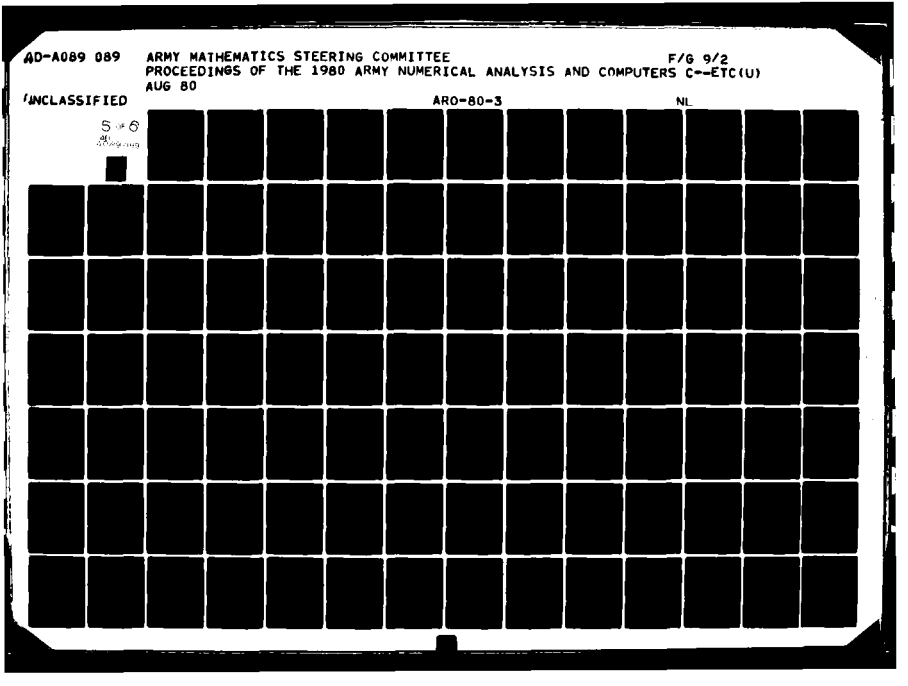

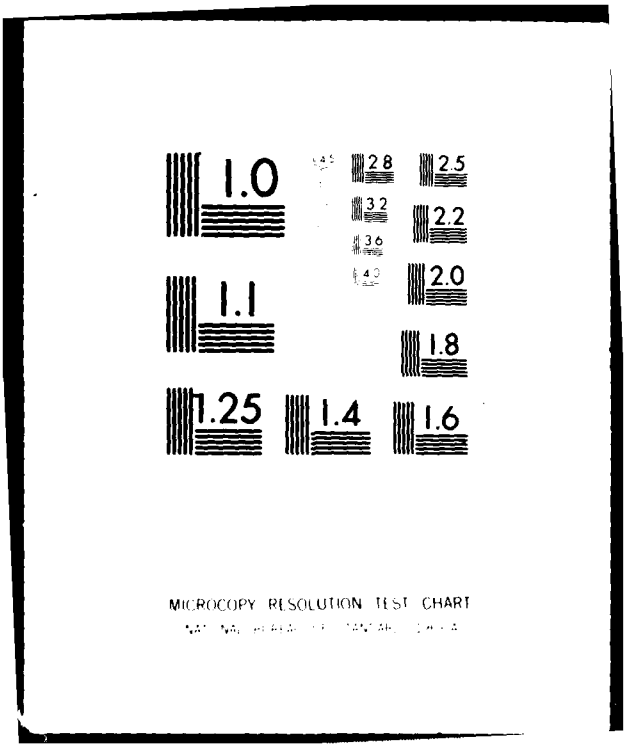
1.0
2.8
2.5
3.2
2.2
3.6
4.0
2.0
1.1
1.8
1.25
1.4
1.6
MICROCOPY RESOLUTION TEST CHART

DATA BASES AND APPLICATIONS

MORTON A. HIRSCHBERG

US ARMY ARRADCOM BALLISTICS RESEARCH LABORATORY

ABERDEEN PROVING GROUND, MARYLAND

PROBLEM

WE HAVE BECOME MASTERS AT THE ART OF DATA COLLECTION BUT HOW ARE WE DOING AT ANALYZING DATA?

Editorial Remarks: This articale consists of a series of unnumbered slides. Most slides take up a full page. This page has three slides on it.

MY VIEW OF THE WORLD

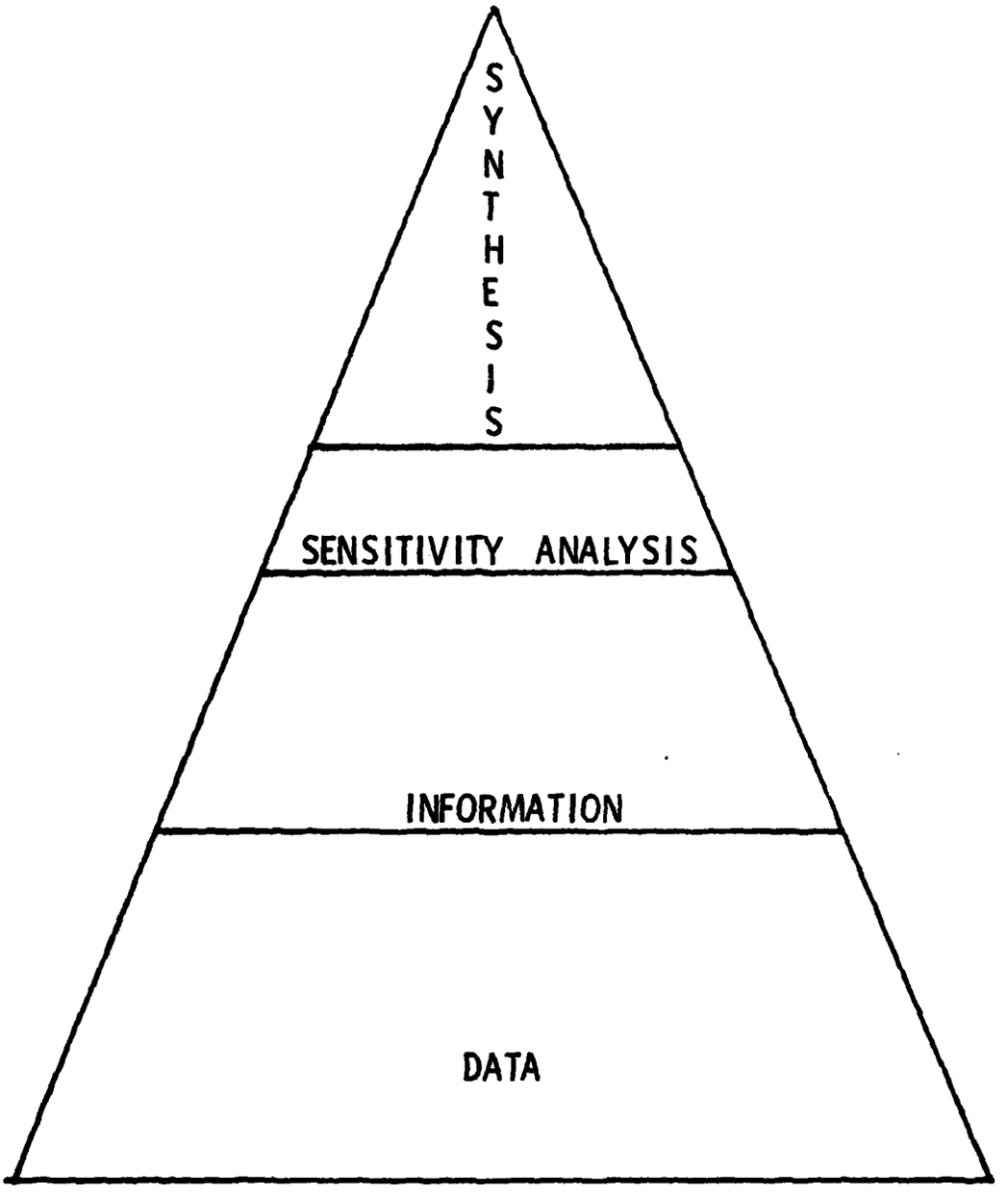

DATA IS A COLLECTION OF OBJECTS IN A PARTICULAR CONTEXT

MEANINGLESS IN ITSELF.

INFORMATION IS A MANIPULATION OF DATA IN A PARTICULAR

CONTEXT MAY NEED TO BE SUPPLEMENTED WITH DATA

FROM OTHER CONTEXTS.

SENSITIVITY ANALYSIS IS TESTING INFORMATION FOR ITS VALIDITY.

SYNTHESIS IS THE EXPLANATION OF INFORMATION.

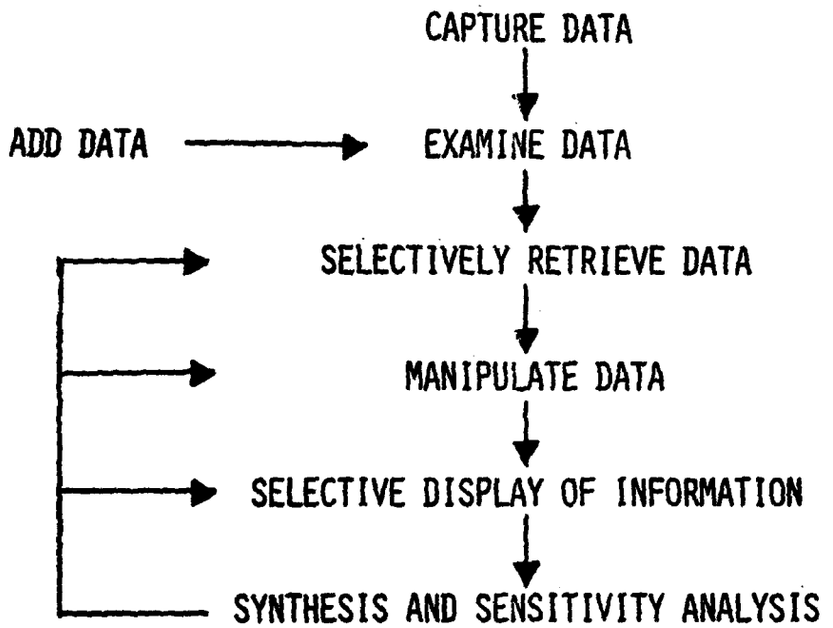

THE DESIGN PROCESS

THE DATA

TEST FIRINGS (GUNS AND MISSILES)

VEHICLE DATA (USAGE, PARTS & SPARES, MAINTENANCE)

VULNERABILITY (OFFENSIVE AND DEFENSIVE)

PERSONNEL (MEASUREMENTS, HISTORICAL, WOUNDING)

CHEMICAL (C&B, FUELS, SMOKE)

TACTICAL (COMMUNICATION, GAMING & MODELING)

MANAGEMENT (PAYROLL, FINANCE, ETC.)

DEVELOP STRATEGIES TO

- COLLECT DATA
- VALIDATE DATA
- SELECTIVELY RETRIEVE AND DISPLAY DATA (REDUCE DATA)
- DERIVE INFORMATION
- VALIDATE INFORMATION
- GENERATE EXPLANATIONS (SYNTHESIZE)

PURPOSES FOR DATA BASE SYSTEMS

STORAGE AND RETRIEVAL

UPDATING

RETRIEVAL AND CALCULATION

- GENERAL RETRIEVAL
- SELECTIVE RETRIEVAL

DATA VALIDATION

DATA ANALYSIS

MAJOR TYPES OF DATA BASE STRUCTURE

- FLAT FILE
- RANDOM ACCESS
- HIERARCHICAL
- NETWORK
- RELATIONAL

FLAT FILE

SEQUENTIAL ACCESS

DIRECTORY

ORDERED ELEMENTS

TAPE OR DISK

RANDOM ACCESS

DIRECTORY

NON SEQUENTIAL ACCESS

DISK

HIERARCHICAL

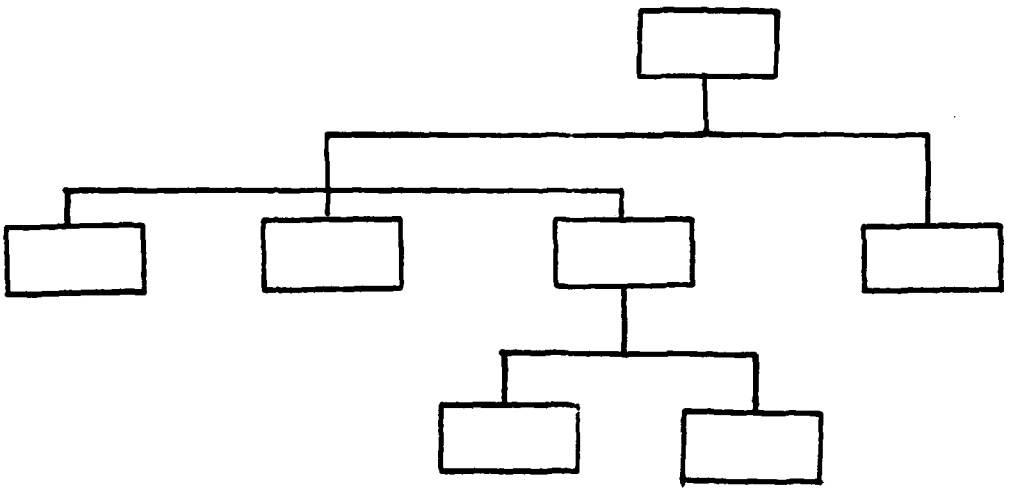

TREE STRUCTURE

HISTORICALLY POPULAR

ADVANTAGES

NATURAL IN FORM

MINIMAL DISTINCTION BETWEEN MODEL AND DATA

BASICALLY SEQUENTIAL

DISADVANTAGES

ADDING

DELETING

UPDATING

NETWORK

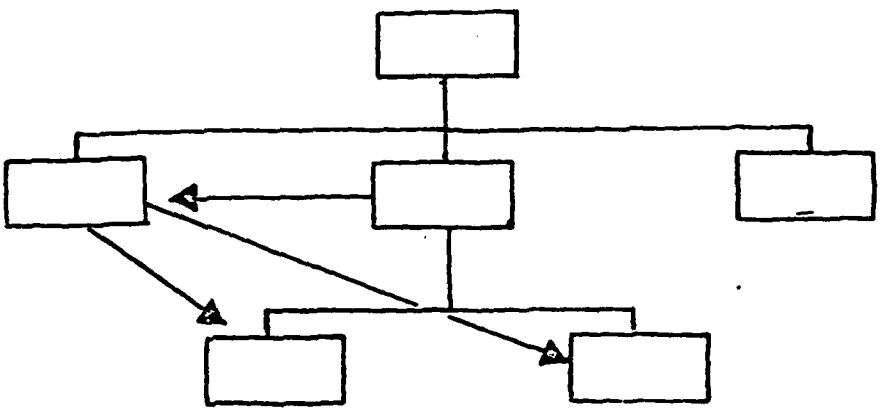

TREE STRUCTURE WITH POINTERS

ADVANTAGES

FLEXIBLE STRUCTURE

EASY TO ADD TO

EASIER TO UPDATE

DISADVANTAGES

DELETING

POINTER INFORMATION

RELATIONAL

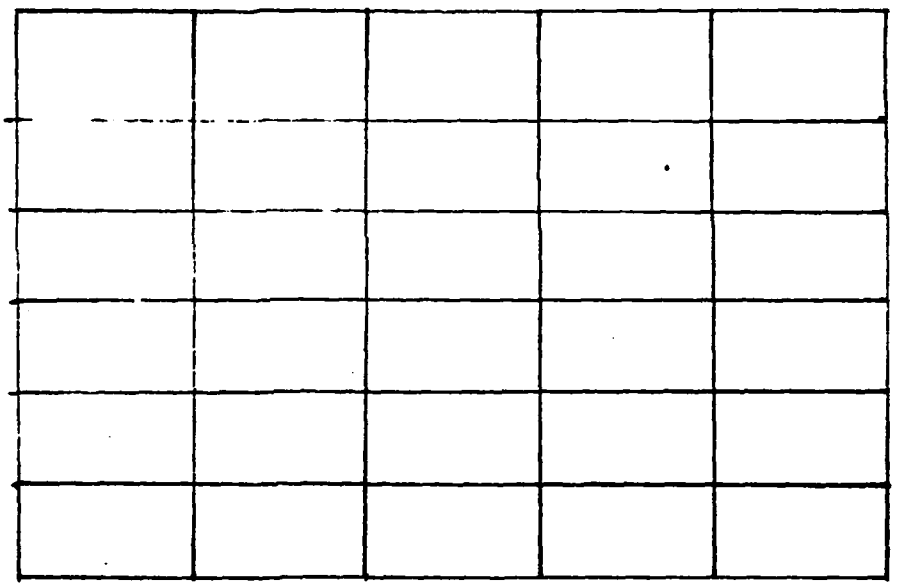

TABLE

ADVANTAGES

NATURAL STRUCTURE

ADDING

DELETING

UPDATING

DISADVANTAGES

NONE!

INTERFACING APPLICATIONS TO A DATABASE

TOOLS

DATA BASE MANAGEMENT SYSTEMS

GRAPHICS

SIMPLE STATISTICS (MEAN, STANDARD DEVIATION, ETC.)

GRANDER STATISTICS (LINEAR AND MULTIPLE REGRESSION)

ERROR BOUNDS

COMPLEX STATISTICS (FACTOR ANALYSIS AND CLUSTERING)

VAGUE ERROR BOUNDS

DIMENSIONAL ANALYSIS (REDUCTION TECHNIQUE)

MODELS (QUEUING AND GAMING)

DATA BASE MANAGEMENT SYSTEMS

CREATABASE

SYSTEM 2000

INGRES

DMS 1100

DMS 170

ORACLE

PARTICULAR TOOLS

GRAPHICS

PAGE PLOTTERS

CAL COMPS

COMPUTERVISION

TEKTRONIX

HEWLETT PACKARD

PARTICULAR TOOLS

STATISTICAL PACKAGES

BMD

SPSS

MATH PACK

STAT PACK

OMNITAB

MULTIPLE REGRESSION

FACTOR ANALYSIS (ANOVA)

CLUSTERING

PARTICULAR TOOLS

REDUCTION, ANALYSIS, MODELING

BUCKINGHAM P_I THEOREM

NASTRAN

GPSS

SIMSCRIPT

DYNAMO

GASP IV

ROUND NO. 1198 TH = 2.54 CM S.O. = 2 C.D. BHN = 260

MASS (GRAMS)	X (CM)	Y (CM)	SHEET NO.	FRAG NO.	MASS (GRAMS)	X (CM)	Y (CM)	SHEET NO.	FRAG NO.
.0084	-19.3	17.8	3	1	.0015	2.3	35.8	3	61
.1600	-16.5	6.6	3	2	.0075	-6.1	34.8	3	62
2.1769	-5.3	3.4	3	3	.0009	-13.2	27.4	3	63
.0421	-16.8	24.1	3	4	.0005	-12.2	27.4	3	64
.0193	-36.8	20.1	3	5	.0067	-10.2	23.6	3	65
.2717	-32.3	40.6	3	6	.0025	-11.4	20.8	3	66
6.7366	-22.4	47.2	3	7	.0075	-16.8	11.9	3	67
.2321	-20.3	39.9	3	8	.0038	-15.7	10.4	3	68
4.9648	-4.8	54.4	3	9	.0001	-14.5	9.9	3	69
.0955	-20.1	39.1	3	10	.0025	-12.4	14.5	3	70
.0181	-27.1	28.8	3	11	.0035	-10.4	14.0	3	71
.0446	-30.5	25.9	3	12	.0032	-9.1	16.3	3	72
.0030	-30.0	20.8	3	13	.0004	-1.8	13.5	3	73
.0051	-31.0	20.6	3	14	.0069	-9.7	13.2	3	74
.0130	-32.0	17.5	3	15	.0045	-7.1	27.4	3	75
.0108	-33.0	11.8	3	16	.0059	-5.1	27.9	3	76
.0162	-38.9	8.9	3	17	.0032	-2.5	22.6	3	77
.0316	-39.9	5.1	3	18	.0006	-2.0	27.9	3	78
.0112	-37.8	3.8	3	19	.0013	-.5	25.4	3	79
.0010	-31.0	3.0	3	20	.0010	-.8	19.1	3	80
.0048	-30.2	3.0	3	21	.0222	-.8	37.1	3	81
.0022	-31.2	6.3	3	22	.0910	18.3	45.0	3	82
.0090	-31.2	8.4	3	23	.0083	9.7	37.1	3	83
.0092	-35.1	8.4	3	24	.0176	4.6	34.3	3	84
.1670	-29.5	36.1	3	25	.0663	13.7	37.6	3	85
.0229	30.0	26.1	3	26	.0578	21.8	34.3	3	86
.0072	-28.2	22.1	3	27	.0050	3.0	32.5	3	87
.2836	-16.4	31.5	3	28	.0022	5.1	30.2	3	88
.0098	-25.9	15.5	3	29	.0020	2.8	29.5	3	89
.2200	-22.9	15.1	3	30	.0038	1.0	23.9	3	90
.0029	-26.1	11.1	3	31	.0100	3.3	24.9	3	91
.0025	-27.2	10.7	3	32	.0020	5.1	30.5	3	92
.0040	-26.9	10.0	3	33	.0034	6.1	35.3	3	93
.0022	-25.7	11.4	3	34	.0022	7.9	33.3	3	94
.0057	-24.1	12.9	3	35	.0166	9.1	34.0	3	95
.0038	-27.2	7.2	3	36	.0183	9.9	33.5	3	96
.0021	-25.4	8.9	3	37	.0062	9.4	32.5	3	97
.0015	-25.1	8.9	3	38	.0211	11.7	33.5	3	98
.0037	-25.4	5.1	3	39	.0043	14.7	33.8	3	99
.0043	-25.4	4.8	3	40	.0044	13.2	31.5	3	100
.0038	-25.1	1.1	3	41	.0015	11.9	28.2	3	101
.0019	-20.3	11.1	3	42	.0050	19.3	31.5	3	102
.0059	-21.3	20.6	3	43	.0064	15.5	30.5	3	103
.0174	-22.6	22.7	3	44	.0080	14.5	29.9	3	104
.0200	-20.3	27.2	3	45	.0065	15.0	27.9	3	105
.3000	-19.3	23.6	3	46	.0022	14.7	28.2	3	106
.0060	-17.3	22.6	3	47	.0027	14.0	27.4	3	107
.0027	-16.8	15.7	3	48	.0032	13.7	25.7	3	108
.0013	-16.7	17.8	3	49	.0015	16.5	24.9	3	109
.0032	-15.7	18.8	3	50	.0018	9.9	26.9	3	110
.0022	-14.5	9.9	3	51	.0037	10.4	26.2	3	111
.0092	-20.3	11.6	3	52	.0024	11.9	25.7	3	112
.0176	-16.5	10.0	3	53	.0018	9.7	24.9	3	113
.0791	-15.9	9.1	3	54	.0025	10.2	25.4	3	114
.0485	-7.9	9.4	3	55	.0008	12.2	23.4	3	115
.0093	-13.7	8.1	3	56	.0010	8.1	20.1	3	116
.0015	-5.8	8.1	3	57	.0016	8.9	20.1	3	117
.0018	-6.1	5.1	3	58	.0010	5.1	16.5	3	118
.0086	-6.6	3.3	3	59	.0001	16.5	19.8	3	119
.0038	-2.0	34.3	3	60	.0008	22.6	23.6	3	120

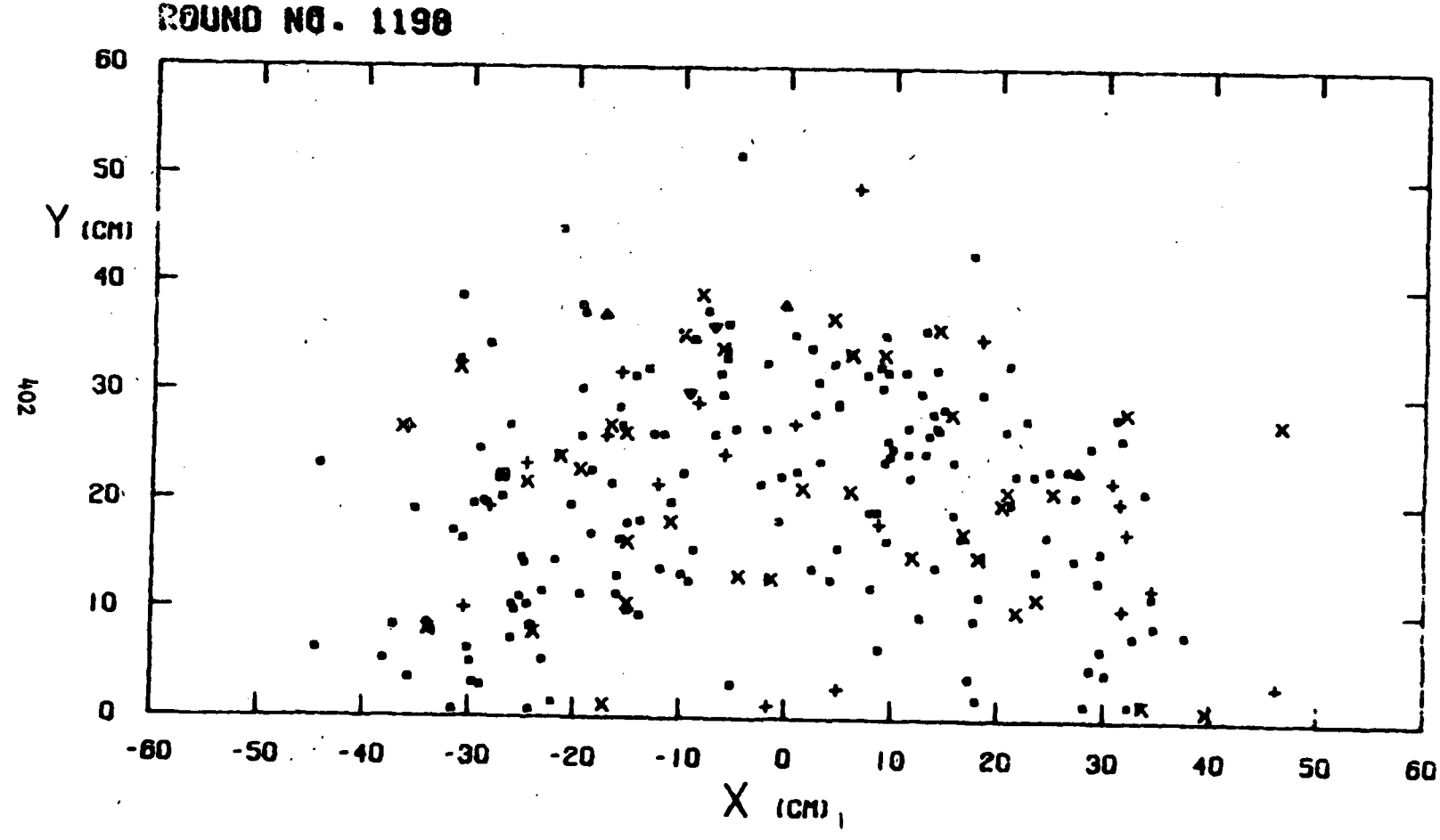
ROUND NO. 1198
60
50
Y (CM)
40
30
20
10
0
-60
-50
-40
-30
-20
-10
0
10
20
30
40
50
60
X (CM)
402

MEAN SPRAY ANGLE AND PERCENTAGE OF HIGH MASS PARTICLES BY CLUSTER

CLUSTER	MEAN SPRAY ANGLE (DEGREES)	PERCENTAGE HIGH MASS PARTICLES
1	15.76	18
2	29.09	77
3	24.88	62
4	28.23	61
5	29.74	60
6	17.71	19
7	21.80	27
8	29.15	50
9	25.80	49
10	31.73	87
11	36.20	100
12	38.76	100

TABLE V

CLUSTER GROUPING BY SPRAY ANGLE

CLUSTER GROUP	MEAN SPRAY ANGLE (DEGREES)	PERCENTAGE HIGH MASS PARTICLES
1,6	16.84	18
3,7,9	24.51	47
2,4,5,8	29.06	61
10,11,12	33.92	92

THE TRUE PURSUITS OF SCIENTIFIC DATA ANALYSIS (AND GOOD ENGINEERING) EXTEND NOT ONLY TO THE ANALYSIS OF NEW DATA IN OLD AND NEW WAYS: BUT, INCLUDE THE INCORPORATION OF OLD DATA TO BE ANALYZED IN (OLD AND) NEW WAYS.

MANAGEMENT INFORMATION SYSTEMS HAVE BECOME ENTITIES ENTIRELY IN THEMSELVES AND NOW OPERATE ACCORDING TO PARKINSON'S LAWS.

NO LONGER REASONABLE IN TERMS OF TIME OR COST TO CONTINUE TO DEVELOP LARGE SPECIAL PURPOSE DATA SYSTEMS.

MAY BE ONLY OF ACADEMIC VALUE TO DEVELOP ANY FURTHER DATA MANAGEMENT SYSTEMS.

ANSWER TO THE DILEMA
(A PROPHECY)

DEVELOP MODULAR SPECIAL PURPOSE PRE- AND POST PROCESSORS (HARDWARE AND/OR SOFTWARE) WHICH WILL WORK IN CONJUNCTION WITH EXISTING COMMERCIALLY AVAILABLE DATA MANAGEMENT SYSTEMS. SUCH PROCESSORS COULD ALLOW A VARIETY OF INDIVIDUALLY TAILORED QUERY AND REPORTING FEATURES, WHILE STILL MAKING USE OF THE DBMS' OWN POWERFUL COMMAND STRUCTURE.

CAUTIONS

BUILD DATA BASE SLOWLY

SELECT DATA MANAGEMENT SYSTEM(S) CAREFULLY

REDUCE THE PROBLEM AS YOU PROCEED

SYNTHESIZE AS YOU PROCEED

A TIME TO RE-THINK SMALL

C. Glenvil Whitacre
Chemical Systems Laboratory
Aberdeen Proving Ground, Maryland 21010

ABSTRACT. The process of adapting a program, now working on a large computer, to a smaller computer, which is more limited in capability but accessible and convenient to the user, is explored. A specific example is used to illustrate the process.

The DOD methodology for computing chemical safety distances had been programmed in the conversational mode on a UNIVAC 1108 system and was offered over AUTOVON lines on a 24-hour basis to the arsenals. The arsenal personnel did not make use of this. The methodology was then studies for possible simplification. Approximations were developed for some functions, and the program was subdivided into five self-contained units. Each was then reduced to one page of FORTRAN and tested in that form. From these, five pocket calculator programs were developed. These were documented and distributed to the arsenals and are now being used.

It is suggested that this approach should be considered for other Army applications in the field.

PRESENTATION. For those of us who consider ourselves old timers in this computer game, we've seen the technology change and the hardware come and go. If you've optimum addressed a drum memory, programmed with plug boards, or been knee-deep in punched paper tape, you're not likely to forget it, although you try. Of course, there were high points. If you ever operated the Burroughs 205 in a dark room, you know where the final scene from Close Encounters comes from.

Then, for some of us, there was a long fight with MISD to keep open-shop access for S and E applications. Having been through all of this, now with easy access to a large system with automatic files and many language processors, why should anyone in this comfortable promised land of milk and honey transfer a program running on that system back to a pocket calculator?

This seems especially unwise if the program has to be subdivided into pieces and parts of it approximated. Yet this is an operation that I have been engaged in for the last couple of years and, at this point, am prepared to defend as a practical solution to this particular problem.

I will describe the problem, some of the stages we went through in attempting to solve it, and then our present solution. This will tell you what the program does and, I hope, will outline a process which may have application to other areas.

I'm thinking here of the military technical manuals and field manuals where any problem has to be reduced to what can be solved on a graph, nomograph, or slide rule. This has generally oversimplified the solution. The present day programmable calculators represent the next step as a computational aid yet are something that can still be carried in the pocket. The artillery people have gone this route, so some are already available in the field.

The mathematics of our sample problem is essentially the moving trivariate Gaussian distribution used to compute the downwind concentration or dosage which would result from the release of vapor or small aerosol. In its basic form, this is not a very difficult calculation; but as we encountered it, there were several complications.

We were applying this to hazard distance calculations needed as guidance in planning the handling and transport of chemical agents within the Department of Defense (DOD). As a result of Public Law 91-190, a requirement was established that all operation plans involving these agents would contain a formal hazards analysis. This analysis would establish a maximum credible event (MCE) for the operation and would compute a downwind hazard distance. This becomes part of the package staffed through DOD, so the methodology had to be formalized to a high degree.

The methodology that was proposed and accepted contained several complications beyond the basic Gaussian. First, the typical solutions for the puff (instantaneous) release or continuous (steady state) release were not adequate for an accidental release such as a spill or a fire. A more complex form called the semicontinuous was developed which could trace the release in time.

The second complication resulted from a property of some of the agents. For these, the physiological effects were dependent on the time over which a given dosage was accumulated. Thus, the downwind dosage was not enough; you also had to trace the time of accumulation to estimate the effect. In the original methodology, this was treated as an iterative procedure, looking at larger and larger time slices at each downwind point to locate the maximum effect.

(Viewgraph 1)*

The third complication came from this infinite series for estimating the reflection from a barrier, such as an elevated temperature inversion. This sums the multiple reflections from that barrier. It's not much in itself, but the first time I included it in a program, I went for the usual 10^{-36} accuracy, and the computer disappeared into a time warp and when it came back, I found it had generated 80,000 terms in the series. After that, a more realistic limit was used. If one traces this reflection far enough, it can be assumed that the vertical distribution is uniform and then this equation, known as the Box Model, can be used.

*Viewgraphs can be found near the end of this article.

This methodology was agreed upon by representatives of the three services and published as a technical paper by the DOD Explosives Safety Board in 1975. All of the arsenals storing or handling chemical agents were directed to use it, but only a couple who still had the original programs on which the methodology was developed could comply.

(Viewgraph 2)

To remedy this, we were tasked to develop a handbook which could be used by the arsenals. This took the form of precomputed solutions presented as graphs of dosage versus downwind distance. This is total dosage from an instantaneous source for neutral stability and a range of values of the height of the mixing layer. (Actually, this graph has been simplified by graphic arts for your benefit; the original was on full log-log paper and you were expected to read it to three digits of accuracy.) This is one of the simpler cases; when you get to the semicontinuous with two-minute correction, the wind speed, time of release, and height of the mixing layer all interact and things get quite complicated.

We developed a system of correction factors for this, but this required reading a number of graphs in succession, and the human variation in results was noticeable. (Safety people don't like variation.)

This handbook was published by US Army Materiel Development and Readiness Command (DARCOM) in March 1977. It was a big book, with 180 pages like this, representing thousands of curves.

(Viewgraph 3)

As a parallel effort, the programs we had used to generate these curves were organized as subroutines under the control of a master program which was written in conversational mode. Most of the numeric data on munition systems and agents were stored as tables and called in by symbolic answers. Once requested, the program asked the first question; this answer determined what the next question would be, and so on to get the information essential for a given solution. A number of output options were provided so that different aspects of the toxic field could be displayed.

Our idea was to provide the handbook as a reference but maintain this program on the Edgewood computer for day-to-day use by the arsenals. A Chemical Systems Laboratory (CSL) technical report was published in June 1977 to document the operation of this program.

We have continued to use this program. US Army Toxic and Hazardous Materiels Agency (THAMA), and the Chemical School use it; US Army Materiel Systems Analysis Activity (AMSAA), Test and Evaluation Command (TECOM), and Aberdeen Proving Ground (APG) Safety Office have requested access to the program. But the remote use we had expected did not develop, at least not over the next year and a half.

The reasons for this lack of interest were many. Getting access to or approval to purchase a terminal was a problem. Most of the arsenals did not have what you might consider "computer people" and they seemed reluctant to get involved with this monster (which might ask embarrasing questions). They complained that AUTOVON was not reliable. Then there was the very real problem that a safety inspection team could say "all the telephones are out" and you were up the creek if you were depending on the computer for answers.

Then in 1978, a series of events led to what we now call the simplified methodology. It produced the same answers (or a slightly safe-sided version of the same answer) but eliminated the infinite series used to compute the transition to the Box Model and the iterative procedure used to develop the two-minute correction.

This started with an attempt to develop a rule of thumb for the handbook users which would give the distance at which the Box Model was safe. This was done by modifying the big program to capture the distance at which the reflective model deviated from the Gaussian by a specified amount and then again when it approached the Box Model by the same amount.

(Viewgraph 4)

This produced tables like this, of distance versus height of the mixing layer and atmospheric stability.

(Viewgraph 5)

To get to the rule of thumb, we then fitted these data with equations of this form, where H_m is the height of the mixing layer and β is the slope of the sigma z curve.

(Viewgraph 6)

It then occurred to me that these two distances, X1 and X2, could be considered as break points between the two forms of the model. The full Gaussian would be used up to X1, and the Box Model beyond X2, and the transition could probably be fit by a log-log segment. This would slightly overestimate the dosage, but that would be all right. This was a safety program. This would eliminate the infinite series and make the equation for each segment rather simple. Here are the equations for total dosage from an instantaneous release.

(Viewgraph 7)

Although this is the simplest form, it is not the semicontinuous and does not have the two-minute correction, but it can solve a number of practical problems, so we tried this in FORTRAN. Now the data, logic, and algebra for this took half a page. And, for the first time, I wondered if something like this could be programmed on a pocket calculator. Of course, we had pocket calculators (they were cheaper than a service call on a Frieden), but I hadn't

taken them seriously as computers up to this time. I had a Texas Instruments SR-52. I dug into the language and was able to get a version of this program to run on the calculator.

I was now fascinated by this approach and began to experiment with the two-minute correction. Using the big program as the standard, I ran it for ranges of variables, captured the final dosage correction factor as a function of distance, and converted this back to an effective time.

(Viewgraph 8)

I then looked at these values and found they could be fitted by an equation of this type.

(Viewgraph 9)

This could be plugged into the dosage correction factor and then into the segment equations.

(Viewgraph 10)

The semicontinuous was a bit more difficult, and the result a bit messy. This is the effective time where t_s is the source time, u is the wind speed, and x is the distance.

(Viewgraph 11)

And this is the equation for segment 1.

This was the most general form of the equation, but I couldn't solve it directly for x, the distance to a given dosage. I would like to have included source geometry (the size of the initial cloud), but this presented a similar problem. However, one often wants to investigate the way dosage decreases with distance, so solving for dosage as a function of x and then interpolating for the specific distance would be a way around all three of these problems. The interpolation could follow the functional form of the equation and be quite accurate.

With this approach, the general equation was subdivided into a system of factors which would represent the difference between the instantaneous, the semicontinuous, and the continuous with and without the two-minute correction. A logic was then designed to recombine these factors as needed to form a specific solution. This took 59 lines of code in FORTRAN, but that included tables of the met parameters, source geometry, and a model for combining the doses from inhalation and deposition on the skin.

We then went to the Texas Instruments Model 59 and were able to program a version of this which would run automatically.

(Viewgraph 12)

Now we could reproduce any one of these thousands of curves from the handbook on call, and this made it possible to design a new handbook based on the pocket calculator programs. This was published as a field handbook in August 1978. To support this program, the field handbook also contained programs for computing the evaporation from a spill and another to select the atmospheric stability following the Turner logic for the Pasquill categories. This was followed by an addendum to the field handbook which contains a program for downwind distance based on concentration. All of the previous work had been in terms of dosage.

The US Army Nuclear and Chemical Agency (USANCA) became interested in this field handbook, and COL Adams placed an announcement in a Surety Information Letter. This must have been sent all over the world, because we began getting requests from US artillery units everywhere. They said they had the TI-59 calculator to do their own trajectory calculations and wanted these programs to add a chemical capability. Their programs are somewhat different, and we haven't gotten any definite feedback yet from artillery units, but we know the arsenals which store chemicals are using the pocket calculator programs on a regular basis.

If we attempt to summarized or draw conclusions from this escapade, we might say there are applications where the big system, even with remote terminals, may not be the most practical. If a programmable pocket calculator is the way to go, the conventional system and FORTRAN are a very convenient, familiar, and rapid way to develop and test short program candidates for the pocket calculator.

In this bigger-is-better world, I would advise anyone who takes this approach to be prepared for a cold to neutral reception. It's hard to impress your boss with very little, and one of these programs in FORTRAN is very little. So when you bring him this little jewel and say "look what I've done this month," he sees a page of FORTRAN and may not be greatly impressed. Even after you ennumerate all of the options and show him what it replaces, there is still an underlying (if unstated) comment, "so what have you been pulling all these years with the old version?".

MIXING LAYER

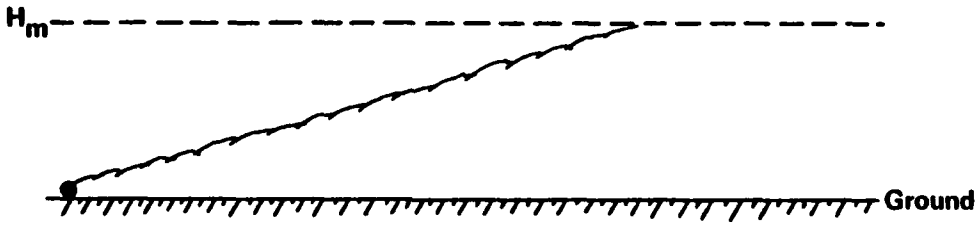

$$R_F = \sum_{i=1}^{\infty} \left\{ \exp\left[-\frac{1}{2} \left(\frac{2iH_m + H}{\sigma_z(x)} \right)^2 \right] + \exp\left[-\frac{1}{2} \left(\frac{2iH_m - H}{\sigma_z(x)} \right)^2 \right] \right\}$$

BOX MODEL

$$D(x) = \frac{Q}{\sqrt{2\pi}\, \sigma_y(x)\, u\, H_m}$$

Viewgraph 1
21 February 1980

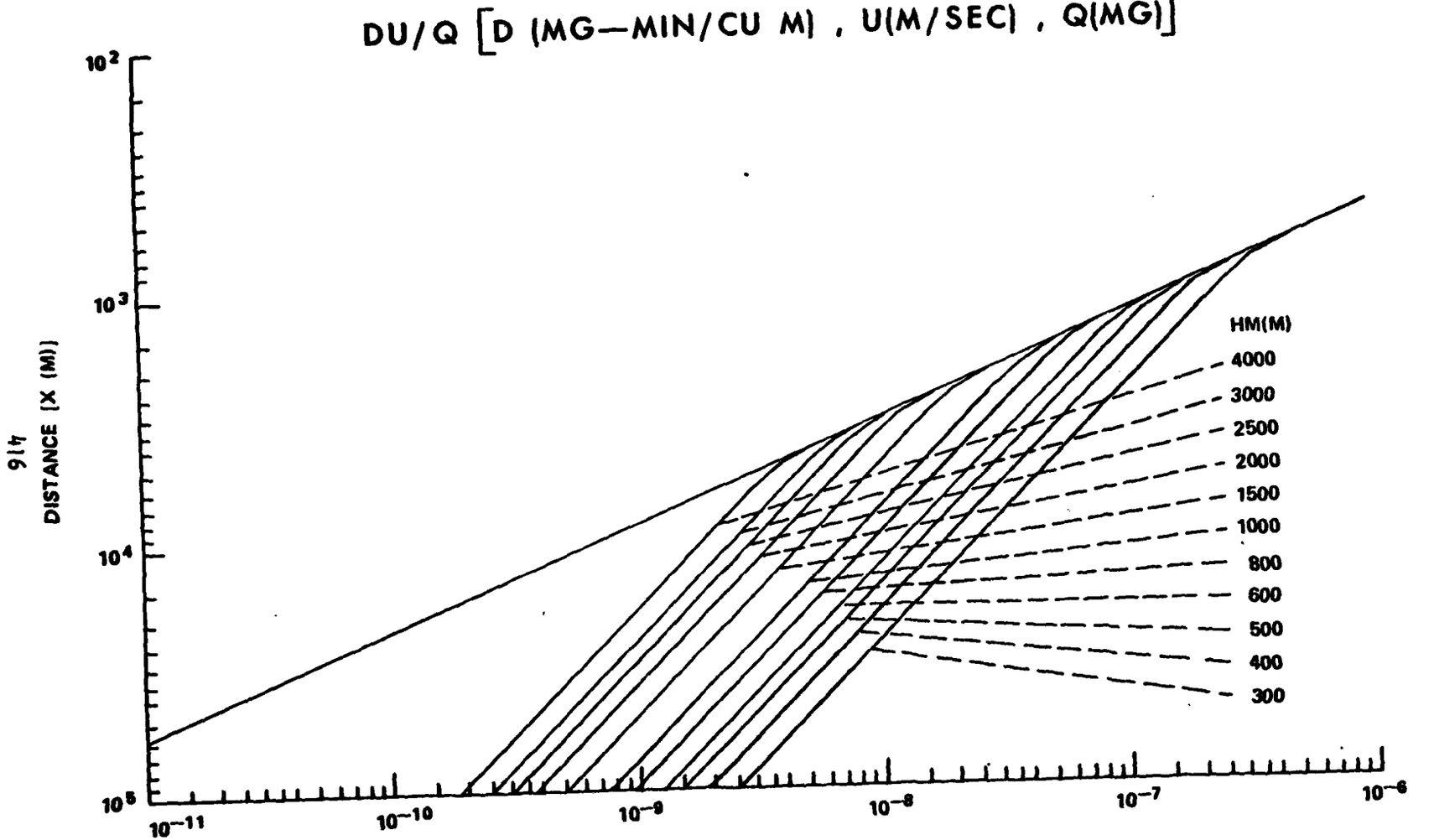

914

Viewgraph 2

February 21, 1980

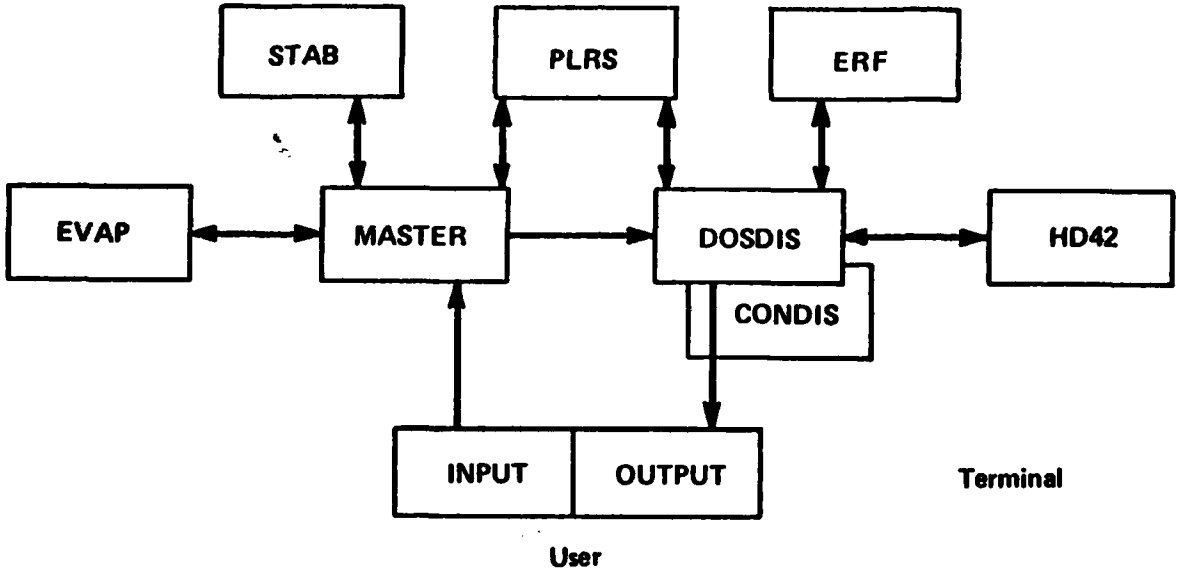

PROGRAM PARTS

Viewgraph 3
February 21, 1980

VALUE OF x_2 AS A FUNCTION OF STABILITY AND H_m

H_m (m)	A	B	C	D	E	F
100	427	955	1862	4074	6918	14454
200	692	1905	4074	9120	16596	36308
300	933	2884	6310	14791	27542	63095
400	1148	3802	8710	20893	39811	91201
600	1514	5754	13804	33113	66069	158489
800	1862	7586	19055	46773	93325	234422
1000	2188	9550	23988	60256	123026	316226
2000	3631	19055	52481	138038	295119	794324

Viewgraph 4
February 21, 1980

TRANSITION ZONE

$$x_1 = C_1 H_m^{1/\beta} \quad (3)$$

$$x_2 = C_2 H_m^{1/\beta} \quad (4)$$

WHERE

x_1 AND x_2 DEFINES THE TRANSITION ZONE (m)

C_1 AND C_2 ARE CONSTANTS FOR EACH STABILITY

β IS THE SLOPE OF THE SIGMA Z CURVE

PARAMETER	A	B	C	D	E	F
C_1	10.5	5.5	6.13	9.49	11.2	15.3
C_2	15.9	9.55	11.2	18.1	21.9	31.1

Viewgraph 5
February 21, 1980

THREE SEGMENT CURVE

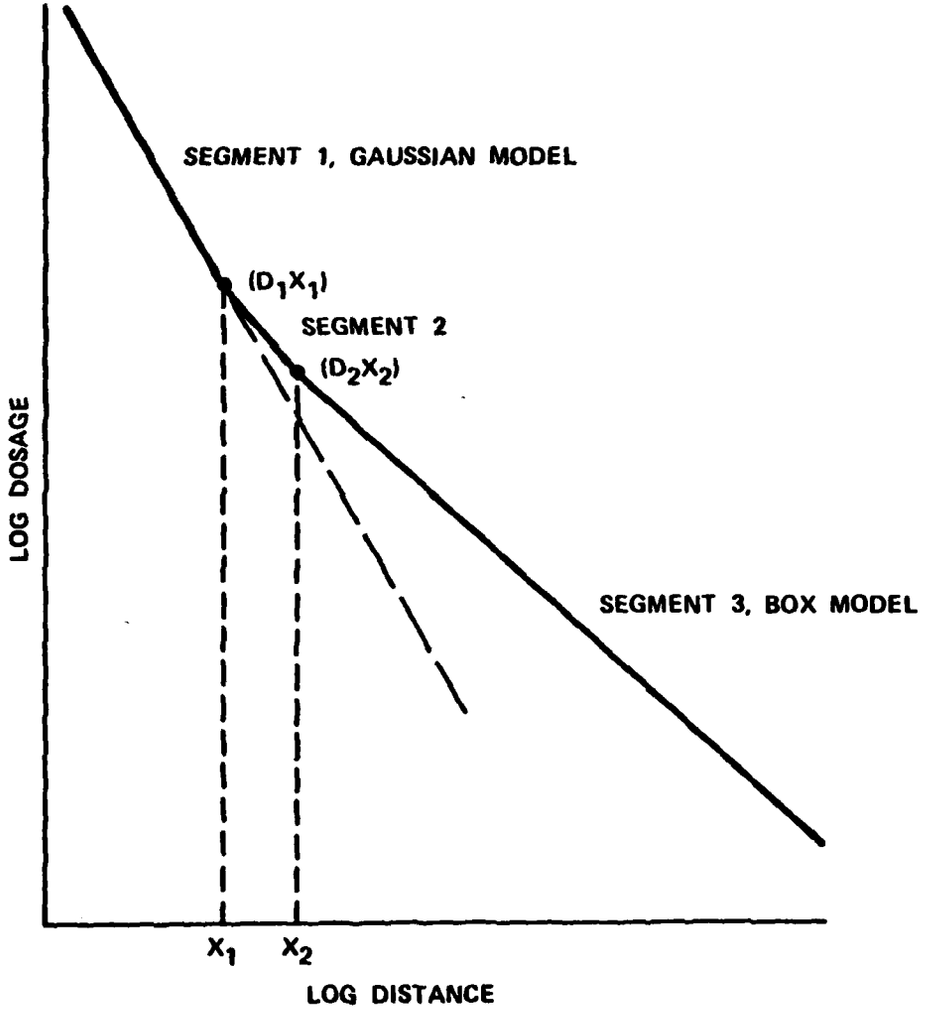

Viewgraph 6
February 21, 1980

TOTAL DOSAGE

SEGMENT 1, $x < x_1$

$$D(x) = \frac{Q}{60\pi\ \sigma_{yl}\ \sigma_{zl}\ u\ x^{\alpha+\beta}} \qquad (6)$$

SEGMENT 3, $x > x_2$

$$D(x) = \frac{Q}{60\ \sqrt{2\pi}\ \sigma_{yl}\ H_m\ x^{\alpha}} \qquad (8)$$

SEGMENT 2, $x_1 < x < x_2$

$$S = \frac{\text{in } (x_2/x_1)}{\text{in } (D_2/D_1)} \qquad (12)$$

$$x = x_1 \left(\frac{D}{D_1}\right)^S \qquad (13)$$

Viewgraph 7
February 21, 1980

TWO-MINUTE CORRECTION

$$t_e = \frac{0.005\,x^{0.9294}}{u} \qquad (14)$$

t_e IS THE EFFECTIVE TIME OF DOSAGE ACCUMULATION (MIN)

0.9294 IS THE SLOPE OF THE SIGMA-x CURVE

$$M = 0.827\,t^{0.274} \quad t > 2 \text{ MIN} \qquad (15)$$

M IS THE FACTOR BY WHICH THE REQUIRED DOSAGE IS INCREASED

t IS THE TIME OF DOSAGE ACCUMULATION (MIN)

Viewgraph 8

February 21, 1980

TWO-MINUTE CORRECTED DOSAGE

SEGMENT 1, $x < x_1$

$$D(x) = \frac{Q}{36.51\ \sigma_{yl}\ \sigma_{zl}\ u^{0.726}\ x^{\alpha + \beta + 0.255}}$$

FOR $x_1 > x > x_T$ (16)

$$x_T = [400\ u]^{1.076}$$

SEGMENT 3, $x > x_2$

$$D(x) = \frac{Q}{29.13\ \sigma_{yl}\ H_m\ u^{0.726}\ x^{\alpha + 0.255}}$$

$x > x_2$ AND x_t (17)

Viewgraph 9
February 21, 1980

SEMICONTINUOUS SOURCE WITH 2-MINUTE CORRECTION

$$t_e = \left[0.281\, t_s^2 + \frac{0.000025}{u^2} \times 1.8588 \right]^{1/2} \qquad (20)$$

SEGMENT 1

$$\left[0.281\, t_s^2 + \frac{0.000025}{u^2} \times 1.8588 \right]^{0.137} x^{\alpha+\beta} = \frac{Q}{155.9\, \sigma_{yl}\, \sigma_{zl}\, u\, D} \qquad x_1 > x > x_{TS} \qquad (21)$$

$$x_{TS} = \left[\frac{(4 - 0.281\, t_s^2)\, u^2}{0.000025} \right]^{0.538} \qquad (22)$$

Viewgraph 10
February 21, 1980

SEMICONTINUOUS SOURCE WITH 2-MINUTE CORRECTION

SEGMENT 3

$$\left[0.281\,t_s^2 + \frac{0.000025}{u^2} \times 1.8588\right]^{0.137} x^{\alpha} = \frac{Q}{124.4\,\sigma_{yl}\,H_m\,D\,u} \qquad x > x_2 \text{ AND } x_{TS} \qquad (23)$$

SEGMENT 2, $x > x_{TS}$

$$D_1 = \frac{Q}{155.9\,\sigma_{yl}\,\sigma_{zl}\,u\,x^{\alpha+\beta}} \left[0.281\,t_s^2 + \frac{0.000025}{u^2} x_1 1.8588\right]^{-0.137} \qquad (24)$$

$$D_2 = \frac{Q}{124.4\,\sigma_{yl}\,H_m\,u\,x^{\alpha}} \left[0.281\,t_s^2 + \frac{0.000025}{u^2} x_2 1.8588\right]^{-0.137} \qquad (25)$$

Viewgraph 11
February 21, 1980

REFERENCES

1.	ORG 40	1970
2.	DODESB TECHNICAL PAPER NO. 10	1975
3.	HANDBOOK FOR CHEMICAL HAZARD PREDICTION	1977
4.	COMPUTER PROGRAM, ARCSL-TR-77049	1977
5.	SIMPLIFIED METHODOLOGY, ARCSL-TR-78010	1978
6.	FIELD HANDBOOK, ARCSL-TR-78036	1978
7.	ADDENDUM, ARCSL-TR-79018	1979
8.	SECOND ADDENDUM, IN PUBLICATION	1979

Viewgraph 12
February 21, 1980

VARIATIONAL METHODS OF CONVOLUTION INTEGRAL AND OF LARGE SPRING CONSTANTS - A NUMERICAL COMPARISON

Julian J. Wu
U.S. Army Armament Research and Development Command
Benet Weapons Laboratory, LCWSL
Watervliet, NY 12189

ABSTRACT. Finite element solution formulations have been carried out for a simple initial value problem based on two different variational statements: that of convolutional integral developed by Gurtin and that of large spring constants adapted by this writer for initial value problems. Numerical results indicate that both generate convergent solution to the given initial value problem of a spring-mass system subjected to a harmonic forcing function.

1. INTRODUCTION. Through a simple initial value problem, this note demonstrates the use of the finite element discretization in conjunction with two variational formulations and compares the numerical results. The variational principles of convolutional integral for initial problems were developed by Gurtin some sixteen years ago (ref. 1 and 2). Since then these formulations have been applied to obtain solution of transient problems (ref. 3 and 4). However, the time dimension was treated separately from the spatial dimensions in the finite element approximation schemes. The viewpoint adopted in this note is that the separate treatment of spatial and time coordinates is unnecessary. Since the initial value problems are nonself-adjoint, the corresponding variational problems can be formulated with the help of adjoint field variables and thus can be used in Ritz-finite element solutions. One such formulation is used here to compare with the formulation using convolution integral in terms of numerical results for a simple initial value problem.

Let us consider a simple mass-spring system. The differential equation of the displacement u(t), a function of time t is

$$m\ddot{u} + ku = f_o \cos \omega_f t \tag{1}$$

where m is the mass, k, the spring constant. A dot ($\cdot$) denotes differentiation with respect to t. The parameters f_o and w_f denote magnitude and frequency respectively, of the forcing function. The initial conditions are given as

$$u(0) = u_0 \quad , \quad \dot{u}(0) = u_1 \tag{2}$$

We shall further use the equations

$$\omega^2 = \frac{k}{m} \quad , \quad f = \frac{f_o}{m}$$

Thus Eq. (1) has the form

$$\ddot{u} + \omega^2 u = f \cos \omega_f t \tag{3}$$

2. VARIATIONAL FORMULATION OF CONVOLUTIONAL INTEGRALS. The variational principle for the problem defined by Eqs. (3) and (2) is (ref. 2):

$$\delta I(u) = 0 \tag{4a}$$

where

$$I = \frac{1}{2} [u(t)*u(t) + \omega^2 t*u(t)*u(t)]$$

$$- [u_0 + \frac{f}{\omega_f^2} + u_1 t - \frac{f}{\omega_f^2} \cos \omega_f t]*u(t) \tag{4b}$$

The operator * defines a convolution integral in the following equation

$$u(t)*v(t) = \int_o^t u(t-\tau)v(\tau)d\tau \tag{5}$$

where u(t) and v(t) are two arbitrary functions of t.

To see that the variational problem of Eqs. (4) is indeed equivalent to the original problem defined by Eqs. (3) and (2), one writes, from Eqs. (4):

$$\delta I = [u(t) + \omega^2 t*u(t) - (u_0 + \frac{f}{\omega_f^2} + u_1 t - \frac{f}{\omega_f^2} \cos \omega_f t)]*\delta u(t) = 0$$

for arbitrary $\delta u(t)$. Thus, $\delta I = 0$ leads to Eq. (6)

$$u(t) + \omega^2 t*u(t) - (u_0 + \frac{f}{\omega_f^2} + u_1 t - \frac{f}{\omega_f^2} \cos \omega_f t) = 0 \tag{6}$$

It is clear from Eq. (6) that $u(0) = u_0$.

Differentiate Eq. (6) once, one has

$$\dot{u}(t) + \omega^2 \int_o^t u(\tau)d\tau - u_1 - \frac{f}{\omega_f} \sin \omega_f t = 0 \tag{7}$$

Eq. (7) gives $\dot{u}(0) = u_1$. Thus both of the initial conditions are satisfied. The differential equation is recovered when Eq. (7) is differentiated once more. Note that in obtaining Eq. (7) the following differentiation formula has been used.

Let

$$F(t) = \int_0^t v(t-\tau)u(\tau)d\tau$$

Then

$$\frac{dF}{dt} = -\int_0^t \frac{\partial v}{\partial \tau}(t-\tau)u(\tau)d\tau + v(0)u(t)$$

3. VARIATIONAL FORMULATION WITH A LARGE "SPRING" CONSTANT. Consider the following variational problem

$$\delta I(u,v) = 0 \tag{8a}$$

with

$$I(u,v) = -\int_0^1 \dot{u}\dot{v}\, dt + \int_0^1 (\omega^2 u - f)v\, dt + \alpha[u(0) - u_0]v(1) - u_1 v(0)$$

In Eqs. (8), u(t) is the physical field variable and v(t) is the adjoint variable. This variational problem is unconstrained since the trial functions of neither u(t) nor v(t) are subject to any end condition requirements. To see that the set of Eqs. (8) is equivalent to the original initial value problem, it is only necessary to carry out the first variation and perform once integration-by-part. Thus, one has

$$\begin{aligned}\delta I(u,v) &= 0 \\ &= \int_0^1 (\ddot{u}+\omega^2 u - f)\delta v\, dt \\ &+ \{\alpha[u(0) - u_0] - \dot{u}(1)\}\delta v(1) + [\dot{u}(0) - u_1]\delta v(0) \\ &+ \int_0^1 (\ddot{v}+\omega^2 v)\delta u\, dt \\ &+ \{\alpha\, v(1) + \dot{v}(0)\}\delta u(0)\ \dot{v}(1)\delta u(1)\end{aligned} \tag{9}$$

It is clear then if one chooses v(t) = 0 and let δv be completely arbitrary, Eqs. (9) reduce to the original initial value problem as α approaches infinity.

4. PROCESS OF FINITE ELEMENT DISCRETIZATION. In case of convolutional integral, the variational equation used is Eq. (6) in Section 2. Rewrite Eq. (6) as

$$\delta I = [u(t) + \omega^2 t * u(t) - F(t)] * \delta u(t) = 0 \tag{10a}$$

where

$$F(t) = u_0 + \frac{f}{\omega_f^2} + u_1 t - \frac{f}{\omega_f^2} \cos \omega_f t \tag{10b}$$

In Eq. (10a), there are three convolution integrals to be evaluated: (a) $u(t)*\delta u(t)$; (b) $\omega^2 t*u(t)*\delta u(t)$; and (c) $F(t)*\delta u(t)$.

(a) For $u(t)*\delta u(t)$:

$$u(t)*\delta u(t) = \int_0^t u(t-\tau)\,du(\tau)\,d\tau$$

Let

$$\bar{\tau} = \tau/t$$

one has then

$$u(t)*\delta u(t) = t \int_0^1 \bar{u}(1-\bar{\tau})\,\delta\bar{u}(\bar{\tau})\,d\bar{\tau}$$

Consider

$$I = \int_0^1 \bar{u}(1-\bar{\tau})\,\delta\bar{u}(\bar{\tau})\,d\bar{\tau}$$

This integral is evaluated by finite element discretization.

$$I = \sum_{i=1}^{L} \int_{\ell_{i-1}}^{\ell_i} \bar{u}(1-\bar{\tau})\,\delta\bar{u}(\bar{\tau})\,d\bar{\tau}$$

Let

$$\ell_o = 0\,, \quad \ell_L = 1\,, \quad \ell_i = \frac{i}{L}$$

$$\xi = \xi^{(i)} = L\,\bar{\tau} - i + 1$$

$$\bar{\tau} = \frac{1}{L}\,[\xi + i - 1]$$

$$d\bar{\tau} = \frac{1}{L}\,d\xi$$

Hence

$$\bar{u}(\bar{\tau}) = \bar{u}[\tfrac{1}{L}\,(\xi+i-1)] = \bar{u}^{(i)}(\xi)$$

$$\bar{u}(1-\bar{\tau}) = \bar{u}[\tfrac{1}{L}\,(L-\xi-i+1)]$$

$$= \bar{u}[\tfrac{1}{L}\,(1-\xi+L-i+1)] = \bar{u}^{(L-i+1)}(1-\xi)$$

Thus

$$I = \sum_{i=1}^{L} \frac{1}{L} \int_0^1 \bar{u}^{(L-i+1)}(1-\xi)\delta\bar{u}^{(i)}(\xi)d\xi$$

Use the matrix representations for the shape function and generalized coordinates. One writes

$$\bar{u}^{(i)}(\xi) = \underset{\sim}{a}^T(\xi)\ \underset{\sim}{U}^{(i)}$$

and

$$\bar{u}^{(L-i+1)}(i-\xi) = a^T(1-\xi)U^{(L-i+1)}$$

Thus

$$I = \sum_{i=1}^{L} \frac{1}{L} \delta\underset{\sim}{U}^{(i)} \int_0^1 \underset{\sim}{a}(\xi)\underset{\sim}{a}^T(1-\xi)d\xi\ \underset{\sim}{U}^{(L-i+1)}$$

Or

$$I = \frac{1}{L} \sum_{i=1}^{L} \delta\underset{\sim}{U}^{(i)T}\ \underset{\sim}{A}\ \underset{\sim}{U}^{(L-i+1)}$$

where

$$\underset{\sim}{A} = \int_0^1 \underset{\sim}{a}(\xi)\underset{\sim}{a}^T(1-\xi)d\xi \qquad (11a)$$

Hence

$$\underset{\sim}{u}(t)*\delta u(t) = tI = \frac{t}{L} \sum_{i=1}^{L} \underset{\sim}{U}^{(i)}{}_A\ \underset{\sim}{U}^{(L-i+1)} \qquad (11b)$$

(b) For $\omega^2 t*u(t)*\delta u(t)$:

The evaluation of this double convolution integral is somewhat more complicated. First consider

$$t*u(t) = \int_o^t (t-\tau)u(\tau)d\tau$$

Then

$$\begin{aligned} I &= [t*u(t)]*\delta u(t) \\ &= \int_o^t \{\int_o^{t-\lambda} (t-\lambda-\tau)u(\tau)d\tau\}\delta u(\lambda)d\lambda \\ &= \int_o^t \int_o^{t-\lambda} (t-\lambda-\tau)u(\tau)\delta u(\lambda)d\tau d\lambda \end{aligned}$$

Again let

$$\bar{\tau} = \frac{\tau}{t} \quad , \quad \bar{\lambda} = \frac{\lambda}{t}$$

Thus $u(\tau)$ becomes $\bar{u}(\bar{\tau})$, $\delta u(\lambda)$ to $\delta\bar{u}(\bar{\lambda})$, etc. One has

$$I = t^3 \int_0^1 \int_0^{1-\bar{\lambda}} (1-\bar{\lambda}-\bar{\tau})\bar{u}(\bar{\tau})\delta\bar{u}(\bar{\lambda})\delta\bar{\tau}d\bar{\lambda} \tag{12}$$

It should be pointed out that the change of variables from τ,λ to $\bar{\tau},\bar{\lambda}$ (so that the limit of integration is changed from t to unit) is carried out after writing down explicitly the <u>double</u> convolutional integral and not before. This is due to the fact that the definition of a convolution integral requires that t appears explicitly in the integrals. To evaluate I of Eq. (12) we write

$$I = t^3\bar{I}$$

and work on $\bar{I}$ instead.

$$\bar{I} = \int_0^1 \int_0^{1-\bar{\lambda}} (1-\bar{\lambda}-\bar{\tau})\bar{u}(\bar{\tau})\delta\bar{u}(\bar{\lambda})d\bar{\tau}d\bar{\lambda}$$

The area of integration in $(\bar{\lambda},\bar{\tau})$ plane is the triangle bounded by lines $\bar{\lambda} = 0$, $\bar{\tau} = 0$ and $\bar{\tau} = 1-\bar{\lambda}$ (shown in shaded area in Figure 1). Using the step function

$$H(1-\bar{\lambda}-\bar{\tau}) = \begin{cases} 1, & \bar{\tau} < 1 - \bar{\lambda} \\ 0, & \bar{\tau} > 1 - \bar{\lambda} \end{cases}$$

one can write

$$\bar{I} = \int_0^1 \int_0^1 H(1-\bar{\lambda}-\bar{\tau})(1-\bar{\lambda}-\bar{\tau})\bar{u}(\bar{\tau})\delta\bar{u}(\bar{\lambda})d\bar{\tau}d\bar{\lambda} \tag{13}$$

Equation (13) will be used for finite element discretization. We shall divide the unit square in $(\bar{\lambda},\bar{\tau})$ plane into smaller squares of L x L (Figure 2). Let

$$\begin{aligned} \xi &= \xi^{(i)} = L\bar{\lambda} - i + 1 \\ \eta &= \eta^{(i)} = L\bar{\tau} - j + 1 \end{aligned} \tag{14}$$

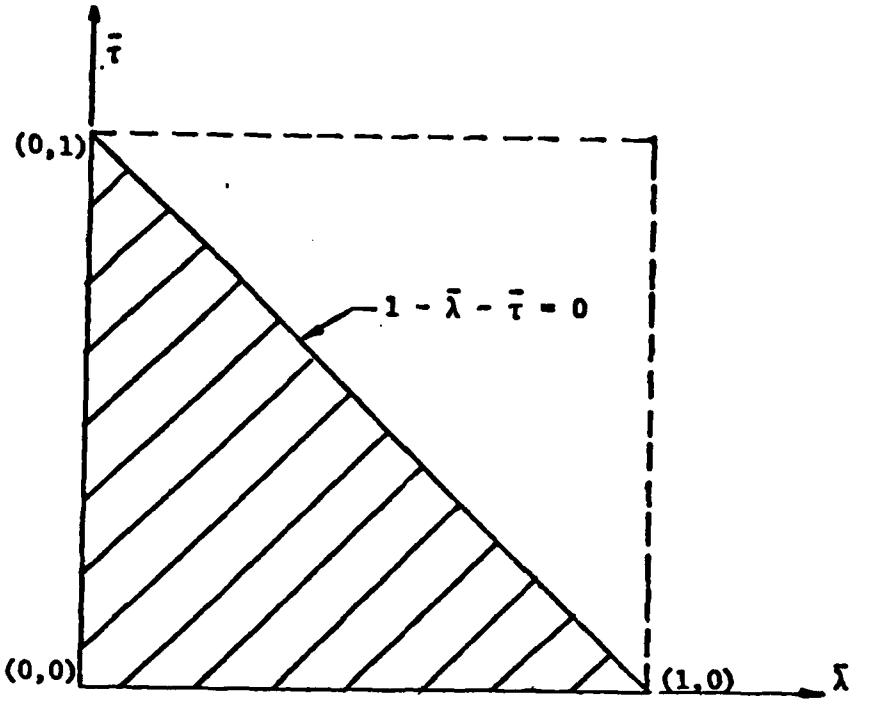

Figure 1. Area of integration for a double integral of convolution: $t*u(t)*\delta u(t)$.

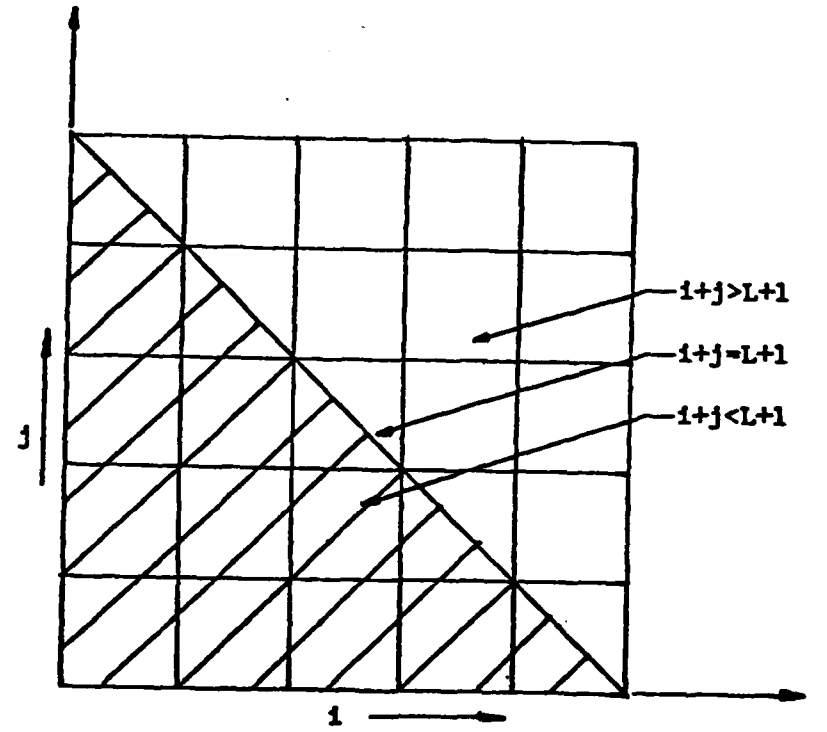

Figure 2. Area of integration using finite elements.

Thus

$$\delta\bar{y}(\bar{\lambda}) \rightarrow \delta\bar{y}^{(i)}(\xi)$$

$$\bar{y}(\bar{\tau}) \rightarrow \bar{y}^{(j)}(\eta)$$

$$1 - \bar{\lambda} - \bar{\tau} = \frac{1}{L}\{L + 1 - i - j + (1-\xi-\eta)\}$$

and

$$\bar{I} = \frac{1}{L^3}\sum_{i=1}^{L}\sum_{j=1}^{L}\int_0^1\int_0^1 H^{(ij)}(L+1-i-j+1-\xi-\eta) \cdot$$

$$\cdot (L+1-i-j+1-\xi-\eta)\bar{y}^{(j)}(\eta)\delta y^{(i)}(\xi)d\eta d\xi \qquad (15)$$

Or,

$$\bar{I} = \sum_{i=1}^{L}\sum_{j=1}^{L} I_{ij}/L^3 \qquad (16)$$

with

$$I_{ij} = \int_0^1\int_0^1 H^{(ij)}(L+1-i-j+1-\xi-\eta) \cdot$$

$$\cdot (L+1-i-j+1-\xi-\eta)\bar{y}^{(j)}(\eta)\delta y^{(i)}(\xi)d\xi d\eta \qquad (17)$$

since $1 - \bar{\lambda} - \bar{\tau} = 0$, $L + 1 - i\ j + (1-\xi-\eta) = 0$.

Or,

$$1 - \xi - \eta = i + j - (L+1)$$

Thus, three cases to consider for $H^{(ij)}$

$$\begin{aligned} &\text{(i)} \quad H^{(ij)} = 1 \ , \ i + j < L + 1 \\ &\text{(ii)} \quad H^{(ij)} = 0 \ , \ i + j > L + 1 \\ &\text{(iii)} \quad H^{(ij)} = H(1-\xi-\eta) \ , \ i + j = L + 1 \end{aligned} \qquad (18)$$

For case (i), one has

$$\bar{I}_{ij} = \int_0^1\int_0^1 (L+2-i-j)\bar{y}^{(j)}(\xi)\delta\bar{y}^{(i)}(\xi)d\eta d\xi$$

$$= \delta\underset{\sim}{Y}^{(i)T}\int_0^1\int_0^1 (L+2-i-j-\xi-\eta)\underset{\sim}{a}(\xi)\underset{\sim}{a}^{T}(\eta)d\eta d\xi\ \underset{\sim}{Y}^{(j)}$$

$$= \delta\underset{\sim}{Y}^{(i)}\ \underset{\sim}{\bar{A}}^{(ij)}\underset{\sim}{Y}^{(j)}$$

$$\underset{\sim}{\bar{A}}^{(ij)} = \int_0^1 \int_0^1 (L+2-i-j-\xi-\eta)\underset{\sim}{a}(\xi)\underset{\sim}{a}^T(\xi)d\eta d\xi$$

For case (ii),

$$I_{ij} = 0$$

For case (iii),

$$I_{ij} = \int_0^1 \int_0^1 H(1-\xi-\eta)(1-\xi-\eta)\bar{y}^{(j)}(\eta)\delta\bar{y}^{(i)}(\xi)d\eta d\xi$$

$$= \int_0^1 \int_0^{1-\xi} (1-\xi-\eta)\bar{y}^{(j)}(\eta)\delta\bar{y}^{(i)}(\xi)d\eta d\xi$$

$$= \delta\underset{\sim}{Y}^{(i)T} \int_0^1 \underset{\sim}{a}(\xi) \int_0^{1-\xi} (1-\xi-\eta)\underset{\sim}{a}^T(\eta)d\eta d\xi \; \underset{\sim}{Y}^{(j)}$$

$$= \delta\underset{\sim}{Y}^{(i)T} \underset{\sim}{\bar{\bar{A}}} \underset{\sim}{Y}^{(j)}$$

$$\underset{\sim}{\bar{\bar{A}}} = \int_0^1 \underset{\sim}{a}(\xi) \int_0^{1-\xi} (1-\xi-\eta)\underset{\sim}{a}^T(\eta)d\eta d\xi$$

Consequently,

$$I = t^3\bar{I}_1 = \frac{t^3}{L^3} \sum_{i=1}^{L} \sum_{j=1}^{L} I_{ij} \tag{19}$$

$$\begin{aligned} i+j < L+1 &\rightarrow I_{ij} = \delta\underset{\sim}{Y}^{(i)}\underset{\sim}{A}^{(ij)}\underset{\sim}{Y}^{(j)} \\ i+j > L+1 &\rightarrow I_{ij} = 0 \\ i+j = L+1 &\rightarrow I_{ij} = \delta\underset{\sim}{Y}^{(i)}\underset{\sim}{\bar{\bar{A}}}\underset{\sim}{Y}^{(j)} \end{aligned} \tag{20}$$

$$\underset{\sim}{\bar{A}}^{(ij)} = \int_0^1 \int_0^1 (L+2-i-j-\xi-\eta)\underset{\sim}{a}(\xi)\underset{\sim}{a}^T(\eta)d\xi d\eta$$

$$\bar{\bar{A}} = \int_0^1 \underset{\sim}{a}(\xi) \int_0^{1-\xi} (1-\xi-\eta)\underset{\sim}{a}^T(\eta)d\eta d\xi \tag{21}$$

And thus

$$\omega^2 t*u(t)*\delta u(t) = \omega^2 t^3 \bar{I} = \frac{\omega^2 t^3}{L^3} \sum_{i=1}^{L} \sum_{j=1}^{L} I_{ij} \tag{22}$$

(c) For $F(t)*\delta u(t)$ with $F(t)$ given in Eq. (10b), one has

$$F(t)*\delta u(t) = (a+bt+c \cos \omega_f t)*\delta u(t)$$

$$= a[1*\delta u(t)] + b[t*\delta u(t)] + c[\cos \omega_f t]*\delta u(t) \tag{23}$$

where, from Eq. (10b):

$$a = u_0 + \frac{f}{\omega_f^2} \quad , \quad b = u_1 \quad , \quad c = -\frac{f}{\omega_f^2} \tag{24}$$

Now, for Eq. (23), one has

$$1*\delta u(t) = \frac{t}{L} \sum_{i=1}^{L} \delta \underset{\sim}{U}^{(i)T} \int_0^1 \underset{\sim}{a}(\xi) d\xi \tag{25}$$

$$t*\delta u(t) = \frac{t^2}{L^2} \sum_{i=1}^{L} \delta \underset{\sim}{U}^{(i)T} \{(L-i+1) \int_0^1 \underset{\sim}{a}(\xi) d\xi - \int_0^1 \xi \underset{\sim}{a}(\xi) d\xi\} \tag{26}$$

and

$$\cos \omega_f t *\delta u(t) = \frac{t}{L} \sum_{i=1}^{L} \delta \underset{\sim}{U}^{(i)T} \int_0^1 \underset{\sim}{a}(\xi) \cos [\frac{\omega_f t}{L} (L-i+1-\xi)] d\xi \tag{27}$$

Now, Eqs. (11b), (22), (23) through (27), a global matrix equation can be written as

$$\delta \underset{\sim}{U}^T \underset{\sim}{K} \underset{\sim}{U} = \delta \underset{\sim}{U}^T \underset{\sim}{F} \tag{28}$$

Or

$$\underset{\sim}{K} \underset{\sim}{U} = \underset{\sim}{F} \tag{29}$$

which is then solved.

The finite element discretization procedure for the variational formulation using a large spring constant has bean described elsewhere (see, for example, ref. 5) and will not be repeated here.

5. NUMERICAL RESULTS. Numerical values of the parameters in the given example as stated in Section 1 are as the following:

$$m = 1.0 , \quad k = 1.0 , \quad f_o = 1.0 , \quad \omega_f = 0.5$$

$$y_0 = 1.0 , \quad y_1 = 1.0$$

Computational results are presented in Tables 1 through 4. Table 1 and 2 compare results of the two methods in an interval of $0 \leq t \leq 10$, which is about the time for a complete forcing cycle. The results for $y(t)$ and $\dot{y}(t)$ are excellent for both methods. As the interval becomes shorter, $0 \leq t \leq 2$ as shown in Table 3 and 4, the convergence is further improved.

TABLE 1. NUMERICAL COMPARISONS BETWEEN TWO UNCONSTRAINED VARIATIONAL METHODS

$0 \leq t \leq 10.0$ 10 Elements

y(t) / t	Convo Integ. M	Spring Const. M	Exact Solution
0	0.999	1.000	1.000
2.0	1.769	1.770	1.768
4.0	-1.094	-1.094	-1.094
6.0	-1.920	-1.920	-1.919
8.0	0.167	0.167	0.167
10.0	0.113	0.114	0.114

TABLE 2. NUMERICAL COMPARISONS BETWEEN TWO UNCONSTRAINED VARIATIONAL METHODS

$0 \leq t \leq 1.0$ 10 Elements

y'(t) / t	Convo Integ. M	Spring Const. M	Exact Solution
0	1.011	1.004	1.000
2.0	-0.675	-0.675	-0.674
4.0	-1.520	-1.518	-1.512
6.0	0.780	0.778	0.773
8.0	0.691	0.690	0.689
10.0	-0.391	-0.385	-0.381

TABLE 3. NUMERICAL COMPARISONS BETWEEN TWO UNCONSTRAINED VARIATIONAL METHODS

$0 \leq t \leq 2.0$ 10 Elements

y(t) / t	Convo Integ. M	Spring Const. M	Exact Solution
0	1.000000	1.000000	1.000000
0.4	1.389154	1.389154	1.389153
0.8	1.713203	1.713203	1.713203
1.2	1.911703	1.911702	1.911701
1.6	1.938251	1.938251	1.938249
2.0	1.768413	1.768416	1.768416

TABLE 4. NUMERICAL COMPARISONS BETWEEN TWO UNCONSTRAINED VARIATIONAL METHODS

$0 \leq t \leq 2.0$ 10 Elements

y'(t) / t	Convo Integ. M	Spring Const. M	Exact Solution
0	0.99999	1.00000	1.00000
0.4	0.91844	0.91843	0.91842
0.8	0.67623	0.67622	0.67621
1.2	0.29662	0.29662	0.29661
1.6	-0.17425	-0.71424	-0.17425
2.0	-0.67425	-0.67413	-0.67403

In conclusion, we have observed that the numerical convergence of the method of large spring constants, in the simple example given, is at least as good as that of the formulation through the variational principle of convolutional integrals. Both are easily adapted for finite element discretization. Due to the fact that the variational principles of convolutional integrals can be formulated only for a very restricted class of problems (of constant coefficients, for example). The alternate approach of large spring constants appears to be quite attractive to obtain solutions of non-self-adjoint problems in general and of initial value problems and initial boundary value problems in particular.

REFERENCES

1. M. E. Gurtin, "Variational Principles for Linear Elastodynamics," Archive for Rational Mechanics and Analysis, 16 (1), p. 34, 1964.

2. M. E. Gurtin, "Variational Principles for Linear Initial-Value Problems," Quarterly of Applied Mathematics, 22 (3), p. 352, 1964.

3. R. E. Nickell and J. L. Sackman, "The Extended Ritz Method Applied to Transient Coupled Thermoelastic Boundary Value Problems," SEL Report 67-3, University of California, Berkeley, CA, 1967.

4. J. Ghahoussi and E. L. Wilson, "Variational Formulation of Dynamics of Fluid-Saturated Porous Elastic Solids," Journal of Engineering Mechanics Division, Proceedings of the American Society of Civil Engineers, EM4, p. 947, 1972.

5. J. J. Wu, "Solutions to Initial Value Problems by Use of Finite Element-Unconstrained Variational Formulations," Journal of Sound and Vibration, Vol. 53, 1977, p. 341-356.

COMPUTATION SCHEMES FOR SENSITIVITY COEFFICIENT OF EXTERIOR BALLISTICS WITH VELOCITY SQUARE DAMPING

C. N. Shen and Julian J. Wu
U.S. Army Armament Research and Development Command
Benet Weapons Laboratory, LCWSL
Watervliet, NY 12189

ABSTRACT. The principal equation of exterior ballistics with velocity square damping term has been integrated analytically in obtaining the solution for tangential velocity in terms of the elevation angle and other parameters. Using the variational method, four equations are obtained. The first one is derived from consideration of terrain slope and the second one is determined by hitting the target. The third and fourth equations are variations of the range and elevation drag functions, respectively.

The computation involves integrals which can be evaluated analytically if the drag coefficient is relatively small. In simplifying the computational procedure we can assign the launch and impact slopes and then compute the drag functions and the terrain slope. However, this procedure is in reverse order because physically the terrain slope is known a priori the rounds are fired. If the terrain slopes and launch slopes are given first, an iteration procedure in computation is required to solve for the impact slopes. The sensitivity coefficients and the range ratios are then computed and plotted for various terrain slopes and launch slopes as the drag coefficients are varied.

1. INTRODUCTION. The research on sensitivity coefficients on ballistics has been discussed in two previous works. The first paper (ref. 1) matches the sensitivity coefficient of exterior ballistics to that of interior ballistics, while the second paper (ref. 2) presents the sensitivity coefficient of exterior ballistics with velocity square damping. This paper continues the work of the latter (ref. 2) and extends the analytic study in order to give numerical solutions of the problem.

The design of a gun involves numerous parameters. These parameters should be in such a combination that the best first round accuracy is given. While the shell leaves the gun it has perturbations for the muzzle elevation angle and the muzzle velocity. The ratio of the two is the sensitivity coefficient of the interior and the exterior ballistics. It is desired to compensate the errors due to uncertain changes of muzzle velocity by the automatic response of the muzzle elevation angle within the gun system. With a correct design this compensation can be made by matching the exterior ballistics to the interior ballistics through the analysis of gun dynamics. This process is called

passive control since there is no external measurement involved nor instrumentation needed for control. This general problem can be formulated by first investigating the sensitivity coefficients for exterior ballistics with velocity square damping.

2. PREVIOUS WORK. In the second paper the principal equation of exterior ballistics has a drag term which, in this case, is proportional to the square of the velocity in the tangential direction of the projectile. The sensitivity coefficient is expressed as the ratio of the initial elevation angle deviation to the initial percentage velocity deviation. The work is to find analytically the sensitivity coefficient of the exterior ballistics with velocity square damping which comes from the nonlinear air resistance for a projectile. This principal equation is integrated analytically in obtaining the solution for tangential velocity in terms of the elevation angle, together with all the necessary initial conditions. The horizontal range and the vertical range are also expressed as integrals of certain function of the elevation angles. In order to obtain the sensitivity coefficient it is necessary to find the perturbations of the horizontal and vertical ranges. This procedure is similar to that of evaluating differentiation under the integral sign. The perturbation of the ranges is the sum of the perturbations due to the initial velocity, the initial elevation angle and the impact elevation angle. By setting to zeroes the range perturbations we can group the coefficients of the perturbations into two separate equations. The ratio of the perturbations for initial elevation angle to that for initial velocity is the sensitivity coefficient for exterior ballistics that we are seeking.

3. RESULT OF PAST RESEARCH. The following results are concluded as:

1. The principal equation of exterior ballistics is derived with the trajectory slope as the independent variable.

2. The closed form solution for the horizontal component of trajectory velocity is determined for the case of exterior ballistics with velocity square damping.

3. The nondimensional range is obtained in terms of an end slope function and a range drag function.

4. Variations of the nondimensional range are expressed as variations of launch velocity.

5. Variations of the range drag function are in terms of the variations of the range drag integral.

6. The range drag integral has parameters in the integrand as well as the upper and lower limits. The variations of the integral are found.

7. The partial derivatives of the range drag integrand are evaluated.

8. The variational equation for the range is in terms of elements involving three integrals as coefficients of three variational parameters.

9. The variational parameters are that of launch velocity, the launch elevation angle, and the impact elevation angle.

10. The average of the end slopes is equal to the terrain slope times the range drag function minus the elevation drag function.

11. Variations of the nondimensional elevation are expressed as variations of the end slopes and the variations of the drag function.

12. The variational equations for the elevation are determined similar to that for the range.

13. Eliminating the variations of impact slope, δq_1, from the set of two variational equations gives the ratio of the coefficients of $\delta v_o/v_o$ and $\delta q_o/(q_o-q_1)$.

14. The sensttivity $\delta\theta_o/(\delta v_o/v_o)$ may be obtained by dividing this ratio $\delta q_o/(\delta v_o/v_o)$ by the quantity $(1+q_o^2)$.

However, numerical calculation of this problem was not carried in that paper (ref. 2).

4. DYNAMICAL EQUATIONS FOR TRAJECTORIES. After several transformations as given in the paper (ref. 2) and summarized in Appendix A, the dynamical equations are simplified as

$$du = \frac{c}{q} u^3 (1+q^2)^{1/2} dq \tag{1}$$

$$dx = -\frac{u^2}{g} dq \tag{2}$$

$$dy = -\frac{u^2}{g} q dq \tag{3}$$

In the above equation the independent variable q is the projectile slope which is related to θ as

$$q = \tan\theta \tag{4}$$

and the dependent variable u is related to v and θ as

$$u = v\cos\theta \tag{5}$$

where g = the acceleration due to gravity
c = the drag coeficient of the projectile
v = the velocity of the projectile
θ = the path inclination (elevation angle)
x = the horizontal distance of the projectile
y = the altitude or vertical distance of the projectile.

The solution for horizontal component of velocity u can be obtained by integrating Eq. (1) to give

$$\frac{1}{u^2} = \frac{1}{u_o^2}\{1-u_o^2\,\frac{c}{g}\,[p(q) - p_o(q_o)\} \tag{6}$$

where

$$p(q) = q(1+q^2)^{1/2} + \ell n[q + (1+q^2)^{1/2}] \tag{7}$$

$$p_o(q_o) = q_o(1+q_o^2)^{1/2} + \ell n[q_o + (1+q_o^2)^{1/2}]\ . \tag{8}$$

$$u_o^2 = v_o^2\sec^{-2}\theta_o = v_o^2(1+q_o^2)^{-1} \tag{9}$$

and

$$q_o = \tan\theta_o \tag{9a}$$

Finally, Eq. (6) takes the form

$$u^2 = \frac{v_o^2}{1+q_o^2}\{1 + \frac{H(q,q_o,v_o^2,c/g)}{1 - H(q,q_o,v_o^2,c/g)}\} \tag{10}$$

where

$$H(q,q_o,v_o^2,c/g) = \frac{c}{g}\,\frac{v_o^2}{1+q_o^2}\,[p(q) - p_o(q_o)] \tag{11}$$

5. SOLUTION FOR NONDIMENSIONAL RANGE. In determining the range x for the trajectory the closed form solution of u^2 in Eq. (10) can be substituted into Eq. (2) to obtain the solution in integral form as

$$x_i - x_o = -\frac{v_o^2}{g(1+q_o^2)}\,[(q_i-q_o) + \int_{q_o}^{q_i}\frac{H(q,q_o,v_o^2,c/g)}{1 - H}\,dq \tag{12}$$

where x_i = range at impact point
x_o = range at initial point
and q_i = projectile slope at impact point.

To non-dimensionalize the range, Eq. (12) is divided by the factor v_o^2/g as

$$X(x_i,x_o,v_o)/\Lambda(q_i,q_o) = G_x(q_i,q_o,v_o^2,c/g) \tag{13}$$

where the nondimensional range is

$$X(x_i,x_o,v_o) = (x_i-x_o)g/v_o^2 \quad , \tag{14}$$

the slope function is

$$\Lambda(q_o,q_i) = \frac{q_o-q_i}{1+q_o^2} \tag{15}$$

and the range drag function due to air resistance is

$$G_x(q_i,q_o,v_o^2,c/g) = 1 - \frac{1}{q_o-q_i}\int_{q_o}^{q_i} \frac{H(q,q_o,v_o^2,c/g)}{1-H}\,dq \quad . \tag{16}$$

6. VARIATION OF THE NONDIMENSIONAL RANGE AND THE SLOPE FUNCTION. In order to obtain a first round hit of the target one of the conditions is that the variation of the range should be zero, i.e., from Eq. (14)

$$\delta(x_i-x_o) = 0 \quad . \tag{17}$$

We take the perturbation for the nondimensional range from Eq. (14) as

$$\frac{\delta X}{X} = \frac{\delta(x_i-x_o)}{x_i-x_o} - \frac{2\delta v_o}{v_o}$$

$$\frac{\delta X}{X} = 0 - \frac{2\delta v_o}{v_o} \quad . \tag{18}$$

The variation of the slope function Λ in Eq. (15) becomes

$$\frac{\delta\Lambda}{\Lambda} = -\frac{\delta q_i}{q_o-q_i} + \frac{\delta q_o}{q_o-q_i} - \frac{2q_o\delta q_o}{1+q_o^2} \quad . \tag{19}$$

Next, taking the variation of Eq. (13) and using the expressions given in Eq. (18) and (19) we have

$$\frac{\delta X}{X} - \frac{\delta \Lambda}{\Lambda} = \frac{\delta G_x}{G_x} \tag{20}$$

or

$$\frac{\delta G_x}{G_x} = -\frac{2\delta v_o}{v_o} + \frac{\delta q_1}{q_o - q_1} - \frac{\delta q_o}{q_o - q_1} + \frac{2q_o \delta q_o}{1+q_o^2} \tag{21}$$

This gives the variation of the range δG_x in terms of the variations of the initial velocity δv_o, and the variations of the initial slope δq_o and that of the impact slope δq_1.

7. THE SOLUTION FOR ELEVATION. The differential equation for elevation was given in Eq. (3) and the solution for u is in Eq. (10).

Substituting Eq. (10) into Eq. (3) gives

$$dy = -\frac{v_o^2}{g(1+q_o^2)}\left[1 + \frac{H(q, q_o, v_o^2, c/g)}{1 - H}\right] q\,dq \quad . \tag{22}$$

Integrating the above one obtains

$$y_1 - y_o = -\frac{v_o^2}{g(1+q_o^2)}\left[\frac{q_1^2 - q_o^2}{2} + \int_{q_o}^{q_1} \frac{qH}{1-H}\,dq\right] . \tag{23}$$

Rearranging yields the relationship between the range Y, the end slope function Λ, and the elevation drag function G_y.

$$Y(y_1, y_o, v_o)/\Lambda(q_1, q_o) = \frac{1}{2}(q_o + q_1) + G_y(q_1, q_o, v_o^2, c/g) \tag{24}$$

where the nondimensional elevation is

$$Y(y_1, y_o, v_o) = \frac{g(y_1 - y_o)}{v_o^2} \quad . \tag{25}$$

Λ is given in Eq. (15), and the elevation drag function is

$$G_y(q_1, q_o, v_o^2, c/g) = -\frac{1}{q_o - q_1}\int_{q_o}^{q_1} \frac{qH(q, q_o, v_o^2, c/g)\,dq}{1-H} \tag{26}$$

8. TERRAIN SLOPE FROM LAUNCH POINT TO TARGET POINT. If Eq. (25) is divided by Eq. (14) with the aid of Eqs. (16) and (26), one obtains

$$\frac{y_1-y_o}{x_1-x_o} \triangleq m = \frac{(1/2)(q_o+q_1) + G_y}{G_x} \tag{27}$$

where m is the terrain slope from launch point to target point, a constant parameter. Therefore,

$$(1/2)(q_o+q_1) + G_y = mG_x \quad . \tag{28}$$

We use Eq. (27) to find the variational equation for the elevation. Taking the variation of Eq. (28) for any given m, we have

$$(1/2)(\delta q_o+\delta q_1) + \delta G_y - m\,\delta G_x = 0 \tag{29}$$

It is noted that δG_y and δG_x are related in Eq. (29), with also the variations δq_o and δq_1.

9. VARIATION OF THE RANGE AND ELEVATION DRAG FUNCTIONS. Work was performed on evaluation of the drag function in the previous paper (ref. 2) which is summarized in Appendix B. This gives the respectful variations of the range and elevation drag functions as

$$\delta G_x = a_v \frac{2\delta v_o}{v_o} + a_1 \frac{\delta q_1}{q_o-q_1} + a_o \frac{\delta q_o}{q_o-q_1} \tag{30}$$

$$\delta G_y = b_v \frac{2\delta v_o}{v_o} + b_1 \frac{\delta q_1}{q_o-q_1} + b_o \frac{\delta q_o}{q_o-q_1} \tag{31}$$

where

$$a_v = \left[-\frac{1}{q_o-q_1} I_{12}\right] \quad , \tag{32}$$

$$a_1 = \left[-\frac{H_1}{1-H_1} - \frac{1}{q_o-q_1} I_{11}\right] \quad ,$$

$$a_o = \left[\frac{2q_o}{1+q_o^2} I_{12} + \frac{1}{q_o+q_1} I_{11} + \left(\frac{c}{g}\right) \frac{v_o^2}{1+q_o^2} \frac{dp_o}{dq_o} I_{02}\right] \quad , \tag{34}$$

$$b_v = \left[-\frac{1}{q_o-q_1} J_{12}\right] \quad , \tag{35}$$

$$b_1 = \left[-\frac{q_1 H_1}{1-H_1} - \frac{1}{q_o-q_1} J_{11}\right] \quad , \tag{36}$$

and

$$b_o = \left[\frac{2q_o}{1+q_o^2} J_{12} + \frac{1}{q_o-q_1} J_{11} + \left(\frac{c}{g}\right) \frac{v_o^2}{1+q_o^2} \frac{dp_o}{dq_o} J_{02}\right] \tag{37}$$

In turn, the integral I_{11}, I_{12}, and I_{02}, and other terms are given as follows.

$$I_{11}(q_o,q_i) = \int_{q_o}^{q_i} \frac{H(q,q_o,v_o^2,c/g)}{1-H}\, dq \quad , \tag{38}$$

$$I_{12}(q_o,q_i) = \int_{q_o}^{q_i} \frac{H}{(1-H)^2}\, dq \quad , \tag{39}$$

$$I_{02}(q_o,q_i) = \int_{q_o}^{q_i} \frac{1}{(1-H)^2}\, dq \quad , \tag{40}$$

$$H_i = H(q=q_i) \tag{41}$$

and

$$\frac{dp_o}{dq_o} = 2(1+q_o^2)^{1/2} \quad . \tag{42}$$

Moreover, the integral J_{11}, J_{12}, and J_{02}, and other terms are given as follows.

$$J_{11} = \int_{q_o}^{q_i} qH(q,q_o,v_o^2,c/g)/(1-H)\, dq \quad , \tag{43}$$

$$J_{12} = \int_{q_o}^{q_i} qH/(1-H)^2\, dq \quad , \tag{44}$$

$$J_{02} = \int_{q_o}^{q_i} q/(1-H)^2\, dq \quad , \tag{45}$$

and

$$G_y = -\frac{1}{q_o-q_i} J_{11} \quad . \tag{46}$$

10. SOLUTION FOR SENSITIVITY COEFFICIENT. It is noted that both Eq. (21) and Eq. (30) give the variation δG_x in terms of variations δv_o, δq_i, and δq_o and the equations are independent of each other. Rewriting these equations as:

$$\delta G_x = G_x\left[-\frac{2\delta v_o}{v_o} + \frac{dq_i}{q_o-q_i} - \frac{\delta q_o}{q_o-q_i} + \frac{2q_o\delta q_o}{1+q_o^2}\right] \tag{47}$$

$$\delta G_x = a_v \frac{2\delta v_o}{v_o} + a_i \frac{\delta q_i}{q_o-q_i} + a_o \frac{\delta q_o}{q_o-q_i} \tag{48}$$

Subtracting Eq. (48) from Eq. (47) and then dividing by G_x gives

$$0 = [-1 - \frac{a_v}{G_x}] \frac{2\delta v_o}{v_o} + [1 - \frac{a_i}{G_x}] \frac{\delta q_i}{q_o - q_i} + [-1 - \frac{a_o}{G_x}] \frac{\delta q_o}{q_o - q_i} + \frac{2q_o \delta q_o}{1+q_o^2} \quad (49)$$

It is also noted that Eq. (31) expresses the variation δG_y in terms of variations δv_o, δq_i, and δq_o, and Eq. (29) relates δG_y and δG_x with the same set of variations. These are rewritten as

$$\delta G_y = b_v \frac{2\delta v_o}{v_o} + b_i \frac{\delta q_i}{q_o - q_i} + b_o \frac{\delta q_o}{q_o - q_i} \quad (50)$$

$$\delta q_i = - \delta q_o + 2m\delta G_x - 2\delta G_y \quad (51)$$

By substituting Eqs. (48) and (50) into (51) we have

$$\delta q_i = - \delta q_o + 2m[a_v \frac{2\delta v_o}{v_o} + a_i \frac{\delta q_i}{q_o - q_i} + a_o \frac{\delta q_o}{q_o - q_i}]$$

$$-2[b_v \frac{2\delta v_o}{v_o} + b_i \frac{\delta q_i}{q_o - q_i} + b_o \frac{\delta q_o}{q_o - q_i}] \quad (52)$$

or

$$0 = \frac{(-2ma_v + 2b_v)}{q_o - q_i} \frac{2\delta v_o}{v_o} + (1 + \frac{-2ma_i + 2b_i}{q_o - q_i}) \frac{\delta q_i}{q_o - q_i} + (1 + \frac{-2ma_o + 2b_o}{q_o - q_i}) \frac{\delta q_o}{q_o - q_i} \quad (53)$$

Equations (49) and (53) are in terms of the variations δv_o, δq_i, and δq_o. Sensitivity coefficients are ratio of δq_o and δv_o, thus δq_i can be eliminated by combining these two equations:

$$0 = [(\frac{-2ma_v + 2b_v}{q_o - q_i})(1 - \frac{a_i}{G_x}) + (1 + \frac{a_v}{G_x})(1 + \frac{-2ma_i + 2b_i}{q_o - q_i})] \frac{2\delta v_o}{v_o}$$

$$+ [(1 + \frac{-2ma_o + 2b_o}{q_o - q_i})(1 - \frac{a_i}{G_x}) +$$

$$(1 + \frac{a_o}{G_x} - \frac{2q_o(q_o - q_i)}{1+q_o^2})(1 + \frac{-2ma_i + 2b_i}{q_o - q_i})] \frac{\delta q_o}{q_o - q_i} \quad (54)$$

If we define the ratio S* as

$$S^* = \frac{\delta q_o/(q_o-q_i)}{\delta v_o/v_o} \tag{55}$$

Then from Eq. (54) this ratio is

$$S^* = (-2)\frac{(\frac{-2ma_v+2b_v}{q_o-q_i})(1-\frac{a_i}{G_x}) + (1+\frac{a_v}{G_x})(1+\frac{-2ma_i+2b_i}{q_o-q_i})}{(1+\frac{-2ma_o+2b_o}{q_o-q_i})(1-\frac{a_i}{G_x}) + (1+\frac{a_o}{G_x}-\frac{2q_o(q_o-q_i)}{1+q_o^2})(1+\frac{-2ma_i+2b_i}{q_o-q_i})} \tag{56}$$

The sensitivity equation is defined as

$$S = \frac{\delta q_o/(1+q_o^2)}{\delta v_o/v_o} \tag{57}$$

which give the relationship

$$S = \frac{q_o-q_i}{1+q_o^2}\,S^* \tag{58}$$

11. ITERATION OF SOLUTIONS. The terrain slope m is usually provided before the computation. Equation (27) shows that this terrain slope is in terms of the range drag function G_x in Eq. (16) and the elevation drag function G_y in Eq. (26). In turn, these drag functions are expressed in terms of the projectile starting slope q_o and its impact slope q_i. Computationally the solution of m for given q_o and q_i is a straight forward substitution procedure using Eqs. (27), (16), and (26). However, since the terrain slope m is known in advance physically and the impact slope q_i is not, we compute instead the impact slope q_i for a given starting slope q_o in Eq. (27). Rewriting this equation we have

$$q_i = -q_o + \frac{2}{q_o-q_i}\int_{q_o}^{q_i}\frac{qH(q,q_o,v_o^2,c/g)dq}{1-H} + 2m - \frac{2m}{q_o-q_i}\int_{q_o}^{q_i}\frac{H(q,q_o,v_o^2,c/g)dq}{1-H} \tag{59}$$

One can guess an initial value for q_i on the right side of the above equation and perform the integration. The value for q_i on the left side can be used as the initial value for q_i on the right side for the second trial. This iteration procedure continues until the value of q_i converges to a numerical solution as its limit.

Equation (59) may be expressed as

$$q_i = -q_o + \frac{2}{q_o - q_i} J_{11} + 2m - \frac{2m}{q_o - q_i} I_{11} \tag{60}$$

where I_{11} and J_{11} are given in Eqs. (38) and (43). These integrals will be evaluated in the next section.

12. EVALUATION OF INTEGRALS. If the drag coefficient cv_o^2/g is small compared to $(1+q_o^2)$ the denominator terms (1-H) and $(1-H)^2$ in Eqs. (38) - (40) and (43) - (45) may be neglected. One obtains from the above equations the following

$$I_{11} \cong I_{12} \cong \int_{q_o}^{q_i} H dq \tag{61}$$

$$I_{02} \cong q_i - q_o \tag{62}$$

$$J_{11} \cong J_{12} \cong \int_{q_o}^{q_i} qH dq \tag{63}$$

$$J_{02} = \frac{1}{2}(q_i^2 - q_o^2) \tag{64}$$

Equation (11) for H may be rewritten as

$$H = K \frac{1}{1+q_o^2} [p(q) - p_o(q_o)] \tag{65}$$

where

$$K = cv_o^2/g \tag{66}$$

and p(q) is given in Eq. (7). Then the integrals I_{11} and I_{12} are

$$I_{11} = I_{12} = KM \tag{67}$$

where

$$M = \frac{1}{1+q_o^2} [P_{q=q_i} - P_{q=q_o} + (q_o - q_i) p_o(q_o)] \tag{68}$$

and

$$P = \int p(q)dq$$

$$= \frac{1}{3}(1+q^2)^{3/2} + q\ell n[q + (1+q^2)^{1/2}] - (1+q^2)^{1/2} \tag{69}$$

Similarly the integrals J_{11} and J_{12} are

$$J_{11} = J_{12} = KN \tag{70}$$

where

$$N = \frac{1}{1+q_o^2}[Q_{q=q_i} - Q_{q=q_o} + \frac{1}{2}(q_o^2 - q_i^2)p_o(q_o)] \tag{71}$$

and

$$Q = \int qp(q)dq$$

$$= \frac{1}{4}q(1+q^2)^{3/2} - \frac{3}{8}q(1+q^2)^{1/2} + (\frac{1}{2}q^2 + \frac{1}{8})\ell n[q + (1+q^2)^{1/2}] \tag{72}$$

In the last section the iteration equation (59) for the solution for q_i now becomes

$$q_i = -q_o + 2(mG_x - G_y) \tag{73}$$

where

$$G_x = 1 - (q_o - q_i)^{-1} KM \tag{74}$$

and

$$G_y = -(q_o - q_i)^{-1} KN \tag{75}$$

We are now able to compute q_i if the quantities m and q_o are given.

The coefficients used in the variation of range and elevation drag functions in Eqs. (32) - (37) give

$$a_v = -(q_o - q_i)^{-1} KM \tag{76}$$

$$a_i = K\{-[p(q_i) - p_o(q_o)] - (q_o - q_i)^{-1} M\} \tag{77}$$

$$a_o = K\{[\frac{2q_o}{1+q_o^2} + (q_o - q_i)^{-1}]M - \frac{dp_o}{dq_o}(q_o - q_i)\} \tag{78}$$

$$b_v = -(q_q - q_i)^{-1} KN \tag{79}$$

$$b_i = K\{-q_i[p(q_i) - p_o(q_o)] - (q_o - q_i)^{-1} N\} \tag{80}$$

and

$$b_o = K\{[\frac{2q_o}{1+q_o^2} + (q_o - q_i)^{-1}]N - \frac{1}{2}(q_o^2 - q_i^2)\frac{dp_o}{dq_o}\} \tag{81}$$

With q_o and q_i known, we are able to compute the coefficients of three a's and three b's as given in the above equations. It is now ready to substitute all the coefficients into Eq. (56) to compute S*. By Eq. (58), in turn, one obtains S, the sensitivity we are seeking.

13. DETERMINATION OF THE EXTREMAL VALUE OF THE DAMPING COEFFICIENT. The assumption that the denominator terms (1-H) may be dropped in evaluating the integrals depends on

$$H << 1 \tag{82}$$

From Eq. (65) this is equivalent to

$$H(q) = K\{\frac{1}{1+q_o^2}[p(q) - p_o(q_o)]\} << 1 \tag{83}$$

where

$$p(q) = \{q(1+q^2)^{1/2} + \ell n[q + (1+q^2)^{1/2}]\} \tag{84}$$

It is noted that

$$H(q_o) = 0 \quad \text{at } q = q_o \tag{85}$$

The extremal value of H(q) can be evaluated at $q = q_i$

$$|H| \leq |H|_{\text{extremal}} = |H(q_i)| = K\frac{1}{1+q_o^2}[p(q_i) - p_o(q_o)]| << 1 \tag{86}$$

The above is conservative in that we use the largest value of |H| for determining the range spread of K. For example if $q_o = 1$ and $q_i = -1$, then

$$\frac{1}{1+q_o^2} p_o(q_o) = (1.414 + \ell n\ 2.414)/2 = 1.147 \tag{87}$$

$$\frac{1}{1+q_o^2} p(q_i) = (-1.414 + \ell n\ 0.414)/2 = -1.147 \tag{88}$$

then

$$K|-1.147 - 1.147| << 1 \tag{89}$$

or

$$K << 0.436 \tag{90}$$

and if $q_o = \sqrt{3}$, and $q_1 = -\sqrt{3}$, then

$$\frac{1}{1+q_o^2} p_o(q_o) = [(1.732)(2) + \ell n\ 3.732]/4 = 1.195 \tag{91}$$

$$\frac{1}{1+q_o^2} p(q_1) = [(-1.732)(2) + \ell n\ 0.268]/4 = -1.195 \tag{92}$$

then

$$K|-1.195 - 1.195| << 1 \tag{93}$$

$$K << 0.418 \tag{94}$$

The maximum of K we chose in this paper is

$$\max(cv_o^2/g) = \max K = 0.20 \tag{95}$$

which satisfies the above requirements for the approximation used in evaluating the integrals.

14. COMPUTATION PROCEDURE. The computation procedure consists of two parts, the iteration procedure for the impact slope q_1 and the sensitivity and range computation after obtaining q_1.

(1) Iteration Procedure - By giving the launch slope q_o one can compute such quantities as $p_o(q_o)$ from Eq. (7), $Pq=q_o$ from Eq. (69) and $Qq=q_o$ from Eq. (72). The iteration procedure starts by assuming an initial impact slope q_1. Then we can obtain $Pq=q_1$ and $Qq=q_1$ from Eqs. (69) and (72), respectively. In addition, we can compute M and N from Eqs. (68) and (71), respectively. By assuming the value of K (i.e., cv_o^2/g) in Eq. (66) the integrals I_{11} and J_{11} are calculated from Eqs. (67) and (70), respectively. With these integrals one can find a new value for the impact slope q_1 by using Eq. (60). This iteration procedure continues until the value of q_1 converges to a numerical solution as its limit.

(2) Sensitivity and Range Computation - With the iterated solution of the impact slope q_1 known, one can proceed to find the sensitivity coefficients and the range. We start to find the range drag function G_x and the elevation drag function G_y from Eqs. (74) and (75), respectively. Next the coefficients a_v, a_1, a_o, b_v, b_1, and b_o can be evaluated by Eqs. (76) - (81).

Substituting these functions and coefficients into Eq. (56) we can get S^*, thus the sensitivity coefficient S can be obtained readily from Eq. (58).

The range X can also be computed by combining Eqs. (13), (15), and (74).

15. NUMERICAL SOLUTIONS. We are using the nondimensional damping coefficient $K = cv_o^2/g = 0.2$ for illustration purpose. The terrain slopes are assumed to be $m = 0$ and $m = 0.2679$ which is corresponding to a terrain angle of 0° and 15° respectively. The launch angle θ_o are varied as follows:

$$\text{for } m = 0, \quad 7.5^\circ \leq \theta_o \leq 82.5^\circ \text{ at intervals of } 7.5^\circ$$

$$\text{for } \tan^{-1} m = 15^\circ, \quad 22.5 \leq \theta_o \leq 75^\circ \text{ at intervals of } 7.5^\circ$$

The results are shown in Tables 1 and 2, and plotted in Figures 2-6. Figure 2 gives the iterated impact angles for various launch angles. The effect of K to the range is fairly large as shown in Figures 3 and 4. However, the effect of the nondimensional drag coefficient K to the sensitivity coefficient is not very large except near the critical sensitivity which magnitude is unbounded as shown in Figures 5 and 6.

16. CONCLUSION. This paper is the third of a sequence. The findings are summarized as follows.

From the first paper (ref. 1) we have:

(1) The error increments in hitting a target are derived and set to zero for a bull's eye landing.

(2) The sensitivity coefficient is defined as the ratio of increments of the initial elevation angle to the increments of the natural logarithm of the velocity.

(3) Without air resistance or damping the maximum range is found to be located at an optimal initial elevation angle, which is half of the sum of 90° and the terrain angle.

(4) Without damping the sensitivity coefficients become infinite at maximum range and zero at minimum range of zero.

(5) The sensitivity coefficient is positive for high trajectories (above 45° initial elevation angle) and negative for low trajectories (below 45° initial elevation angle).

(6) Due to uncertainty of muzzle velocity deviation a gun may be designed by matching the interior ballistics to the exterior ballistics. This is to give automatically and instantly a proportional deviation of its initial elevation angle when the shell leaves the muzzle during firing for the first round.

The second paper (ref. 2) investigated the problem when the principal equation of exterior ballistics has a drag term which is proportional to the square of velocity. The paper is to find analytically the sensitivity coefficient. A sequence of nonlinear transformation was used before the sensitivity problem can be studied. The variation of various parameters is investigated, including the variation under an integral sign.

The present paper continues the work of the second and converts it into a different analytical form that is suitable for numerical computation. The solution for sensitivity coefficients is condensed into a single formula with the terms readily computable from a set of parameters. An iteration procedure is used in the computation. Some integrals are approximated in order to obtain their analytical solution forms.

The effect of velocity square damping to the range can be large, especially at the maximum range. However, the effect of velocity square damping to the sensitivity coefficient is usually small, except near the maximum range.

TABLE 1. RANGE AND SENSITIVITY COEFFICIENTS FOR FLAT TERRAIN

For m = 0 θ_o	q_o	$\frac{cv_o^2}{g}$	θ_1 (degree)	q_1	X	S
7.5°	0.13165	0	- 7.5000	-0.131652	0.258819	-0.267949
		0.20	- 7.7808	-0.136641	0.249773	-0.268020
15.0°	0.26794	0	-15.0000	-0.267949	0.500000	-0.577350
		0.20	-16.1583	-0.289738	0.465538	-0.578836
22.5°	0.41421	0	-22.5000	-0.414213	0.707106	-1.000000
		0.20	-25.0595	-0.467574	0.636169	-1.011472
30.0°	0.57735	0	-30.0000	-0.577350	0.866025	-1.732050
		0.20	-34.2094	-0.679841	0.755507	-1.804402
37.5°	0.76732	0	-37.5000	-0.767326	0.965925	-3.732050
		0.20	-43.1708	-0.938106	0.821550	-4.422821
45.0°	1.00000	0	-45.0000	-1.000000	1.000000	∞
		0.20	-51.4995	-1.257153	0.835103	14.3160
52.5°	1.30322	0	-52.5000	-1.303225	0.965925	3.732050
		0.20	-58.9394	-1.660305	0.798363	2.645294
60.0°	1.73205	0	-60.0000	-1.732105	0.866025	1.732050
		0.20	-65.5374	-2.198108	0.714006	1.342668
67.5°	2.41421	0	-67.5000	-2.414213	0.707106	1.000000
		0.10	-69.0956	-2.618147	0.647751	0.915074
		0.20	-71.6039	-3.006806	0.585294	0.796916
75.0°	3.73205	0	-75.0000	-3.732050	0.500000	0.577350
		0.10	-76.0085	-4.013342	0.459463	0.529802
		0.20	-77.5372	-4.524636	0.417197	0.465626
82.5°	7.59575	0	-82.5000	-7.595754	0.258819	0.267949
		0.10	-82.9614	-8.099269	0.238697	0.245899
		0.20	-83.6382	-8.969194	0.217891	0.217213

TABLE 2. RANGE AND SENSITIVITY COEFFICIENTS FOR 15° TERRAIN

For m = + 0.2679 θ_o	q_o	$\frac{cv_o^2}{g}$	θ_1(degree)	q_1	X	S
22.5°	0.41421	0	6.932362	0.121586	0.249772	-0.278596
		0.10	6.783131	0.118944	0.245353	-0.278737
		0.20	6.619309	0.116045	0.240893	-0.278891
30.0°	0.57735	0	-2.379286	-0.041550	0.464175	-0.634112
		0.10	-3.002055	-0.052443	0.448368	-0.636174
		0.20	-3.751089	-0.065562	0.432262	-0.638617
37.5°	0.76732	0	-13.03583	-0.231526	0.628688	-1.214643
		0.10	-14.38786	-0.256530	0.598311	-1.230168
		0.20	-16.14129	-0.289416	0.567092	-1.250663
45.0°	1.00000	0	-24.90070	-0.464200	0.732100	-2.732736
		0.10	-26.98236	-0.509137	0.688258	-2.877936
		0.20	-29.80982	-0.572933	0.642910	-3.107193
52.5°	1.30322	0	-37.50354	-0.767425	0.767364	∞
		0.10	-39.96784	-0.838143	0.714885	32.535621
		0.20	-43.37056	-0.944680	0.660410	13.127275
60.0°	1.73205	0	-50.10622	-1.196250	0.732075	2.731708
		0.10	-52.42571	-1.299732	0.678076	2.405832
		0.20	-55.62687	-1.461933	0.622002	2.031230
67.5°	2.41421	0	-61.97076	-1.878413	0.628640	1.214358
		0.10	-63.73921	-2.026837	0.580688	1.105513
		0.20	-66.17359	-2.264476	0.531007	0.968816
75.0°	3.73205	0	-72.62684	-3.196250	0.464108	0.633962
		0.10	-73.71086	-3.422142	0.428564	0.581436
		0.20	-75.20812	-3.787022	0.391874	0.514330
82.5°	7.59575	0	-81.93802	-7.059954	0.249690	0.278489
		0.10	-82.41359	-7.508239	0.230773	0.255652
		0.20	-83.07899	-8.238227	0.211307	0.226622

REFERENCES

1. Shen, C. N., "On the Sensitivity Coefficient of Exterior Ballistics and Its Potential Matching to Interior Ballistics Sensitivity," Proceedings of the Second US Army Symposium on Gun Dynamics at the Institute on Man and Science, Rensselaerville, NY, September 1978, sponsored by USA ARRADCOM.

2. Shen, C. N., "Sensitivity Coefficient of Exterior Ballistics With Velocity Square Damping," Transactions of the Twenty-Fifth Conference of Army Mathematicians, ARO Report 80-1, January 1980, pp. 267-282.

APPENDIX A

DYNAMICAL EQUATIONS FOR TRAJECTORIES AND VARIABLE TRANSFORMATIONS. For a constant mass travelling in a vertical plane with no lift and applied thrust, but having drag and velocity vectors contained in the plane of symmetry as shown in Figure 1, the dynamical equations of motion are (ref. 1):

$$\frac{dx}{dt} - v \cos \theta = 0 \tag{A1}$$

$$\frac{dy}{dt} - v \sin \theta = 0 \tag{A2}$$

$$m\left(g \cos \theta + v \frac{d\theta}{dt}\right) = 0 \tag{A3}$$

$$\frac{d^2x}{dt^2} = -\frac{D \cos \theta}{m} \tag{A4}$$

It is noticed that deviations due to anomalies in the azimuth direction are not considered here.

By differentiating Eq. (A1) with respect to t one obtains

$$\frac{d^2x}{dt^2} = \frac{d}{dt}(v \cos \theta) \tag{A5}$$

Substituting into Eq. (A4) we have

$$\frac{d}{dt}(v \cos \theta) = -\frac{D \cos \theta}{m} \tag{A6}$$

Solving for $d\theta/dt$ in Eq. (A3) one obtains

$$\frac{d\theta}{dt} = \frac{-g \cos \theta}{v} \tag{A7}$$

Equation (A7) indicates that the differential equations can be transformed from the time domain in t to the angle domain in θ. Equations (A6), (A1), and (A2) are divided by Eq. (A7) in achieving this transformation as

$$\frac{d(v \cos \theta)}{d\theta} = \frac{Dv}{mg} \tag{A8}$$

$$\frac{dx}{d\theta} = -\frac{v^2}{g} \tag{A9}$$

$$\frac{dy}{d\theta} = -\frac{v^2}{g}\tan\theta \tag{A10}$$

Equation (A8) is called the principal equation of exterior ballistics (ref. 2). It can be integrated if the drag D is a known function of velocity v.

The head wind drag is a velocity square damping term given as

$$D = mcv^2 \tag{A11}$$

where

$$c = c_w\left(\frac{\pi}{4}d^2\right)(\rho/2) \tag{A12}$$

c_w = the dimensionless resistant coefficient
d = the diameter of projectile

and ρ = the air density.

Thus the principal equation of exterior ballistics (Eq. (A8)) becomes

$$\frac{d}{d\theta}(v\cos\theta) = \frac{cv^3}{g} \tag{A13}$$

A further transformation of the dependent variable is necessary by letting

$$u = v\cos\theta \tag{A14}$$

where u is the horizontal component of the projectile velocity. Then the dynamical Eqs. (A13), (A9), and (A10) become

$$\frac{du}{d\theta} = \frac{c}{g}u^3\sec^3\theta \tag{A15}$$

$$\frac{dx}{d\theta} = -\frac{u^2}{g}\sec^2\theta \tag{A16}$$

$$\frac{dy}{d\theta} = -\frac{u^2}{g}\sec^2\theta\tan\theta \tag{A17}$$

To simplfy further the form of the dynamical equations another transformation of the independent variable is made by letting

$$\frac{dq}{d\theta} = \sec^2\theta = 1+q^2 \tag{A18}$$

APPENDIX B

VARIATION OF THE DRAG FUNCTIONS. As given by Eq. (54) in the previous paper (ref. 2) the variation of the range drag function δG_x is

$$\delta G_x = \left[- \frac{I_{12}}{q_o - q_1} \frac{2\delta v_o}{v_o} + - \frac{H_{q=q_1}}{1-H_{q=q_1}} \frac{I_{11}}{q_o - q_1} \right] \frac{\delta q_1}{q_o - q_1} + \left[\frac{2q_o I_{12}}{1+q_o^2} + \frac{I_{11}}{q_o - q_1} + \frac{c}{g} \frac{v_o^2}{1+q_o^2} \frac{dp_o I_{02}}{dq_o} \right] \frac{\delta q_o}{q_o - q_1} \tag{B1}$$

It is noted that the difference of the end slope is not zero, i.e., $q_o - q_1 \neq 0$. Therefore, the problem does not become singular. We have expressed the variation δG_x in terms of the variational parameters.

As given by Eq. (77) in the previous paper (ref. 2) the variation of the elevation drag function δG_y is

$$\delta G_y = \left[- \frac{J_{12}}{q_o - q_1} \right] \frac{2\delta v_o}{v_o} + \left[- \frac{q_1 H_{q=q_1}}{1-H_{q=q_1}} - \frac{J_{11}}{q_o - q_1} \right] \frac{\delta q_1}{q_o - q_1} + \left[\frac{2q_o J_{12}}{1+q_o^2} \frac{J_{11}}{q_o - q_1} \frac{c}{g} \frac{v_o^2}{1+q_o^2} \frac{dp_o J_{02}}{dp_o} \right] \frac{\delta q_o}{q_o - q_1} \tag{B2}$$

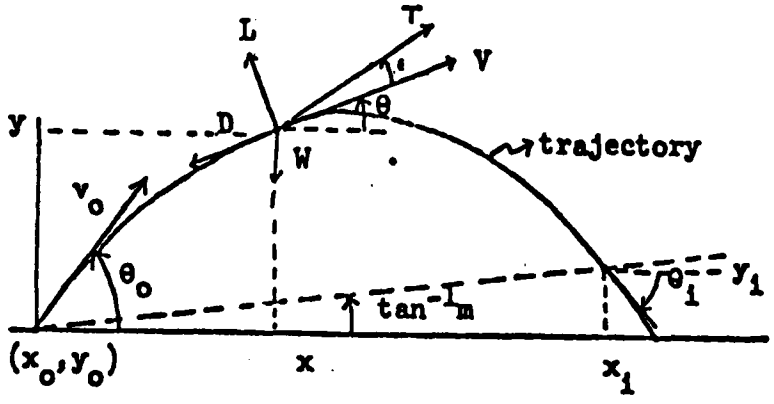

Fig. 1. Forces, Slopes, and Initial and Final Parameters for a Trajectory

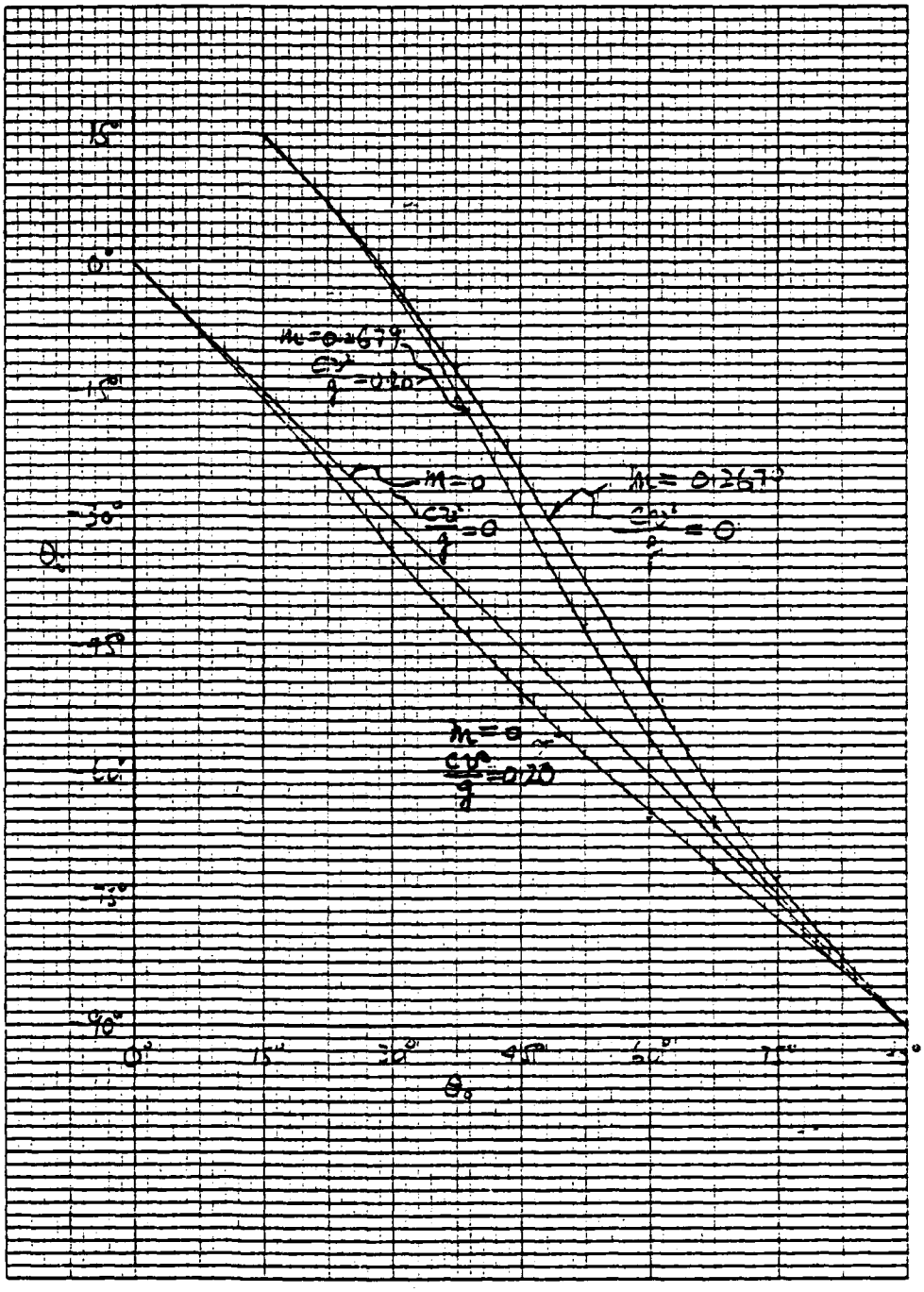

Figure 2. Impact Angle vs. Launch Angle for Different Target Slopes and Damping Coefficients.

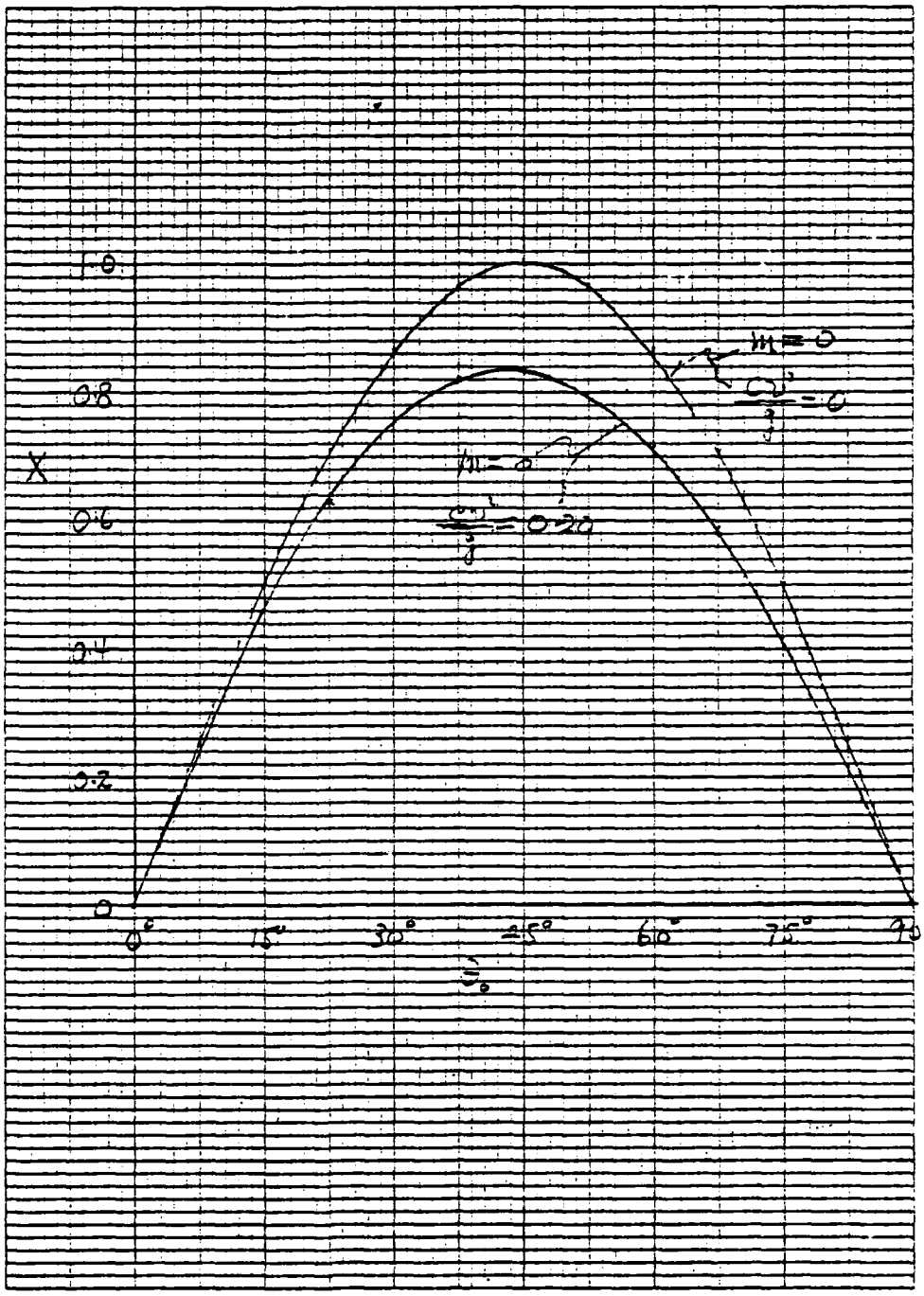

Figure 3. Nondimensional Range vs. Launch Angle for Horizontal Target and Different Damping Coefficients.

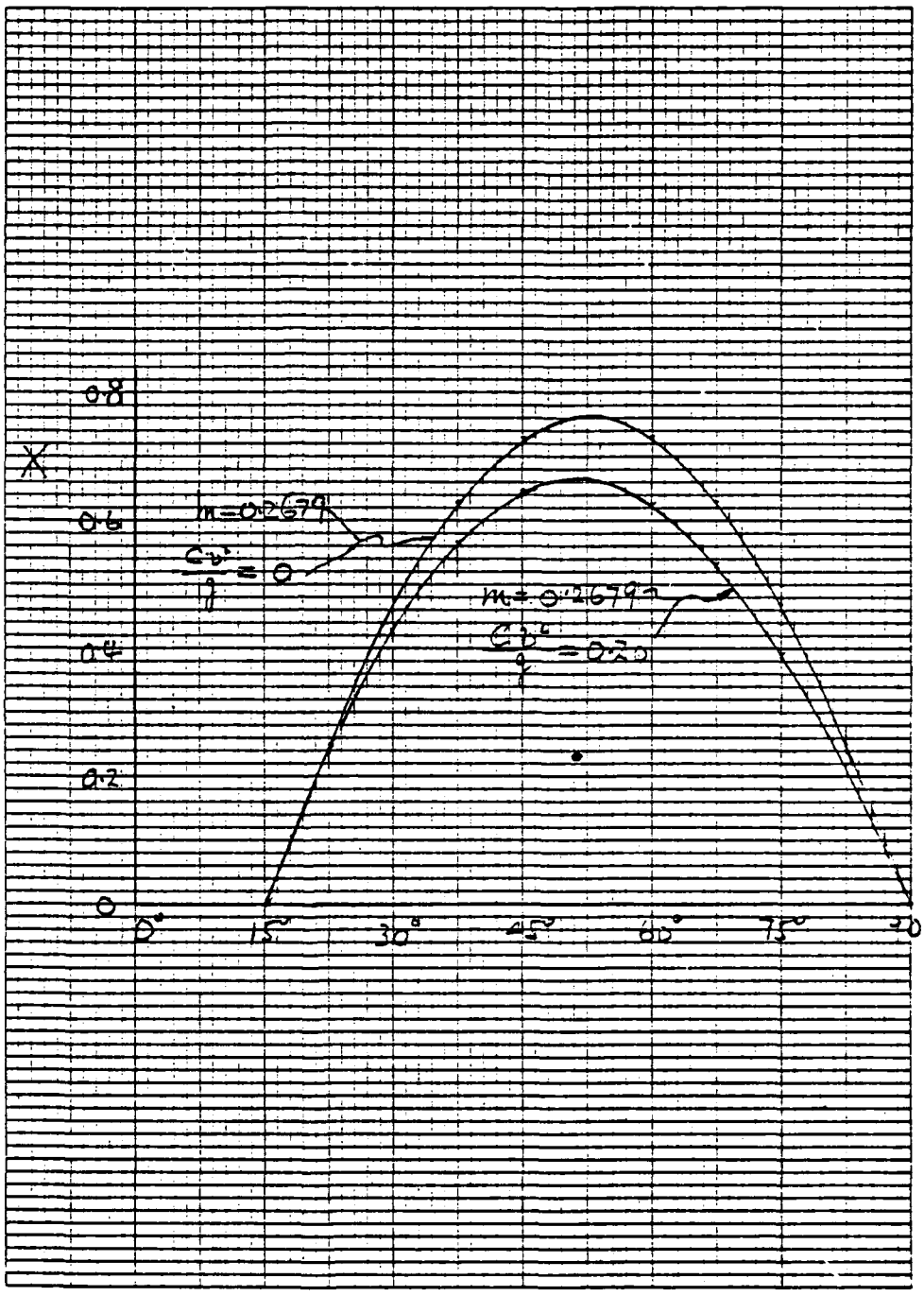

Figure 4. Nondimensional Range vs. Launch Angle for Upgrade Targets and Different Damping Coefficients.

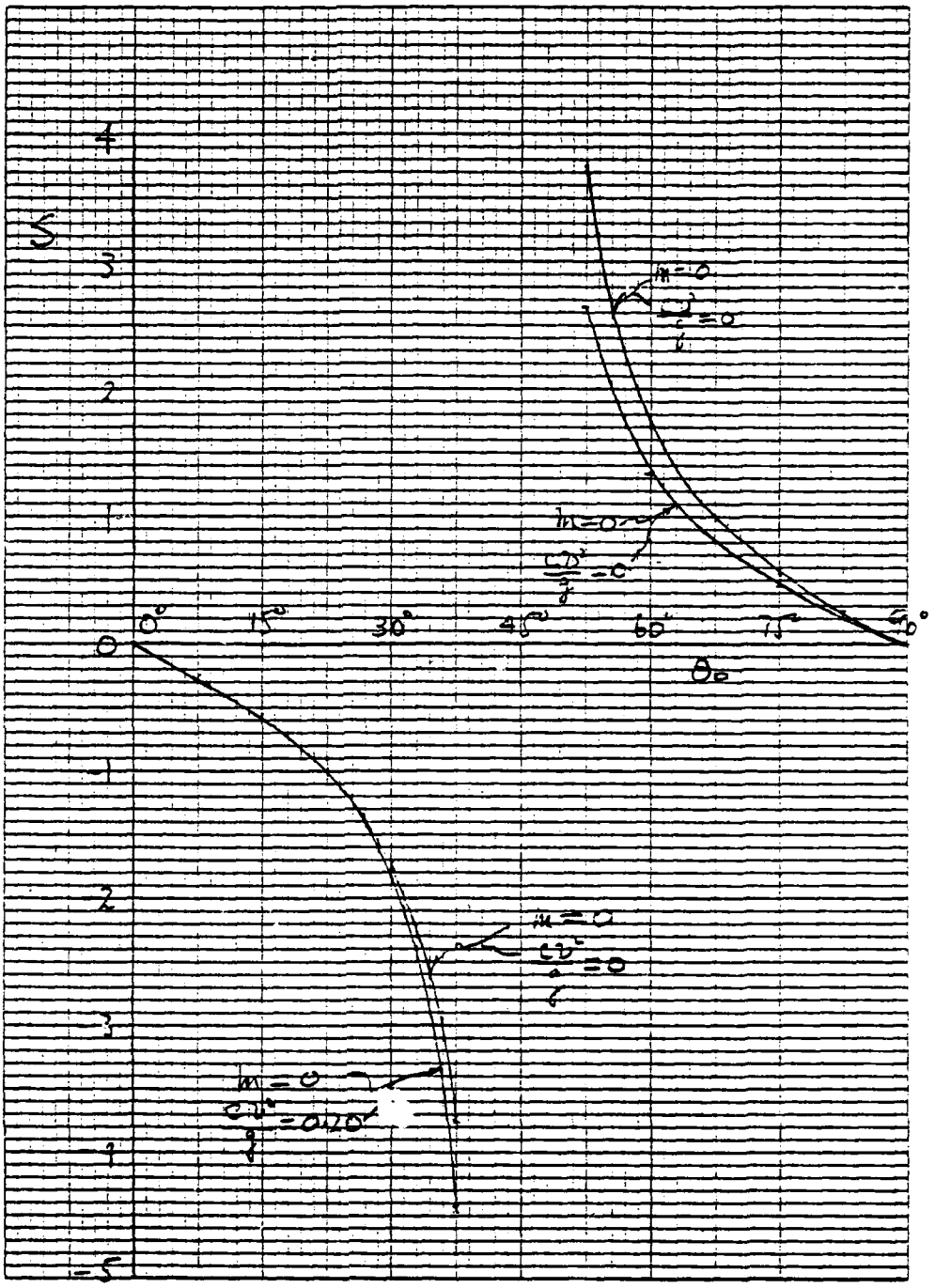

Figure 5. Sensitivity Coefficient vs. Launch Angle for Horizontal Target and Different Damping Coefficients.

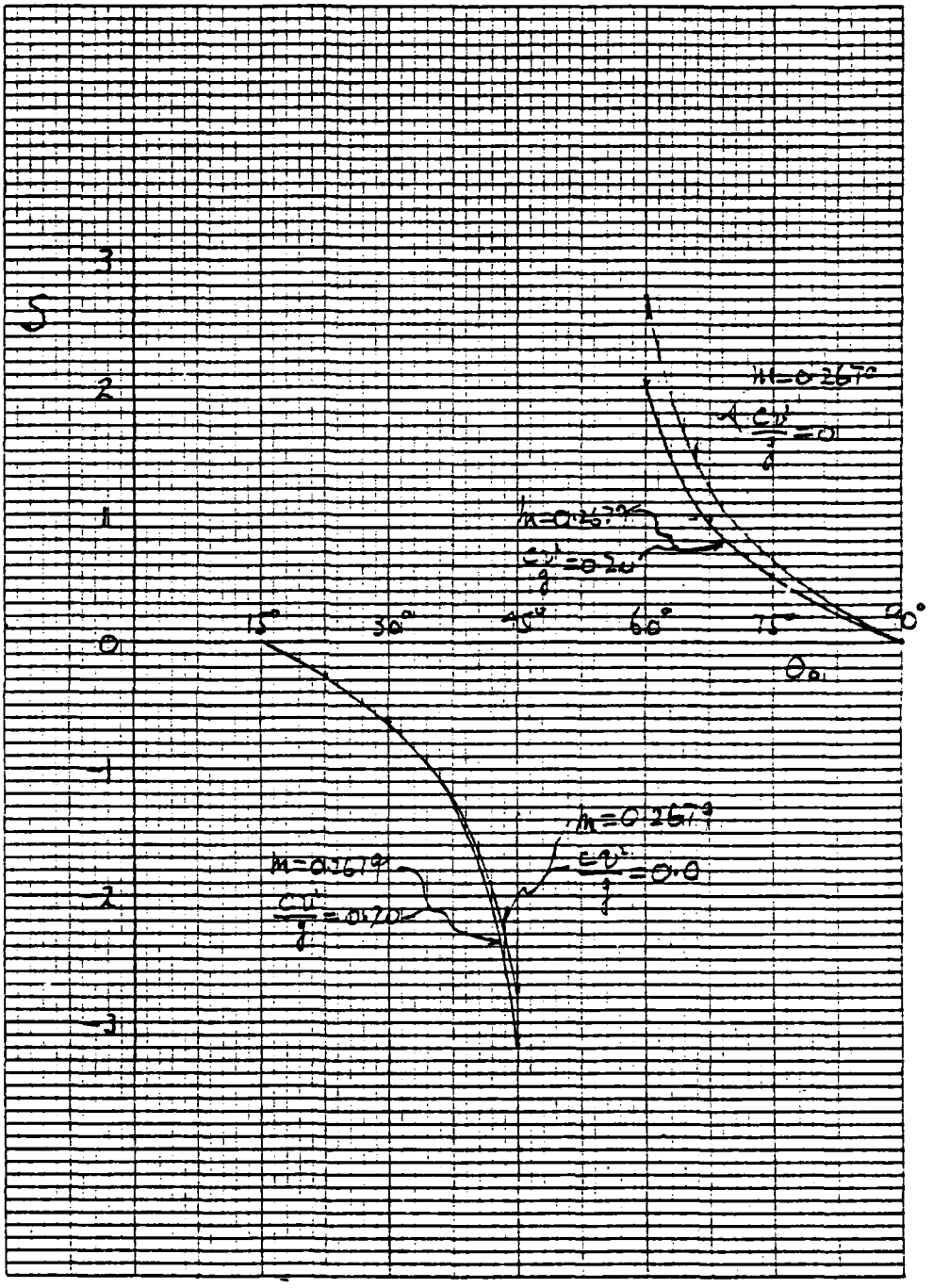

Figure 6. Sensitivity Coefficient vs. Launch Angle for Upgrade Targets and Different Damping Coefficients.

DESIGN OF SUPERCRITICAL SWEPT WINGS

Paul Garabedian and Geoffrey McFadden
Courant Institute of Mathematical Sciences, New York University
New York, N. Y. 10012

ABSTRACT. Two-dimensional codes for the design and analysis of transonic airfoils are now in common use. Codes have been developed to analyze the transonic flow past a swept wing in three-dimensional space. In this paper a computational method to design supercritical swept wings will be discussed that is based on a well posed free boundary problem for the velocity potential.

1. THE ROLE OF COMPUTATIONAL FLUID DYNAMICS. There has been a great deal of interest lately in problems of transonic aerodynamics related to shockless airfoils and supercritical wings. Computational fluid dynamics has turned out to be a very successful tool in this field. For two-dimensional flow, computer codes to design and analyze supercritical wing sections are now in common use. But for swept wings in three-dimensional flow many mathematically challenging problems remain open. It is to some of these that we shall address ourselves here.

The transonic flow past a swept wing can be described realistically by a velocity potential ϕ. Weak shock waves are represented by adding to the partial differential equation for ϕ artificial viscosity terms that may or may not be in conservation form. Iterative schemes to solve corresponding sets of difference equations numerically are obtained by adding further terms that involve differentiation with respect to an artificial time parameter t. This leads to a partial differential equation for ϕ of the form

$$\sum \left(c^2 \delta_{jk} - \phi_{x_j}\phi_{x_k}\right)\phi_{x_j x_k} = h \min\left(1-M^2, 0\right) \sum |\phi_{x_j}| \phi_{x_k} \phi_{x_j x_j x_k} + \sum \alpha_j \phi_{x_j t} + \beta \phi_t ,$$

where c is the speed of sound determined by Bernoulli's law, $M = |\nabla\phi|/c$ is the Mach number, h is a small positive number related to mesh size, and α_j and β are coefficients specifying the iterative scheme. The normal derivative of ϕ is put equal to zero on the surface of the wing, and the vortex sheet behind is modeled by a linearized boundary condition.

The boundary value problem we have described has been used to develop codes for the calculation of transonic flow past an oblique wing or a swept wing [3,6]. For the implementation, parabolic coordinates x and y are introduced in planes perpendicular to the wing. At each span station z this is accomplished so as to achieve good resolution at the leading and trailing edges. Through a substitution of the form

$$Y = y - f(x,z)$$

a further transformation is made to a rectangular domain

$$-1 \leq X \leq 1, \quad 0 \leq Y \leq 1, \quad 0 \leq Z \leq 1$$

that is convenient for the computation. Thus the surface of the wing $y = f(x,z)$ is mapped onto a region of the plane $Y = 0$, with X varying primarily in the direction of the flow and Z indicating the span station. This formulation of the problem is well adapted to questions of design that require changes in the function f.

Meaningful runs of the swept wing code can be made on a mesh of 96×12×16 points using only 100 time cycles. Such calculations are relatively easy on a computer of the capacity of the CDC 6600. However, the lift is slow to converge because in three dimensions it is hard to correlate circulation with an asymptotic expansion for ϕ at infinity. Thus it becomes desirable to seek a version of the code that would run efficiently on modern parallel computers like the STAR or CRAY. The most successful attack on this problem so far has been through vectorization of the calculation of the coefficients in the partial differential equation for ϕ, which is where the bulk of the computing is done [8]. This can be implemented over either lines or planes in the space of the coordinates X, Y and Z.

The drag has not been calculated very accurately in three dimensions, especially when conservation form of the equation for the velocity potential ϕ has been dropped in order to simulate boundary layer effects. We have under consideration an improved algorithm to compute the wave drag using equations for the conservation of momentum. Moreover, examination of computed pressure distributions does seem to give a physically significant measure of the performance of supercritical wings that can be relied on in practice.

A more ambitious undertaking is the design of swept wings with prescribed pressure distributions. At transonic speeds it is onerous to ask for shockless flow in three dimensions [9]. However, we shall discuss in the next section a method of artificial viscosity that does seem to offer some prospect of improving the design and reducing the drag of swept wings in various three-dimensional configurations. The scheme provides an alternative to outright minimization of the drag [5]. It is based on a free boundary problem in which the speed is prescribed continuously over a portion of the wing. The free boundary problem seems to be well posed provided that shocks satisfying a suitable entropy inequality are allowed to appear in the interior of the flow.

2. A TRANSONIC FREE BOUNDARY PROBLEM. Two-dimensional codes have been written to design an airfoil with a given pressure distribution. For transonic flow we have at our disposal two possible approaches to this problem. One of them is to introduce complex characteristic coordinates in the hodograph plane so as to obtain a shockless airfoil whose pressure distribution only deviates from the prescribed data in the supersonic zone [2]. The other is to add artificial viscosity in the physical plane so that shocks are smeared out while the data are fitted perfectly over the whole profile [7].

The hodograph method has the advantage that it determines supercritical wing sections with low levels of wave drag automatically. The method of artificial viscosity is relatively easy to implement as a robust code, but it allows shocks with significant wave drag to remain inside the flow even when the pressure

at the profile is smooth. To apply the design codes one must exercise some skill in choosing the pressure distribution that is assigned. The theory of shockless airfoils can be helpful in making an initial choice (cf. Figs. 1 and 2). To eliminate shocks it is desirable to use a pressure distribution that is peaky near the leading edge of the wing as well as smooth at the rear of the supersonic zone.

Because the hodograph method fails in three-dimensional space, we rely on artificial viscosity to develop a code for the design of supercritical swept wings. Our work is based on the references cited earlier [3,6,8].

To avoid questions of closure and other complications with the geometry, we formulate a free boundary problem in which the pressure, or, rather, the speed, is assigned over only a limited part of the surface of the wing. Let $y = f(x,z)$ be the equation of that surface, let ϕ stand for the velocity potential of a corresponding flow with given speed at infinity, let $q = |\nabla\phi|$, let $y = f_0(x,z)$ represent a surface that is supposed to lie inside the eventual wing, and let $q_0(x,z)$ specify a prescribed distribution of speed. For the design problem we ask that $f(x,z) \geq f_0(x,z)$ everywhere, assuming that $y > f(x,z)$ defines the region of flow. In addition, we ask that the free boundary condition

$$Q(f,f_x,f_z) = q_0(x,z)^2 - q(x,z)^2 = 0$$

be fulfilled wherever the strict form $f(x,z) > f_0(x,z)$ of the inequality holds. It will be seen that these requirements define a wing on which the prescribed values q_0 of the speed are taken on only at points where they are sufficiently big. The result is a patch of wing surface on which unwanted shocks may be smoothed out.

The free boundary problem that we have described can be solved numerically by an iterative scheme generalizing one that has been applied successfully to analogous questions arising in computational magnetohydrodynamics [1]. Let both ϕ and f depend on the artificial time parameter t, and suppose that ϕ satisfies the partial differential equation formulated above for transonic flow. We allow the surface $y = f(x,z,t)$ to vary with t according to the following rules. For all t we require that $f \geq f_0$. However, when $f > f_0$ we put

$$a_1\left(\phi_x f_{xt} + \phi_z f_{zt}\right) + f_t = Q + a_2\left(Q_{f_x} Q_x + Q_{f_z} Q_z\right) ,$$

with the coefficients a_1 chosen to make the scheme converge. This partial differential equation for f is approximated by finite difference equations determining the free surface in the limit as $t \to \infty$. The extra terms on the right are suggested by the Lax-Wendroff scheme, whereas those on the left are motivated by linearized flow theory (cf. [4]). To solve the difference equations for f we march in a direction opposed to the flow.

A preliminary version of a code that implements our design concept has been written. Computational experience with convergence of the method is encouraging. More specifically, the addition of the term in f_{xt} facilitates convergence

when the flow is transonic. Our success is perhaps surprising in view of the fact that flux is stationary at sonic speed. The rate of convergence for the new design code becomes even faster than that for older swept wing codes because the difficulty with slow convergence of the lift can be circumvented by the simple device of fixing the section lift coefficient at each span station while varying the corresponding angles of attack and twist.

We have yet to develop the code into an engineering tool of practical significance. It can be applied, in a fashion suggested by wind tunnel techniques, to add material to an underlying wing structure so as to obtain supercritical flow with only weak shocks of negligible wave drag. As a first example we have attempted to suppress the shocks at the root section of a swept wing that was constructed from shockless airfoils. Figs. 3 and 4 show the pressure distribution on the upper and lower surfaces of the wing before and after application of the design code. The reduction in drag is disappointing, but this may be attributed to poor accuracy. Engine nacelles or a possible fuselage can be modeled in the computation by imposing a linearized boundary condition at the wall.

ACKNOWLEDGEMENT. This work was supported by NASA Grants NGR-33-015-201 and NSG-1579.

REFERENCES

1. F. Bauer, O. Betancourt and P. Garabedian, A Computational Method in Plasma Physics, Springer Series in Computational Physics, Springer-Verlag, New York, 1978.

2. F. Bauer, P. Garabedian and D. Korn, Supercritical Wing Sections III, Lecture Notes in Economics and Mathematical Systems, vol. 150, Springer-Verlag, New York, 1977.

3. F. Bauer, P. Garabedian, D. Korn and A. Jameson, Supercritical Wing Sections II, Lecture Notes in Economics and Mathematical Systems, vol. 108, Springer-Verlag, New York, 1975.

4. W. Davis, "Techniques for developing design tools from the analysis methods of computational aerodynamics," AIAA Paper 79-1529, 1979.

5. R. Hicks and P. Henne, "Wing design by numerical optimization," AIAA Paper 77-1247, 1977.

6. A. Jameson and D. Caughey, "Numerical calculation of the transonic flow past a swept wing," ERDA Research and Development Report COO-3077-140, Courant Institute of Mathematical Sciences, New York University, 1977.

7. G. McFadden, "An artificial viscosity method for the design of supercritical airfoils," DOE Research and Development Report COO-3077-158, Courant Institute of Mathematical Sciences, New York University, 1979.

8. R. Smith, J. Pitts and J. Lambiotte, "A vectorization of the Jameson-Caughey NYU transonic swept-wing computer program FLO-22-VI for the STAR-100 computer," NASA TM-78665, 1978.

9. N. Yu, "Efficient transonic shock-free wing redesign procedure using a fictitious gas method," AIAA Journal, vol. 18 (1980), pp. 143-148.

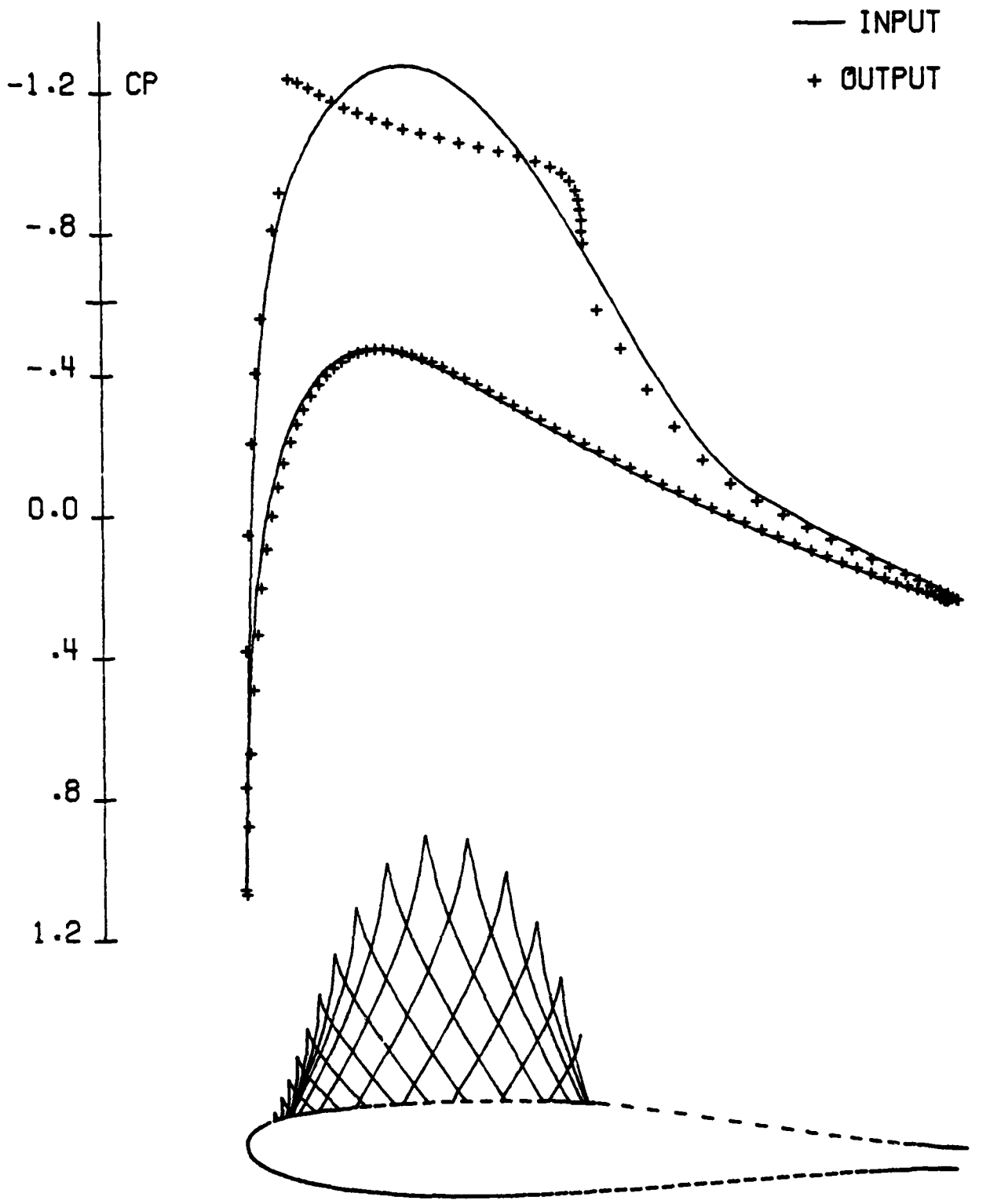

Fig. 1. Modification of the NACA 0012 by the hodograph method.

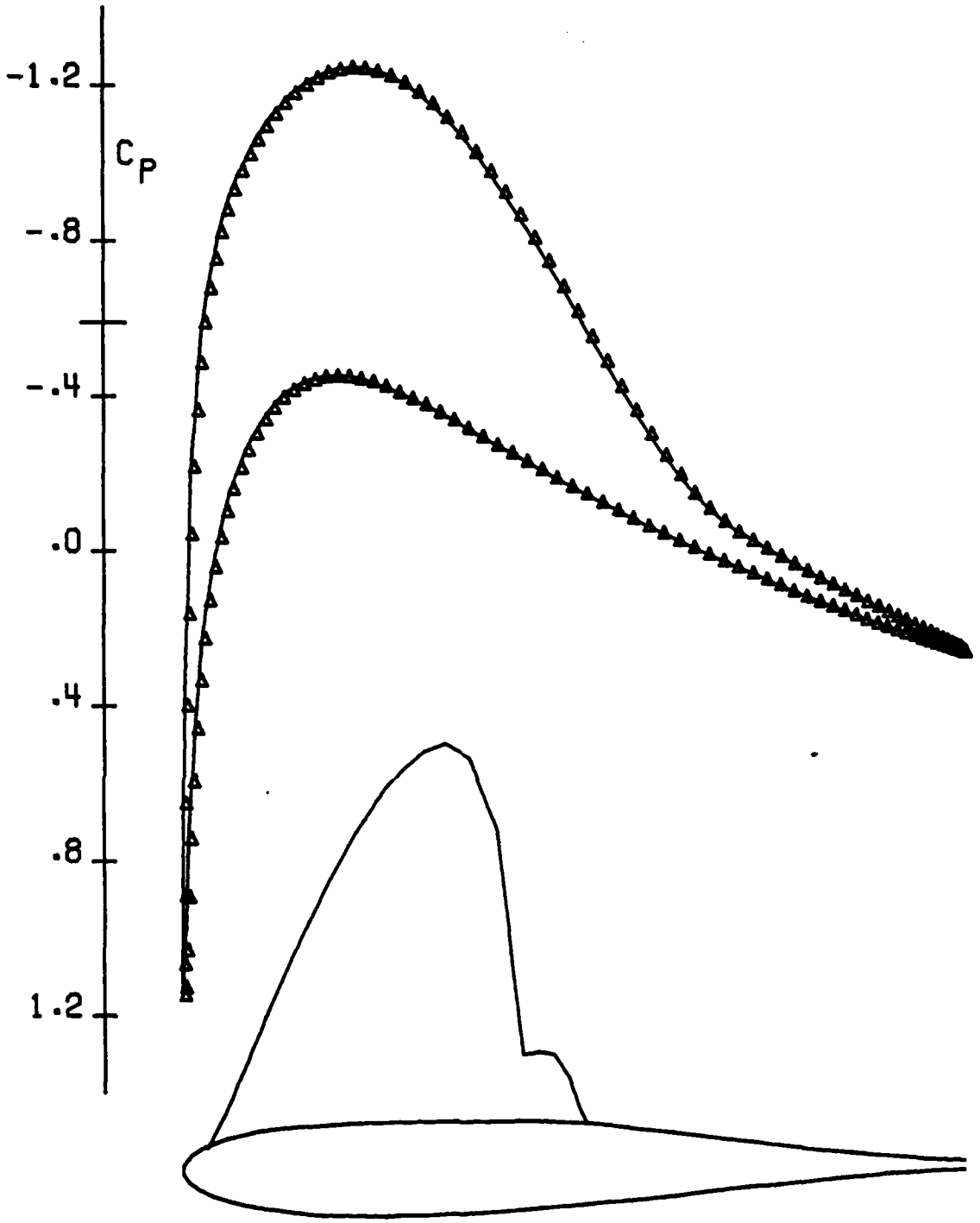

VISCOUS DESIGN M*N=160*30 NCY= 159 EPS1=0.000

— ANALYSIS M=.751 ALP= 2.00 CL= .434 CD=.0038

Δ INPUT CP T/C= .124 DQ= .85E-03 DPHI= .76E-04

Fig. 2. Modification of the NACA 0012 using artificial viscosity.

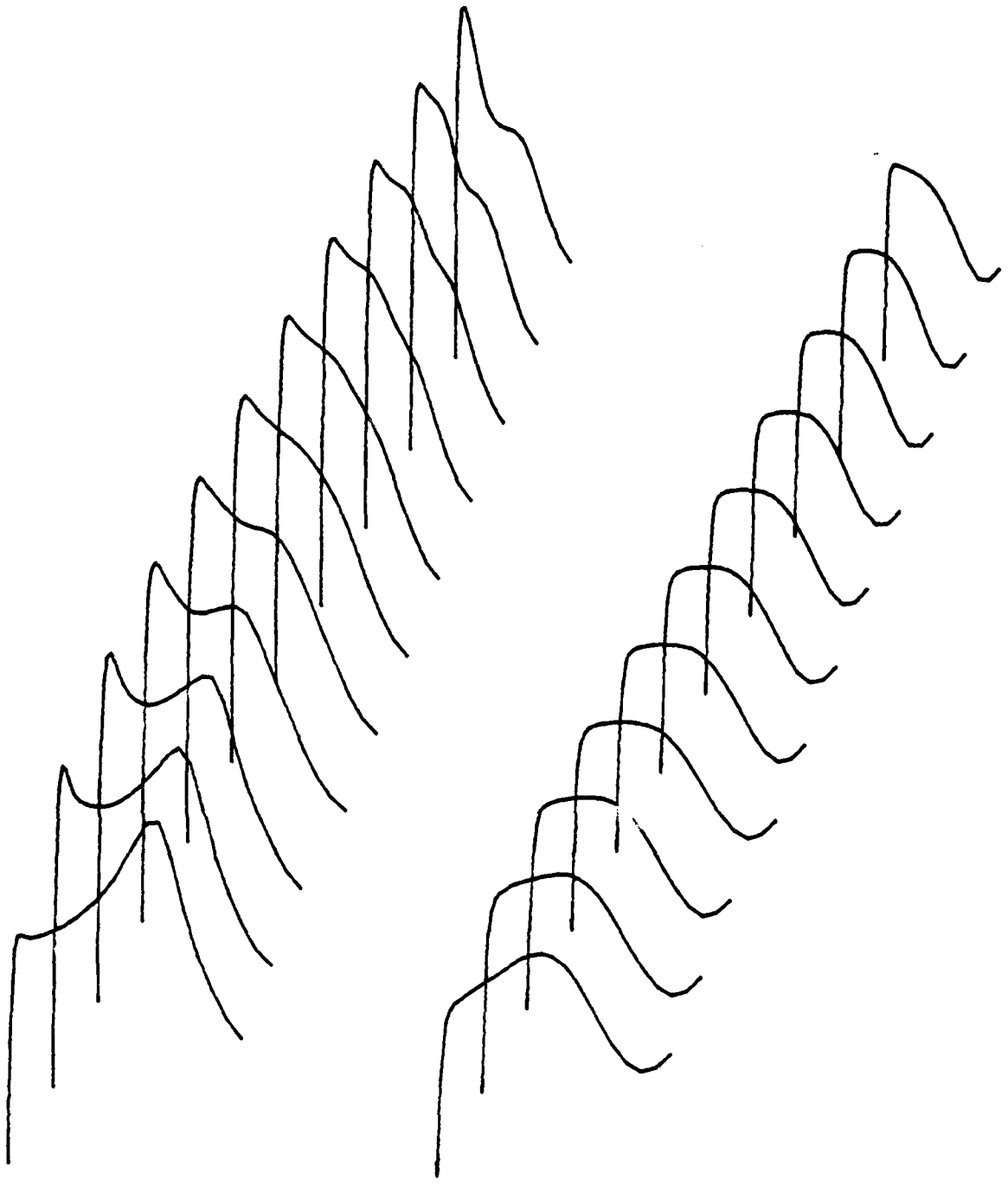

Fig. 3. Pressure on a swept wing showing a shock near the wall.

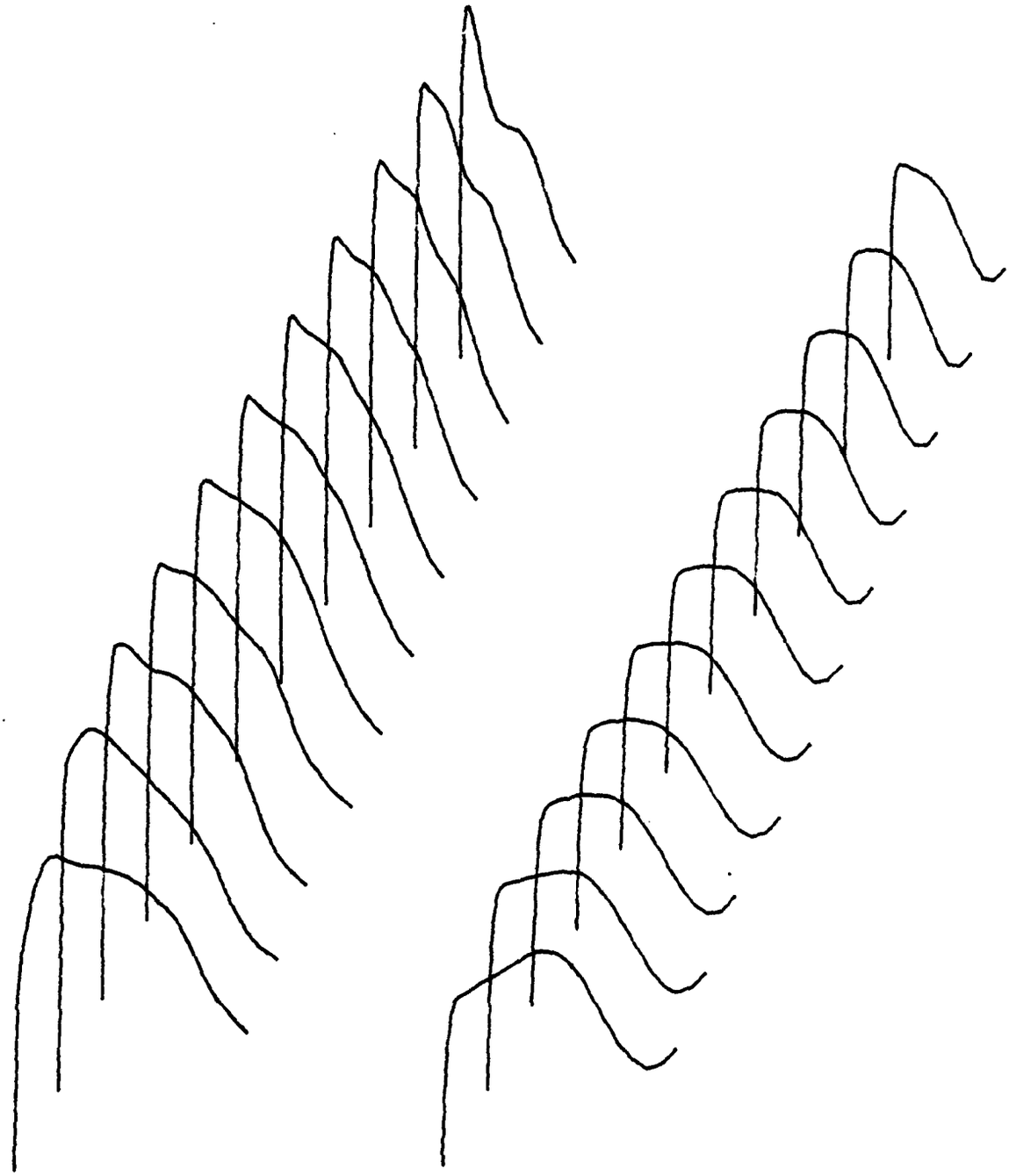

Fig. 4. Smoothed pressure on the swept wing after design.

LIST OF REGISTERED ATTENDEES

Essam H. Atta
Ames Research Center
Moffett Field, CA 94035

J. M. Ball
University of California-Berkeley
Berkeley, CA 94720

Richard Beam
Ames Research Center
Moffett Field, CA 94035

Paul T. Boggs
US Army Research Office
Research Triangle Park, NC 27709

James R. Brasseur
Ames Research Center
Moffett Field, CA 94035

Frank Caradonna
Ames Research Center
Moffett Field, CA 94035

Aivars Celmins
Ballistic Research Laboratory
Aberdeen Proving Ground, MD 21005

Jagdish Chandra
US Army Research Office
Research Triangle Park, NC 27709

Peter C. T. Chen
Watervliet Arsenal
Watervliet, NY 12189

Leslie Chow
Ames Research Center
Moffett Field, CA 94035

Michael Crandell
MRC, University of Wisconsin
Madison, WI 53706

William R. Van Dalsem
Ames Research Center
Moffett Field, CA 94035

Richard E. Dickson
Army Missile Command
Huntsville, AL 35803

F. Carroll Dougherty
Ames Research Center
Moffett Field, CA 94035

Paul R. Garabedian
Courant Institute, N.Y.U.
New York, NY 10012

James Glimm
Rockefeller University
New York, NY 10021

Gene H. Golub
Stanford University
Stanford, CA 94305

Peter M. Goorjian
Ames Research Center
Moffett Field, CA 94035

Robert M. Hackett
US Army Missile Command
Redstone Arsenal, AL 35809

Kristin A. Hessenius
Ames Research Center
Moffett Field, CA 94035

Raymond M. Hicks
Ames Research Center
Moffett Field, CA 94035

Satoru I. Hirayama
Ames Research Center
Moffett Field, CA 94035

Morton A. Hirschberg
Ballistic Research Laboratory
Aberdeen Proving Ground, MD 21005

Dewey H. Hodges
Ames Research Center
Moffett Field, CA 94035

Terry L. Holst
Ames Research Center
Moffett Field, CA 94035

C. C. Horstman
Ames Research Center
Moffett Field, CA 94035

Ching-Mao Hung
Ames Research Center
Moffett Field, CA 94035

Mamorie Inouye
Ames Research Cehter
Moffett Field, CA 94035

James A. Jeske
Ames Research Center
Moffett Field, CA 94035

Henry E. Jones
Ames Research Center
Moffett Field, CA 94035

Lyndell S. King
Ames Research Center
Moffett Field, CA 94035

Clarence W. Kitchens, Jr.
Ballistic Research Laboratory
Aberdeen Proving Ground, MD 2100

Allen L. Kuhl
R&D Associates
Marina Del Ray, CA 90291

J. O. Lambert
Ames Research Center
Moffett Field, CA 94035

Harold Law
AVRADCOM, HQ
St. Louis, MO 63166

Anthony Leonard
Ames Research Center
Moffett Field, CA 94035

R. E. Lottero
Ballistic Research Laboratory
Aberdeen Proving Ground, MD 2100

Robert MacCormack
Ames Research Center
Moffett Field, CA 94035

Thomas L. Mann
Ballistic Research Laboratory
Aberdeen Proving Ground, MD 2100

J. E. Marsden
University of California-Berkeley
Berkeley, CA 94720

W. James McCrosky
Ames Research Center
Moffett Field, CA 94035

Anmeel B. Mehta
Ames Research Center
Moffett Field, CA 94035

Joel P. Mendoza
Ames Research Center
Moffett Field, CA 94035

J. D. Murphy
Ames Research Center
Moffett Field, CA 94035

John A. Nohel
MRC, University of Wisconsin
Madison, WI 53706

Larry Olson
Ames Research Center
Moffett Field, CA 94035

Seymour V. Parter
University of Wisconsin
Madison, WI 53706

Richard H. Petersen
Ames Research Center
Moffett Field, CA 94035

Victor L. Peterson
Ames Research Center
Moffett Field, CA 94035

George Reddien
Southern Methodist University
Dallas, TX 75275

Walter A. Reinhardt
Ames Research Center
Moffett Field, CA 94035

J. Barkley Rosser
MRC, University of Wisconsin
Madison, WI 53706

Vernon J. Rossow
Ames Research Center
Moffett Field, CA 94035

James A. Schmitt
Ballistic Research Laboratory
Aberdeen Proving Ground, MD 21005

Gregory R. Shubin
Naval Surface Weapons Center
Silver Springs, MD 20910

Irving C. Statler
Ames Research Center
Moffett Field, CA 94035

Michael Steuerwalt
Los Alamos Scientific Laboratory
Los Alamos, NM 87545

Lloyd N. Trefethen
Stanford University
Stanford, CA 94305

John R. Viegas
Ames Research Center
Moffett Field, CA 94035

Marcel Vinokur
Ames Research Center
Moffett Field, CA 94035

Robert F. Warming
Ames Research Center
Moffett Field, CA 94035

Chia Ping Wang
US Army Natick R&D Command
Natick, MA 01760

C. Glenvil Whitacre
Chemical Systems Laboratory
Aberdeen Proving Ground, MD 21010

Carroll O. Wilde
U. S. Military Academy
West Point, NY 10994

James T. Wong
Ames Research Center
Moffett Field, CA 94035

Julian J. Wu
Watervliet Arsenal
Watervliet, NY 12189

Helen M. C. Yee
Ames Research Center
Moffett Field, CA 94035

Yung H. Yu
Ames Research Center
Moffett Field, CA 94035

AD-A089 089 ARMY MATHEMATICS STEERING COMMITTEE F/G 9/2
PROCEEDINGS OF THE 1980 ARMY NUMERICAL ANALYSIS AND COMPUTERS C--ETC(U)
AUG 80

UNCLASSIFIED ARO-80-3 NL

6 of 6

END
DATE FILMED
10-80
DTIC

UN

SECURITY CLASSIFICATI

REPO

1. REPORT NUMBER
ARO Report 80-

4. TITLE (and Subtitle)
Proceedings of
and Computers

7. AUTHOR(s)

9. PERFORMING ORGANI.

11. CONTROLLING OFFIC
Army Mathematic
the Chief of Re

14. MONITORING AGENCY
Army Research C
ATTN: DRXRO-MA
P. O. Box 12211
Research Triang

DISTRIBUTION STATE
Approved for pu
report are not
unless so desig

17. DISTRIBUTION STATE

18. SUPPLEMENTARY NO
This is a techn
Computers Confe
engineering as

19. KEY WORDS (Continue
fluid discontir
transonic roto
discontinuity
computation fo
predictor-corr
Fourier transf
approximation
root searching
Schwarz-Christ
Shoenberg appr
full potential
bifurcation br
iterative sche
Navier-Stokes

DD FORM 1 JAN 73 1473

UNCLASSIFIED

SECURITY CLASSIFICATION OF THIS PAGE (When Data Entered)

REPORT DOCUMENTATION PAGE	READ INSTRUCTIONS BEFORE COMPLETING FORM
1. REPORT NUMBER: ARO Report 80-3	2. GOVT ACCESSION NO.: AD-A089089
3. RECIPIENT'S CATALOG NUMBER	
4. TITLE (and Subtitle): Proceedings of the 1980 Army Numerical Analysis and Computers Conference,	5. TYPE OF REPORT & PERIOD COVERED: Interim technical report
	6. PERFORMING ORG. REPORT NUMBER
7. AUTHOR(s)	8. CONTRACT OR GRANT NUMBER(s)
9. PERFORMING ORGANIZATION NAME AND ADDRESS	10. PROGRAM ELEMENT, PROJECT, TASK AREA & WORK UNIT NUMBERS
11. CONTROLLING OFFICE NAME AND ADDRESS: Army Mathematics Steering Committee on behalf of the Chief of Research, Development and Acquisition	12. REPORT DATE: August 1980
	13. NUMBER OF PAGES: 480
14. MONITORING AGENCY NAME & ADDRESS (if different from Controlling Office): Army Research Office, ATTN: DRXRO-MA, P. O. Box 12211, Research Triangle Park, NC 27709	15. SECURITY CLASS. (of this report)
	15a. DECLASSIFICATION/DOWNGRADING SCHEDULE

16. DISTRIBUTION STATEMENT (of this Report)

Approved for public release; distribution unlimited. The findings in this report are not to be construed as an official Department of the Army position, unless so designated by other authorized documents.

17. DISTRIBUTION STATEMENT (of the abstract entered in Block 20, if different from Report)

18. SUPPLEMENTARY NOTES

This is a technical report resulting from the 1979 Army Numerical Analysis and Computers Conference. It contains papers on computer aided designs and engineering as well as papers on numerical analysis.

19. KEY WORDS (Continue on reverse side if necessary and identify by block number)

fluid discontinuities
transonic rotor flows
discontinuity tracking methods
computation for shocks
predictor-corrector methods
Fourier transform evaluation
approximation methods
root searching algorithm
Schwarz-Christoffel transformations
Shoenberg approximations
full potential equation
bifurcation branches
iterative schemes
Navier-Stokes equations
motions of a flat plate
software
interior ballistic codes
finite element analysis
breech ring analysis
over-strained tubes
vector computers
queueing models
data bases
from large to small computers
variational methods
computational schemes
suppression of shocks on swept wings

DD FORM 1 JAN 73 1473 EDITION OF 1 NOV 65 IS OBSOLETE

UNCLASSIFIED

SECURITY CLASSIFICATION OF THIS PAGE (When Data Entered)